Hetero-junction and Nanomaterial Systems for Metal Oxide Semiconductor based Gas Sensing

Anupriya J. T. Naik

This thesis is submitted in partial fulfilment of the requirement for the Degree of Doctor of Engineering
(Eng.D)

Department of Chemistry
Faculty of Mathematical and Physical Sciences
UCL

2015

I, Anupriya Jai Tilak Naik, confirm that the work presented in this thesis is my own. Where information has been derived from other sources, I confirm that this has been indicated in the thesis.

Abstract

Investigations into a number of hetero-junction and nanoceramic materials systems for metal oxide semiconductor (MOS) gas sensing for potential environmental and bio-sensing applications are presented.

The hetero-junction study encompasses investigations into various composite n-n hetero-contact systems such as WO_3-ZnO and SnO_2-ZnO and a p-n hetero-contact system, specifically CTO (Chromium Titanium Oxide) - ZnO. The facile fabrication of various arrays of hetero-junction MOS gas sensor devices has been demonstrated. A simple change in the compositional contribution of an individual metal oxide within a composite, exhibits the ability to tune the composite's responsivity and selectivity. The hetero-junction systems were characterized by various techniques including Scanning Electron Microscopy (SEM), Raman spectroscopy, X-Ray Diffraction (XRD) and X-Ray Photoelectron Spectroscopy (XPS) and the influence of the physical and chemical properties of these materials towards the associated gas sensing properties, deduced. Further, the influence of fundamental properties of junctions such as contact potential and packing structure, towards the sensing properties, are also discussed.

The nanomaterials study encompasses investigation into ZnO semiconducting oxides fabricated by various emerging fabrication technologies including Continuous Hydrothermal Flow Synthesis (CHFS) and other relatively high temperature routes. The chemical and physical properties of the nanoceramics have been investigated by various techniques including Transmission Electron Microscopy (TEM), Scanning Electron Microscopy (SEM) and Brunauer Emmett Teller (BET) surface area measurements. The investigation demonstrates emerging techniques for the production of nanomaterials, which can be successfully used in MOS gas sensing for the desired applications. Further, the study shows that the behaviour of the nanomaterials is complex and material surface area is not the only deterministic factor of enhanced responsivities, but microstructural factors such as morphology and particle size, as well as heat-treatment conditions are all influential over the overall sensing properties.

This thesis presents an overview of emerging material systems for MOS gas sensing applications.

Acknowledgements

I would like to take this opportunity to sincerely thank my supervisors Prof. Ivan P. Parkin and Dr. Russell Binions for giving me the chance to undertake this project, and for the support they have given to me to experiment and steer the research in areas of my interest, without which this thesis would not have been possible. I would also like to express my heartfelt gratitude to them for all their help and guidance throughout my time at UCL, both during my undergraduate and postgraduate years, and for all the opportunities that they have given to me.

I would also like to thank the EPSRC, the Molecular Modelling and Materials Science Doctoral Training Centre (M^{3}S DTC) and Silicon Labs for their support in funding this research; without their support, this project would not have been possible.

My many thanks to members of the academic staff, particularly Mr. Martin Vickers, Dr. Steve Firth, Dr. Robert Palgrave and Prof. Jawwad Darr; the technical and support staff, in particular Mr. Len Parrish, Mr. Charles Willoughby, Mr. Joe Nolan, Dr. Jorg Sassmannshausen, Mr. Dave Ladd, Mr. Tony Field, Mr. Tom Bridges, and Mr. Tony Bernard and staff at the BOC group at UCL, particularly Dr. Geoffrey Kirby and Mr. James Britz, for all their help and support, which saw this project through till the end, and without whom, this research could not have been accomplished. I would also like to thank Dr. Sanjayan Sathasivam, Dr. Robert Gruar, Dr. Chris Tighe, Dr. Kristin Poduska and Miss Jessica Ellis for their help in the completion of various aspects of this project.

I would like to express my profound gratitude to Dr. Ayodele Afonja and Dr. Leon Cavanagh for sharing their expertise and training me in the UCL gas sensor lab (G15) and for their guidance throughout various stages of the project.

In particular, I would like to say thank you to my lab partner Miss Emma Newton for her friendship and with whom I spent hours of laughing and problem-solving in G15, and who has truly made my time in the lab enjoyable and very memorable.

Special thanks also go to past and current members of the Parkin and/or Binions research groups, in particular Dr. Michael Warwick, Mr. William Peveler, Mr. David Pugh, Miss Paula Tarttelin Hernandez and Mr. Gwyn Evans.

Finally, I take this opportunity to convey my inexpressible gratitude to my parents Maya and Jai Naik, for being my pillars of support and for all their love, perseverance, guidance and direction, and without whom I could never have reached this far.

Contents Page

Abstract **3**

Acknowledgements **4**

Contents Page **5**

List of Figures **10**

List of Tables **24**

List of Figures in Appendix **28**

List of Tables in Appendix **29**

List of Acronyms **30**

Chapter 1 : Introduction **31**

1.1 Gas Sensor Technology 31

1.2 Metal Oxide Semiconductor (MOS) Sensors 34

1.3 Interpretation of Sensor Response Trace/Curve 37

1.4 n-type and p-type Semiconductors 38

1.4.1 Intrinsic Semiconductors 38

1.4.2 Extrinsic Semiconductors: n-type and p-type Semiconductors 38

1.5 Gas Sensing Mechanism in MOS Sensors 41

1.6 Thick-Film vs. Thin-Film Metal Oxide Gas Sensing Materials 43

1.7 Physicals and Chemical Influences on Gas Response 47

1.7.1 Microstructural effects 47

1.7.2 Acidic/Basic nature of metal oxides 50

1.7.3 Morphological effects 51

1.8 Metal Oxides of Interest 51

1.8.1 Zinc Oxide (ZnO) 52

1.8.2 Tin Oxide (SnO_2) 54

1.8.3 Tungsten Oxide (WO_3) 55

1.8.4 Chromium Titanium Oxide (CTO = $Cr_{2-x}Ti_xO_3$) 56

1.9 New Materials in Metal Oxide Gas Sensing 58

1.9.1 Mixed Metal Oxide Gas Sensors 59

1.9.2 Hetero-junctions 62

1.10 Target Analytes of Interest 68
1.10.1 Nitrogen Dioxide (NO_2) (Oxidising Gas) 68
1.10.2 Ethanol (Reducing Gas) 68
1.10.3 NH_3 (Reducing Gas) 69
1.10.4 Acetone (Reducing Gas) 70
1.10.5 CO (Reducing Gas) 71
1.10.6 Toluene (Reducing Gas) 72
1.11 Project Aims 73
1.12 Summary of Thesis 74
Chapter 2 : Materials and Experimental Method 75
2.1 Materials Investigated 75
2.2 Sensor Fabrication 77
2.2.1 Single metal oxide sensor devices 80
2.2.2 Composite metal oxide sensor devices 80
2.3 Sensor Devices and Materials Syntheses 81
2.3.1 Chapter 3: WO_3-ZnO composite system 81
2.3.1.1 Synthesis of $ZnWO_4$ 81
2.3.2 Chapter 4: SnO_2-ZnO composite system 82
2.3.3 Chapter 5: CTO-ZnO composite system 83
2.3.3.1 Synthesis of $Cr_{1.95}Ti_{0.05}O_3$ (CTO) 83
2.3.4 Chapter 6: nanostructured ZnO system 84
2.3.4.1 Synthesis of Nanostructured ZnO Materials via CHFS 85
2.3.4.2 ZnO Ceramic Samples from other high temperature synthetic methods 86
2.4 Material characterisation 87
2.4.1 Scanning Electron Microscopy (SEM) 87
2.4.2 Transmission Electron Microscopy (TEM) 87
2.4.3 X-Ray Diffraction (XRD) 88
2.4.3.1 Bruker D4 Endeavour Powder X-ray Diffractometer (PXRD) 88
2.4.3.2 Bruker Discover D8 Diffractometer with a wide angle Gadds detector 88
2.4.3.3 Bruker D8 Discover D8 diffractometer with Vantec 500 detector 88
2.4.4 Raman Spectroscopy 88
2.4.5 X-Ray Photoelectron Spectroscopy (XPS) 89
2.4.6 Brunauer-Emmett-Teller (BET) surface area measurements 89
2.5 Gas Sensing Characterisation 90
Chapter 3 : WO_3-ZnO based n-n hetero-junction system 99
3.1 Introduction 99

3.2 Results and Analysis 102
3.2.1 Scanning Electron Microscopy (SEM) 102
3.3 XRD (X-Ray Diffraction) 107
3.4 Raman Spectroscopy 110
3.5 X-Ray Photoelectron Spectroscopy (XPS) 113
3.6 Gas Sensing 114
3.6.1 Gas Sensing Properties of $ZnWO_4$ 114
3.6.2 Gas Sensing Properties of WO_3-ZnO hetero-junction system 116
3.6.2.1 Ethanol Sensing 116
3.6.2.2 NO_2 Sensing 124
3.6.3 Further Gas Sensing Studies 131
3.6.3.1 CO Sensing 131
3.6.3.2 NH_3 Sensing 133
3.6.3.3 Acetone Sensing 134
3.7 Summary and Conclusions 138

Chapter 4 : SnO_2-ZnO based n-n hetero-junction system 140

4.1 Introduction 140
4.2 Results and Analysis 141
4.2.1 Scanning Electron Microscopy (SEM) 141
4.2.2 X-Ray Diffraction (XRD) 145
4.2.3 Raman Spectroscopy 147
4.2.4 X-Ray Photoelectron Spectroscopy 148
4.2.5 Gas Sensing Characterisation 149
4.2.5.1 Ethanol Sensing 149
4.2.5.2 NO_2 Sensing 167
4.2.6 Further Gas Sensing Studies 174
4.2.6.1 NH_3 Sensing 174
4.2.6.2 Acetone Sensing 176
4.2.6.3 CO Sensing 178
4.3 Summary and Conclusions 181

Chapter 5 : CTO-ZnO based p-n hetero-junction system 184

5.1 Introduction 184
5.2 Results and Analysis 188
5.2.1 Verification of success of CTO synthesis 188
5.2.1.1 Scanning Electron Microscopy (SEM) 188
5.2.1.2 X-Ray Diffraction (XRD) 189

5.2.1.3 X-Ray Photoelectron Spectroscopy (XPS) 191
5.2.1.4 Raman Spectroscopy 193
5.2.2 Pre-Gas Sensing Material characterisation 194
5.2.2.1 Scanning Electron Microscopy (SEM) 194
5.2.2.2 X-Ray Diffraction (XRD) 197
5.2.2.3 Raman Spectroscopy 198
5.2.3 Post Gas Sensing Material characterisation 201
5.2.3.1 Observed Colour Change in Gas Sensor Materials 201
5.2.3.2 Scanning Electron Microscopy (SEM) 202
5.2.3.3 X-Ray Diffraction (XRD) 204
5.2.3.4 Raman Spectroscopy 206
5.2.3.5 X-Ray Photoelectron Spectroscopy (XPS) 208
5.2.3.6 Gas Sensing Properties of $ZnCr_2O_4$ (Zinc Chromite) 209
5.2.4 Gas Sensing 211
5.2.4.1 Ethanol Sensing 211
5.2.4.2 NO_2 Sensing 222
5.2.5 Further Gas Sensing Studies 228
5.2.5.1 CO Sensing 229
5.2.5.2 NH_3 Sensing 230
5.2.5.3 Acetone Sensing 231
5.2.5.4 Toluene Sensing 235
5.3 Summary and Conclusions 239
Chapter 6 : Emerging ZnO Materials for MOS Sensing 241
6.1 Introduction 241
6.2 Results and Analysis: Nanomaterials based on Continuous Hydrothermal Flow Synthesis (CHFS) 244
6.2.1 Transmission Electron Microscopy (TEM) 244
6.2.2 Scanning Electron Microscopy (SEM) 249
6.2.3 Powder X-Ray Diffraction (PXRD) 251
6.2.4 Raman Spectroscopy 252
6.2.5 Brunauer-Emmet-Teller (BET) Surface Area measurements and Crystallite size 253
6.2.6 Gas Sensing 254
6.2.6.1 Ethanol Sensing 254
6.2.6.2 NO_2 Sensing 259
6.2.7 Key influential factors effecting responsivity order of ZnO samples A, B and C. 263
6.2.7.1 Effect of particle size and morphology 263
6.2.7.2 Effect of heat-treatment 264
6.2.7.3 Effect of neck formation 265

6.2.8 Further Gas Sensing Studies 269

6.3 Results and Analysis: ZnO ceramics synthesised via Molten-Salt synthesis, Solid-State metathesis and Hydrothermal synthesis 273

6.3.1 Scanning Electron Microscopy (SEM) 273

6.3.2 PXRD (Powder X-Ray Diffraction) 275

6.3.3 Gas Sensing 276

6.3.3.1 Ethanol Sensing 276

6.3.3.2 NO_2 Sensing 281

6.3.4 Further Gas Sensing Studies 286

Summary and Conclusions 289

Chapter 7 : Final Conclusions and Future Work 290

7.1 Final Conclusions 290

7.1.1 Cross Comparisons 291

7.1.2 Sources of Error 299

7.1.3 Application Possibilities 300

7.1.4 Drawbacks 302

7.2 Future Work 303

Publications 306

References 307

Appendix 332

List of Figures

Figure 1–1. a) MOS gas sensor substrate strip with the face comprising of gold interdigitated electrodes and the back comprising of a platinum heater track and (b) semiconducting metal oxide film partially deposited on to face of sensor substrate and corresponding back of sensor substrate with platinum heater track to heat metal oxide film to desired operating temperature. 34

Figure 1–2. Typical response signal from metal oxide semiconductor gas sensor upon exposure to gaseous analyte. The diagram indicates when the pulse of gas is switched on and when it is switched off. Further, t_{90} represents the response time of the sensor device to reach 90% of its maximum response and t_{-90} is the recovery time of the sensor device to be within 10% of the baseline value. {Diagram redrawn and adapted from O.A.Afonja [37]}. 37

Figure 1–3. Band Diagrams for (ai) n-type semiconducting oxide when T = 0 K, (aii) n-type semiconducting oxide when temperature is applied, (b) intrinsic semiconductor when temperature is applied, (ci) p-type semiconductor when T = 0 K and (cii) p-type semiconducting oxide when temperature is applied. {Diagrams (ai), (aii), (ci) and (cii) adapted and redrawn from Turton [42] and Atkins and de Paula [44] and diagram (b) adapted and redrawn from Turton [42] and Hofman [43]}. 40

Figure 1–4. Gas sensing mechanism of n-type semiconducting oxide upon interaction with (a) air, in which an electron depletion layer (EDL) is formed on the surface of the metal oxide, upon interaction with O_2 molecules and subsequent adsorption and ionisation of oxygen species on its surface and (b) the target analyte CO (a reducing gas), which interacts with the adsorbed ionic oxygen species on the surface of the metal oxide, forming the product CO_2 and releasing electrons in the process. This induces a decrease in the width of the electron depletion layer, and resultantly increases the conductivity of the n-type metal oxide. The gold percolation arrows illustrate the direction of electron conduction in the material. {Diagram redrawn and adapted from Kim *et al.* [46]}. 41

Figure 1–5. Illustration of diffusion/permeation pathway of the gaseous reactants and products in (a) porous metal oxide gas sensing film or where particles in the gas sensing film are loosely packed and (b) in tightly packed metal oxide gas sensing film or where particles are agglomerated together. The blue arrows represent the pathways of gas diffusion of the reactant analyte molecules and the pink presents the pathways of diffusion of the decomposed/oxidised products. {Diagram redrawn and adapted from Sharma *et al*. [63]}........................46

Figure 1–6. (a) The geometry of a solid composed of fused spherical particles, with the three key regions: the surface, the bulk and the particle boundary. The lilac dashed line represents the length to which the surface extends, which is equivalent to the Debye length or the Depletion Layer – (this represents the depth to which electrons are depleted on the surface of the metal oxide, upon surface adsorption of oxygen ions on the surface of the metal oxide) and (b) A network resistor model representing the three key regions of the gas sensitive material: the particle boundary, the surface and the bulk. The model illustrates how each region relates to each other within a solid composed of fused spherical particles {Diagram redrawn and adapted from Naisbitt *et al*. [65]}...47

Figure 1–7. Models illustrating the crystallite size effects and their determination of the element controlling the responsivity. In (a), the crystallite size is siginificantly larger than twice the Debye length and the responsivity Is grain boundary controlled. In (b), the crystalite size is similar to the twice the Debye length and the responsivity is neck controlled and in (c), the crystallite size is much smaller than twice the size of the Debye layer, and so the responsivity is grain controlled. {Diagram redrawn and adapted from Sharma *et al*. [63]}...................................49

Figure 1–8. Hexagonal wurtzite ZnO crystal structure in which Zn^{2+} ions (represented as Zn) and O^{2-} ions (represented as O) are tetrahedrally co-ordinated. {Diagram redrawn and adapted from Ozgur *et al*. [78] and [80]}...53

Figure 1–9. Tetragonal SnO_2 crystal structure in which Sn^{2+} ions (represented as Sn) are six-fold co-ordinated to three-fold O^{2-} (represented as O) ions. {Diagram redrawn and adapted from [95]}...54

Figure 1–10. Crystal structure of WO_3 showing corner sharing WO_6 octahedra. {Diagram redrawn and adapted from Zheng *et al*. [102]} 55

Figure 1–11. Layer of corundum crystal structure of Cr_2O_3, with hexagonally closed packed O^{2-} ions (represented as O) in octahedral co-ordination with Cr^{3+} ion (represented as Cr). {Diagram redrawn and adapted from [121]}. 57

Figure 1–12. Energy band diagram for (ai) two isolated n-type semiconductors (valence band not shown) with ϕ2 < ϕ1 and (aii) the corresponding hetero-junction band structure for an ideal n-n interface (i.e. when the charge carrier exchange occurs through Fermi level alignment) & (bi) isolated p-type and n-type semiconductor with ϕ2 < ϕ1 and (bii) the corresponding hetero-junction band structure for a p-n interface.In the diagram, ϕ1 and ϕ2 represent the work-functions, Ec1 and Ec2 represent the conduction bands, Ev1 and Ev2, Eg1 and Eg2 represent the band gaps, Ef1 and Ef2 represent the Fermi energy levels and Ex1 and Ex2 represent the electron affinities of semiconductors 1 and 2 respectively, Evac is the vacuum level, ELvac is the local vacuum level and ∆Ec is the conduction band discontinuity and ∆Ev is the valence band discontinuity. {Diagram (ai) and (aii) redrawn and adapted from Wager [163] and diagram (bi) and (bii) redrawn and adapted from van der Krol *et al*. [165] and Roy [166]}. 63

Figure 1–13. Random packing structure of hetero-contact device where purple circles represent metal oxide grains of material A and the green circles represent the metal oxide grains of material B. {Diagram adapted and redrawn from Yamazoe *et al*. [170]}. 67

Figure 1–14. Packing structures of (a) layer-by-layer hetero-contact device. Here the purple circles represent metal oxide grains of material A and green circles represent metal oxide grains of material B and (b) core-shell hetero-contact device. Here the purple circles represent the metal oxide grains of material A and green circles represent shells of material B, which encapsulates material A. {Diagram (a) adapted and redrawn from Yamazoe *et al*. [170]}. 67

Figure 2–1. Schematic of MOS sensor device fabrication process implemented for all sensor devices investigated in this thesis. 77

Figure 2–2. (a) Screen-printable ink fabricated with agate pestle and mortar, (b) DEK 1202 screen-printer for screen-printing inks on to MOS sensor substrates, (c) Single wide gap sensor substrate chip with interdigitated gold electrodes on top and platinum heater track at bottom, (d) SEM images of wide gap sensor substrates top and bottom, (e) SEM images of measured electrode spacing on wide gap substrate, (f) Infra-Red (IR) heat lamp for drying screen-printed layers, (g) muffle furnace for heat-treating sensor chips and (h) Macgregor DC601 parallel gap resistance welder for spot welding of Pt wires onto individual MOS gas sensor chips. 79

Figure 2–3. Schematic of Continuous Hydrothermal Flow Synthesis (CHFS) pilot plant, where P-1, P-2 and P-3 represent pump 1 from which super critical water and pump 2 and pump 3 from which the precursors, are pumped into the confined jet mixer (CJM) / Reactor. PT in the schematic represents a Pressure Transducer and PD represents a Pulsation Dampener. Figure from [143, 196]. 85

Figure 2–4. Schematic of the gas sensing rig used for gas sensing experiments. In the schematic, the MFC represents a Mass Flow Controller, the SV represents a Solenoid Valve, and NO and NC represent open and close ports respectively, through which the gas is allowed access to the exhaust or test cell, respectively.{Diagram from O.A. Afonja [194]}. 90

Figure 2–5. Image of the gas sensing rig used for gas sensing experiments. 91

Figure 2–6. Circular test cell in which gas sensors are placed radially from the centre from where the gas and air inlet is located. The arrow leads to a picture of the sensor mount, in which the 4-pin sensor housing is seated. 92

Figure 2–7. Illustration of the direction of the gas flow that the sensor device experiences when placed in gas sensing rig. 92

Figure 2–8. Wheatstone Bridge heater circuit. 93

Figure 2–9. Circuit diagram of Wheatstone bridge circuit. {Diagram redrawn and adapted from O.A. Afonja [194]}. 93

Figure 2–10. Potentiostat circuit board. 94

Figure 2–11. Circuit diagram of inverting operational amplifier segment of potentiostat measurement circuit. The sensor resistance is calculated using the following components of the circuit: Vp, the sensor device probe voltage, Rs, the unknown resistance of the sensor device, Rfb, the resistance of the feedback resistor and Vs, the measured potential across the sensor device. {Diagram redrawn and adapted from O.A. Afonja [194]}. 94

Figure 2–12. Illustration of the two-point potential measurement of the sensor material being made across the gold pads of sensor substrates. 95

Figure 3–1. Schematic of WO_3 core nanorods and WO_3-ZnO core-shell nanorod architectures fabricated by An *et al*. [209]. 100

Figure 3–2. SEM images of (a) 100 wt.% WO_3 x 10,000 magnification, (b) 100 wt.% WO_3 x 20,000 magnification, (c) 90 wt.% WO_3 – 10 wt.% ZnO x 10,000 magnification, (d) 90 wt.% WO_3 – 10 wt.% ZnO x 20,000 magnification, (e) 70 wt.% WO_3 – 30 wt.% ZnO x 10,000 magnification, (f) 70 wt.% WO_3 – 30 wt.% ZnO x 20,000 magnification, (g) 50 wt.% WO_3 – 50 wt.% ZnO (area 1) x 10,000 magnification, (h) 50 wt.% WO_3 – 50 wt.% ZnO (area 1) x 20,000 magnification, (i) 50 wt.% WO_3 – 50 wt.% ZnO (area 2) x 10,000 magnification, (j) 50 wt.% WO_3 – 50 wt.% ZnO (area 2) x 20,000 magnification, (k) 30 wt.% WO_3 – 70 wt.% ZnO x 10,000 magnification, (l) 30 wt.% WO_3 – 70 wt.% ZnO x 20,000 magnification, (m) 10 wt.% WO_3 – 90 wt.% ZnO x 10,000 magnification, (n) 10 wt.% WO_3 – 90 wt.% ZnO x 20,000 magnification, (o) 100 wt.% ZnO x 10,000 magnification and (p) 100 wt.% ZnO x 20,000 magnification. All materials were screen-printed and heat-treated at 600 ºC before imaging. 103

Figure 3–3. SEM images of (a) 100 wt.% $ZnWO_4$ x 10,000 magnification and (b) 100 wt.% $ZnWO_4$ x 20,000 magnification. The material was screen-printed and heat-treated at 600 ºC before imaging. 106

Figure 3–4. XRD patterns of (a): 100 wt.% WO_3, 90 wt.% WO_3 – 10 wt.% ZnO, 70 wt.% WO_3 – 30 wt.% ZnO, 50 wt.% WO_3 – 50 wt.% ZnO and 30 wt.% WO_3 – 70 wt.% ZnO sensor devices and (b): 10 wt.% WO_3 – 90 wt.% ZnO and 100 wt.% ZnO sensors. The strongest reflections of WO_3 are indicated in black and ZnO are in red. The peaks marked with an * correspond to the tertiary phase, $ZnWO_4$. All materials were screen-printed and heat-treated at 600 °C, prior to XRD measurements. 107

Figure 3–5. PXRD pattern of pure zinc tungstate ($ZnWO_4$), experimentally synthesised by a solid-state method reported by Phani *et al*. [192]. 109

Figure 3–6. Raman patterns of (a): 100 wt.% WO_3, 90 wt.% WO_3 – 10 wt.% ZnO, 70 wt.% WO_3 – 30 wt.% ZnO, 50 wt.% WO_3 – 50 wt.% ZnO and 30 wt.% WO_3 – 70 wt.% ZnO sensor devices and (b): 10 wt.% WO_3 – 90 wt.% ZnO and 100 wt.% ZnO sensors. The modes of WO_3 are indicated in black and ZnO are in red. The modes marked with an * correspond to the tertiary phase, $ZnWO_4$. All materials were screen-printed and heat-treated at 600 °C, prior to Raman spectroscopy measurements. 110

Figure 3–7. Raman pattern of pure zinc tungstate ($ZnWO_4$), experimentally synthesised by a solid-state method reported by Phani *et al*. [192]. The peak with the asterix (*) is the high intensity $ZnWO_4$ peak that was observed in the Raman patterns of the composite materials in Figure 3–6. 112

Figure 3–8. XPS relative binding energies (B.E.) (calculated by taking the difference between the B.E. of the Zn $2p_{3/2}$ peak and the B.E. of the W $4f_{7/2}$ peak) for all the associated WO_3-ZnO composites as a function of wt.% WO_3 in each composite. 113

Figure 3–9. (a) Conductive response of $ZnWO_4$ at 350 °C exposed to increasing concentrations: 5, 10, 20, 40, 80 and 100 ppm ethanol gas and (b) Resistive response of $ZnWO_4$ at 300 °C exposed to increasing concentrations: 100, 200, 400 and 800 ppb NO_2 gas. 114

Figure 3–10. Conductive response traces of the WO_3-ZnO system towards 10, 20, 40, 80 and 100 ppm ethanol gas, at an operating temperature of 350 °C. 116

Figure 3–11. Conductive response of WO_3-ZnO system towards 10, 20, 40, 80 and 100 ppm ethanol gas, at an operating temperature of 350 °C. 120

Figure 3–12. Conductive response of WO_3-ZnO system towards 100 ppm ethanol as a function of increasing operating temperature. 122

Figure 3–13. Resistive response traces of the WO_3-ZnO system towards 100, 200, 400 and 800 ppb NO_2 gas, at an operating temperature of 300 °C. The inset projects the resistive response of the system towards 100 ppb NO_2. 124

Figure 3–14. Resistive responses of WO_3-ZnO system towards 100, 200, 400 and 800 ppb NO_2 gas, at an operating temperature of 300 °C. 128

Figure 3–15. Resistive responses of WO_3-ZnO system towards 800 ppb NO_2 gas, as a function of increasing operating temperature. 130

Figure 3–16. Resistive responses of WO_3-ZnO system against 1000 ppm CO at an operating temperature of 350 °C. 132

Figure 3–17. (a) Conductive responses and (b) Resistive responses of the WO_3-ZnO system against 20 ppm NH_3 at an operating temperature of 350 °C. 133

Figure 3–18. Conductive responses of WO_3-ZnO system towards 1, 2, 4, 6, 8 and 10 ppm acetone gas, at an operating temperature of 350 °C. 134

Figure 4–1. SEM images of (a) 100 wt.% ZnO x 10,000 magnification, (b) 100 wt.% ZnO x 20,000 magnification, (c) 90 wt.% ZnO – 10 wt.% SnO_2 x 10,000 magnification, (d) 90 wt.% ZnO – 10 wt.% SnO_2 x 20,000 magnification, (e) 70 wt.% ZnO – 30 wt.% SnO_2 x 10,000 magnification, (f) 70 wt.% ZnO – 30 wt.% SnO_2 x 20,000 magnification, (g) 50 wt.% ZnO – 50 wt.% SnO_2 x 10,000 magnification, (h) 50 wt.% ZnO – 50 wt.% SnO_2 x 20,000 magnification, (i) 30 wt.% ZnO – 70 wt.% SnO_2 x 10,000 magnification, (j) 30 wt.% ZnO – 70 wt.% SnO_2 x 20,000 magnification, (k) 10 wt.% ZnO – 90 wt.% SnO_2 x 10,000 magnification, (l) 10 wt.% ZnO – 90 wt.% SnO_2 x 20,000 magnification, (m) 100 wt.% SnO_2 x 10,000 magnification and (n) 100 wt.% SnO_2 x 20,000 magnification. All materials were screen-printed and heat-treated at 600 ºC before imaging. 142

Figure 4–2. SEM image of 100 wt.% SnO_2 at x 50,000 magnification. 143

Figure 4–3. XRD patterns of pure and composite sensors based on SnO_2 and ZnO metal oxides, in the SnO_2-ZnO composite system. All materials were screen-printed and heat-treated at 600 °C, prior to XRD measurements. 145

Figure 4–4. XRD pattern of SnO_2 rutile from the ICSD reference database [264, 265]. 146

Figure 4–5. Raman spectra of all sensor devices within SnO_2-ZnO composite system. All sensors were heat-treated at 600 °C, prior to Raman spectroscopy measurements. 147

Figure 4–6. XPS data of the relative binding energies (calculated by taking the difference between the B.E. of the Zn $2p_{3/2}$ peak and the B.E. of the Sn $3d_{5/2}$ peak) for all the associated composites as a function of wt.% SnO_2 in each composite. 148

Figure 4–7. Conductive response traces of SnO_2-ZnO system towards 10, 20, 40, 80 and 100 ppm ethanol gas, at an operating temperature of 300 °C. The inset zooms into the conductive response traces against 10 ppm of the analyte. 149

Figure 4–8. Schematic of random packing structure of metal oxide grains in 50 wt.% ZnO - 50 wt.% CTO and 30 wt.% ZnO – 70 wt.% ZnO sensor devices. In the diagram the green circles represent the smaller ZnO particles and the larger purple circles, the larger SnO_2 agglomerates. Although the diagram presents the grains and agglomerates to be perfectly spherical for simplicity, this perfect spherical nature is not assumed. 151

Figure 4–9. Conductive response of SnO_2-ZnO system towards 10, 20, 40, 80 and 100 ppm ethanol gas, at an operating temperature of 300 °C. 157

Figure 4–10. Conductive response traces of SnO_2-ZnO system towards 10, 20, 40, 80 and 100 ppm ethanol gas, at an operating temperature of 200 °C. The inset zooms into the conductive response traces of all sensor devices towards 10 ppm ethanol. 159

Figure 4–11. Conductive response of SnO_2-ZnO system towards 10, 20, 40, 80 and 100 ppm ethanol gas, at an operating temperature of 200 °C. 161

Figure 4–12. Conductive response traces of SnO_2-ZnO system towards 10, 20, 40, 80 and 100 ppm ethanol gas, at an operating temperature of 500 °C. 162

Figure 4–13. Conductive responses of SnO_2-ZnO system against 100 ppm ethanol gas, as a function of increasing operating temperature. 164

Figure 4–14. Conductive Responses of a) 100 wt.% SnO_2, (b) 90 wt.% SnO_2 – 10 wt.% ZnO, (c) 70 wt.% SnO_2 - 30 wt.% ZnO, (d) 50 wt.% SnO_2 – 50 wt.% ZnO, (e) 30 wt.% SnO_2- 70 wt.% ZnO, (f) 10 wt.% SnO_2- 90 wt.% ZnO and (g) 100 wt.% ZnO sensor devices as a function of increasing operating temperature against 10, 20, 40, 80 and 100 ppm ethanol. 166

Figure 4–15. Resistive response traces of SnO_2-ZnO system towards 100, 200, 400 and 800 ppb NO_2 gas, at an operating temperature of 300 °C. The inset projects the resistive responses of the array towards 200 ppb NO_2. 167

Figure 4–16. Resistive response bar graph of SnO_2-ZnO system towards 400 ppb NO_2 gas, at an operating temperature of 300 °C. 169

Figure 4–17. Resistive (and Conductive) response traces of SnO_2-ZnO system towards 100 ppb NO_2 gas, at an operating temperature of 300 °C. 170

Figure 4–18. Resistive responses of SnO_2-ZnO system towards 800 ppb NO_2 gas as a function of increasing operating temperature. 171

Figure 4–19. (a) Conductive responses and (b) Resistive responses of the SnO_2-ZnO system against 20 ppm NH_3 at an operating temperature of 300 °C. 174

Figure 4–20. Conductive responses of SnO_2-ZnO system towards 1, 2, 4, 6, 8 and 10 ppm acetone gas, at an operating temperature of 300 °C. 176

Figure 4–21. Conductive responses of SnO_2-ZnO system towards 100, 200, 400, 600, 800 and 1000 ppm CO gas, at an operating temperature of 300 °C. 178

Figure 5–1. Synthesised CTO powder screen-printed onto gas sensor substrate and fired at 600 ºC, prior to imaging. The CTO powder was fabricated by a solid-state ceramic ‘shake and bake’ method..........................188

Figure 5–2. XRD patterns of as-synthesised $Cr_{1.95}Ti_{0.05}O_3$ and eskolaite from the ICSD reference database [264, 294]. The CTO powder was fabricated by a solid-state ceramic ‘shake and bake’ method. 189

Figure 5–3. XRD patterns of as-synthesised $Cr_{1.95}Ti_{0.05}O_3$, TiO_2 (predominantly rutile phase) used in the synthesis of CTO and TiO_2 (pure rutile phase) from the ICSD reference database [264, 297]. The asterixed (*) peak in the TiO_2 pattern indicates the 101 lattice place of the anatase phase. The CTO powder was fabricated by a solid-state ceramic ‘shake and bake’ method. 190

Figure 5–4. (a) XPS spectrum of (a) Cr 2p core level, (b) Ti 2p core level and (c) O 1s core level in as-synthesised $Cr_{1.95}Ti_{0.05}O_3$. The CTO powder was fabricated by a solid-state ceramic ‘shake and bake’ method. 191

Figure 5–5. Raman spectrum of screen-printed 100 wt.% CTO sensor and commercial Cr_2O_3 and TiO_2 powders used in the synthesis of CTO using a 514.5 nm green argon-ion laser. The asterixed (*) peak indicates the presence of the anatase phase of TiO_2 in the commercial titania powder. The CTO powder was fabricated by a solid-state ceramic ‘shake and bake’ method. 193

Figure 5–6. SEM images of a) 100 wt.% ZnO x 10,000 magnification, b) 100 wt.% ZnO x 20,000 magnification, c) 90 wt.% ZnO - 10 wt.% CTO x 10,000 magnification, d) 90 wt.% ZnO - 10 wt.% CTO x 20,000 magnification, e) 70 wt.% ZnO – 30 wt.% CTO x 10,000 magnification, f) 70 wt.% ZnO – 30 wt.% CTO x 20,000 magnification, g) 50 wt.% ZnO – 50 wt.% CTO x 10,000 magnification, h) 50 wt.% ZnO – 50 wt.% CTO x 20,000 magnification, i) 30 wt.% ZnO – 70 wt.% CTO x 10,000 magnification, j) 30 wt.% ZnO – 70 wt.% CTO x 20,000 magnification, k) 10 wt.% ZnO – 90 wt.% CTO x 10,000 magnification, l) 10 wt.% ZnO – 90 wt.% CTO x 20,000 magnification, m) 100 wt.% CTO x 10,000 magnification and n) 100 wt.% CTO x 20,000 magnification. All materials were screen-printed and heat-treated at 600 ºC before imaging. 195

Figure 5–7. XRD patterns prior to gas sensing experiments of all pure and composite sensors based on $Cr_{1.95}Ti_{0.05}O_3$ and ZnO metal oxides in the CTO-ZnO composite system. All materials were screen-printed and heat-treated at 600 ºC, prior to XRD measurements. Alumina and Gold reflections from MOS sensor substrate were visible and have also been indicated. 197

Figure 5–8. Raman spectra prior to gas sensing experiments of all pure and composite sensors based on $Cr_{1.95}Ti_{0.05}O_3$ and ZnO metal oxides in the CTO-ZnO composite system. All materials were screen-printed and heat-treated at 600 ºC, prior to Raman measurements. 198

Figure 5–9. Pre- and post-gas sensing coupled images of each sensor device based on $Cr_{1.95}Ti_{0.05}O_3$ and ZnO metal oxides: a) 100 wt.% CTO, b) 90 wt.% CTO - 10 wt.% ZnO, c) 70 wt.% CTO – 30 wt.% ZnO, d) 50 wt.% CTO – 50 wt.% ZnO, e) 30 wt.% CTO – 70 wt.% ZnO, f) 10 wt.% CTO – 90 wt.% ZnO and g) 100 wt.% ZnO, within the CTO-ZnO composite system. 201

Figure 5–10. Post-gas sensing SEM images of a) 100 wt.% ZnO, b) 90 wt.% ZnO - 10wt.% CTO, c) 70 wt.% ZnO – 30 wt.% CTO, d) 50 wt.% ZnO - 50wt.% CTO, e) 10 wt.% ZnO – 90 wt.% CTO and f) 100 wt.% CTO sensor materials all x 20,000 magnification. 202

Figure 5–11. XRD patterns taken after gas sensing experiments of all pure and composite sensors based on $Cr_{1.95}Ti_{0.05}O_3$ and ZnO metal oxides in the CTO-ZnO composite system. 204

Figure 5–12. XRD patterns of zinc chromite, $ZnCr_2O_4$, from the ICSD reference database [264, 308]. 205

Figure 5–13. Raman spectra taken after gas sensing experiments of all pure and composite sensors based on $Cr_{1.95}Ti_{0.05}O_3$ and ZnO metal oxides in the CTO-ZnO composite system. 206

Figure 5–14. XPS spectrum of O 1s core level in the pre- and post-gas sensing sensor devices within CTO-ZnO composite system. 208

Figure 5–15. Conductive response of 100 wt.% ZnO, 90 wt.% ZnO – 10 wt.% CTO and 70 wt.% ZnO – 30 wt.% CTO sensor devices against 10, 20 and 40 ppm ethanol at 200, 250, 300, 350 and 400 °C. 211

Figure 5–16. Resistive response of 50 wt.% ZnO – 50 wt.% CTO, 30 wt.% ZnO – 70 wt.% CTO, 10 wt.% ZnO – 90 wt.% CTO and 100 wt.% CTO sensor devices against 10, 20 and 40 ppm ethanol at 200, 250, 300, 350 and 400 °C. 213

Figure 5–17. Schematic of packing structure of metal oxide grains in 10 wt.% ZnO - 90 wt.% CTO sensor device. In the diagram the green circles represent the smaller CTO particles and the larger purple circles, the larger ZnO particles. Although the diagram presents the grains to be perfectly spherical for simplicity, this perfect spherical nature is not assumed. 215

Figure 5–18. Schematic of packing structure of metal oxide grains in 30 wt.% ZnO - 70 wt.% CTO sensor device. In the diagram the green circles represent the smaller CTO particles and the larger purple circles, the larger ZnO particles. Although the diagram presents the grains to be perfectly spherical for simplicity, this perfect spherical nature is not assumed. 217

Figure 5–19. (a) Conductive response traces of 100 wt.% ZnO, 90 wt.% ZnO – 10 wt.% CTO and 70 wt.% ZnO – 30 wt.% CTO sensor devices at 350 °C, (b) Resistive response traces of 50 wt.% ZnO – 50 wt.% CTO, 30 wt.%

ZnO – 70 wt.% CTO, 10 wt.% ZnO – 90 wt.% CTO and 100 wt.% CTO sensor device at 350 ºC, (c) Conductive response traces of 100 wt.% ZnO, 90 wt.% ZnO – 10 wt.% CTO and 70 wt.% ZnO – 30 wt.% CTO sensor devices at 250 ºC and (d) Resistive response traces of 50 wt.% ZnO – 50 wt.% CTO, 30 wt.% ZnO – 70 wt.% CTO, 10 wt.% ZnO – 90 wt.% CTO and 100 wt.% CTO sensor at 250 ºC, all against increasing concentrations of ethanol. 219

Figure 5–20. Resistive response of 100 wt.% ZnO, 90 wt.% ZnO – 10 wt.% CTO and 70 wt.% ZnO – 30 wt.% CTO sensor devices against 100, 200 and 400 ppb NO_2 at 300, 350 and 400 °C. 222

Figure 5–21. Conductive response of 50 wt.% ZnO – 50 wt.% CTO, 30 wt.% ZnO – 70 wt.% CTO, 10 wt.% ZnO – 90 wt.% CTO and 100 wt.% CTO sensor devices against 100, 200 and 400 ppb NO_2 at 300, 350 and 400 °C. 224

Figure 5–22. (a) Resistive response traces of 100 wt.% ZnO, 90 wt.% ZnO – 10 wt.% CTO and 70 wt.% ZnO – 30 wt.% CTO sensor devices and (b) Conductive response traces of 50 wt.% ZnO – 50 wt.% CTO, 30 wt.% ZnO – 70 wt.% CTO, 10 wt.% ZnO – 90 wt.% CTO and 100 wt.% CTO sensor devices towards 100, 200 and 400 ppb NO_2, at 300 ºC. 226

Figure 5–23. (a) Resistive response of 100 wt.% ZnO, 90 wt.% ZnO – 10 wt.% CTO, 70 wt.% ZnO – 30 wt.% CTO and (b) Conductive response of 50 wt.% ZnO – 50 wt.% CTO, 30 wt.% ZnO – 70 wt.% CTO, 10 wt.% ZnO – 90 wt.% CTO and 100 wt.% CTO sensor devices against 200, 400, 600 and 800 ppm CO at an operating temperature of 350 °C. 229

Figure 5–24. Resistive response of 100 wt.% ZnO, 90 wt.% ZnO – 10 wt.% CTO, 70 wt.% ZnO – 30 wt.% CTO, 50 wt.% ZnO – 50 wt.% CTO, 30 wt.% ZnO – 70 wt.% CTO, 10 wt.% ZnO – 90 wt.% CTO and 100 wt.% CTO sensor devices against 5, 10 and 20 ppm NH_3 at an operating temperature of 350 °C. 230

Figure 5–25. (a) Conductive response of 100 wt.% ZnO, 90 wt.% ZnO – 10 wt.% CTO and 70 wt.% ZnO – 30 wt.% CTO sensor devices and (b) Resistive response of 50 wt.% ZnO – 50 wt.% CTO, 30 wt.% ZnO – 70 wt.% CTO, 10 wt.% ZnO – 90 wt.% CTO and 100 wt.% CTO sensor devices against 2, 4, and 8 ppm of acetone at 300 and 350 °C. 231

Figure 5–26. Resistive response of 50 wt.% ZnO – 50 wt.% CTO, 30 wt.% ZnO – 70 wt.% CTO, 10 wt.% -90 wt.% CTO and 100 wt.% CTO sensor devices against 10, 20 and 40 ppm toluene at 300 and 350 °C. 235

Figure 6–1. TEM images of as-prepared CHFS ZnO nanomaterials where (a) is of ZnO sample A with scale bar of 100 nm, (b) is of ZnO sample A with scale bar of 20 nm, (c) is of ZnO sample B with scale bar of 100 nm, (d) is of ZnO sample B with scale bar of 20 nm, (e) is of ZnO sample C with scale bar of 100 nm and (f) ZnO sample C with scale bar of 20 nm. Samples A, B and C were prepared by CHFS which involved a reaction of ambient flows of 0.1, 0.2, 0.45 M of Zn $(NO_3)_2.6H_2O$ aqueous solution and KOH aqueous solution respectively (each flowing at 200 mL min^{-1}), with a supercritical water flow at 450 °C and 240 bar (flowing at 400 mL min^{-1}) in a confined jet mixer......244

Figure 6–2. Particle size distribution calculated from TEM imaging of ZnO sample A prepared by CHFS which involved reaction of ambient flows of 0.1 M of Zn $(NO_3)_2.6H_2O$ aqueous solution and KOH aqueous solution (each flowing at 200 mL min^{-1}) with supercritical water flow at 450 °C and 240 bar (flowing at 400 mL min^{-1}) in a confined jet mixer......245

Figure 6–3. Particle size distribution calculated from TEM imaging of ZnO sample B prepared by CHFS which involved reaction of ambient flows of 0.2 M of Zn $(NO_3)_2.6H_2O$ aqueous solution and KOH aqueous solution (each flowing at 200 mL min^{-1}) with supercritical water flow at 450 °C and 240 bar (flowing at 400 mL min^{-1}) in a confined jet mixer......246

Figure 6–4. Particle size distribution calculated from TEM imaging of ZnO sample C prepared by CHFS which involved reaction of ambient flows of 0.45 M of Zn $(NO_3)_2.6H_2O$ aqueous solution and KOH aqueous solution (each flowing at 200 mL min^{-1}) with supercritical water flow at 450 °C and 240 bar (flowing at 400 mL min^{-1}) in a confined jet mixer......246

Figure 6–5. SEM images of (a) and (b) ZnO A at x 100,000 and x 40,000 magnification respectively, (c) and (d) ZnO B at x 100,000 and x 40,000 magnification respectively and (e) and (f) ZnO C at x 100,000 and x 40,000 magnification, respectively, after screen-printing onto gas sensor substrates and heat-treating at 600 °C. Samples A, B and C were prepared by CHFS which involved a reaction of ambient flows of 0.1, 0.2, 0.45 M of Zn $(NO_3)_2.6H_2O$ aqueous solution and KOH aqueous solution respectively (each flowing at 200 mL min^{-1}) with supercritical water flow at 450 °C and 240 bar (flowing at 400 mL min^{-1}) in a confined jet mixer. 249

Figure 6–6. PXRD patterns of as-prepared CHFS ZnO samples ZnO A, ZnO B and ZnO C. Samples A, B and C were prepared by CHFS which involved a reaction of ambient flows of 0.1, 0.2, 0.45 M of Zn $(NO_3)_2.6H_2O$ aqueous solution and KOH aqueous solution respectively (each flowing at 200 mL min^{-1}), with a supercritical water flow at 450 °C and 240 bar (flowing at 400 mL min^{-1}) in a confined jet mixer......251

Figure 6–7. Raman spectra of as-prepared CHFS ZnO samples ZnO A, ZnO B and ZnO C. Samples A, B and C were prepared by CHFS which involved a reaction of ambient flows of 0.1, 0.2, 0.45 M of Zn $(NO_3)_2.6H_2O$ aqueous solution and KOH aqueous solution respectively (each flowing at 200 mL min^{-1}), with a supercritical water flow at 450 °C and 240 bar (flowing at 400 mL min^{-1}) in a confined jet mixer......252

Figure 6–8. BET surface area vs. approximated Crystallite Size (Scherrer equation) of as-prepared CHFS samples ZnO A, ZnO B and ZnO C. Samples A, B and C were prepared by CHFS which involved a reaction of ambient flows of 0.1, 0.2, 0.45 M of Zn $(NO_3)_2.6H_2O$ aqueous solution and KOH aqueous solution respectively (each flowing at 200 mL min^{-1}), with a supercritical water flow at 450 °C and 240 bar (flowing at 400 mL min^{-1}) in a confined jet mixer....253

Figure 6–9. Conductive response traces of CHFS ZnO samples: ZnO A, ZnO B and ZnO C at 350 °C against 5, 10, 20, 40 and 80 ppm of ethanol. Samples A, B and C were prepared by CHFS which involved a reaction of ambient flows of 0.1, 0.2, 0.45 M of Zn $(NO_3)_2.6H_2O$ aqueous solution and KOH aqueous solution respectively (each flowing at 200 mL min^{-1}), with a supercritical water flow at 450 °C and 240 bar (flowing at 400 mL min^{-1}) in a confined jet mixer....254

Figure 6–10. Conductive response of CHFS ZnO samples: ZnO A, ZnO B and ZnO C at 350 °C against 10, 20, 40 and 80 ppm of ethanol. Samples A, B and C were prepared by CHFS which involved a reaction of ambient flows of 0.1, 0.2, 0.45 M of Zn $(NO_3)_2.6H_2O$ aqueous solution and KOH aqueous solution respectively (each flowing at 200 mL min^{-1}), with a supercritical water flow at 450 °C and 240 bar (flowing at 400 mL min^{-1}) in a confined jet mixer....256

Figure 6–11. Resistive response traces of CHFS ZnO samples: ZnO A, ZnO B and ZnO C at 250 °C against 100, 200, 400 and 800 ppb of NO_2. Samples A, B and C were prepared by CHFS which involved a reaction of ambient flows of 0.1, 0.2, 0.45 M of Zn $(NO_3)_2.6H_2O$ aqueous solution and KOH aqueous solution respectively (each flowing at 200 mL min^{-1}), with a supercritical water flow at 450 °C and 240 bar (flowing at 400 mL min^{-1}) in a confined jet mixer....259

Figure 6–12. Resistive response of CHFS ZnO samples: ZnO A, ZnO B and ZnO C against increasing concentrations of NO_2 at 250 °C. Samples A, B and C were prepared by CHFS which involved a reaction of ambient flows of 0.1, 0.2, 0.45 M of Zn $(NO_3)_2.6H_2O$ aqueous solution and KOH aqueous solution respectively (each flowing at 200 mL min^{-1}), with a supercritical water flow at 450 °C and 240 bar (flowing at 400 mL min^{-1}) in a confined jet mixer....261

Figure 6–13. Conductive response of CHFS ZnO samples: ZnO A, ZnO B and ZnO C as a function of increasing operating temperature against 80 ppm of ethanol. Samples A, B and C were prepared by CHFS which involved a reaction of ambient flows of 0.1, 0.2, 0.45 M of Zn $(NO_3)_2.6H_2O$ aqueous solution and KOH aqueous solution respectively (each flowing at 200 mL min^{-1}), with a supercritical water flow at 450 °C and 240 bar (flowing at 400 mL min^{-1}) in a confined jet mixer....267

Figure 6–14. Resistive response of CHFS ZnO samples: ZnO A, ZnO B and ZnO C as a function of increasing operating temperature against 800 ppb of NO_2. Samples A, B and C were prepared by CHFS which involved a reaction of ambient flows of 0.1, 0.2, 0.45 M of Zn $(NO_3)_2.6H_2O$ aqueous solution and KOH aqueous solution respectively (each flowing at 200 mL min^{-1}), with a supercritical water flow at 450 °C and 240 bar (flowing at 400 mL min^{-1}) in a confined jet mixer....267

Figure 6–15. Conductive responses of CHFS ZnO samples: ZnO A sensor at 300 °C, ZnO B at 400 °C and ZnO C 350 °C against 8 ppm acetone and 600 ppm CO. The inset presents the resistive response of the sensor devices at the same operating temperatures against 20 ppm NH_3. Samples A, B and C were prepared by CHFS which involved a reaction of ambient flows of 0.1, 0.2, 0.45 M of Zn $(NO_3)_2.6H_2O$ aqueous solution and KOH aqueous solution respectively (each flowing at 200 mL min^{-1}), with a supercritical water flow at 450 °C and 240 bar (flowing at 400 mL min^{-1}) in a confined jet mixer. 269

Figure 6–16. Conductive response of CHFS ZnO sensor devices: ZnO A at 300 °C, ZnO B at 400 °C and ZnO C at 350 °C as a function of increasing concentrations of acetone. Samples A, B and C were prepared by CHFS which involved a reaction of ambient flows of 0.1, 0.2, 0.45 M of Zn $(NO_3)_2.6H_2O$ aqueous solution and KOH aqueous solution respectively (each flowing at 200 mL min^{-1}), with a supercritical water flow at 450 °C and 240 bar (flowing at 400 mL min^{-1}) in a confined jet mixer. 271

Figure 6–17. SEM images of (a) & (b) MS ZnO at x 10,000 & x 20,000 magnification respectively, (c) & (d) SS ZnO at x 10,000 & x 20,000 magnification respectively and (e) & (f) Zn ZnO at x 10,000 & x 20,000 magnification, respectively, after screen-printing onto gas sensor substrates and heat-treating at 600 °C. The ZnO ceramics were prepared by three different synthesis methods: Molten-Salt synthesis (MS-ZnO), Solid-State metathesis (SS-ZnO) and Hydrothermal synthesis (Zn-ZnO). 273

Figure 6–18. PXRD patterns of Zn ZnO, SS ZnO and MS ZnO samples. The ZnO ceramics were prepared by three different synthesis methods: Molten-Salt synthesis (MS-ZnO), Solid-State metathesis (SS-ZnO) and Hydrothermal synthesis (Zn-ZnO). 275

Figure 6–19. Conductive response traces of MS ZnO, SS ZnO and Zn ZnO sensor devices against increasing concentrations of ethanol at an operating temperature of 400 °C. The ZnO ceramics were prepared by three different synthesis methods: Molten-Salt synthesis (MS-ZnO), Solid-State metathesis (SS-ZnO) and Hydrothermal synthesis (Zn-ZnO). 276

Figure 6–20. Conductive response of MS ZnO, SS ZnO and Zn ZnO sensor devices as a function of increasing ethanol concentration at an operating temperature of 400 °C. The ZnO ceramics were prepared by three different synthesis methods: Molten-Salt synthesis (MS-ZnO), Solid-State metathesis (SS-ZnO) and Hydrothermal synthesis (Zn-ZnO). 278

Figure 6–21. Conductive response traces of MS ZnO, SS ZnO and Zn ZnO sensor devices against increasing concentrations of ethanol at an operating temperature of 300 °C. The ZnO ceramics were prepared by three different synthesis methods: Molten-Salt synthesis (MS-ZnO), Solid-State metathesis (SS-ZnO) and Hydrothermal synthesis (Zn-ZnO). 280

Figure 6–22. Resistive response traces of MS, SS ZnO and Zn ZnO sensor devices against increasing concentrations of NO_2 at an operating temperature of 300 °C. The ZnO ceramics were prepared by three different synthesis methods: Molten-Salt synthesis (MS-ZnO), Solid-State metathesis (SS-ZnO) and Hydrothermal synthesis (Zn-ZnO). 281

Figure 6–23. Resistive response traces of MS, SS and Zn ZnO sensor devices against increasing concentrations of NO_2 at an operating temperature of 350 °C. The ZnO ceramics were prepared by three different synthesis methods: Molten-Salt synthesis (MS-ZnO), Solid-State metathesis (SS-ZnO) and Hydrothermal synthesis (Zn-ZnO)........282

Figure 6–24. Resistive responses of SS ZnO and Zn ZnO sensor devices as a function of increasing operating temperature against 800 ppb of NO_2. The ZnO ceramics were prepared by two different synthesis methods: Solid-State metathesis (SS-ZnO) and Hydrothermal synthesis (Zn-ZnO). 284

Figure 6–25. Conductive responses of SS ZnO and Zn ZnO sensor devices as a function of increasing operating temperature against 80 ppm of ethanol. The ZnO ceramics were prepared by two different synthesis methods: Solid-State metathesis (SS-ZnO) and Hydrothermal synthesis (Zn-ZnO). 284

Figure 6–26. Conductive responses of SS and Zn ZnO sensor devices at 350 °C against 8 ppm Acetone and 600 ppm CO. The inset presents the resistive responses of both sensor devices at 350 °C against 20 ppm NH_3. The ZnO ceramics were prepared by two different synthesis methods: Solid-State metathesis (SS-ZnO) and Hydrothermal synthesis (Zn-ZnO). 286

Figure 6–27. Conductive responses of ZnO sensor devices: SS ZnO and Zn ZnO as a function of increasing concentrations of acetone at the specific optimal operating temperatures, which was 350 °C for both devices. The ZnO ceramics were prepared by two different synthesis methods: Solid-State metathesis (SS-ZnO) and Hydrothermal synthesis (Zn-ZnO). 288

List of Tables

Table 2–1. All materials investigated in thesis, corresponding supplier, and associated Chapter number and associated Chapter title within which the material has been investigated. 76

Table 2–2. Composition of Metal Oxide A (MO A) and Metal Oxide B (MO B) used as a basis for the formation and investigation of all composite sensor devices in this thesis. 80

Table 2–3. All MOS sensor devices fabricated for Chapter 3, which investigates the application of a system of WO_3-ZnO n-n hetero-junction composite devices for MOS sensing. Those sensor devices with an asterix (*) are single component metal oxide MOS sensor devices, all others are dual component metal oxide MOS sensor devices..........81

Table 2–4. All MOS sensor devices fabricated for Chapter 4, which investigates the application of a system of SnO_2-ZnO n-n hetero-junction composite devices for MOS sensing. Those sensor devices with an asterix (*) are single component metal oxide MOS sensor devices, all others are dual component metal oxide MOS sensor devices..........82

Table 2–5. All MOS sensor devices fabricated for Chapter 5, which investigates the application of an system of CTO-ZnO p-n hetero-junction composites for MOS sensing. All sensor devices were fabricated by screen-printing method, details of which have been given in Chapter 2. Those sensor devices with an asterix (*) are single component metal oxide MOS sensor devices, all others are dual component metal oxide MOS sensor devices..........83

Table 2–6. All MOS sensor devices fabricated for Chapter 6, which investigates emerging ZnO semiconducting metal oxides for MOS sensing. In the study nanostructured ZnO sample A, ZnO sample B and ZnO sample C were fabricated by Continuous Hydrothermal Flow Synthesis (CHFS), and MS-ZnO was fabricated by Molten-Salt synthesis, SS-ZnO was fabricated by Solid-State metathesis and Zn-ZnO was fabricated by Hydrothermal synthesis. All sensor devices were fabricated by screen-printing method, details of which have been given in Chapter 2. All sensor devices are asterixed (*) indicating single metal oxide component MOS sensor devices. .84

Table 2–7. Summary of CHFS synthesis conditions for the fabrication of ZnO sample A, sample B and sample C, that were characterised for their materials and gas sensing properties in Chapter 6. Fabrication of samples A, B and C involved a reaction of ambient flows of 0.1, 0.2, 0.45 M of Zn $(NO_3)_2.6H_2O$ aqueous solution and KOH aqueous solution respectively (each flowing at 200 mL min^{-1}) with a supercritical water flow at 450 °C and 240 bar (flowing at 400 mL min^{-1}) in a confined jet mixer. 86

Table 2–8. ZnO ceramic samples prepared by Molten-Salt synthesis (MS-ZnO), Solid-State metathesis (SS-ZnO) and Hydrothermal synthesis (Zn-ZnO) supplied by Dr. Kristin Poduska and her research group at Memorial University, New Foundland, Canada. 86

Table 2–9. Example of a gas testing method file for a NO_2 test, containing 12 phases. The original concentration of the NO_2 cylinder was 1000 ppb, however upon dilution with dry air, concentrations in the range of 50 – 800 ppb could be achieved. Each MFC was set a % of full scale flow into the test cell, which was 100%. In phases where the SV is set to 0, flow from the associated MFCs is directed to the exhaust, ensuring that the total flow inside the test cell is always only 100%. Where the SV is set to 1, flow from the associated MFCs is directed to the test cell. No water was added to the Dreschel bottles during anytime of testing and so the dry air flows could be split between a dry air and its corresponding wet air MFC. 97

Table 3–1. Average conductive responses of sensors devices in WO_3-ZnO system from all repeat tests against various ethanol concentrations at 350 °C and associated errors in the form of 95% CIs. 117

Table 3–2. Average resistive responses of sensor devices in WO_3-ZnO system from all repeat tests against various NO_2 concentrations at 300 °C and associated errors in the form of 95% CIs.......................................125

Table 3–3. Average resistive responses of sensor devices in WO_3-ZnO system from all repeat tests against 1000 ppm CO at 350 °C and associated errors in the form of 95% CIs. 132

Table 3–4. Average responses of sensor devices in WO_3-ZnO system from all repeat tests against 20 ppm NH_3 350 °C and associated errors in the form of 95% CIs. 134

Table 3–5. Average conductive responses of sensor devices in WO_3-ZnO system from all repeat tests against 1, 2, 4, 6, and 10 ppm acetone at 350 °C and associated errors in the form of 95% CIs. 137

Table 4–1. Average conductive responses of sensors devices in SnO_2-ZnO system from all repeat tests against various ethanol concentrations at 300 °C and associated errors in the form of 95% CIs. 150

Table 4–2. Average resistive responses of sensor devices in SnO_2-ZnO system from all repeat tests against 400 ppb and 800 ppb NO_2 concentrations at 300 °C and associated errors in the form of 95% CIs. 167

Table 4–3. Average responses of sensor devices in SnO_2-ZnO system from all repeat tests against 20 ppm NH_3 300 °C and associated errors in the form of 95% CIs. 175

Table 4–4. Average conductive responses of sensor devices in SnO_2-ZnO system from all repeat tests against 1, 2, 4, 6, 8 and 10 ppm acetone at 300 °C and associated errors in the form of 95% CIs. 177

Table 4–5. Average conductive responses of sensor devices in SnO_2-ZnO system from all repeat tests against 100, 200, 400, 600, 800 and 1000 ppm CO at 300 °C and associated errors in the form of 95% CIs. 179

Table 4–6. Response magnitudes of sensor devices within SnO_2-ZnO composite system against various concentrations of ethanol, NO_2, acetone, and CO gas at 300 °C (the associated optimal operating temperature). Where device responses were observed to be below 1.5, associated cells have been block filled. 181

Table 5–1. Raman peak positions of Cr_2O_3 (Eskolaite) observed in the literature [302] vs. Raman peak positions observed for the same compound experimentally. 199

Table 5–2. Raman peak positions of Cr_2O_3 (Eskolaite) observed in the literature [302] vs. Raman peak positions observed experimentally for the 90 wt.% ZnO – 10 wt.% CTO composite sensor device. 200

Table 5–3. Average responses of sensor devices in CTO-ZnO system from all repeat tests against various ethanol concentrations at 350 °C and associated errors in the form of 95% CIs. 220

Table 5–4. Average responses of sensor devices in CTO-ZnO system from all repeat tests against various ethanol concentrations at 250 °C and associated errors in the form of 95% CIs. 220

Table 5–5. Average responses of sensor devices in CTO-ZnO system from all repeat tests against various NO_2 concentrations at 300 °C and associated errors in the form of 95% CIs. 227

Table 5–6. Average responses of sensor devices in CTO-ZnO system from all repeat tests against various CO concentrations at 350 °C and associated errors in the form of 95% CIs. 229

Table 5–7. Average resistive responses of sensor devices in CTO-ZnO system from all repeat tests against various NH_3 concentrations at 350 °C and associated errors in the form of 95% CIs. 231

Table 5–8. Average responses of sensor devices in CTO-ZnO system from all repeat tests against various acetone concentrations at 300 °C and associated errors in the form of 95% CIs. 232

Table 5–9. Average responses of sensor devices in CTO-ZnO system from all repeat tests against various acetone concentrations at 350 °C and associated errors in the form of 95% CIs. 232

Table 5–10. Average resistive responses of sensor devices in CTO-ZnO system from all repeat tests against various toluene concentrations at 300 °C and associated errors in the form of 95% CIs. 236

Table 5–11. Average resistive responses of sensor devices in CTO-ZnO system from all repeat tests against various toluene concentrations at 350 °C and associated errors in the form of 95% CIs. 236

Table 5–12. Response magnitudes of CTO-ZnO composite system against various concentrations of ethanol, NO_2, acetone, and toluene gas at operating temperatures of 300 and 350 °C. The devices highlighted in orange are those which exhibited n-type conductive behaviour and those in green are those which exhibited p-type conductive behaviour. Where devices responses were observed to be below 1.5, associated cells have been block filled. 238

Table 6–1. Average conductive responses of sensor devices in CHFS ZnO system from all repeat tests against various ethanol concentrations at 350 °C and associated errors in the form of 95% CIs. 255

Table 6–2. Average resistive responses of sensor devices in CHFS system from all repeat tests against various NO_2 concentrations at 250 °C and associated errors in the form of 95% CIs. 259

Table 6–3. Comparison of conductive responses of ZnO A, ZnO B and ZnO C sensor devices at 300 °C, 400 °C and 350 °C respectively, against 8 ppm acetone and 10 ppm ethanol. Samples A, B and C were prepared by CHFS which involved a reaction of ambient flows of 0.1, 0.2, 0.45 M of Zn $(NO_3)_2.6H_2O$ aqueous solution and KOH aqueous solution respectively (each flowing at 200 mL min^{-1}), with a supercritical water flow at 450 °C and 240 bar (flowing at 400 mL min^{-1}) in a confined jet mixer. 270

Table 6–4. Average conductive responses of sensor devices in CHFS system from all repeat tests against various acetone concentrations at corresponding operating temperatures, and associated errors in the form of 95% CIs. 271

Table 6–5. Average conductive responses of sensor devices in Molten-Salt synthesis ZnO (MS-ZnO), Solid-State metathesis ZnO (SS-ZnO) and Hydrothermal synthesis ZnO (Zn-ZnO) system from all repeat tests against various ethanol concentrations at 400 °C and associated errors in the form of 95% CIs. 277

Table 6–6. Average resistive responses of sensor devices in Molten-Salt synthesis ZnO (MS-ZnO), Solid-State metathesis ZnO (SS-ZnO) and Hydrothermal synthesis ZnO (Zn-ZnO) system from all repeat tests against various NO_2 concentrations at 350 °C and associated errors in the form of 95% CIs. 283

Table 6–7. Comparison of conductive responses of SS ZnO and Zn ZnO sensor devices at 350 °C against 8 ppm acetone and 10 ppm ethanol. The ZnO ceramics were prepared by two different synthesis methods: Solid-State metathesis (SS-ZnO) and Hydrothermal synthesis (Zn-ZnO). 287

Table 6–8. Average conductive responses of sensor devices in Molten-Salt synthesis ZnO (MS-ZnO), Solid-State metathesis ZnO (SS-ZnO) and Hydrothermal synthesis ZnO (Zn-ZnO) system from all repeat tests against various acetone concentrations at 350 °C and associated errors in the form of 95% CIs. 288

List of Figures in Appendix

Figure A - 1. Repeat test of WO_3-ZnO composite system when exposed to increasing concentrations of ethanol at an operating temperature of 350 °C as presented in the main body of thesis in Figure 3–10.......................332

Figure A - 2. Figure 3–10 reproduced from main body of thesis. 332

Figure A - 3. Repeat test of SnO_2-ZnO composite system when exposed to increasing concentrations of ethanol at an operating temperature of 300 °C as presented in the main body of thesis in Figure 4–7..........................333

Figure A - 4. Figure 4–7 reproduced from main body of thesis 333

Figure A - 5. Repeat test of SnO_2-ZnO composite system when exposed to increasing concentrations of ethanol at an operating temperature of 200 °C as presented in the main body of thesis in Figure 4–10.......................334

Figure A - 6. Figure 4–10 reproduced from main body of thesis. 334

Figure A - 7. Repeat test of CTO-ZnO composite system when exposed to increasing concentrations of ethanol at 250 °C in (ai) and (aii) as presented in the main body of thesis in Figure 5–19 (c) and (d). 335

Figure A - 8. Figure 5–19 (c) and (d) reproduced from main body of thesis. 335

Figure A - 9. Repeat test of CTO-ZnO composite system when exposed to increasing concentrations of NO_2 at 300 °C in (bi) and (bii) as presented in the main body of thesis in Figure 5–22 (a) and (b). 336

Figure A - 10. Figure 5–22 (a) and (b) reproduced from main body of thesis..336

Figure A - 11. Repeat test of CHFS ZnO system against increasing concentrations of NO_2 at 300 °C as presented in the main body of thesis in Figure 6–11. 337

Figure A - 12. Figure 6–11 reproduced from main body of thesis 337

Figure A - 13. Repeat test of MS ZnO, SS ZnO and Zn ZnO sensor devices against increasing concentrations of ethanol at an operating temperature of 300 °C. The ZnO ceramics were prepared by three different synthesis methods: Molten-Salt synthesis (MS-ZnO), Solid-State metathesis (SS-ZnO) and Hydrothermal synthesis (Zn-ZnO) as presented in the main body of thesis in Figure 6–21. 338

Figure A - 14. Figure 6–21 reproduced from main body of thesis. 338

List of Tables in Appendix

Table A - 1. Baseline resistance ranges in ohms for all sensor devices studied within WO_3-ZnO composite system at operating temperatures of 500, 450, 400, 350 and 300 ^{o}C. 339

Table A - 2. Baseline resistance ranges in ohms for all sensor devices studied within SnO_2-ZnO composite system at operating temperatures of 500, 450, 400, 350 and 300 ^{o}C. 340

Table A - 3. Baseline resistance ranges in ohms for all sensor devices studied within CTO-ZnO composite system at operating temperatures of 500, 450, 400 and 350 ^{o}C. 340

Table A - 4. Baseline resistance ranges in ohms for all sensor devices studied within nanostructured ZnO material systems at operating temperatures of 500, 450, 400, 350 and 300 ^{o}C. 341

List of Acronyms

CHFS	-	Continuous Hydrothermal Flow Synthesis
CI	-	Confidence Interval
EDL	-	Electron Depletion Layer
HAL	-	Hole Accumulation Layer
MOS	-	Metal Oxide Semiconductor
MFC	-	Mass Flow Controller
MS - ZnO	-	Molten Salt synthesised ZnO
PXRD	-	Powder X-Ray Diffraction
SV	-	Solenoid Valve
SEM	-	Scanning Electron Microscopy
SS - ZnO	-	Solid State synthesised ZnO
TEM	-	Transmission Electron Microscopy
TLV	-	Threshold Limit Value
XPS	-	X-Ray Photoelectron Spectroscopy
XRD	-	X-Ray Diffraction
Zn - ZnO	-	Hydrothermally synthesised ZnO

Chapter 1 : Introduction

1.1 Gas Sensor Technology

Chemical gas sensing technology stands as a prominent area of research and development in a diverse number of academic and industrial fields, in particular those spanning the physical sciences, materials science and electronics engineering. This motivation is driven by the significance of this technology in a diverse number of areas such as environmental monitoring, the security sector, medical diagnostics and the food industry [1, 2]. Recently, in an article by ‘Global Industry Analysts Inc.’, it was reported that the global chemical sensing market is projected to reach $17.28 billion dollars by 2015 [3].

Amongst the chemical sensor technologies that span the capability to detect gases, electrochemical sensors, optical sensors, thermal sensors, and chemiresistive sensors are examples of the most widely used detection technologies in the field [4, 5].

Of all the mentioned sensor types, electrochemical sensor technology is the largest and oldest group of chemical sensor types [6], in which an electric signal is generated when a chemical oxidation or reduction reaction occurs (between the gas and the electrodes) in an electrochemical cell [7]. During the process of this electrochemical reaction, chemical changes occur at the electrodes, as well as charge conduction taking place through the bulk of the electrolyte (which is in contact with the electrode) [6]. Chemical modulation of the reactions that occur at the electrodes, as well as the charge transport, serve as a basis of the sensing process [6], with the generated electric current from the reaction being measured. Advantages of this technology are the immediate generation of electric signals i.e. quick response times [8], as well as the linearity which allows ease of calibration and more precise detection of low concentration ranges [7]. However the nature of the transduction principle, limits the technology to gases which are active to oxidation and reduction reactions; and inadvertently introduces cross-sensitivity issues as one or more gas in the environment where detection is taking place, may be susceptible to reduction or oxidation as well the target gas [7]. Further, the detection limits of this technology are poor with respect to that of other sensor technologies.

Optical gas sensing is a significantly more modern technology to that of electrochemical, and is a technique which works on the basis of spectroscopic methods, based on the chemical principles of adsorption and emission [4]. An Infra-Red (IR) sensor is a classic example used for gas sensing and works on the principle of molecular absorption, whereby the gas which has a particular IR absorption fingerprint, will absorb a particular wavelength from the broad range of wavelengths emitted by the IR source. A filter will filter out all wavelengths except that which is absorbed by the gas, and an IR detection unit will detect the absorbed wavelength and in this way the gas is detected [4]. The mode of detection is commended due to its stability, sensitivity, selectivity in comparison to methods which are not optical. Further, the techniques are not disturbed by harsh environments or poisoning caused by some gases and thus have long shelf lives. However, the large and delicate nature of the technique means that its miniaturisation and mobility are limited; large spaces are required for its operation and large costs are required for maintenance purposes [4, 9]. In particular with miniaturised optical sensors, getting appropriate paths lengths is vital in order to enable appropriate responsivities.

Thermal sensors are generally used for combustible gas detection and work on the principle of a resistance change of a semiconducting catalytic material, which has a temperature dependent conductivity [10]. When the target combustible gas comes into contact with the catalytic material of the thermal sensor, an exothermic combustion reaction takes place releasing heat which causes the temperature of the catalytic material to rise [10]. When the temperature of the sensor has equilibrated (promoted by heat conduction), the resulting temperature difference between the material and the ambient is measured indirectly by measuring the change in resistance of the material by an integrated thermistor [10]. The extent of heat released by the reaction, is dependent on the concentration of the target combustible analyte in the air and as such, the method is able to detect the concentration of the target gas in the environment [10]. The nature of the detection method makes it essential to find selective catalysts for combustible gases, otherwise it can suffer from cross-sensitivity issues. Further the method is only limited to the detection of inflammable gases such as hydrogen, hydrogen sulphide and carbon monoxide [4, 10].

The final group of sensors, chemiresistive sensors, work on the principle of a gas sensor element exhibiting a change in resistance or conductance, upon exposure to the target analyte. The change in resistance of the element is promoted by surface induced adsorption, desorption and oxidation reactions of the analyte molecules upon its surface and subsequent change in charge carrier concentration [11, 12]. Usually the gas sensor element is a high operating temperature ceramic semiconducting metal oxide, and as such chemiresistive sensors are more popularly called Metal Oxide Semiconducting (MOS) gas sensors, which is the technology of focus in this thesis. Detailed introduction to this technology, the mechanism by which gas response occurs and the advantages and disadvantages in comparison to the other technologies, have been presented further in this Chapter in sections 1.2, 1.4 and 1.5. The Taguchi sensor [11, 13, 14], alluded to further in section 1.8.2, is one of the oldest and most commonly used chemical sensors based on MOS technology and is a device built around pressing and sintering powdered metal oxide materials.

Independent of the transduction function of the technology utilised for gas sensing applications, all sensor devices are desired to encapsulate some fundamental properties that make them useful for practical applications, some of which have already been alluded to above. The most fundamental of these is the responsivity which is the output of the sensor as a function of the quantity applied to its input, which is very commonly and incorrectly called the sensitivity [15]. The selectivity is another property; which is a term used to describe if a sensor responds selectively to a group of analytes or specifically to a single analyte [5]. A fast response time, which is the time taken for a sensor to respond from zero concentration to a step change in concentration [5] and a fast recovery time (which is the exact opposite of the response time) are also important factors that dictate assimilation of the kinetics of the device and its applicability in environments, particularly where immediate warning is required. Both these kinetic terms are usually represented as the t_{90} and t_{-90} respectively, which have been introduced further in this Chapter in section 1.3. The reproducibility of the sensor device in terms of its response and its manufacture is also an important factor for practical reasons, which will support the reliability of the sensor device, which is particularly important for life-threatening applications. An extension to the reproducibility, is the repeatability of the response of single device for reliable and practical purposes and a long shelf life [5]. The stability and baseline stability of the sensor as a measure of the performance of the sensor for a period of time is another important measure of the reliability of the device, with the drift of the device used as a measure of this factor [5]. A lower power consumption of a sensor device is a further attractive quality and ensures economic viability, making it attractive for expansive industrial applications. The linearity of the device (associated values of which are specified for a certain concentration range) which is a relative measure of an experimentally determined calibration graph from an ideal straight line [5] is another important factor which adds to the reliability of the device and supports the ability to model the behaviour of the sensor. A final requirement of any practical sensor that is to be used in practice, is resistance towards humidity as well as harsh environmental conditions, which demand the need for robust and durable sensor devices.

1.2 Metal Oxide Semiconductor (MOS) Sensors

As introduced above, within the large assortment of chemical gas sensors, metal oxide semiconductor (MOS) based gas sensors, illustrated in Figure 1–1, are one of the most widely investigated technologies [16, 17].

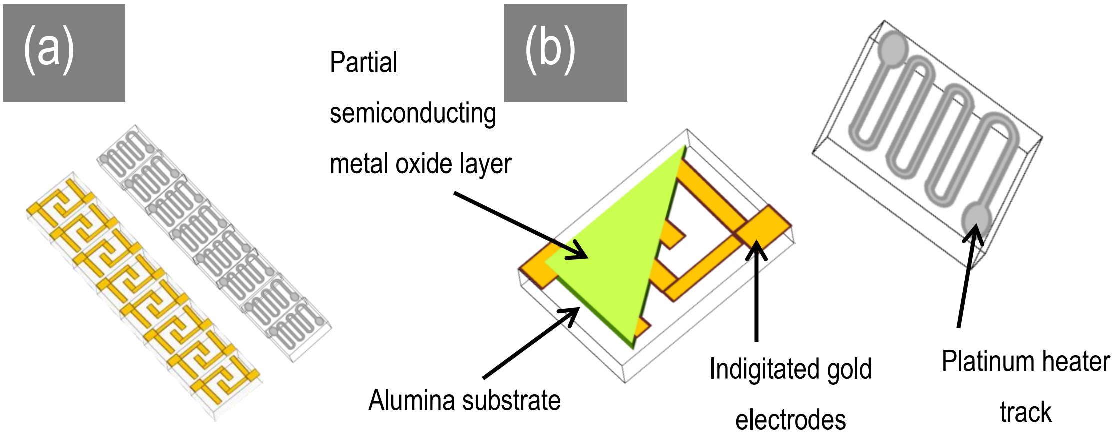

Figure 1–1. a) MOS gas sensor substrate strip with the face comprising of gold interdigitated electrodes and the back comprising of a platinum heater track and (b) semiconducting metal oxide film partially deposited on to face of sensor substrate and corresponding back of sensor substrate with platinum heater track to heat metal oxide film to desired operating temperature.

Such sensor devices consist of an insulating substrate such as alumina, which encompasses screen-printed gold interdigitated electrodes on the top and a platinum heater track at the bottom, illustrated in Figure 1–1 (a). A semiconducting metal oxide film such as WO_3, ZnO, SnO_2, In_2O_3 or Cr_2O_3 is deposited onto the top of the substrate on the gold electrodes using thick-film methods such as screen-printing or thin-film methods such as CVD, amongst a variety of other examples [18, 19]. When integrated into a circuit, the printed gas responsive semiconducting metal oxide can be heated to higher temperatures of operation via the platinum heater track at the bottom. Such sensors are usually operated at temperatures of 200 - 400 °C [20]. The device is then able to exhibit changes in its electrical resistance (or conductance) due to surface mediated chemical decomposition/oxidation reactions with the various target analytes it is exposed to [21].

MOS sensor technology has many advantages and the concentrated research effort behind the technology arise due its economic and easy fabrication process which imply low production costs for the manufacturer. At the back end, utilisation of the device for the end-user is very simple [12] with no training required. As such, this technology is commercially very attractive in comparison to larger and/or more complex optical sensors and electrochemical sensors. Further, controllable, well-established and commercially attractive printing processes such as screen-printing [12], introduced further in section 1.6, can be used in conjunction with this technology for the deposition of the gas responsive metal oxide, adding to the commercial scalability of the technology and the production of devices which exhibit repeatable response characteristics.

The development of deposition technologies such as chemical vapour deposition, physical vapour deposition and sputtering techniques, among a host of others, for the deposition of 1- dimensional thin films and 2-dimensional nanostructures which are gas responsive, have allowed the advancement of research and development of next generation sensor devices, which have improved response performances, due to the inherently large surface area associated to the deposited materials. Such techniques have also allowed the potential to miniaturize MOS sensor devices, which conventionally are based on bulky substrates, requiring large heating powers due to their bulky nature [12, 22]. The large power consumption is a severe drawback of MOS technology, however the development of advanced deposition technologies of the gas responsive films, allow the miniaturization of the device onto micro-fabricated substrates [22].

In terms of performance, MOS sensor devices are associated to large responsivities to the target analytes, robustness and quick response and recovery times. The high operating temperatures required by the technology, allows for control of the response and recovery kinetics depending on the application. Unlike electrochemical sensors however, room temperature operation of MOS sensors results in poor responses, and as such the technology is limited to high temperature applications [4]. However unlike thermal pellistors which are limited to the detection of inflammable gases, MOS sensors are open to sensing a host of analytes which are not inflammable such as NO_2 [23] , NH_3 [24], CO_2 [12], HCl [25] and SO_2 [26]. As such, the commercial applicability of MOS sensors is open to wider variety of settings. Some of the aforementioned gases however, such as H_2S, NH_3 and SO_2 can result in the conditioning of the surface of the metal oxide resulting in surface poisoning, sensor drift, and alteration of the gas sensing properties of the material, another drawback of MOS sensor technology [27-30]. Such conditioning problems can however be overcome with temperature pulsing techniques which can regenerate the surface of the metal oxide and aid to bring back the original properties of the sensor device.

Apart from surface poisoning, the presence of humidity can lead to drift of MOS sensors, particularly n-type metal oxides, due to the nature of their sensing mechanism via the Electron Depletion Layer (EDL), which has been illustrated further in section 1.5. However p-type metal oxides in contrast, have a greater resistance to humidity due to electron conduction through the Hole Accumulation Layer (HAL) (illustrated in section 1.5 and in section 5.1, Chapter 5) making them more applicable materials for practical purposes. The lack of selectivity of MOS sensors is another key drawback of the technology and as such, the technology suffers from cross-sensitivity issues, making it difficult to interpret which gas the response signal observed, belongs to [12, 30]. Section 1.9 in this Chapter, alludes to various solutions that have been developed to overcome selectivity issues with MOS sensors. MOS sensors also suffer from poor repeatability issues, which subsequently effects the reliability. Factors such as the method of temperature control, cross-sensitivity and surface poisoning which leads to drift, are examples that contribute its lack of repeatability and thus lack of linearity.

The responsivity, as well as the stability and the selectivity [31, 32], are imperative in establishing the performance of this solid-state gas sensor [21]. In particular, excellent responsivity towards the target analyte(s) is logically one of the most fundamental requirements of a sensing device and is significantly influenced by parameters such as the microstructure, morphology and composition of the gas sensitive MOS layer [33-35]. These parameters have a profound effect on the response because the gas sensing mechanism is predominantly a surface process, constituting complex and speculative surface reactions, such as redox as well as adsorption and desorption processes [17, 36]. Thus, the ability of the MOS sensor to function effectively is also very much influenced by the surface characteristics of the gas sensitive material.

1.3 Interpretation of Sensor Response Trace/Curve

A typical response trace from a MOS gas sensor device, when exposed to a pulse of the target analyte for a given time period, has been presented in Figure 1–2, which has been redrawn and adapted from O.A.Afonja [37].

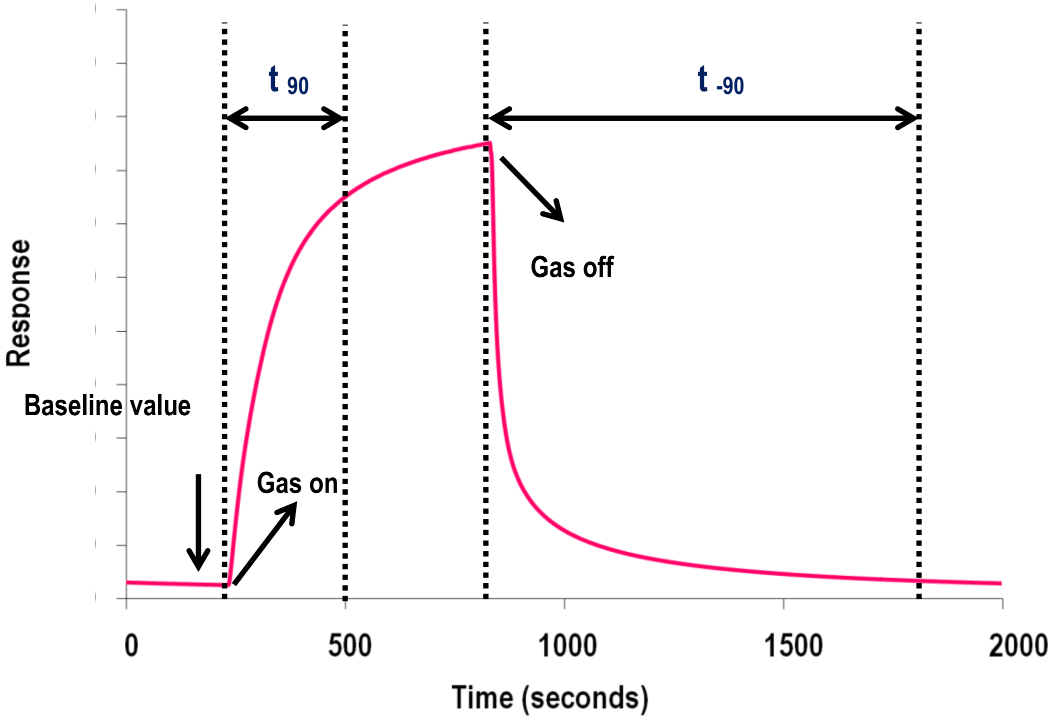

Figure 1–2. Typical response signal from metal oxide semiconductor gas sensor upon exposure to gaseous analyte. The diagram indicates when the pulse of gas is switched on and when it is switched off. Further, t_{90} represents the response time of the sensor device to reach 90% of its maximum response and t_{-90} is the recovery time of the sensor device to be within 10% of the baseline value. {Diagram redrawn and adapted from O.A.Afonja [37]}.

Figure 1–2 presents a typical sensor response trace obtained from the exposure of a MOS sensor device to a gas pulse. The sensor trace demonstrates the responsivity of the material towards the analyte with respect to baseline response which is 1 (calculated as R_0/R_0). The conductive response of a sensor device is defined as a ratio of the sensor resistance during exposure to air (R_0) over the resistance of the sensor during exposure to the target gas (R_g) i.e. the conductive response = R_0/R_g. The resistive response in contrast is defined as a ratio of the resistance of the sensor during exposure to the target gas (R_g) as a ratio of the sensor resistance during exposure to air (R_0) i.e. resistive response = R_g/R_0 [38].

The response trace also allows assimilation of the response and recovery kinetics for the sensor device before and after exposure of a certain pulse of the target analyte, respectively. The response of a sensor device is defined as the time it takes for the sensor to reach 90 % of its final response and is denoted as t_{90}. The recovery of a sensor device is defined as the time it takes for the sensor to reach to 10% of the baseline response value and is denoted as t_{-90} [39]. Figure 1–2 presents the regions within which both the response and recovery times lie; ideally a sensor device should respond and recover in the 10s of seconds [40] to the target analyte for practical applications. The figure also shows that the equilibration of the response trace i.e. the response trace reaching steady state or saturation is likely to occur with a longer duration of gas exposure.

1.4 n-type and p-type Semiconductors

Semiconductors are classed into two groups, the first being intrinsic semiconductors and the second being extrinsic semiconductors. Extrinsic metal oxides, contain impurities or defects in the form of a loss of oxygen species (donor impurity) which can leave behind extra electrons in the lattice, i.e. creation of excess negative charge carriers, producing an n-type semiconductor. Alternatively, they can be in the form of extra oxygen species, which introduce electronic holes in the lattice, i.e. excess positive charge carriers, producing a p-type semiconductor [41].

1.4.1 Intrinsic Semiconductors

Intrinsic semiconductors contain no impurities, and as such these materials contain an equivalent number of charge carriers in the valence band (holes) and in the conduction band (electrons). At absolute zero temperature, the probability of the conduction band being occupied is zero, and the probability of the valence band being occupied is 1 [42]. When the temperature is increased to a high enough temperature, electrons in the valence band have enough energy to jump across the band gap to the conduction band, leaving vacant holes in the valence band. Because of the ideal nature of the semiconductor, for every electron that is excited to the conduction band, a hole is generated in the valence band. In such semiconductor the Fermi level is placed at the centre of the semiconductor, given that the probability of occupation of both bands is 50 % [42]. Figure 1–3 (b), illustrates the band diagram of an intrinsic semiconductor.

1.4.2 Extrinsic Semiconductors: n-type and p-type Semiconductors

In extrinsic semiconductors, the conductivity is controlled by the introduction of acceptor impurities or donor impurities in the semiconductor lattice [42-44]. In the case of n-type semiconductors, donor impurities are introduced into the lattice. These impurities contain a donor electron, which is occupied within a donor state. [42]. The donor electrons only require very little energy to be able to enter the conduction band, as they have very small binding energies, implying that the donor state is located just below the conduction band [42, 43]. The excitation of the donor electrons to the conduction band is how an n-type semiconductor conducts. In such a semiconductor, the position of the Fermi level is positioned depending on two extremes of temperature [42]. At absolute zero [42], all electron states up to and including the donor state, are occupied, implying that the lowest vacant state would be in the conduction band. Thus, the Fermi level is placed half way between the donor state and the conduction band. At higher temperatures [42] however, the intrinsic carriers becomes comparable to the number of donor electrons, and so the material behaves like an intrinsic semiconductor with the Fermi level close to the centre of the band gap [42]. Schematic of the band diagrams of an n-type semiconductor are shown in Figure 1–3 (a) and (ai).

In contrast in a p-type semiconducting oxide, acceptor impurities are introduced into the lattice. These impurities contain an acceptor hole, which is occupied within an acceptor state [42]. In order for holes to conduct in the valence band, the acceptor holes need to be ionised [42]. This is done by exciting a valence electron up to the acceptor state and in this way; the p-type semiconductor conducts. Little energy is required for the valence electrons to be excited to the acceptor state, as they have very small binding energies, implying that the acceptor state lies close to the valence band [42, 43]. The positon of the Fermi level, again like the n-type semiconducting oxide lies in different positions, depending on the temperature of operation. At high temperatures it behaves like an intrinsic semiconductor, however at absolute zero, the higher occupied state is at the top of the valence band and the lowest occupied state is at the acceptor level, so the Fermi level is half way between the acceptor state and valence band [42]. Schematic of the band diagrams of a p-type semiconductor are shown in Figure 1–3 (c) and (ci).

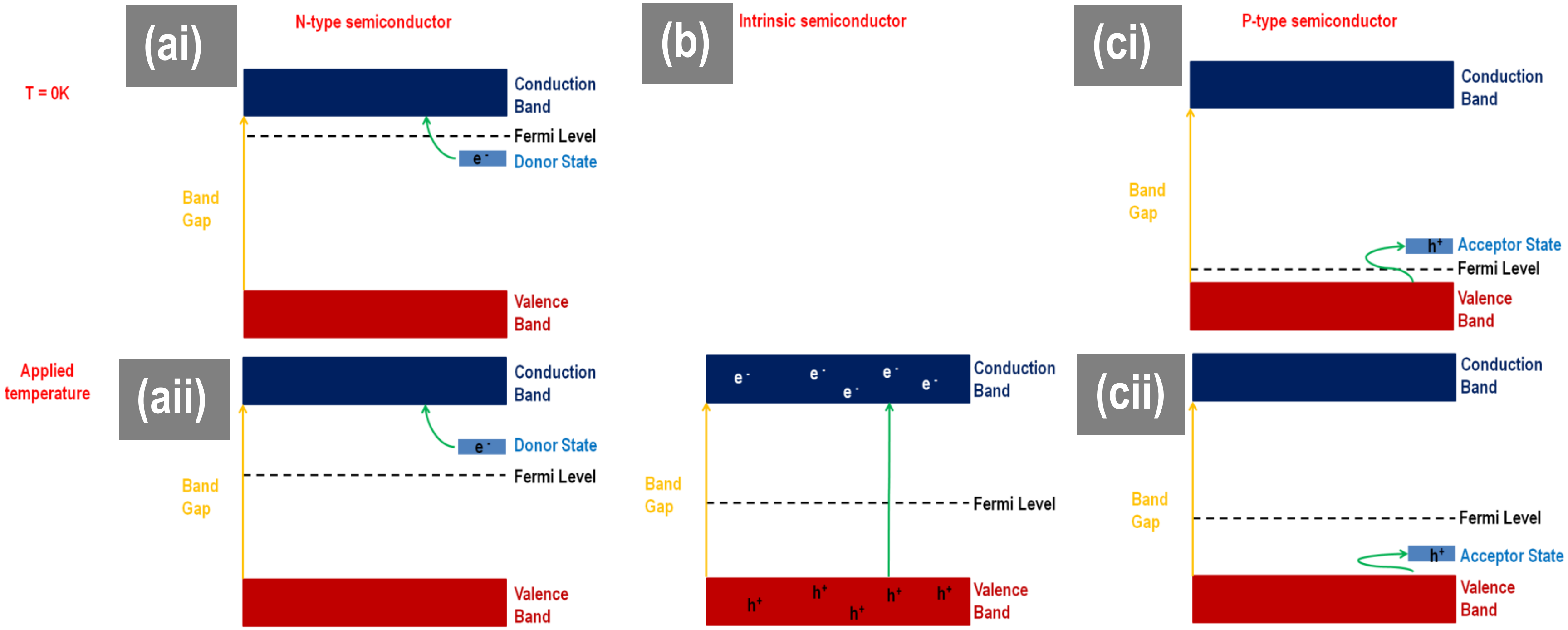

Figure 1–3. Band Diagrams for (ai) n-type semiconducting oxide when T = 0 K, (aii) n-type semiconducting oxide when temperature is applied, (b) intrinsic semiconductor when temperature is applied, (ci) p-type semiconductor when T = 0 K and (cii) p-type semiconducting oxide when temperature is applied. {Diagrams (ai), (aii), (ci) and (cii) adapted and redrawn from Turton [42] and Atkins and de Paula [44] and diagram (b) adapted and redrawn from Turton [42] and Hofman [43]}.

1.5 Gas Sensing Mechanism in MOS Sensors

The gas sensing mechanism of semiconducting metal oxides is predominantly a surface process, constituting complex and speculative surface reactions, examples being redox [4] as well as adsorption and desorption processes [17, 36]. These reactions directly cause a change to the population of charge carriers in the semiconducting oxide materials, which are the source of the electrical resistance (or conductance) changes observed [12].

Figure 1–4 illustrates the conduction-oxidation response mechanism [1, 45, 46] of an n-type semiconducting oxide such as WO_3, ZnO or SnO_2, with the aid of diagrams which have been modified and adapted from a report by Kim *et al*. [46].

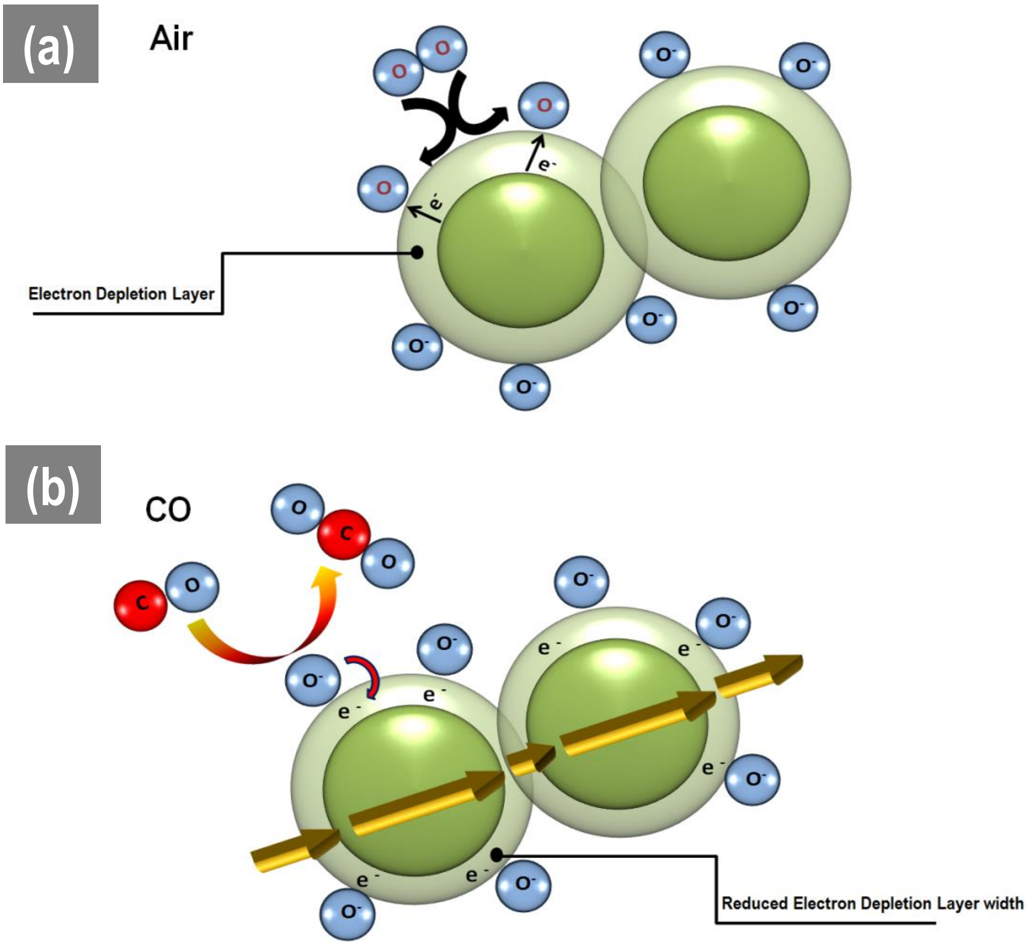

Figure 1–4. Gas sensing mechanism of n-type semiconducting oxide upon interaction with (a) air, in which an electron depletion layer (EDL) is formed on the surface of the metal oxide, upon interaction with O_2 molecules and subsequent adsorption and ionisation of oxygen species on its surface and (b) the target analyte CO (a reducing gas), which interacts with the adsorbed ionic oxygen species on the surface of the metal oxide, forming the product CO_2 and releasing electrons in the process. This induces a decrease in the width of the electron depletion layer, and resultantly increases the conductivity of the n-type metal oxide. The gold percolation arrows illustrate the direction of electron conduction in the material. {Diagram redrawn and adapted from Kim *et al.* [46]}.

Figure 1–4 shows that the reaction initiates with the adsorption of oxygen molecules from the air, on the surface of the n-type particles, in the form of various anionic oxygen species such as O^- or O^{2-}; the exact type of anionic oxygen species is dependent on the operating temperature of the sensor [1, 45]. For these anionic oxygen species to form and stabilise on the surface of the metal oxide, the oxygen molecules from ambient air need to be reduced by the uptake of electrons (i.e. they need to be ionized) [46]. These electrons are extracted from the conduction band of the metal oxide and trapped at its surface. This process leads to the formation of an electron depletion layer (EDL) or space-charge layer at the surface of the metal oxide, which is a zone depleted of electrons [1, 45, 46].

Following this, the second part of the reaction may occur, which is illustrated Figure 1–4 part (b). Here the target analyte, in this case CO (which is a reducing gas) undergoes oxidation reactions with the adsorbed anionic oxygen species forming CO_2 molecules, which desorb off the surface, and in the process of the oxidation reaction, remnant electrons are released into the EDL / space-charge layer. This reaction causes a decrease in the thickness of the EDL and as a result of this release of electrons back into the bulk of the material, which in effect implies a change in the charge carrier concentration of the material, a decrease in the height of the potential barrier (also called the Schottky barrier) between the two consecutive n-type grains occurs. As such, an increase in the conductance of the material is then observed [1, 45]. The electron conduction that occurs in the gas sensitive material is represented by the gold percolation arrows observed in Figure 1–4 part (b).

Had the n-type material been exposed to an oxidising gas such as NO_2, a resistance increase in the material would have been observed. This is due to trapping of and subsequent abstraction of electrons from the bulk of the material upon exposure to the oxidising gas, leading to a decrease in the charge carrier concentration in the bulk and an increase in the size of the electron depletion layer. Resultantly, an increase in the potential barrier height is induced and an increase in the resistance of the gas sensitive material is observed.

Conversely with p-type semiconducting oxides such as $Cr_{2-x}Ti_xO_3$ (chromium titanium oxide) – shortened to CTO hence forth [47, 48], Cr_2O_3, NiO, CuO or Co_3O_4 [18, 46, 49], the reaction initiates with the adsorption of oxygen molecules from the air, on the surface of the p-type particles, in the form of various anionic oxygen species such as O^- or O^{2-}. The formation of the anionic species on the surface of the p-type semiconducting oxide forms a hole accumulation layer (HAL) [46] at the surface of the p-type particles due to the dominant population of holes in the valence band of p-type semiconductors and the attraction of the electrons to stabilise the oxygen species on the surface [46]. When the p-type materials are then exposed to a reducing environment of CO, the CO molecules will interact with the surface adsorbed oxygen anions and release electrons into the material, which interact with the positive holes in the HAL through electron-hole recombination reactions, reducing the concentration of the holes in the HAL [46]. As such, the resistance of the p-type material will increase upon exposure to a reducing gas.

Upon interaction with an oxidising gas, the concentration of electrons on the surface of the p-type semiconducting oxide will decrease as the oxidising gas will abstract them from the surface, resulting in an increase in the conductivity of the material as the extracted electrons result in the generation of holes in the valence band [49].

1.6 Thick-Film vs. Thin-Film Metal Oxide Gas Sensing Materials

In general, the gas sensitive MOS layer is classified either as a product of thick-film or thin-film materials fabrication technology. Thick-films are in the broad μm range of thickness values and are generally produced by screen printing; such sensors are termed “first generation” devices [31]. Screen printing is a very attractive commercial process with the ability to mass produce a large number of sensor chips in one printing cycle. Further, the controlled deposition associated to the technique ensures consistent printing and limits the batch-to-batch variability between each sensor device. The technique is simple and requires forming a printable viscous paste of the desired metal oxide powder, by mixing the powder with an organic vehicle. The organic vehicle contains a binder which ensures strong adherence of the printed metal oxide to the substrate. The formed ink is then printed onto an alumina tile, with one tile containing more than 200 sensor chips. As highlighted, the ability to print a large number of sensor chips simultaneously, is commercially attractive and ensures repeatability between each device. The shapes of the gas responsive layer to be printed onto the individual chips on the alumina tile, are dictated by a screen which contains a stencil of the shapes. The ink is pressed down through and along the screen onto the alumina tile using a squeegee. The print is then dried and further prints can be made, depending on the thickness desired. Finally the printed layer is heat-treated to burn off the organic vehicle and ensure strong adherence between the sensing layer and the tile.

Another method of thick-film deposition is drop coating which as the name suggests encompasses the deposition of drops of the gas responsive metal oxide material onto the sensor substrate [50]. The method involves the creation of a metal oxide solution, a known volume of which can be dropped onto the sensor substrate by the use of a calibrated volumetric pipette. The solution is prepared using a solvent and thus after deposition, evaporation of the solvent leads to a dry deposit of the metal oxide [51]. In comparison to screen printing, the preparation of a group of sensor devices cannot occur simultaneously, but rather individually. Further irreproducibility between devices is inherent to the technique unlike screen-printing. Despite the drawbacks of the technique, drop coating has been reported to lead to highly stable and reproducible sensors with large responsivities and was adapted as a thick film deposition technique for the large-scale commercialisation of metal oxide sensors by AppliedSensor GmbH, Germany, for the automotive industry [52, 53]. Further, the technique is compatible with miniature MOS sensor device fabrication, which uses micro-hotplate technology. This is possible by utilising capillaries for drop coating deposition, helping to fabricate devices with significantly lower power consumption, than the bulky counterparts [52].

Flame spray pyrolysis (FSP) is another method for thick-film deposition, which encompasses spraying liquid precursors, which form a flame [52]. Reaction of the precursors occurs in gas phase with subsequent particle formation. The method has been shown to be compatible with large MOS sensor substrates as well as smaller hotplate based devices and has been reported as having effective control over morphological characteristics, with annealing not required for films which are a few micrometres thick [52].

In contrast to thick-film technology, thin-film technology targets the production of films which are in the low µm range - nm range of thickness and is based on more complex deposition methods such as chemical vapour deposition (CVD) or physical vapour deposition (PVD) such as Aerosol Assisted Chemical Vapour Deposition [54, 55], Atmospheric Pressure Vapour Deposition [33, 56], electron beam evaporation and sputtering [52], amongst others [35, 56, 57], and sensors associated to such materials are termed “second generation” devices [31]. The PVD techniques involve physical processes such as evaporation or sputtering for vapour formation from liquid or solid sources followed by subsequent transport and deposition [58], whereas the CVD process involves the formation of a vapour from a volatile precursor, followed by the transport and chemical reaction of the vapour phases upon a heated surface [59], with both processes resulting in the formation of thin films. Both techniques are particularly complementary to miniature gas sensor devices, as they both commonly used in the semiconductor industry [52].

Sol-gel based techniques are another method of thin film deposition; a method which involves the formation of a colloidal suspension of precursor species, called a sol. Gelation of the sol then allows cross-linking between the precursor species. For the formation of a ceramic film, the sol undergoes evaporation, forming a highly porous xerogel film. Heating the film then causes the formation of a dense ceramic material upon the substrate surface [60].

The key difference between both thick- and thin- film technologies is that thin-films, potentially provide greater control of the gas sensor material and further, are associated to a more automated production process. CVD technology in particular, affords films which are economical, strongly bound and reproducible with low impurity levels and thus in many ways, this is an advantageous technique compared to thick-film technology [56, 61]. However, the dense films produced via thin-film techniques generally suffer from reduced sensing performance compared to their thick-film counterparts [32, 62].

Greater porosity of the gas sensing material, which thick-film technology generally provides, in comparison to thin film technology, is an important requirement as it encourages an augmented material surface area [21] which in-turn implies an increase in the reaction sites for the target analyte on the sensing material [2].

Lee *et al*. [63, 64] had reported that in a thick porous metal oxide (specifically SnO_2) film, fabricated via a metal organic decomposition route, that consisted of loosely interconnected small crystallites, the grain boundaries were present in all directions within the sensor matrix. These crystallites provided significant number of surface sites for the surface reactions to occur. In contrast, they had reported that in a compact SnO_2 thin film, fabricated via Metal Organic Chemical Vapour Deposition (MOCVD), which consisted of a dense columnar structure, only a limited surface area which is exposed to the gas, could contribute to the overall responsivity. Sharma *et al*. [63] resultantly concluded that the responsivity of high surface area porous gas sensors reside in the number of high-resistivity grain boundary point contacts, and that to promote the responsivity of a material, the number of these contact points should be maximised.

Figure 1–5, redrawn and adapted from a review by Sharma *et al*. [63] presents the variation in particle density of a thick screen-printed film in (a) versus a thin-film in (b) and illustrates the extent of gas permeation throughout the sensor matrix. Figure 1–5 (a) shows the advantage of using a thick-film which promotes greater permeation and diffusion of the gaseous reactant and product molecules throughout the sensor matrix, with contact of the gaseous molecules seen to occur with the surface and the bulk of the material. Figure 1–5 (b) shows the limitation of using a thin-film of semiconducting material, which due to its increased density, limits the permeation of the gaseous reactant and product molecules to predominantly the surface of the material.

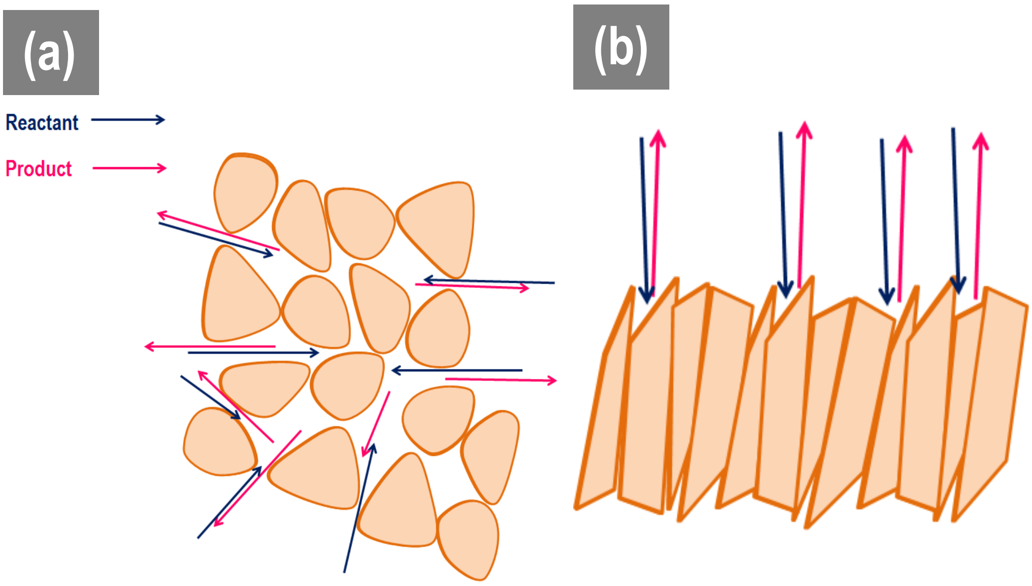

Figure 1–5. Illustration of diffusion/permeation pathway of the gaseous reactants and products in (a) porous metal oxide gas sensing film or where particles in the gas sensing film are loosely packed and (b) in tightly packed metal oxide gas sensing film or where particles are agglomerated together. The blue arrows represent the pathways of gas diffusion of the reactant analyte molecules and the pink presents the pathways of diffusion of the decomposed/oxidised products. {Diagram redrawn and adapted from Sharma *et al*. [63]}.

1.7 Physicals and Chemical Influences on Gas Response

The gas sensor response of a metal oxide is affected by many of its inherent physical and chemical properties, some of which include the microstructure, the acid and basic properties of the metal oxide and the morphology. The impact of these properties on the response characteristics are briefly discussed here.

1.7.1 Microstructural effects

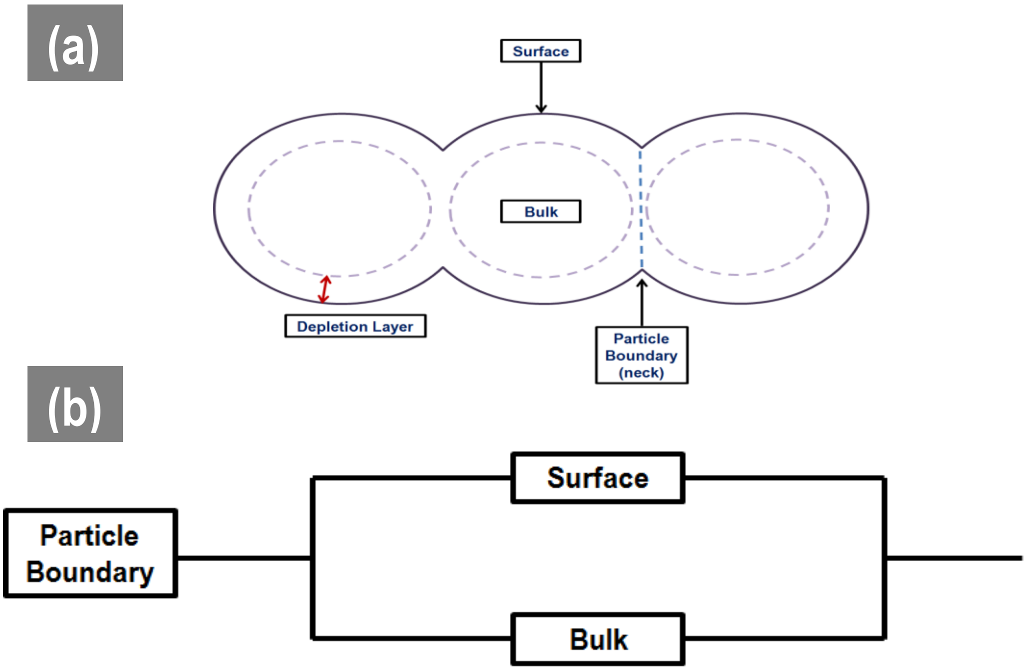

Figure 1–6. (a) The geometry of a solid composed of fused spherical particles, with the three key regions: the surface, the bulk and the particle boundary. The lilac dashed line represents the length to which the surface extends, which is equivalent to the Debye length or the Depletion Layer – (this represents the depth to which electrons are depleted on the surface of the metal oxide, upon surface adsorption of oxygen ions on the surface of the metal oxide) and (b) A network resistor model representing the three key regions of the gas sensitive material: the particle boundary, the surface and the bulk. The model illustrates how each region relates to each other within a solid composed of fused spherical particles {Diagram redrawn and adapted from Naisbitt *et al*. [65]}.

One of the key parameters influencing the responsivity of a sensor is the microstructure of the material, a property associated to the porosity and extent of sintering of the gas sensing material matrix [65]. Williams *et al*. [65, 66] have highlighted, in a number of studies, the importance of the role of microstructure of a gas sensing material on the gas sensor response. They have demonstrated this through comparing the three main regions of the gas sensitive material, which are the surface, the bulk and the particle boundary to a simple model based on a network of three resistors as seen in Figure 1–6 (b) [65].

In this model, the surface and the bulk are in parallel to each other, whilst the particle boundary is in series to both. An assumption of the model is that the accessible surface is the only gas responsive element and therefore it is the only region that can exhibit a change in resistivity upon exposure to the target analyte. Thus from the three regions of the gas responsive element, the surface region which can extend to a size which is equal to the depth of the Debye length (alternatively called the Electron Depletion Layer (EDL) or space charge region)[63], is gas responsive. In contrast, the bulk of the material has an invariant resistance which does not contribute to the responsivity, and therefore is associated to a resistance independent of the concentration of the gas. The net accessible surface (which is gas responsive) is made up of the surface and the particle boundary. The contribution of the particle boundary to the accessible surface is dependent on the extent to which the material is sintered. When sintered, necks between the particles are formed at the particle boundaries; for highly sintered materials, only the outer region of the neck will be gas sensitive, whilst the inner region will not, as it contributes to the bulk. As such, the necks in this situation are practically non-resistive, implying that the electrons need to surmount a lower energy barrier to move through the highly sintered grains. For less sintered materials, the whole of the neck will be considered as contributing to the surface, and thus it is gas sensitive. In such a case, the necks are associated to larger energy barriers that the electrons need to overcome. For materials where the particles are barely touching, a Schottky barrier may exist between the particles. The second situation is generally the case for practical MOS sensors. If both the neck and the surface are responsive as per the second case, then they are both contributory to the net responsivity of the material. If the responsivities of the surface and the neck are equivalent, then both the surface and the neck will be in series to each other in the circuit.

In contrast, the as-drawn diagram illustrating the parallel arrangement of the surface and bulk regions in Figure 1–6(b), suggests that only the surface is contributory however, changing the magnitude of one region, will still lead to a change of the other. This model therefore exemplifies the importance of the role of the surface and the particle boundary of the gas sensitive material in gas response. Apart from sintering, the network resistor model can also be applied for effects like agglomeration, where loose agglomeration and dense agglomeration are likely to behave in similar way to loosely sintered and heavily sintered materials [67].

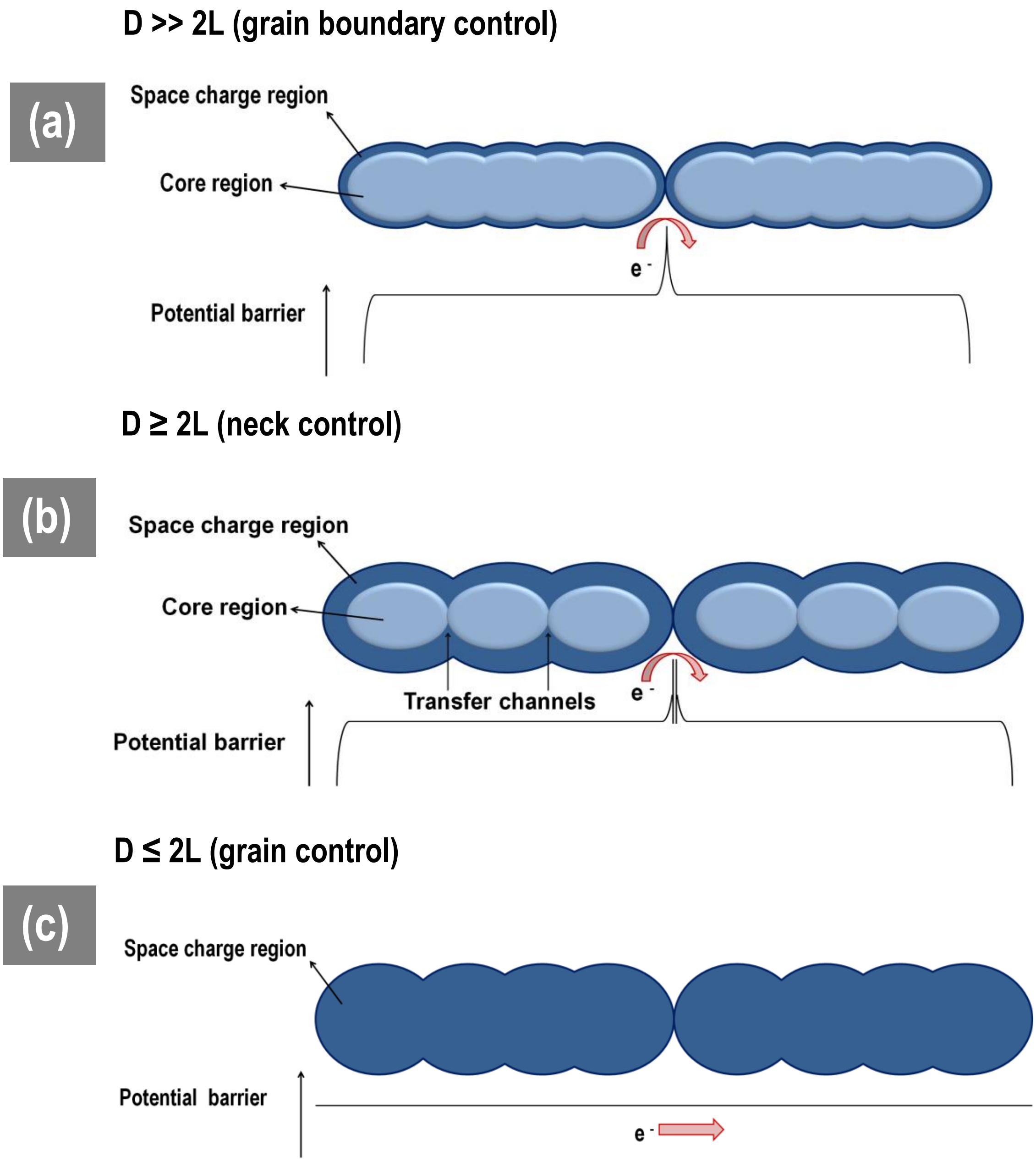

Figure 1–7. Models illustrating the crystallite size effects and their determination of the element controlling the responsivity. In (a), the crystallite size is siginificantly larger than twice the Debye length and the responsivity Is grain boundary controlled. In (b), the crystalite size is similar to the twice the Debye length and the responsivity is neck controlled and in (c), the crystallite size is much smaller than twice the size of the Debye layer, and so the responsivity is grain controlled. {Diagram redrawn and adapted from Sharma *et al*. [63]}.

Grain boundary contributions to the overall responsivity of a material, are particularly size dependent. Xu *et al*. [63, 68] had proposed schematic models, consisting of a chain of crystallites to address what governed the gas responsivity of their porous SnO_2 based semiconductor sensors. The group had come up with three models [68] which have been redrawn and adapted from Sharma *et al.* [63] and presented in Figure 1–7. Xu *et al*. had suggested that when the size of the crystallite (D) was larger than twice the size of the Debye layer (L), then the grain boundary contacts were attributed to the highest resistance and the gas sensing materials were grain boundary controlled as observed in Figure 1–7(a). At this stage the size of the particles are very large and therefore the surface: bulk ratio is very small. As the size of the grain (D) reduces and become equivalent to twice the size of the Debye layer (L), then the necks become more resistant and therefore they dominate the gas responsivity as observed in Figure 1–7(b). The extent of contribution of the neck to the overall responsivity is then determined by the extent of sintering. Finally if the size of the grain (D) becomes significant smaller than twice the size of the Debye layer (L), then the grain themselves become the most resistive and gas responsivity is controlled by the grains as seen in Figure 1–7 (c). This latter model is associated to the highest response of all three models because very small grains are thought to be associated to a very large surface : bulk contributions and as such thought to be associated to no bulk region, and therefore the whole of the grain is thought to contribute to the surface region [12]. This model therefore illustrates the size effects of grains on the responsivity of the materials, with smaller sized particles attributed to largest responsivities.

1.7.2 Acidic/Basic nature of metal oxides

The acidic or basic nature of the metal oxide is another factor that can affect the response properties of a metal oxide; this is through a direct impact on the nature of the oxygen species of the oxide. The oxygen species on the surface, depending on the pH of the metal oxide, can play a role to influence the catalytic decomposition pathway of the target analyte. The catalytic decomposition pathway of such metal oxides is usually demonstrated in literature with ethanol as a popular example analyte [69]. The decomposition of ethanol has been described to undertake a dehydrogenation reaction upon a basic metal oxide, resulting in the formation of acetal and hydrogen as the intermediates as seen in Equation 1–1.

Equation 1–1

$$2C_2H_5OH \rightarrow 2C_2H_4O + H_2$$

In contrast, the decomposition of the ethanol on an acidic oxide undergoes a dehydration reaction to ethene and water as seen in Equation 1–2.

Equation 1–2 $$C_2H_5OH \rightarrow C_2H_4 + H_2O$$

In either case, the intermediates further breakdown into CO, CO_2 and H_2O. Xu *et al*. [69] have reported on the alcohol sensing mechanism of ZnO based sensors, and have interpreted the responsiveness of ZnO which is a basic oxide, to be dependent on the conversion ratio of ethanol to acetal. The group report that ZnO is actually more responsive to acetal, which is what makes ZnO a solid choice for ethanol sensing. This shows that the acidic or basic nature of a metal oxide determines the responsivity of the metal oxide towards a particular analyte. It has also been reported that responsivity to acidic gases such as H_2S or basic gases such as NH_3, can be increased by incorporation of a corresponding acidic or basic oxide, respectively, forming adsorption sites for the gases [22]. Metal oxides such as WO_3 can also act as acid or base catalysts, with brief details of its catalytic nature presented further in section 1.8.3.

1.7.3 Morphological effects

The morphology of a material is associated to the size and shape of the particles within the metal oxide material, which together control the overall surface area of contact with the target analyte. The smaller a particle and the greater the number of dimensions it has, the larger number of surface sites the material has for the surface induced oxidation reactions, and as such this can lead to an enhanced responsivity of the gas sensing materials, as opposed to a material having much larger particles with lower dimensions. Chapter 6, section 6.1 alludes to the various morphologies of ZnO that have been researched and developed, giving an idea of the variety of morphologies that have potential in gas sensing applications. Korotchenkov [70] has reported that various studies show that the development of high surface area materials can lead to the development of highly responsive metal oxide gas sensors. However, such materials do suffer from a disadvantage of low temporal and thermal stability [70], leading to significant sintering of the particles. This results in a decrease in porosity and thus a reduced number of surface sites, for analyte interaction; this then relates back to the microstructural effects on the gas sensing properties, and as such the morphology and microstructure are inter-related. A more detailed study on the effects of morphology on the gas sensor response has been discussed in Chapter 6.

1.8 Metal Oxides of Interest

A host of metal oxide materials are used for MOS technology, with examples being n-type ZnO, WO_3, SnO_2, In_2O_3, γ-Fe_2O_3 and p-type Cr_2O_3, CTO, CuO [71-73] and Co_3O_4. Some of the metal oxides given here are those which have been reported to exhibit significant gas responsivity. However due to issues of stability, In_2O_3, SnO_2 and WO_3 have been mainly adopted as materials for practical applications [74].

Despite the stability and responsivity of the metal oxides as single component materials, sensitizers are usually added to them in the form of noble metal oxide nanoparticles, metal oxide nanoparticles, a second metal oxide powder or a binder. These are added to enhance the responsivity characteristics of the base metal oxide and the selectivity, as explained further in section 1.9. Sensitizer materials are all called foreign and antenna materials [74, 75] and are added to be able to optimize a combination of both the receptor and the transduction function. Very established examples of such systems are the SnO_2 doped Pt and a combination of SnO_2-PdO which are well-known combinations for effective CO and hydrocarbon sensing [74]. Other examples of sensitized metal oxide gas sensing materials are Au- and Pt- WO_3 for NH_3 sensing [74, 75], CuO-SnO_2 for H_2S sensing [74, 75], SnO_2-Co_3O_4 for CO sensing, SnO2-AgO for H_2 sensing, In_2O_3-PdO for CO and odorant gases, SnO_2-La_2O_3-Pt and SnO_2-CaO for ethanol sensing, SnO_2-Fe_2O_3 for NO_2 sensing, amongst a whole host of other combinations [74]. Some of these sensitizers such as Pt, PdO, AgO_2 and CuO are examples of oxidising catalysts for reducing gases [74] and as such the catalytic activity of these sensitizers contributes to their overall antenna / sensitizing effect.

The next part of this section will give a brief introduction to the semiconducting metal oxides that are specifically of interest to this thesis. These are ZnO, SnO_2, WO_3 and CTO, with specific advantages of these metal oxides as gas sensing materials, highlighted.

1.8.1 Zinc Oxide (ZnO)

ZnO is an n-type semiconducting oxide, with a direct band gap 3.37 eV – 3.44 eV [76, 77] at room temperature, known to be associated to three crystal structures: hexagonal wurtzite, cubic zinc blende and cubic rock-salt (which is rarely observed) [76, 78, 79]. The hexagonal wurtzite phase is the most thermodynamically stable form, under ambient conditions, in which the Zn^{2+} and O^{2-} ions are tetrahedrally co-ordinated [76, 78-80] as observed in Figure 1–8.

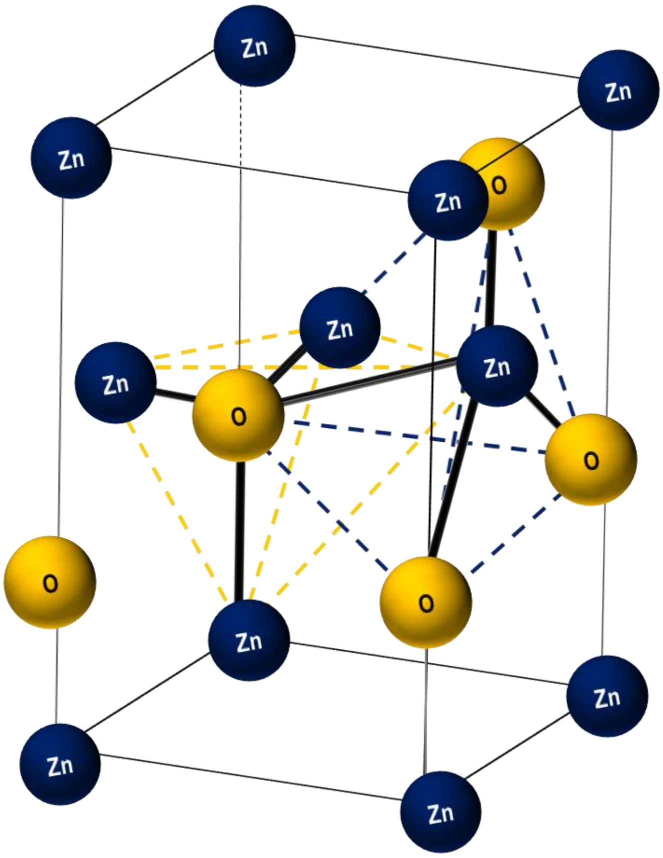

Figure 1–8. Hexagonal wurtzite ZnO crystal structure in which Zn^{2+} ions (represented as Zn) and O^{2-} ions (represented as O) are tetrahedrally co-ordinated. {Diagram redrawn and adapted from Ozgur *et al*. [78] and [80]}.

The electrical, optical and thermal properties specific to ZnO have made it attractive for an system of applications [76]. For example, it is used in the pigments industry due to its high refractive index [76, 81] and its high temperature stability, making it suitable for incorporation into ceramics [76]. Further, the incorporation of ZnO into various clinical products is also well-established, due to its antimicrobial properties [76, 82].

The response and variation of the metal oxide's electrical resistance to various gases, makes it a prime candidate for gas sensing applications [76]. Further, ZnO has been associated to adopting a variety of morphological architectures. In particular, in terms of 1D nanostructures, it is one of the most popular oxides studied [76, 79, 83, 84]. A host of examples of ZnO based 1D nanostructures has been given in Chapter 6, section. 6.1. The ability to adopt an system of high surface area morphological architectures is a key advantage for gas sensing applications, in which the contribution of surface is the most influential on the overall response properties.

ZnO is one of the most investigated gas sensing materials alongside SnO_2 [18] and its nanostructured forms in particular, have been reported by various studies to be successful for the detection of both oxidising and reducing gases which include: NO_2 [85], ethanol [69], and acetone [86] amongst a range of other gases [18, 79]. Doping of the metal oxide with metals such as Aluminium [18, 87], Indium and Gallium [18, 88] has been observed to effect an enhancement in the response properties of ZnO towards NH_3 and amine based gaseous species e.g. trimethylamine.

Apart from its predominance in nanostructured materials gas sensor research, ZnO has been reported as popular in the application of hetero-structure based systems [18] with popular examples in the literature being ZnO-CuO systems [89, 90] and ZnO-SnO_2 systems [91-93].

1.8.2 Tin Oxide (SnO_2)

SnO_2 is another n-type semiconducting metal oxide, with a band gap of 3.6 eV [94], which adopts a tetragonal rutile crystal structure in which the Sn^{2+} ions are six-fold co-ordinated to three-fold co-ordinated O^{2-} ions [94, 95] as observed in Figure 1–9.

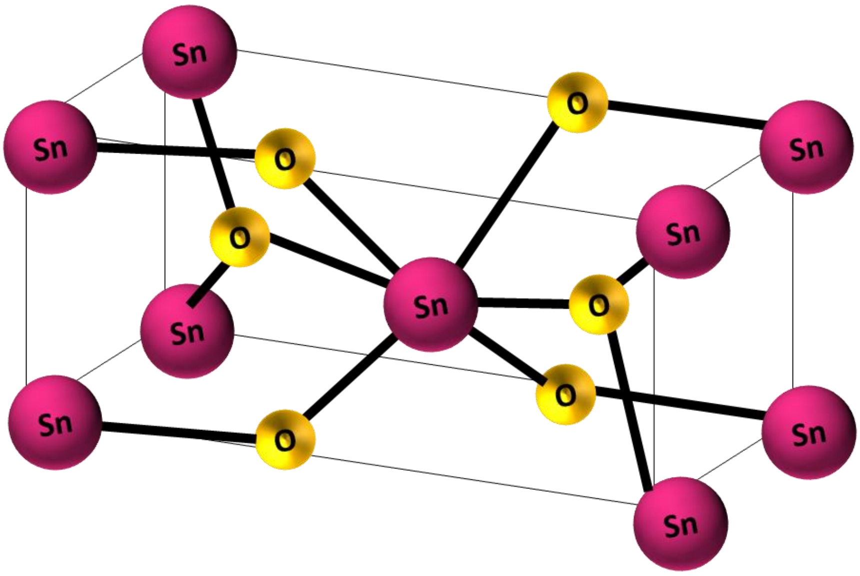

Figure 1–9. Tetragonal SnO_2 crystal structure in which Sn^{2+} ions (represented as Sn) are six-fold co-ordinated to three-fold O^{2-} (represented as O) ions. {Diagram redrawn and adapted from [95]}.

The metal oxide is particularly well known for three major applications, which include optoelectronic applications, heterogeneous catalysis and solid-state sensing [94]. The electrical conductivity and optical transparency of the metal oxide, make it a prime candidate as Transparent Conducting Oxides (TCOs) for optoelectronic applications such as liquid crystal displays (LCDs), plasma display panels and light emitting diodes (LEDs) [94, 96-98].

SnO_2 is the most utilized semiconducting metal oxide of all metal oxides for MOS gas sensing [18, 94] since it was the first metal oxide to be patented by Taguchi as a chemiresistive gas detecting device in the early 70s [13, 20]. SnO_2 has been reported as a popular choice towards the detection of mainly reducing combustible and poisonous gases such as CH_4 and CO respectively [99, 100], amongst a range of other inflammable and toxic types such as LPG, ethanol and CO_2 [101]. The metal oxide is associated to low baseline resistances and stability, making it an established choice for a MOS based gas sensor.

1.8.3 Tungsten Oxide (WO_3)

WO_3 has been shown in the literature as a versatile wide band gap n-type semiconducting metal oxide, possessing a band gap value of 2.62 eV at room temperature, when in the monoclinic bulk form[102]. The metal oxide with the crystals of the metal oxide generally formed by WO_6 octahedra which share the corner and edges [102] as seen in Figure 1–10.

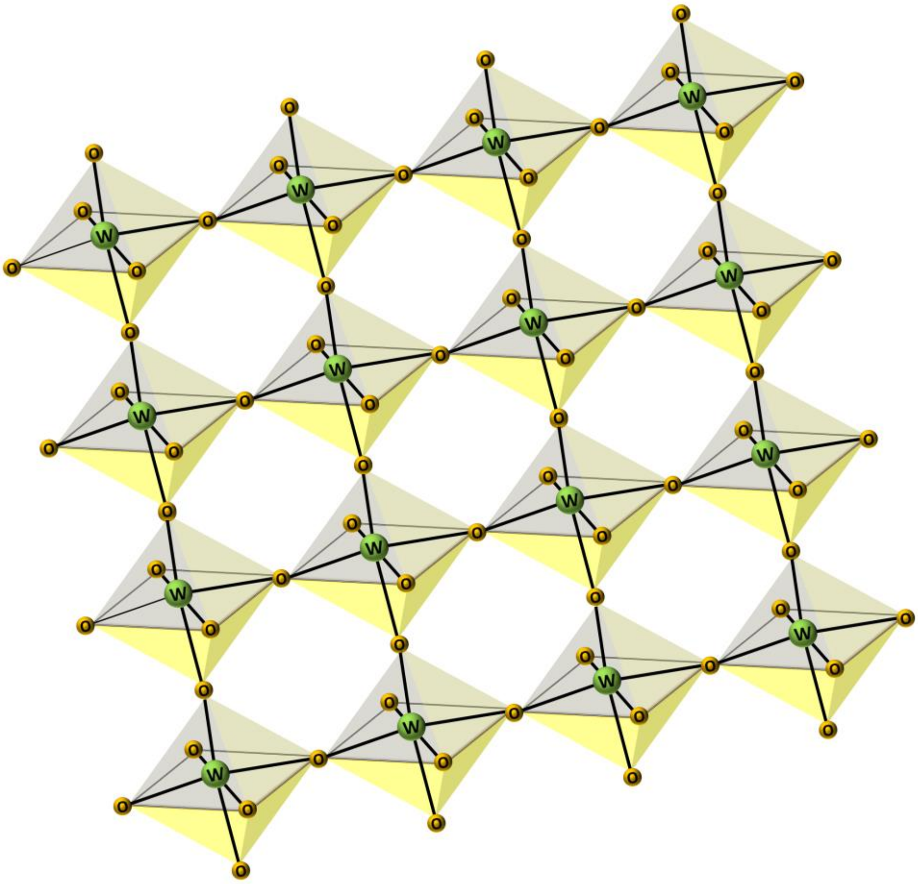

Figure 1–10. Crystal structure of WO_3 showing corner sharing WO_6 octahedra. {Diagram redrawn and adapted from Zheng *et al*. [102]}

The crystal phase of WO_3 is reported to change with temperature, with the most important ones between room temperature and higher temperatures of 800 °C being the monoclinic phase (γ-WO_3) obtained between 17 °C – 330 °C and orthorhombic phase (β-WO_3) adopted at higher operating temperatures of 330 °C – 740 °C [102].

An assortment of applications of this metal oxide have been reported in the literature, which include photocatalysis [103, 104], electrochromic and photochromic coatings [105], and solid-state gas sensing [54, 106, 107].

WO_3 is the key semiconducting metal oxide, with both its thick and thin films known for their sensing properties of NO_2 [18, 23, 38, 55, 108-110]. Further it has been reported as a particularly attractive metal oxide semiconductor, as it is contributes to catalytic oxidation and reduction reactions, by acting as a solid acid/alkaline catalyst and such provides Bronsted or Lewis acid/base sites (i.e. H^+/OH^- species) or a combination of both upon which oxidation or reduction catalysis can occur [111, 112].

In particular for NO_x compounds, pure WO_3 has outstanding sensitivity at both low and more elevated temperatures [18]. WO_3 has also been reported as an established candidate for sensing O_3, CO, H_2S [17, 18, 113] and is also a promising metal oxide as it exhibits less cross-sensitivity at low operating temperatures, than other metal oxides [18]. When doped with noble or transition metals such as copper and vanadium, WO_3 has been observed to be an effective sensor candidate for NH_3 and amine based analytes [18, 114, 115].

1.8.4 Chromium Titanium Oxide (CTO = $Cr_{2-x}Ti_xO_3$)

CTO ($Cr_{2-x}Ti_xO_3$, where x = 0.05 – 0.4), which is also called titanium substituted chromium oxide, was the first p-type gas sensitive material to be commercialised by City Technology. [116]. CTO is a solid solution of TiO_2 in Cr_2O_3, which can occur due to the very similar ionic radii (0.060 ±0.001 nm) of both Cr^{3+} and Ti^{4+} species [48, 117, 118]. Thus, the crystal structure adopted by CTO is analogous to Cr_2O_3, the latter of which is presented Figure 1–11, with compounds adopting a corundum (Al_2O_3) crystal structure which consists of layers of distorted hexagonally closed packed O^{2-} ions with the Cr^{3+} ions occupying two-thirds of the octahedral holes [47, 48, 116, 119-121].

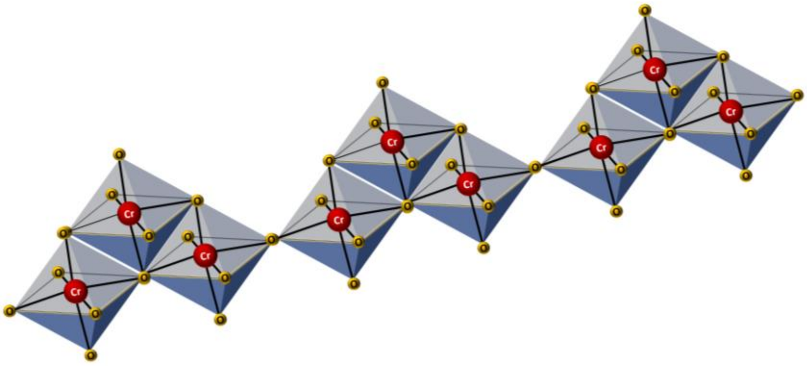

Figure 1–11. Layer of corundum crystal structure of Cr_2O_3, with hexagonally closed packed O^{2-} ions (represented as O) in octahedral co-ordination with Cr^{3+} ion (represented as Cr). {Diagram redrawn and adapted from [121]}.

In comparison to SnO_2, CTO has been associated to various advantages which include baseline stability, negligible humidity interference and selectivity [116]. The lower humidity interference and therefore greater baseline stability of this material, is due to its p-type nature and the reasoning behind this, has been presented in significant detail in Chapter 5. CTO has been reported in the literature to be prepared via two key methods which are either by a high temperature solid-state reaction route between Cr_2O_3 and TiO_2 [47, 120, 122] or via a sol-gel route method [116, 117]. The former poses an advantage as a commercially attractive method. However, is also associated to negative factors that can impact the gas sensing properties. These disadvantages are poor chemical homogeneity, introduction of chemical impurities and poor microstructural control during the sintering stage of fabrication. The latter method in contrast is reported to be an ideal way to control particle size, shape and sample purity [116]. Apart from these two methods of CTO fabrication for thick film devices, emerging methods for thin film devices of the material such as electrostatic spray assisted vapour deposition by Du *et al*. [123] and Atmospheric Pressure Chemical Vapour Deposition (APCVD) by Shaw *et al*. [124] have also been reported in the literature.

Niemeyer [125] reported that the addition of TiO_2 to Cr_2O_3 reduced the conductivity of the material by reducing the Cr (VI) acceptor state (empty Cr 3d states) density of the surface region. A high density of Cr (VI) surface accepter states in the surface region, results in very little variation in the conductivity of the material. This is because when oxygen adsorbs on the surface of the metal oxide, it also acts as a surface accepter state and therefore the net responsivity of the surface to the variation in the surface acceptor state density is minimal, implying minimal response to a variation in surface oxygen concentration [125]. Given that oxygen is primarily responsible for the gas sensing transduction function, a significant response to a variation in its concentration needs to be induced, to achieve effective responses. Ti substitution, enhanced by its surface segregation, can induce effective responses by decreasing the surface concentration of the Cr (VI) acceptor state density. This reduction resultantly increases the resistance of the material, inducing a greater response of the material upon adsorption of oxygen acceptor states on the surface i.e. a variation of the surface oxygen concentration [125]. Apart from its presence on the surface, the presence of Ti^{4+} ions in the bulk implies it also decreases the bulk acceptor state density, hence decreasing the conductivity of the bulk region. Since the bulk contributes to limiting the gas sensing performance, in contrast to the surface, then a decrease in the bulk acceptor states acts to enhance the gas sensing performance of the material [125]. This decrease of the overall conductivity of the CTO material, particularly at the surface, by the substitution of Ti^{4+} as well as the surface segregation of Ti^{4+}, are said to control the gas sensing behaviour and show that the addition of Ti^{4+} ions to the matrix of Cr_2O_3 has a particularly advantageous and influential effect on the overall gas sensing properties of CTO [125].

CTO has been reported successful for the detection of reducing gases such as ethanol [116, 124, 126], acetone [127], NH_3 [48, 122, 128, 129], H_2S [130], CO [130] and very recently a report on the responsivity of CTO towards NO_2 [120] has been reported.

1.9 New Materials in Metal Oxide Gas Sensing

Currently significant research is being carried out to investigate novel gas sensing materials for MOS technology, which may potentially help to enhance the responsivity and selectivity associated to these sensing devices. A few examples of such material systems include nanostructured metal oxides [19, 35], metal oxides with noble nanoparticles [54, 72], complex oxides [131-135] and metal oxide based composites [45, 89, 91, 92, 136]. In particular, it is both the former and the latter, that this thesis will focus on; namely metal oxide based composite materials and metal oxide based nanomaterials for MOS gas sensing technology.

Section 1.8 alluded to some of the sensitized metal oxide systems that use catalytic metal dopants and other minority metal oxide dopants, as established and conventional ways for improving responsivity and selectivity. Apart from the use of catalysts and promoters or more surface specific additives as a method of improving responsivity and selectivity, another method includes the use of filters or chromatographic columns to discriminate between gases on the basis of molecular size or other physical properties [137]. One example of such a route includes the use of zeolites as catalytic filter layers, which are deposited on top of the metal oxide of interest [23, 138, 139]. Such zeolitic layers are thought to take part in the catalytic breakdown of certain gaseous analytes in a mixed analyte atmosphere, and as such make the sensor device selectively response to a particular gas. Alternatively, the zeolites take part in the catalytic conversion of a target analyte to a by-product which the sensor device is more likely to be responsive too, in comparison to its response towards the target gas. A third method of improving selectivity is changes in the analyte concentration and the sensor operating temperature, in particular temperature modulation is a very effective method [137]. Lee has reported that the simplest way to observe temperature-dependent dynamic sensor response is to switch the sensor power supply on and off, in the presence or absence of gas. Such an approach he has reported, was adopted by Hiranaka *et al*. [137, 140] on Taguchi type Figaro SnO_2 sensors. The group had exposed sensors pre-heated to a temperature corresponding to 5 V, and then switched off the power and the sensor response monitored over a period of 60 seconds. The resulted in a transient response in which the sensor peaked at a time characteristic of the analyte gas and to a lesser degree, its concentration. In this way the group demonstrated the possibility for a sensor device to distinguish between different target analytes [137]. Another method to improve the responsivity and selectivity is through the physical preparation of the sensor material [137], varying for example the morphological and microstructural characteristics for example the development of technologies for the development of vast of nanomaterials, which have an enhanced surface area, ideal for MOS sensor technology.

The research and development of nanomaterials for metal oxide gas sensing is a well-established line of research [1, 2, 19, 141]. The advantage of a reduced crystallite size has been highlighted in the previous section (1.7) and therefore the prime reason for the research and development of nanomaterials for metal oxide gas sensing application has been established. Further, the larger surface to bulk ratios in nanomaterials, makes it clear that the yield of surface reactions are enhanced compared to larger particle sizes. In this thesis, the specific aim in the research study of nanomaterials (specifically ZnO nanomaterials), is the demonstration of the emerging synthetic routes, in particular Continuous Hydrothermal Flow Synthesis (CHFS) [142, 143], as successful for the fabrication for nanostructured metal oxides. Further the aim is to demonstrate the potential these nanostructured materials hold for MOS gas sensing applications. As such, a detailed introduction to this unique part of the thesis has been presented in Chapter 6, which discusses the nanomaterial research investigation.

Since the main focus of the research presented here however, is on hetero-junction based materials systems, the next two sections will give a brief introduction to such systems as well as a brief introduction on the theoretical and qualitative basis behind the utilisation of such materials in gas sensing applications.

1.9.1 Mixed Metal Oxide Gas Sensors

The utilisation of gas sensitive materials based on semiconducting metal oxide mixtures in the solid state gas sensing field is a relatively fresh trend of research and development [36]. Intensive studies into these materials is based on the knowledge that a multiple number of desired parameters in semiconducting metal oxide materials exist, with catalytic activity, large sensitivity, effective adsorption ability and thermodynamic stability being just some examples. However, difficulty lies in attempting to find all these benefits in a single oxide [45]. The fabrication and utilisation of mixed metal oxides can potentially lead to novel materials which encompass many of these desired properties required in a gas sensor and thus lead to enhanced sensitivities and selectivities towards the target analyte(s) [24, 36, 144-147].

In a recent article by Kaciulis *et al*. [148] it was reported that one of the aims of using a mixed metal oxide system in gas sensing technology, is improvement in the gas selectivity through a combination of the catalytic properties of some oxides with the effective sensitivity of other oxides. Wang *et al*. [45], also reported various studies on binary oxide materials as sensitive materials in gas sensing applications, one example being a ZnO-SnO_2 system fabricated through a mechanical mixture of the individual oxides [91]. This system was generally attributed to significantly higher responses towards 1-butanol gas, than sensors made from the individual components alone. The synergistic coupling of SnO_2 as a dehydrogenator of butanol to butanal and ZnO as an effective catalyst for the breakdown of butanal, was considered to be the reason behind the effectiveness of this system.

A large number of groups, some of them cited here [144, 148, 149], have established that mixed oxide systems can be classified into three different groups [149]. These are as either compounds, as solid solutions or as neither of the first two. An example of the first is the ZnO-SnO_2 system mentioned previously, forming compounds such $ZnSnO_3$ and Zn_2SnO_4, which have been shown to be candidates for ethanol and hydrogen detection [144, 149-151]. An example of a solid solution system is TiO_2-SnO_2 system reported by Radecka *et al*. [149, 152] who investigated this system for the detection of hydrogen gas. The final group is one where neither compounds nor solid solutions are formed, an example being a TiO_2-WO_3 system reported by Zhu *et al*. [153] for the detection of benzene, toluene and xylene (BTX) [154]. Such systems contain an intimate mixture of metal oxides which are interacting with each other potentially via weak Van der Waals forces of interaction, and thus this implies that there is no strong chemical bonding between the individual components [155]. Interestingly Trakhtenberg *et al*. [144] suggest that only systems in this latter category of the three, can actually be regarded as composite materials.

One of the key factors determining the particular type of mixed oxide system formed is the corresponding fabrication method and preparation conditions [148, 155] via which the mixed oxide system is made. This implies that the preparation method plays a very influential role in determining the type and strength of interactions formed between the individual components in the mixed oxide material. Reddy *et al*. [155] for example, report that a mixed oxide material consisting of TiO_2 and ZrO_2 can be formed by physically mixing the individual components together, which results in a weak Van der Waals force of interaction or they can be formed such that chemical bonds are established between the individual components, in the form of Ti-O-Zr linkages. The existence of chemical bonding between the components, leads to a mixed oxide system which has very different physiochemical and reactivity properties in comparison to a system made by simple mechanical mixing of the two components [148, 155]. This therefore demonstrates that the preparation method and the conditions employed during fabrication of the mixed oxide system, can result in very different mixed oxide materials which may constitute the same individual components, but are so different due to the extent of interaction that exists between the individual metal oxide components within the system. Further, it implies that solid solutions and compounds which are associated to strong chemical interactions of the components, may lead to nicer dispersion of the individual oxides in the mixed oxide system. In contrast mechanical mixtures would constitute an uneven distribution or polarisation of the individual components in the mixture, as they are associated to very weak forces of interaction [155]. Apart from influencing the chemical nature of the mixed oxide system formed, the fabrication method equally plays an important role in controlling the overall microstructure of a gas sensitive material. As mentioned earlier, the microstructure of gas sensitive materials contributes significantly to their responsivity and therefore differing fabrication and deposition methods of single and mixed oxide compounds such as screen-printing, sol-gel, CVD, PVD e.g. sputtering [144, 148] can ultimately lead to very different gas sensitive materials.

A more theoretical approach of the enhancement effect of binary mixed oxide materials has been reported by Zakrzewska [149], among other research groups [156], who report that the formation of mixed oxides modifies the electronic structure of the bulk and the surface components of the system. The former includes the band gap, the position of the Fermi level and transport properties; and such properties are affected mainly in compound and solid solution phases of mixed oxide systems. The surface component of the system, is affected in all phases of mixed oxide systems, and is expected to be influenced by new boundaries between grains constituting different chemical composition. All of these factors are expected to contribute positively towards the gas sensing characteristics and in particular, it is the boundaries that exist between the grains of the semiconducting oxide materials of different chemical composition, which are reported as the basis of the enhancement of utilising composite systems in gas sensing [18] in a number of sources of literature.

This boundary enhancement effect is termed hetero-junction enhancement or hetero-contact enhancement. Hetero-junction enhancement in composite sensors has been reported in a number of literature reports [75, 156, 157]. The following section will give a brief introduction about the theory of hetero-junctions and their role in gas sensing applications.

1.9.2 Hetero-junctions

Junctions are fundamental to all composite systems and are usually classified as either being graded or abrupt. Graded junctions are those attributed to a gradual change of composition over macroscopic dimensions. Examples of where graded junctions occur are during a film growth process where a change in composition of the film occurs or an change in composition through the occurrence of inter-diffusion or homogenous mixing at high temperatures in processes such as alloying [158]. Abrupt junctions in contrast, are those where a change in property occurs over a distance that is comparable to or less than the width of the space-charge region [158, 159]. In regular semiconductors, according to Schubert, the chemical transition from one semiconductor to another semiconductor is abrupt, suggesting that in general, most junctions formed are abrupt [160]. Another classification that junctions can be subdivided into, are homo-junctions and hetero-junctions. The former exists at the interface of the same semiconductor material or alternatively, this can be rephrased as an interface where the same band gap exists at both of sides of the interface. A difference that can exist on either side of the homo-junction is a difference in doping; where the material exists as a n-type semiconductor on one side of the junction and as a p-type semiconductor on the other side of the junction; an example could be the interface between n-TiO_2 and p-TiO_2 [161, 162].

The hetero-junction in contrast, exists at the interface between two very different semiconductor materials, i.e. those which have different band gaps, and therefore different work functions from each other. It is this latter category which is of importance to this thesis; as the experimental investigations, have focussed upon bringing two very different semiconducting oxides together and characterising their gas sensing properties. A further sub-classification exists within the group of hetero-junctions in the form of isotype and anisotype junctions. The isotype is the interface between two p-type or two n-type semiconductors [163], whilst anisotype is the interface between an n-type and a p-type semiconductor; this thesis presents investigations into both types of systems.

It has been widely stated in a number of sources of literature that when two solids, which have different work functions, are brought into contact, the Fermi level of the two solids must be in thermal equilibrium. This equilibrium state is reached when the electrons from the material with the lower work function flow to the adjacent material, until the Fermi levels equilibrate [164]. Zakrzewska [149] reports that it is believed that this equilibration of the Fermi levels through a mixed oxide semiconductor is responsible for the associated electrical and gas-response properties, although he does not report on how the gas sensing enhancement effect actually occurs. However his report on the equilibration of the Fermi levels has been justified in a number of different sources, of which Figure 1–12 {Diagram redrawn and adapted from Wager [163] , van der Krol *et al.* [165] and Roy [166]} is one example illustration.

Figure 1–12 (ai) and (aii) present band diagrams for an ideal abrupt n-n hetero-junction and (bi) and (bii) present band diagrams for an ideal p-n hetero-junction. Figure 1–12 (ai) and (bi) are the band diagrams between two n-type and a p-type and n-type semiconductors prior to intimate contact, respectively. Figure 1–12 (aii) and (bii) are the band diagrams after the corresponding two semiconductors are in intimate contact.

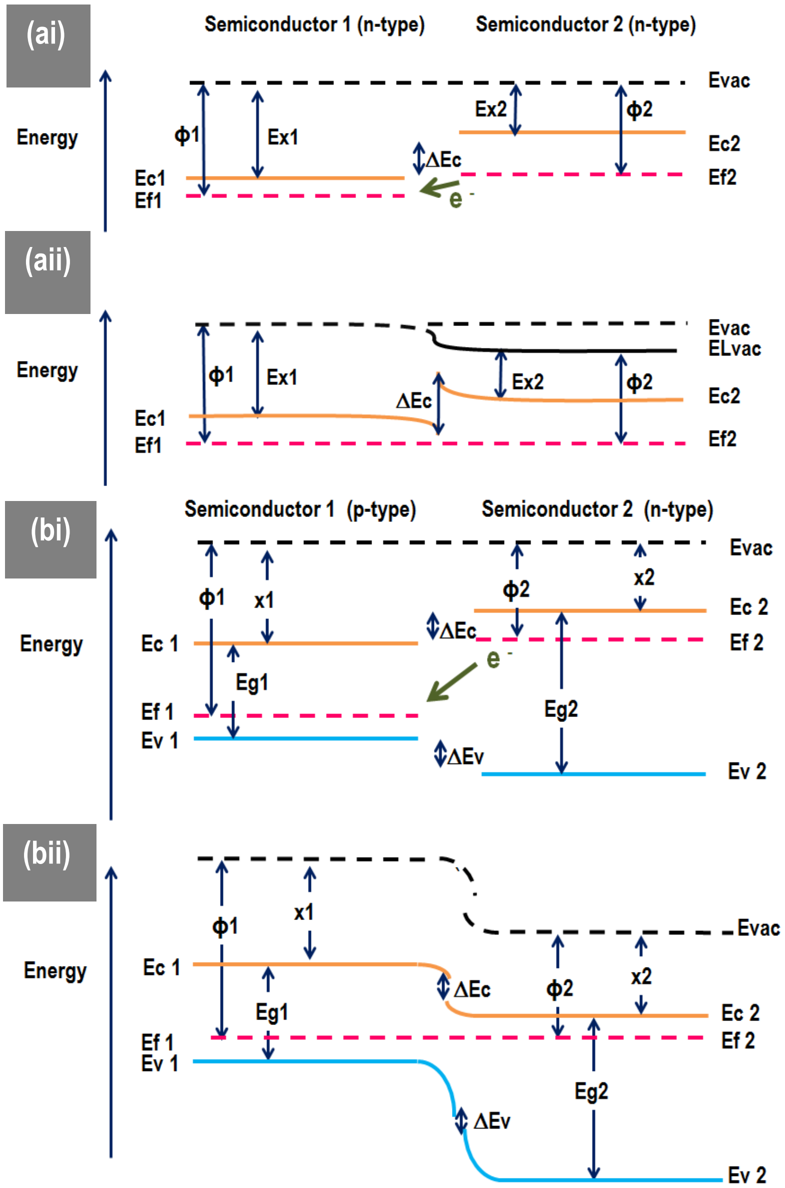

Figure 1–12. Energy band diagram for (ai) two isolated n-type semiconductors (valence band not shown) with $\phi2 < \phi1$ and (aii) the corresponding hetero-junction band structure for an ideal n-n interface (i.e. when the charge carrier exchange occurs through Fermi level alignment) & (bi) isolated p-type and n-type semiconductor with $\phi2 < \phi1$ and (bii) the corresponding hetero-junction band structure for a p-n interface.In the diagram, ϕ1 and ϕ2 represent the work-functions, Ec1 and Ec2 represent the conduction bands, Ev1 and Ev2, Eg1 and Eg2 represent the band gaps, Ef1 and Ef2 represent the Fermi energy levels and Ex1 and Ex2 represent the electron affinities of semiconductors 1 and 2 respectively, Evac is the vacuum level, ELvac is the local vacuum level and ΔEc is the conduction band discontinuity and ΔEv is the valence band discontinuity. {Diagram (ai) and (aii) redrawn and adapted from Wager [163] and diagram (bi) and (bii) redrawn and adapted from van der Krol *et al*. [165] and Roy [166]}.

It can be seen from Figure 1–12 that electron flow occurs from semiconductor 2, which has the lower work function, to semiconductor 1, which has the higher work function, until the equilibration of the Fermi levels of both solids has occurred, when the two component n-type oxides are in contact with each other. Such a hetero-junction is commonly termed an n-n type junction or interface. This illustrates that Fermi levels equilibrate as a result of the local exchange of charge carriers i.e. electrons or holes [167]. The energy bands of both semiconductors bend upon contact of the two materials, because the exchange of charge carriers that occurs during the Fermi level equilibration, causes the energies of these charge carriers to change, resulting in curvature to the energy diagram at the interface [163, 167]. The negative curvature of the conduction band in semiconductor 1 indicates the transfer of the negative charge from semiconductor 2 to semiconductor 1.

Roy, [166] explained that bringing together semiconductors of different energy gaps and work-functions results in the energy band discontinuities at the interfacial region due to the alignment of the Fermi level to achieve thermal equilibrium.

The phenomenon of Fermi level equilibration, upon contact of two differing semiconducting oxides, has also been reported in a recent publication by Zeng *et al*. [168]. Here the group reported on the enhanced gas sensing properties of SnO_2 nanosphere functionalised TiO_2 nanobelts towards various VOCs such as methanol, ethanol, formaldehyde and acetone and compared the gas sensing characteristics of this hybrid oxide system, to pure TiO_2 nanobelts. In this study, they had reiterated like most other sources of literature, the phenomenon of Fermi level equilibration upon contact of the two different n-type oxides. As mentioned earlier, for pure n-type semiconducting oxides, adsorption of O_2 molecules occurs on the surface of the gas sensitive oxide in the form of various anionic species, through extraction of electrons from the conduction band and subsequent trapping of the electrons on the surface of the material. This process causes the formation of a space-charge region – a zone which is depleted of electrons. Subsequent reaction of the adsorbed oxygen species on the surface of the gas sensitive material, with reducing gases will release electrons back into the space-charge layer and decrease its thickness. Release of electrons back into the bulk of the material also implies an increase in conductivity of the gas sensitive material. In the case of the hybrid system Zeng *et al*. explain that additional to the depletion layer that forms at the surface of both the oxides individually, further depletions occur at the interface between the SnO_2 nanospheres and the TiO_2 nanobelts, upon alignment of the Fermi levels between both oxides, due to significant adsorption of oxygen species at this interfacial region. The adsorption of the oxygen species at the interfacial region promotes, easier injection of electrons to the conduction band through thermally induced charge transfer, enhancing the conductivity of the hybrid oxides in an atmosphere of VOCs. This suggests that these additional depletions in the interfacial region, are critical in contributing to the enhancement of the gas response properties of these hybrid materials, in comparison to the pure metal oxides. The group conclude that the contact regions between both semiconducting oxides, play a critical role in inducing more active gas reactions and improving the response properties of this hybrid system. Thus the interfacial regions, where the hetero-junction effects occur, act as additional reaction sites by enhancing the adsorption of oxygen species, promoting the system to be highly responsive.

In another study, Beckermann *et al.* [169] had reported that the p-n junctions that existed between the Co_3O_4 and ZnO metal oxides in the Co_3O_4 and ZnO nanocomposites they had fabricated by plasma enhanced chemical vapour deposition (PECVD), played a significant role in the responsivity of their optimal composite sensor towards ethanol, acetone and NO_2. They had reported that the p-n junction produced an improved charge separation at the interfacial region between both the metal oxides. This charge separation region they reported was thought to induce an enhanced conduction modulation when the composite material was exposed to the target analytes, which resultantly enhanced the responsivity of the material.

In another study by Yoon *et al*. [89] the CO gas sensing properties of a p-n hetero-junction system based on CuO-ZnO composites were reported. They had found that CuO-ZnO composites in which the CuO was doped with aluminium (Al), were seen to exhibit substantial responsivities towards CO, particularly at high loadings of Al-doped CuO in the ZnO metal oxide matrix. The group had reported that increasing the loading of the Al-doped CuO in ZnO matrix i.e. increasing the composite nature of the gas sensing material, would result in the fractions of n-p (ZnO - CuO) and p-p (CuO - CuO) contacts to increase, while those of n-n (ZnO – ZnO) contacts would decrease. Thus the two most probable paths of charge carrier percolation would be the n-n (ZnO–ZnO) contacts and the n-p (ZnO - CuO) contacts (not the p-p contacts as the host matrix was ZnO into which CuO was being loaded, so the ZnO was still the dominant metal oxide). In such a scenario, the resistive n-p hetero-contacts they reported are likely to dominate the percolation of charge carriers through the composite, as opposed to the n-n homo-contacts. This is because of the higher resistance potential energy barriers that exist at the p-n hetero-contacts as opposed to the lower resistance potential energy barriers that exist at the n-n hetero-contacts. Thus a change in the analyte environment around the p-n junction is likely to contribute significantly to the overall responsivity of the sample. These examples show the advantages of using n-n or p-n hetero-junction materials systems for gas sensing applications.

Yamazoe *et al*. [170, 171] complement the theory of the Fermi level alignment, by introducing the concept of the contact potential, $q\delta_p$ seen in Equation 1–3.

Equation 1–3

$$q\delta_p = E_{F2(f)} - E_{F1(f)} = q\phi_{1(f)} - q\phi_{2(f)}$$

In Equation 1–3 [170, 171] $q\phi_{1(f)}$ and $q\phi_{2(f)}$ or $E_{F1(f)}$ and $E_{F2(f)}$ are work function or Fermi levels of grain 1 and grain 2 or material 1 and 2, at free state respectively. They suggest that this component is always generated in the presence of a hetero-contact or a contact between grains where non-uniformity exists at both sides, such as the difference in size of both grains or difference in their chemical composition. This contact potential or electrostatic potential compensates for the difference in Fermi level that existed between both grains, prior to contact. The electrostatic equilibrium inherently induces a difference in the conduction band edge, δ_{EC}, between the contacting grains which is generated to establish an exchange current across the contact at equilibrium.

Yamazoe *et al*. have shown that the contact potential acts to attenuate the drift mobility, μ, of electrons that travel in the direction against it, and as such influences the resistance (increasing the resistance) of the associated hetero-contact [170, 171]. The implication is that the hetero-contact is sensitive to a change in the ambient gaseous environment and is affected in two ways by gaseous analytes. The first way, which is well established in gas sensing theory, is through change in the electron density on the surface of the grains, which is a receptor function effect of the gas sensitive grains. The second is through the change in drift mobility of electron flow, which is the contact potential effect. This therefore shows that the hetero-contact resistance is more sensitive compared to homo-contact resistance and as such exploitation of hetero-contacts, can render a new generation of gas sensitive materials [170, 171].

Depending on the way the two component oxides are mixed and the way the grains of each are positioned with respect to each other, an effective use of the change in the electron mobility can occur, which changes the resistance of the hetero-contact in such a way, that it is possible to enhance the response of the composite device as compared to a conventional single component semiconducting metal oxide device. Yamazoe *et al*. term the way in which the metal oxides are mixed and the grains are positioned with respect to each other as the 'packing structure' and they report that this packing structure significantly influences the role of the contact potential, towards the enhancement of composite materials in a gas sensing application [170, 171].

The group report that for randomly distributed grains as seen in Figure 1–13 or a one- or two-dimensional packing scenario, a large number of homo-contacts maybe present in parallel to the hetero-contacts and thus, the effect of the hetero-contacts will be significantly diminished as the homo-contacts, which are unable to modulate the drift mobility, μ, will dominate this packing structure. The presence of a large number of parallel homo-contacts, potentially makes them analogous to a rate-limiting step in a chemical reaction, i.e. their abundant presence, will not lead to a significant enhancement in the gas sensing properties of the composite materials.

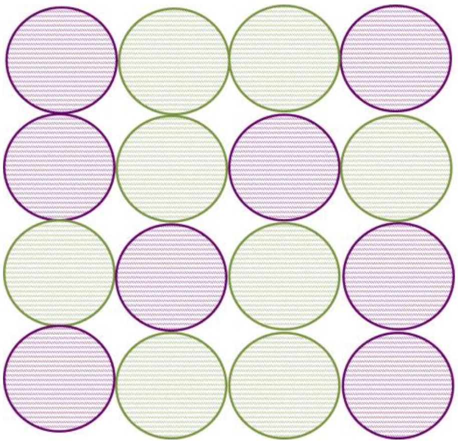

Figure 1–13. Random packing structure of hetero-contact device where purple circles represent metal oxide grains of material A and the green circles represent the metal oxide grains of material B. {Diagram adapted and redrawn from Yamazoe *et al*. [170]}.

In contrast to the random packing structure or a one- or two-dimensional scenario, hetero-contacts are suggested to be more influential in layer-by-layer structures or core-shell packing structures as seen in Figure 1–14 or in a three-dimensional scenario and potentially some two-dimensional scenarios. In such systems, the percolation pathways will be hetero-contact dominated and thus the effect of the hetero-contacts will be significant, implying such systems to be associated to enhanced gas sensing properties [170, 171].

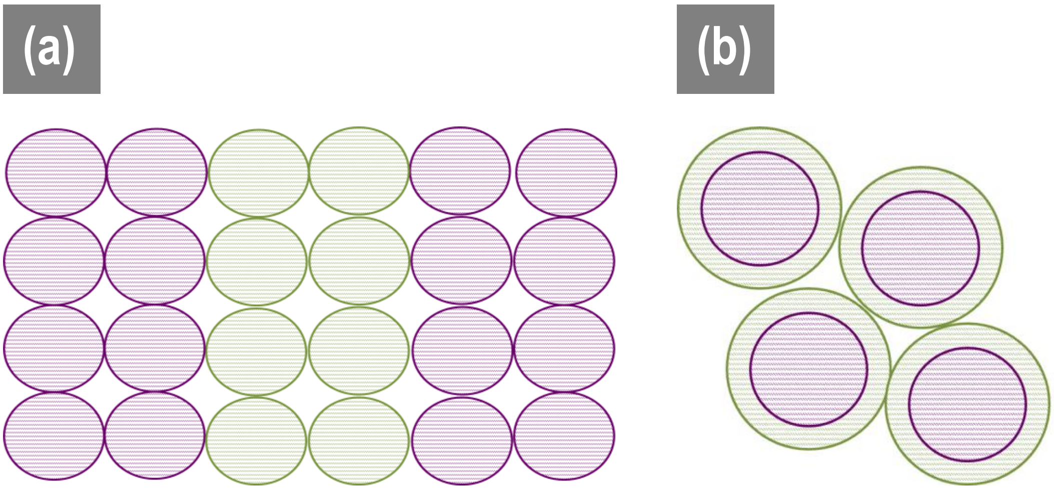

Figure 1–14. Packing structures of (a) layer-by-layer hetero-contact device. Here the purple circles represent metal oxide grains of material A and green circles represent metal oxide grains of material B and (b) core-shell hetero-contact device. Here the purple circles represent the metal oxide grains of material A and green circles represent shells of material B, which encapsulates material A. {Diagram (a) adapted and redrawn from Yamazoe *et al*. [170]}.

Thus Yamazoe *et al*. suggest that the effectiveness of the mixing in the hetero-junction devices and metal oxide deposition techniques, will heavily influence the packing of the grains and therefore ultimately the overall responsivity of the material. This shows that the influence of hetero-contacts on the sensing properties of the composite system, is significantly dependent on the extent of mixing and the positioning of the grains. Their reports are potentially indicative of behaviours of varying composite systems, differing through a number of fabrication methods.

1.10 Target Analytes of Interest

In this section, an overview of the target analytes of interest (in this thesis), sources of their exposure, importance of their detection as well as their surface oxidation reaction mechanisms with metal oxide surfaces, are presented. Specific ranges of the analytes that the sensor devices reported in this thesis can be applied towards, have been summarised in Chapter 7, section 7.1.3, after evaluating their response performances.

1.10.1 Nitrogen Dioxide (NO_2) (Oxidising Gas)

Cars, power plants and combustion engines are a major cause of polluting nitrogen oxides (NOx) in the air, such as NO and NO_2 [38, 172]. Of these gases, NO_2 is the most toxic, with a Threshold Limit Value (TLV) of 3 ppm [38, 172]. The respiratory system is the target system under attack from NO_2, causing adverse health conditions like asthma, emphysema, bronchitis and eventually heart disease, leading to hospitalisation and premature deaths [173]. The severity of exposure to this analyte, illustrates the importance for the detection of NO_2 in the environment.

Reports in the literature have suggested that the surface oxidation reaction of NO_2 on the surface of a n-type semiconducting metal oxide has been reported to undergo direct chemisorption on the surface and abstract electrons as seen in Equation 1–4 [16, 23]:

Equation 1–4

$$NO_2 + e^- \rightarrow NO_2^-$$

1.10.2 Ethanol (Reducing Gas)

Ethanol detection is particularly important in the food and drinks industries. Quality control processes such as the food packaging safety is one example where ethanol gas sensors are used [174]. Industrial processes such as fermentation and distillation, can cause the concentration of ethanol to reach toxic levels, with irritation of the eyes, nose and skin, and alcohol poisoning being the possible symptoms, depending on exposure levels [175]. 1000 ppm is the Threshold Limit Value (TLV) or maximum concentration of acceptable ethanol exposure in a work place [175, 176]. This VOC (volatile organic compound) is also a key bio-marker for detection of alcohol content from breath samples of drunk drivers [177] and is therefore key in road safety control and regulation, with the legal limit of the blood alcohol content in the UK reported to be 7.5 parts per thousand [178].

The surface oxidation reaction of ethanol has been proposed to undergo two possible reactions on the surface of an n-type metal oxide depending on whether the oxide surface is acidic or basic [69]. On the surface of an acidic oxide the alcohol is reported to undergo a dehydration reaction, which forms ethene as an intermediate, as seen in Equation 1–5 and Equation 1–6 as follows [69]:

Equation 1–5 $$C_2H_5OH \rightarrow C_2H_4 + H_2O$$

Equation 1–6 $$C_2H_4 + 3O_2^{2-} \rightarrow 2CO_2 + 2H_2O + 6e^-$$

On the surface of a basic oxide, the reaction is thought to undergo a dehydrogenation reaction, which forms acetal as an intermediate, as follows [69, 179]:

Equation 1–7 $$2C_2H_5OH \rightarrow 2CH_3CHO + H_2$$

Equation 1–8 $$2CH_3CHO + 5O_2^{2-} \rightarrow 4CO_2 + 4H_2O + 10e^-$$

The conversion of the ethanol to acetal i.e. the dehydrogenation reaction, has been reported as the dominant reaction to occur on the surfaces of ZnO [69], SnO_2 [180] and WO_3 [181].

1.10.3 NH_3 (Reducing Gas)

The control of ammonia gas is important in variety of different environments, one prominent example being the food industry where the detection and control of the analyte is important in being able to determine the freshness of food [114]. The gas is also important in agricultural applications in order to control the farming environment for human comfort [114] and is an important precursor to food and fertilizers for the nutritional needs to all living organisms [38]. The detection of the volatilite is also important in the automotive industry for combustion exhaust control in diesel engines, for the reduction of toxic NO_X emissions. Toxic concentration of NO_X emissions are lowered by the selective catalytic reduction (SCR) with NH_3, the latter of which is injected into the exhaust system converting the NO_X to N_2 in the process [114, 182]. Interestingly, the analyte is also important as the building block in the direct or indirect synthesis of many pharmaceuticals and used as a component in household cleaning products [38]. These applications illustrate that the detection of ammonia is widespread and is crucial as it is caustic and hazardous to human life, particularly when the concentration is above the Threshold Limit Value (TLV) of 25 ppm [38].

The oxidation reaction mechanism of the reducing gas NH_3 is complex as it is reported to occur via a number of routes, resulting in several competitive processes taking place at the same time. Three of the main reactions that occur for NH_3 decomposition have been presented in Equation 1–9, Equation 1–10 and Equation 1–11 below [114, 115]:

Equation 1–9
$$2NH_3 + 3O^- \rightarrow N_2 + 3H_2O + 3e^-$$

Equation 1–10
$$2NH_3 + 5O^- \rightarrow 2NO + 3H_2O + 5e^-$$

Equation 1–11
$$2NH_3 + 4O^- \rightarrow N_2O + 3H_2O + 4e^-$$

The dominance of Equation 1–10 in NH_3 decomposition reactions can lead to an unconventional switch in semiconductor behaviour (for example an n-type semiconductor can exhibit p-type response behaviour towards the reducing gas) [114, 115]. This is because nitrous oxide is known to be very unstable and can readily oxidise to NO_2, which is a well-established oxidising gas [114], causing a switch in semiconducting behaviour of the sensor device towards the original NH_3 analyte. In the case of an n-type material, conventional response towards NH_3 would be an increase in conductive response and if NH_3 is converted to an oxidising gas, then an increase in resistive response is observed. For a p-type semiconducting oxide, the opposite behaviour would be observed i.e. increase in resistive response upon NH_3 exposure and an increase in conductive response, if NH_3 converts to an oxidising gas.

1.10.4 Acetone (Reducing Gas)

Acetone has been reported to be a key biomarker for patients suffering from diabetes with the levels of acetone found in the breath of a diabetes sufferer being above 1.8 ppm [23]. The analyte is also an important biomarker for ketosis control [183]. Ketosis is a condition characterised by ketone bodies such as acetone and acetoacetate, in the blood, which are produced from the fat stores when blood glucose levels are low. Factors that can cause ketosis could be prolonged fasting, unbalanced diabetes or an in-take of ketogenic diets as well as high fat, low carbohydrate and low protein diets [184, 185]. The need to detect acetone as a biomarker for the determination of potential health issues is at significantly lower concentrations, in comparison to the threshold limit value (TLV) of the analyte which has been reported to be 500 ppm [176]. Acute inhalation of the analyte has been reported by the Centre of Diseases and Control (CDC) to induce the effect of narcosis, and inflammation of the respiratory tract, stomach and small intestine [186].

The surface oxidation reaction mechanism of acetone vapour on the surface of an n-type semiconducting oxide has been proposed to undergo two possible surface reactions [107, 187], which comprise either oxidation with an oxygenated anion (Equation 1–12 - Equation 1–14) or oxidation via a reaction with a hydroxyl species (Equation 1–15 - Equation 1–17).

Equation 1–12 $$CH_3CO\,CH_3(gas)+O^- \rightarrow CH_3C^+O + CH_3O^- + e^-$$

Equation 1–13 $$CH_3C^+O \rightarrow C^+H_3 + CO$$

Equation 1–14 $$CO + O^- \rightarrow CO_2 + e^-$$

Or

Equation 1–15 $$CH_3CO\,CH_3(gas)+OH^- \rightarrow CH_3CH\,O + CH_3O^-$$

Equation 1–16 $$CH_3COCH_3(gas)+O^- \rightarrow CH_3CO\,C^+H_2 + OH^- + e^-$$

Equation 1–17 $$CH_3CHO\,(gas) + O_{(bulk)} \rightarrow CH_3COOH + O_{(vacancies)}$$

1.10.5 CO (Reducing Gas)

Carbon Monoxide is a very well-studied odourless toxic gas, the main source of its production being the incomplete combustion reactions of fuels [38] and it is common to find this analyte emitted from car exhausts and in fires. The gas is particularly toxic as it has been reported to irreversibly bind to the Fe centre of the haemoglobin metal-protein complex, which is the key protein that delivers oxygen to the body via blood [12, 38]. The irreversible binding means that oxygen can no longer be absorbed by the molecule which reduces the level of oxygen transport around the body and increases the transport of CO, causing significant exposure of the body to CO and ultimately death [12, 38]. The extent of harm of CO as a function of concentration of exposure has been presented in a literature study by Fine *et al.* [12, 23], who have reported that concentration of 35 ppm can cause dizziness and headaches within 6 - 8 hours of exposure, with the TLV of the analyte reported to be 25 ppm [176]. Concentrations above 800 ppm of the analyte have been reported to cause death with a maximum of 30 minutes [12, 23].

The oxidation reaction mechanism of CO vapour (illustrated earlier with the gas sensing mechanism), on the surface of an n-type semiconducting oxide has been proposed as follows [46]:

Equation 1–18 $$CO\,(gas) + O^- \rightarrow CO_2 + e^-$$

1.10.6 Toluene (Reducing Gas)

Toluene is one of the main VOCs contributing to environmental pollution alongside other VOCs such as benzene, ethylbenzene, and xylene all of which are collectively known as BTEX [188]. Among the group of VOCs in BTEX, benzene is the most commonly used chemical in industrial processes for the manufacture of rubber, lubricants, dyes, detergents, drugs, pesticides, etc. However the carcinogenicity of benzene deems its use very limited and is therefore replaced with toluene [188]. Apart from the importance of toluene detection in process monitoring, it is also important in applications such as environmental monitoring and work place safety and efficiency in bioremediation [154]. Toluene has also interestingly been reported as a primary pathogen for the cause of ‘sick house syndrome’, which is an illness attributed to occupants in a building primarily due to poor indoor air quality [189, 190]. Exposures to high concentrations of toluene are hazardous and life-threatening with the volatilite primarily known to be attributed to neurotoxicity [189, 191]. The TLV of the volatilite has been reported to be 50 ppm [176].

The decomposition of toluene is reported to be complex, with Santra *et al*. [192] only reporting the first stage of the decomposition reaction on the surface of an n-type semiconducting metal oxide, presented in Equation 1–19:

Equation 1–19 $$C_7H_8 + 2O^- \leftrightarrow C_7H_6O + H_2O + 2e^-$$

Trushkin *et al*.[193] however had reported a more detailed stage by stage decomposition mechanism of the analyte when it is was subjected to atmospheric pressure glow discharge in an atmosphere of $N_2 : O_2 : H_2O$ gas mixture. The decomposition reactions have been presented below in three stages. In some stages of the reactions, specifically in stage 1: Equation 1–21 and stage 2: Equation 1–24, the group had presented the decomposition reaction of the analyte with a hydroxyl radical species. Such reactions they suggested were likely to be due to the humidity caused by the presence of water vapour in the plasma. In the case of MOS sensing, it is likely that the reaction of the hydroxyl species will take place in a humid atmosphere, where water vapour is introduced into the gas flow. In the case of a dry atmosphere however, it is likely that the reaction will take place with anionic oxygen species.

Equation 1–20 $$C_6H_5CH_3 + O \rightarrow C_6H_5CH_2 + OH$$

Equation 1–21 $$C_6H_5CH_3 + OH \rightarrow C_6H_5CH_2 + H_2O$$

Equation 1–22 $$C_6H_5CH_2 + O \rightarrow C_6H_5CHO + H$$

Equation 1–23 $$C_6H_5CHO + O \rightarrow C_6H_5CO + OH$$

Equation 1–24 $$C_6H_5CHO + OH \rightarrow C_6H_5CO + H_2O$$

1.11 Project Aims

The research and development of new materials in MOS based gas sensing is a growing field. The applications of hetero-junction systems has various advantages that a single metal oxide system cannot provide; key factors being the synergy, specifically the combination of the sensing strengths and catalytic properties of the individual metal oxides as well as the specific compositional contribution of each metal oxide to the hetero-junction system. A second advantage being the electronic enhancement effects of a combination of two semiconducting oxides. Applications of nanomaterials is a mature subject in MOS sensing technology, however emerging routes to fabrication of new nanostructured materials are continuously being developed, particularly those techniques which have potential commercial viability. The aim of this thesis is to present a comprehensive materials and gas sensing characterisation investigation of emerging hetero-junction and nanomaterials systems for MOS semiconductor gas sensing.

The novelty of the hetero-junction research in this thesis is three-fold. The first lies in the route of the design of the systems of the various hetero-junction systems, specifically the compositions of hetero-junction devices prepared and the fabrication of the MOS sensor devices. The second lies in some of the combinations of metal oxides used, for example WO_3-ZnO; this combination of metal oxides has been studied before, however not to the extensive detail presented here. The combination of CTO-ZnO on a sensor is novel and has not been reported before. The final novelty lies in the method through which the sensors have been characterised for their gas sensing properties; this testing has been conducted in a novel gas sensing rig, designed and developed by O.A.Afonja [194].

Particular aims with the research associated to the hetero-junction systems are:

- To determine if responsivities are improved with particular combinations of mixtures of metal oxides with respect to the single metal oxide counterpart
- To understand which particular combinations of metal oxides give the best responses and interpret the enhancement effects
- To assimilate which particular combinations of metal oxides give poor responses, with respect to the single metal oxide counterpart, and interpret possible causes
- To aim to interpret any possible electronic interactions or synergistic effects with the various hetero-junction systems investigated
- To understand if random packing structures are an effective way to promote hetero-junction enhancement effects

- To understand if selectivity can be achieved with such hetero-junction systems
- Finally to understand potential effects of microstructure, material composition, junction effect, packing structure, temperature and analyte concentration on the general behaviour of the material systems

The nanomaterials research part of this thesis establishes new emerging technologies, such as CHFS, among a host of other relatively high temperature techniques, for the synthesis of nanostructured metal oxides (specifically ZnO) for MOS gas sensing. The gas sensing properties of CHFS based materials have been reported previously in the literature [142, 143], however a comprehensive gas sensing characterisation study has not yet been conducted. The novelty of the investigation in this thesis lies in the comprehensive gas sensing characterisation of newly fabricated CHFS based ZnO materials, screen-printing as a deposition method for these materials as well the materials and gas sensing characterisation study of newly synthesised ZnO ceramics fabricated by various high temperature synthesis routes.

Particular aims with the research associated to the nanomaterials systems are:

- To identify influential microstructural factors on the response behaviours of nanomaterials
- To assess the potential of emerging fabrication technologies as a route to synthesis of ZnO nanomaterials for MOS gas sensing

1.12 Summary of Thesis

The following Chapters present investigations of the applications of a variety of emerging hetero-junction and nanomaterial material systems for MOS gas sensing applications. Chapter 2 presents the method of sensor device fabrication, gives an overview of all metal oxides investigated and synthesis details and introduces the materials and gas sensing characterisation techniques used to undertake the research. Chapter 3 is the first experimental Chapter which presents a material and gas sensing characterisation study of an n-n hetero-junction system based on WO_3 - ZnO composites. Chapter 4 furthers the investigation of the application of n-n hetero-junction systems, focussing on a material and gas sensing characterisation study of a SnO_2 – ZnO composite system. Chapter 5 extends the application of the hetero-junction system approach to MOS sensing, however introduces a p-n hetero-junction system based on CTO and ZnO composites. The final experimental Chapter 6 extends the theme of the application of ZnO based materials to MOS gas sensing, focusing on emerging nanostructured ZnO fabrication technologies and materials. The concluding Chapter, Chapter 7 concludes the main findings from the various investigations in the thesis and proposes investigations that can be conducted in future work to further explore the potential of the materials systems investigated.

Chapter 2 : Materials and Experimental Method

This Chapter presents an overview of all materials used in the fabrication of the various systems of sensor devices, presented in this thesis. Further, details of all the instruments and techniques used for elucidation of the physical and chemical characteristics of the materials, and for their functional gas sensing characterisation, throughout this thesis, have also been presented in this Chapter. Experimental procedures specific to a certain Chapter, for example the fabrication of a specific material or particular system of sensors, have also been presented here.

2.1 Materials Investigated

Table 2–1 presents all materials (solid-state powders) which have been fully characterised and investigated for their gas sensing properties in this thesis. Further, it specifies the supplier of the chemical, and the Chapter number and associated title within which the material has been reported. Many metal oxide samples were synthesised 'in-house', i.e. in laboratories at UCL, and the associated Chapter and section within it, have been indicated and should be referred to for detailed experimental fabrication procedure. Some metal oxide samples have been supplied by internal/external sources and where this is the case, these sources have been acknowledged.

Table 2–1. All materials investigated in thesis, corresponding supplier, and associated Chapter number and associated Chapter title within which the material has been investigated.

Material	Supplier	Chapter	Chapter title
WO_3	New Metals Chemicals Ltd.	3	WO_3-ZnO based n-n hetero-junction system.
Zinc Tungstate $ZnWO_4$	Synthesised 'in-house', See section 2.3.1.1.	3	As above
Acid SnO_2	Keeling and Walter.	4	SnO_2-ZnO based n-n hetero-junction system.
CTO ($Cr_{2-x}Ti_xO_3$) Where X = 0.05 i.e. $Cr_{1.95}Ti_{0.05}O_3$	Synthesised 'in-house' See section 2.3.3.1.	5	CTO-ZnO based p-n hetero-junction system.
ZnO	Sigma Aldrich.	3 4 5	See above. See above. As above.
Nanostructured ZnO (3 samples) Fabricated via Continuous Hydrothermal Flow Synthesis	Synthesised 'in-house', See section 2.3.4.1.	6	Emerging ZnO Materials for MOS sensing.
Nano- and Micron-sized ZnO fabricated via: Molten Salt synthesis, Solid-State metathesis and Hydrothermal synthesis methods (3 samples)	Dr. Kristin Poduska, Memorial University, Canada.	6	As above

2.2 Sensor Fabrication

Figure 2–1 presents a schematic of the sensor fabrication process that was used throughout this thesis for the build-up of all MOS sensor devices.

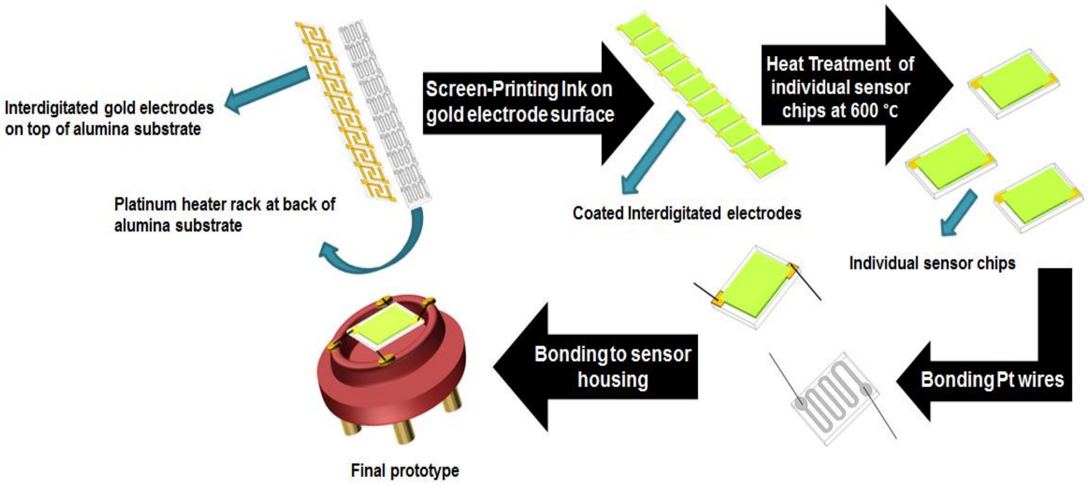

Figure 2–1. Schematic of MOS sensor device fabrication process implemented for all sensor devices investigated in this thesis.

Within each Chapter, a system of sensors associated to a particular material or combination of materials, was investigated. Each sensor device within the system was fabricated by forming a screen-printable ink of the constituent metal oxide(s) with an organic vehicle, ESL 400 (Agmet Ltd.), in an agate pestle and mortar, illustrated in Figure 2–2 (a). Each device either constituted a single metal oxide or a composite of two metal oxides – details of how both types of inks were fabricated, have been presented below in sections 2.2.1 and 2.2.2, respectively. Once the inks were formed, they were screen-printed using a DEK 1202 screen-printer (DEK) (Figure 2–2 (b)), onto a gas sensor substrate strip containing 23 2 x 2 mm wide gap alumina chips (Capteur Sensors), which consisted of interdigitated gold electrodes on the top, with a gap of 171 ± 10 µm between the electrodes, and a platinum heater track on the bottom, as observed in Figure 2–2 (c), (d) and (e). Four layers of each ink were screen-printed onto the individual strips, and each layer was dried under an Infra-Red (IR) lamp seen in Figure 2–2 (f), for 10 ± 2 minutes to ensure it was dry before the subsequent layer was printed, preventing potential smudging effects. Once the ink layers were printed, individual chips from the strip were broken and heat-treated in a muffle furnace (Elite Thermal Systems Limited), seen in Figure 2–2 (g), at 600 °C for 1 hour. Reasons for heat-treatment were two-fold, the first to ensure that the organic vehicle (used to form the inks) was burnt off to prevent its interference with the gas sensing performance of the materials; and the second was to ensure that the screen-printed material adhered well to the alumina substrate. The ramp rate of the furnace, to increase the temperature from ambient conditions to 600 °C, was set at 5 °C / minute, ensuring the materials experienced a gradual increase, rather than sudden increase, in temperature. After the printed sensor chips were heat-treated, 50.8 µm platinum wires (0.002 inches in diameter, 99.95% metal basis, Alfa Aesar) were spot welded to the platinum pads at the back and gold pads on the top of the individual chips, using a Macgregor DC601 parallel gap resistance welder, seen in Figure 2–2 (h). In a final step, the chips were further spot-welded to the high density polyethylene 4-pin sensors housings, producing the final device prototypes as observed in Figure 2–1, to carry out physical, chemical and functional analysis.

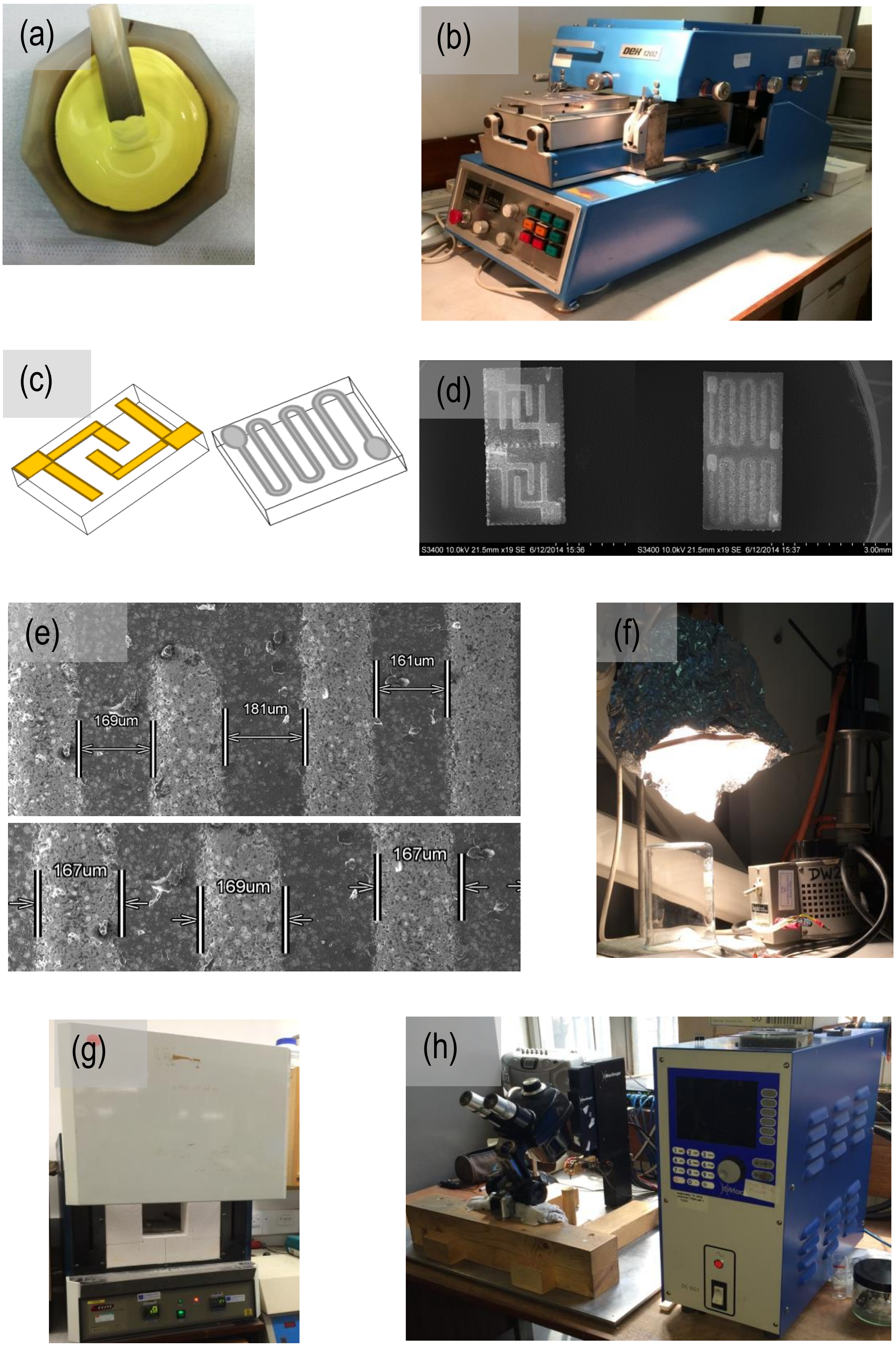

Figure 2–2. (a) Screen-printable ink fabricated with agate pestle and mortar, (b) DEK 1202 screen-printer for screen-printing inks on to MOS sensor substrates, (c) Single wide gap sensor substrate chip with interdigitated gold electrodes on top and platinum heater track at bottom, (d) SEM images of wide gap sensor substrates top and bottom, (e) SEM images of measured electrode spacing on wide gap substrate, (f) Infra-Red (IR) heat lamp for drying screen-printed layers, (g) muffle furnace for heat-treating sensor chips and (h) Macgregor DC601 parallel gap resistance welder for spot welding of Pt wires onto individual MOS gas sensor chips.

2.2.1 Single metal oxide sensor devices

Single metal oxide sensors were fabricated as the pure counterparts in each composite system studied in Chapter 3, Chapter 4 and Chapter 5 or were fabricated as part of the Chapter focussing on emerging technologies for the fabrication of nanostructured semiconducting metal oxides in Chapter 6. Each sensor consisted of 100 weight percent (wt.%) of the individual metal oxide powder in order to fabricate the associated sensor.

In the fabrication of such devices, a screen-printable ink of a single metal oxide material was prepared by mixing a certain mass of the single metal oxide powder with an appropriate mass of organic vehicle ESL 400 (Agmet Ltd.), which allowed for the production of the appropriate consistency of ink for subsequent screen-printing, using an agate pestle and mortar. All powders were ground with the organic vehicle, until the ink had a smooth viscous consistency. Further fabrication of the sensor devices followed the method described in section 2.2.

Details (i.e. compositions and concentrations) of the single metal oxide sensor devices have been tabulated in the appropriate table in the individual Chapter, and can be identified in the tables as those devices with an asterix beside them. Details include the chemical composition of the metal oxide, its mass and the mass of ESL 400, required to make the corresponding ink for each device.

2.2.2 Composite metal oxide sensor devices

In the case of each composite system studied, fabrication of a system of composite sensor devices involved simple mechanical mixing of certain masses of two metal oxides, with ESL 400 (Agmet Ltd.) in an agate pestle and mortar. Variable masses of each metal oxide was used in order to achieve a certain weight percent (wt.%) of each component metal oxide within the composite mixture. The composite sensors in each system were always fabricated with a fixed set of ratios between both metal oxides denoted in Table 2–2 as Metal Oxide A (MO A) and Metal Oxide B (MO B):

Table 2–2. Composition of Metal Oxide A (MO A) and Metal Oxide B (MO B) used as a basis for the formation and investigation of all composite sensor devices in this thesis.

wt.% MO A – wt.% MO B
10 wt.% - 90 wt.%
30 wt.% - 70 wt.%
50 wt.% - 50 wt.%
70 wt.% - 30 wt.%
90 wt.% - 10 wt.%

After the formation of an appropriate consistency of composite inks, the fabrication of the sensor devices followed the method described in section 2.2.

Details (i.e. compositions and concentrations) of the component metal oxides within the composite metal oxide sensor devices have been tabulated in the appropriate table in section 2.3. Details include the chemical composition of the individual metal oxides, their masses and the mass of ESL 400, required to make the corresponding ink for each device.

2.3 Sensor Devices and Materials Syntheses

This section presents the compositions of the individual sensor devices fabricated and studied in each Chapter, as well as specific synthesis details of various materials prepared in each Chapter.

2.3.1 Chapter 3: WO_3-ZnO composite system

The metal oxide semiconductor (MOS) sensor devices fabricated for this Chapter have been presented in Table 2–3 with composition details of the WO_3 and ZnO pure and composite inks used in the fabrication of the associated sensor devices. Additionally in this Chapter, a $ZnWO_4$ sensor was fabricated. This was to understand the response effects that this tertiary phase, which was present in all the WO_3-ZnO composites, had on the composite sensor devices. Description of the synthesis of this tertiary phase has been presented in section 2.3.1.1.

Table 2–3. All MOS sensor devices fabricated for Chapter 3, which investigates the application of a system of WO_3-ZnO n-n hetero-junction composite devices for MOS sensing. Those sensor devices with an asterix (*) are single component metal oxide MOS sensor devices, all others are dual component metal oxide MOS sensor devices.

Sensor device	Metal oxide powder(s) & mass (g)	Metal oxide powder(s) & moles (mol)	Mass of ESL 400 (g)
***100 wt.% WO_3**	**WO_3 – 3.44**	**WO_3 – 0.015**	**2.41**
90 wt.% WO_3 – 10 wt.% ZnO	**WO_3 – 1.80 ZnO – 0.20**	**WO_3 – 0.008 ZnO – 0.002**	**1.10**
70 wt.% WO_3 – 30 wt.% ZnO	**WO_3 – 2.12 ZnO – 0.92**	**WO_3 – 0.009 ZnO – 0.011**	**1.20**
50 wt.% WO_3 – 50 wt.% ZnO	**WO_3 – 2.84 ZnO – 2.86**	**WO_3 – 0.012 ZnO – 0.035**	**2.39**
30 wt.% WO_3 – 70 wt.% ZnO	**WO_3 – 0.62 ZnO – 1.42**	**WO_3 – 0.003 ZnO – 0.017**	**0.95**
10 wt.% WO_3 – 90 wt.% ZnO	**WO_3 – 0.22 ZnO – 1.83**	**WO_3 – 0.001 ZnO – 0.022**	**1.15**
***100 wt.% ZnO**	**ZnO – 2.00**	**ZnO – 0.025**	**1.10**
***100 wt.% $ZnWO_4$**	**$ZnWO_4$ – 1.52**	**$ZnWO_4$ – 0.005**	**1.18**

2.3.1.1 Synthesis of $ZnWO_4$

In this study, the presence of a tertiary phase, $ZnWO_4$, within the WO_3-ZnO composites, was detected via X-Ray Diffraction (XRD) and Raman spectroscopy characterisation methods. To understand the influence of this compound on the responsivity of the composite sensor devices, it was synthesised prior to subsequent functional and material characterisation, through a solid-state synthesis method reported by Phani *et al*. [195]. Some modifications were made to the method reported in literature.

Synthesis encompassed ball milling equimolar ratios of WO_3 (New Metals Chemicals Ltd.) and ZnO (Sigma Aldrich) powders in 20 mL of ethanol in a Nannetti Speedy 1 ball mill. The mixture was ball milled, with 6 mm alumina grinding balls for 6 minutes. Following milling, the mixture and residue were decanted (removing the alumina media in the process) and washed with ethanol, with the final mixture suspended in ~ 150 mL solvent. After evaporation of the solvent, the mixture was dried in a furnace (Elite Thermal Systems Limited) at 100 °C, for 24 hours which ensured removal of any remaining ethanol. The dry light yellow powder was then ground in an agate pestle and mortar and sieved through a 150 μm sieve before being fired again, this time at 1000 °C for 16 hours, resulting in the final product, a white powder.

2.3.2 Chapter 4: SnO_2-ZnO composite system

The metal oxide semiconductor (MOS) sensor devices fabricated for this Chapter have been presented in Table 2–4 with composition details of the SnO_2 and ZnO pure and composite inks used in the fabrication of the associated sensor devices.

Table 2–4. All MOS sensor devices fabricated for Chapter 4, which investigates the application of a system of SnO_2-ZnO n-n hetero-junction composite devices for MOS sensing. Those sensor devices with an asterix (*) are single component metal oxide MOS sensor devices, all others are dual component metal oxide MOS sensor devices.

Sensor device	Metal oxide powder(s) & mass (g)	Metal oxide powder(s) & moles (mol)	Mass of ESL 400 (g)
***100 wt.% SnO_2**	**SnO_2 – 2.10**	**SnO_2 – 0.014**	**1.61**
90 wt.% SnO_2 – 10 wt.% ZnO	**SnO_2 – 1.83 ZnO – 0.21**	**SnO_2 – 0.012 ZnO – 0.003**	**1.24**
70 wt.% SnO_2 – 30 wt.% ZnO	**SnO_2 – 1.42 ZnO – 0.62**	**SnO_2 – 0.009 ZnO – 0.008**	**0.74**
50 wt.% SnO_2 – 50 wt.% ZnO	**SnO_2 – 1.51 ZnO – 1.52**	**SnO_2 – 0.010 ZnO – 0.019**	**1.08**
30 wt.% SnO_2 – 70 wt.% ZnO	**SnO_2 – 0.60 ZnO – 1.41**	**SnO_2 – 0.004 ZnO – 0.017**	**0.85**
10 wt.% SnO_2 – 90 wt.% ZnO	**SnO_2 – 0.21 ZnO – 1.80**	**SnO_2 – 0.001 ZnO – 0.022**	**1.06**
***100 wt.% ZnO**	**ZnO - 2.00**	**ZnO – 0.025**	**1.18**

2.3.3 Chapter 5: CTO-ZnO composite system

The MOS sensor devices fabricated for this Chapter have been presented in Table 2–5 with composition details of the CTO and ZnO pure and composite inks used in the fabrication of the associated sensor devices. The synthesis of CTO was done in–house and has been presented in section 2.3.3.1.

Table 2–5. All MOS sensor devices fabricated for Chapter 5, which investigates the application of an system of CTO-ZnO p-n hetero-junction composites for MOS sensing. All sensor devices were fabricated by screen-printing method, details of which have been given in Chapter 2. Those sensor devices with an asterix (*) are single component metal oxide MOS sensor devices, all others are dual component metal oxide MOS sensor devices.

Sensor device	Metal oxide powder(s) & mass (g)	Metal oxide powder(s) & moles (mol)	Mass of ESL 400 (g)
***100 wt.% CTO**	**CTO - 1.36**	**CTO – 0.009**	**1.37**
90 wt.% CTO – 10 wt.% ZnO	**CTO – 2.71 ZnO – 0.31**	**CTO – 0.018 ZnO – 0.004**	**3.57**
70 wt.% CTO – 30 wt.% ZnO	**CTO – 2.11 ZnO – 0.93**	**CTO – 0.014 ZnO – 0.011**	**2.80**
50 wt.% CTO – 50 wt.% ZnO	**CTO – 1.40 ZnO – 1.41**	**CTO – 0.009 ZnO – 0.017**	**2.43**
30 wt.% CTO – 70 wt.% ZnO	**CTO – 0.90 ZnO – 2.10**	**CTO – 0.006 ZnO – 0.026**	**3.01**
10 wt.% CTO – 90 wt.% ZnO	**CTO – 0.31 ZnO – 2.71**	**CTO – 0.002 ZnO – 0.033**	**2.57**
***100 wt.% ZnO**	**ZnO - 2.16**	**ZnO – 0.027**	**2.15**

2.3.3.1 Synthesis of $Cr_{1.95}Ti_{0.05}O_3$ (CTO)

The CTO in this study, with target stoichiometry: $Cr_{1.95}Ti_{0.05}O_3$, was synthesised through a solid-state ceramic ‘shake and bake’ method, in accordance with studies reported by Henshaw *et al.* [122, 126] and Dawson *et al.* [126, 128]. Some modifications were made to the methods reported in literature.

Synthesis of $Cr_{1.95}Ti_{0.05}O_3$ was carried out by ball milling stoichiometric amounts of TiO_2 powder (Sigma Aldrich) and Cr_2O_3 powder (Sentury Reagents, 99.9%) in 32 mL of Iso-Propyl-Alcohol (IPA) (Emplura, Merck). The mixture was ball milled, with 6 mm alumina grinding balls in a Nannetti Speedy 1 ball milling machine for 15 minutes in three intervals of 5 minutes each, forming a viscous mixture. After evaporation of the solvent, the powder was dried at 100 ºC in a furnace (Elite Thermal Systems Limited) for 5 hours to ensure complete evaporation of any remaining IPA. The dried powder was then ground in an agate pestle and mortar and sieved through a 150 µm sieve, before undergoing further heat-treatment again; this time at 900 ºC for 12 hours, for the final product to form.

2.3.4 Chapter 6: nanostructured ZnO system

The MOS sensor devices fabricated for this Chapter have been presented in Table 2–6 with composition details of the ZnO inks used in the fabrication of each device. The synthesis of CHFS based ZnO materials was done in-house, details of which have been presented in section 2.3.4.1.

Table 2–6. All MOS sensor devices fabricated for Chapter 6, which investigates emerging ZnO semiconducting metal oxides for MOS sensing. In the study nanostructured ZnO sample A, ZnO sample B and ZnO sample C were fabricated by Continuous Hydrothermal Flow Synthesis (CHFS), and MS-ZnO was fabricated by Molten-Salt synthesis, SS-ZnO was fabricated by Solid-State metathesis and Zn-ZnO was fabricated by Hydrothermal synthesis. All sensor devices were fabricated by screen-printing method, details of which have been given in Chapter 2. All sensor devices are asterixed (*) indicating single metal oxide component MOS sensor devices.

Sensor device	ZnO Mass (g)	ZnO Moles (mol)	Mass of ESL 400 (g)
***100% Nano ZnO sample A (CHFS)**	**0.61**	**0.007**	**1.46**
***100% Nano ZnO sample B (CHFS)**	**1.33**	**0.016**	**1.53**
***100% Nano ZnO sample C (CHFS)**	**1.31**	**0.016**	**1.88**
***100% ZnO (MS ZnO) (Molten-Salt synthesis)**	**0.45**	**0.006**	**0.24**
***100% ZnO (SS ZnO) (Solid-State Metathesis)**	**0.61**	**0.007**	**0.87**
***100% ZnO (ZN ZnO) (Hydrothermal synthesis)**	**0.87**	**0.011**	**0.79**

2.3.4.1 Synthesis of Nanostructured ZnO Materials via CHFS

ZnO nanomaterials were synthesised via a CHFS process on a pilot plant scale, a schematic of which has been presented in Figure 2–3 [143, 196]. Detailed literature which includes information on the actual CHFS process and the rig's construction and its validation can be found in literature [196-199].

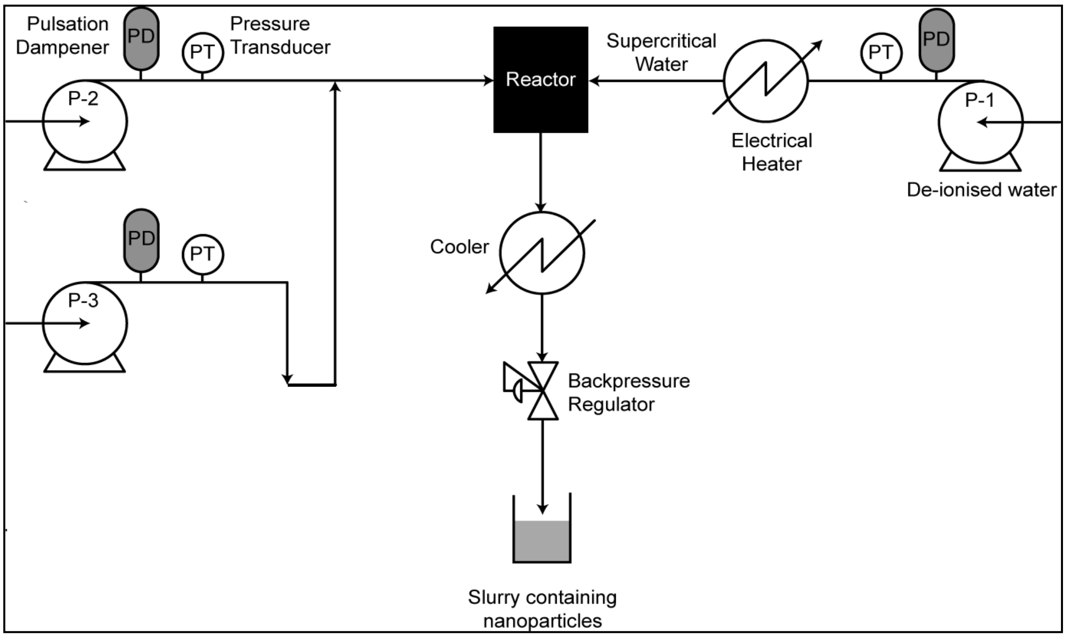

Figure 2–3. Schematic of Continuous Hydrothermal Flow Synthesis (CHFS) pilot plant, where P-1, P-2 and P-3 represent pump 1 from which super critical water and pump 2 and pump 3 from which the precursors, are pumped into the confined jet mixer (CJM) / Reactor. PT in the schematic represents a Pressure Transducer and PD represents a Pulsation Dampener. Figure from [143, 196].

For the syntheses of CHFS based nanostructured ZnO, zinc (II) nitrate hexahydrate [$Zn(NO_3)_2.6H_2O$] (Sigma Aldrich), potassium hydroxide (KOH) pellets (Alfa Aesar) and 10 MΩ deionised water were used.

CHFS based ZnO nanomaterials were produced by reacting a supercritical water flow issuing from P-1 at 450 °C, 240 bar (400 mL min^{-1}) with an ambient temperature flow of precursor solutions issuing from P-2 ($Zn(NO_3)_2.6H_2O$ aqueous solution) and P-3 (KOH aqueous solution), both at 200 mL min^{-1}, in a confined jet mixer (CJM) [196] yielding a reaction point temperature of 335 °C. When the precursors and supercritical water were fully mixed, rapid hydrolysis and dehydration of the zinc salt led to the formation of many particle nucleates with minimal growth. After formation in the CJM, the particles were cooled in flow and collected as a slurry at the end of the process, after passing through a back pressure regulator which was used to maintain a pressure of 240 bar. The slurry was cleaned by centrifuging (4500 rpm), then decanting and replacing the supernatant with clean deionised water, ensuring to shake each time to encourage re-dispersion of the solids. This centrifugation process was carried out a number of times till the supernatant reached close to neutrality, indicated by pH indicator paper. After cleaning, all slurries were subsequently dried in a freeze drier (Virtis Genesis 35 XL) by slowly heating a sample from -60 °C to 25 °C, over 24 hours under vacuum of 100 mTorr generating the final material. In a final step, all materials were ground in an agate pestle and mortar to attain them in free flowing powder form before further processing. A summary of the synthesis conditions employed for each fabricated CHFS based metal oxide sample, has been presented in Table 2–7**.**

Table 2–7. Summary of CHFS synthesis conditions for the fabrication of ZnO sample A, sample B and sample C, that were characterised for their materials and gas sensing properties in Chapter 6. Fabrication of samples A, B and C involved a reaction of ambient flows of 0.1, 0.2, 0.45 M of Zn $(NO_3)_2.6H_2O$ aqueous solution and KOH aqueous solution respectively (each flowing at 200 mL min^{-1}) with a supercritical water flow at 450 °C and 240 bar (flowing at 400 mL min^{-1}) in a confined jet mixer.

Sample No.	Sample Name	P-2 (Zn/M)	P-3 (KOH/M)	Q_{P-2} (ml min^{-1})	Q_{P-3} (ml min^{-1})	Q_{SW} (ml min-^{1})
1	ZnO A	0.1	0.1	200	200	400
2	ZnO B	0.2	0.2	200	200	400
3	ZnO C	0.45	0.45	200	200	400

P-2 = precursor concentration issuing from pump 2, P-3 = precursor concentration issuing from pump 3, Q_{P-2} = volumetric flow of precursor from pump 2, Q_{P-3} = volumetric flow of precursor from pump 3, Q_{SW} = volumetric flow of supercritical water issuing from pump 1.

2.3.4.2 ZnO Ceramic Samples from other high temperature synthetic methods

This Chapter also reports on various ZnO ceramic samples, prepared by molten-salt synthesis, solid-state metathesis and hydrothermal synthesis provided by Dr. Kristin Poduska and her research group from Memorial University, New Foundland, Canada. These samples have been tabulated in Table 2–8.

Table 2–8. ZnO ceramic samples prepared by Molten-Salt synthesis (MS-ZnO), Solid-State metathesis (SS-ZnO) and Hydrothermal synthesis (Zn-ZnO) supplied by Dr. Kristin Poduska and her research group at Memorial University, New Foundland, Canada.

Sample No.	Sample Name	Synthesis Method
1	MS - ZnO	Molten-Salt synthesis
2	SS - ZnO	Solid-State metathesis
3	Zn - ZnO	Hydrothermal synthesis

2.4 Material characterisation

This section presents the details of all the material characterisation techniques that were used to investigate the chemical and physical properties of the metal oxide materials.

2.4.1 Scanning Electron Microscopy (SEM)

Top down Scanning Electron Microscopy (SEM) imaging was carried out on a JEOL JSM-6301F field emission scanning electron microscope (FE-SEM) instrument in secondary electron mode. Prior to analysis, all samples were carbon coated using an Edwards Auto 306 vacuum carbon coater, to prevent charging of the sample and enhance its conductivity during imaging. The acceleration voltage used for all samples was 5 kV and the probe current (μA) was very much sample dependent and varied according to the magnitude that gave the best image clarity. Data acquisition was conducted with SemAFORE software and images were taken at magnifications of x 10,000, x 20,000, x 30,000, x 40,000, x 50,000 and x 100,000. 4-5 images were taken per sample at different areas across the sample to ensure the images obtained were representative of the whole sample.

Images of the sensor chips and measurements of the wide gap electrode spacings within them, were taken using a Hitachi S-3400N environmental scanning electron microscope (E-SEM) instrument. Sensor chips were mounted on flat sensor stubs and imaged using an accelerating voltage of 10.0 kV, and the probe current was in the μA range in both secondary and back-scattered electron modes.

2.4.2 Transmission Electron Microscopy (TEM)

Transmission Electron Microscopy (TEM) imaging was carried out on all nanomaterials investigated in this thesis. The instrument used to conduct the imaging was a 200 keV JSM-2100 Transmission Electron Microscope instrument, which used a Lanthanum Hexaboride LaB_6 electron source. Samples were prepared by creating a dispersion of each in methanol through ultrasonication, and drop coating onto carbon-coated grids (Holey carbon film, 300 mesh Cu, Agar Scientific), after which imaging was conducted. A number of images, at a variety of magnifications, were taken to ensure the images were representative of each sample as a whole and to obtain detailed image analysis. All images were acquired using Gatan Digital Micrograph software and particle size distributions determined using imageJ software.

2.4.3 X-Ray Diffraction (XRD)

X-Ray Diffraction (XRD) data was obtained from a number of different instruments throughout this project. Details of each instrument are given in this section.

2.4.3.1 Bruker D4 Endeavour Powder X-ray Diffractometer (PXRD)

XRD patterns of all powder samples were obtained using a Bruker D4 Endeavour powder X-Ray Diffractometer instrument using Cu $K\alpha_{1+2}$ radiation (λ = 1.546 Å). DIFFRAC Plus XRD software was used for instrument control, data acquisition and diffraction data processing. Crystallite sizes of nanomaterials were evaluated from diffraction patterns acquired on the Bruker D4 diffraction instrument, using fityK software [200].

2.4.3.2 Bruker Discover D8 Diffractometer with a wide angle Gadds detector

XRD patterns of some thick-film sensor devices, investigated at the early-mid stage of this project, were taken using a Bruker Discover D8 diffractometer with a wide angle Gadds detector using Cu $k\alpha_{1+2}$ radiation (λ = 1.546 Å) in reflection mode using a glancing incident angle of 5°. The X-Ray generator operated at 40 kV and 40 mA. The scans were taken using a 0.5 mm collimator with $\theta 1$ = 5 ° and $\theta 2$ = 22 °, (frame width 34 °) with 2 frames per scan, with each frame having a total count of 200 seconds. Gadds software was used for instrument control, data acquisition and 2-D diffraction data processing.

2.4.3.3 Bruker D8 Discover D8 diffractometer with Vantec 500 detector

XRD patterns of some thick-film sensor devices, investigated towards the latter stage of this project, were taken using a Bruker D8 Diffractometer with a Vantec 500 detector using Cu $k\alpha_{1+2}$ radiation (λ = 1.546 Å) source. The X-Ray generator operated at 50 kV and 100µA. XRD patterns were collected using a 0.3 mm collimator, over range of 20 ° – 65 ° with a time step of 100 second / step and 4 steps / scan. Diffrac.Commander software was used for instrument control, data acquisition and 2-D diffraction data processing.

All XRD patterns were evaluated using EVA software and data extracted to plottable formats using convx and PowDLL converter softwares.

2.4.4 Raman Spectroscopy

Raman spectroscopy of all samples was carried out using a Renishaw inVia Raman (Renishaw Raman System 1000) microscope using a green argon-ion laser of wavelength 514.5 nm. The laser power varied with each sample and was chosen on the basis that it gave the pattern with optimum clarity peaks and at the same time did not saturate the signal. The exposure times were 10 seconds /scan. 4-5 scans were taken in different areas across the sample, to ensure the scans obtained were representative of the whole sample.

2.4.5 X-Ray Photoelectron Spectroscopy (XPS)

X-ray Photoelectron Spectroscopy (XPS) was carried out using a Thermo K-Alpha spectrometer using monochromated Al Kα radiation, with survey scans collected over the 0 – 1400 eV binding energy range with 1 eV step size and a pass energy of 200 eV. Higher resolution scans (step size: 0.1 eV) were carried out around the principle peaks for each element and were collected at a pass energy of 50 eV. All XPS data was evaluated and extracted into a plottable format using Casa XPS software. All XPS spectra were charge corrected against the reference C 1s peak at 284.6 eV [201-203] .

2.4.6 Brunauer-Emmett-Teller (BET) surface area measurements

Brunauer-Emmet-Teller (BET) surface area measurements were carried out on CHFS nanomaterials using N_2 in a Micromeritics ASAP 2420 instrument with six parallel analysis stations. The samples were degassed at 150 °C for 12 hours prior to measurements.

2.5 Gas Sensing Characterisation

Gas sensing experiments were carried out using an in-house automated test rig, developed by O. A. Afonja [194], a schematic of which is presented in Figure 2–4 and an image of which is presented in Figure 2–5.

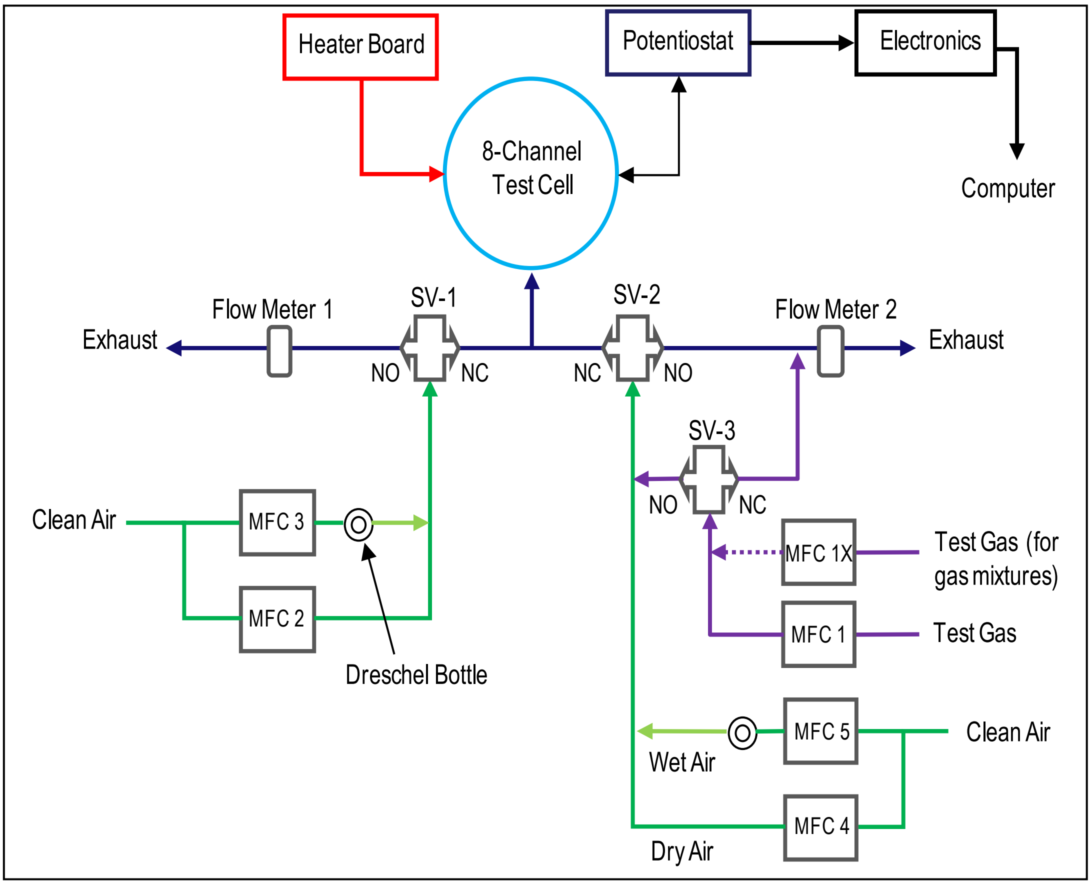

Figure 2–4. Schematic of the gas sensing rig used for gas sensing experiments. In the schematic, the MFC represents a Mass Flow Controller, the SV represents a Solenoid Valve, and NO and NC represent open and close ports respectively, through which the gas is allowed access to the exhaust or test cell, respectively.{Diagram from O.A. Afonja [194]}.

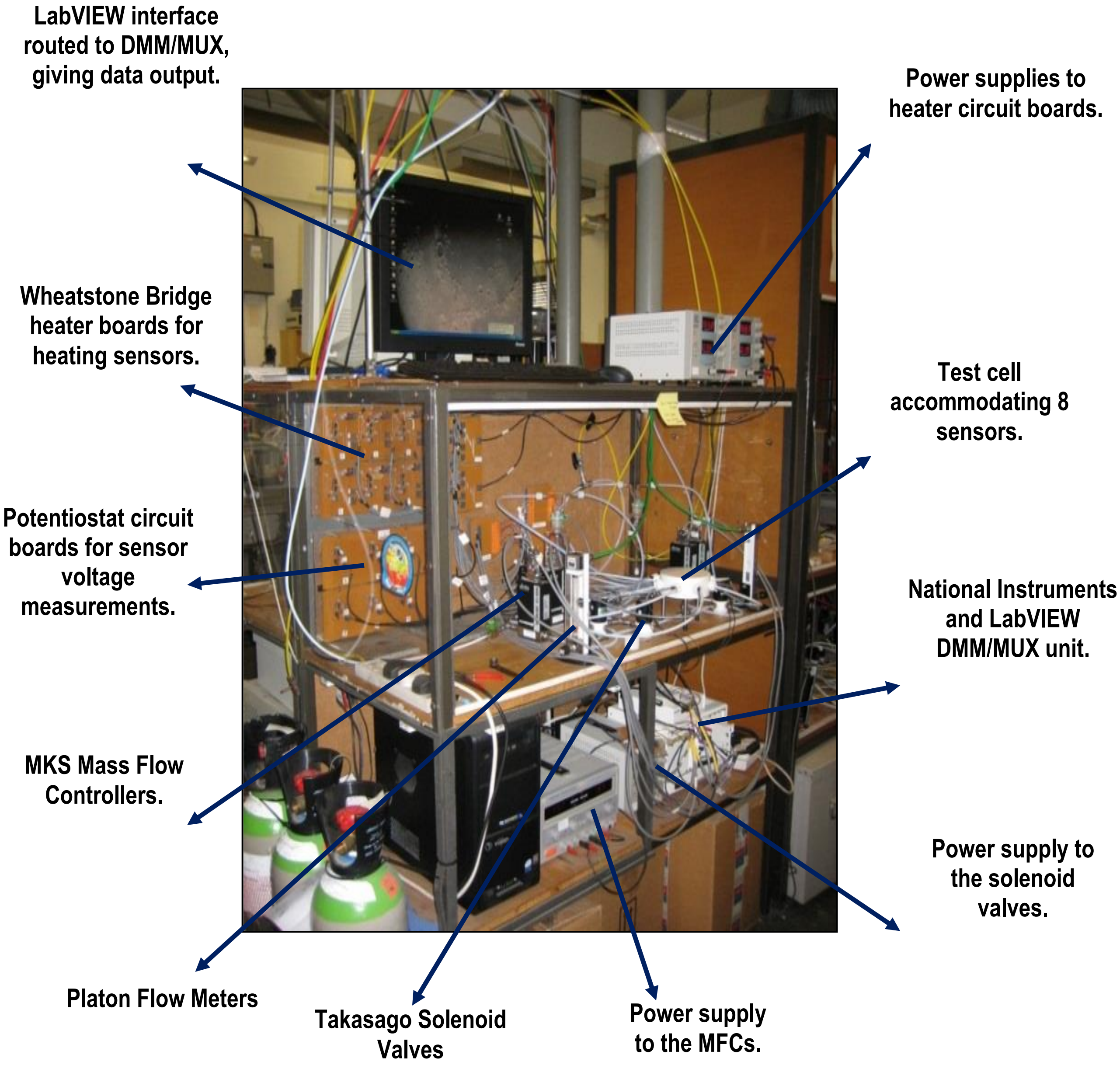

Figure 2–5. Image of the gas sensing rig used for gas sensing experiments.

As observed in Figure 2–4, the rig contained a test cell which was made of solid Polytetrafluoroethylene (PTFE), a material which has established chemical inertness to a wide variety of chemicals [204]. The cell was able to accommodate eight sensors at any one time and all sensors were situated radially and equidistant around a circular test cell, as seen in Figure 2–6, from the centre, where the air/gas inlet was located allowing all sensors to "experience" the exposure conditions synchronously. The total internal volume of the 8 channel test cell, calculated by the summation of the volume of each of the 8 channels, was 34 cm^3 [205]. This small internal volume of the test cell, ensured minimal lag in the gas flow towards the sensors and allowed for short measurements times [204]. The direction of the gas flow was at right angles to the sitting position of the sensor devices in the gas rig as observed in Figure 2–7.

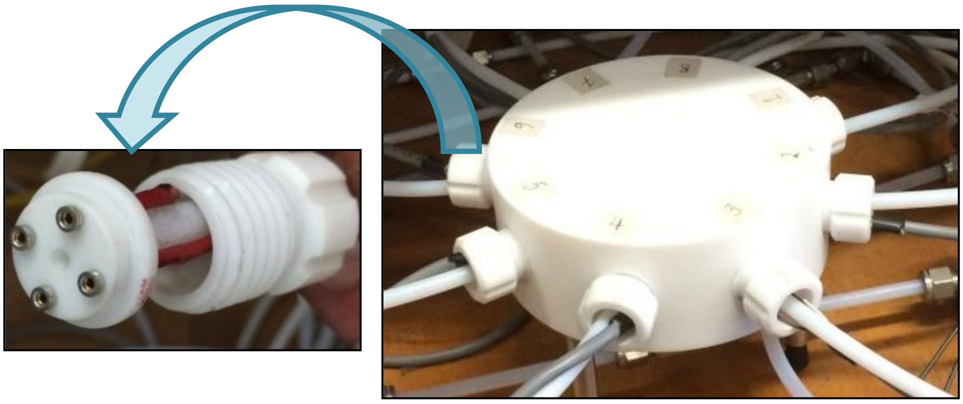

Figure 2–6. Circular test cell in which gas sensors are placed radially from the centre from where the gas and air inlet is located. The arrow leads to a picture of the sensor mount, in which the 4-pin sensor housing is seated.

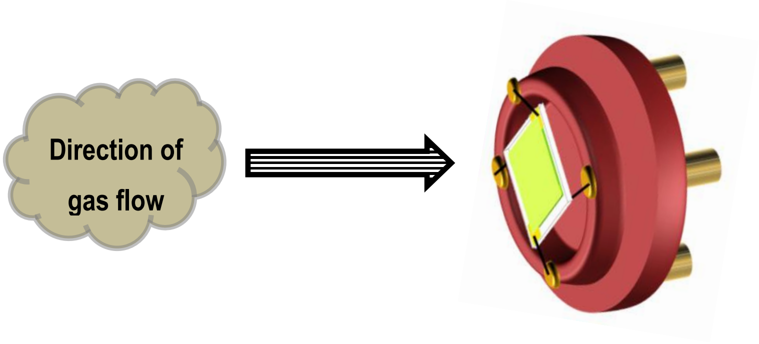

Figure 2–7. Illustration of the direction of the gas flow that the sensor device experiences when placed in gas sensing rig.

The sensors were held at constant operating temperatures via a Wheatstone Bridge heater driver circuit, an image of which is presented in Figure 2–8 and circuit diagram of which is presented in Figure 2–9, which were connected to each sensors' platinum heater track. The heater circuits were used to set the sensors at a range of operating temperatures between 250 °C and 500 °C, in 50 °C increments. The desired operating temperature was established via an iterative heater calculation programme written by Dr. Keith Pratt in Microsoft Excel [206]. The programme provides the voltage ratios required between A-B and B-C as illustrated in Figure 2–9, to provide the appropriate current, based on ambient conditions, through the selection of appropriate resistance values on the circuit's potentiometer, in order to establish the desired operating temperature [206].

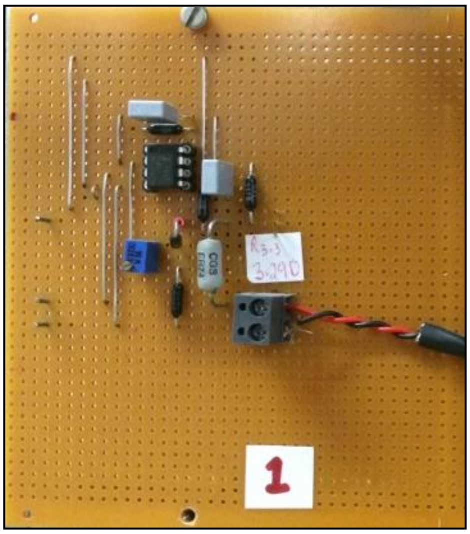

Figure 2–8. Wheatstone Bridge heater circuit.

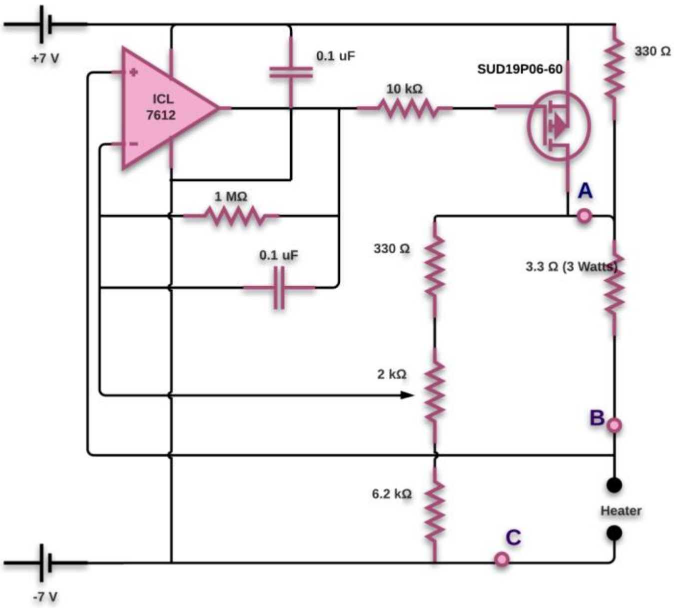

Figure 2–9. Circuit diagram of Wheatstone bridge circuit. {Diagram redrawn and adapted from O.A. Afonja [194]}.

Sensor conductance measurements were obtained through potentiostat circuits, presented in Figure 2–10. Specifically, the measurement sections of the potentiostat circuits were based on an inverting operational amplifier, a circuit diagram of which is presented Figure 2–11. The potential value was measured across the gold electrodes as illustrated in Figure 2–12 and could be converted to the associated resistance using the inverting operational amplifier equation seen in Equation 2–1:

Equation 2–1
$$v_{out} = -v_{in} \times {R_{fb}}/{R_{in}}$$

In the equation, v_{out} is equivalent to V_{sensor} and is the measured output voltage, v_{in} is the probe voltage, which is 100 mV, R_{fb} the feedback resistor value and R_{in} is equivalent to R_{sensor}, which is the unknown resistance of the sensor material to be calculated.

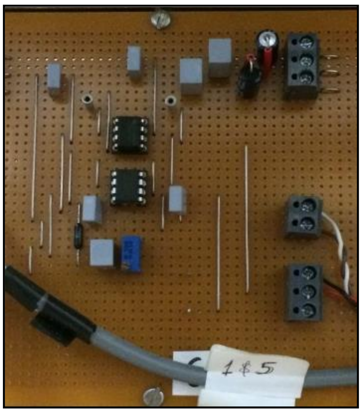

Figure 2–10. Potentiostat circuit board.

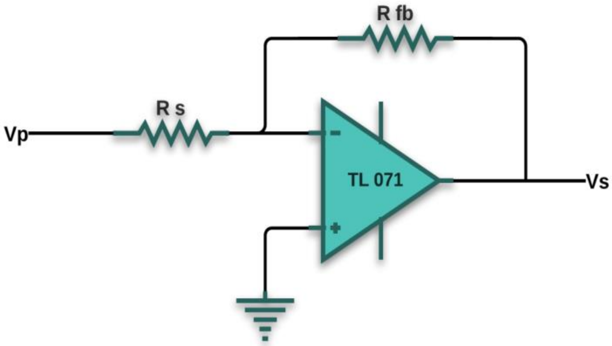

Figure 2–11. Circuit diagram of inverting operational amplifier segment of potentiostat measurement circuit. The sensor resistance is calculated using the following components of the circuit: Vp, the sensor device probe voltage, Rs, the unknown resistance of the sensor device, Rfb, the resistance of the feedback resistor and Vs, the measured potential across the sensor device. {Diagram redrawn and adapted from O.A. Afonja [194]}.

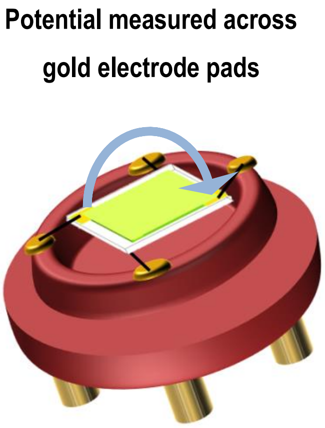

Figure 2–12. Illustration of the two-point potential measurement of the sensor material being made across the gold pads of sensor substrates.

Raw resistance data was transformed into conductive response and resistive response values in this thesis. The conductive and resistive responses were calculated as ratios of R_0/R_g and R_g/R_0, respectively. For each test cycle, the baseline value R_0 of an individual sensor, was calculated by taking its average resistance in air, in the first thirty seconds, prior to the first gas purge. This value of R_0 was then kept as a static value for the corresponding test cycle, and resistance of the sensor device factored against its corresponding R_0 value. Thus the absolute responses have been calculated as opposed to the relative responses - where each response value is calculated by taking R_0 to be the value prior to the corresponding gas injection. The R_0 value was calculated this way, as it ensured a standard baseline resistance value of the device, which was not in any way affected by a pre-conditioned gas sensor surface, that could subsequently change the resistance value.

The sensor devices were tested against a range of gases, which comprised of an oxidising gas: NO_2 in air, (100 – 800 ppb) and various reducing gases: ethanol in synthetic air, (5 - 100 ppm), acetone in air, (1 – 10 ppm), CO in synthetic air, (100 - 1000 ppm), NH_3 in air, (5 - 20 ppm) and toluene in synthetic air (10 – 50 ppm); all gas tests were carried out under dry air conditions and no water was added to the Dreschel bottles throughout the duration of this investigation. A variety of concentrations of each gas was obtained through dilution of the original concentration with compressed air (79% nitrogen, 21% oxygen). All gases were obtained from the British Oxygen Company. All concentrations of the gases tested were below the accredited toxic limit values (TLV) levels described in Chapter 1, except for CO, where higher concentrations than the TLV level were required for a quantifiable sensor response to be observed.

The gas delivery part of the rig observed in Figure 2–4 consisted of 5 MKS mass flow controllers (MFCs), 3 Takasago solenoid valves (SVs) and 2 Platon flow meters [194]. Gas supply to the test cell was controlled by MFC-1 which could be used in conjunction with MFC-4 for diluting the gas with dry air to the desired concentration or with both MFC-4 and MFC-5 to obtain the diluted gas mixture in a humid atmosphere. In the absence of any water in the Dreschel bottles, the dry air flow could be split between both MFC-4 and MFC-5, to obtain a dilute mixture of the gas in dry air; this is analogous to diluting the target gas with full flow of the dry air through only MFC-4. MFC-2 supplied dry air to determine the baseline resistance of the sensors in dry air and MFC-2 and MFC-3 together combined, enabled the determination of the baseline resistance of the sensors under humid conditions. Once again, in the absence of any water in the Dreschel bottles, the dry air flow could be split between both MFC-2 and MFC-3, for determination of the baseline resistance of the sensors in dry air; this is analogous supplying the full flow of dry air through only MFC-2, to determine the baseline resistance of the sensors. In the case of this experimental work, as no water was added to the Dreschel bottles during any period of the investigation, the dry air flows were split between MFC-4 and MFC-5 for diluting the target gas in dry air and between MFC-2 and MFC-3 for determination of the baseline line resistance of the sensor in dry air.

In this investigation, the required concentration of a particular gaseous analyte was achieved by varying the flow rate through MFC-1 (controlling target gas flow) and MFC-4 and MFC-5 combined (controlling dry air flow) and the baseline of the sensors in dry air was determined by splitting the dry air flow between MFC-2 and MFC-3.

The SVs in the gas delivery part of the system controlled the delivery of the gas and air (from the MFCs) to the test cell and the exhaust and were controlled by binary numbers 0 and 1, where 0 represented flow in the direction of the NO (normally open) port towards exhaust and 1 represented flow in the direction of the NC (normally closed) port towards the test cell as seen in Figure 2–4. SV-1 controlled the baseline air flowing from MFC-2 and MFC-3. SV-2 controlled the air (which was mixed with the target gas) flowing from MFC-4 and MFC-5. SV2 also controlled the gas flow into the test cell and therefore by default when SV-2 was set to 1, then SV-3 had to always be set to 0. If SV-3 were set to 1, the gas would by-pass the cell and flow to the exhaust, as observed in the schematic in Figure 2–4.

When setting up a gas test method file, the value assigned to an individual MFC was a % value of the full scale flow into the test cell. The total flow directed to the test cell always add up to 100%, which was representative of a total full scale flow of 1L/min, i.e. 100% = 1L/min or 1000 cc/min into the test cell. The minimum flow value of a MFC was set to 5%, which represented 5% of the total full scale flow of a MFC which was 1L/min i.e. 5% = 50 mL/min or 50 cc/min; any value below 5% was thought to be subject to fluctuations and errors and so 5% was a standard minimum flow rate. Thus whatever value was assigned to MFC 1 represented a % of the original concentration of the target gas, delivered to the test cell.

Table 2–9, presents an example of a gas test method file for a NO_2 test (original concentration in cylinder = 1000 ppb). A minimum flow rate of 5% was kept on all MFCs throughout most phases, so as not to hold the MFCs low powered state, which allowed a smooth transition to a high powered state, with an increased flow rate, in the succeeding phase. However despite the MFCs being set on 5%, the associated SV was always set to 0, and so the flow of gas/air always by-passed the test cell and went straight to the exhaust, so as to not disturb the input flow into the test cell in any way and ensure that the full scale flow into the cell was always 100% or 1L.

Table 2–9. Example of a gas testing method file for a NO_2 test, containing 12 phases. The original concentration of the NO_2 cylinder was 1000 ppb, however upon dilution with dry air, concentrations in the range of 50 – 800 ppb could be achieved. Each MFC was set a % of full scale flow into the test cell, which was 100%. In phases where the SV is set to 0, flow from the associated MFCs is directed to the exhaust, ensuring that the total flow inside the test cell is always only 100%. Where the SV is set to 1, flow from the associated MFCs is directed to the test cell. No water was added to the Dreschel bottles during anytime of testing and so the dry air flows could be split between a dry air and its corresponding wet air MFC.

Phase No.	Time (seconds)	MFC-1 (Gas)	MFC-2 (Dry Air)	MFC-3 (Wet Air)	MFC-4 (Dry Air)	MFC-5 (Wet Air)	SV-1 (MFC - 2/3)	SV-2 (MFC - 4/5)	SV-3 (MFC - 1)	NO_2 concentration (ppb)
0	20	0	0	0	0	0	0	0	0	0
1	1200	5	50	50	5	5	1	0	0	0
2	600	5	5	5	47.5	47.5	0	1	0	50
3	1200	5	50	50	5	5	1	0	0	0
4	600	10	5	5	45	45	0	1	0	100
5	1200	5	50	50	5	5	1	0	0	0
6	600	20	5	5	40	40	0	1	0	200
7	1200	5	50	50	5	5	1	0	0	0
8	600	40	5	5	30	30	0	1	0	400
9	1200	5	50	50	5	5	1	0	0	0
10	600	80	5	5	10	10	0	1	0	800
11	1200	5	50	50	5	5	1	0	0	0

In the table, phase 1 shows all MFCs were held in a powered low state and reset themselves for the first 20 seconds of the test, ensuring that a previous test setting is not carried over, just in case it was stopped in the middle of testing. In phase 2, a full scale flow of dry baseline air is directed into the test cell via SV-1 for 30 minutes followed by phase 3 in which 50 ppb of NO_2 is directed to the test cell via SV-2 for 10 minutes. Within each gas sensing test, sensor devices were exposed to a particular concentration of the target analyte for 600 seconds and dry air for 1200 seconds. A longer time was given in baseline air for the sensor to recover after exposure to the target analyte from the proceeding phase.

All gas sensing experiments were repeated in triplicate to ensure the responsivities observed were repeatable, with one type of each sensor device from each system, characterised for gas sensing behaviour. The gas sensing results of the final repeat test (graphical form) have been presented in the thesis with examples of various preceding repeat tests (in graphical form) presented in the Appendix.

Further throughout each section, average responses (calculated from all repeat tests) of the sensor devices from some of the gas sensing tests, and the associated errors in the form of 95% confidence intervals (CIs), have been tabulated. The 95% confidence interval (CI) is a useful method of estimating variability in gas sensing based experiments, as it assumes a random order in the response magnitude with sequential tests conducted. These error values indicate the interval which has a 95% probability of containing the average response value, illustrate the variability and repeatability of the response measurements and indicate the stability of sensor performance.

Generally, response results were seen to be repeatable and stable at low concentrations of gas exposure, but were associated to greater variation at the highest concentrations of gas exposure and/or with composite materials consisting of a significant contribution of both metal oxides. In most cases, preceding repeat tests showed a response signal for all devices, but in some cases where the response magnitude of the device was very high (usually towards the highest concentrations of analyte exposure) capping out of the signal was observed, due to the electronic limits of the digital multimeter integrated into the gas rig. This limited the calculations of errors on sporadic response magnitudes of some devices, and where this is the case, this has been indicated in the error tables. Brief error analysis has been presented in the summary and conclusion sections of most chapters, and a more detailed analysis of potential sources of error in the response measurements, have been discussed in Chapter 7. The baseline resistance ranges for each sensor device have also been tabulated in the Appendix for reference.

Chapter 3 : WO_3-ZnO based n-n hetero-junction system

In this first experimental Chapter, an in-depth investigation of materials and gas sensing characterisation study based on a n-n hetero-junction system of WO_3 and ZnO composites is presented.

3.1 Introduction

Literature on the gas sensing properties of a hybrid system containing WO_3 and ZnO are very limited, and more work is required to explore the potential of this combination of metal oxides. The combination of certain proportions of both these metal oxides, has been reported as an effective way to enhance gas sensing performance [207]. For example, in a recent study by Siriwong *et al*. [207], a report on the gas sensing properties of WO_3 doped ZnO nanoparticles made by Flame Spray Pyrolysis were reported. In their study, they prepared control ZnO nanoparticles as well as doping varying concentrations of WO_3 (0.25 mol.%, 0.5 mol.% and 0.75 mol.%) into ZnO nanoparticles. TEM imaging showed the particles to be attributed to spheroidal and hexagonal morphologies of size 5 - 25 nm and rod like morphologies with width of 5 – 10 nm and lengths of 10 - 25 nm. The nanoparticles were deposited onto gas sensor substrates by spin-coating and gas sensing characteristics tested against NO_2, CO and H_2 at operating temperatures between 300 °C – 400 °C. When exposed to increasing concentrations of NO_2 gas between 1 - 50 ppm at an operating temperature of 400 °C, the 0.5 mol% WO_3-ZnO sensor exhibited the highest resistive response with a 5-fold enhanced response with respect to the pure ZnO counterpart toward 50 ppm of NO_2, showing the properties of a ZnO film could be dramatically improved by addition of a specific amount of WO_3. Interestingly, the gas sensing responsivities of the doped nanoparticulate films were seen to decrease as a function of operating temperature, but that of the pure ZnO particles was seen to increase, showing the films had different temperature-conductance profiles [20, 137, 208]. Exposure of the sensors towards 100 ppm of CO as a function of increasing operating temperatures showed that the WO_3 doping had very little effect to the responsivity, with respect to the pure ZnO counterpart, and that all sensors showed negligible response towards the gas compared to NO_2. The same observation had occurred when the materials were exposed to 2000 ppm $H_{2,}$ with the WO_3 doping having no effect on the responsivity of the films. The group had concluded that the combination of the appropriate proportion of each of the oxides was a useful approach to enhance gas sensing-performance of the multi-component metal oxide system. Further, the group had reported that the preparation technique would considerably affect the physical, chemical and gas sensing properties of the mixed-oxide sensors because these factors are dependent on the essential surface activity of the layers, which are of course controlled by the method of fabrication.

In another more recent study by An *et al.* [209], a report on the enhanced NO_2 gas sensing properties of WO_3-ZnO core-shell architectures was reported. The hybrid materials were prepared by a dual method; the first encompassed the fabrication of the WO_3 core by catalyst-free thermal evaporation of WO_3 powder and graphite in an oxidising atmosphere, producing WO_3 nanorods and the latter encompassed atomic layer deposition (ALD) of ZnO around the WO_3 nanorods, producing WO_3-ZnO core-shell architectures. A schematic of these architectures has been presented in Figure 3–1.

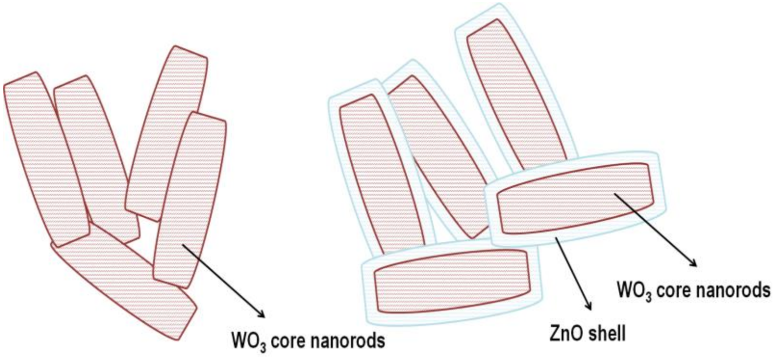

Figure 3–1. Schematic of WO_3 core nanorods and WO_3-ZnO core-shell nanorod architectures fabricated by An *et al*. [209].

The nanorod sample was prepared as a gas sensor by dispersion of the individual fabricated nanorod metal oxide materials into a mixture of deionised water and iso-propyl alcohol (IPA) and subsequent drop coating of the dispersion onto gas sensor substrates, forming multi-networked core-shell WO_3-ZnO nanorod sensors. The nanorods were seen to exist in a few tens to a few hundreds of nm in width and few tens of micrometres in length. When sensors were operated at 300 °C and exposed to increasing concentrations of NO_2 in the range 1 – 5 ppm, it was found that the bare WO_3 sensor showed responses of 7, 14, 19, 26 and 30 % towards 1, 2, 3, 4, and 5 ppm NO_2. In contrast the WO_3-ZnO core-shell hybrid nanorods were seen to show responses of 50, 87, 143, 201 and 281 % towards 1, 2, 3, 4 and 5 ppm NO_2, showing enhancements of 7, 6, 8, 8 and 9 with respect to the pure WO_3 counterparts. The WO_3-ZnO core-shell combination was reported to be attributed to a 5 times higher response than previous results of SnO_2-ZnO core-shell nanofibres, which were exposed to the same concentrations.

The group had explained the enhancement effect of the WO_3-ZnO hybrid system by a space charge model, whereby adsorption of NO_2 molecules on the surface of the hybrid metal oxide results in an increase in the size of the depletion layer or space charge layer on the surface. This is because the NO_2 molecules were thought to be able to deplete electrons from both the WO_3 and ZnO materials, as the surface layer size was an order of the Debye length. Thus, they proposed that the hetero-junction existing at the interface of both metal oxides was an important factor contributing to the enhancement of the device, as the transport of electrons is modulated by the hetero-junction, when they are depleted from both the WO_3 core and ZnO shell. Further, upon switching off the NO_2 gas, the electrons are released back into the conduction band of not only the ZnO shell, but also of the WO_3 core via the hetero-junction. As such, the hetero-junction was thought to act as a lever which could modulate the electron transfer (facilitation or restraint) in the hybrid system by adjusting the height of the effective energy barriers at the hetero-interfaces, resulting in the enhanced gas sensing properties observed.

The literature studies illustrate the effective gas sensing properties of a combination of both WO_3 and ZnO against NO_2 and suggest that the enhancement effects in such systems are complex, with a variety of factors such as specific combinations of both metal oxides as well as the hetero-junctions that exist at the interface, being influential factors contributing to the enhancement of the hybrid system.

In this investigation, an in-depth materials and gas sensing characterisation study on a hetero-junction system based on WO_3 and ZnO composites is presented. Based on literature searches, this is the first study based around composite packing structures of both metal oxides and a first to present the gas sensing properties of the hybrid system, against such an extensive range of analytes.

3.2 Results and Analysis

3.2.1 Scanning Electron Microscopy (SEM)

SEM imaging characterisation of all seven sensors in the WO_3-ZnO composite system was carried out to observe the microstructure of each material. The SEM images of all sensor materials in the WO_3-ZnO system presented in Figure 3–2.

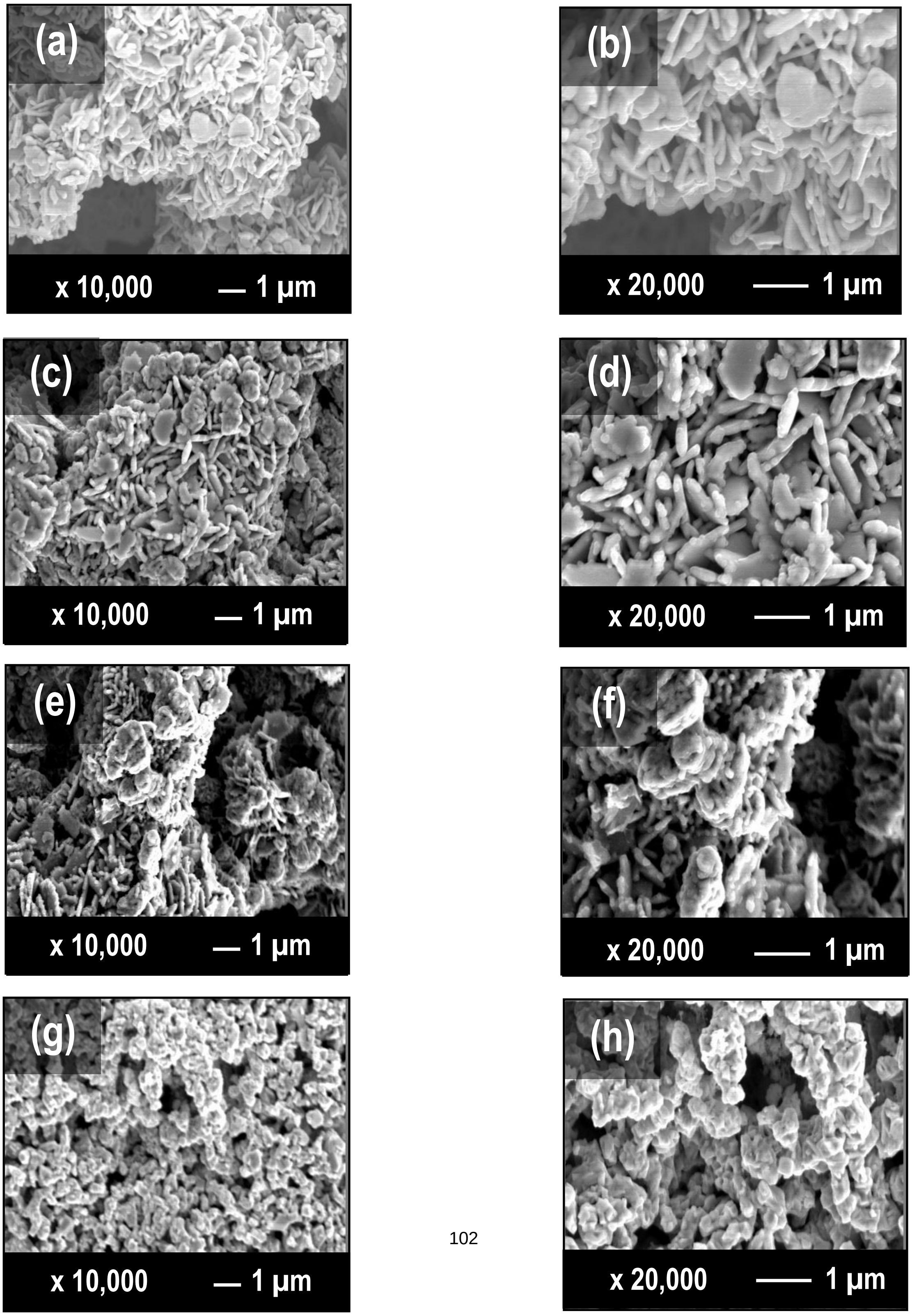

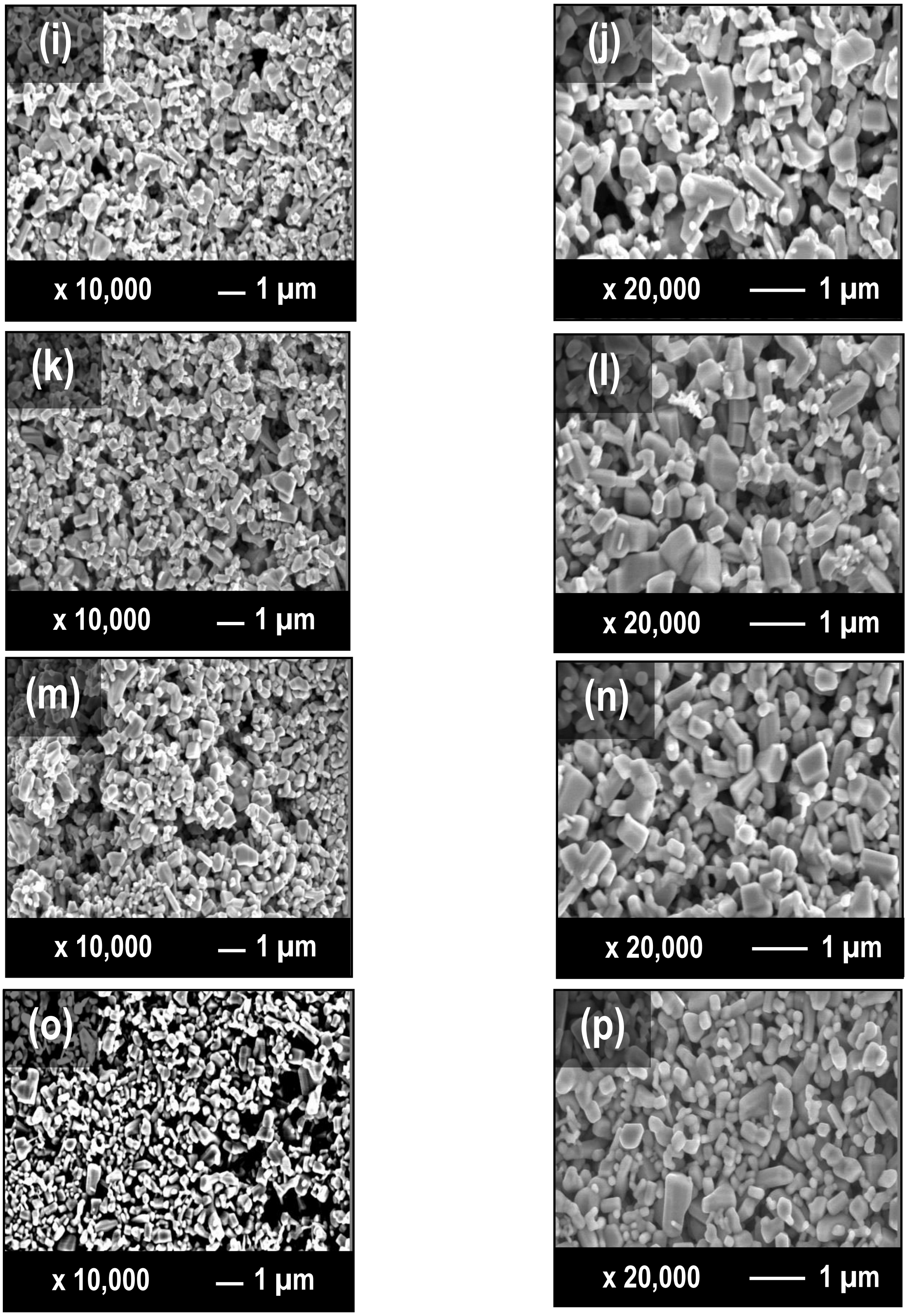

Figure 3–2. SEM images of (a) 100 wt.% WO_3 x 10,000 magnification, (b) 100 wt.% WO_3 x 20,000 magnification, (c) 90 wt.% WO_3 – 10 wt.% ZnO x 10,000 magnification, (d) 90 wt.% WO_3 – 10 wt.% ZnO x 20,000 magnification, (e) 70 wt.% WO_3 – 30 wt.% ZnO x 10,000 magnification, (f) 70 wt.% WO_3 – 30 wt.% ZnO x 20,000 magnification, (g) 50 wt.% WO_3 – 50 wt.% ZnO (area 1) x 10,000 magnification, (h) 50 wt.% WO_3 – 50 wt.% ZnO (area 1) x 20,000 magnification, (i) 50 wt.% WO_3 – 50 wt.% ZnO (area 2) x 10,000 magnification, (j) 50 wt.% WO_3 – 50 wt.% ZnO (area 2) x 20,000 magnification, (k) 30 wt.% WO_3 – 70 wt.% ZnO x 10,000 magnification, (l) 30 wt.% WO_3 – 70 wt.% ZnO x 20,000 magnification, (m) 10 wt.% WO_3 – 90 wt.% ZnO x 10,000 magnification, (n) 10 wt.% WO_3 – 90 wt.% ZnO x 20,000 magnification, (o) 100 wt.% ZnO x 10,000 magnification and (p) 100 wt.% ZnO x 20,000 magnification. All materials were screen-printed and heat-treated at 600 ºC before imaging.

SEM imaging characterisation of the sensor devices showed that the WO_3 particles observed in Figure 3–2 (a) and (b) were attributed to flat-faced platelet like morphologies with particle sizes observed to be as large as 1 µm in width and 0.125 µm in height. In contrast the ZnO particles observed in Figure 3–2 (o) and (p) were attributed to 3-dimensional cuboid shapes with rounded edges, with particle observed to be in the range of 0.1 µm to 1 µm.

A variation in the overall microstructure of the composite materials as a function of changing concentration of both metal oxides was observed, however minimal difference was observed between the 100 wt.% WO_3 and 90 wt.% WO_3 – 10 wt.% ZnO sensor devices , observed in Figure 3–2 (a) & (b) and (c) & (d), respectively and in the 10 wt.% WO_3 – 90 wt.% ZnO and 100 wt.% ZnO sensor devices, observed in Figure 3–2 (m) & (n) and (o) & (p), respectively, with the host metal oxides dominating the microstructure in the composite devices. This suggested that both composites devices were significantly homo-contact dominated, with the localised dispersion of WO_3-ZnO hetero-contacts present within the sensor matrix. In contrast, the 50 wt.% WO_3 – 50 wt.% ZnO and 30 wt.% WO_3 – 70 wt.% ZnO sensor devices observed in Figure 3–2 (i) & (j) and (k) & (l), showed more of a heterogeneous dispersion of both metal oxide grains within the sensor matrix, suggesting that the presence of WO_3-ZnO hetero-contacts were more delocalised within and around the WO_3–WO_3 and ZnO-ZnO homo-contacts.

The ability of gas molecules to not only interact with the material surface, but also with the body of the material, was evident through low agglomerated network of metal oxides grains in most devices. Thus, voids between the grain interfaces suggested the provision of pathways for gas molecules to diffuse and percolate through the body of the sensor matrix. Such a microstructure is favourable for gas sensing applications as it inherently increases the surface site interaction of the target analyte(s), leading to a higher yield of surface reactions between the analyte and the metal oxide surface, and ultimately increasing the responsivity of the material towards the target analyte. In contrast, a more compact gas sensing film inhibits the pathways for gas diffusion and as such, the target analyte interacts predominantly with the surface and in comparison, has limited interaction with the body of the sensor material.

In some devices however, gross intimate contact between the metal oxide grains was observed, an example being the 70 wt.% WO_3 - 30 wt.% ZnO sensor device observed in Figure 3–2 (e) and (f). Such intimate contact of the grains was suggestive of extensive agglomeration between the grains, which suggested a lower diffusion pathway of the gas molecules into the body of the sensor matrix. However despite the large inter-grain agglomeration, spaces between the agglomerates suggested that inter-agglomerate diffusion of the gas molecules was apparent in the sensor device, suggesting that diffusion of the gas molecules into the body of the sensor matrix could occur.

The 50 wt.% WO_3 - 50 wt.% ZnO device was observed to be associated to a contrast in grain contact within the sensor matrix. One part of the sample, observed in Figure 3–2 (g) and (h) was seen to be associated to extensive agglomeration between the grains, however another region of the sample, observed in Figure 3–2 (i) and (j) was seen to be associated to loosely held grains. The observed inhomogeneous microstructure of the sample, suggested a disadvantage in the preparation method (i.e. mechanical mixing) of the composite inks. Sun *et al*. [210] had reported in their study, where they had mixed powders (Cr_2O_3 and WO_3) using sonication and then drop-coated the suspension onto gas sensor substrates, that the irreproducibility that was associated to mixing powders was due to differences in the size and density differences of the particles and the different settling dynamics upon depositing the ink onto the alumina substrate.

The difference in particle sizes between both metal oxides suggested that within the composite, not only were hetero-junction effects introduced by the presence of grains of differing chemical natures, but also they were present due to the stark contrast in grains sizes. Yamazoe *et al*. [170, 171] had reported on hetero-junction effects within devices incorporating grains which were non-uniform. They had reported that the simplest factor in hetero-junction devices that contributed to the non-uniformity between the grains, was the differences in grain sizes between the grains. Thus, in the WO_3–ZnO composite system that was examined here, multiple in-homogeneities existed to exert hetero-junction enhancement effects, which are expected to play a positive role in the overall gas-sensing properties of the materials.

Evidence of fusing between the hetero-contacts in most sensor devices was not evident, however some localised fusing between the homo-contacts, in the sensor materials rich in WO_3 or ZnO, was observed. It is likely that higher thermal energy would be required to promote the fusing and sintering of the hetero-contacts, with reports in the literature suggesting that sintering of a composite material is difficult to achieve [89]. Too much thermal energy however, has a number of unfavourable implications associated to it. The first, specific to this WO_3-ZnO composite system, is the formation of the tertiary phase zinc tungstate, $ZnWO_4$, which was experimentally found present in the composite sensor devices, as a minor phase, after heat-treatment at 600 °C, data of which has been presented further in the Chapter in sections 3.3 and 3.4. Secondly, under very high-temperature conditions the microstructure suitable for gas-sensing applications will be compromised, with the formation of profuse "open necks" between the grains [65, 211]. These necks inhibit the formation of potential energy barriers between the grains, thus creating paths of low resistance for the charge carriers to travel across, such a microstructure restricts the surface-site accessibility of the gas as the neck region contributes to the bulk of the material; both these factors contributing to reducing the overall responsivity of the gas sensitive material [65]. Low sintering between grains in contrast, promotes the formation of a "closed neck" [65, 211] case, where there exists more resistive potential barriers between the grains that charge carriers must overcome. Further, such a microstructure promotes more contact of the surface of gas sensitive material with the analyte, as the neck contributes to the surface component of the gas sensitive material [65]. Such a microstructure would enhance the overall gas sensing properties of the material. This apparent difference in extent of sintering, suggests a possible influence of microstructure on the electron percolation pathways between the different composites and variation in the extent of surface site accessibility of the analyte within the individual composites.

SEM imaging of the solid-state synthesised $ZnWO_4$ was also conducted and the associated images have been presented in Figure 3–3.

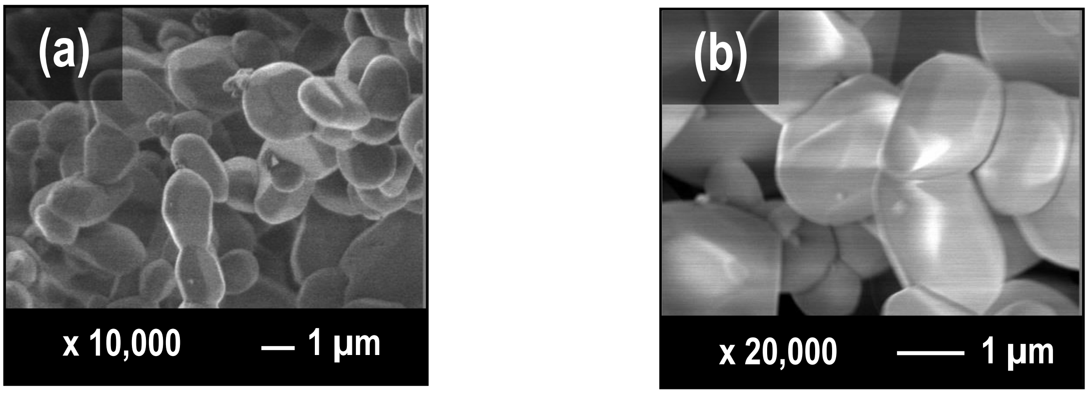

Figure 3–3. SEM images of (a) 100 wt.% $ZnWO_4$ x 10,000 magnification and (b) 100 wt.% $ZnWO_4$ x 20,000 magnification. The material was screen-printed and heat-treated at 600 ºC before imaging.

SEM images of the sensor device of the tertiary phase, $ZnWO_4$, shown in Figure 3–3 (a) and (b) was in stark contrast to the microstructure of the WO_3 and ZnO pure and composite sensor devices. The images show huge grain sizes, larger than 1 µm, with sintering evident between the grains. This is a likely result of firing the compound to 1000 °C for 16 hours, during the solid-state synthesis method. Yamazoe *et al.* [170] have reported that the formation of gross necks in the literature has been reported under harsh conditions, of which firing at 1000 °C, is experimentally as seen above, an example. As such, the sintered necks are likely to contribute insignificantly to the overall material resistance and therefore this material is likely to be associated to low gas responsivity, if any, in comparison to the pure and composite WO_3 and ZnO based materials. However the inherent responsivity of $ZnWO_4$ is not expected to diminish completely despite its highly sintered microstructure; only the amplitude of its response signal is expected to be lower in comparison to the response magnitude from a microstructure, which has many more grain boundaries. Firing at excessive temperatures for long periods of time does promote grain growth [65, 195] and as such, the microstructure obtained experimentally here, can be justified.

The $ZnWO_4$ was experimentally in this thesis synthesised by a solid-state method reported by Phani *et al.*[195]. The difference in microstructure of the tertiary phase obtained in this thesis to that reported in the literature[195], could be attributed to the fact that Phani *et al.* fired the final $ZnWO_4$ at 1000 °C for 24 hours, as opposed to the 16 hour period that the $ZnWO_4$ was heat-treated at, experimentally.

3.3 XRD (X-Ray Diffraction)

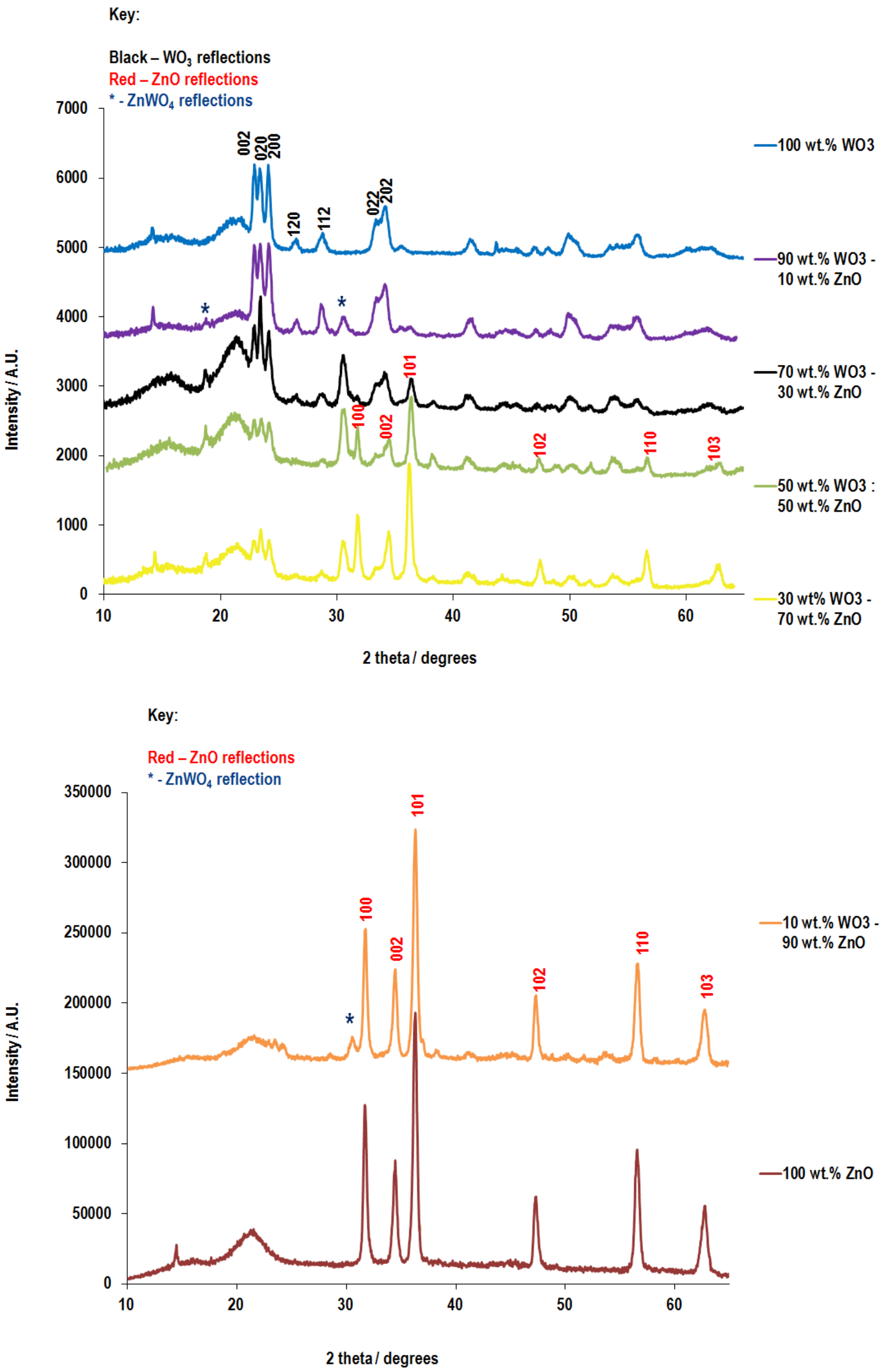

Figure 3–4. XRD patterns of (a): 100 wt.% WO_3, 90 wt.% WO_3 – 10 wt.% ZnO, 70 wt.% WO_3 – 30 wt.% ZnO, 50 wt.% WO_3 – 50 wt.% ZnO and 30 wt.% WO_3 – 70 wt.% ZnO sensor devices and (b): 10 wt.% WO_3 – 90 wt.% ZnO and 100 wt.% ZnO sensors. The strongest reflections of WO_3 are indicated in black and ZnO are in red. The peaks marked with an * correspond to the tertiary phase, $ZnWO_4$. All materials were screen-printed and heat-treated at 600 °C, prior to XRD measurements.

Glancing angle X-Ray Diffraction (XRD) seen in Figure 3–4 showed that both WO_3 and ZnO samples were crystalline. Phase identification analysis found that that commercial WO_3 powder corresponded to randomly oriented monoclinic γ-crystal phase matching the reference pattern (ICDD 43-1035). The random orientation of the WO_3 crystallites in the samples, was indicated by the large intensities of the three closely spaced reflections (002, 020, 200) [109] in the region of 22-25 °2θ.

The commercial ZnO powder matched the reference ZnO pattern (ICDD 36-1451) [212], indicating that the ZnO corresponded to a hexagonal wurtzite crystallite structure [77, 213, 214].

The XRD patterns of the composite samples were clearly indicative of the change in ratio of WO_3 and ZnO, with the ZnO diffraction peaks becoming more intense and the WO_3 peaks concurrently decreasing in intensity, as the concentration of ZnO increased with respect to a decrease in concentration of WO_3. Further, the patterns indicated that the composite materials were physically composites and not chemical compounds or solid solutions, evidenced through clearly distinguishable XRD peaks of both individual metal oxides and absence of any peak overlap between them.

XRD patterns of all the composites indicated the presence of $ZnWO_4$, as minority phase. The peaks at approximately 18.6 °2θ and 30.55 °2θ corresponding to this tertiary phase (seen in Figure 3–5) have been marked with an asterix (*). Empirical evidence suggests through the comparison of the peak intensities of $ZnWO_4$ between each composite pattern, and the $ZnWO_4$:ZnO relative peak ratios of each composite pattern that the concentration of this tertiary phase increases as the concentration of ZnO decreases and that of WO_3 begins to increase. A limit is reached at the 50 wt.%:50 wt.% WO_3:ZnO composite, after which further increase in WO_3 composition and a subsequent decrease in ZnO, results in less $ZnWO_4$ formation. A similar observation in variation of zinc tungstate content relative to ZnO and WO_3 concentration, has been observed and reported previously in the literature [111]. The formation of this phase was inevitable due to exposure of the composite to the large thermal energy from firing the sensors at 600 °C.

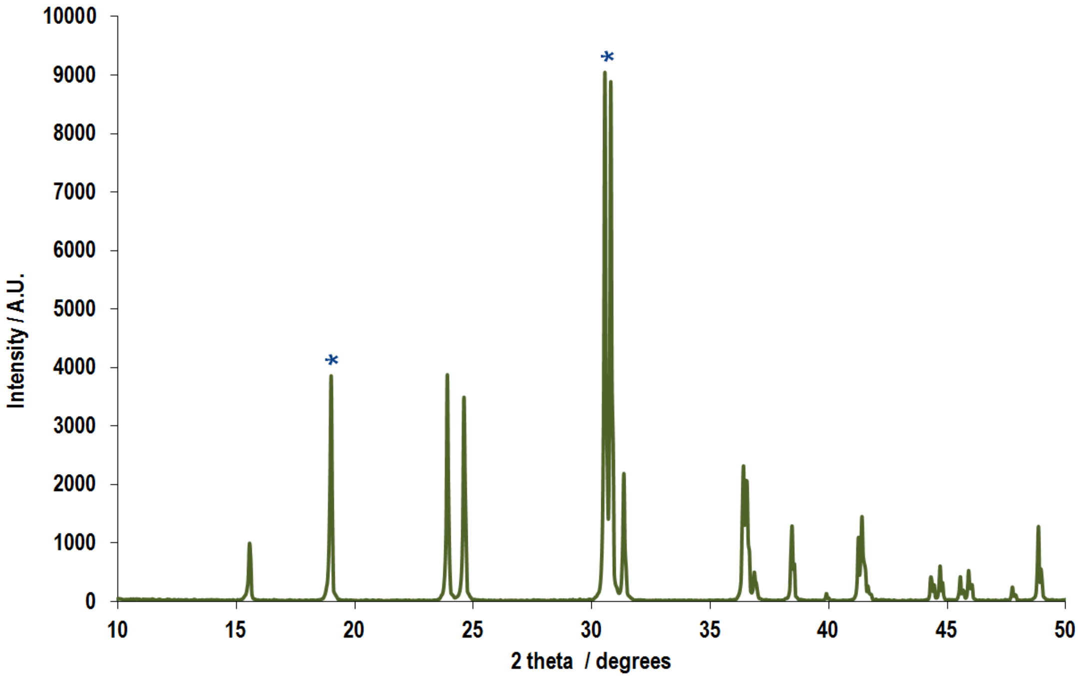

Figure 3–5. PXRD pattern of pure zinc tungstate ($ZnWO_4$), experimentally synthesised by a solid-state method reported by Phani *et al*. [192].

PXRD of the tertiary phase, $ZnWO_4$, has been presented in Figure 3–5. The experimental pattern was in agreement with the reference pattern corresponding to JCPDS 15-0774 [215], with tungstate adopting a pure monoclinic wolframite structure. The two peaks which have been marked with an asterix (*), are those which could be identified in the XRDs of the WO_3-ZnO composite materials, presented in Figure 3–4.

3.4 Raman Spectroscopy

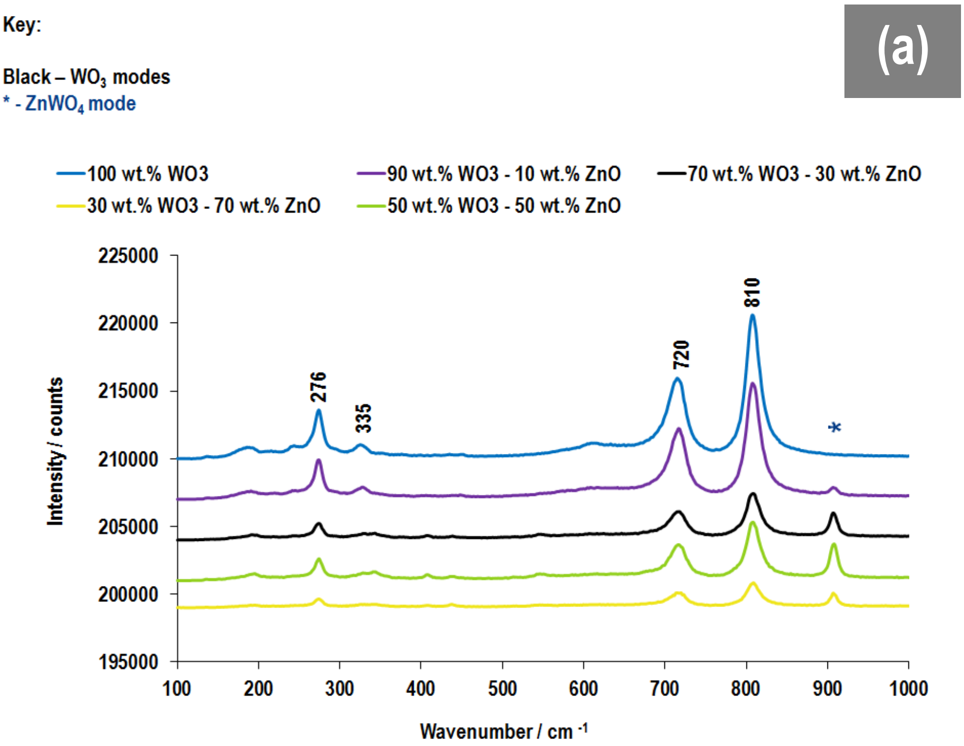

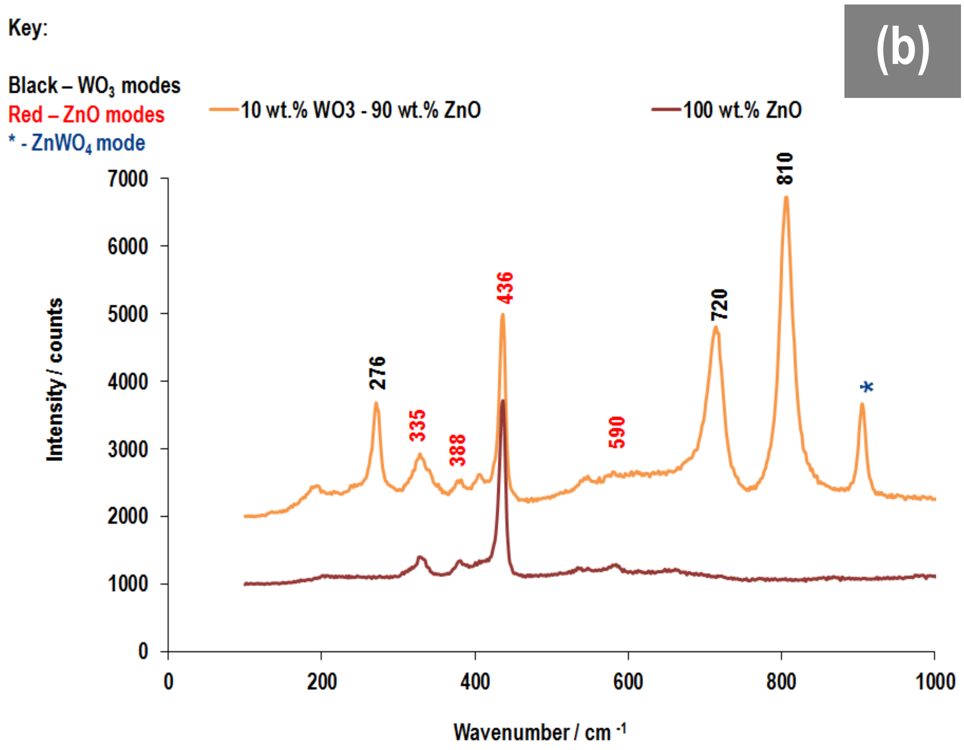

Figure 3–6. Raman patterns of (a): 100 wt.% WO_3, 90 wt.% WO_3 – 10 wt.% ZnO, 70 wt.% WO_3 – 30 wt.% ZnO, 50 wt.% WO_3 – 50 wt.% ZnO and 30 wt.% WO_3 – 70 wt.% ZnO sensor devices and (b): 10 wt.% WO_3 – 90 wt.% ZnO and 100 wt.% ZnO sensors. The modes of WO_3 are indicated in black and ZnO are in red. The modes marked with an * correspond to the tertiary phase, $ZnWO_4$. All materials were screen-printed and heat-treated at 600 °C, prior to Raman spectroscopy measurements.

Raman spectroscopy in Figure 3–6 corroborated the findings from the XRD characterisation, with the spectrum of WO_3 in Figure 3–6 (a) showing the Raman shifts at 810 cm^{-1}, 720 cm^{-1}, 335 cm^{-1} and 276 cm^{-1}. All of these bands have been observed in similar positions in the literature before, with the former two attributed to the W-O-W stretching modes of the bridging oxygen and the latter two attributed to the associated bending modes of monoclinic γ-WO_3 [34, 55, 103, 216, 217].

Bands observed experimentally for ZnO in Figure 3–6 (b) at 335 cm^{-1}, 388 cm^{-1}, 436 cm^{-1}, have also been observed and reported in the literature, with the first and last being associated to a second order Raman spectrum, occurring due to zone boundary phonon modes of the ZnO crystal: $3E_{2H}$-E_{2L} (335 cm^{-1}) and E_{2H} (436 cm^{-1}) and the band observed at 388 cm^{-1} corresponding to the A_1(TO) phonon mode of the ZnO crystal [218-220].

Figure 3–6 (a) shows that most composites show mainly the presence of WO_3, with ZnO being largely unidentifiable, as WO_3 is a much greater scatterer than ZnO. This is because vibrational frequencies are atomic mass dependent, with WO_3 having a significantly greater molecular mass than ZnO. However, the 10 wt.%:90 wt.% WO_3:ZnO sample observed in Figure 3–6 (b) shows evidence of each component within the composite system being individually identifiable and present.

Appearance of the stretch at 911cm^{-1}, marked with an asterix (*), was observed only in the composite materials, but not in the pure oxides. The appearance of this peak has been observed as the most intense peak in the Raman spectra of $ZnWO_4$, presented in Figure 3–7, and is attributed to a WO_6 symmetric stretch vibration, which is associated to the isolated WO_6 wolframite crystal structure of $ZnWO_4$ [221-223].

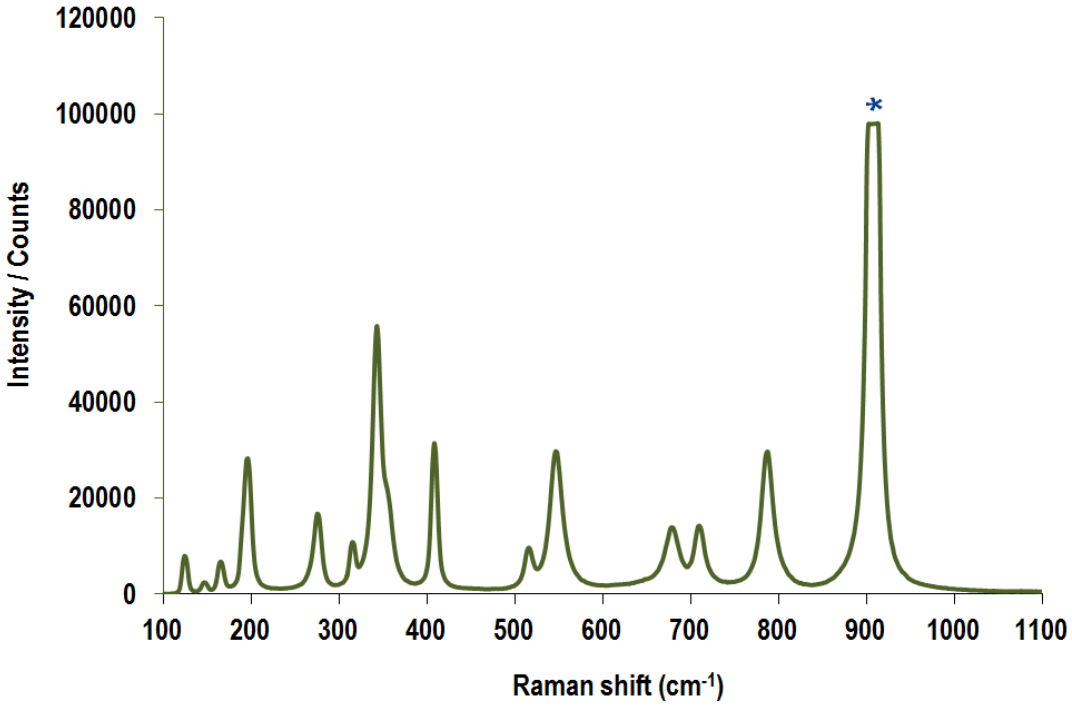

Figure 3–7. Raman pattern of pure zinc tungstate ($ZnWO_4$), experimentally synthesised by a solid-state method reported by Phani *et al*. [192]. The peak with the asterix (*) is the high intensity $ZnWO_4$ peak that was observed in the Raman patterns of the composite materials in Figure 3–6.

Figure 3–7 presents the Raman spectrum of $ZnWO_4$, which was in agreement with Raman patterns reported in the literature, such as that by Kalinko *et al*. [222] and Liu *et al*. [221] . These groups report that the vibrational frequencies at 908 cm^{-1}, 788 cm^{-1} and 409 cm^{-1} are associated to the symmetric stretching vibration associated to the isolated WO_6 wolframite crystal structure of $ZnWO_4$ [223].

3.5 X-Ray Photoelectron Spectroscopy (XPS)

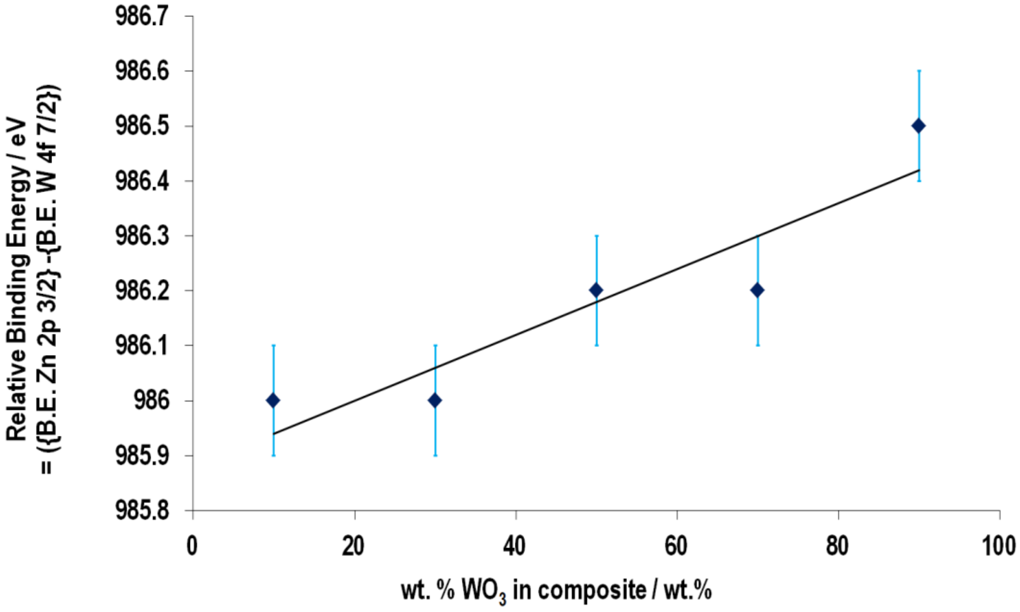

Figure 3–8. XPS relative binding energies (B.E.) (calculated by taking the difference between the B.E. of the Zn $2p_{3/2}$ peak and the B.E. of the W $4f_{7/2}$ peak) for all the associated WO_3-ZnO composites as a function of wt.% WO_3 in each composite.

XPS measurements were conducted on all sensors within the system, with two binding energy peaks of each metal observed for the corresponding metal oxide. All spectra (with a ± 0.1 eV experimental measurement error) were standardized against the C1s binding energy of 284.6 eV obtained from the reference database [201] and from literature [202, 203]. For all WO_3 containing samples, a W $4f_{7/2}$ peak in the range of 35-36 eV was observed and for all ZnO containing samples, a Zn $2p_{3/2}$ peak occurred in the range of 1021-1023 eV. All the observed peaks were experimentally in agreement with the reference database [201] and accompanied by spin-orbit doublets. For the Zn species, Zn $2p_{3/2}$ and Zn $2p_{1/2}$ splitting values in the range of 22.9 – 23.2 eV were in close agreement to literature values [224]. For the W species, W $4f_{7/2}$ and W $4f_{5/2}$ splitting values in the range of 2.0 - 2.2 were in close agreement to literature values [225, 226]. XPS did not show evidence of any remnants such as silica from the organic vehicle in any of the sensor devices. Calculation of the relative binding energies, by finding the difference between the binding energies of the Zn $2p_{3/2}$ and the W $4f_{7/2}$ peaks, as a function of increasing WO_3 composition in the composites, gave evidence of interactions taking place between the individual oxides. Since XPS binding energies are referenced to the Fermi Level (E_F), a change in the relative positions of the W and Zn core levels indicates a change in E_F relative to the energy levels in WO_3 and ZnO phases. Figure 3–8 shows that the difference between the W and Zn core lines increases as a function of increasing WO_3 phase fraction, showing that the ZnO energy levels move down and the WO_3 energy levels move up relative to E_F. This is consistent with increasing electron donation from WO_3 to ZnO. As such, the Fermi level of WO_3 effectively decreases, whilst that of the ZnO effectively increases, maintaining the equilibration of the Fermi level throughout all the composites in the system. As these shifts occur as a function of changing composition, a change in the relative binding energy is observed. XPS data therefore gave evidence of an electronic interaction within the hetero-junction mixed-oxide system.

3.6 Gas Sensing

3.6.1 Gas Sensing Properties of $ZnWO_4$

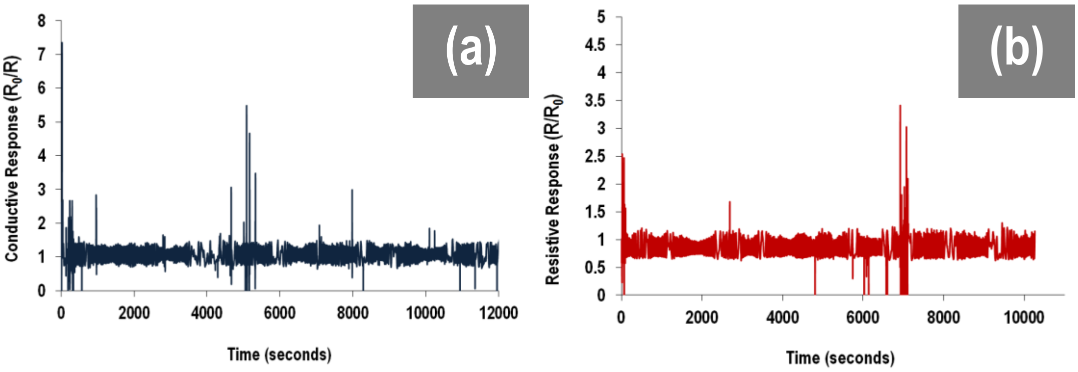

Figure 3–9. (a) Conductive response of $ZnWO_4$ at 350 °C exposed to increasing concentrations: 5, 10, 20, 40, 80 and 100 ppm ethanol gas and (b) Resistive response of $ZnWO_4$ at 300 °C exposed to increasing concentrations: 100, 200, 400 and 800 ppb NO_2 gas.

The observation of the presence of $ZnWO_4$ in the composite materials, prompted investigation of the responsivity of the tertiary phase against the two main test gases NO_2 and ethanol, that have been investigated against all systems reported in this thesis. Figure 3–9 presents the responsivity of the tertiary phase against increasing concentration of both analytes at the optimal operating temperatures of the WO_3-ZnO composite system (presented further in the Chapter) which was 300 °C against NO_2 as seen in Figure 3–15 and 350 °C against ethanol as seen in Figure 3–12. Figure 3–9 (a) presents the conductive response of $ZnWO_4$ against increasing ppm concentrations of ethanol and Figure 3–9 (b) presents the resistive response of $ZnWO_4$ against increasing ppb concentrations of NO_2. The figures show that the tertiary phase was associated to no responsivity towards both analytes, suggesting that its presence in the composite materials had no role towards promoting the responsivity of the materials.

In the literature, the number of reports on $ZnWO_4$ as a gas sensor are very limited, but a few do exist [227, 228]. In one report, Cao *et al.*[227] had reported on the use of nanosized $ZnWO_4$ for a cataluminescence sensor – a sensor which emits cataluminescence in the process of catalytic oxidation, in this case for the detection of ether. Specifically, the process involves the emission of electromagnetic radiation (most commonly in the UV-Vis or Infrared region), due to the catalytic oxidation of organic molecules on solid catalyst surfaces. The surfaces generally yield the excited intermediates of the organic molecules in the excited electronic states, producing light when they recover back to the ground electronic state. The group had reported that the sensor had performed optimally at an operating temperature of 330 °C with a detection limit of 8.7 ppm ether. When exposed to a range of VOCs at 200ppm that included ethanol, acetone and ether, the sensor was found to be selective to ether, with no responsivity towards ethanol and hardly any towards acetone.

In another study by Tamaki *et al*. [228], the group had observed $ZnWO_4$ to exhibit a responsivity of 2.6 and 1.8 towards 200 ppm NO at 450 °C and 500 °C, respectively and responsivities of 34.7 and 14.8 towards 50 ppm NO_2 at 450 °C and 500 °C, respectively. The response behaviour of this material, alongside other metal tungstates, had been attributed to p-type behaviour. This literature study [228] suggests that this tungstate may be responsive towards NO_2 gas at very high concentrations in the ppm range. In contrast, the concentrations studied in this thesis are in the ppb range. Further reports in the literature have also shown $ZnWO_4$ to be a potential candidate as a humidity sensor [229].

Given that the presence of the tertiary phase was minimal in comparison to the content of the individual oxides in the various composite mixtures, inferred from empirical evidence of relative intensities of $ZnWO_4$ versus the WO_3 and ZnO reflections, in the XRD patterns in Figure 3–4, and given that the tertiary phase showed no responsivity towards ethanol and NO_2 as observed in Figure 3–9, analysis suggested that the tertiary phase did not play an active role towards enhancing the response of the composite systems. This inference is in contrast to a report of the function of $ZnWO_4$ in ZnO and WO_3 composites reported by Ge *et al.*[111]. The group reported that an appropriate amount of the tungstate phase in WO_3-ZnO composites, can act to enhance the gas sensing properties.

The SEM of $ZnWO_4$ in Figure 3–3 showed that the microstructure of the synthesised tertiary material is significantly different to that of the system of WO_3-ZnO composites observed in Figure 3–2, with the $ZnWO_4$ seen to have larger particle sizes and fused grains. As such, it can be argued that its microstructure may have played a role in inhibiting the responsivity of this compound. However, MOS sensor responsivity is promoted through the fundamental principle that the surface sites of the gas sensitive material can adsorb [1, 45, 230], and subsequently stabilise the adsorption of the ionised oxygen species [137]. The reaction of the adsorbed oxygen species with the target analyte will promote a change in the charge carrier concentration, resulting in changing the resistance (increase or decrease) of the semiconducting oxide. Thus the inherent response characteristic of a material, if any, is always present, independent of the microstructure of the material. The microstructure would however, play a significant role in the amplification of the response trace, depending on size effects, in terms of particle size, agglomeration and thickness of the film and the extent of sintering [1, 65, 231].

3.6.2 Gas Sensing Properties of WO_3-ZnO hetero-junction system

This section presents an in-depth gas sensing functionality study of all sensor devices in the WO_3-ZnO composite system against ppm concentrations of ethanol and ppb concentrations of NO_2. Further gas sensing studies against a range of reducing gases: CO, NH_3 and acetone has also been presented. Results of all sensor devices within the system have been presented here, except the 70 wt.% WO_3 – 30 wt.% ZnO sensor device, which was attributed to significant electrical digitisation to its response signals, which invalidated subsequent interpretation and analysis of the response behaviour. A second device of this composition was built and tested to confirm the effect seen with this composition and again the second device confirmed that this particular composition was attributed to significant noise.

3.6.2.1 Ethanol Sensing

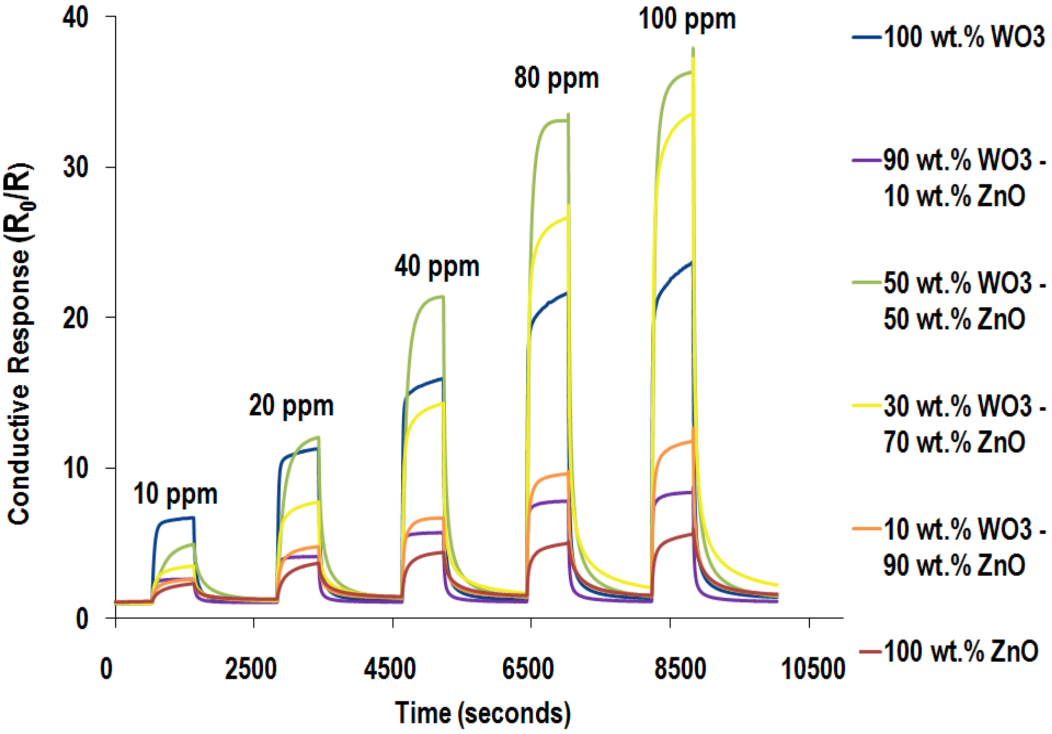

Figure 3–10. Conductive response traces of the WO_3-ZnO system towards 10, 20, 40, 80 and 100 ppm ethanol gas, at an operating temperature of 350 °C.

The conductive response of the WO_3-ZnO system against increasing concentrations of ethanol at an operating temperature of 350 °C, have been presented in Figure 3–10. Tabulation of the mean responses values of the devices in the WO_3-ZnO system from the repeat tests against exposure towards the various ethanol concentrations at 350 °C and the associated 95% confidence intervals have been presented in Table 3–1.

Table 3–1. Average conductive responses of sensors devices in WO_3-ZnO system from all repeat tests against various ethanol concentrations at 350 °C and associated errors in the form of 95% CIs.

	10 ppm		**20 ppm**		**40 ppm**		**80 ppm**		**100 ppm**	
Device	Average Response	95% CI	Average Response	95% CI	Average Response	95% CI	Average Response	95% CI	Average Response	95% CI
100 wt.% WO_3	6.69	±0.20	11.62	±0.35	16.62	±1.32	22.85	±2.35	25.09	±2.72
90 wt.% WO_3 – 10 wt.% ZnO	2.68	±0.10	4.24	±0.10	7.77	±1.24	8.35	±0.58	9.23	±0.65
50 wt.% WO_3 – 50 wt.% ZnO	4.83	±0.20	11.86	±0.71	20.20	±2.34	33.08	±3.27	36.18	±3.85
30 wt.% WO_3 – 70 wt.% ZnO	3.61	±0.12	8.54	±0.66	14.30	±0.01	28.11	±4.89	32.41	±9.44
10 wt.% WO_3 – 90 wt.% ZnO	2.83	±0.25	5.52	±0.64	5.90	±0.21	10.77	±1.10	13.22	±1.58
100 wt.% ZnO	2.46	±0.38	4.15	±0.72	3.93	±1.95	6.44	±2.18	6.82	±2.82

350 °C was the temperature at which most of the sensor devices within the system exhibited optimal response performance, except for the 100 wt.% ZnO sensor device which was seen to perform optimally at 450 °C, as seen further in Figure 3–12. The observed increase in the conductive response of the system of devices against ethanol, suggested that the conductivity occurred via the n-type percolation pathways that were present between the WO_3 - WO_3 n-n homo-contacts and ZnO - ZnO n-n homo-contacts in the pure and composite materials and the WO_3 – ZnO n-n hetero-contacts in the composite materials, with both metal oxides being well-established to exhibit n-type semiconductor behaviour i.e. an increase in conductivity upon exposure to ethanol [220, 232].

Figure 3–10 showed evidence of the enhanced response of some of the composite devices in comparison to one or both of the pure counterparts devices: 100 wt.% WO_3 and 100 wt.% ZnO. The largest response was observed by the 50 wt.% WO_3 – 50 wt.% ZnO composite device which had a response of 37.9 towards 100 ppm at 350 °C, attributed to a 1.6-fold better performance than the pure WO_3 sensor and a 6.6-fold better performance than the pure ZnO sensor under the same experimental conditions. The 30 wt.% WO_3 – 70 wt.% ZnO sensor device was also seen to exhibit an enhanced response of 37.2 towards 100 ppm ethanol, which was a 1.6-fold better response than the pure WO_3 sensor and a 6.6-fold better response than the pure ZnO sensor device. Thus, the results gave evidence of an enhancement effect of a multi-component metal oxide system on the responsivity in comparison to the single metal oxide systems. Both the 50 wt.% WO_3 – 50 wt.% ZnO and the 30 wt.%

WO_3 - 70 wt.% ZnO devices, were seen from the SEM characterisation in Figure 3–3 (i) & (j) and (k) & (l) respectively, to contain a random dispersion of both metal oxides which suggested that the packing structures of both composite materials were attributed to WO_3 –ZnO hetero-contacts as well as WO_3-WO_3 and ZnO-ZnO homo-contacts. The random dispersion of both metal oxide grains observed was suggestive that both devices may have been attributed to a large concentration of delocalised contact potentials [170, 171], which played a role to enhance the responsivity of the materials, by modulating the electron drift mobility and as such increase its overall response function [170, 171]. In particular, the higher resistance energy barriers that have been postulated to exist between to inequivalent grains [170], can act to increase the resistance of the hetero-contact, making it more sensitive to the atmosphere around it [170].

These results are in stark contrast to theory postulated by Yamazoe *et al.*[170, 171] who argued that a random packing structure of hetero-contacts has limited contribution to the overall transduction function of the device, due to competition between the homo-contacts and hetero-contacts connected in parallel, which act to cancel each other out, and as a result the transduction function can hardly change. However, the experimental evidence presented in Figure 3–10 suggests that random 2-dimensional distribution of hetero-contacts [170, 171] can play an effective role in gas sensing applications. Further, the hetero-junctions in this study were not only due to the chemical inhomogeneity of both metal oxide materials, but also due to the differences in the particle sizes between the WO_3 and ZnO grains [170, 171]. Significant differences in the particle size have been reported to increase the resistance of the hetero-contact [170, 171] and act to enhance the overall transduction function of the device.

Figure 3–10 further shows that the two sensor devices which were dominated by the host matrix of metal oxide grains i.e. the 90 wt.% WO_3 – 10 wt.% ZnO device, which was dominated by the WO_3 grains and the 10 wt.% WO_3 – 90 wt.% ZnO device, which was dominated by the ZnO grains, also showed enhanced responses with respect to the pure ZnO sensor device. In particular the 10 wt.% WO_3 – 90 wt.% ZnO device showed that the ability to enhance the responsivity of a sensor (with respect to pure ZnO sensor device) by a simple change in the concentration of WO_3 and ZnO. However the relatively low responses of both these composite devices with respect to other composites in the system, maybe accounted for by the route of conduction being dominated by homo-contacts. The percolation pathways in devices where the homo-contacts are more dominant than the hetero-contacts, are practically non-resistive. This implies that the electrons need to surmount a lower energy barrier to move through the same individual grains in the body of the material. This reasoning may justify the lower response of the 90 wt.% WO_3 – 10 wt.% ZnO device and the 10 wt.% WO_3 – 90 wt.% ZnO device with respect to the 50 wt.% WO_3 – 50 wt.% ZnO and the 30 wt.% WO_3 - 70 wt.% ZnO devices.

As the concentration of ethanol increased, Figure 3–10 showed that the devices showed a gradual drift in the baseline. The behaviour was particularly apparent for the two best performing composites: the 50 wt.% WO_3 – 50 wt.% ZnO and the 30 wt.% WO_3 - 70 wt.% ZnO sensor devices. Such behaviour is thought to be induced by the production of H_2O from the combustion reactions of the ethanol molecules on the surface of the metal oxides [69], which have been presented in Chapter 1. H_2O molecules are thought to split at the surface of a metal oxide in the form of OH^- and H^+ ions [12]. The OH^- ions are thought to introduce electrons to the surface of the metal oxide, which act to increase the conductivity of an n-type material [12]. Further, the H^+ ions are also thought to increase the conductivity of the n-type material, by reacting with surface oxygen atoms and promoting the formation of negative holes [12]. N-type semiconductors in particular, are responsive to this introduction of electrons to their surface, as the EDL, positioned on the surface, is the layer through which conductivity takes place in such semiconducting oxides. In particular the dominant drift of both of the best performing composites may be accounted by their stronger intermolecular bonding to the water molecules, than other sensors devices within the system.

Figure 3–10 shows that in terms of linear range of response, a steep increase in the response magnitudes of the 50 wt.% WO_3 – 50 wt.% ZnO and 30 wt.% WO_3 – 70 wt.% ZnO sensor devices was evident as the ethanol concentration was increased from 20 ppm to 40 ppm to 80 ppm. This behaviour may have been due to the larger number of surface sites available in these multi-component materials to accommodate the increasing number of ethanol molecules as a function of increasing concentration of exposure, and as such promote an increased yield of ethanol combustion reactions per unit time. Such a steep increase in linear range, as a function of increasing ethanol concentration, was not evident in the pure metal oxides and those composites associated to the 90 wt.% - 10 wt.% and 10 wt.% - 90 wt.% ratios. In contrast, these materials displayed a shallow increase in response magnitude as a function of increasing ethanol concentration, which may be attributed to the limited number of reaction sites available in the materials, due to either absence or limited number of interfacial regions between WO_3 and ZnO. This behaviour has been presented more clearly in Figure 3–11, which shows the larger gradient of linear range for the 50 wt.% WO_3 – 50 wt.% ZnO and 30 wt.% WO_3 – 70 wt.% ZnO devices and shallower gradients of the homo-contact dominated sensor devices in the system.

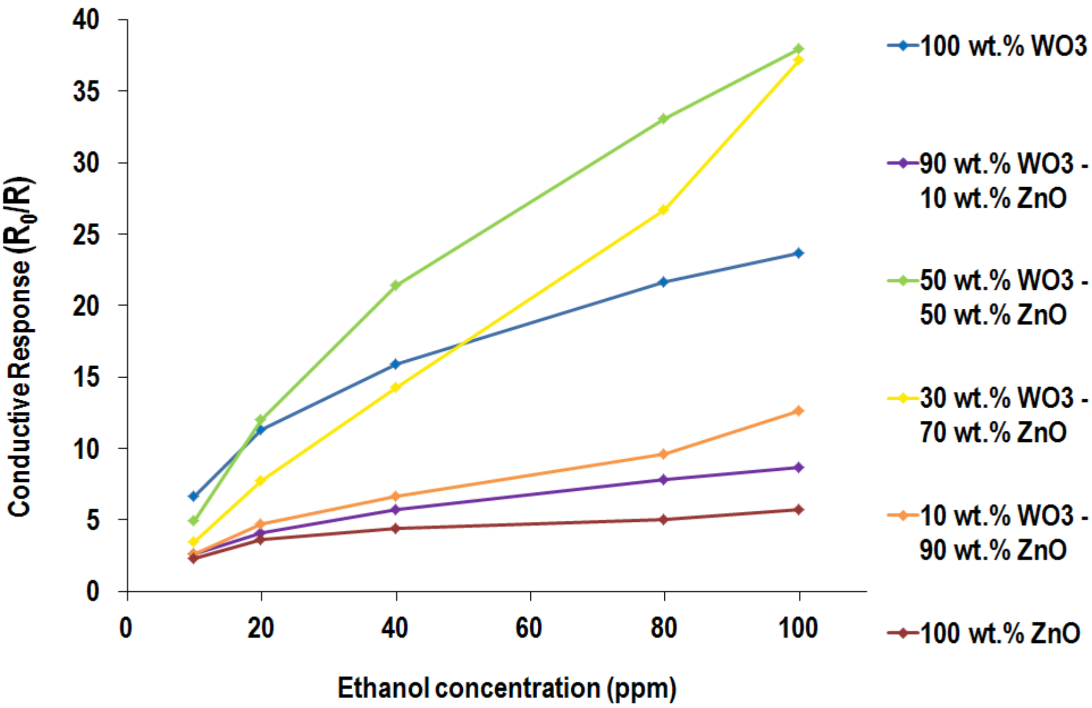

Figure 3–11. Conductive response of WO_3-ZnO system towards 10, 20, 40, 80 and 100 ppm ethanol gas, at an operating temperature of 350 °C.

The presence of an enhanced number of reaction sites in a mixed oxide system has been reported by Zeng *et al*. [168] who had reported on the enhanced gas sensing properties of SnO_2 nanosphere functionalised TiO_2 nanobelts toward various VOCs, such as methanol, ethanol, formaldehyde and acetone. The group had observed enhanced gas sensing properties of the hybrid oxides compared to the sole TiO_2 nanobelts. When discussing the gas sensing mechanism, they had reported that the hybrid oxides are associated to additional depletion regions that occur at the interfaces between the SnO_2 nanospheres and the TiO_2 nanobelts and that the hetero-junctions that exist between the interface of both the metal oxides, serve as additional reaction sites. The enhanced number of the reaction sites promoted by the significant dispersion of hetero-contacts within the packing structures of both the 50 wt.% WO_3 – 50 wt.% ZnO and 30 wt.% WO_3 – 70 wt.% ZnO composites, may explain the unsaturated shark-fin nature of the response traces observed with these composite materials and suggests a larger number of reaction sites available for the given number of ethanol molecules, that the materials are exposed to.

Due to the baseline drift at 80 ppm and 100 ppm of ethanol exposure, response and recovery times have been evaluated at the lower concentration of 40 ppm, where the baseline is observed to be stable. Calculations of the t_{90} (40 ppm) values of the 100 wt.% WO_3 and 100 wt.% ZnO devices were 45 and 200 seconds, respectively. In contrast, the 50 wt.% WO_3 – 50 wt.% ZnO and 30 wt.% WO_3 – 70 wt.% ZnO sensor devices were 173 and 133 seconds respectively. The calculations suggested no particular order of the response times (i.e. no correlation with the varying composition of the individual metal oxide), however suggested that the WO_3 device responded the fastest, which was evident from its flat 'box' type [106] saturated response towards 40 ppm of the analyte, seen in Figure 3–10. In contrast, the ZnO material was seen to be attributed to very slow response, observed by its slow unsaturated 'shark-fin' [33] response in the same figure. The response time of the 30 wt.% WO_3 – 70 wt.% ZnO composite was seen to lie in between both the WO_3 and ZnO materials, suggesting that its response was influenced by the speedy response of the WO_3 and slow response of the ZnO. The 50 wt.% WO_3 - 50 wt.% ZnO composite sensor device was seen to be slower than the 30 wt.% WO_3 – 70 wt.% ZnO composite sensor. The response speed difference between both composites was indicated by the greater curvature of the 50 wt.% WO_3 - 50 wt.% ZnO composite, which indicated the slower and unsaturated behaviour of the sensor, in comparison to the 30 wt.% WO_3 - 70 wt.% ZnO composite, which was attributed to greater flatness in its response behaviour, indicating some saturation of the surface sites. The recovery times of the same four sensor devices after 40 ppm ethanol exposure i.e. the t_{-90} (40 ppm) values, were seen to be 606 seconds (100 wt.% WO_3), 507 seconds (100 wt.% ZnO), 918 seconds (50 wt.% WO_3 - 50 wt.% ZnO) and 892 seconds (30 wt.% WO_3 - 70 wt.% ZnO). The recovery times suggested that the composite materials were slower than both the pure metal oxide counterparts, which suggests slower diffusion of the ethanol molecules through the composite matrices during recovery period, in comparison to the pure metal oxide counterparts. A potentially larger number of surface sites in the composites, due to the hetero-contact interfaces, may also suggest longer desorption times of the all the molecules per unit time in comparison to the pure metal oxides, which are thought to have a lower number of surface sites, as they are dominated solely by homo-contacts. Further, slower recoveries of the composites indicate stronger intermolecular forces between the hetero-junctions and the surface adsorbed chemical species, in comparison to the pure metal oxides. Evaluation of the response and recovery kinetics and responsivities of the various sensors in the system, suggests the compromise of the kinetics for larger responsivities of the composite materials.

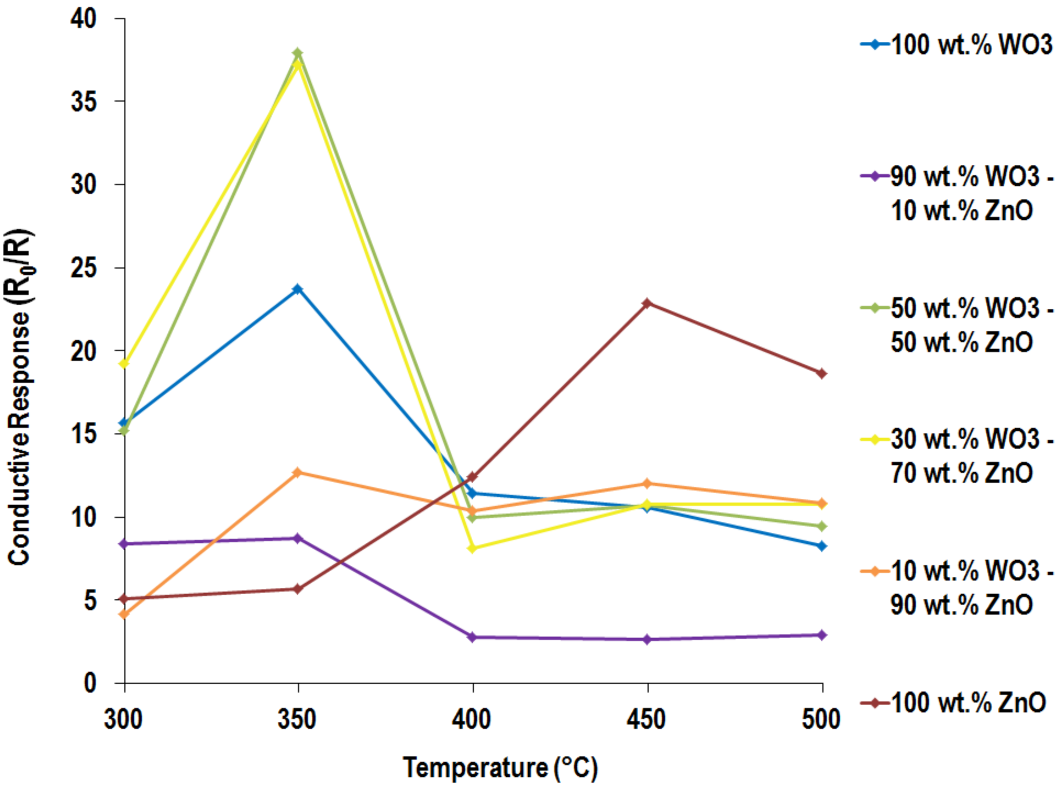

Figure 3–12. Conductive response of WO_3-ZnO system towards 100 ppm ethanol as a function of increasing operating temperature.

Figure 3–12 presents the conductive response of the system of sensors towards 100 ppm ethanol as a function of increasing operating temperature. The figure illustrates that 350 °C was the optimal operating temperature for almost all sensor devices, except for the 100 wt.% ZnO sensor device which was seen to exhibit optimal performance at 450 °C.

The behaviour of increasing responsivity of ZnO towards ethanol as a function of increasing operating temperature has been reported previously in the literature. For example, in a literature report by Singh *et al*. [233] nanoparticulate and nanorod based ZnO powders, of hexagonal wurtzite crystal structure were synthesised and thick-films of these materials were coated onto gas sensor substrates. These sensors were tested against 250 ppm ethanol vapour at different operating temperatures (150 °C – 400 °C). A similar trend in response characteristics was observed between the sensors, as a function of operating temperature, with their responsivities of the sensors increasing between 150 °C – 400 °C and then decreasing upon further increasing the operating temperature. Xu *et al*. [69] have also observed the increase in the response of a ZnO sensor towards ethanol as a function of increasing operating temperature and have accounted for the gas response behaviour of ZnO being strongly dependent on the conversion of ethanol to acetal; with greater conversion of the alcohol to the aldehyde reported to occur as a function of increasing operating temperature.

An interesting observation from Figure 3–12 is the gradual cross over in conductive response at 400 °C, between the 100 wt.% WO_3 and 100 wt.% ZnO sensor devices, with respect to each other, as the operating temperature increased from 300 °C to 500 °C. The figure illustrates that the ZnO material is more responsive than WO_3 to ethanol at higher operating temperatures (as discussed earlier) and WO_3 is more responsive to ethanol at lower operating temperatures. A possible explanation for this cross over behaviour as a function of increasing temperature could be associated to the optimum combustion environment as a function of temperature, associated to the particular semiconducting oxide. The number of ionised oxygen species that adsorb on the surface of the sensor material, is expected to increase as a function of operating temperature until a maximum limit of adsorption is reached (this is governed by the equilibrium between adsorption and thermally driven desorption) [234]. The response towards ethanol is therefore dependent on this magnitude of oxygen ion adsorption, with a larger number of adsorbed oxygen species implying a greater number of combustion reactions of the analyte. The greater the combustion rate of ethanol, the larger number of electrons released back into the space-charge layer and therefore the larger the response of the material toward the target gas [235-237]. The variation of the optimal performance of MOS sensor devices as a function of temperature modulation is a well know phenomenon, with all gas sensitive metal oxide materials known to be associated to characteristic temperature-conductance profiles [20, 137, 208], where the response is seen to be the greatest at a moderate operating temperature, but lowest at both its highest and lowest extremes. Complexities such as the stability of the surface oxygen species adsorbed on the surface of the different materials and also the differing optimum oxidising temperatures of the target analytes, are factors which have been reported to influence the shape of these profiles [238]. Chemical and physical factors, such as the rates of adsorption and desorption of oxygen and the target analytes, or of oxidation products, the rate of surface decomposition of target analytes, the charge-carrier concentration (in the conduction band as well as the electron depletion layer) also contribute to the response of the sensor and thus its conductance-temperature profile [137, 239].

Figure 3–12 shows that as the operating temperature of the system was increased, the responsivity of most of the hybrid sensors converged and deteriorated in performance, with respect to their responsivities at lower operating temperatures. This indicates the breakdown of the hetero-junction enhancement effects at the higher operating temperatures, which can be accounted for by understanding the effect of elevated temperatures on the overall potential energy barrier of the system [240].

Increasing the operating temperature implies an increase in thermal energy. This increased thermal energy promotes a decrease in the work-function of the semiconductors, as thermally induced charge transfer within the semiconductors is energetically easier. As such, the charge carrier distribution within these semiconductors is subsequently affected, with a large number of electrons occupying the conduction bands. The relative decrease in work-function within the semiconductors and between them at an n-n interface, will therefore promote the junction effect to act negatively on the response. This is because the energy barrier for Fermi level equilibration is reduced, resulting in a decrease in the energy barrier for the local exchange of charge carriers across both semiconductors. As such, the effective energy barrier and resistance at the junction is decreased, weakening the overall junction effect. Hence higher temperatures cannot promote junction effects to play effective roles in enhancing gas sensing response and so the composites were seen to respond less than they had at lower operating temperatures.

3.6.2.2 NO_2 Sensing

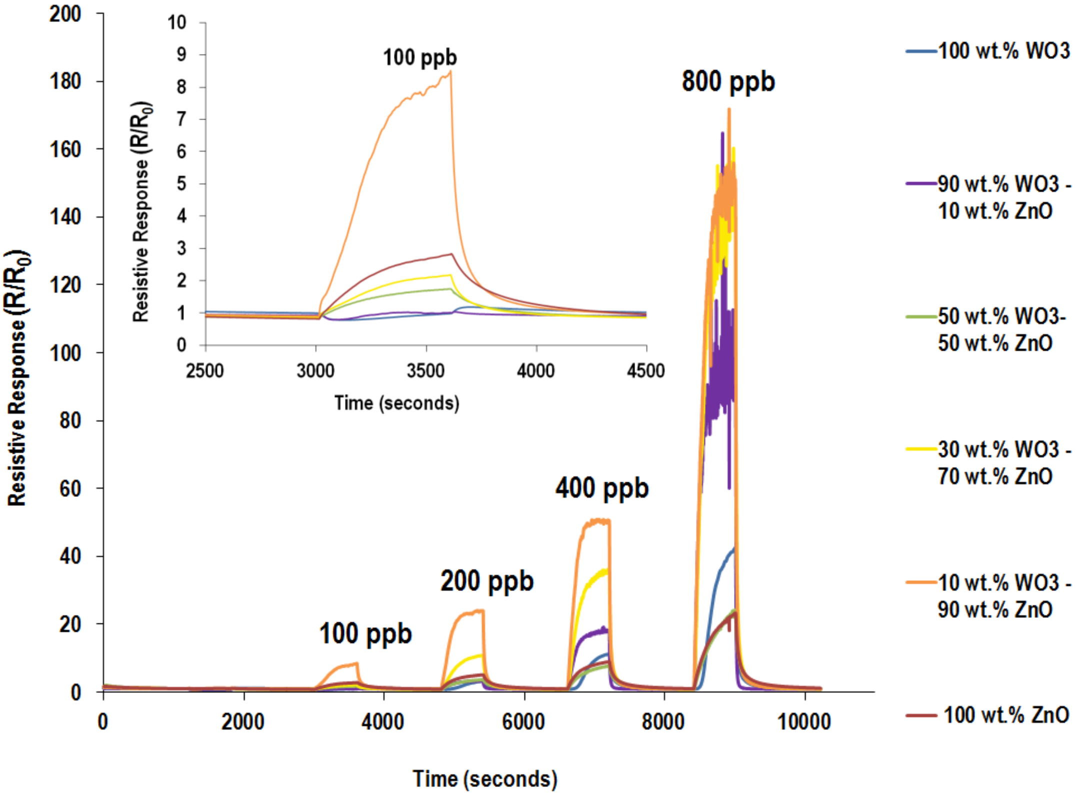

Figure 3–13. Resistive response traces of the WO_3-ZnO system towards 100, 200, 400 and 800 ppb NO_2 gas, at an operating temperature of 300 °C. The inset projects the resistive response of the system towards 100 ppb NO_2.

Figure 3–13 presents the resistive response traces of the system of sensors at the optimal operating temperature of 300 °C. Tabulation of the mean responses values of the sensor devices in the WO_3-

ZnO system from the repeat tests against exposure towards the various NO_2 concentrations at 300 °C and the associated 95% confidence intervals have been presented in Table 3–2.

Table 3–2. Average resistive responses of sensor devices in WO_3-ZnO system from all repeat tests against various NO_2 concentrations at 300 °C and associated errors in the form of 95% CIs.

	100 ppb		**200 ppb**		**400 ppb**		**800 ppb**	
Device	Average Response	95% CI	Average Response	95% CI	Average Response	95% CI	Average Response	95% CI
100 wt.% WO_3	2.38	±1.35	5.26	±3.46	15.50	±4.16	53.29	±7.33
90 wt.% WO_3 – 10 wt.% ZnO	2.23	±1.20	12.52	±6.09	15.72	±5.20	Electronic capping out	
50 wt.% WO_3 – 50 wt.% ZnO	2.46	±0.69	4.89	±1.18	8.40	±0.79	25.26	±3.49
30 wt.% WO_3 – 70 wt.% ZnO	4.87	±2.64	18.08	±6.11	36.84	±1.15	Electronic capping out	
10 wt.% WO_3 – 90 wt.% ZnO	8.65	±0.15	25.29	±1.27	47.34	±6.39	157.52	±7.36
100 wt.% ZnO	2.87	±0.04	5.56	±0.43	9.96	±0.93	26.54	±3.49

300 °C was the optimal operating temperature of most sensor devices, except for the 50 wt.% WO_3 – 50 wt.% ZnO sensor device which was seen to exhibit slightly better performance at 350 °C, as observed further in Figure 3–15. All sensors were seen to demonstrate the expected increase in resistive response at all concentrations of NO_2, as expected with n-type semiconducting oxides, suggesting that the conduction took place via the n-type percolation paths of metal oxides.

The figure illustrates that most of the composite sensors within the system, displayed an enhanced response to NO_2 over the whole concentration range with respect to the pure metal oxide counterparts. The best device was observed to be the 10 wt.% WO_3 - 90 wt.% ZnO sensor device, which was attributed to a response of 148 towards 800 ppb NO_2, a 7-fold enhanced response than the pure ZnO sensor and a 3.5-fold better response than the pure WO_3 sensor. This suggested that an incremental addition of WO_3 to the host metal oxide ZnO, makes for an excellent material for NO_2 detection. The enhanced performance of this material was surprising, as it constituted a greater proportion of ZnO than WO_3, however WO_3 is a well-established material for the detection of NO_2 [241] with the WO_3 seen to response better towards NO_2 than ZnO, as observed in Figure 3–13. The 90 wt.% WO_3 - 10 wt.% ZnO sensor device was also seen to display a substantially significant response towards 800 ppb NO_2 again showing that an incremental addition of ZnO to the host metal oxide WO_3, makes for an excellent material for NO_2 detection. SEM imaging in Figure 3–2 gave evidence of the microstructures of both these composite being dominated by the host metal oxides, suggesting that the packing structures of both devices to be homo-contact dominated with a low frequency of hetero-contacts present. Such packing structures are likely to be attributed to highly localized contact potentials [170, 171], with the associated response results showing such combinations of WO_3 and ZnO, to be effective for NO_2 detection.

The 30 wt.% WO_3 – 70 wt.% ZnO sensor device was also seen to perform well against NO_2, with the highest response of 140 towards 800 ppb NO_2, which was a 6-fold enhanced response with respect to the pure ZnO sensor and a 3.3-fold enhanced response with respect to the pure WO_3 sensor, demonstrating the effectiveness of this hetero-junction system for NO_2 detection. Interestingly however, the 50 wt.% WO_3 – 50 wt.% ZnO sensor device (which was one of the best performing composites for ethanol detection) was the only composite seen to show a relatively low response to the analyte, with the best response of 24.4 towards 800 ppb. This may be due to an insignificant change in charge carrier concentration and change in size of electron depletion layer upon interaction with NO_2.

In comparison to literature reports by An *et al*. [209] and Siriwong *et al*. [207], the WO_3-ZnO composites reported in this Chapter are better with high responsivities towards ppb levels of NO_2 in comparison to the ppm levels of NO_2 that both groups have evaluated their WO_3-ZnO hybrid sensors against.

All sensors demonstrated the expected increase in resistive response at all concentrations of the oxidising gas, except for the 100 wt.% WO_3 and 90 wt.% WO_3 – 10 wt.% ZnO sensor devices, which were seen to show a p-type behaviour (i.e. decrease in resistive response) towards 100 ppb of the analyte, as observed in the inset of Figure 3–13. Such p-type behaviour of WO_3 towards NO_2 has been reported previously in the literature by Wu *et al.* [242]. In their, study the group prepared hexagonal WO_3 nanorods via a hydrothermal process and spin-coated them onto an alumina substrate with interdigitated Pt electrodes. The NO_2 sensing characteristics of the nanorod sensor was evaluated by testing it against 0.5 ppm – 50 ppm NO_2 between operating temperatures in the range of 25 °C – 250 °C. Specifically, when they had exposed their sensor to 1 ppm of NO_2 between 25 °C – 250 °C, they had found that the temperature effected a change in response behaviour of the material. The nanorod film was seen to be attributed to conventional n-type resistive response at temperatures between 50 °C – 250 °C, but showed p-type behaviour at lower temperatures of 25 °C – 50 °C. The group [242] had evaluated this switch in behaviour, as a function of operating temperature, to be associated to the formation of an inversion layer at the surface of the WO_3 nanorods. The inversion layer in the case of a n-type metal oxide is produced if the negative charge is too excessive which results in the reduction of electrostatic potential in the depletion layer with respect to the number of holes, forming an inversion layer [242]. Wu *et al*. had reported that the surface of the WO_3 sample contained a space layer as well as a surface layer, the latter which was induced by the presence of dangling bonds, structural defects and gas adsorption. Specifically in their case, they had found the presence of mixed phases in their WO_3 sample to include non-stoichiometric as well as tetragonal WO_x species, which were associated to a large number of oxygen vacancies V_o^{2+}. The stabilisation of the vacancies they reported was achieved via adsorption of oxygen species from the air. Adsorption of further oxygen molecules occurs on the surface when the nanorod sensor is exposed to the air and form chemisorbed oxygen species by capturing electrons from the adsorption sites on the oxide surface. Therefore ultimately, the concentration of the negative charge was too excessive on the surface of the metal oxide, which led to the decrease in the electrostatic potential in the space charge layer with respect to the concentration of holes, resulting in the formation of an inversion space-charge layer. At higher operating temperatures, the greater energy in the system would promote the desorption of the negative surface adsorbed NO_2 species, causing an increase in the electrostatic potential in the space charge layer, with respect to the electron concentration, increasing the size of the depletion layer, leading to an increase in the resistance of the material.

In the case of this WO_3-ZnO composite study, the p-type behaviour was observed with the 100 wt.% WO_3 and 90 wt.% WO_3 – 10 wt.% ZnO devices, at the lowest NO_2 exposure concentration. Such behaviour, at lower NO_2 concentrations, has been observed previously before in the literature [29, 242, 243]. A lower concentration implies a lower number of NO_2 molecules to interact with the metal oxide surface and as such a reduced number of electron abstracted from the conduction band of the metal oxide, in contrast to a high concentration of NO_2. As such, the concentration of electrons in the metal oxide surface is higher at a lower exposure concentration of NO_2 [29, 243] implying that the change in size of the space charge layer may have been minimal with respect to the concentration of holes. This then relates back to the idea of Wu *et al*. [242] that an excessive number of charge carriers in the surface may have led to a decrease in the electrostatic potential in the space charge layer, with respect to the concentration of holes, resulting in the formation of an inversion space-charge layer and therefore the decrease in the resistance. Further, the inverted behaviour specific to the two devices that were both dominated by WO_3, may also suggest structural defects in the WO_3, which may have also contributed the unconventional p-type behaviour.

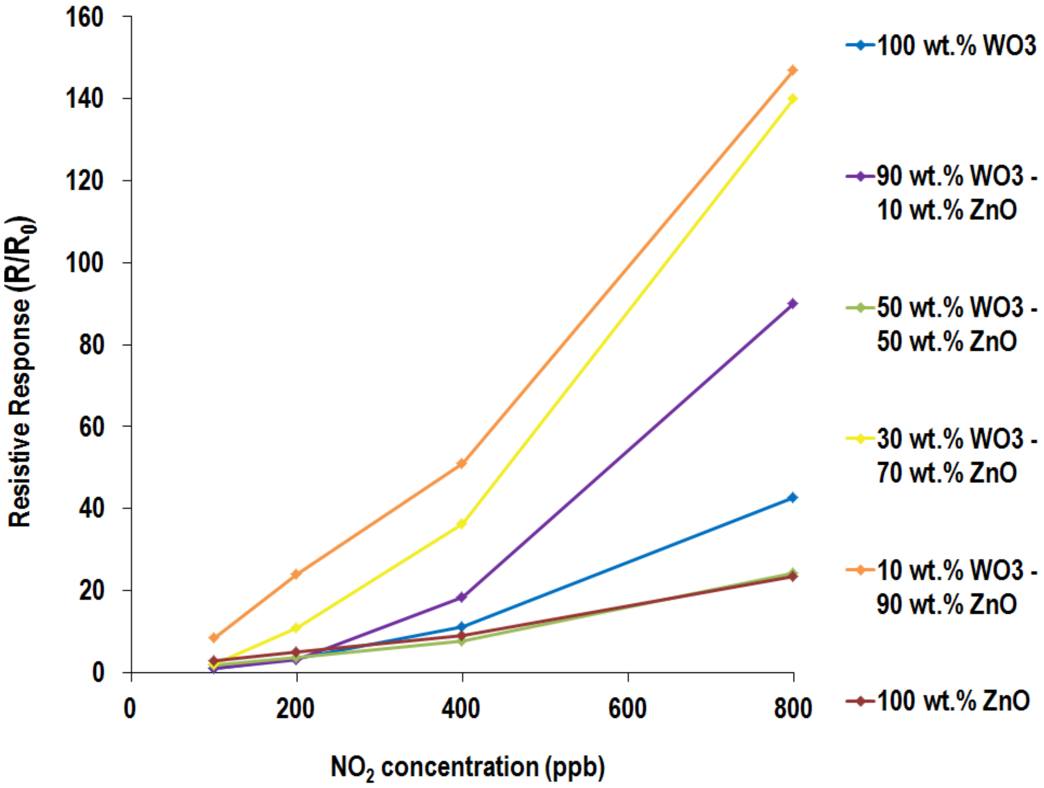

Figure 3–14. Resistive responses of WO_3-ZnO system towards 100, 200, 400 and 800 ppb NO_2 gas, at an operating temperature of 300 °C.

Figure 3–14 shows that the increase in resistive response of most of the composite materials as a function of increasing NO_2 concentration, was attributed to a significant change in response amplitude particularly between 400 ppb and 800 ppb NO_2. In comparison, the pure metal oxide counterparts did not show a substantial increase. This trend is more clearly presented in Figure 3–14, which shows a larger rate of change of resistive response in most of the composite materials, particularly between 400 ppb and 800 ppb NO_2, in comparison to the shallow rate of change of response of the 50 wt.% WO_3 – 50 wt.% ZnO sensor device and the pure metal oxide materials. This steep increase of the composites indicates their ability to accommodate the increasing number of NO_2 molecules in the increasing exposure concentrations. In contrast, the behaviour of the pure 100 wt.% WO_3 and 100 wt.% ZnO sensors and the 50 wt.% WO_3 – 50 wt.% ZnO composite sensor indicated that these materials were unable to occupy the increasing concentrations of NO_2 molecules. Such large increases in the response amplitude as a function of increasing NO_2 concentrations, have also been observed with zeolite systems, for example in a report by Varsani *et al*. [23]. In their study, Varsani *et al*. had reported the steep response behaviour of WO_3 modified with H-ZMS 5 as a function of increasing NO_2 concentration, particularly between 200 ppb and 400 ppb of the analyte, as a result of a catalytic effect of the zeolite, which may have acted to chemically modify the NO_2 molecules diffusing towards the material, to form a product to which the underlying WO_3 was more sensitive towards. Thus it is possible that a synergistic catalytic effect through a combination of specific amounts of WO_3 and ZnO, may be contributing to the enhanced combustion of NO_2, effectively changing the charge carrier concentration which induces significant increase in the resistance of the composite materials.

In terms of kinetics, the two best performing composite devices: 10 wt.% WO_3 – 90 wt.% ZnO and 30 wt.% WO_3 – 70 wt.% ZnO at 300 °C were attributed to t_{90} (400 ppb) values of 208 and 328 seconds, respectively. In contrast, both the pure metal oxide counterparts: WO_3 and ZnO, were associated to t_{90} (400 ppb) values of 443 and 390 seconds, respectively. The response and recovery kinetics were calculated at 400 ppb and not 800 ppb, due to the electronic noise associated to both composite devices at the highest concentration of exposure, observed in Figure 3–13, which made kinetic evaluation difficult. The response values were not seen to be attributed to any form of order between the four sensor devices (i.e. no correlation with the varying composition of the individual metal oxide) however, the faster responses of the composites in comparison to the pure counterparts suggested faster diffusion of the oxidising analyte molecules into the matrix of the composite materials than the pure metal oxides, yielding rapid and a larger number of surface reactions per unit time, accounting for their enhanced responsivities as well as faster response times. The recoveries of the four devices after exposure to 400 ppb of the analyte i.e. the t_{-90} (400 ppb) values were 818 seconds (10 wt.% WO_3 – 90 wt.% ZnO), 822 seconds (30 wt.% WO_3 – 70 wt.% ZnO), 710 seconds (100 wt.% WO_3) and 953 (100 wt.% ZnO). The values suggested that the recoveries of the composite devices existed between both the pure metal oxides, implying that the recoveries may have been influenced by the chemical properties of both metal oxides and a synergistic effect between them.

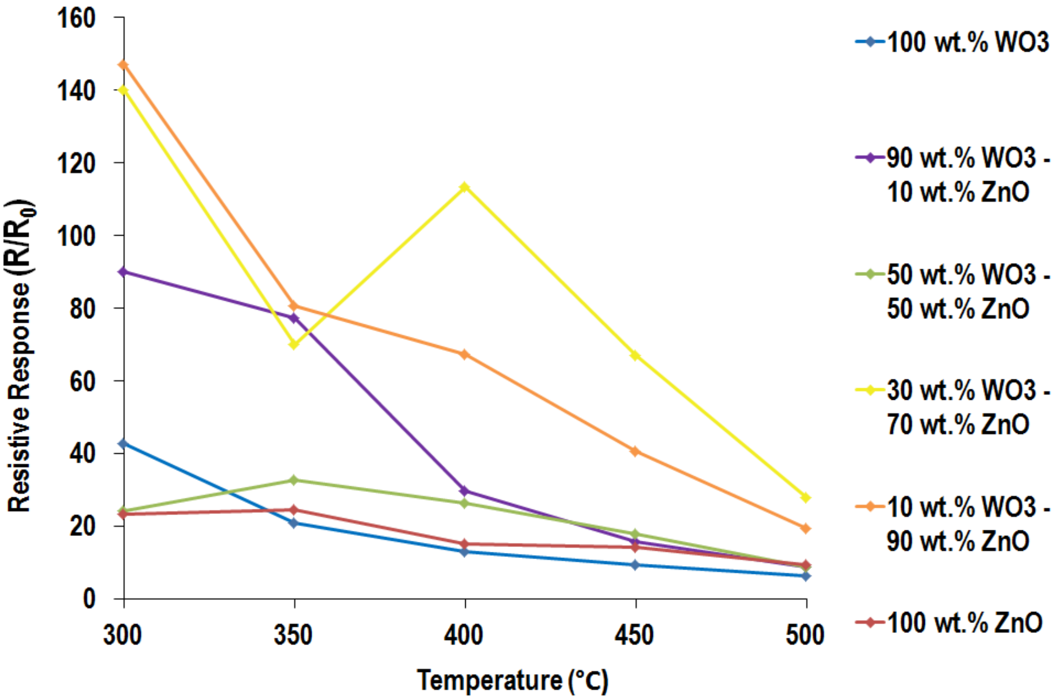

Figure 3–15. Resistive responses of WO_3-ZnO system towards 800 ppb NO_2 gas, as a function of increasing operating temperature.

Figure 3–15 presents the resistive responses of the system of sensors towards 800 ppb of NO_2 as a function of increasing operating temperature. Within the range of tested operating temperatures from 300 °C – 500 °C, the graph shows that 300 °C was the optimal operating temperature of most sensor devices against exposure to NO_2. However, given the nature of the response trend as a function of temperature i.e. increasing response magnitude as a function of decreasing operating temperature, then it is possible lower operating temperatures may have promoted better response performances of the sensor devices. As such the optimal operating temperature can be lower than 300 °C and further testing at lower operating temperature would aid to assimilate this. As the operating temperature was increased, the response of all devices was seen to decrease, with responses converging at the highest operating temperature of 500 °C. The higher operating temperature leads to higher thermal energy in the system [234], which promotes instantaneous adsorption and desorption reactions, leading to incomplete surface reactions, yielding an overall reduced number of surface combustion reactions and therefore a reduced responsivity magnitude.

At the lower end of the operational temperature range, in which lies the optimal performance of the sensors, the kinetics are inherently slower than at higher temperatures in the range of 450 °C – 500 °C. This is due to the lack of the thermal energy to drive the kinetics of diffusion, adsorption and desorption, and thus temperature is a contributory factor to the slow recoveries observed. However, as explained earlier in the Chapter, one of the advantages of the lower temperatures of operation for such hetero-junction based materials, is the retained nature of the hetero-junction enhancement effects. As such, the composite sensor devices are seen to perform optimally at 300 °C – 350 °C, exhibiting increased resultant change in charge carrier, resulting in increased response amplitudes.

3.6.3 Further Gas Sensing Studies

The system of WO_3-ZnO sensor devices was tested for selectivity against a range of reducing gases: acetone, CO and NH_3 (and ethanol presented earlier) by conducting further gas sensing studies, at an operating temperature of 350 °C. This was the optimal operating temperature of most sensor devices, when exposed to the main reducing gas of interest: ethanol, as observed in Figure 3–12.

Figure 3–16 and Figure 3–17 show that the system was seen to perform poorly (relative to the performances against ethanol (Figure 3–10) and acetone (Figure 3–18)) against the highest tested concentrations of CO (1000 ppm) and NH_3 (20 ppm), respectively, with responsivities towards both analytes being close to the baseline response of 1. In particular this was true of the responses observed against NH_3. In the case of CO, some of the devices were seen to be attributed to higher responses than 1, but were still relatively poor given that the CO exposure concentration was 1000 ppm. However the poor response performance towards CO and NH_3, demonstrated the selectivity of the devices towards a target gas such as ethanol acetone or NO_2, if put in a mixed gas atmosphere.

3.6.3.1 CO Sensing

Figure 3–16 presents the resistive responses of the WO_3-ZnO composite system against the highest tested concentration of CO exposure which was 1000 ppm. Tabulation of the mean responses values of the sensor devices in the WO_3-ZnO system from the repeat tests against exposure towards 1000 ppm CO at 350 °C and the associated 95% confidence intervals have been presented in

Table 3–3. All devices were seen to show responsivities above a baseline response of 1, with the highest response of 2.5 associated to the 30 wt.% WO_3 – 70 wt.% ZnO sensor device, exhibiting a higher response than both the pure WO_3 and ZnO counterparts, which showed responses of 2.0 and 1.5, respectively. The significantly low response of the devices towards 1000 ppm, suggested that exposure to lower concentrations would have shown negligible response, close to baseline response.

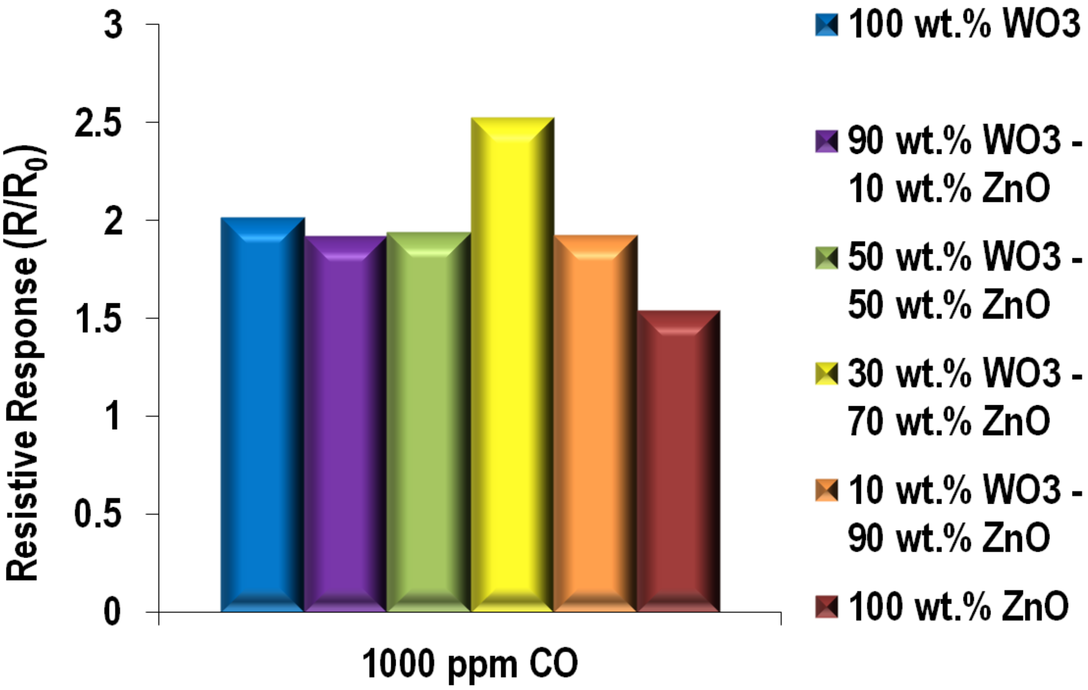

Figure 3–16. Resistive responses of WO_3-ZnO system against 1000 ppm CO at an operating temperature of 350 °C.

Table 3–3. Average resistive responses of sensor devices in WO_3-ZnO system from all repeat tests against 1000 ppm CO at 350 °C and associated errors in the form of 95% CIs.

	1000 ppm	
Device	Average Response	95% CI
100 wt.% WO_3	2.00	±0.03
90 wt.% WO_3 – 10 wt.% ZnO	1.96	±0.07
50 wt.% WO_3 – 50 wt.% ZnO	2.03	±0.18
30 wt.% WO_3 – 70 wt.% ZnO	2.47	±0.12
10 wt.% WO_3 – 90 wt.% ZnO	1.94	±0.04
100 wt.% ZnO	1.50	±0.09

Interestingly all devices exhibited unconventional p-type behaviour towards the reducing gas. Such behaviour can be justified with reports from the literature that suggest that surfaces of transition metal oxides, within temperature ranges of 200 °C – 400 °C are known to be attributed to the formation of an inversion layer on the conduction surface due to oxygen adsorption [244, 245], which can cause a switch in the direction of response. In the case of this study however, the exclusive p-type behaviour of the whole system towards CO in comparison to that observed with NH_3 in Figure 3–17 and acetone in Figure 3–18, against which most devices showed n-type behaviour, suggested a unique interaction of

CO with the surface of the materials [23] or the possibility that CO may be functioning as a surface acceptor [244, 246].

3.6.3.2 NH_3 Sensing

The response results at 350 °C of the system against 20 ppm NH_3, which was the largest concentration of the analyte that the system was exposed to, have been presented in Figure 3–17. Tabulation of the mean responses values of the sensor devices in the WO_3-ZnO system from the repeat tests against exposure towards 20 ppm NH_3 at 350 °C and the associated 95% confidence intervals have been presented in Table 3–4. All sensor devices showed responsivities close to baseline response (1), with the largest response (conductive) of 1.25 exhibited by the 50 wt.% WO_3 – 50 wt.% ZnO device. The responsivities of the devices in the region of the baseline response in general, indicated the poor response of the materials against the analyte. Interestingly the 100 wt.% WO_3 and 30wt.% WO_3 – 70 wt.% ZnO devices exhibited p-type response behaviour towards the reducing gas, in comparison to all other sensor devices in the system which exhibited conventional n-type behaviour.

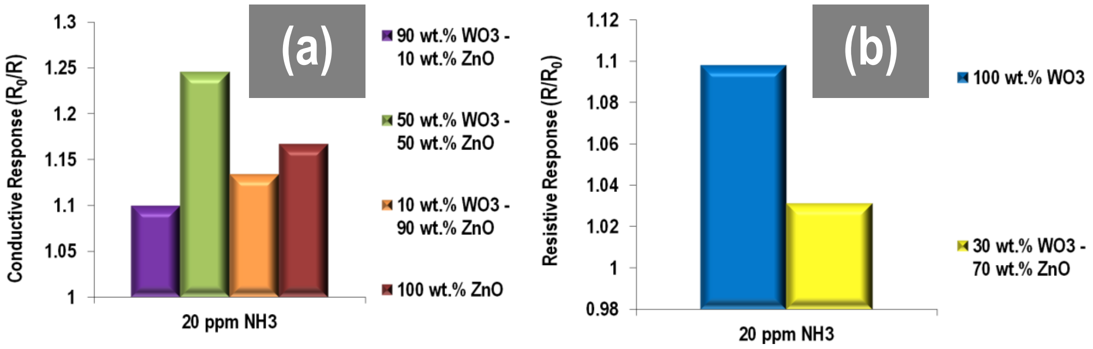

Figure 3–17. (a) Conductive responses and (b) Resistive responses of the WO_3-ZnO system against 20 ppm NH_3 at an operating temperature of 350 °C.

Such an n- to p- type response change has been observed previously with WO_3 sensors and NH_3 [114, 115]. This is because NH_3 under goes oxidation reactions on the surface of metal oxides [114, 115], and the reaction process can follow one of many routes, allowing several possible competing processes to all take place at the same time. One of the reactions leads to the combustion of NH_3 to NO as explained in Chapter 1, which is easily converted to NO_2 in the presence of oxygen. WO_3 is a well-established metal oxide known for its responsivity NO_2, which may have resulted in the increase in resistive response observed for WO_3 sensor device and also the 30 wt.% WO_3 – 70 wt.% ZnO sensor device.

Table 3–4. Average responses of sensor devices in WO_3-ZnO system from all repeat tests against 20 ppm NH_3 350 °C and associated errors in the form of 95% CIs.

	20 ppm NH_3	
Device	Average	95% CI
100 wt.% WO_3	1.10	±0
90 wt.% WO_3 – 10 wt.% ZnO	1.09	±0.01
50 wt.% WO_3 – 50 wt.% ZnO	1.25	±0.01
30 wt.% WO_3 – 70 wt.% ZnO	1.04	±0.01
10 wt.% WO_3 – 90 wt.% ZnO	1.11	±0.04
100 wt.% ZnO	1.14	±0.04

3.6.3.3 Acetone Sensing

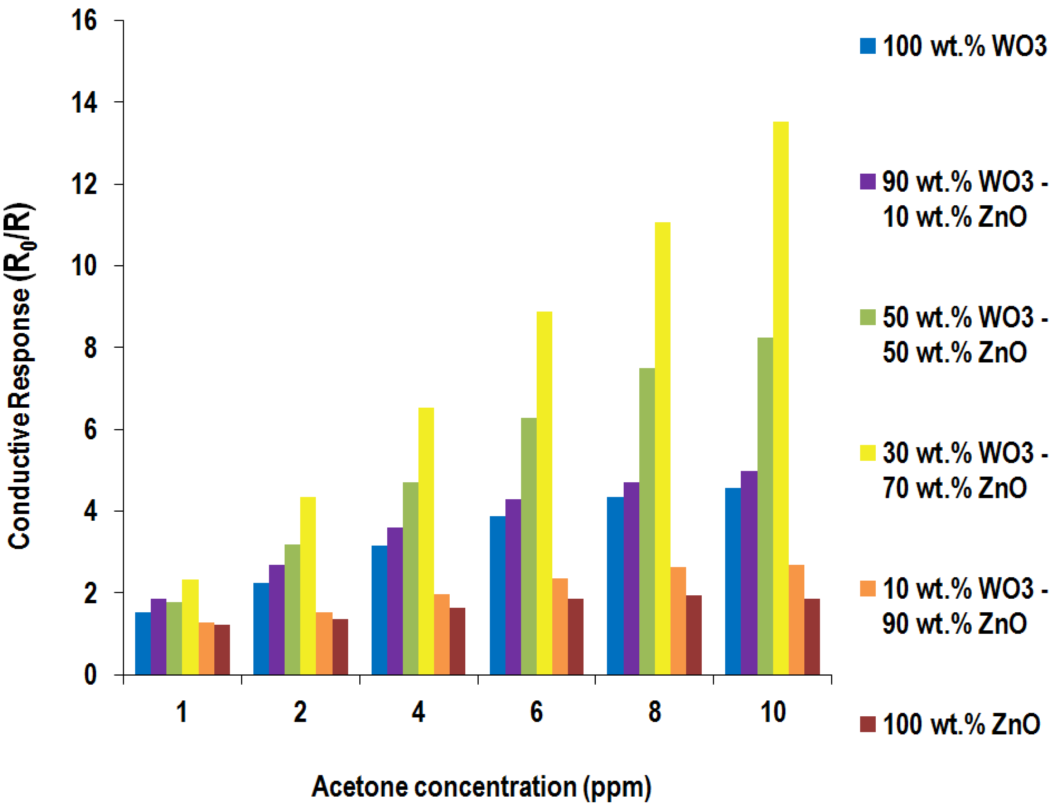

Figure 3–18. Conductive responses of WO_3-ZnO system towards 1, 2, 4, 6, 8 and 10 ppm acetone gas, at an operating temperature of 350 °C.

Figure 3–18 presents the conductive response of the system of WO_3-ZnO sensor devices against increasing concentrations of acetone at an operating temperature of 350 °C. Tabulation of the mean responses values of the sensor devices in the WO_3-ZnO system from the repeat tests against exposure towards the various acetone concentrations at 350 °C and the associated 95% confidence intervals have been presented in Table 3–5. The response behaviour towards acetone exemplifies the enhanced response characteristics of the mixed-oxide composites, with the highest observed response of 13.5 exhibited by the 30 wt.% WO_3 – 70 wt.% ZnO device towards 10 ppm of acetone, which was a 2.9-fold enhanced response with respect to the pure WO_3 counterpart (which exhibited a response of 4.6) and a 7.1-fold enhanced response with respect to the pure ZnO counterpart (which exhibited a response of 1.9). The response of this composite was followed by the response of the 50 wt.% WO_3 – 50 wt.% ZnO device, which displayed the second best performance. Both these composites were also seen to dominate the conductive responses when exposed to 80 ppm and 100 ppm ethanol seen in Figure 3–10. The results therefore suggest the suitability of both these devices, with the specific WO_3 –ZnO ratios, for effective detection of VOC's.

In terms of the pure counterparts, Figure 3–18 showed that the response amplitude of the 100 wt.% ZnO sensor hardly changed as a function of increasing acetone concentration and that of the 100 wt.% WO_3 sensor was also seen to increase in amplitude only very slightly. In comparison, the responses of the 30 wt.% WO_3 – 70 wt.% ZnO device was seen to increase rapidly, illustrating less saturation and greater number of surface sites to accommodate the increasing concentration of acetone molecules with time. Both the 90 wt.% WO_3 – 10 wt.% ZnO and 10 wt.% WO_3 – 90 wt.% ZnO devices were seen to exhibit very similar responses to the pure WO_3 and ZnO sensor devices, respectively. This was accounted for by the domination of the host metal oxides in each of their packing structures observed by SEM imaging in Figure 3–2 (c) & (d) and (m) & (n), respectively, with the frequency of the hetero-contacts being localised and minimal. Instead both the 50 wt.% WO_3 – 50 wt.% ZnO and 30 wt.% WO_3 – 70 wt.% ZnO sensor devices were seen by SEM imaging in Figure 3–2 (i) & (j) and (k) & (l) to be associated to a dispersion of both metal oxide grains, which suggests the prevalence and delocalisation of hetero-contacts in their packing structures.

Interestingly in a study by Anno *et al*. [247] ZnO based semiconductor sensors for the detection of acetone and capronaldehyde in a vapour of consommé soup was reported. The detection of acetone was carried out as it was reported to be an important flavour component of the soup. One of the ZnO sensors that the group fabricated was a 5 wt.% WO_3-ZnO composite material. The fabrication of the composite first involved the formation of ZnO powder which was prepared by the neutralisation of $ZnCl_2$ with ammonia, with the resulting precipitate filtered, dried and calcined in air at 600 °C for 5 hours. The addition of 5 wt.% WO_3 was conducted by mixing an associated aqueous precursor salt solution with the ZnO powder followed by evaporation to dryness and calcining in air at 600 °C for 5 hours. A sensor element in the form of a sintered block was formed from the powdered material. Gas sensing experiments were conducted in a wet atmosphere as water is a key component of soup. The electrical resistance of the sample was measured by measuring the electrical conductivity of the material in wet air and wet acetone gas, to obtain the responsivity of the material. The gas of the aqueous acetone solution was prepared by bubbling it through with dry air. The resulting concentration of the acetone in the sample gas was determined by analysis of the conversion product CO_2, formed when the acetone was passed over an oxidation catalyst: Pt-alumina, via gas chromatography. Studies showed that a sensor element consisting of pure ZnO, had only limited responsivity towards 20 ppm acetone at 500 °C. However the addition of WO_3 (associated to a large electronegativity) dramatically increased the responsivity towards 20 ppm acetone to 60 at the same operating temperature. As the responsivity towards acetone correlated with additives with a high electronegativity, the group suggested that acidic surfaces were more favourable for the detection of acetone. As suggested previously in Chapter 1, section 1.8.3, WO_3 acts as a solid acid/alkaline catalyst and such provides Bronsted or Lewis acid sites, or a combination of both upon which oxidation or reduction catalysis can occur [111, 112]. As an acid catalyst, WO_3 is a source of H^+ species which can catalyse the oxidation and catalytic breakdown of acetone and in this way, the composite material was able to response to acetone better in the presence of WO_3. In a cross-sensitivity study at 500 °C towards other important flavour components such as capronaldehyde, methylpyrozine, and dimethylsulfide in consommé soup, (all at 20 ppm concentrations), the WO_3-ZnO element showed selectivity towards 20 ppm acetone. The group had concluded that the enhanced responsivity of the WO_3-ZnO composite was attributed to its acidic surface, over which oxidation of acetone occurred through the formation of intermediates such as CO and CO_2. Further they had reported that the modest catalytic activity of the composite allowed the acetone molecules as well as intermediates such as CO, to diffuse into the inner region of the sensor body and react with the adsorbed oxygen species, which also contributed to the high responsivity of the composite material. This study suggests that the acidic properties of the WO_3-ZnO composites studied in this thesis, may have also contributed to their enhanced acetone responsivity properties, with respect to the pure counterparts.

Comparison of the conductive responses of the devices between 10 ppm ethanol and 10 ppm acetone, showed that both the 50 wt.% WO_3 – 50 wt.% ZnO and 30 wt.% WO_3 – 70 wt.% ZnO sensor devices, in particular the latter device showed selectivity towards 10 ppm acetone. Comparison of the response values and 95% CIs of the two devices towards 10 ppm ethanol at 350 °C as seen in Table 3–1, and towards 10 ppm acetone at 350 °C as seen in Table 3–5, show that the response and errors do not overlap, and as such the selectivity is demonstrated. The other sensor devices however, displayed very close conductive responses towards both analytes and therefore discrimination was not as apparent. Kim *et al*. [248] have reported that discrimination between ethanol and acetone is difficult to achieve due to the similar chemical natures of both gases. However the WO_3-ZnO composite sensors here show that specific combinations of both WO_3 and ZnO can potentially achieve discrimination between both analytes.

Table 3–5. Average conductive responses of sensor devices in WO_3-ZnO system from all repeat tests against 1, 2, 4, 6, and 10 ppm acetone at 350 °C and associated errors in the form of 95% CIs.

	1 ppm		**2 ppm**		**4 ppm**		**6 ppm**		**8 ppm**		**10 ppm**	
Device	Average Resistance	95% CI	Average Resistance	95% CI	Average Resistance	95% CI	Average Resistance	95% CI	Average Resistance	95% CI	Average Resistance	95% CI
100 wt.% WO_3	1.54	±0.04	2.19	±0.10	3.04	±0.26	3.71	±0.33	4.14	±0.40	4.33	±0.43
90 wt.% WO_3 – 10 wt.% ZnO	1.95	±0.20	2.70	±0.01	3.56	±0.11	4.21	±0.13	4.62	±0.15	4.89	±0.17
50 wt.% WO_3 – 50 wt.% ZnO	1.80	±0.20	3.22	±0.04	4.80	±0.43	6.61	±0.95	7.82	±0.99	8.75	±1.27
30 wt.% WO_3 – 70 wt.% ZnO	2.41	±0.20	4.36	±0.04	6.46	±0.15	8.77	±0.20	10.94	±0.23	12.76	±1.45
10 wt.% WO_3 – 90 wt.% ZnO	1.27	±0.00	1.52	±0.02	1.95	±0.04	2.34	±0.05	2.70	±0.15	2.74	±0.08
100 wt.% ZnO	1.22	±0.02	1.35	±0.05	1.60	±0.07	1.81	±0.09	1.91	±0.09	1.83	±0.05

3.7 Summary and Conclusions

Results of the investigation have shown that the combination of WO_3 and ZnO metal oxides in composite form was an effective and versatile strategy for obtaining enhanced responsivities, in comparison to the pure metal oxide counterparts. In particular, the combination of metal oxides proved to be particularly effective for the detection of ethanol, NO_2 and acetone.

The highest resistive response against NO_2, was displayed by the 10 wt.% WO_3 - 90 wt.% ZnO sensor device, which showed a response of 147 at 300 °C and a conductive response of only 4 towards 100 ppm ethanol at the same operating temperature. This was one of the best performing composites for NO_2 and displayed superior resistive responsivity towards 800 ppb NO_2, across the whole range of operating temperatures between 300 °C – 500 °C. In comparison for ethanol, the device showed poor conductive responsivities across the same operating temperature range. This indicated that the device was able to discriminate between both the reducing and oxidising gas. For ethanol, the best performing composite was the 50 wt.% WO_3 – 50 wt.% ZnO device, which showed a conductive response of 37 against 100 ppm of the analyte at 350 °C. The same device was seen to exhibit a resistive response of 33 towards 800 ppb NO_2 at the same operating temperature. Between 300 °C - 500 °C, the device was seen to be attributed to similar responsivities between both ethanol and NO_2, and as such this device could not clearly discriminate between both ethanol and NO_2.

At 350 °C, gas sensing tests towards a variety of reducing gases showed that the system responded poorly towards 1000 ppm CO and 20 ppm NH_3, with most sensor devices showing responses (conductive/resistive) close to a baseline response of 1. However significant conductive responsivities towards acetone were observed, particularly at concentrations of 2 ppm and higher, with the best performing composite sensor device seen to be the 30 wt.% WO_3 – 70 wt.% ZnO material. This composite was seen to be associated to enhanced conductive responsivities, with respect to the pure counterparts, at all concentrations of acetone exposure between 1 – 10 ppm. The maximum conductive response of this composite against acetone was of 14 against 10 ppm of the analyte.

Comparison of the conductive responses of the system of devices between 10 ppm ethanol and 10 ppm acetone at 350 °C, showed that both the 50 wt.% WO_3 – 50 wt.% ZnO and 30 wt.% WO_3 – 70 wt.% ZnO sensor devices, in particular the latter device, showed selectivity towards 10 ppm acetone. This behaviour indicated that in a mixed atmosphere of both ethanol and acetone, both the 50 wt.% WO_3 – 50 wt.% ZnO and 30 wt.% WO_3 – 70 wt.% ZnO sensor devices maybe more selective to acetone.

The enhanced responsivities of the composite metal oxides with respect to the pure counterparts, were thought to be influenced by a combination of hetero-junction enhancement effects as well as the superior sensing properties of the individual metal oxides. XPS analysis did suggest an electronic interaction between both metal oxides, which supported the hypothesis of the influence of hetero-junction enhancement effects towards some of the enhanced responsivities of the composite devices.

Error analysis of the response values throughout the study, showed that in general the responses between repeat tests were repeatable. This was particularly apparent at exposures towards low concentrations of all analytes and with materials which were either pure or biased by the wt.% of either of the metal oxides. Further, lower error magnitudes were observed towards acetone, CO and NH_3 in comparison to the higher concentrations of ethanol and NO_2, towards which the devices were attributed to significant error. In particular, exposure towards 100 ppm ethanol, resulted in for example the 30 wt.% WO_3 – 70 wt.% ZnO sensor device being associated to an error of ±9.4 and the 10 wt.% WO_3 – 90 wt.% ZnO sensor device was associated to an error of ±7.4 towards 800 ppb NO_2. The trends of the error values showed that both analytes towards which the group of sensors were most responsive towards i.e. ethanol and NO_2, were associated to the largest errors. This suggested the possibility of several surface by-products forming or additional reactions occurring on the surface of the metal oxide device, promoting interference of the response magnitudes. The behaviour also suggested potential instability of such composite devices. In contrast, towards the lower concentrations of ethanol and NO_2 and towards all exposed concentrations of CO, NH_3 and acetone, the devices showed lower responsivities and also lower errors magnitudes, suggesting that the formation of interfering by-products or additional reactions occurring on the surface was lowered, due to the lowered concentrations of exposure or due to lack of reactivity. The error values suggest that comparative responsivity and selectivity between the best performing composite materials was difficult to conclude, due to the overlap of error ranges. However, the enhanced response of these composites with respect to the pure counterparts was evident. A more detailed discussion of error sources has been presented in Chapter 7.

Chapter 4 : SnO_2-ZnO based n-n hetero-junction system

In the previous Chapter an in-depth materials and gas sensing characterisation study an n-n hetero-junction system based on WO_3 and ZnO composites was presented. In this Chapter, an in-depth investigation of a materials and gas sensing characterisation study of another n-n hetero-junction composite system, this time based on SnO_2 and ZnO composites, is presented.

4.1 Introduction

Hetero-junction material systems based on the combination of SnO_2 and ZnO are one of the most investigated mixed metal oxide systems studied and applied to vapour sensing technology, as evidenced from the large number of reports in the literature [91, 93, 145, 156, 248-259].

In the past, reports on the gas sensing studies of the SnO_2-ZnO hybrid systems have differed through the route by which the composite system has been fabricated and subsequently deposited onto gas sensing substrates. Various examples include simple mechanical mixing of powders of both metal oxides resulting in the formation of physical mixtures of the two components and subsequent screen-printing inks of the mixtures [91, 145, 156], combinatorial solution deposition to form thin films of the combination of oxides [248] to more advanced techniques such as vapour growth method or a combination of electro-spinning and Atomic Layer Deposition (ALD) to form more complex ZnO-SnO_2 core shell nanowire type structures [93, 249-254], among other processes. The utilization of this combination of metal oxides, subject to fabrication method, have been shown to promote enhanced responses towards a variety of environmentally important analytes such as NO_2 [251], CO [250], VOCs [91, 145, 248, 256, 259] and hydrogen [254], in comparison to one or both of the single metal oxide counterparts.

The observed effective enhancement with a combination of both these oxides has been reasoned due to a number of factors which primarily include hetero-junction enhancement effects [248-250] but also the synergistic advantages and catalytic activity of both metal oxide materials towards various compounds [91]. A number of literature studies, which have investigated this combination of both these metal oxides, have been referred to throughout this Chapter.

In this investigation, a study of a composite system based on a combination of SnO_2 and ZnO, has been presented.

4.2 Results and Analysis

4.2.1 Scanning Electron Microscopy (SEM)

SEM imaging characterisation of all seven sensors in the SnO_2-ZnO composite system was carried out to gauge into the microstructure of each material. The SEM images of all sensor materials in the SnO_2-ZnO system presented in Figure 4–1, have been spread over the next two pages.

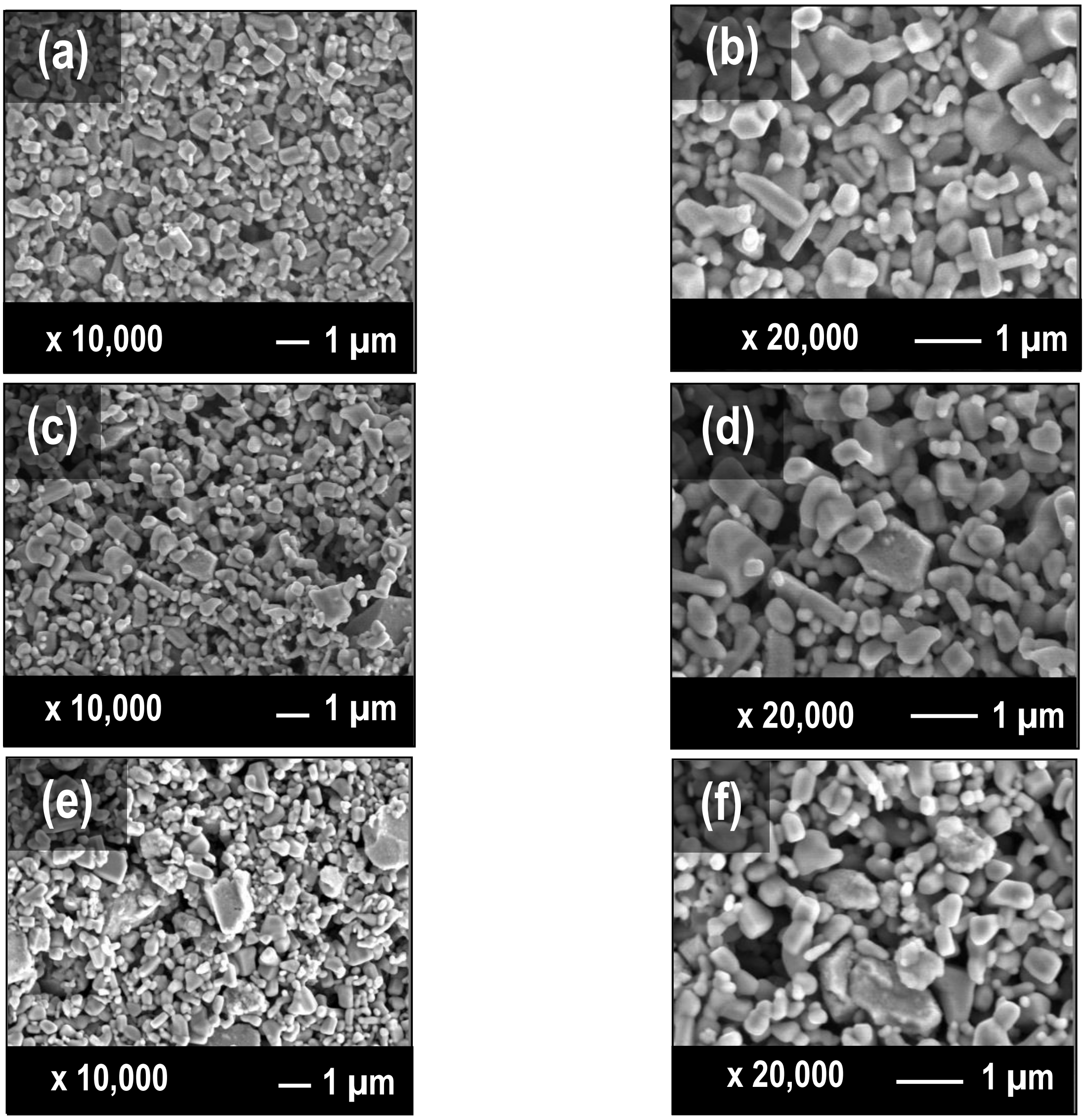

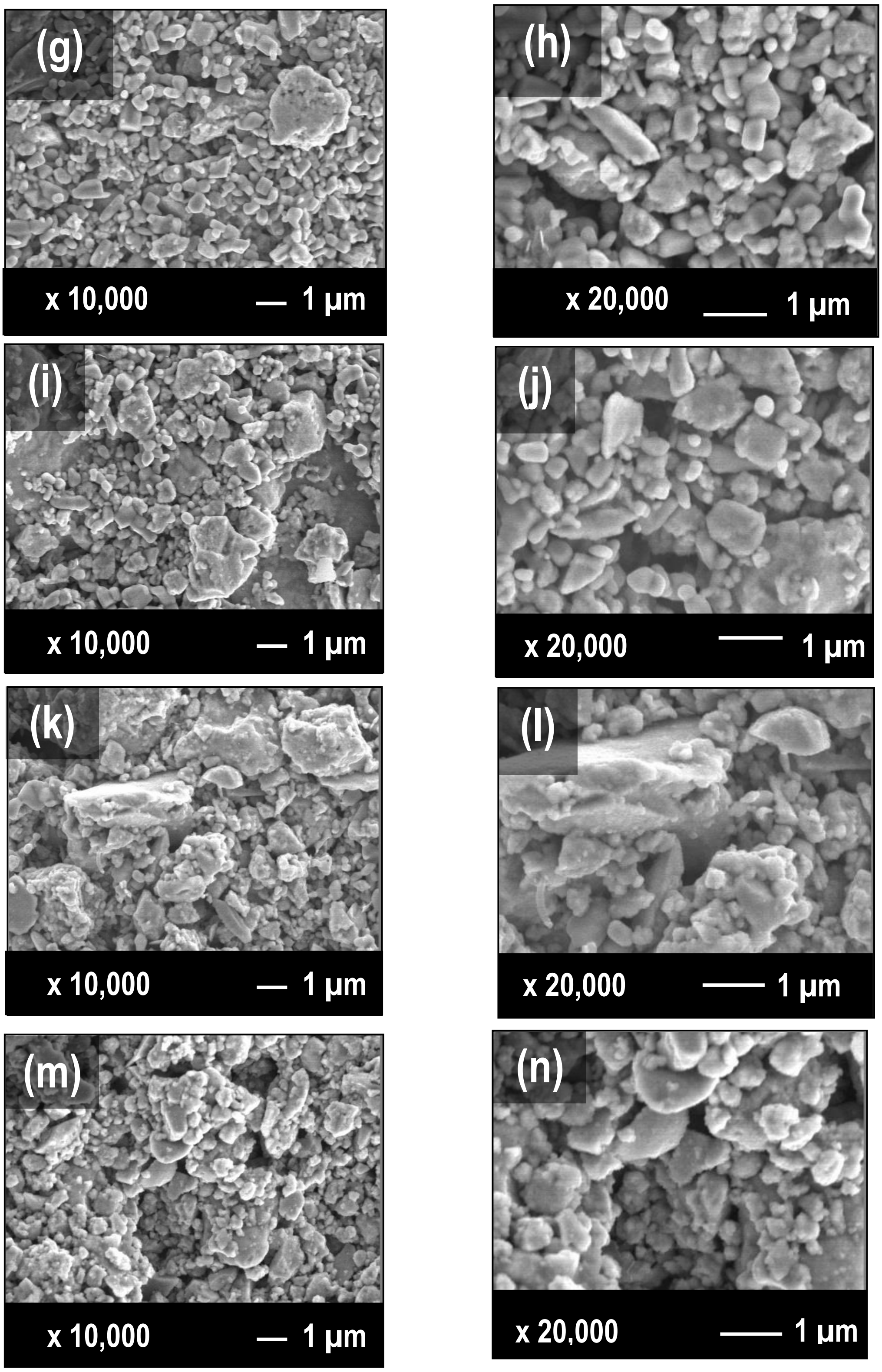

Figure 4–1. SEM images of (a) 100 wt.% ZnO x 10,000 magnification, (b) 100 wt.% ZnO x 20,000 magnification, (c) 90 wt.% ZnO – 10 wt.% SnO_2 x 10,000 magnification, (d) 90 wt.% ZnO – 10 wt.% SnO_2 x 20,000 magnification, (e) 70 wt.% ZnO – 30 wt.% SnO_2 x 10,000 magnification, (f) 70 wt.% ZnO – 30 wt.% SnO_2 x 20,000 magnification, (g) 50 wt.% ZnO – 50 wt.% SnO_2 x 10,000 magnification, (h) 50 wt.% ZnO – 50 wt.% SnO_2 x 20,000 magnification, (i) 30 wt.% ZnO – 70 wt.% SnO_2 x 10,000 magnification, (j) 30 wt.% ZnO – 70 wt.% SnO_2 x 20,000 magnification, (k) 10 wt.% ZnO – 90 wt.% SnO_2 x 10,000 magnification, (l) 10 wt.% ZnO – 90 wt.% SnO_2 x 20,000 magnification, (m) 100 wt.% SnO_2 x 10,000 magnification and (n) 100 wt.% SnO_2 x 20,000 magnification. All materials were screen-printed and heat-treated at 600 ºC before imaging.

SEM imaging of the sensor devices showed that the ZnO sample observed in Figure 4–1 (a) and (b) consisted of 3-dimensional cuboid shaped particles with curved edges, with a broad particle size distribution ranging between 0.1 to 1 µm, corroborating with the observation from Chapter 3. The morphology of the SnO_2 material observed in Figure 4–1 (m) and (n) was attributed to smooth and jagged rock-like clumps ranging from a size of 0.25 µm to as large as 1.75 µm. The image of the 10 wt.% ZnO – 90 wt.% SnO_2 in Figure 4–1 (l) showed that some of the SnO_2 clumps were as large as 4 µm.

Careful inspection of a higher magnification of the SnO_2 sample at x 50,000 observed in Figure 4–2, showed that the rock-like clumps were actually agglomerates made up of spherical nano-SnO_2 particles of sizes less than 100 nm.

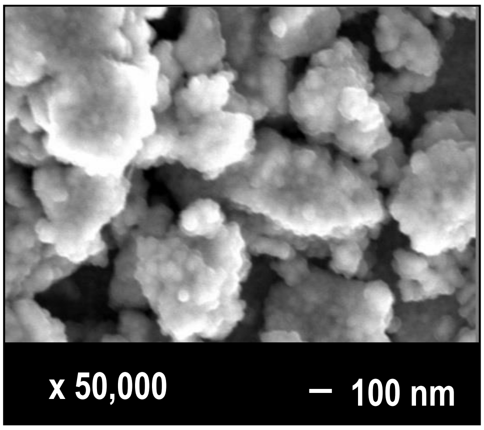

Figure 4–2. SEM image of 100 wt.% SnO_2 at x 50,000 magnification.

The nanograin sizes of the SnO_2 sample suggest a large surface to bulk ratio of the SnO_2 grains inherent to all nano-sized materials. Such nanomaterials are likely to agglomerate as observed via SEM imaging in Figure 4–2 owing to the lower thermal stability of nanomaterials, due to a greater ratio of surface to bulk component. Prior to SEM imaging, all sensor devices were heat-treated at 600 °C, which would have likely caused the SnO_2 particles to agglomerate together. SnO_2 nanoparticles are known to sinter at temperatures as low as 400 °C [260], suggesting that heat-treatment at 600 °C may have promoted some sintering between the nano-structured SnO_2 metal oxide grains, subsequently impacting the gas sensing performance. An agglomerated microstructure is not preferred for gas sensing applications due to a reduction in diffusion pathways for the gas molecules to travel into the bulk of the metal oxide, suggesting the surface site interaction is limited between the analyte molecules and the solid metal oxide.

Despite the effective inter-grain agglomeration between the SnO_2 nanograins, the agglomerates themselves were seen to be loosely held together within the sensor matrix as observed in Figure 4–1 (m) and (n) and Figure 4–2, suggesting the provision of diffusion pathways between the agglomerates [70] for the gaseous molecules to travel into and out of the body of the sensor matrix. The pure ZnO sensor sample in Figure 4–1 (a) and (b) showed that the ZnO grains were loosely held within the matrix of the material. Thus in contrast to the pure SnO_2 material, where the diffusion pathways are seen to be present between the agglomerates within the sensor matrix, the ZnO sample showed that the diffusion pathways exist in between the ZnO grains within the sensor matrix.

The stark contrast in the particle sizes of both metal oxides also suggested that within the composite, not only were hetero-junction effects introduced by the presence of grains of differing chemical natures, but also they were present due to the difference in grains size. Yamazoe *et al.* [170, 171] had reported on hetero-junction effects within devices incorporating grains which were non-uniform. They had reported that the simplest factor in hetero-junction devices that contributed to the non-uniformity between the grains, was the differences in grain sizes between the grains. This suggests that even in a sample which consists of particles of the same chemical nature i.e. a pure SnO_2 sample for example, differences in the grain sizes between the SnO_2 particles can induce contact potential enhancement effects, within the matrix of the sensing material. Therefore, this suggests that unless any sample contains superior particle size homogeneity, which is very ideal to realistically achieve, it is associated to hetero-junction enhancement effects. In the case of the SnO_2–ZnO composite system examined here, multiple in-homogeneities existed to exert hetero-junction enhancement effects, which are expected to play a positive role in the overall gas-sensing properties of the materials.

As the concentration of ZnO and SnO_2 were varied, SEM imaging showed a variation in the microstructure of the sensor devices, however microstructures of the 90 wt.% ZnO – 10 wt.% SnO_2 and the 10 wt. ZnO - 90 wt.% SnO_2 composite devices, were seen to be dominated by the dominant metal oxide i.e. ZnO and SnO_2 respectively as observed in Figure 4–1 (c) & (d) and (k) & (l), respectively and as such, the microstructures of these composites resembled those of the corresponding pure metal oxides. This suggested domination of homo-contact dominated percolation paths within the sensor matrix of each composite device and a homo-contact dominated packing structure. The 70 wt.% ZnO – 30 wt.% SnO_2, 50 wt.% ZnO - 50 wt.% SnO_2 and 30 wt.% ZnO - 70 wt.% SnO_2 composite devices observed in Figure 4–1 (e) & (f), (g) & (h) and (i) and (j) were seen to be associated to a dispersion of both metal oxide materials, suggestive of a hetero-contact dominated packing structure in these devices.

SEM imaging did not show evidence of significant fusing between the ZnO and SnO_2 grains in the composite materials, which gave evidence of the composite nature of the devices. Within the pure metal oxide materials, significant inter-grain agglomeration and sintering was seen between the SnO_2

nano-grains, however the agglomerates remained independent of each other. With the ZnO material, some fusing was observed between the ZnO particles as observed in Figure 4–1 (b) and (d).

SEM imaging in general showed evidence of loosely held grains within the metal oxide matrices. Such a microstructure in the thick-film devices ensured diffusion pathways for the analyte molecules to diffuse through, deep into the body of the sensor matrix and react with surface sites in the bulk as well as on the surface of the materials. Thus, the microstructural nature of the thick-films increased the surface site accessibility of the analyte molecules. The microstructure of the composite thick-films as well as the packing structure and hetero-junctions that existed between the hetero-interfaces are likely to all influence the overall gas sensing properties of the system of devices.

4.2.2 X-Ray Diffraction (XRD)

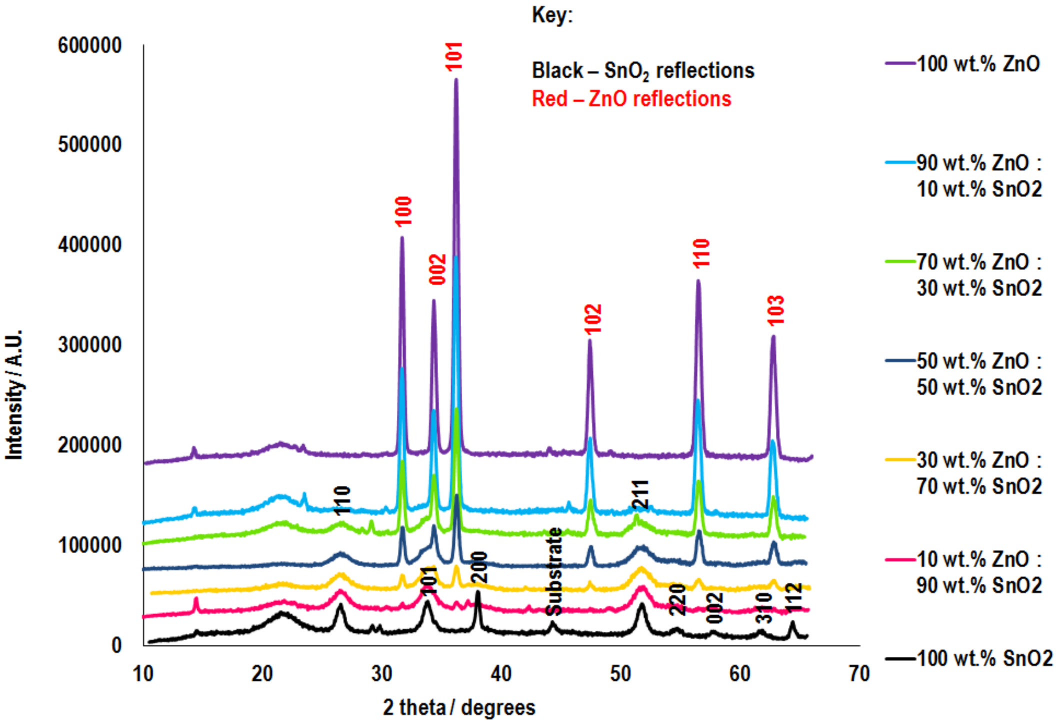

Figure 4–3. XRD patterns of pure and composite sensors based on SnO_2 and ZnO metal oxides, in the SnO_2-ZnO composite system. All materials were screen-printed and heat-treated at 600 °C, prior to XRD measurements.

The glancing angle XRD patterns of the devices within the SnO_2 and ZnO composite system are presented in Figure 4–3. The crystalline nature of both metal oxide compounds was confirmed through the observation of the sharp defined peaks of both metal oxides. The XRD pattern of the SnO_2 sample, confirmed that the metal oxide crystallised in a tetragonal rutile structure, matching the reference pattern (JCPDS No. 41-1445) [261-263] seen in Figure 4–4 obtained from the ICSD database via the National Chemical Database Service [264], which stored the SnO_2 rutile XRD data from a study by

Bolzan *et al*. [265]. The strongest reflections of rutile have been presented in Figure 4–4. The XRD pattern of ZnO as discussed in Chapter 3, showed that the metal oxide adopted a wurtzite hexagonal crystal structure (JCPDS No. 36-1451) [77, 213, 214].

The patterns showed the variation in the concentration of the SnO_2 and ZnO components through the gradual change in intensity of the associated peaks in ascending or descending order. The observation of the peaks of the individual metal oxide crystal phases indicated that all materials existed in composite form. An observation of the alumina substrate was evident with the pure SnO_2 sensor.

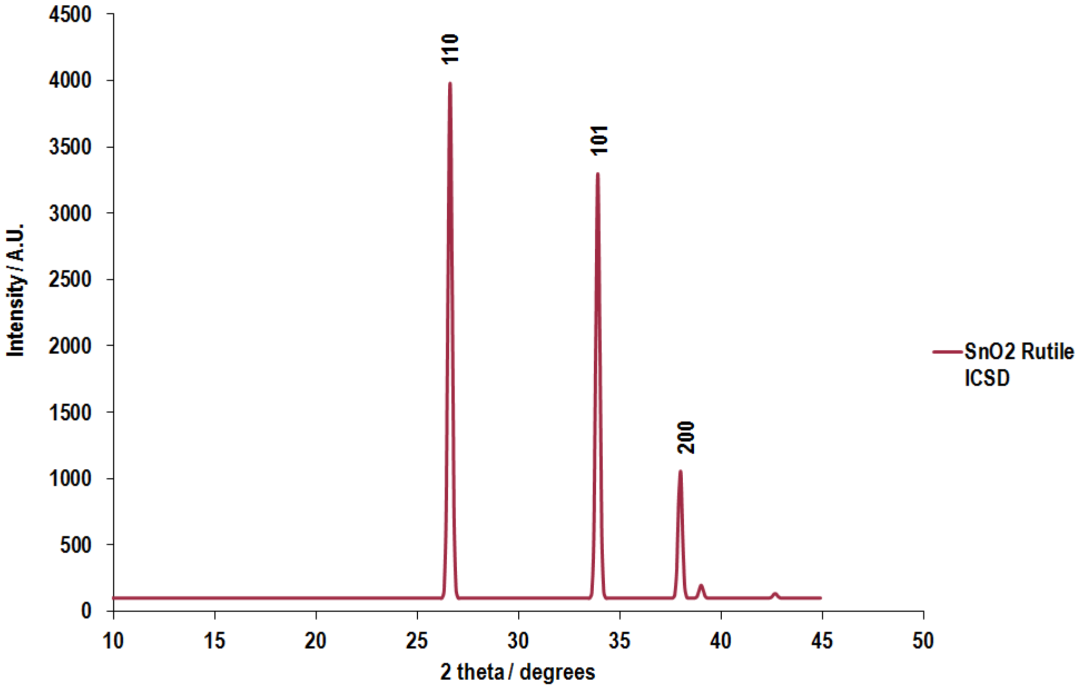

Figure 4–4. XRD pattern of SnO_2 rutile from the ICSD reference database [264, 265].

Further confirmation of the composite nature of the materials was confirmed by the absence of any reflections associated to the formation of any tertiary phases that could have formed due to the solid-state reaction of both metal oxides. The absence of the tertiary phase was confirmed by comparison of the experimental data with the reference patterns of the possible tertiary phases that could have formed, which were $ZnSnO_3$ perovskite [151, 266] and $ZnSn_2O_4$ spinel [266]. The latter of these compounds, zinc orthostannate, is the most stable tertiary phase that crystallises via the solid-state reaction of both metal oxides at temperatures above 600 °C [266] and former is the metastable tertiary phase formed as an intermediate of the solid-state reaction, at 300 – 500 °C [266]. This suggests that any gas sensing behaviour observed was purely due to the presence of both metal oxide phases and was not influenced in any way by the presence of a tertiary phase.

4.2.3 Raman Spectroscopy

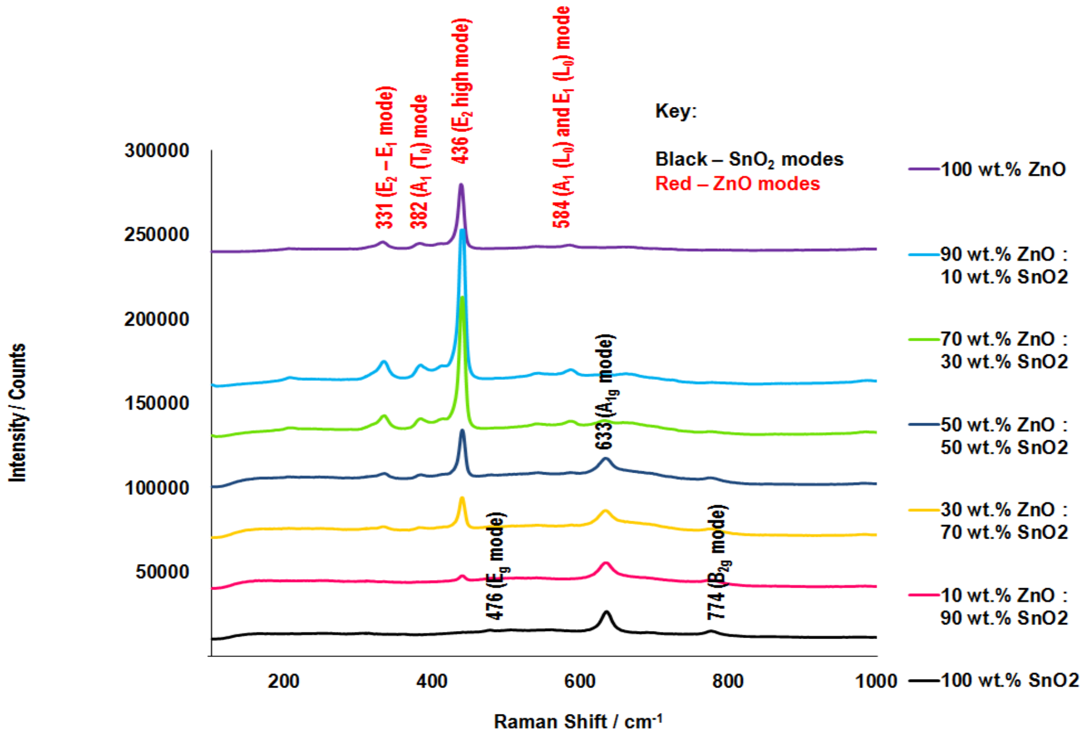

Figure 4–5. Raman spectra of all sensor devices within SnO_2-ZnO composite system. All sensors were heat-treated at 600 °C, prior to Raman spectroscopy measurements.

Raman spectra of the sensor devices within the SnO_2-ZnO system, have been presented in Figure 4–5. The results corroborated with XRD showing that the Raman bands of SnO_2 matched those of a tetragonal rutile phase [263]. The three bands of SnO_2 observed in the Raman data are reported to be the three most fundamental peaks of rutile SnO_2, associated to the E_g (476 cm^{-1}), A_{1g} (633 cm^{-1}) and

B_{2g} (774 cm^{-1}) vibrational modes. The Raman bands of the ZnO sample were in agreement with a wurtzite hexagonal structure [218-220], in-depth analysis of which has been discussed in Chapter 3.

The Raman data showed presence of both metal oxides within the mixed metal oxide materials, giving evidence of the composite nature of the mixtures. No peaks observed to any tertiary phases were observed in the Raman spectra, corroborating with XRD data, of the presence of only the two metal oxide phases in the materials.

4.2.4 X-Ray Photoelectron Spectroscopy

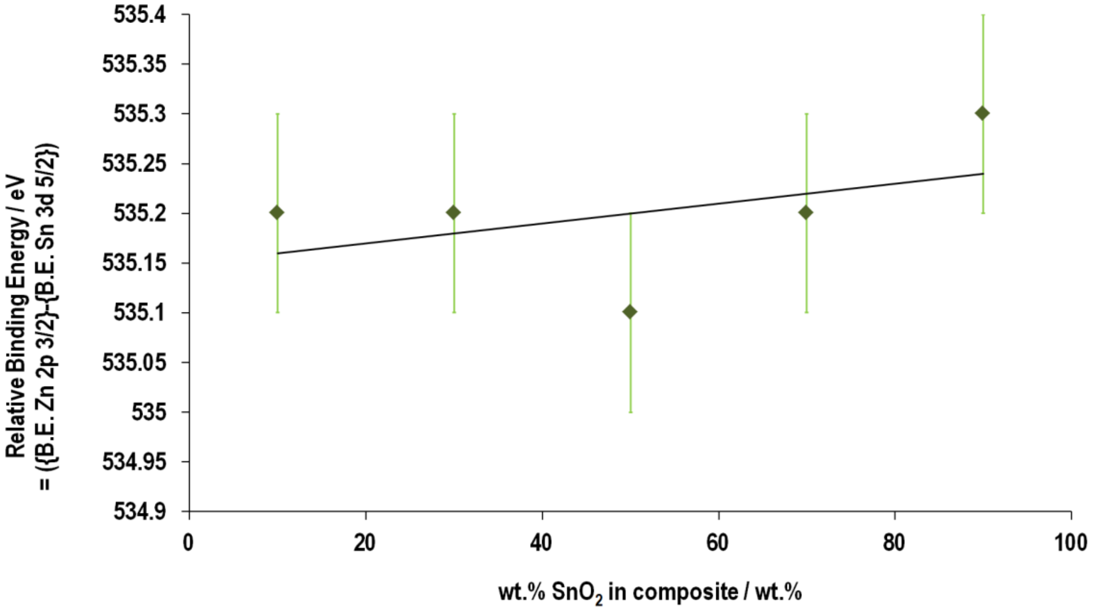

Figure 4–6. XPS data of the relative binding energies (calculated by taking the difference between the B.E. of the Zn $2p_{3/2}$ peak and the B.E. of the Sn $3d_{5/2}$ peak) for all the associated composites as a function of wt.% SnO_2 in each composite.

XPS measurements were conducted on all sensors within the SnO_2 – ZnO system, with two binding energy peaks of each metal observed for the corresponding metal oxide. All spectra (with a ± 0.1 eV experimental measurement error), were standardized against the C1s binding energy of 284.6 eV obtained from the reference database [201] and from literature [202, 203]. For all SnO_2 containing samples, a Sn $3d_{5/2}$ peak in the range of 486 - 487 eV was observed and for all ZnO containing samples, a Zn $2p_{3/2}$ peak occurred in the range of 1021-1023 eV. All the observed peaks were experimentally in agreement with the reference database [201] and accompanied by spin-orbit doublets. For the Sn species, $3d_{5/2}$ and $3d_{3/2}$ splitting values in the range of 8.4 – 8.7 eV were in close agreement with literature values [98] and for Zn species: $Zn2p_{3/2}$ and $Zn2p_{1/2}$ splitting values in the range of 23.0 – 23.1 eV which were also in close agreement with literature values [224]. XPS did not show evidence of any remnants such as silica from the organic vehicle in any of the sensor devices.

Calculation of the relative binding energies, by finding the difference between the binding energies of the Zn $2p_{3/2}$ and the Sn $3d_{5/2}$ peaks, as a function of increasing SnO_2 composition in the composites, showed evidence of a slight increase in the relative positions of the Sn and Zn core levels, as a function of increasing SnO_2 concentration, however these were within the instrumental error of the XPS instrument. As explained in Chapter 3 the XPS binding energies are referenced to the Fermi Level (E_F) and thus a change in the relative positions of the Sn and Zn core levels indicates a change in E_F relative to the energy levels in SnO_2 and ZnO phases. However, the experimental data showed that the net change in the relative binding energies between the Sn and Zn core lines was generally within the instrumental error of the XPS instrument, which suggested a very weak electronic interaction, if any, between both metal oxide components.

4.2.5 Gas Sensing Characterisation

4.2.5.1 Ethanol Sensing

The conductive response traces against increasing concentrations of ethanol at an operating temperature of 300 °C, have been presented in Figure 4–7. Tabulation of the mean responses values of the sensor devices in the SnO_2-ZnO system from the repeat tests against exposure towards the various ethanol concentrations at 300 °C and the associated 95% confidence intervals have been presented in Table 4–1.

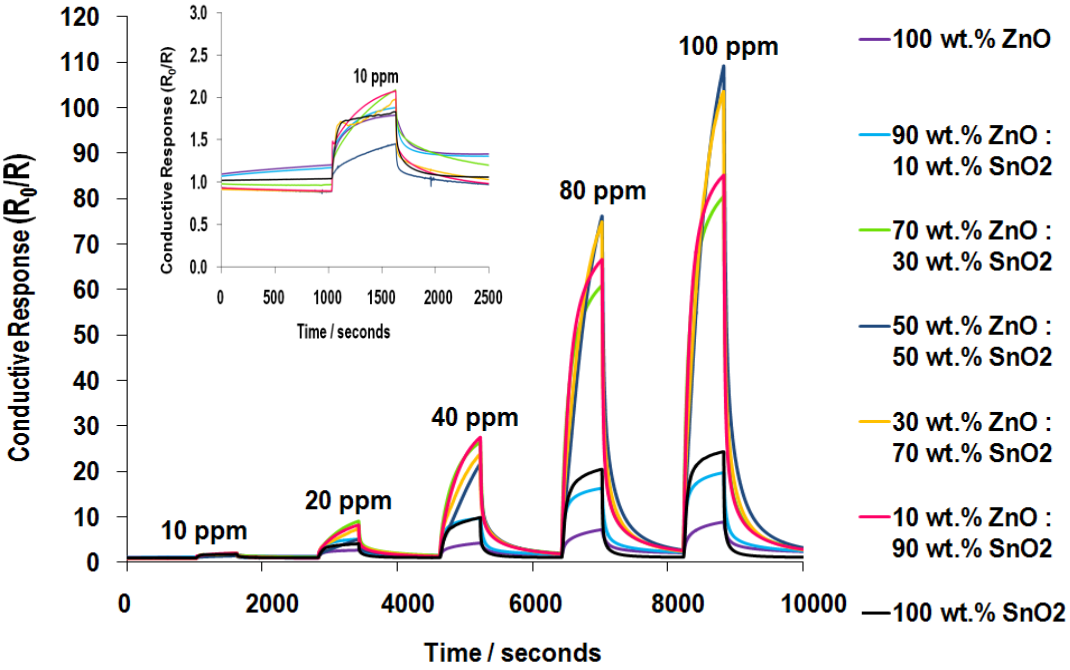

Figure 4–7. Conductive response traces of SnO_2-ZnO system towards 10, 20, 40, 80 and 100 ppm ethanol gas, at an operating temperature of 300 °C. The inset zooms into the conductive response traces against 10 ppm of the analyte.

Table 4–1. Average conductive responses of sensors devices in SnO_2-ZnO system from all repeat tests against various ethanol concentrations at 300 °C and associated errors in the form of 95% CIs.

	10 ppm		20 ppm		40 ppm		80 ppm		100 ppm	
Device	Average Response	95% CI	Average Response	95% CI	Average Response	95% CI	Average Response	95% CI	Average Response	95% CI
SnO_2	1.79	±0.04	4.21	±0.07	10.08	±0.18	20.67	±0.26	24.15	±0.75
90 wt.% SnO_2 – 10 wt.% ZnO	2.53	±0.45	10.09	±1.78	32.87	±5.29	78.34	±11.93	99.54	±14.70
70 wt.% SnO_2 – 30 wt.% ZnO	2.19	±0.21	8.6	±1.19	26.32	±2.41	79.35	±8.67	109.09	±10.89
50 wt.% SnO_2 – 50 wt.% ZnO	1.75	±0.30	6.28	±1.12	25.40	±3.65	84.96	±14.06	Electronic capping out	
30 wt.% SnO_2 – 70 wt.% ZnO	2.28	±0.19	9.31	±0.46	26.21	±2.28	59.91	±6.43	79.76	±9.39
10 wt.% SnO_2 – 90 wt.% ZnO	1.83	±0.06	4.90	±0.39	9.39	±0.86	15.96	±1.52	19.79	±2.11
100 wt.% ZnO	1.81	±0.08	2.87	±0.15	4.61	±0.36	7.61	±0.39	9.43	±0.70

300 °C was the temperature at which most of the sensors exhibited optimal response performance (as observed further on in Figure 4–13) except for the 100 wt.% ZnO and 90 wt.% ZnO – 10 wt.% SnO_2 sensor devices, both of which exhibited optimal performance at a higher temperature of 350 °C. The observed increase in conductive response of all devices against the reducing analyte is inherent to the nature of the n-type conductivity of both SnO_2 and ZnO metal oxides, whose conductive response is seen to increase upon exposure to ethanol [248]. The response behaviour therefore gave evidence that the conductivity within the pure and composite materials occurred via the n-type percolation paths that existed between the ZnO-ZnO and SnO_2-SnO_2 homo-contacts and the ZnO-SnO_2 hetero-contacts (the latter of which is only attributed to the composite materials).

The response traces in Figure 4–7 showed evidence of an enhanced response of the composite devices compared to both the 100 wt.% SnO_2 and 100 wt.% ZnO pure counterpart devices. The highest response achieved was against 100 ppm ethanol by the 50 wt.% ZnO - 50 wt.% SnO_2 device which exhibited a response of 109.1, a 4.5-fold increase with respect to the pure SnO_2 counterpart (which displayed a response of 24.4) and a 12.3-fold enhancement with respect to the pure ZnO counterpart (which was associated to a response of 8.9), towards the same concentration of the analyte.

This evidence demonstrates the enhanced response characteristics of a mixed-oxide system based on SnO_2 and ZnO composites. The 30 wt.% ZnO – 70 wt.% SnO_2 composite device also exhibited a response close to the 50 wt.% ZnO – 50 wt.% SnO_2 device, with a response of 103.6 towards 100 ppm ethanol which was a 4.2-fold enhanced response with respect to the pure SnO_2 counterpart and a 11.6-fold enhanced response compared to the pure ZnO counterpart, both against 100 ppm ethanol.

Both composite devices in terms of the mole ratios of ZnO:SnO_2 observed in Table 2–4, are associated to a significant contribution of both metal oxide components, suggesting that the packing structures [170, 171] of the sensor materials are associated to a random dispersion of SnO_2 and ZnO grains amongst each other to include SnO_2-ZnO hetero-contacts as well as ZnO-ZnO and SnO_2-SnO_2 homo-contacts, as observed in the illustrated schematic in Figure 4–8.

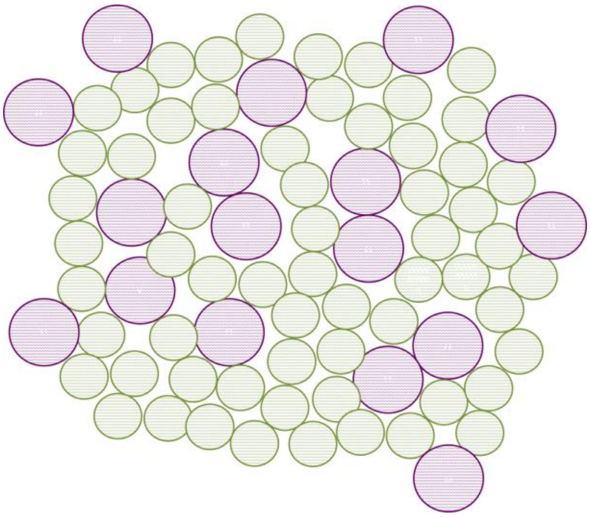

Figure 4–8. Schematic of random packing structure of metal oxide grains in 50 wt.% ZnO - 50 wt.% CTO and 30 wt.% ZnO – 70 wt.% ZnO sensor devices. In the diagram the green circles represent the smaller ZnO particles and the larger purple circles, the larger SnO_2 agglomerates. Although the diagram presents the grains and agglomerates to be perfectly spherical for simplicity, this perfect spherical nature is not assumed.

The dispersion of both metal oxide grains within the sensor matrix, is further evident from the SEM images of the 50 wt.% ZnO – 50 wt.% SnO_2 and 30 wt.% ZnO – 70 wt.% SnO_2 devices observed in Figure 4–1 (h) and (j), respectively. This dispersion of the SnO_2 and ZnO hetero-contacts within the matrix of the two sensor materials, is indicative of delocalised contact potentials, which may act to enhance the gas sensing response behaviour. As explained in Chapter 1, the enhancement effect is influenced by the modulation of the drift mobility of electrons travelling against the contact potential (which occurs through scattering away electrons that do not possess sufficient energy to overcome the energy barrier that exists between the hetero-contacts). As such the contact potential induces a potential energy barrier and therefore a resistance at the hetero-contact, making it more sensitive to a change in the atmosphere around it [170, 171].

Hetero-junction enhancement effects have been postulated in the literature as a key influential factor in the enhancement effects observed in SnO_2-ZnO mixed oxide systems. Haeng Yu *et al*. [92] for example, reported on the CO gas sensing properties of ZnO–SnO_2 composites. In their study, they had formed pellets containing mixtures of ZnO and SnO_2, with each pellet containing different mol % concentrations of ZnO and SnO_2. Upon exposure to 200 ppm of the analyte, the composite materials were attributed to enhanced responsivities with respect to the pure ZnO and SnO_2 counterparts. In particular, the enhancement effect of those composites which contained a significant contribution of both SnO_2 and ZnO metal oxides, were reported to be associated to the heterogeneous interfaces that existed between the ZnO and SnO_2 phases. The materials that were associated to increasing ZnO concentration into the SnO_2 matrix (specifically 20 mol% – 60 mol % ZnO), were reported to be associated to a significant number of SnO_2/ZnO grain boundaries, which were reported to contribute to the enhancement in gas response properties.

In another study by Song *et al*. [253] who had investigated a highly sensitive ethanol sensor based on mesoporous ZnO-SnO_2 nanofibres, the group had reported that the hetero-junction structure between the SnO_2 and ZnO interface, plays an important role to improve the sensing properties in such mixed oxide materials. Further, they had reported that it was well-established that an additional second component in a metal oxide semiconductor sensor could be exploited, with the interface between both metal oxides promoting an active site for the surface redox processes, suggesting an increased number of surface sites in a hetero-junction material, and further promoting free charge carriers which act to enhance the electronic conductance of the oxide films [168].

The experimental evidence presented in Figure 4–7 shows that a random packing structure of hetero-contacts can act to drastically enhance the transduction function of the sensor device. In this study, not only was the contact potential component influenced by the chemical non-uniformity between both component metal oxides, but was influenced by the significant difference in particle sizes of both component metal oxides [170]. Significant differences in the particle size have been reported to increase the resistance of the hetero-contact [170] and act to enhance the overall transduction function of the device.

Figure 4–7 further shows that the 10 wt.% ZnO – 90 wt.% SnO_2 and 70 wt.% ZnO – 30 wt.% SnO_2 sensor devices also exhibited enhanced responses in comparison to the pure ZnO and SnO_2 counterparts, with the former exhibiting a response of 85.1 against 100 ppm ethanol (a 3.5-fold enhancement compared to the pure SnO_2 device and a 9.6-fold enhance compared to the pure ZnO device) and the latter exhibiting a response of 80.5 towards 100 ppm ethanol (a 3.3-fold enhanced response compared to the pure SnO_2 device and 9-fold enhanced response compared to the pure ZnO device). Both these devices however were not associated to responses as pronounced as the 50 wt.% ZnO – 50 wt.% SnO_2 and the 30 wt.% ZnO – 70 wt.% SnO_2 composite devices.

Comparison of the contributions of metal oxides in the 10 wt.% ZnO – 90 wt.% SnO_2 and 70 wt.% ZnO – 30 wt.% SnO_2 from Table 2–4 shows that in the former device, there was a significantly greater contribution of the SnO_2 material, with the packing structure indicative of ZnO grains dispersed in the host matrix of SnO_2 grains. In the latter device, the contribution of the ZnO was significantly greater than that of the SnO_2, and therefore the packing structure was suggestive of SnO_2 grains dispersed in the host matrix of ZnO grains. SEM imaging corroborates with the suggested packing structures of both devices, showing that the 10 wt.% ZnO – 90 wt.% SnO_2 device as observed in Figure 4–1 (I) was dominated by SnO_2 grains and the 70 wt.% ZnO – 30 wt.% SnO_2 device Figure 4–1 (f) was dominated by the ZnO grains. Thus for both devices, the ratio of the homo-contacts (of the dominant metal oxide):hetero-contacts was large, suggesting that the homo-contacts were more competitive than the hetero-contacts and the devices consisted of more localised contact-potentials. This suggests why both composite devices did not perform as well as the 50 wt.% ZnO – 50 wt.% SnO_2 and the 30 wt.% ZnO – 70 wt.% SnO_2 composite sensors.

The percolation pathways of devices where the homo-contacts are more dominant than the hetero-contacts, are practically non-resistive. This implies that the electrons need to surmount a lower energy barrier to move through the same individual grains in the body of the material. This reasoning may aid in justifying the lower response of the 10 wt.% ZnO – 90 wt.% SnO_2 and 70 wt.% ZnO – 30 wt.% SnO_2 composites compared to the 50 wt.% ZnO – 50 wt.% SnO_2 and the 30 wt.% ZnO – 70 wt.% SnO_2 composite devices. The significant response however of both the 10 wt.% ZnO – 90 wt.% SnO_2 and 70 wt.% ZnO – 30 wt.% SnO_2 devices with respect to the pure SnO_2 and ZnO counterparts, suggested that packing structures contained localized contact potentials that played a role to enhance the response function of the devices. Such packing structures were also observed to be effective as gas sensing materials in the Chapter 3 focussing on a WO_3-ZnO composite system.

The 90 wt.% ZnO – 10 wt.% SnO_2 composite device was the only mixed metal oxide sensor that displayed a response behaviour which was slightly better than the ZnO counterpart, but worse than the pure SnO_2 counterpart. The device exhibited a response of 19.8 towards 100 ppm ethanol, which was a 2-fold enhanced response compared to the unmodified ZnO sensor but a 1.2-fold times poor response compared to the unmodified SnO_2 sensor, both against 100 ppm ethanol. The composition of this particular device as observed in Table 2–4, showed that its matrix was dominated almost totally by the ZnO grains with very little contribution of the SnO_2 material. This suggested that the fraction of the SnO_2 grains that were present within the sea of ZnO grains, were limited. As such, the percolation pathways were mainly dominated by the ZnO-ZnO homo-contacts, with hardly any percolation paths between the SnO_2-ZnO hetero-contacts, which did not influence the performance of the device with respect to the unmodified ZnO counterpart.

Apart from the hetero-junction enhancement effects associated to the SnO_2 and ZnO binary system, the synergy of the combination of both metal oxides can be postulated as playing a key role in influencing the enhanced response behaviour observed. De Lacy Costello *et al*. [91] have reported that both SnO_2 and ZnO are well known dehydrogenation catalysts for VOCs such as methanol and 2-butanol and ethanol [267, 268]. The group itself had reported on the catalytic and vapour sensing properties of various SnO_2 – ZnO composite devices: 1) 25 mass%:75 mass%, 2) 50 mass%:50 mass% and 3) 75 mass%:25 mass% SnO_2 – ZnO, at 350 °C towards 1-butanol. They had reported that composites of both metal oxides were more responsive to butanol than the pure metal oxide counterparts; and had attributed this behaviour to the synergistic action of both metal oxides towards the catalytic breakdown of butanol via a dehydrogenation route (as opposed to a dehydration route). The dehydrogenation has been observed to be the more dominant pathway of the catalytic breakdown of ethanol on the surface of metal oxides [69, 180, 181]. Specifically, they had reported that the SnO_2 was very effective in the dehydrogenation of butanol to butanal, and the ZnO was particularly effective not only at the dehydrogenation of the butanol to butanal, but further for the breakdown of butanal. As such they reported that combining both metal oxides was attributed to enhanced responsivity towards the analyte, due to the independent but synergistic catalytic butanol breakdown mechanisms of each metal oxide. In a similar way, the catalytic dehydrogenation of ethanol may also have been influenced by the synergistic combination of both SnO_2 and ZnO metal oxides.

In comparison to the observed responses to ethanol exhibited by the SnO_2-ZnO composite system presented in this thesis, de Lacy Costello *et al.* [145] had reported a very similar study on SnO_2 and ZnO composite sensors for the detection of ethanol. The group had fabricated pastes containing a variation of the mass % ratios of both metal oxides (100:0, 75:25, 50:50, 25:75, 0:100 SnO_2:ZnO) and then applied 3 mg of the prepared paste using a micro spatula to alumina sensor substrates. The pastes were equilibrated at room temperature for 24 hours, followed by heat-treatment at 350 °C for another 24 hours, prior to gas sensing tests. All sensors were tested at an operating temperature of 350 °C toward ppb concentrations of ethanol. The group had observed enhanced response characteristics of the composite sensors, with respect to the pure metal oxide counterparts when exposed to both 10 ppb and 100 ppb of ethanol. In particular the 25 mass%:75 mass% SnO_2:ZnO sensor device was the most responsive and exhibited a maximum response of 86 % change in conductivity, compared to 22 % exhibited by the pure SnO_2 sensor device and 60 % exhibited by the pure ZnO sensor device, all against 100 ppb ethanol. Although a direct comparison cannot be made between the literature study and that being reported here, the sensor devices reported by de Lacy Costello *et al*. [145] are seen to be very responsive, with the ability to detect ppb levels of ethanol, 100 times less concentrated than the concentrations studied experimentally in this thesis. However both studies do establish the enhancement effects achieved through a combination of SnO_2 and ZnO metal oxides.

In another study by Song *et al.* [93] who had reported on the characterization of ZnO–SnO_2 nano-fibres for an ethanol sensor, the group prepared the nano-fibres through in-situ electro-spinning technique and calcination. Three samples of nano-fibres were prepared with the molar ratios of the precursor sols of the Zn:Sn being varied in the ratios of 2:1, 1:1 and 1:2. Each sample of nano-fibres was mixed with water to form individual pastes, which were then coated around a ceramic tube, which contained pre-printed gold electrodes and which was temperature controlled by an inserted Ni-Cr wire. When the materials were operated at 300 °C, against increasing concentrations of ethanol, the ratio of 2:1 Zn:Sn sol prepared nano-fibres out-performed the other two sample of nano-fibres, with a response of just above 10 for 50 ppm ethanol and a response of 19 towards 100 ppm ethanol. In contrast the other two samples showed responses of 5 towards 50 ppm and responses in the range of 8-10 towards 100 ppm of the analyte. No responsivity comparisons were made by the group between the mixed oxide sensors and the pure SnO_2 and ZnO counterparts. Although a direct comparison is not possible between the literature and this thesis study, the results of responsivities obtained in this thesis are better than those obtained by Song *et al*. [93].

The kinetic behaviour observed from the response traces of the system in Figure 4–7, showed that the response of the composite materials was significantly slower than that of the pure metal oxide materials. This was indicated by the slower unsaturated shark-fin response traces of all the composite materials (except the 90 wt.% ZnO – 10 wt.% SnO_2 composite), as opposed to the saturated almost box-type traces (with slight shark-fin characteristics) of the pure metal oxides. The two best performing composite materials: 50 wt.% ZnO – 50 wt.% SnO_2 and 30 wt.% ZnO – 70 wt.% SnO_2 were attributed to a t_{90} (100 ppm) of 463 seconds and 425 seconds and a t_{-90} (100 ppm) of 1096 and 1035 seconds, respectively. In contrast the pure SnO_2 and ZnO counterparts were attributed to a t_{90} (100 ppm) of 236 seconds and 241 seconds towards 100 ppm ethanol and a t_{-90} (100 ppm) of 702 and 778 seconds, respectively. Thus the two composites responded almost twice as slowly and recovered almost 1.5 times as slowly as the pure counterparts. This illustrates the compensation of the kinetics of response and recovery, for the enhanced responsivity of composite materials and suggests that the composite need to be catalytically modified to optimise the kinetics of response and recovery.

The shark-fin behaviour of the response traces of both composites was suggestive of unsaturated sensor surfaces, with 10 minutes of ethanol exposure proving to be insufficient time to attain steady-state saturation. This unsaturated behaviour was suggestive of a large number of reaction sites, with adsorbed oxygen anions readily available to react, in both composite materials for the given concentration of ethanol exposure, or alternatively, too large concentrations of ethanol for the given number of reaction sites. The shark-fin behaviour was very gradual for these two best performing composites, which suggested very slow response behaviour. In stark contrast, the pure metal oxide materials exhibited saturated behaviour within the 10 minutes of exposure to ethanol, suggesting the presence of a limited number of reaction sites, or a limited number of adsorbed oxygen anions available, for the given concentration of ethanol exposure.

As discussed in Chapter 3, an enhanced number of reaction sites in a mixed oxide system has been reported by Zeng *et al*. [168] who had reported on the enhanced gas sensing properties of SnO_2 nanosphere functionalised TiO_2 nanobelts toward various VOCs, such as methanol, ethanol, formaldehyde and acetone. The group reported that the hybrid oxides are associated to additional depletion regions that occur at the interface between the SnO_2 nanospheres and the TiO_2 nanobelts and that the hetero-junctions that exist between the interfaces of both the metal oxides, serve as additional reaction sites. Thus, the enhanced number of the reaction sites promoted by the significant dispersion of hetero-contacts within the packing structures of both the 50 wt.% ZnO – 50 wt.% SnO_2 and 30 wt.% ZnO – 70 wt.% SnO_2 composites, can explain the unsaturated shark-fin nature of their response traces, and suggests a larger number of reaction sites available for the given number of ethanol molecules in the exposure. As such, the reaction sites of the composite materials are unsaturated and therefore associated to slower response times. In contrast, a limited number of reaction sites in the pure metal oxide materials suggest faster saturation of the surfaces, accounting for the faster response times.

The shark-fin behaviour for the 10 wt.% ZnO – 90 wt.% SnO_2 and 70 wt.% ZnO – 30 wt.% SnO_2 composites, was less pronounced (compared to the 30 wt.% ZnO – 70 wt.% SnO_2 and 50 wt.% ZnO – 50 wt.% SnO_2 devices) and therefore both associated devices were attributed to relatively faster kinetics, with a t_{90} (100 ppm) of 294 and 299 seconds and a t_{-90} (100 ppm) of 1073 and 1063 seconds, respectively. The faster behaviour of both these composites suggested a reduced number of reaction sites of interaction for the given number of ethanol molecules they were exposed to, justified by the homo-contact dominated packing-structures of both composites.

The recoveries of all composite sensors were observed to be significantly slower than of the pure metal oxides, observed by comparison of the t_{-90} values and indicated by their gradual return to baseline response. In stark contrast, faster recovery of the pure metal oxides was indicated by the steep gradient of return back to baseline upon switching off the ethanol gas. The faster return back to baseline was suggestive of a limited number of ethanol molecules that desorbed from the limited number of available reaction sites in the pure materials i.e. the desorption yield was significantly lower in the pure materials than in the composite materials. The slower recovery of the composite materials suggested that the composites have a greater number of occupied surface sites, due to the presence of the hetero-junction interfaces, and therefore needed more time to fully recover back to baseline response.

It was interesting to observe the cross over behaviour between the four best performing composite materials, with the 10 wt.% ZnO – 90 wt.% SnO_2 and 70 wt.% ZnO – 30 wt.% SnO_2 devices exhibiting the best performance towards 10, 20 and 40 ppm ethanol and then the 30 wt.% ZnO – 70 wt.% SnO_2 and 50 wt.% ZnO – 50 wt.% SnO_2 devices crossing-over between 40 ppm and 80 ppm and exhibiting the best performance towards 80 ppm and 100 ppm ethanol. This demonstrated how a simple change in the composition of a composite material, could tune the selectivity of the sensors towards particular analyte concentrations. Further, it showed how a simple change in composition of the metal oxides could manipulate the yield of the ethanol combustion reactions, which influenced the concentration of charge carriers released into the electron depletion layer (EDL) of the metal oxide, ultimately determining the magnitude of conductive response.

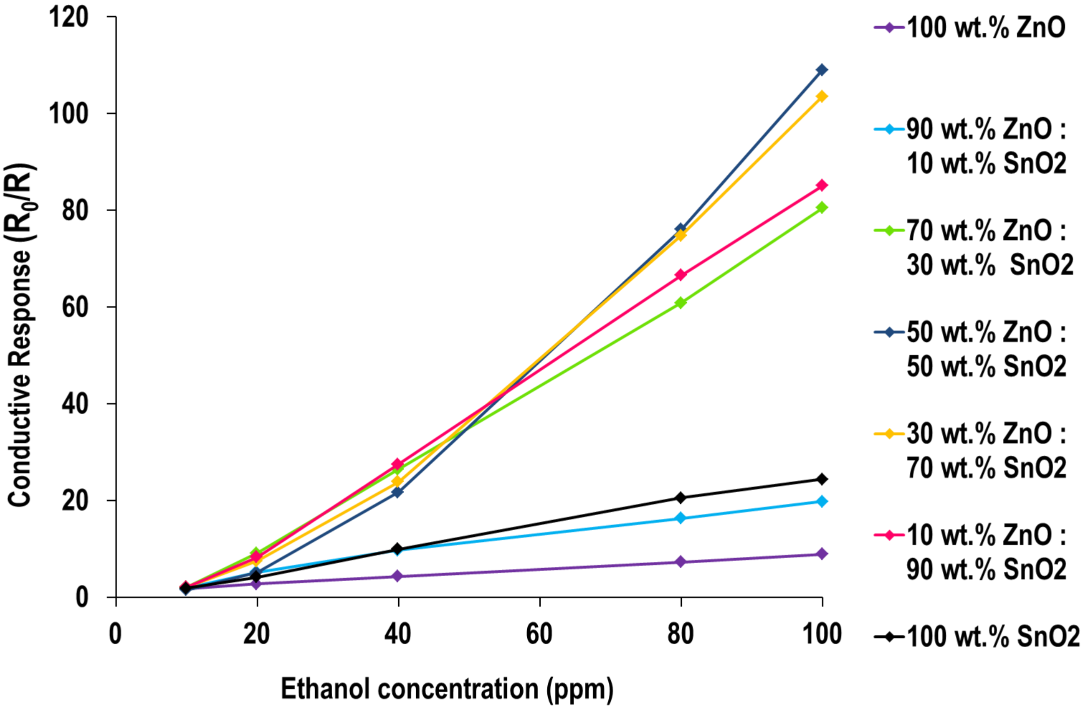

Figure 4–9. Conductive response of SnO_2-ZnO system towards 10, 20, 40, 80 and 100 ppm ethanol gas, at an operating temperature of 300 °C.

Figure 4–9 presents the increase in the conductive response of the sensor devices within the SnO_2 – ZnO composite system as a function of increasing concentration of ethanol at an operating temperature of 300 °C. The graph presents a steep increase in response magnitude of the four best performing composite materials, and in stark contrast, the shallow increase in the magnitude of the pure metal oxide devices and the 90 wt.% ZnO – 10 wt.% SnO_2 device. The steep rate of increase in response magnitude or linear range of the four best performing composite devices, suggests that the number of available reaction sites in their corresponding sensor matrices, are able to occupy the increasing number of ethanol molecules, As such, the yield of ethanol combustion reactions is effectively increasing with these materials, as the concentration of ethanol exposure increases. The large number of reaction sites, may be accounted for by the presence of a larger number of hetero contacts between the SnO_2 and ZnO grains, accounted for by the small mole ratio of SnO_2:ZnO in the corresponding sensor matrices from Table 2–4, Chapter 2. The pure ZnO and SnO_2 materials as well the 90 wt.% ZnO – 10 wt.% SnO_2 sensor device in contrast, are unable to occupy the increasing number of ethanol molecules that they are exposed to as a function of time, accounted for by the homo-contact dominated packing structure. One of the key observances from Figure 4–9, is the poor response of the 90 wt.% ZnO - 10 wt.% SnO_2 sensor device towards ethanol as opposed to the much larger response of the 10 wt.% ZnO – 90 wt.% SnO_2 sensor device, given that both are homo-contact dominated materials. This observation can however be justified by calculation of the mole ratio of the metal oxides in each sensor; with the former having a SnO_2:ZnO ratio of 1 : 22 and the latter having a ratio of 1 : 0.25. The ratios show that the 90 wt.% ZnO - 10 wt.% SnO_2 is significantly more homo-contact dominated by the ZnO grains, and is effectively as good as a pure metal oxide. The 10 wt.% ZnO – 90 wt.% SnO_2 sensor device in contrast has a lower ratio of both grains, and therefore is likely to comprise a larger number of hetero-contacts, which aid to enhance its response behaviour. This example shows how a simple change in the compositional contribution of either metal oxide can significantly tune the response properties of such devices.

The shallower linear range of the pure ZnO material relative to the pure SnO_2 material, suggests that the ZnO material has limited surface adsorption sites compared to SnO_2. This is unusual as SEM imaging shows that the ZnO material constitutes particles in the range of 0.1 μm – 1 μm size and the SnO_2 material is observed to constitute agglomerates in the μm range, some larger than 2-3 μm. Thus, the particle sizes suggest that the SnO_2 materials should have a shallower linear range due to the larger particle sizes and therefore reduced surface area. However, this behaviour may be explained by differences in density that exist at the junction of the grains, with the ZnO having greater density between the grain and therefore limiting the diffusion pathways for the gas molecules to travel into the matrix of the material. In contrast, the SnO_2 material maybe associated to lower density at the junctions between the grains, providing greater pathway for gas diffusion.

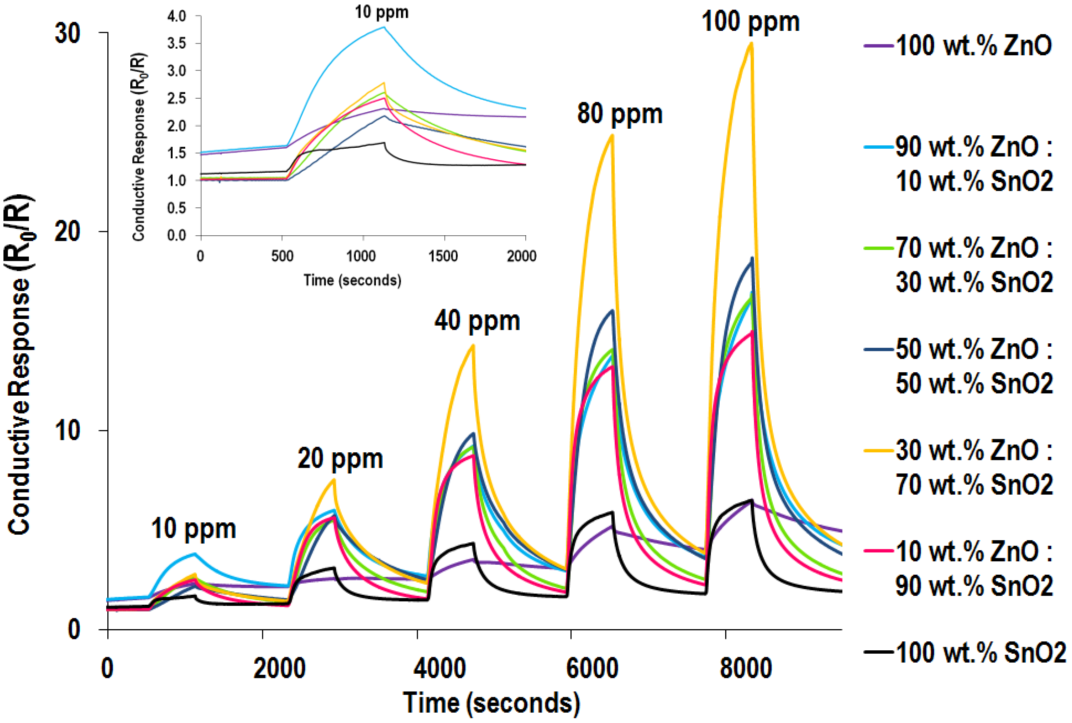

Figure 4–10. Conductive response traces of SnO_2-ZnO system towards 10, 20, 40, 80 and 100 ppm ethanol gas, at an operating temperature of 200 °C. The inset zooms into the conductive response traces of all sensor devices towards 10 ppm ethanol.

The operating temperature of 300 °C was the optimal temperature of operation for the system of sensor devices, with a large distribution of response magnitudes exhibited by the system of sensor devices, against the range of concentrations of ethanol exposure. In contrast, Figure 4–10 shows that at the lowest temperature of operation which was 200 °C, the poor response performance of all sensor devices, narrowed the distribution of conductive response magnitudes observed.

The highest response observed at 200 °C was of the 30 wt.% ZnO – 70 wt.% SnO_2 sensor device of 25.5 against 100 ppm ethanol, which was a 5.4-fold enhanced response with respect to the pure SnO_2 and 10.6-fold enhanced response with respect to the pure ZnO counterparts, against the same concentration of ethanol exposure. The response traces of the sensor devices in Figure 4–10 showed the responses to be associated to significant drift accounted for by the unstable baseline, which increasingly drifted as a function of time and as the concentration of ethanol exposure increased. The traces showed that 20 minutes was not enough to recover the devices back to baseline response and that further recovery time e.g. 30 minutes, was required to fully recover the surface of the materials.

The lack of resistance of the n-type metal oxides to humidity, aids to explain the drift towards higher conductive responses observed in the sensor devices in Figure 4–9. Further the lower operating temperature implies that the surface of the metal oxides are not fully recovered in comparison to higher operating temperatures, suggesting potential interference of the surface adsorbed species which act to modulate the stability of the sensor devices.

Due to the lack of complete recovery of the sensor surfaces, prior to the introduction of a new concentration of ethanol, the responses observed at 200 °C were greater than the true response magnitudes. This observation was warranted by the nature of the response calculations, where the R_0 value was kept static throughout calculation of the responses as explained earlier in Chapter 2, section 2.5. Had the relative response ratio been calculated as a ratio of the span of the individual response trace, where the R_0 value was the resistance prior to gas injection, then the relative response could be calculated, despite the baseline drift. The best performing composite, the 30 wt.% ZnO – 70 wt.% SnO_2 device, was attributed to a t_{90} (10 ppm) of 241 seconds at 200 °C and the same composite exhibited a t_{90} (10 ppm) of 36 seconds at 300 °C. The same composite exhibited a t_{-90} (10 ppm) recovery time of 716 seconds when at 200 °C and a t_{-90} (10 ppm) recovery time of 357 seconds when at 300 °C. A concentration of 10 ppm ethanol was the best concentration for comparison of the t_{90} and t_{-90} values between the different temperatures of operation, as the baseline was stable at both operating temperatures, prior to exposure to this specific concentration of ethanol. Comparison of the t_{90} and t_{-90} values between both operating temperatures at the higher concentration regions, was difficult as the baseline drift artificially shortened these values at 200 °C, due to incomplete recovery of the surface of the material. This incomplete recovery was warranted in accordance to the nature of the t_{90} and t_{-90} calculations which were calculated with respect to the absolute R_0 values, as opposed to the relative R_0 values, to maintain consistency with response calculations.

Comparison of the t_{90} and t_{-90} values between 200 °C and 300 °C, showed that the kinetics of the surface reactions were thermally induced, with quicker response and recovery times at 300 °C. Increased operating temperatures are likely to quicken the rate of the ethanol surface combustion reactions with the surface adsorbed oxygen anions and therefore quicken the response of the sensor material towards the exposed analyte. However, increasing the operational temperature is also likely to reduce the residence time of the adsorbed oxygen anions on the surface of the metal oxide, in comparison to a reduced operating temperature. As such, this implies a low stability of adsorption of the anionic oxygen species or a very high level of diffusion of the analyte molecules, which statistically reduces the overall yield of ethanol surface reactions that are probable. Thus a higher temperature, provides greater energy to the ethanol molecules to desorb and diffuse away from the metal oxide surface as well as reduce their stability of adsorption, and as such leads to faster regeneration/recovery of the metal oxide surface.

The best response performance of most of the sensors at an operating temperature of 300 °C, suggested this was the ideal operating temperature. A number of reasons can contribute to this observation, with the first being an ideal environment for the promotion of the hetero-junction enhancement effects with an ideal potential energy barrier level, which is controls the local exchange of charge carriers across both semiconductors. The second reason being that 300 °C was a suitable temperature to promote synergistic dehydrogenation reactions of ethanol, with the sensors being potentially responsive and reactive towards the by-products of the ethanol combustion reactions under these temperature conditions. A third reason maybe that this temperature may have promoted the required concentration of electrons in the conduction band of the n-type semiconductors, in contrast to lower operating temperatures. Thus, the increased electron density in the conduction band is likely to have stabilised sufficient number of oxygen ions on the surface of the metal oxides. Subsequently, this is likely to yield the optimal number of ethanol surface reactions, increasing the concentration of electrons released back in to the conduction bands of the n-type semiconductors, and therefore promote the best responsivity of the materials.

As observed in Figure 4–10, at the lower operating temperature of 200 °C, the hetero-junction enhancement effects were still visible with enhanced response of the composite materials with respect to the pure counterparts. The narrowed distribution of response magnitudes of the system of sensors observed at this reduced operating temperature, presented more clearly in Figure 4–11, suggested however, that the temperature played a significant role to swamp the hetero-junction enhancement effects.

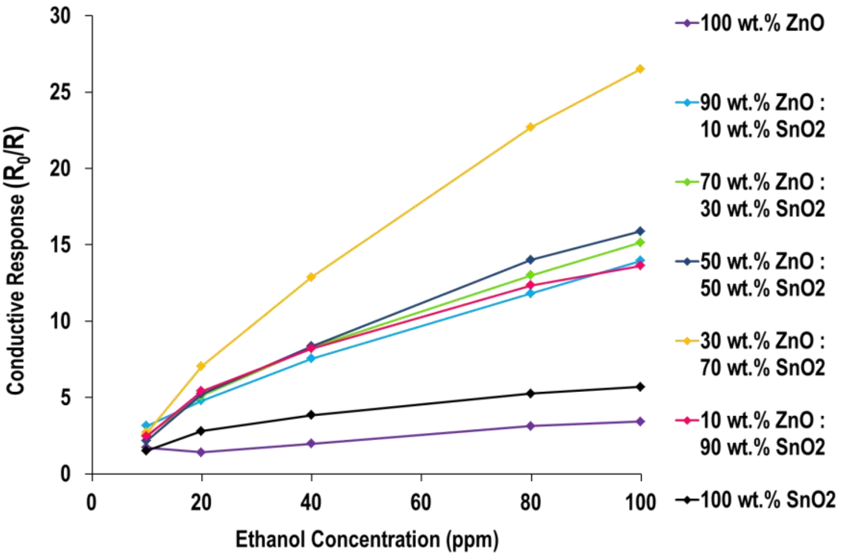

Figure 4–11. Conductive response of SnO_2-ZnO system towards 10, 20, 40, 80 and 100 ppm ethanol gas, at an operating temperature of 200 °C.

This can be explained by understanding that at reduced operating temperatures, the thermal energy of the system is low. The lower thermal energy suggests that the thermally induced charge transfer within the semiconductors is subsequently more difficult, with a reduced number of electrons occupying the conduction bands of both metal oxides. This suggests that the work-function between the interfacial region of SnO_2 and ZnO at the n-n interface, will impact the junction effect on the responsivity in a negative way as the energy barrier for the Fermi level equilibration is increased, resulting in an increased energy barrier for the local exchange of charge carriers across both semiconductors. In such a situation, the resistance at the junction is increased. The charge carriers have less than available energy to overcome the increased energy barriers between the grains and therefore lower operating temperatures are unlikely to promote the hetero-junction enhancement effects, and hence the composites are seen to exhibit weakly enhanced response behaviour. Further, the reduced occupation of electrons in the conduction band suggests a lower occupation of oxygen anions on the surface of the metal oxides, and therefore a lower yield of surface reactions between the ethanol molecules and the adsorbed oxygen anions, lowering the overall response magnitude of the device at 200 °C.

The conductive response of the system of sensors at the highest operating temperature of 500 °C seen in Figure 4–12 showed that responses of all sensor devices significantly decreased in comparison at the response magnitudes observed at the lower operating temperatures of 200 °C and 300 °C.

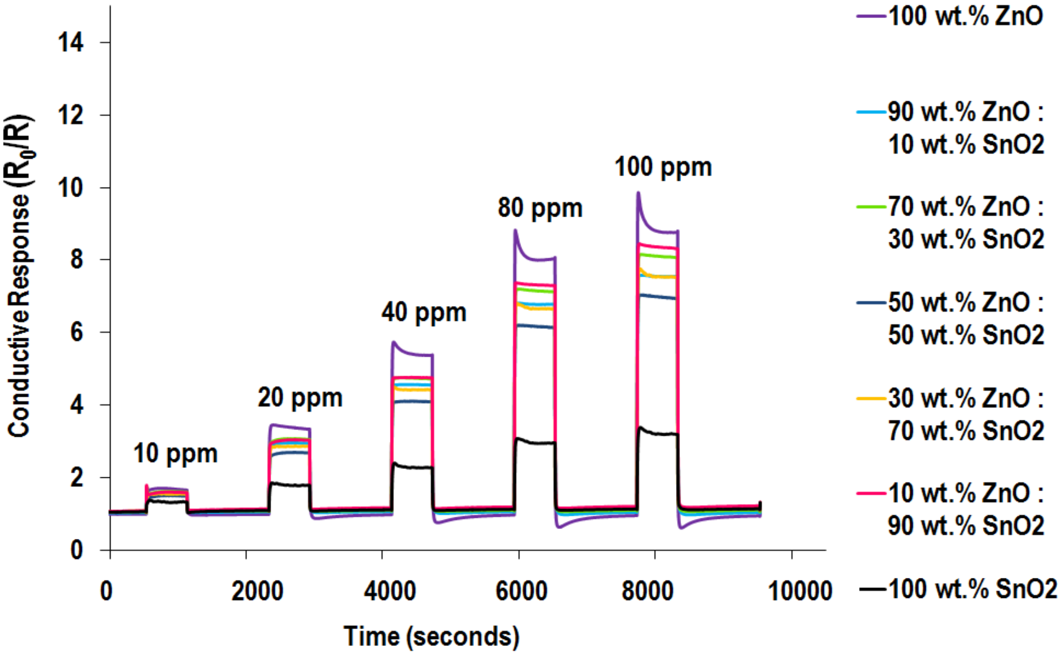

Figure 4–12. Conductive response traces of SnO_2-ZnO system towards 10, 20, 40, 80 and 100 ppm ethanol gas, at an operating temperature of 500 °C.

The highest response observed was attributed to the ZnO sensor of 9.9 towards 100 ppm ethanol. The composites were attributed to responses which were lower than the pure ZnO sensor, showing that the hetero-junction enhancement effects diminished at the higher operating temperature. Further, they all exhibited very similar responses at the higher temperature of operation, and therefore no discrimination between the response magnitudes were observed in comparison to that observed at 200 °C and 300 °C. In comparison to the pure ZnO sensor, the pure SnO_2 sensor exhibited a conductive response of 3.4 towards the same concentration of 100 ppm, which may be accounted for by the ZnO materials as a better dehydrogenation catalyst of ethanol at the higher operating temperature. As reported in Chapter 3, Xu *et al.*[69] reported that the gas response of ZnO is strongly dependent on the conversion of ethanol to acetal, and the conversion of the alcohol to the aldehyde is reported to increase as a function of increasing operating temperature.

The response traces of the pure ZnO metal oxide device were interesting as they were attributed to fast 'box' like [106] 'pseudo' n-type behaviour, particularly towards 80 ppm and 100 ppm ethanol. Here 'pseudo' suggests lack of full conventional n-type behaviour, but instead a mix of both n-type and p-type response characteristics. The fast response of the ZnO device was justified by its t_{90} (100 ppm) of 9.2 seconds and t_{-90} (100 ppm) value of 10.9. The 'pseudo' n-type response behaviour of the ZnO sensor device, suggested that the concentration of ethanol molecules may have been significantly higher than the concentration of adsorbed oxygen anions on the surface of the metal oxides. A higher operating temperature is likely to severely decrease the residence time of the oxygen anions on the surfaces of the metal oxides. As such, the rate of depletion of electrons from the conduction bands of the metal oxides, due to the instantaneous adsorption and desorption of the oxygen anions from the surfaces, is likely to be accelerated. Thus the statistical probability of the ethanol surface reactions is lowered. Further, the lowered electron density in the conduction band is likely to promote p-type conductivity. Another cause of the p-type behaviour may have been a reaction which occurred between the ethanol molecules and the surface of the ZnO material, which promoted the formation of an oxidising by-product. Exposure to such a species, can cause the resistance of the material to increase. The observation of both n-type and p- type responses in this case, suggest different time scales of interaction towards both the reducing and oxidising species, warranted by each species being associated to different adsorption and desorption isotherms.

In contrast, all other sensor devices exhibited fast 'box' like [106] saturated steady-state n-type behaviour which suggested complete saturation of the metal oxide surfaces. At the higher temperatures of operation, the frequency of ethanol reactions is expected to increase dramatically [234]. As such the saturation of the response signal is expected as a greater number of surface combustion reactions imply a greater removal of the oxygen anions from the metal oxide surfaces [234]. As such with higher and higher concentrations of ethanol, a limit is reached as to the amount of oxygen that can be removed from the surface and as such a saturated response is observed [234]. The steady-state nature of the response curves suggests the adsorption and desorption reactions of the gaseous species are thermodynamically and kinetically equilibrated, implying the rate of the reaction of the ethanol molecules with the surface adsorbed oxygen anions is as fast as the subsequent formation and desorption of the reaction products formed as a result of those reactions. The SnO_2 sensor was attributed to a t_{90} (100 ppm) of 17 seconds and a t_{-90} (100 ppm) value of 16 seconds at this higher temperature of operation. Analogously, the two best performing composites observed in Figure 4–7, which were the 50 wt.% ZnO – 50 wt.% SnO_2 and 30 wt.% ZnO – 70 wt.% SnO_2 sensor devices were attributed to a t_{90} (100 ppm) of 12.4 seconds and 11.2 seconds and t_{-90} (100 ppm) values of 17.6 seconds and 9.8 seconds, exhibiting the enhanced speed of response and recovery as a function of increased operating temperature.

Figure 4–13 presents the conductive response of the system of sensors towards 100 ppm ethanol as a function of increasing operating temperature. The figure illustrates that 300 °C was the optimal operating temperature for almost all sensor devices within the system, with the 90 wt.% ZnO – 10 wt.% SnO_2 and pure ZnO sensor devices performing optimally at a higher operating temperature of 350 °C.

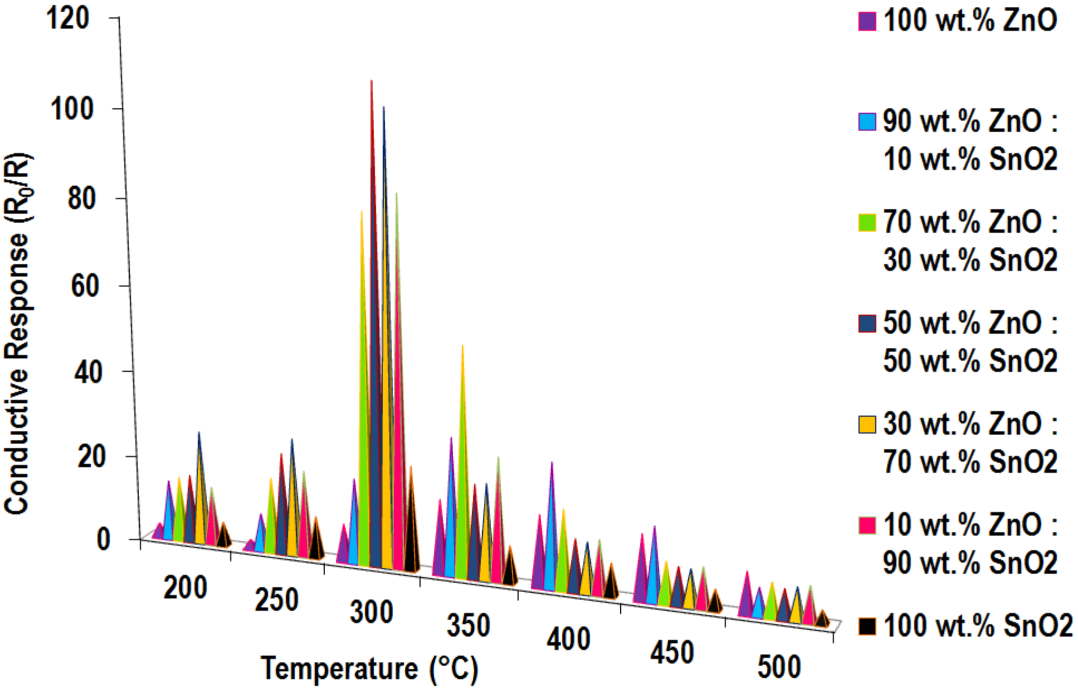

Figure 4–13. Conductive responses of SnO_2-ZnO system against 100 ppm ethanol gas, as a function of increasing operating temperature.

A deconvolution of Figure 4–13 of the conductive response magnitudes as a function of increasing operating temperature of the individual sensor devices, against 100 ppm and all other tested concentrations of ethanol, has been presented in Figure 4–14. Figure 4–14 (b), (c) and (d) show that the 90 wt.% SnO_2 – 10 wt.% ZnO, 70 wt.% SnO_2 – 30 wt.% ZnO and the 50 wt.% SnO_2 – 50 wt.% ZnO devices were all dominated by the SnO_2 material, with all devices exhibiting the optimal performance at 300 °C, analogous to the pure SnO_2 sensor device presented in Figure 4–14 (a). In contrast, the 90 wt.% ZnO – 10 wt.% SnO_2 device presented in Figure 4–14 (f), was dominated by the ZnO material, with the device exhibiting the optimal performance at 350 °C, analogous to the pure ZnO sensor device presented in Figure 4–14 (g). The 30 wt.% SnO_2 – 70 wt.% ZnO sensor device presented in Figure 4–14 (e) however, showed optimal performance at 300 °C analogous to the pure SnO_2 material but was also attributed to a significant contribution of the ZnO material, with the pyramidal curve observed in Figure 4–14 (a), (b), (c) and (d), for the SnO_2 dominated materials, being slightly distorted for the 30 wt.% SnO_2 – 70 wt.% ZnO device. Thus, the deconvolution aids to illustrate the contribution of the both metal oxides to the overall enhanced response properties of the composite devices towards ethanol and further explain the enhanced behaviour of the 30 wt.% SnO_2 – 70 wt.% ZnO composite device observed in Figure 4–7 and Figure 4–10, in comparison to all other composites within the system.

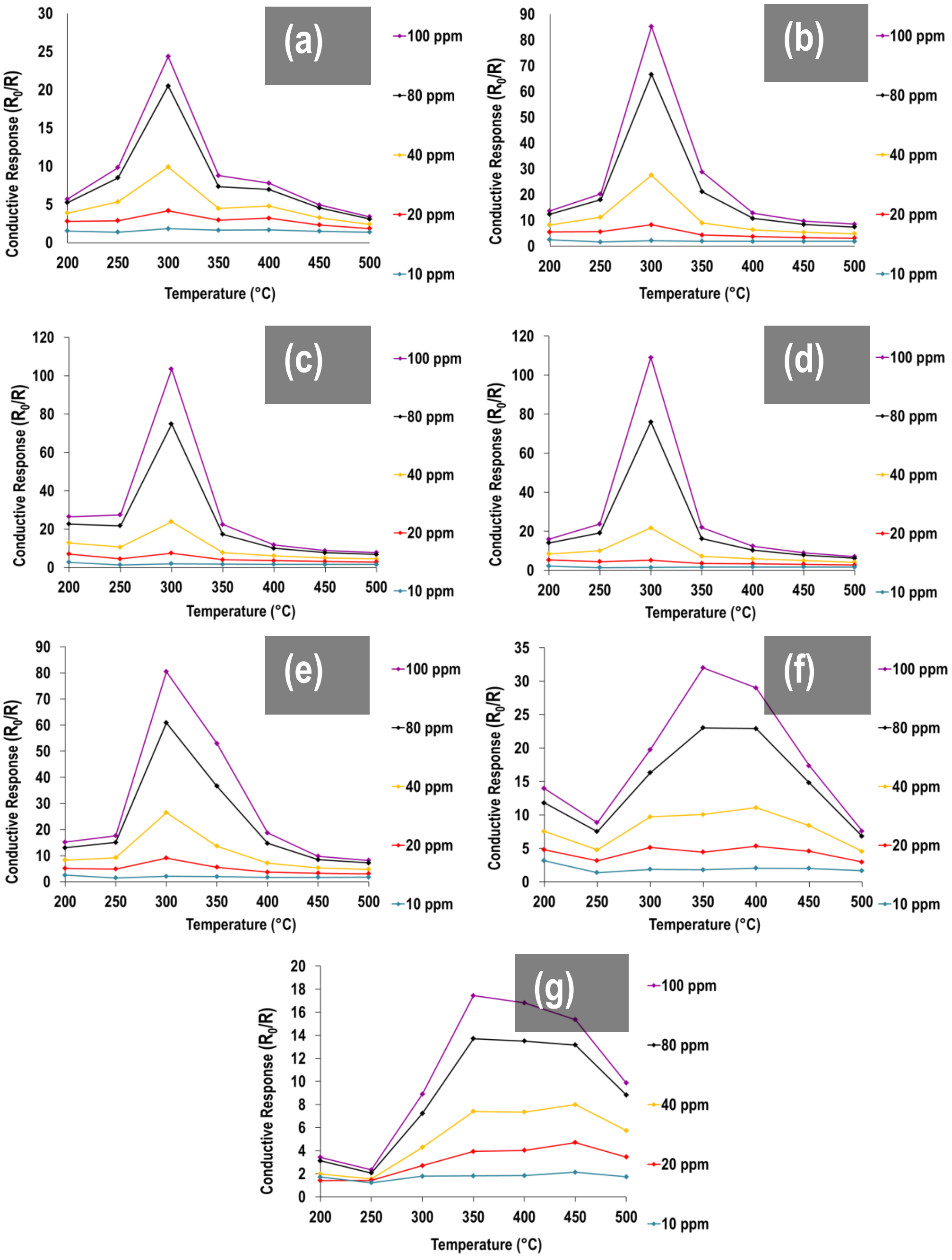

Figure 4–14. Conductive Responses of a) 100 wt.% SnO_2, (b) 90 wt.% SnO_2 – 10 wt.% ZnO, (c) 70 wt.% SnO_2 - 30 wt.% ZnO, (d) 50 wt.% SnO_2 – 50 wt.% ZnO, (e) 30 wt.% SnO_2- 70 wt.% ZnO, (f) 10 wt.% SnO_2- 90 wt.% ZnO and (g) 100 wt.% ZnO sensor devices as a function of increasing operating temperature against 10, 20, 40, 80 and 100 ppm ethanol.

4.2.5.2 NO_2 Sensing

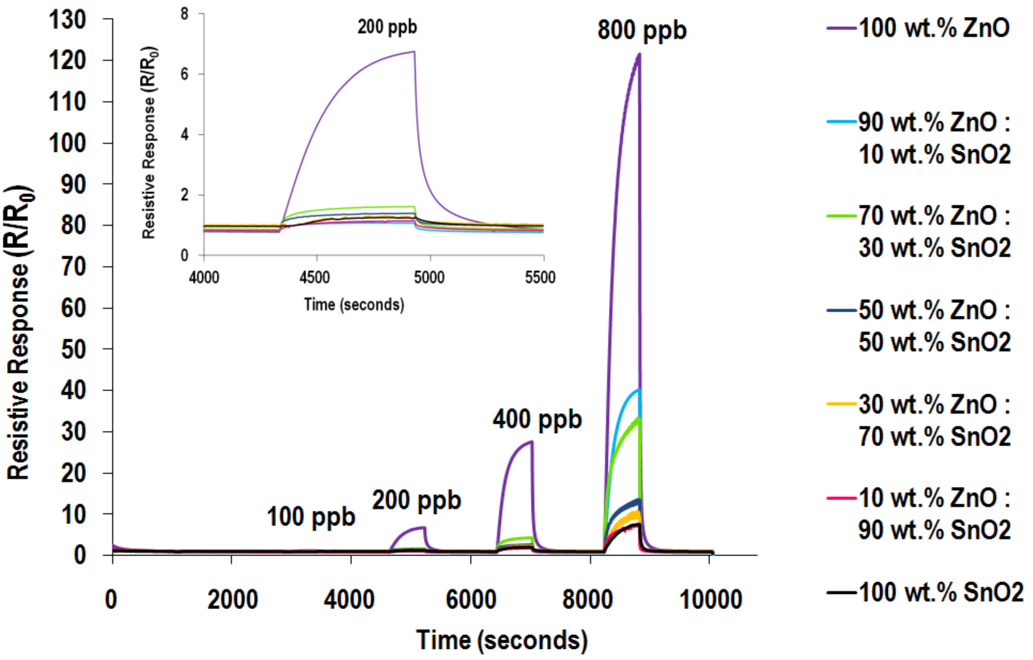

Figure 4–15. Resistive response traces of SnO_2-ZnO system towards 100, 200, 400 and 800 ppb NO_2 gas, at an operating temperature of 300 °C. The inset projects the resistive responses of the array towards 200 ppb NO_2.

Figure 4–15 illustrates the resistive response traces of the system of sensors against increasing concentrations of NO_2 at the optimal operating temperature of 300 °C. Tabulation of the mean responses values of the sensor devices in the SnO_2-ZnO system from the repeat tests against exposure towards the various NO_2 concentrations at 300 °C and the associated 95% confidence intervals have been presented in Table 4–2.

Table 4–2. Average resistive responses of sensor devices in SnO_2-ZnO system from all repeat tests against 400 ppb and 800 ppb NO_2 concentrations at 300 °C and associated errors in the form of 95% CIs.

	400 ppb		800 ppb	
Device	Average Response	95% CI	Average Response	95% CI
100 wt.% SnO_2	1.88	±0	7.59	±0.09
90 wt.% SnO_2 – 10 wt.% ZnO	1.75	±0.13	6.77	±0.94
70 wt.% SnO_2 – 30 wt.% ZnO	2.28	±0.08	10.26	±0.50
50 wt.% SnO_2 – 50 wt.% ZnO	2.65	±0.17	13.35	±1.13
30 wt.% SnO_2 – 70 wt.% ZnO	4.36	±0.20	33.28	±0.04
10 wt.% SnO_2 – 90 wt.% ZnO	3.32	±2.48	39.86	±1.06

Figure 4–15 indicates that the resistive response order of the system of devices increased as a function of increasing ZnO concentration or as a function of decreasing concentration of SnO_2, when exposed to 800 ppb NO_2. At this highest concentration of NO_2 exposure, the results show that the system did not exhibit hetero-junction or synergistic enhancement effects when exposed to the oxidising gas, in stark contrast to what was observed for ethanol. Towards 800 ppb, the pure ZnO sensor device exhibited the strongest resistive response (of all sensor devices) of 121.6 and the pure SnO_2 sensor in contrast exhibited the weakest resistive response (of all sensors devices) of 10.7. A deconvolution of the responses of the system towards 400 ppb and 200 ppb at 300 °C, has been presented further in Figure 4–16 and Figure 4–17, respectively. Figure 4–15 showed that as the concentration of NO_2 was increased from 200 ppb to 800 ppb, a large increase in the response of the ZnO sensor device was observed. This suggested the lack of occupation of the surface sites when exposed to 200 ppb of NO_2, and therefore a low response magnitude. At 800 ppb however, the surface sites of the material were significantly occupied, causing the response magnitude to increase significantly. In particular a change in the response mechanism was observed by the ZnO sensor between 400 ppb and 800 ppb, observed through the sudden increase in the response at 800 ppb. This can be accounted for by an increase in the size of the electron depletion layer (Debye Length) due to the increase in concentration of NO_2 molecules in the 800 ppb purge, which are likely to have abstracted a significant number of electrons upon interaction with the ZnO surface [45, 269]. If the size of the ZnO grains, particularly those in the region of 0.1 µm or less, are comparable to twice the size of the Debye Length, then the space charge region can develop within the crystallites of the grains, inducing grain controlled which is the most responsive [270], as opposed to grain boundary controlled conductivity [45, 269]. In most cases, it is most likely to develop in 1-dimensional materials of a length comparable to the Debye length [45], however the steep increase in response suggests some form of similar mechanism occurring here. In contrast the, agglomeration of the SnO_2 nanoparticles into agglomerates of sizes which are in the µm range, some larger than 2-3 µm, suggest that the grain controlled conduction mechanism is difficult to achieve and therefore such a large increase in the response behaviour is not observed.

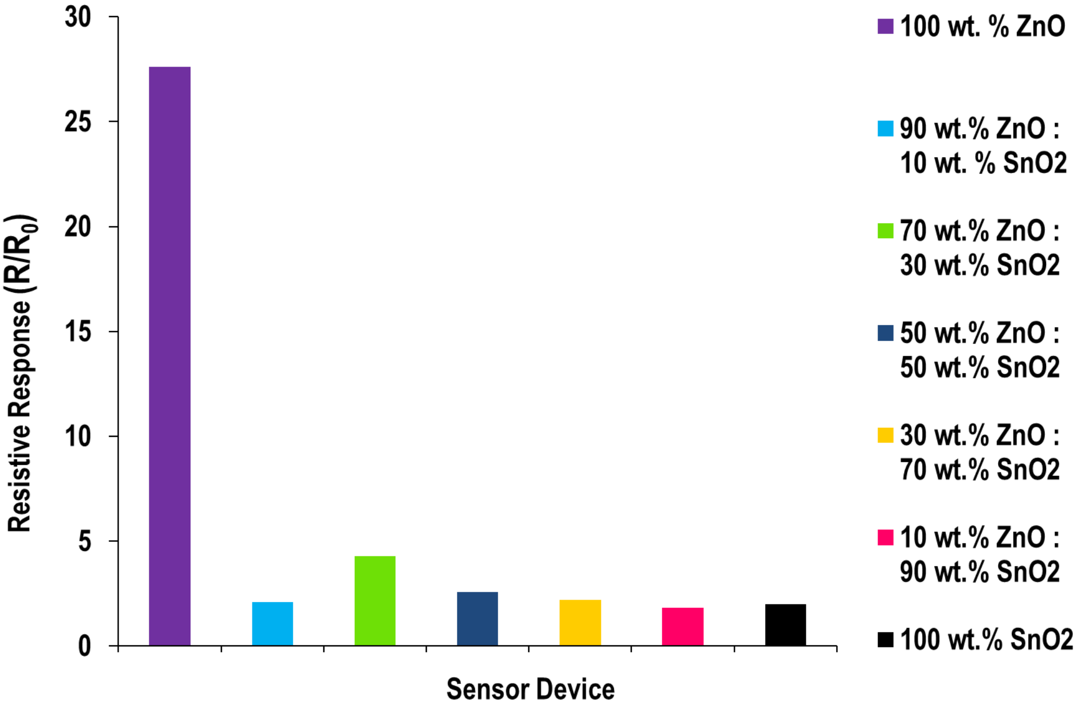

Figure 4–16. Resistive response bar graph of SnO_2-ZnO system towards 400 ppb NO_2 gas, at an operating temperature of 300 °C.

The resistive response of the system towards 400 ppb NO_2 at 300 °C in Figure 4–16 is presented in more detail in Figure 4–16. Figure 4–16 shows that the pure ZnO sensor device exhibited the best performance even at this lower concentration of exposure, with a response magnitude of 26.8. The 70 wt.% ZnO – 30 wt.% SnO_2 device was observed to be the best performing composite material attributed to a response of 3.5, however the discriminatory behaviour between all the other sensor devices within the system was poor. The response magnitudes of the 50 wt.% ZnO – 50 wt.% SnO_2, 30 wt.% ZnO – 70 wt.% SnO_2, 10 wt.% ZnO – 90 wt.% SnO_2 and 100 wt.% SnO_2 decreased consecutively as a function of decreasing ZnO concentration, showing that the response at this concentration, were mainly dominated by increasing concentration of ZnO or decreasing concentration of SnO_2.

The response traces of the system against 100 ppb at 300 °C that was too shallow to observe in Figure 4–15 and has been projected in Figure 4–17.

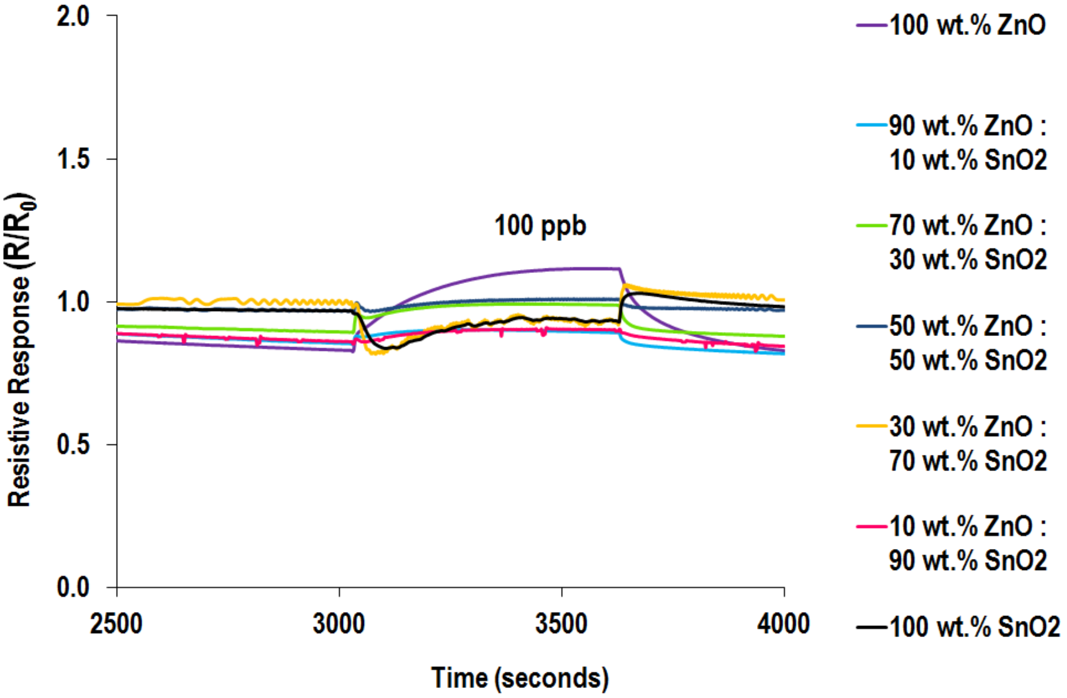

Figure 4–17. Resistive (and Conductive) response traces of SnO_2-ZnO system towards 100 ppb NO_2 gas, at an operating temperature of 300 °C.

The figure shows that the response of the system of sensor devices, towards this concentration of NO_2 was negligible, however did present some interesting features. The 100 wt.% ZnO, 90 wt.% ZnO – 10 wt.% SnO_2, 70 wt.% ZnO – 30 wt.% SnO_2, 50 wt.% ZnO – 50 wt.% SnO_2 and 10 wt.% ZnO – 90 wt.% SnO_2 devices were all attributed to an increase in resistive response, exhibiting n-type behaviour. However the 30 wt.% ZnO - 70 wt.% SnO_2 and 100 wt.% SnO_2 devices in contrast, exhibited a decrease in the resistive response (or increase in conductive response), which was unconventional for an n-type material. In this case, it is likely that the p-type behaviour of both devices towards NO_2 was associated to oxygen-induced band bending as the p-type behaviour was only observed towards the lowest concentration of NO_2 [271]. The presence of defects that cause fundamental changes to the electronic structure and properties of the materials, may also be responsible for the p-type behaviour of n-type materials [271]. Examples of defects are for example the surface oxygen species which exist as interstitial oxygen ions. In such a case the hole density (associated to the holes corresponding to the interstitial oxygen ions) would dominate the electron density at the surface of the metal oxide [271]. However the formation of interstitial oxygen ions would need to be induced by high-energy irradiation. Further, such species would also promote the p-type behaviour at higher concentrations of NO_2

exposure, which was not observed here. Another contributory factor for the unconventional response may have been the reduced ratio of NO$_2$ molecules:surface oxygen species may have also promoted an inverse behaviour of the metal oxide. Kida *et al*. [272] reported that the resistance change of a material, when exposed to NO$_2$, is dependent on the NO$_2$ concentration. Further, they reported that during NO$_2$ sensing, O$_2$ adsorption reactions compete with NO$_2$ adsorption reactions to extract electrons from the oxide surface. If the NO$_2$ adsorbs more strongly to the oxide surface than the O$_2$, then the electrical resistance of the material is seen to increase. Thus the resistance decrease at 200 ppb, suggests that the O$_2$ adsorption as likely to have been more competitive than NO$_2$ adsorption, due to a higher O$_2$ partial pressure, leading to an observed decrease in the resistance of the material. The higher concentration of 400 ppb NO$_2$, is likely to have increased the ratio of NO$_2$ molecules:surface oxygen species, switching the behaviour of the n-type materials back to normal.

Figure 4–18 presents the resistive response of the system of sensors towards 800 ppb NO$_2$, as a function of increasing operating temperature. The figure established that the pure ZnO sensor dominated the response at all operating temperatures and that the response magnitudes of the rest of the system, decreased as a function of decreasing concentration of ZnO at all operational temperatures. Further the figure illustrates that the response of the sensor devices decreases as a function of increasing operating temperature with the optimal response of the sensors at 300 °C.

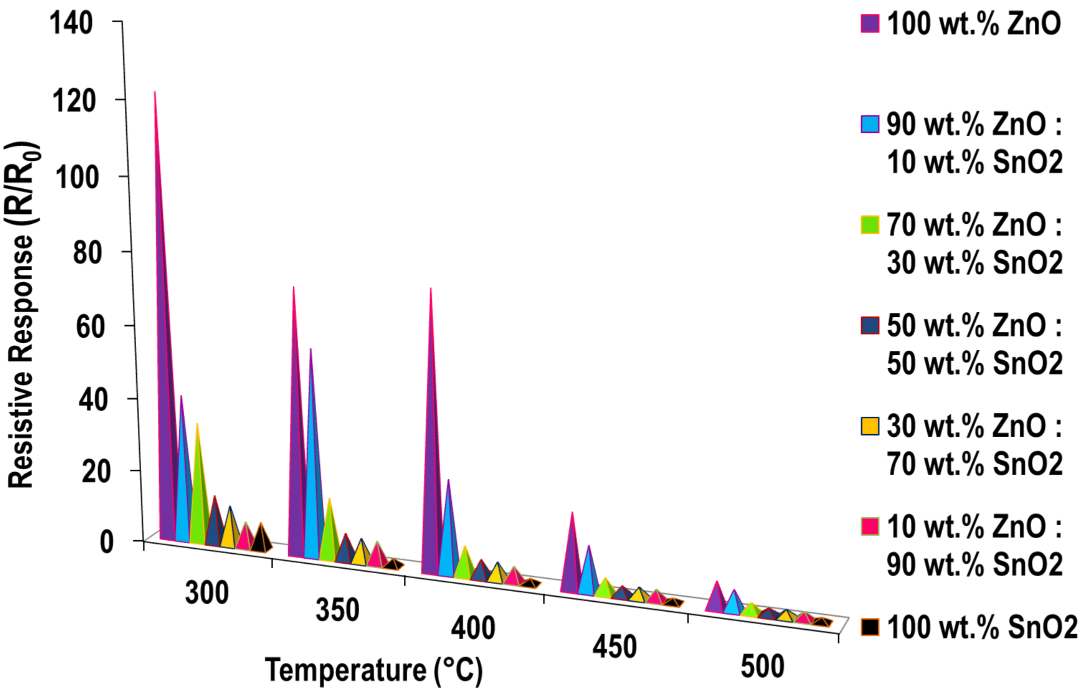

Figure 4–18. Resistive responses of SnO$_2$-ZnO system towards 800 ppb NO$_2$ gas as a function of increasing operating temperature.

The application of SnO_2 and ZnO composites for NO_2 detection has been reported in the literature. Park *et al.* [251] had reported on a hybrid SnO_2-ZnO nanofibre based highly sensitive NO_2 sensor, which was prepared via electrospinning and pulsed laser deposition methods. Specifically the nanofibre contained a ZnO nanofibre core which was enveloped by a SnO_2 shell layer. The sensor was reported to exhibit a relatively high response at working temperatures between 180 °C – 200 °C towards a concentration of 3.2 ppm NO_2, with the highest resistive response observed of 100 at 180 °C. Further, when the sensor was held constant at an operating temperature of 200 °C and exposed to increasing concentrations of NO_2 from 400 ppb to 4 ppm, the resistive response of the hybrid sensor was observed to increase from 6 to 105. In stark contrast, the pure ZnO nanofibre counterpart was seen to exhibit a response of less than 1.15 against all concentrations of NO_2 at the same operating temperature. The group had attributed the enhanced response of the hybrid sensor to two potential factors. The first was the incorporation of the small SnO_2 crystallites which provided extra adsorption sites, due to the hetero-junction nature of the material and therefore facilitated the surface reactions. The second was the ability of charge transfer to take place easily between both metal oxides due to the similarity in their work-functions, which made the interface barrier very low and therefore charge transfer a facile process. They suggested that the facile electronic interaction between the SnO_2 and ZnO contributed to the enhancement, as the number of individual surface reactions were proportional to the number of available electrons. This justification as a factor of enhancement is contradictory to theories presented in the literature [170, 171]. According to the group, the hetero-junction enhancement effects are due to the facile charge transfer between the hetero-interfaces, which suggests that the energy barrier for Fermi level equilibration is reduced, resulting in a decrease in the energy barrier for the local exchange of charge carriers across both semiconductors. However, in such a case, the effective energy barrier and resistance at the junction is decreased, which acts to weaken the overall junction effect and as such, the group have wrongly argued the hetero-junction enhancement effect.

Song *et al*. [93] whose report was alluded to earlier in the Chapter, had reported that their nanofibre sensor prepared with the molar ratio of the precursor sols of Zn:Sn of 2:1, which exhibited a response of 19 towards 100 ppm ethanol, only showed a response of 1 towards 100 ppm NO_2, demonstrating the poor NO_2 response properties of the mixed oxide sensor. Interestingly, the nanofibres prepared in this literature study were composites of SnO_2 and ZnO analogous to the experimental study in this thesis, and unlike those prepared by Park *et al*. [251], who had reported more core-shell type structures. This suggests that the packing structure of the metal oxides with respect to each other, can significantly influence the responsivity and selectivity towards particular analytes, and that those packing structures containing composites of both SnO_2 and ZnO are better suited for VOC detection.

In another study, Xu *et al*. [273] reported on the NO_2 gas sensing properties of SnO_2 – ZnO porous nano-solids by a solvo-thermal hot-press (SHP) method. They reported that a porous nano-solid is an intermediate state between nanoparticles and dense nano-ceramics and contains interconnected SnO_2 and ZnO nanoparticles which form a framework with numerous pores. When exposed to 35 ppm NO_2, the composites were seen to exhibit enhanced responses compared to the pure SnO_2 porous nanosolid counterpart. The best response of 75 was observed at 225 °C by a composite sensor containing SnO_2 loaded with 20 wt.% ZnO, which was a 1.7-fold enhanced response with respect to a pure SnO_2 sensor which showed a response of 45. The group however did not report the responses of the composite materials, with respect to a pure ZnO counterpart. In contrast to the SnO_2-ZnO composites reported in this thesis and in the literature by Song *et al*. [93], the composites prepared by Xu *et al*. [273] did exhibit high responsivities towards NO_2. Interestingly, when the same composite (SnO_2 loaded with 20 wt.% ZnO) was coated with polyaniline, forming a n-p hetero-junction based sensor, the resistive response towards 35 ppm NO_2, increased to a maximum of 375, at an operating temperature of 180 °C. The enhancement was thought to be associated to optimal microstructure of the SnO_2 loaded with 20 wt.% ZnO and aniline composite as well as hetero-junction enhancement effects. The SnO_2-ZnO-polyaniline based sensing material was also reported to exhibit selectivity towards NO_2, with minimal response towards ethanol.

The literature examples illustrate the variation of responses and selectivities and complexities of the enhancement processes achieved against NO_2 (and ethanol) from a host of SnO_2-ZnO based mixed oxide systems.

4.2.6 Further Gas Sensing Studies

Further gas sensing studies of the SnO_2 – ZnO system were conducted towards a range of reducing gases: acetone, CO and NH_3 at an operating temperature of 300 °C. This was the temperature at which most sensors in the system performed optimally against the key reducing gas: ethanol, as seen in Figure 4–13. These studies were conducted to assess the response and selectivity of the system towards reducing vapours including ethanol, which was evaluated earlier in the Chapter.

Focus was on testing the system against various concentrations of acetone and CO, as the system proved to be poor at responding towards NH_3 as observed in Figure 4–19.

4.2.6.1 NH_3 Sensing

The response results of the system against 20 ppm NH_3, which was the largest concentration the system was exposed to, have been presented in Figure 4–19. Tabulation of the mean responses values of the sensor devices in the SnO_2-ZnO system from the repeat tests against exposure towards 20 ppm NH_3 at 300 °C and the associated 95% confidence intervals have been presented in Table 4–2.

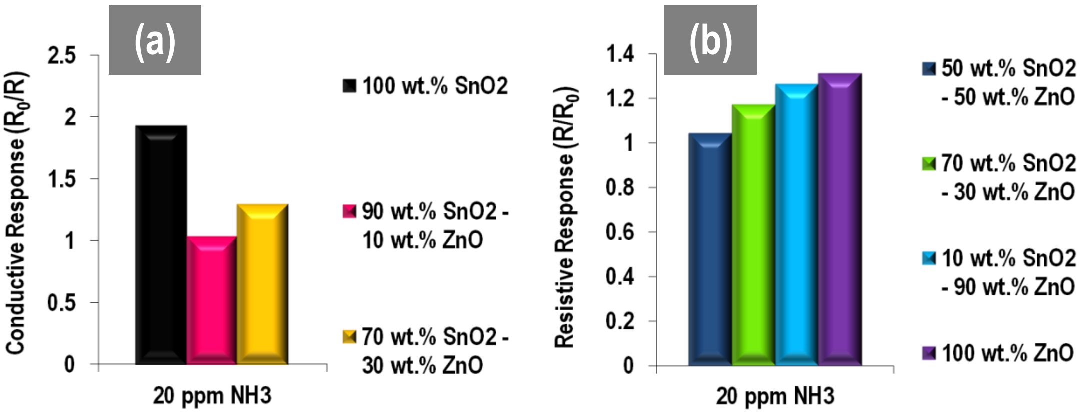

Figure 4–19. (a) Conductive responses and (b) Resistive responses of the SnO_2-ZnO system against 20 ppm NH_3 at an operating temperature of 300 °C.

Table 4–3. Average responses of sensor devices in SnO_2-ZnO system from all repeat tests against 20 ppm NH_3 300 °C and associated errors in the form of 95% CIs.

	20 ppm	
Device	Average Response	95% CI
100 wt.% SnO_2	1.89	±0.08
90 wt.% SnO_2 – 10 wt.% ZnO	1.1	±0.12
70 wt.% SnO_2 – 30 wt.% ZnO	1.35	±0.11
50 wt.% SnO_2 – 50 wt.% ZnO	1.03	±0.02
30 wt.% SnO_2 – 70 wt.% ZnO	1.18	±0.02
10 wt.% SnO_2 – 90 wt.% ZnO	1.29	±0.06
100 wt.% ZnO	1.35	±0.08

Most of the sensors in the system were attributed to responses close to the baseline response of 1, with only the pure SnO_2 showing a response of 2. Interestingly, the SnO_2, 90 wt.% SnO_2 – 10 wt.% ZnO and 70 wt.% SnO_2 – 30 wt.% ZnO sensor devices were seen to be attributed to conventional n-type response characteristics against the analyte, however all other n-type devices, which had a significant contribution of ZnO, were attributed to unconventional p-type response behaviour. Such resistive response of n-type materials against NH_3, was observed in Chapter 3 with the WO_3-ZnO composite system and has been reported in the literature due to the NH_3 under-going oxidation reactions on the surface of metal oxides [114, 115]. The reaction process can follow one of many routes, allowing several possible competing processes to all take place at the same time. These reactions of NH_3 molecules upon the surface of a semiconducting metal oxide, have been alluded to in Chapter 1, section 1.10.3.

4.2.6.2 Acetone Sensing

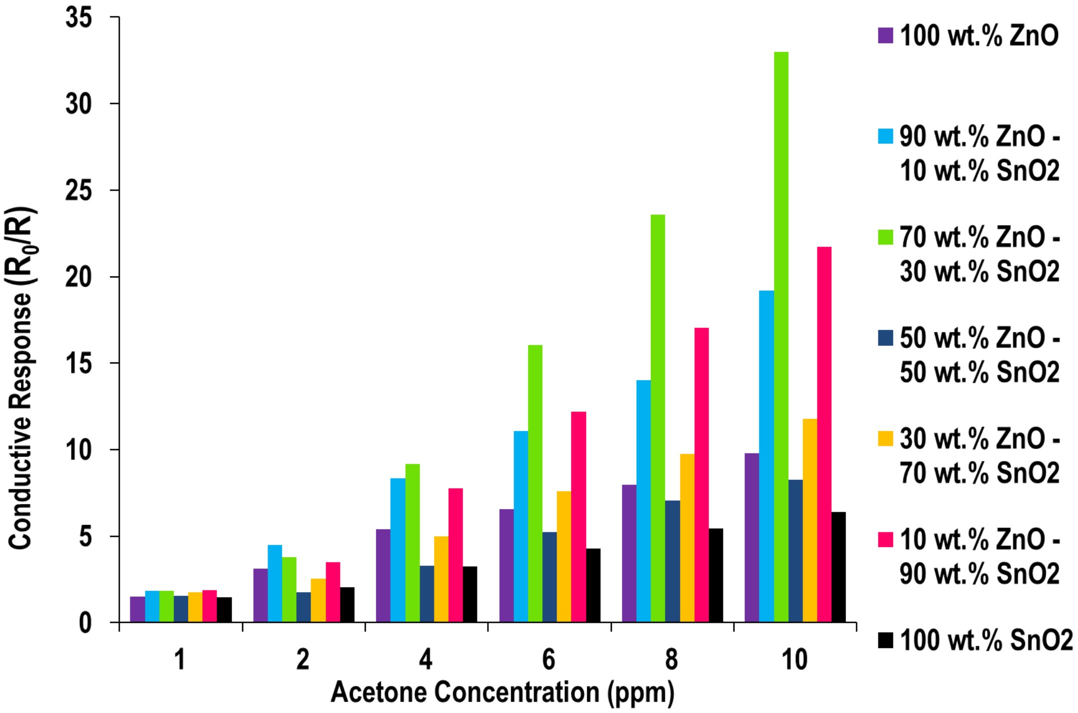

Figure 4–20. Conductive responses of SnO_2-ZnO system towards 1, 2, 4, 6, 8 and 10 ppm acetone gas, at an operating temperature of 300 °C.

Figure 4–20 presents the conductive responses of the system of sensor devices against increasing concentrations of acetone gas at an operating temperature of 300 °C. Tabulation of the mean responses values of the sensor devices in the SnO_2-ZnO system from the repeat tests against exposure towards various acetone concentrations at 300 °C and the associated 95% confidence intervals have been presented in Table 4–4. The graph shows that the sensors were responsive to a concentration as low as 1 ppm acetone. As the concentration of acetone exposure was increased, the graphs show that the response of the system randomises. This randomisation is in terms of response order of the devices, with respect to each other. The 70 wt.% ZnO - 30 wt.% SnO_2 sensor was the best performing composite sensor device of the system, with the best response of 32.9 towards 10 ppm of the analyte. This was a 5.5-fold enhanced response with respect to the pure SnO_2 counterpart (which exhibited a response of 6.4) and a 3.3-fold enhanced response compared the pure ZnO counterpart (which exhibited a response of 9.8) at the same analyte concentration of 10 ppm. The particularly enhanced response of this composite, against the poor response of both the individual metal oxides is suggestive of synergistic and hetero-junction effects playing a role to enhance the response characteristics. Comparison of Figure 4–20 with respect to an exposure of 10 ppm of ethanol at the same operating temperature, observed in Figure 4–7, shows the system of SnO_2-ZnO sensor devices were more selective towards 10 ppm acetone. Comparison of the response values and 95% CIs of the devices towards 10 ppm ethanol at 300 °C as seen in Table 4–1 and towards 10 ppm acetone at 300 °C as seen in Table 4–4, show that the response and errors do not overlap, and as such the selectivity is demonstrated.

Table 4–4. Average conductive responses of sensor devices in SnO_2-ZnO system from all repeat tests against 1, 2, 4, 6, 8 and 10 ppm acetone at 300 °C and associated errors in the form of 95% CIs.

	1 ppm		**2 ppm**		**4 ppm**		**6 ppm**		**8 ppm**		**10 ppm**	
Device	Average Response	95% CI	Average Response	95% CI	Average Response	95% CI	Average Response	95% CI	Average Response	95% CI	Average Response	95% CI
100 wt.% SnO_2	1.34	±0.08	1.29	±0.50	2.30	±0.63	3.22	±0.72	4.15	±0.86	5.03	±0.94
90 wt.% SnO_2 – 10 wt.% ZnO	1.38	±0.33	1.96	±1.02	4.79	±1.97	8.04	±2.80	11.32	±3.91	14.19	±5.17
70 wt.% SnO_2 – 30 wt.% ZnO	1.29	±0.31	1.47	±0.71	3.14	±1.23	5.08	±1.70	6.77	±2.07	7.81	±2.77
50 wt.% SnO_2 – 50 wt.% ZnO	1.21	±0.22	1.02	±0.50	2.35	±0.65	3.95	±0.88	5.36	±1.19	6.02	±1.56
30 wt.% SnO_2 – 70 wt.% ZnO	1.52	±0.22	2.35	±0.98	6.20	±2.09	11.36	±3.56	16.59	±5.57	21.63	±9.37
10 wt.% SnO_2 – 90 wt.% ZnO	1.62	±0.26	2.90	±1.27	5.77	±2.13	8.07	±2.64	10.34	±3.27	13.23	±5.10
100 wt.% ZnO	1.41	±0.16	1.76	±0.98	3.23	±1.62	4.28	±1.85	5.21	±2.23	6.49	±2.85

The highest response observed against 10 ppm ethanol was 2.1 by the 10 wt.% ZnO - 90 wt.% SnO_2 sensor device. Thus of the two VOCs, the system can be established as being selective towards acetone. In particular, the conductive response of the 70 wt.% ZnO - 30 wt.% SnO_2 composite is seen to increase exponentially as a function of increasing acetone concentration, which suggests that the surface of the composite remains unsaturated upon each exposure concentration introduced. In contrast, the conductive response magnitudes of the pure metal oxides, in particular the SnO_2 material, are seen to increase gradually and slowly as a function of increasing acetone concentration, which indicates the saturation of the surfaces as a function of the increased concentration. A similar behaviour of the devices was observed as a function of increasing ethanol concentration, and can be accounted for by the increased number of reaction sites in the composite materials, due to the presence of the hetero-contacts in the composite materials.

In a study by Kim *et al*. [248] who had reported on the selective detection of ethanol using SnO_2–ZnO thin film gas sensors prepared by combinatorial solution deposition, the group had reported that special attention was paid towards the discrimination of their sensors towards ethanol and acetone, due to the similar chemical natures of both gases. The nature of the reported sensor fabrication involved repetitive combinatorial drop coating of sols of both metal oxides followed by subsequent drying a number of times, and then finally heat-treatment of the sensor device at 600 °C, to form the SnO_2-ZnO thin film sensor. A film that contained equal volume (870 µl) of each of the SnO_2 and ZnO sol i.e. a 50 % - 50 % sensor, was seen to exhibit a response of 4.69 towards 200 ppm ethanol and 2.30 towards 200 ppm acetone, at an operating temperature of 300 °C and hence there composite exhibited selectivity towards ethanol (exhibiting a response that was double that of acetone). In general, they had found that other composites they had formed; 75 % - 25 % SnO_2-ZnO and 25 % - 75 % SnO_2-ZnO, also exhibited selectivity towards ethanol, exhibiting response magnitudes which were twice that of acetone. This selectivity remained at operating temperatures of 250 °C and 300 °C, but began to fail at 400 °C where the response magnitude towards both analytes was indistinguishable. Comparatively, the SnO_2-ZnO composites investigated in this thesis, are better than those reported by Kim *et al*. in terms of response performance, with the ability to exhibit larger responses towards concentrations of acetone which are 1/20 or less than those reported by Kim *et al*. and concentrations of ethanol which are ½ of or less than those reported by Kim *et al*.

Kim *et al*. [248] reported that the gas sensing behaviour of MOS sensors in other works published in the literature, had usually achieved similar responses between ethanol and acetone, regardless of the metal oxide used but that discrimination between both analytes was necessary for applications requiring precise and reliable screening of intoxicated drivers and patients suffering from diabetes [248]. In particular the SnO_2-ZnO composites investigated experimentally for this thesis, are particularly useful for the second application as the breath of a diabetic patient can contain acetone vapour [248, 274], with the concentrations of the analyte being as high as 300 ppm for those suffering from a diabetic coma [248, 275]. Thus the low detection limit of the sensor devices demonstrated here, are potentially useful for such applications.

4.2.6.3 CO Sensing

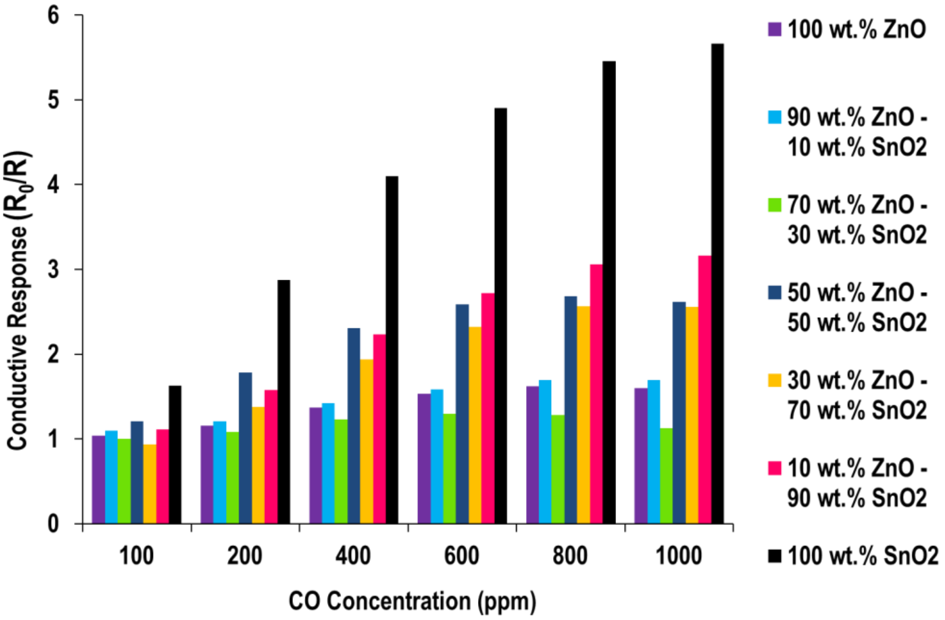

Figure 4–21. Conductive responses of SnO_2-ZnO system towards 100, 200, 400, 600, 800 and 1000 ppm CO gas, at an operating temperature of 300 °C.

Figure 4–21 presents the conductive responses of the system of SnO_2–ZnO sensor devices against increasing concentrations of CO at an operating temperature of 300 °C. Tabulation of the mean responses values of the sensor devices in the SnO_2-ZnO system from the repeat tests against exposure towards the various CO concentrations at 300 °C and the associated 95% confidence intervals have been presented in Table 4–5.

Table 4–5. Average conductive responses of sensor devices in SnO_2-ZnO system from all repeat tests against 100, 200, 400, 600, 800 and 1000 ppm CO at 300 °C and associated errors in the form of 95% CIs.

	100 ppm		**200 ppm**		**400 ppm**		**600 ppm**		**800 ppm**		**1000 ppm**	
Device	Average Response	95% CI	Average Response	95% CI	Average Response	95% CI	Average Response	95% CI	Average Response	95% CI	Average Response	95% CI
100 wt.% SnO_2	1.67	±0.07	2.86	±0.05	4.02	±0.16	4.82	±0.16	5.32	±0.28	5.58	±0.17
90 wt.% SnO_2 – 10 wt.% ZnO	1.09	±0.05	1.48	±0.20	1.94	±0.57	2.31	±0.80	2.55	±1.01	2.62	±1.07
70 wt.% SnO_2 – 30 wt.% ZnO	0.97	±0.07	1.30	±0.16	1.69	±0.48	1.96	±0.72	2.12	±0.88	2.09	±0.92
50 wt.% SnO_2 – 50 wt.% ZnO	1.17	±0.09	1.61	±0.34	2.02	±0.58	2.23	±0.71	2.31	±0.75	2.20	±0.82
30 wt.% SnO_2 – 70 wt.% ZnO	1.01	±0.02	1.08	±0.01	1.20	±0.06	1.25	±0.09	1.26	±0.05	1.15	±0.03
10 wt.% SnO_2 – 90 wt.% ZnO	1.09	±0.00	1.22	±0.01	1.38	±0.08	0.99	±1.17	1.60	±0.18	1.68	±0.05
100 wt.% ZnO	1.05	±0.01	1.18	±0.03	1.35	±0.04	1.48	±0.10	1.51	±0.22	1.57	±0.06

The graph illustrates that the pure SnO_2 sensor was associated to the best response behaviour of all sensor devices with a maximum response of 5.7 observed against 1000 ppm CO. The pure ZnO sensor in contrast was associated to a response of 1.6 towards the same concentration of CO. In general the response graph shows that the response of the sensors increased as a function of increasing concentration of SnO_2 and decreasing concentration of ZnO, which is analogous to the behaviour observed against NO_2, however for the oxidising gas the trend was observed to be an increase in resistive response as a function of increasing concentration of ZnO and decreasing concentration of SnO_2. Thus the response trend observed against CO was observed to be dominated by the presence of SnO_2.

With respect to ethanol and acetone responsivities, Figure 4–21 confirms that the responses towards CO were poor and that selectivity of the system is towards acetone. Further a difference in the variable contributing to the enhanced responses was visible between all three reducing analytes, with greater synergistic catalysis and hetero-junction enhancement effects contributing to the extensive response of the composite materials towards both ethanol and acetone, and in contrast dominance of the SnO_2 metal oxide concentration, contributing towards the responsivities observed against CO.

Some studies in the literature have been reported on the SnO_2-ZnO sensing properties of CO. One such study was by Haeng Yu *et al*. [92] mentioned earlier. In their study, they had formed pellets containing mixtures of ZnO and SnO_2, with each pellet containing different mol % concentrations of ZnO and SnO_2. Upon exposure to 200 ppm of the analyte, the composite materials were attributed to enhanced responsivities with respect to the pure ZnO and SnO_2 counterparts. In particular, the enhancement effect of those composites which contained a significant contribution of both SnO_2 and ZnO metal oxides, was reported to be associated to the heterogeneous interfaces that existed between the ZnO and SnO_2 phases. The materials that were associated to increasing ZnO concentration into the SnO_2 matrix (specifically 20 mol % – 60 mol % ZnO), were reported to be associated to a significant number of SnO_2 / ZnO grain boundaries, which were reported to contribute to the enhancement in gas response properties. The responsivities of the ZnO dominated composites were also seen to increase with the addition of SnO_2 and this was attributed to the promotion of a greater porosity, through the reduction in the ZnO grain size, through the addition of SnO_2. Composites rich in SnO_2 were seen to exhibit some of the highest responses with respect to other composites in the system, which is analogous to what was observed in this thesis, and this was promoted by the ZnO dissolution into the SnO_2 matrix.

In another study by Yue *et al*. [276] ZnO-SnO_2 composite nanofibres were fabricated by an electrospinning method and tested against CO. The group has observed that all composites which varied by wt.% loading of ZnO into the SnO_2 (0 wt.% , 0.5 wt.%, 1.0 wt.% and 1.5 wt.%), when tested against 100 ppm CO, exhibited enhanced gas sensing properties in comparison to the pure SnO_2 counterpart, which exhibited a response of 1 (baseline response). In particular, the 1 wt.% ZnO-SnO_2 composite was seen to exhibit the highest response of 16 at an operating temperature of 360 °C, which was a 16-fold enhancement with respect to the pure SnO_2 counterpart. Interestingly, the group had tested the composite materials against a range of other gases, which included ethanol and acetone, at a concentration of 100 ppm, at an operating temperature of 360 °C. The composites exhibited very low responsivities against both VOCs, with prominent selectivity towards CO, which was a stark contrast to the observations made with the SnO_2-ZnO composite system in this thesis. The enhanced responsivities of the composite materials against CO were reported by Yue *et al*. to be promoted by an increased number of surface sites in the hybrid structure as well as the presence of ZnO-SnO_2 hetero-junctions.

These literature studies exemplify the range of fabrication methods of hybrid metal oxide sensor materials based on ZnO and SnO_2 and also justify the complexity of deducing the enhancement effects upon their application for the detection of CO.

4.3 Summary and Conclusions

Table 4–6 summarises the responsivities of the SnO_2-ZnO sensor system against ethanol, NO_2, acetone and CO at 300°C. Where device responses were below 1.5, associated cells have been block filled.

Table 4–6. Response magnitudes of sensor devices within SnO_2-ZnO composite system against various concentrations of ethanol, NO_2, acetone, and CO gas at 300 °C (the associated optimal operating temperature). Where device responses were observed to be below 1.5, associated cells have been block filled.

	100 Z	90 Z–10 S	70 Z–30 S	50 Z–50 S	30 Z–70 S	10 Z–90 S	100 S
Ethanol (300 °C)							
10 ppm	1.8	1.9	2.1	1.5	2.0	2.1	1.8
20 ppm	2.7	5.1	9.1	5.1	7.5	8.3	4.2
40 ppm	4.3	9.7	26.5	21.7	23.9	27.5	9.9
80 ppm	7.2	16.3	60.9	76.0	74.8	66.6	20.5
100 ppm	8.9	19.6	80.5	109.0	103.5	85.1	24.4
NO_2 (300 °C)							
200 ppb	6.0	■	■	■	■	■	■
400 ppb	26.8	■	3.5	1.6	■	■	■
800 ppb	120.8	39.5	32.5	12.6	10.2	6.5	6.6
Acetone (300 °C)							
1 ppm	1.5	1.8	1.8	1.5	1.8	1.9	1.5
2 ppm	3.1	4.5	3.8	1.8	2.5	3.5	2.1
4 ppm	5.4	8.3	9.2	3.3	5.0	7.8	3.3
6 ppm	6.6	11.1	16.0	5.2	7.6	12.2	4.3
8 ppm	8.0	14.0	23.6	7.1	9.6	17.0	5.5
10 ppm	9.8	19.2	33.0	8.3	11.8	21.7	6.4
CO (300 °C)							
100 ppm	■	■	■	■	■	■	1.6
200 ppm	■	1.2	■	1.8	■	1.6	2.9
400 ppm	■	1.4	■	2.3	1.9	2.2	4.1
600 ppm	1.5	1.6	■	2.6	2.3	2.7	4.9
800 ppm	1.6	1.7	■	2.7	2.6	3.1	5.5
1000 ppm	1.6	1.7	■	2.6	2.6	3.2	5.7

Key:

100Z – 100 wt.% ZnO

90Z – 10S – 90 wt.% ZnO – 10 wt.% SnO_2

70Z – 30S – 70 wt.% ZnO – 30 wt.% SnO_2

50Z – 50S – 50 wt.% ZnO – 50 wt.% SnO_2

30Z – 70S – 30 wt.% ZnO – 70 wt.% SnO_2

10Z – 90S – 10 wt.% ZnO – 90 wt.% SnO_2

100S – 100 wt.% SnO_2

Results and analysis from this study showed that the system of SnO_2 – ZnO composite sensors were most effective for the detection of both ethanol and acetone. In particular, the composite materials were seen to exhibit significantly better response behaviours than the pure counterparts towards both analytes.

The best performing composite towards ethanol was seen to be the 50 wt.% ZnO-50 wt.% SnO_2 sensor device at 300 °C with a response of 109 towards 100 ppm of the analyte. The 70 wt.% ZnO-30 wt.% SnO_2 sensor device was the best candidate for acetone sensing, with the largest observed response of 33 towards 10 ppm of the analyte at 300 °C.

Comparison of the responsivities of the SnO_2–ZnO system towards 10 ppm acetone and 10 ppm ethanol indicated that if the system were put in a mixed atmosphere of 10 ppm of both analytes, it could potentially discriminate between ethanol and acetone, and exhibit selectivity towards acetone. These results thus showed that a simple change in the concentration of the individual metal oxides within the composites, could tune the responsivity and selectivity of the devices towards a particular analyte, specifically a VOC based analyte.

In contrast to the extensive responsivities of the composite materials towards both VOCs, the combination of both metal oxides did not prove successful in the detection of NO_2 or CO, with the responsivities increasing in order of increasing ZnO concentration for the former analyte, and increasing in order of increasing SnO_2 concentration for the latter analyte. This behaviour may be accounted by the better responsivity of SnO_2 towards CO, but poor responsivity towards NO_2 and vice versa for ZnO. Thus the response towards both NO_2 and CO were seen to be dominated by the concentration composition of each metal oxide.

The enhanced responsivities of the composite materials towards both the VOCs, with respect to the pure counterparts was difficult to pin point. However, the synergy of both metal oxides as oxidation combustion catalysts for both VOCs is likely to be the prime reason for their effective performance. In particular this was reasoned because the combination of both metal oxides showed no enhancements effects upon exposure to NO_2 and CO, but only towards ethanol and acetone. The influence of the hetero-junction enhancement effects that existed due to the chemical as well particle size inhomogeneity of both metal oxide materials was thought to be a supporting response enhancement factor. Evidence of an electronic interaction between the SnO_2 – ZnO composites was not evident from XPS, however, the steep increase in response amplitudes of the composite sensors, particularly towards ethanol (at the optimal operating temperature), with respect to the pure counterparts, suggested electronic effects may have played a contributory role, to enhance the response by such significant amplitudes.

Error analysis of the mean response values throughout the study showed that in general, responses between the repeat tests were repeatable. This was particularly apparent at exposures towards low concentrations of all analytes and with materials which were either pure or biased by the wt.% of either of the metal oxides. Further, lower error magnitudes were observed towards NO_2, CO and NH_3 in comparison to the higher concentrations of ethanol and acetone, towards which the devices were attributed to significant error. In particular, exposure towards 100 ppm ethanol resulted in for example, the 90 wt.% SnO_2 – 10 wt.% ZnO, the 70 wt.% SnO_2 – 30 wt.% ZnO and the 30 wt.% SnO_2 –70 wt.% ZnO sensor devices being attributed to an error of ±14.7, ±10.9 and ±9.4, respectively. These devices were three of the best performing devices towards the analyte. In a similar way, all three devices were attributed to errors of ±5.2, ±2.8 and ±9.4 respectively towards 10 ppm acetone, of which the last device had the largest response. The trends of the error values showed that the two analytes towards which the group of sensors were most responsive towards i.e. ethanol and acetone were associated to the largest errors. This suggested the possibility of several surface by-products forming or additional reactions occurring on the surface of the metal oxide device, promoting interference of the response magnitudes. The behaviour also suggested potential instability of these composite devices. In contrast, towards the lower concentrations of ethanol and acetone and towards all exposed concentrations of NO_2, CO and NH_3, the devices showed lower responsivities and also lower error magnitudes, suggesting that the formation of interfering by-products or additional reactions occurring on the surface was lowered, due to the lowered concentrations of exposure or due to lack of reactivity. The error values suggest that comparative responsivity and selectivity between the best performing composite materials was difficult to conclude, due to the overlap of error ranges - this was particularly apparent towards larger concentrations of ethanol exposure at 80 and 100 ppm and larger concentration of acetone exposure at 8 ppm and 10 ppm. However, the enhanced response of these composites with respect to the pure counterparts was evident, as well as the selectivity of the individual gas sensor device towards a particular analyte e.g. selectivity towards acetone when put in mixed atmosphere of acetone and ethanol. A more detailed discussion of error sources has been presented in Chapter 7, section 7.1.2.

Chapter 5 : CTO-ZnO based p-n hetero-junction system

In the previous two Chapters, investigations of the materials and gas sensing properties of two n-n hetero-junction composite systems were presented. This Chapter continues on the theme of hetero-junction systems for metal oxide semiconductor (MOS) based gas sensing, however presents a study of the materials and gas sensing properties of a p-n hetero-junction composite system based on CTO, with specific stoichiometry $Cr_{1.95}Ti_{0.05}O_3$*, and ZnO i.e. CTO-ZnO composites.*

5.1 Introduction

The development of chemiresistor sensors based on p-type semiconducting metal oxides such as NiO [277], CuO [278, 279], Cr_2O_3 [210, 280], CTO [47, 48] and Co_3O_4 [169, 281], has been relatively low key and is still at a nascent stage [46]. In contrast, the development of chemiresistor sensors based on n-type semiconducting oxides such as SnO_2, WO_3, ZnO and In_2O_3, have been at the forefront of MOS sensor technology, with novel strategies being developed to better their performance, and research and development being conducted for their use in new applications [46].

This distinction between the popularity of both p- and n- type semiconducting metal oxides comes down fundamentally to their response characteristics, where the former is associated to significantly poor response magnitudes than the latter [46, 278, 282, 283]. Pokhrel *et al*. [282] and Hubner *et al*. [278] had justified this phenomenon based on Cr_2O_3 and CuO conduction models respectively, which they reported could be valid for all p-type semiconducting metal oxide materials used as gas sensing materials [278, 282, 283].

They have reported that the lower response signals of p-type MOS gas sensors, are accounted by the fact that the resistance of the electron depletion layer (EDL) does not dominate the overall resistance of the p-type semiconductor, as it does with n-type semiconducting oxides [278, 282, 283]. Instead for p-type semiconductors, as described in Chapter 1, conduction through the hole accumulation layer (HAL) dominates the overall sensing layer resistance [46, 278]. When an oxidation reaction occurs between a reducing gas e.g. CO and the surface adsorbed oxygen anionic species on the surface of a p-type semiconductor, the release of electrons from the oxidation reaction back into the material, will indeed decrease the concentration of holes in the hole accumulation layer (HAL) and cause an increase in the resistance of the material [46]. However, this decrease in the concentration of holes occurs through electron-hole recombination reactions, in which the negative charges of the electrons cancel out the positive charges of the holes, leaving the resultant charge to be null [46, 278], which ultimately leads to insignificant change in the chemiresistivity of the p-type semiconductor (upon exposure to CO). Equation 5–1 and Equation 5–2 illustrate the electron-hole recombination reaction that occurs on the surface of a p-type material when exposed to CO [278], where O_2^{air} represents oxygen from the atmosphere, *S* an adsorption site on the surface of the metal oxide, O^- an anionic adsorbed oxygen species and *h*+, a hole in the HAL, generated through electron transfer to the surface-acceptor sites to stabilise adsorption of the oxygen ions [278, 284].

Equation 5–1
$$\tfrac{1}{2}O_2^{air} + S \leftrightarrow O_{(ad)}^{-} + h^{+}$$

Equation 5–2
$$CO + O_{(ad)}^{-} + h^{+} \rightarrow CO_2 + S$$

The extent of the contribution of the HAL towards the overall resistance change is dependent on its thickness relative to the size of the p-type particles. If the particle sizes are twice the size of the HAL, suggesting significant bulk contribution and minimised surface (i.e. HAL) contribution to the overall resistance change, then the chemiresistive change in the p-type material would be minimised further. This exemplifies how the microstructure of a p-type material can influence its overall responsivity.

Although conductivity through the HAL, poses a significant disadvantage to the overall responsivity of p-type materials toward the target analytes, one of the key advantages of this route of conduction, is the inherent resistance of the material, to humidity. When water interacts with a metal oxide surface, it is thought to split into OH^- and H^+ ions [12]. The OH^- ions are thought to introduce electrons to the surface of the metal oxide [12]. In the case of p-type materials, these electrons would be introduced into the HAL decreasing the concentration of holes through electron-hole recombination reactions, leaving the resultant charge to be null [46, 278], ultimately leading to insignificant change in the chemiresistivity of the p-type semiconductor (towards humidity). Further, the H^+ ions are also thought to react with surface oxygen anions, resulting in the same effect as the OH- ions on the p-type semiconducting device. In contrast, when in contact with an n-type material, the release of electrons in the EDL, will act to increase its conductivity [12, 285], making such materials very responsive to humidity and therefore unsuitable for applications where humidity is present. This exemplifies the importance of p-type semiconducting oxides for practical applications.

To find a solution to the low responsivity signals of p-type semiconducting oxides, a number of strategies are being developed to enhance their gas response properties, to be able to use them for practical applications. These strategies include tuning of the morphology of the nanostructures [46, 73] to enhance the surface contribution to overall conductivity of the p-type material, electronic sensitization of the p-type semiconducting oxides through doping [46, 286] or loading noble metals or metal oxides to chemically sensitize the p-type metal oxides [46, 72, 287].

Of the three key strategies, the approach taken in this thesis is the third one of chemical sensitisation of a p-type metal oxide by loading a second n-type metal oxide, through a composite approach, which extends the theme of hetero-junction based composite systems to a p-n combination of semiconducting metal oxides.

The study of p-n hetero-junction systems for gas sensing is one of emerging interest, enabling the possibility of increasing both the response and selectivity of the overall composite material [46]. A number of studies have been reported on such sensing systems such as CuO - ZnO [89, 288, 289], Cr_2O_3 – ZnO [290, 291], Cr_2O_3 – WO_3 [210] and Cr_2O_3 – Fe_2O_3 [292] among other p - n metal oxide combinations. The gas sensing enhancement of such systems has been attributed to a number of reasons, some which are specific to the combination of metal oxides used, and some more general associated to hetero-junction enhancement effects which were described in Chapter 1.

One example of such a system was recently published by Barrecca *et al*. [72] who had reported that a CuO - TiO_2 nanocomposite represents one of the most appealing p - n systems due to the synergistic combination of attractive properties of both metal oxides; the low band gap of p-type CuO and high reactivity of n-type TiO_2. Further the group reported that the hetero-junction existing between both materials is expected to produce an enhanced charge carrier life time, which would be an advantage to both the catalysis and sensing performance of the system. The group had specifically reported on CuO - TiO_2 nanocomposite and CuO –TiO_2 nanocomposite functionalised with Au nanoparticles systems, prepared by a combined route of CVD and RF sputtering. They had found their systems to be responsive to ethanol, hydrogen and ozone, with the former system showing a response of 50 at 200 ºC towards 300 ppb O_3 and a response of 1 at 200 ºC towards 100 ppm ethanol; and the latter system showing a response of 500 towards the same concentration of O_3 at 100 ºC and a response of about 3 towards 100 ppm ethanol at 200 ºC. Results suggested their systems were selective and responsive towards oxidising environments.

A more recent report on a p - n hetero-junction gas sensing system was published by Sun *et al*. [210] who had investigated several composites of p-type Cr_2O_3 and n-type WO_3 as a hetero-junction architecture where both metal oxides were placed adjacent to each other (like a p - n diode type junction). In their composite system, they varied the ratio of WO_3:Cr_2O_3 in weight % ratios of 1:1, 3:1, 9:1 and 11:1 wt.%. They evaluated the response properties of these composites against various concentrations of NO and CO diluted with 20% O_2 and 80% N_2. The 9:1 WO_3:Cr_2O_3 composite as an example, exhibited an increase in resistance towards a concentration of 20 ppm of NO, however exhibited almost no change in resistance (due to cancellation of conductivities of both metal oxides) towards the same concentration of CO. This suggested that putting them in a mixed atmosphere of NO and CO, would allow the sensors to be able to selectively discriminate towards NO. Evaluation of the sensing properties of the adjacent composite architectures of WO_3 and Cr_2O_3 was conducted by exposing the hetero-junction sensors towards a mixed atmosphere of ppb levels of NO mixed with varying ppm levels of CO. In a mixed atmosphere of 63 ppb NO with varying ppm levels of CO (3 - 20 ppm), the hetero-junction sensor was able to demonstrate responsivity and selectivity towards the 63 ppb of NO, whilst discriminating against the ppm levels of CO. The group had reported that the sensors exploited the different majority carriers (electrons and holes) of both metal oxides to develop responsivity and selectivity towards ppb levels of NO, which is usually at levels of less than 10 ppb in healthy humans, whilst discriminating against CO at ppm levels, which is a known toxic gas.

CO gas sensitivity was also reported by Yoon *et al.* [89], who had studied the application of a CuO - ZnO composite system for the detection of this analyte. They had found that a CuO - ZnO composite, which contained 10 mol% CuO doped with 1 at.% Al added to ZnO powder, displayed a resistive response of 12.2 at 180 ^{o}C, towards 200 ppm CO at 23% relative humidity. This was one of the largest responses the group observed from the range of CuO - ZnO composite sensors fabricated. The enhancement was associated to a number of factors. The first was the decreased density of the material due to the doping of Al, suggesting greater surface site accessibility of the analyte molecules with the matrix of sensing material. Al doping also increased the resistance of the CuO, which acted to increase the responsivity of the sample. Further, the large concentration of CuO was influential on reducing the optimal operating temperature of the sensor, which exemplified the ability to engineer an optimal concentration of the metal oxide within the composite, to tune its sensor performance. Finally, the sensitivity of the p-n grain boundary upon exposure to gas was also thought to contribute to the enhanced response performance, where the hetero-interfacial regions between the CuO - ZnO contacts dominated the resistive behaviour of the gas sensing material, compared with the homo-interfacial regions between the CuO - CuO contacts and the ZnO – ZnO contacts.

Reports in the literature show that the enhancement effects in p - n hetero-junction sensor devices are as complex as the n - n hetero-junction systems discussed in the previous two Chapters, and it is difficult to pin-point any one particular factor as solely influential on the enhanced responsivities observed.

In this investigation, an in-depth materials and gas sensing characterisation study on a p – n hetero-junction system based on CTO and ZnO composites has been presented. Based on literature searches, this is the first study done on this specific combination of metal oxides.

5.2 Results and Analysis

5.2.1 Verification of success of CTO synthesis

5.2.1.1 Scanning Electron Microscopy (SEM)

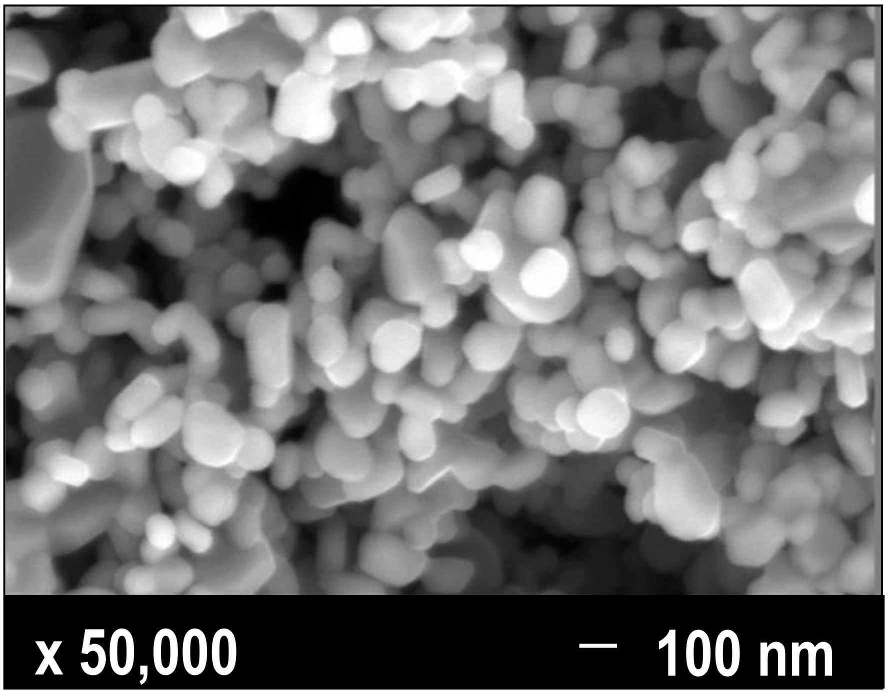

Figure 5–1. Synthesised CTO powder screen-printed onto gas sensor substrate and fired at 600 ºC, prior to imaging. The CTO powder was fabricated by a solid-state ceramic 'shake and bake' method

SEM imaging of the syntheised CTO ($Cr_{1.95}Ti_{0.05}O_3$) powder (screen printed and fired at 600 ºC) seen in Figure 5–1, showed the associated particles demonstrated small spherical and oval behaviour with sizes of about 100 nm – 200 nm. In comparison to the CTO powder fabricated in this study, Chabanis *et al*. [116] who had synthesised a range of $Cr_{2-x}Ti_xO_3$ powders (x = 0.05, 0.1, 0.2 and 0.4) via a sol-emulsion-gel route, had reported a range of sizes of their powders. The size of their sol spheres, was dependent on the rate of stirring, which was required in their synthesis process to mix appropriate proportions of chromia and titania sols together, to form their range of CTO sols. They had reported that the more intense the stirring speed, the smaller the size of the final CTO particles. A stirring speed of 2000 rotations per minute (rpm) led to a particle size of 10 µm, whereas a stirring speed as high as 20500 rpm, led to the formation of 0.7 µm. Peter *et al*. [120] who had prepared CTO via a ceramic synthesis method, analogous to that used in this thesis, had formed undispersed particles with sizes < 1 µm. A more detailed investigation of particle size distribution using laser scattering showed that the average particle size was 260 nm, with 95% of particles < 500 nm. This evidence suggests that ball-milling is a harsh powder processing technique and can lead to the formation of significantly smaller particle sizes. Peter *et al*. also reported that the nm particle sizes they achieved, confirmed adequate size reduction by the milling process [120].

5.2.1.2 X-Ray Diffraction (XRD)

The XRD pattern of the as-made CTO ($Cr_{2-x}Ti_xO_3$) powder, with a target composition of $Cr_{1.95}Ti_{0.05}O_3$ (where x = 0.05) presented in Figure 5–2, indicated that the compound adopted a single phase corundum crystal structure analogous to eskolaite, Cr_2O_3, i.e. CTO is iso-structural with Cr_2O_3 (JCPDS No. 38-1479) [293]. This was evident as the XRD peaks of CTO matched the reference pattern of eskolaite, also presented in Figure 5–2. The reference pattern was retrieved from the ICSD database via the National Chemical Database Service [264], which stored the eskolaite XRD data from a study by Hill *et al*. [294], and the miller indices were indexed with reference to various studies in the literature [116, 295].

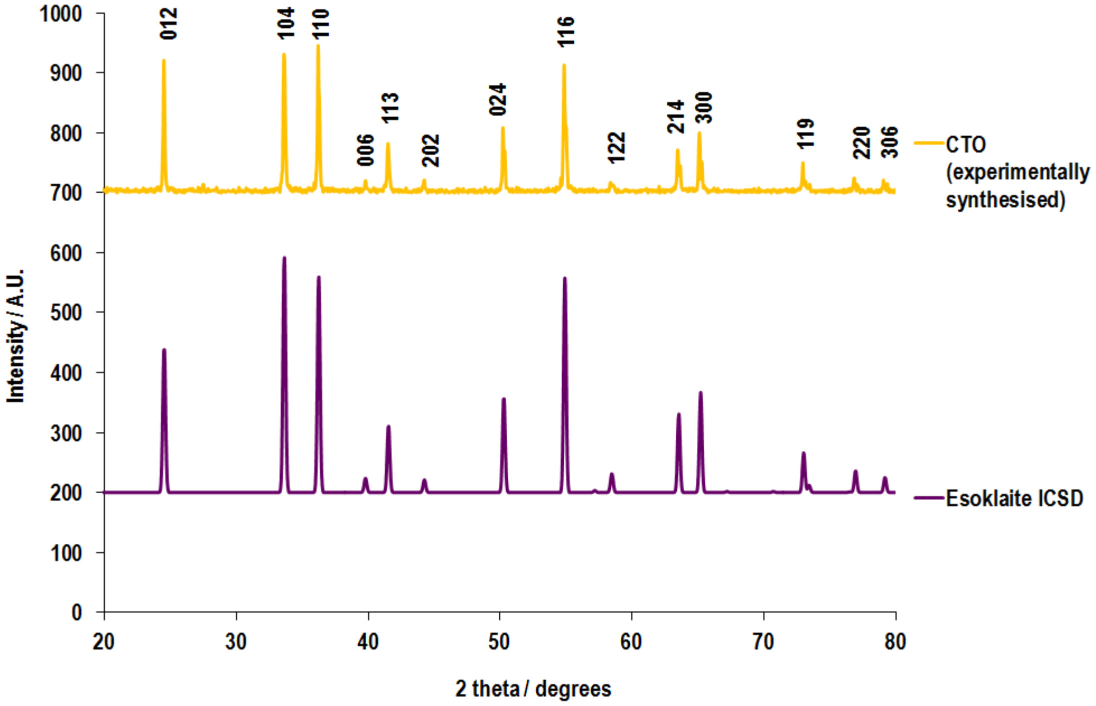

Figure 5–2. XRD patterns of as-synthesised $Cr_{1.95}Ti_{0.05}O_3$ and eskolaite from the ICSD reference database [264, 294]. The CTO powder was fabricated by a solid-state ceramic ‘shake and bake’ method.

Chabanis *et al*. [116] reported the formation of $Cr_{1.95}Ti_{0.05}O_3$ by a sol-emulsion-gel route and observed this compound to be iso-structural with eskolaite, concurring with observations seen in Figure 5–2. Jayaraman *et al*. [48] prepared various samples of $Cr_{2-x}Ti_xO_3$, where x was varied from 0.1 - 0.4, by a solid-state chemical reaction pathway, analogous to this thesis. The group observed all CTO compounds to be iso-structural with Cr_2O_3, however a gradual emergence of $CrTiO_3$ as a minor phase was also reported, particularly at a higher stoichiometry of Ti species (Ti = 0.4) [116]. The iso-structural nature of CTO (where x= 0.1 - 0.5) with Cr_2O_3 has also been observed in other relevant literature focussing on the preparation of CTO compounds via a solid-state chemical reaction pathway [47, 120]. The Ti stoichiometry limit in these and other studies to maintain a single phase has been observed to be at Ti ≤ 0.2 - 0.3 [47, 116, 296], whilst others have reported it to be as high as Ti ≤ 0.4 [47, 122].

Observation of the single phase of the synthesised CTO, justified the formation of a solid solution of TiO_2 in the Cr_2O_3 matrix [116]. Further evidence of the successful synthesis of CTO as a solid solution, is the absence of the TiO_2 peaks in the CTO XRD pattern as seen in Figure 5–3, suggesting that the Ti atoms migrated to the Cr_2O_3 lattice sites [120]. The TiO_2 used in the synthesis of CTO was predominantly rutile phase, which was confirmed by direct match of the TiO_2 XRD pattern with reference pattern of the rutile phase, obtained from a literature resource within the ICSD [264, 297], also plotted in Figure 5–3. The miller indices of the TiO_2 rutile phase have been indexed with reference to a study by Yan *et al*. [298]. The asterixed (*) single peak in the TiO_2 pattern at 25.4 °, in Figure 5–3, indicates the presence of a small amount of the anatase phase of TiO_2 [244], corresponding to the 101 lattice plane of anatase. The presence of this peak suggested the use of impure TiO_2, for the synthesis of CTO. The most crucial step in the synthesis of CTO, is the substitution of the Cr vacancies by Ti, with XRD being reported as the most common technique used to verify the success of it [117, 120], as shown in Figure 5–3.

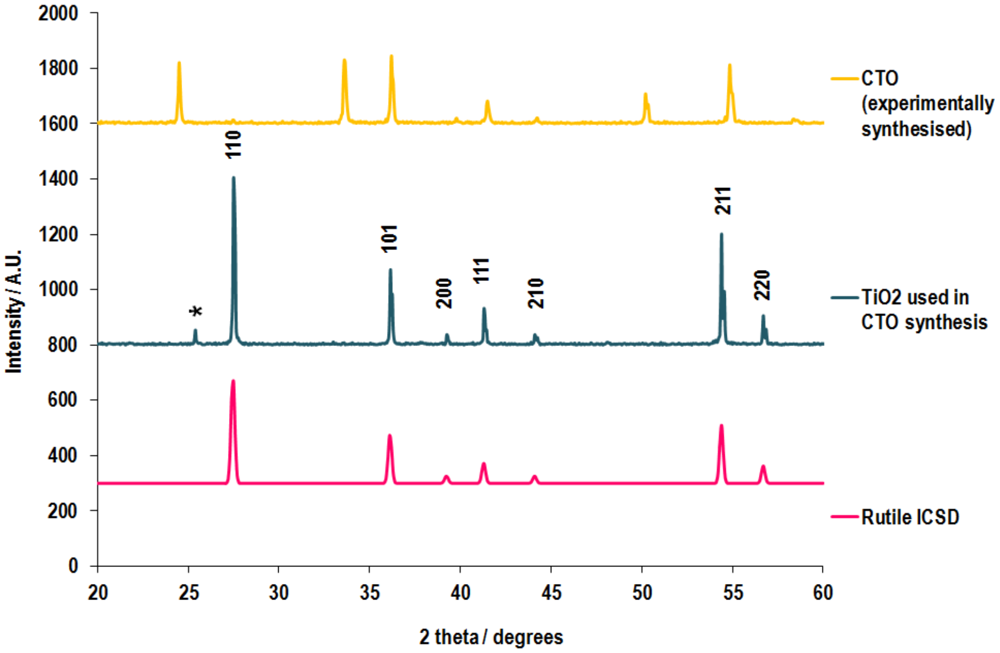

Figure 5–3. XRD patterns of as-synthesised $Cr_{1.95}Ti_{0.05}O_3$, TiO_2 (predominantly rutile phase) used in the synthesis of CTO and TiO_2 (pure rutile phase) from the ICSD reference database [264, 297]. The asterixed (*) peak in the TiO_2 pattern indicates the 101 lattice place of the anatase phase. The CTO powder was fabricated by a solid-state ceramic 'shake and bake' method.

5.2.1.3 X-Ray Photoelectron Spectroscopy (XPS)

XPS spectra of the Cr 2p, Ti 2p and 1 Os core levels of the as-synthesised CTO have been presented in Figure 5–4 (a), (b) and (c). The positions of Cr 2p $_{3/2}$ and Ti 2p $_{3/2}$ components at around 577 eV and 458 eV are attributed to Cr^{3+} and Ti^{4+}, respectively [122]. Comparison of the positions of the Cr 2p $_{3/2}$ and Ti 2p $_{3/2}$ components, are in good agreement with literature values for the same composition, $Cr_{1.95}Ti_{0.05}O_{3}$, reported by Chabanis *et al*. [116]. Other doctoral and literature studies, which report XPS measurements for $Cr_{2-x}Ti_{x}O_{3}$ where x = 0.1 - 0.3, have also reported the positions of both components in similar regions to those obtained experimentally [118, 122, 123, 127, 299] and the values also concur with literature values obtained from XPS reference database [201]. Doublets of the 2p components associated to the Cr and Ti species due to spin-orbit splitting effects were observed, with the splitting between the peaks observed to be 9.5 and 5.7 eV, respectively. These splitting values are in close agreement with previous studies [123, 299].

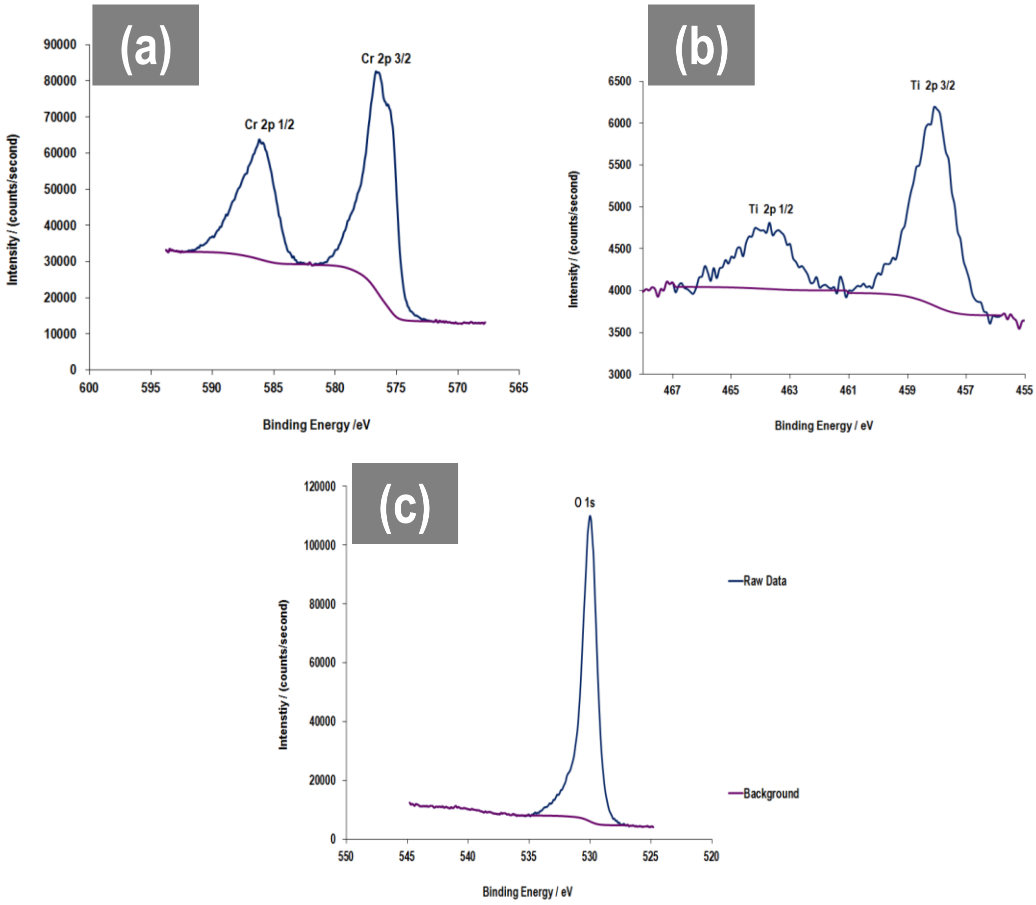

Figure 5–4. (a) XPS spectrum of (a) Cr 2p core level, (b) Ti 2p core level and (c) O 1s core level in as-synthesised $Cr_{1.95}Ti_{0.05}O_{3}$. The CTO powder was fabricated by a solid-state ceramic 'shake and bake' method.

The atomic % of Cr : Ti in the solid solution was calculated by evaluating the integrated area under the individual XPS curves of each species, using Casa XPS software. The Cr : Ti at.% ratio calculated from XPS analysis was 97.8:2.2 at.% which was close to the target at.% ratio of $Cr_{1.95}Ti_{0.05}O_3$ of 97.5:2.5 at.%. The experimental ratio suggested that surface segregation of the Ti^{4+} cations was not apparent and that the Ti^{4+} species were more likely to be dispersed throughout the bulk and the surface of the material.

Surface segregation/enrichment of Ti^{4+} species in CTO has been observed in multiple studies [47, 116-118, 122] and has been accounted for by a segregation driving force due to electrostatic charge effects [47, 118]. Niemeyer [125] reported that the surface segregation of the Ti^{4+} ions relieved the strain caused by defects in the CTO material prepared by the solid-state route.

Afonja [299] reported, material characterisation of two samples of $Cr_{2-x}Ti_XO_3$ where (x = 0.2), one prepared by a sol-gel method and the other by conventional solid-state ceramic synthesis; it was found that the former had more apparent surface segregation than the latter. Chabanis *et al*. [116] reported that the sol-gel route, accounted for a better mixing of the Cr_2O_3 and TiO_2 phases, particularly on the nanometre scale, resulting in a better Ti^{4+} species distribution than the solid-state route. These studies therefore suggest that the solid-state synthesis route to $Cr_{1.95}Ti_{0.05}O_3$, may have affected the titanium distribution in the sample, which subsequently influenced the overall segregation of the species. The conventional solid-state method as a route to CTO has been criticised [116, 123] for the poor chemical homogeneity in the resulting product. Further, it has also been criticised as the milling process has the potential to introduce chemical impurities into the sample. Such impurities if present, may have also acted to influence the atomic % of Ti. Due to these disadvantages, the sol-gel method has been commended as a better route to the formation of CTO compounds, with a better degree of purity of sample [116, 300]. However the solid-state ceramic synthesis route was used in this thesis as an application of a commercially viable process for the production of composite sensors.

5.2.1.4 Raman Spectroscopy

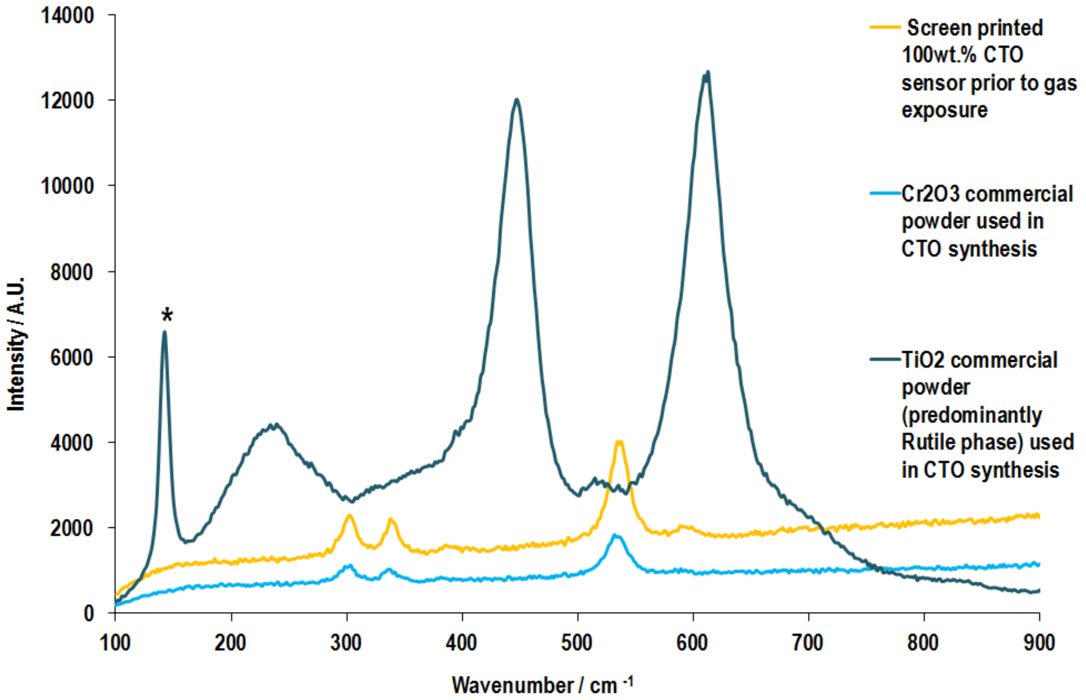

Figure 5–5. Raman spectrum of screen-printed 100 wt.% CTO sensor and commercial Cr_2O_3 and TiO_2 powders used in the synthesis of CTO using a 514.5 nm green argon-ion laser. The asterixed (*) peak indicates the presence of the anatase phase of TiO_2 in the commercial titania powder. The CTO powder was fabricated by a solid-state ceramic ‘shake and bake’ method.

Raman spectroscopy of the precursor metal oxides TiO_2 and Cr_2O_3 powders were compared to the synthesised $Cr_{1.95}Ti_{0.05}O_3$ – in the form a screen-printed sensor, which was heat-treated and prepared for use in gas sensing (i.e. the Raman spectrum of the material was taken prior to gas sensing experiments). The peak positions of TiO_2 (predominantly rutile phase, with presence of the anatase phase indicated by the peak marked with by an * [301]) and Cr_2O_3, were in accordance with the observed values and positions in the literature [302-305]. Detailed analysis of the Raman peak positions of the Cr_2O_3 commercial powder (precursor to CTO) and the synthesised CTO compound has been presented in section 5.2.2.3. TiO_2 is a strong Raman scatterer and hence even the smallest amount of TiO_2 which may have not been in solid-solution form, would have been a strong enough scatter, with its peaks clearly visible in the CTO Raman spectrum [120]. Raman spectroscopy therefore corroborated with the XRD characterisation and justified the successful synthesis of $Cr_{1.95}Ti_{0.05}O_3$. The use of Raman spectroscopy as an analytical technique for the evaluation of the successful synthesis of CTO, has also been reported by Peter *et al*. [120] and Du *et al*.[123].

5.2.2 Pre-Gas Sensing Material characterisation

5.2.2.1 Scanning Electron Microscopy (SEM)

SEM characterisation of all seven sensors in the CTO-ZnO composite system was carried out to investigate the microstructure of each material. The SEM images of all sensor materials in the CTO-ZnO system presented in Figure 5–6.

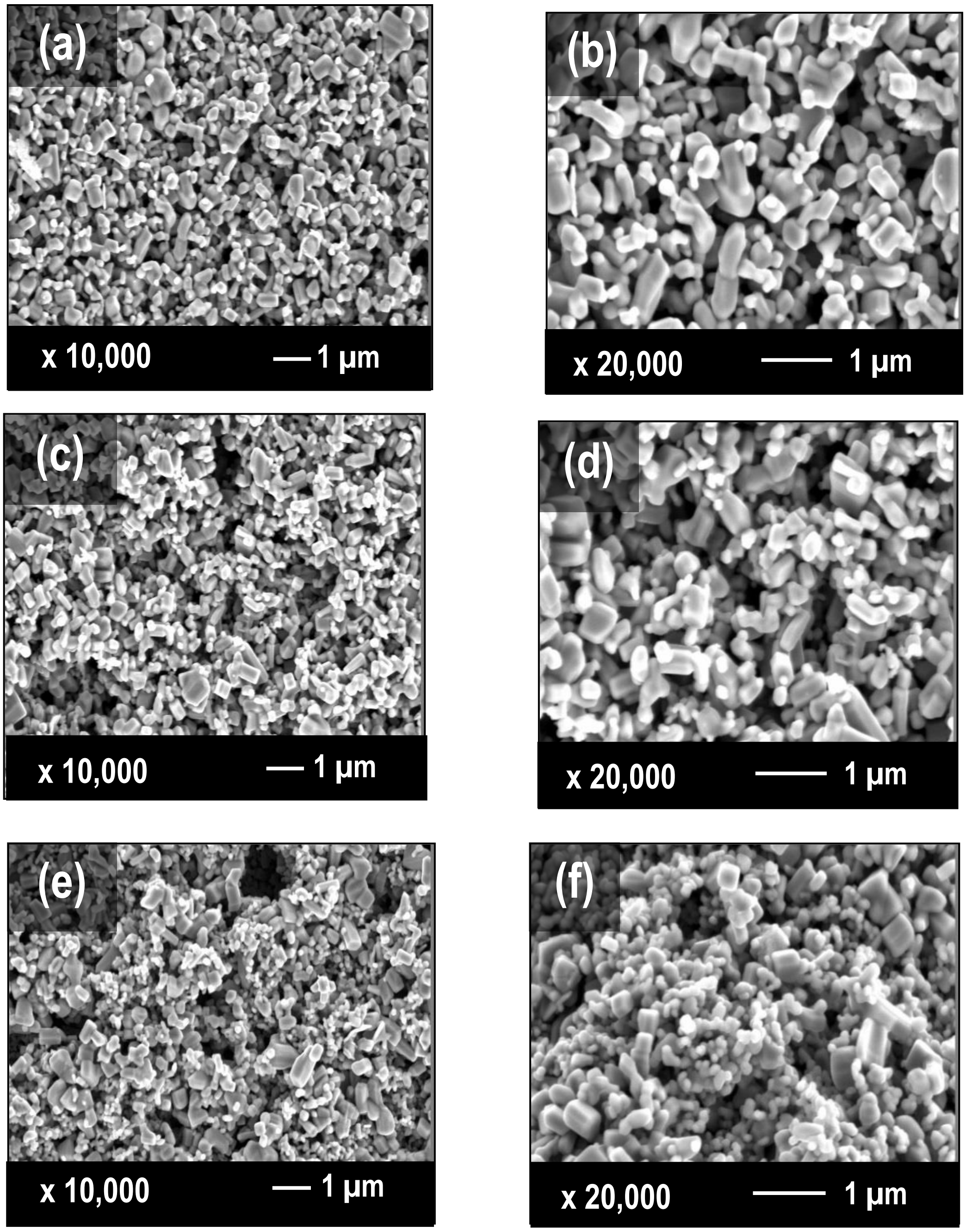

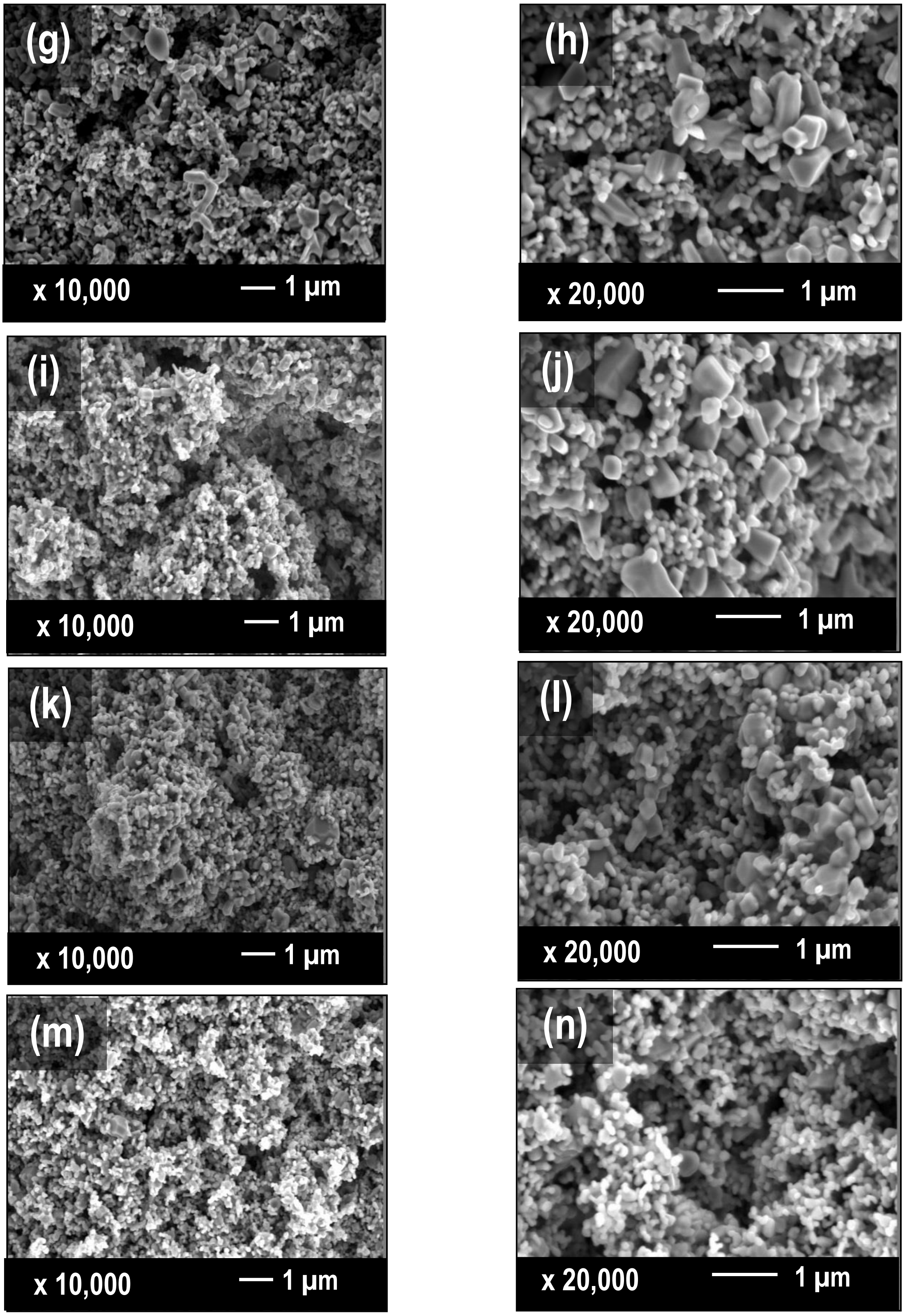

Figure 5–6. SEM images of a) 100 wt.% ZnO x 10,000 magnification, b) 100 wt.% ZnO x 20,000 magnification, c) 90 wt.% ZnO - 10 wt.% CTO x 10,000 magnification, d) 90 wt.% ZnO - 10 wt.% CTO x 20,000 magnification, e) 70 wt.% ZnO – 30 wt.% CTO x 10,000 magnification, f) 70 wt.% ZnO – 30 wt.% CTO x 20,000 magnification, g) 50 wt.% ZnO – 50 wt.% CTO x 10,000 magnification, h) 50 wt.% ZnO – 50 wt.% CTO x 20,000 magnification, i) 30 wt.% ZnO – 70 wt.% CTO x 10,000 magnification, j) 30 wt.% ZnO – 70 wt.% CTO x 20,000 magnification, k) 10 wt.% ZnO – 90 wt.% CTO x 10,000 magnification, l) 10 wt.% ZnO – 90 wt.% CTO x 20,000 magnification, m) 100 wt.% CTO x 10,000 magnification and n) 100 wt.% CTO x 20,000 magnification. All materials were screen-printed and heat-treated at 600 ºC before imaging.

SEM of the system of sensor devices showed a gradual evolution in the morphology as a function of changing concentrations of ZnO and CTO components. Figure 5–6 (a) & (b) show that the pure ZnO particles exhibited 3-dimensional cuboid shapes with rounded edges, with broad particle size distribution ranging from 0.1 µm to 1 µm, as observed in Chapter 3 and Chapter 4.

In contrast, Figure 5–6 (m) & (n) show that the CTO particles exhibited agglomerated spherical like behaviour with sizes of about 100 nm. The smaller particle size of the CTO was likely a result of the harsh frictional grinding of the ball-milling process and is suggestive of the CTO possessing a large surface to bulk ratio, advantageous for gas sensing applications, which is inherently a surface process.

A significant difference in the particle sizes of both the metal oxides, which was also observed in Chapter 4, indicated that hetero-junctions were not only introduced by the presence of particles of differing chemical natures, but were also present due to the stark contrast in particle sizes, in this case between the CTO and ZnO. In the case of the CTO – ZnO composite system examined here, multiple in-homogeneities existed, in particular the dimensional, chemical and electronic nature to potentially exert hetero-junction enhancement effects which may have contributed to playing an influential role towards the overall gas-sensing properties of the materials.

Images of the sensor microstructures in Figure 5–6 showed that the metal oxide particles were generally loosely held within the sensor matrices, which is a key advantage of utilising thick-film technology for MOS sensing, as discussed in Chapter 1. The loosely held grains indicated provision for the gaseous molecules interact with the body of the sensor matrices as well as their surfaces. Thus, diffusion pathways existed, for the gaseous molecules to percolate into and out of the sensor body as well as internally within the body of the sensor matrix and as such, increased the surface site accessibility of the analyte molecules. Comparatively, the CTO particles were attributed to greater agglomeration than the ZnO particles, which can be observed by comparison of Figure 5–6 (b) and (n). This indicated reduced surface site accessibility of the analyte molecules within the body of the CTO sensor matrix in comparison to the ZnO sensor matrix.

The SEM micrographs of the 70 wt.% ZnO – 30 wt.% CTO, 50 wt.% ZnO – 50 wt.% CTO and 30 wt.% ZnO – 70 wt.% CTO sensor devices observed in Figure 5–6 (e) & (f), (g) & (h) and (i) & (j) respectively, gave evidence of the dispersion of the individual metal oxides interspersed, suggesting a hetero-contact dominated packing structure within the devices and delocalised contact potentials, within the bodies of the sensor matrices. In contrast, those composites which were dominated by the host matrix of an individual metal oxide such as the 90 wt.% ZnO – 10 wt.% CTO and the 10 wt.% ZnO - 90 wt.% CTO sensor devices observed in Figure 5–6 (c) & (d) and (k) and (l) respectively, showed the microstructure to be dominated by the dominant metal oxide and therefore were suggestive of a packing structure attributed to homo-contact dominated electron percolation paths, with localised hetero-contacts within the body of the matrix.

As described in Chapter 1, the extent of agglomeration and sintering in a gas sensing material, determines the particles' surface and bulk contribution towards the gas sensing performance [65]. The visibility of the generally loosely held grains of both metal oxides in all composite sensor devices suggested that the surfaces of the individual grains were available for interaction with the gas molecules, thus aiding the surface site accessibility of the analyte molecules.

5.2.2.2 X-Ray Diffraction (XRD)

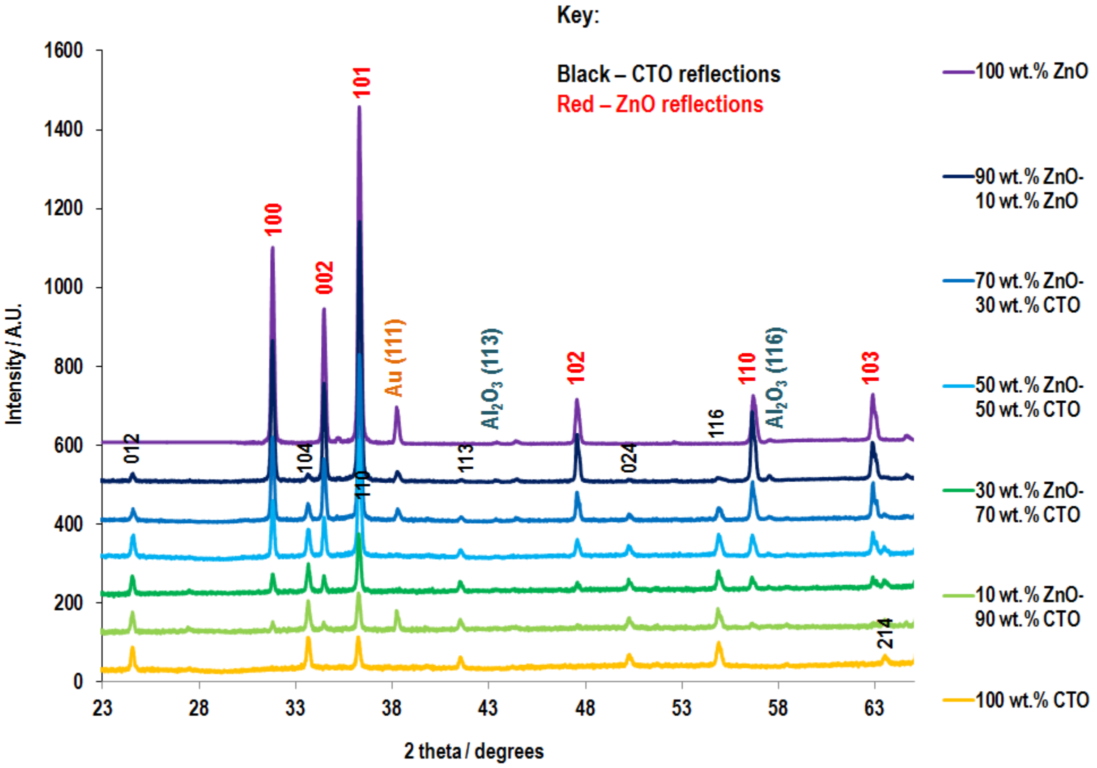

Figure 5–7. XRD patterns prior to gas sensing experiments of all pure and composite sensors based on Cr$_{1.95}$Ti$_{0.05}$O$_3$ and ZnO metal oxides in the CTO-ZnO composite system. All materials were screen-printed and heat-treated at 600 °C, prior to XRD measurements. Alumina and Gold reflections from MOS sensor substrate were visible and have also been indicated.

XRD patterns of the individual sensor materials based on Cr$_{1.95}$Ti$_{0.05}$O$_3$ and ZnO metal oxides, within the CTO-ZnO composite system before exposing them to gas, have been presented in Figure 5–7. XRD confirmed the crystalline nature of both compounds, indicated by the sharp defined peaks observed for both materials. The XRD patterns of CTO, confirmed it still maintained the corundum crystallite structure, analogous to eskolaite (JCPDS No. 38-1479) [290, 293], after heat-treatment. The pattern of ZnO as discussed in Chapter 3 and Chapter 4, adopted a wurtzite hexagonal crystal structure (ICDD No. 36-1451) [77, 213, 214]. The patterns showed the variation in concentration of CTO and ZnO in the system through a gradual change in the intensity of the associated peaks in ascending or descending order. The observation of the peaks of both metal oxide crystal phases, indicated that all materials in the system were mechanically mixed composites. An observation of a gold peak in some of the patterns at 38.2° is associated to the inter-digitated gold electrodes and the two shallow peaks at 43.3° and 52.5° are associated to the alumina, both from the MOS sensor substrate.

5.2.2.3 Raman Spectroscopy

The Raman spectra of the individual sensor materials based on $Cr_{1.95}Ti_{0.05}O_3$ and ZnO metal oxides, within the CTO-ZnO system before exposing them to gas, have been presented in Figure 5–8.

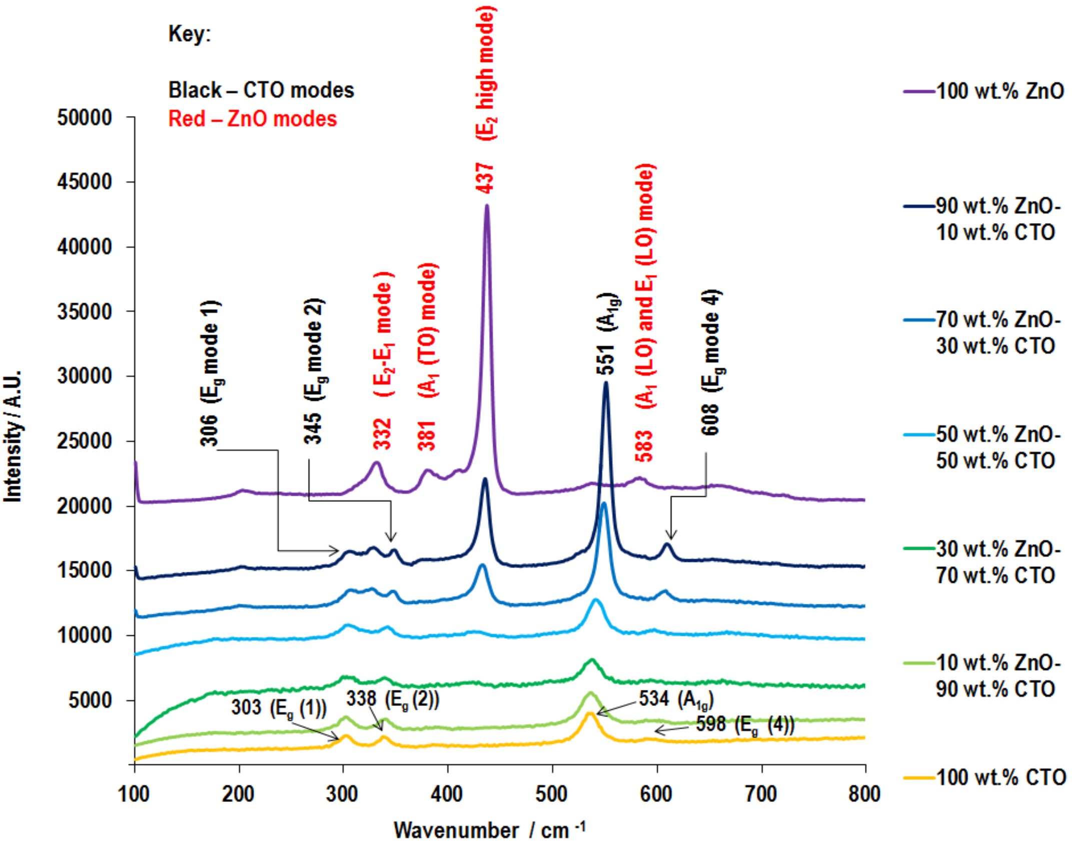

Figure 5–8. Raman spectra prior to gas sensing experiments of all pure and composite sensors based on $Cr_{1.95}Ti_{0.05}O_3$ and ZnO metal oxides in the CTO-ZnO composite system. All materials were screen-printed and heat-treated at 600 °C, prior to Raman measurements.

Raman spectroscopy identified the individual CTO and ZnO phases within the mixed oxide materials. This corroborated with XRD measurements, showing that the materials containing both CTO and ZnO, were composite mixtures. Raman spectroscopy of the pure CTO sensor, i.e. the 100 wt.% CTO sensor device, matched the Raman pattern of the Cr_2O_3 precursor, as observed in Figure 5–5. This observation corroborated with the XRD data, confirming that CTO was iso-structural to Cr_2O_3. Careful observation showed that the peak positions of both the Cr_2O_3 precursor and CTO, were red shifted and significantly broader in comparison to the peak positions of the bulk Eskolaite reference pattern reported in the literature [120, 302, 305, 306]. The peak positions of the Raman bands of Cr_2O_3 observed in the literature [302] vs. those observed experimentally in this thesis, have been presented in Table 5–1.

Table 5–1. Raman peak positions of Cr_2O_3 (Eskolaite) observed in the literature [302] vs. Raman peak positions observed for the same compound experimentally.

Source	**Cr_2O_3: Literature [302]**	**Cr_2O_3: precursor used experimentally**
Raman Band: E_g Mode 4	**609.7 cm^{-1}**	**598 cm^{-1}**
Raman Band: A_{1g}	**551.1 cm^{-1}**	**534 cm^{-1}**
Raman Band: E_g Mode 3	**523.4 cm^{-1}**	**Not observed**
Raman Band: E_g Mode 2	**349.8 cm^{-1}**	**338 cm^{-1}**
Raman Band: E_g Mode 1	**306.3 cm^{-1}**	**303 cm^{-1}**

Comparison of the positions of the Raman bands of Cr_2O_3 between literature [302] and experiment in Table 5–1, shows that only E_g Mode 1 at ca. 300 cm^{-1} was observed to be in similar positions between both sources, with a red shift of less than 5 cm^{-1} between the values. The other observable Raman bands are red shifted by more than 10 cm^{-1} in experiment, with respect to the literature values. In particular the A_{1g} mode which is referred to as the main Raman band of Cr_2O_3 [302], showed the largest red shift of 17 cm^{-1}.

Such red shift behaviour or "wavenumber evolution" [302] for Cr_2O_3, particularly of the A_{1g} peak, has been observed previously by Zuo *et al.* [305, 306]. The group who were investigating the Raman spectra of nano-structured Cr_2O_3, have related this phenomenon to structural disorder in the Cr_2O_3, in the form of oxygen deficiency. They report that the oxygen deficiency is dependent on the grain size of the material; a decrease in the grain size (up to 10 nm) causes the oxygen deficiency to increase, leading to the red shift (of 17 cm^{-1}) and broadening of the A_{1g} band. In contrast, an increase in the grain size via annealing, to sizes > 100 nm, causes the oxygen deficiency to decrease, resulting in a blue shift of the A_{1g} band, which is more defined and sharper, and in excellent agreement with bulk Eskolaite peak positions in the literature. This reasoning suggests potential structural disorder or defects and oxygen deficiency in the Cr_2O_3 precursor used experimentally in this thesis , which promotes red shifting and broadening of the associated Raman bands, and this also accounts for the red shifts observed in the Raman pattern of the synthesised CTO**.**

Interestingly, Figure 5–8 presents evidence that as the CTO concentration decreased and that of ZnO increased in the composites, the peak associated to the A_{1g} band became sharper, more defined and its position blue shifted towards higher wavenumbers, approaching the peak position of bulk Eskolaite reported in the literature [302]. As such, the 90 wt.% ZnO – 10 wt.% CTO sensor device was associated to Eskolaite peaks in excellent agreement with literature values of bulk Eskolaite reference peaks, as observed in Table 5–2.

Table 5–2. Raman peak positions of Cr_2O_3 (Eskolaite) observed in the literature [302] vs. Raman peak positions observed experimentally for the 90 wt.% ZnO – 10 wt.% CTO composite sensor device.

Source	**Cr_2O_3: Literature [302]**	**90 wt.% ZnO – 10 wt.% CTO sensor: Experiment**
Raman Band: E_g Mode 4	**609.7 cm^{-1}**	**608**
Raman Band: A_{1g}	**551.1 cm^{-1}**	**551**
Raman Band: E_g Mode 3	**523.4 cm^{-1}**	**Not observed**
Raman Band: E_g Mode 2	**349.8 cm^{-1}**	**345**
Raman Band: E_g Mode 1	**306.3 cm^{-1}**	**306**

Using the explanation by Zuo *et al*., this blue shift and increased sharpness of the Raman peaks, particularly the A_{1g} peak, observed as a function of changing concentrations of CTO and ZnO, could be accounted for change in oxygen concentration in the composites. In particular, as the concentration of CTO decreases and that of ZnO increases, the presence of ZnO may provide greater oxygen species for the amount of CTO available and this therefore causes the A_{1g} mode to blue shift and become sharper and defined. Further the presence of increasing ZnO concentration and decreasing CTO concentration, indicates an enhanced change in the dipole moment of the A_{1g} mode which is accounted for by the increased intensity of the associated peak.

Mougin *et al*. [302], also reported the in situ Raman monitoring of Cr_2O_3 scale growth for stress determination.. The group had followed in situ isothermal oxidation of a chromium sheet to form a Cr_2O_3 layer, at 750 °C under 150 mbar of O_2. In their study, they had observed the wavenumbers of Cr_2O_3 band red shifted as a function of increasing oxidation temperature from 25 °C – 750 °C. They reported that this red shift was accounted for by induced oxide and thermal stresses and a variation in compressibility of the material between the two temperatures, with compression being greater at higher temperatures. In relation to the study by Zuo *et al*., the study by Mougin *et al*. suggests that the influence of higher temperatures is similar to that of increasing the oxygen deficiency in Cr_2O_3. As such the overall influence on the shifting and sharpening of peaks, maybe be accounted for by due to potential defects and associated compression effects due to the defects and disorder in the Cr_2O_3 lattice, due to various physical effects of the oxygen ions.

Peter *et al*. [120], who reported the synthesis of $Cr_{2-x}Ti_xO_3$, where x = 0.2 via the conventional solid-state route, observed Raman bands for CTO to be in excellent agreement with bulk Eskolaite peak positions in the literature [123, 302]. This suggested that the precursor Cr_2O_3 material in their study had reduced structural defects than the Cr_2O_3 precursor used in this thesis.

5.2.3 Post Gas Sensing Material characterisation

5.2.3.1 Observed Colour Change in Gas Sensor Materials

Figure 5–9 illustrates the colour change of the gas sensor materials that was observed post-gas sensing (i.e. after completion of gas sensing characterisation of all sensor devices and subsequent removal of the devices from the gas sensing rig), in comparison to the original colour of the sensor materials pre-gas sensing. The colour change was apparent specifically in the composite materials and therefore indicated that some form of chemical reaction had occurred between both the component oxides. Post-gas sensing analysis was conducted on the sensor devices, to investigate the observed change, the results of which have been presented in the following sections.

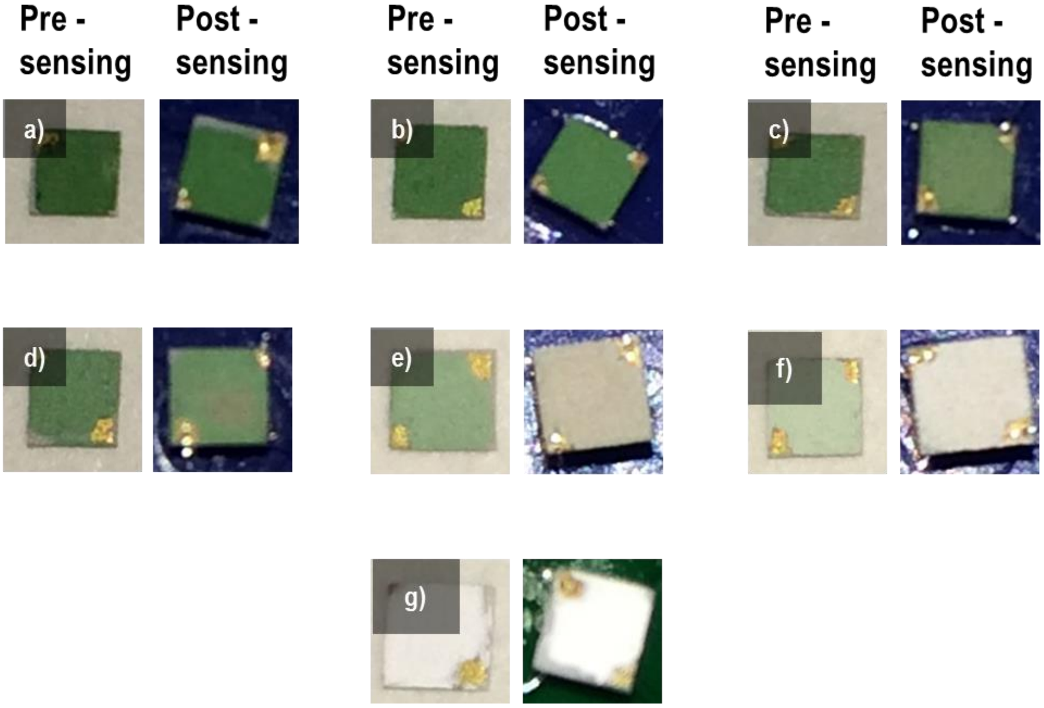

Figure 5–9. Pre- and post-gas sensing coupled images of each sensor device based on Cr$_{1.95}$Ti$_{0.05}$O$_3$ and ZnO metal oxides: a) 100 wt.% CTO, b) 90 wt.% CTO - 10 wt.% ZnO, c) 70 wt.% CTO – 30 wt.% ZnO, d) 50 wt.% CTO – 50 wt.% ZnO, e) 30 wt.% CTO – 70 wt.% ZnO, f) 10 wt.% CTO – 90 wt.% ZnO and g) 100 wt.% ZnO, within the CTO-ZnO composite system.

5.2.3.2 Scanning Electron Microscopy (SEM)

SEM images of all sensor materials in the CTO-ZnO composite system, post -gas sensing, have been presented in Figure 5–10. The objective was to investigate any apparent change in microstructure, as a result of the chemical change observed.

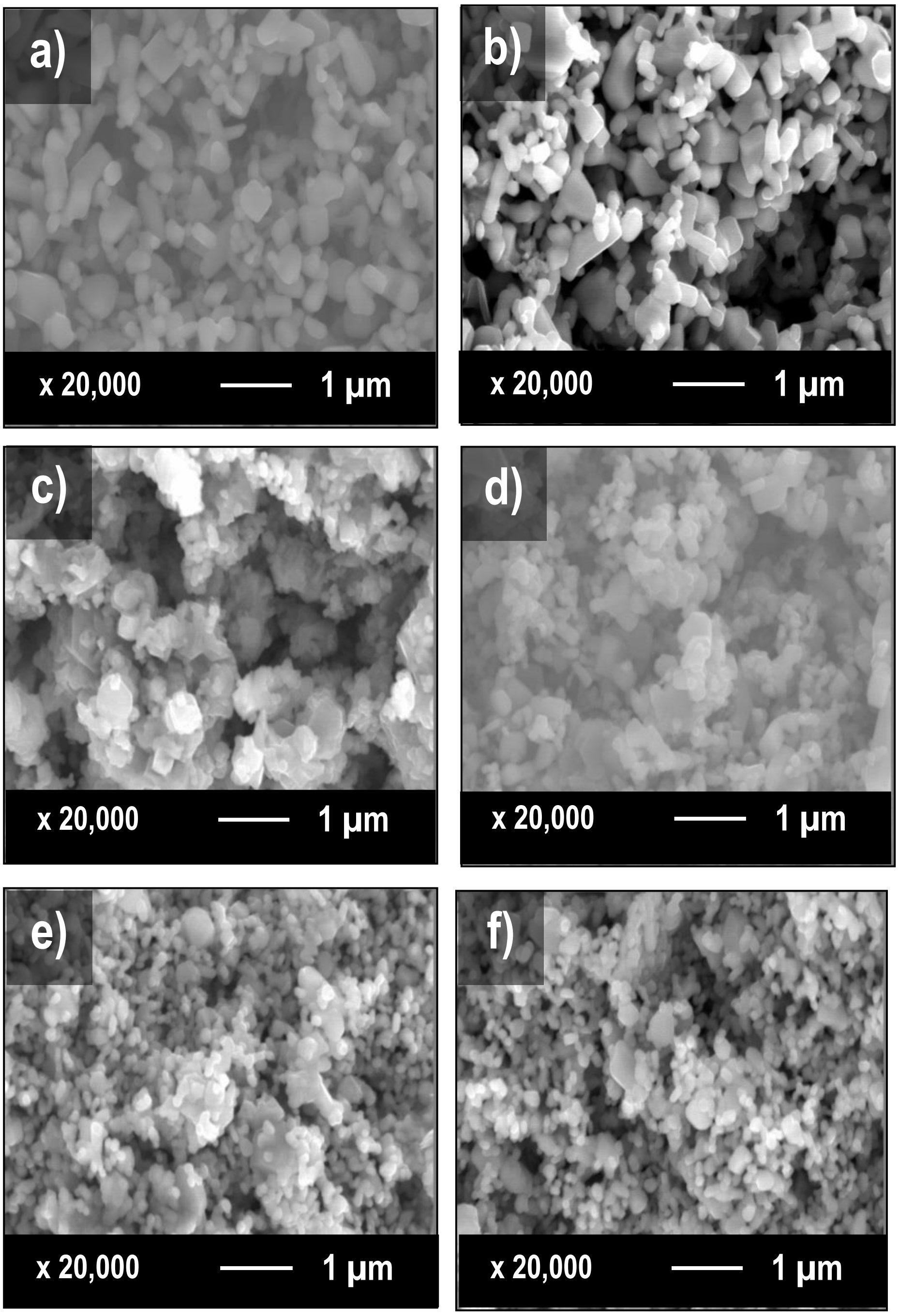

Figure 5–10. Post-gas sensing SEM images of a) 100 wt.% ZnO, b) 90 wt.% ZnO - 10wt.% CTO, c) 70 wt.% ZnO – 30 wt.% CTO, d) 50 wt.% ZnO - 50wt.% CTO, e) 10 wt.% ZnO – 90 wt.% CTO and f) 100 wt.% CTO sensor materials all x 20,000 magnification.

SEM imaging post-gas sensing, showed no appreciable difference in the microstructure of the 100 wt.% ZnO (Figure 5–10 (a)), 90 wt.% ZnO - 10 wt.% CTO (Figure 5–10 (b)), 100 wt.% CTO (Figure 5–10 (f)) and 90 wt.% CTO – 10 wt.% ZnO (Figure 5–10 (e)) sensor devices, in comparison to the pre-gas sensing counterparts presented in Figure 5–6.

The morphological characteristics of the individual metal oxides in terms of particle size, shape and loosely held grains was still maintained. The 70 wt.% ZnO – 30 wt.% CTO and 50 wt.% ZnO – 50 wt.% CTO composite sensor devices in Figure 5–10 (c) and (d) respectively, showed greater agglomeration of the metal oxides, however the images suggested these to be representative of the composite materials rather than of any form of chemical reaction, as the individual CTO and ZnO particles were still visible within the matrices of the gas sensing materials. As mentioned previously in Chapter 3, one of the drawbacks of the manual mechanical mixing as a route to formation of the composite materials, is the possibility of an in-homogenous microstructure within the sensor matrix. Sun *et al*. [210] also mentioned that the irreproducibility with mixing powders for composite formation, arises from the size and density differences of the particles and the different settling dynamics once the ink has been deposited onto the alumina substrate. This justifies that the overall difference in microstructure is statistically likely to be a result of the inhomogeneity associated to the preparation process of the composite materials, with limited evidence to suggest that it has occurred due to the observed chemical change.

In conclusion, SEM imaging did not show any apparent change in the microstructure of the materials as a result of the chemical change that was observed.

5.2.3.3 X-Ray Diffraction (XRD)

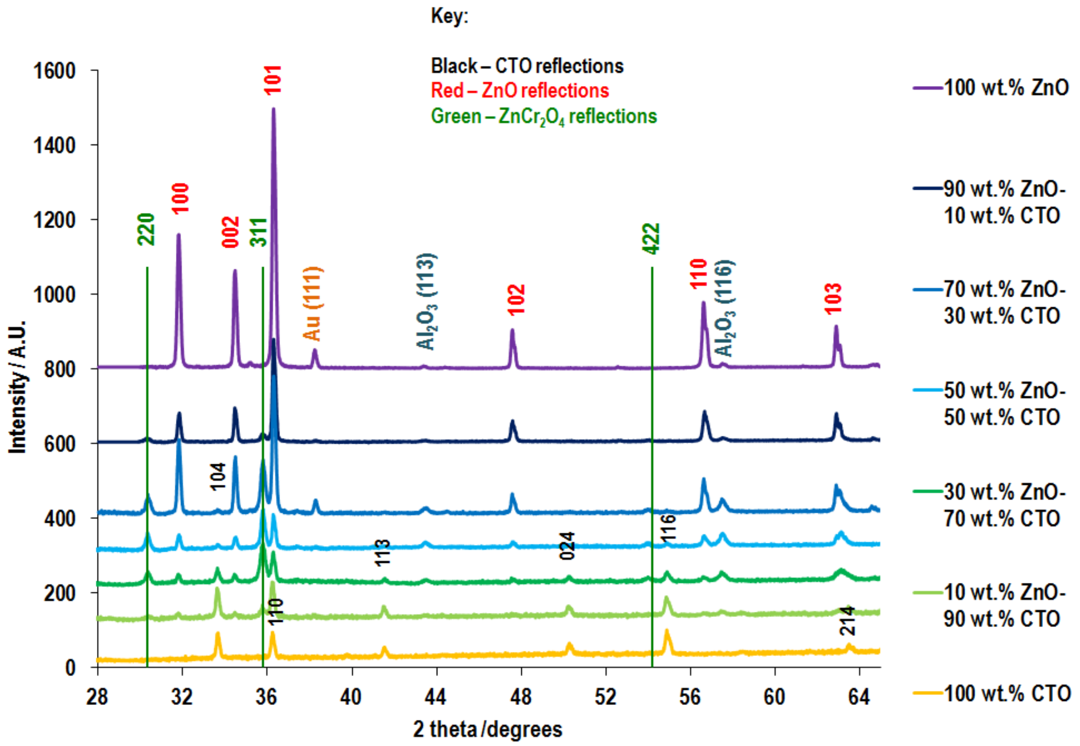

Figure 5–11. XRD patterns taken after gas sensing experiments of all pure and composite sensors based on $Cr_{1.95}Ti_{0.05}O_3$ and ZnO metal oxides in the CTO-ZnO composite system.

The XRD patterns of the individual sensor devices within the CTO-ZnO composite system, after gas sensing experiments, have been presented in Figure 5–11. Analysis of the patterns showed that the crystalline nature of the materials was maintained, evident through the sharp defined peaks of the individual metal oxides. Further, peaks associated to both metal oxide phases were all present, indicating that the composite nature of the materials was also maintained. However, three additional peaks; at 30.3 °, 35.9 ° and 54.1 ° were observed in the composite materials (not pure metal oxides), which were not present prior to gas sensing. This indicated the formation of a new tertiary phase, specifically spinel zinc chromite, $ZnCr_2O_4$, in the composite mixtures, which suggested a solid-state reaction between Cr_2O_3 and ZnO had occurred. The XRD peak positions of the tertiary phase observed experimentally, were in direct correlation to reports in the literature and were indexed to the cubic phase of $ZnCr_2O_4$, (ICDD No. 01-087-0028) [264, 307, 308]. Some of the reflections observed experimentally were the most intense reflections of the compound as observed in the reference pattern presented in Figure 5–12 obtained from the ICSD database [264, 308]. The reflection indexed 511 at 57.5 ° in $ZnCr_2O_4$ as seen in Figure 5–12, was not evident in the composites. The likely reasoning behind this was because the Al_2O_3 116 reflection from the alumina substrate, was located in the same position of 57.5 ° and had greater intensity, and as a result swamped observation of the high angle $ZnCr_2O_4$ reflection.

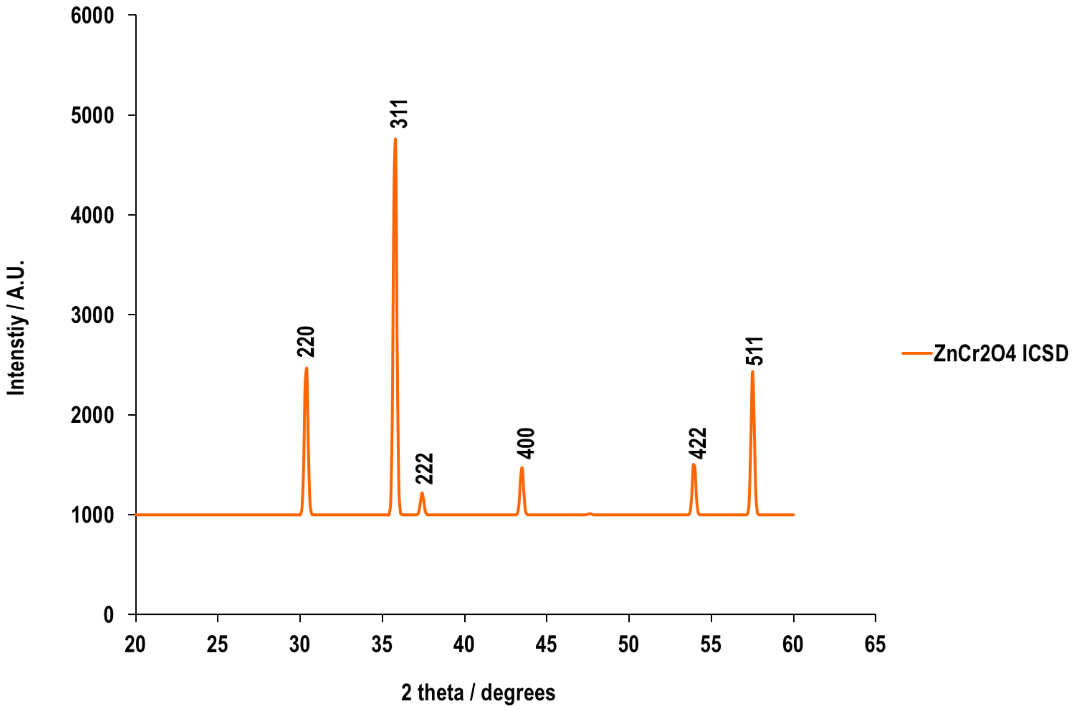

Figure 5–12. XRD patterns of zinc chromite, $ZnCr_2O_4$, from the ICSD reference database [264, 308].

5.2.3.4 Raman Spectroscopy

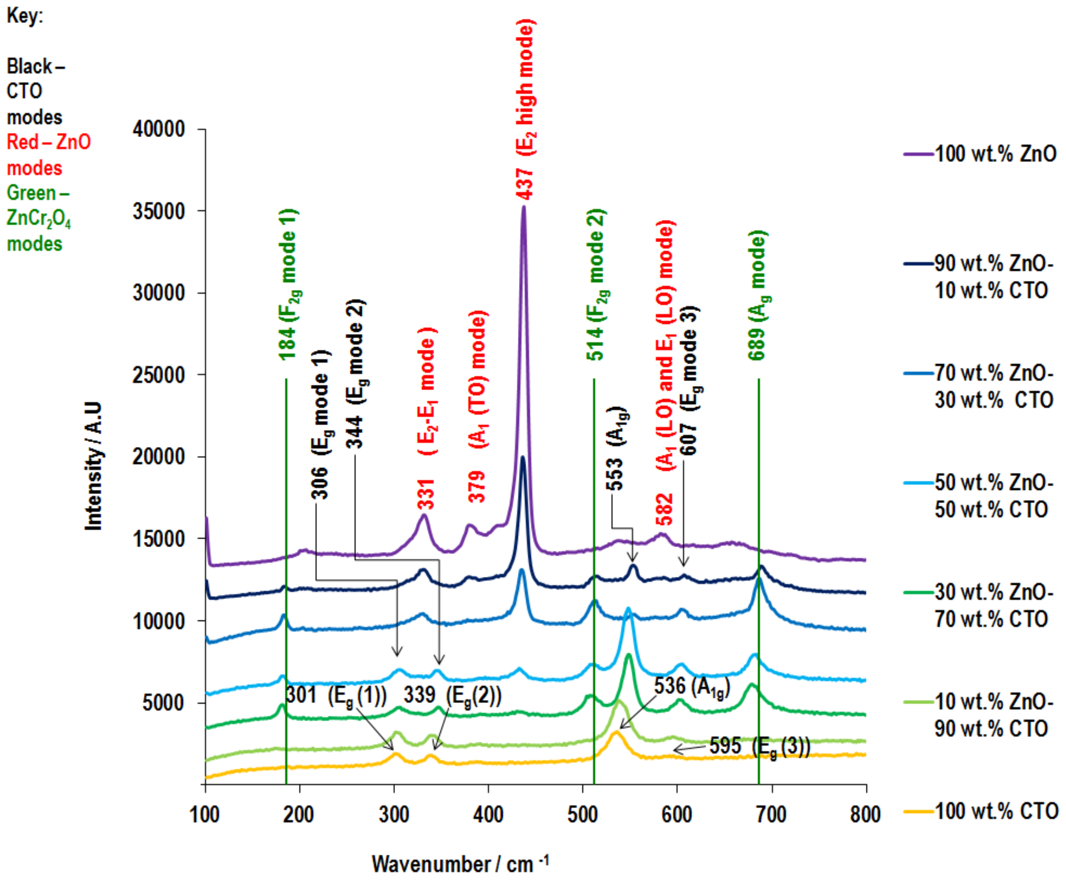

Figure 5–13. Raman spectra taken after gas sensing experiments of all pure and composite sensors based on $Cr_{1.95}Ti_{0.05}O_3$ and ZnO metal oxides in the CTO-ZnO composite system.

Raman spectroscopy identified the individual modes of both component oxides within the CTO-ZnO composite system as observed in Figure 5–13 suggesting that the composite nature of the materials was still maintained. However, extra modes within the composites were seen after gas sensing experiments. The bands were confirmed to be associated to the tertiary phase $ZnCr_2O_4$, as per comparison of the observed experimental bands with the literature and were associated to the spinel having a cubic crystal structure [307, 309].

The formation of $ZnCr_2O_4$ has been reported by Wang *et al.* [309] by high-temperature solid-state reaction of stoichiometric amounts of ZnO and Cr_2O_3. The group had not reported the temperature of the reaction at which they formed the spinel as their study was more focussed on an in-situ Raman study on the transformation of the phase upon application of high pressure. Vargas-Hernandez *et al.* [310] reported that the optimal formation of the spinel phase is obtained by conducting the solid-state reaction between stoichiometric amounts of both component oxides for 24 hours at 750 °C. Marinkovic

Stanojevic *et al*. [311] in contrast reported making the spinel phase by dry grinding together equimolar amounts of both component oxides in a vibro-mill, prior to firing the mixture at 900 °C for 4 hours. These synthesis approaches suggest that a similar solid-state reaction must have taken place between both metal oxides in the composite sensor devices. However, heat-treatment at 600 ºC prior to gas sensing analysis, did not promote the solid-state reaction between ZnO and Cr_2O_3. Had it done so, the $ZnCr_2O_4$ phase would have been evident in the pre-gas sensing XRD and Raman data. This is perhaps not surprising as 600 ºC is relatively lower than those temperatures reported by Vargas-Hernandez *et al*. and Marinkovic Stanojevic *et al*. This suggests that exposures to temperatures in the range of 200 ºC - 500 ºC, over the period when the gas sensing experiments were conducted, may have promoted the formation of the spinel i.e. the formation of remnant spinel phase is a result of slow solid-state reaction, which seems to have occurred during exposure to 200 ºC - 500 ºC during gas sensing experiments. Given that the ratios of both metal oxides varied between the composites, then a varying stoichiometry of the spinel phase is likely to have formed in each composite sensor device.

5.2.3.5 X-Ray Photoelectron Spectroscopy (XPS)

XPS analysis was conducted before and after gas sensing analysis to understand any surface changes that may have occurred prior to and post gas exposure. Of all the species present, the spectroscopic technique was seen to show a change in the oxygen environment of the samples as presented in Figure 5–14.

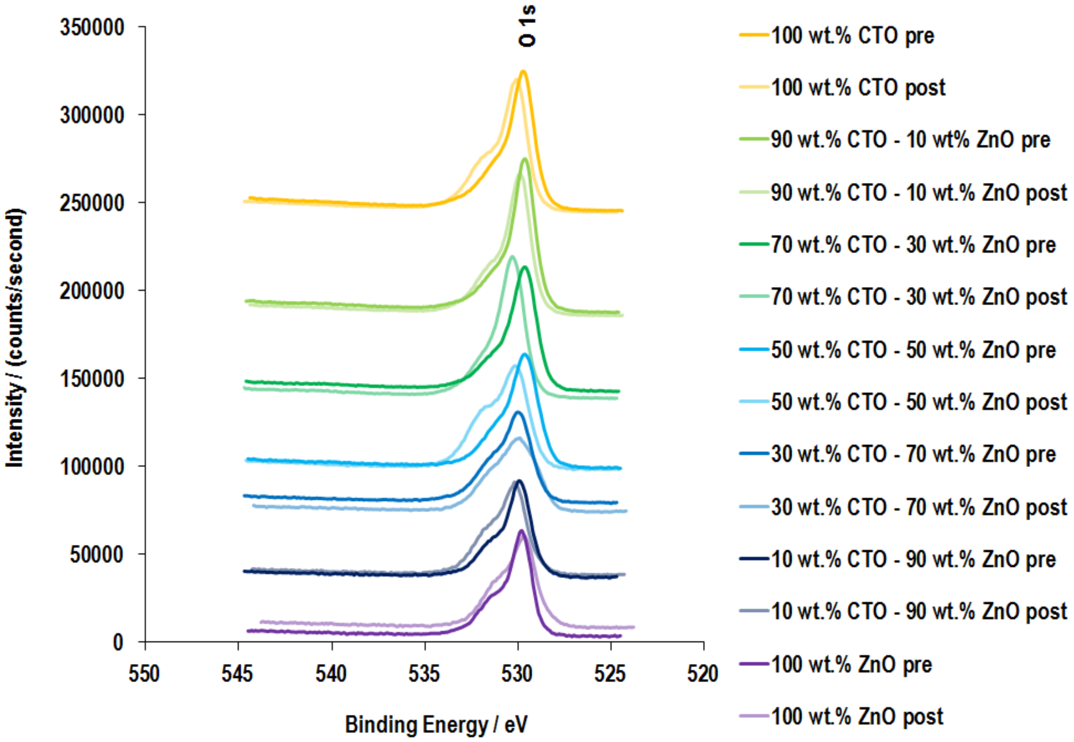

Figure 5–14. XPS spectrum of O 1s core level in the pre- and post-gas sensing sensor devices within CTO-ZnO composite system.

Spectra of the O 1s core level presented in Figure 5–14 showed a prominent shoulder at a higher binding energy in the O 1s peak in the post-gas sensing samples, which was only weakly present in some of the materials prior to gas sensing. This shoulder peak is attributed to the presence of hydroxyl species (OH^-) on the surface of the metal oxides [312, 313], which can be accounted for by the exposure of the sensor devices to a variety of gases, in particular the VOCs as such ethanol. The combustion of ethanol on the surface of a semiconducting metal oxide leads to the formation of H_2O as a by-product [69, 314]. H_2O has been reported to split into the OH^- and H^+ species [12] upon the metal oxide surface, promoting hydroxylation to occur through two potential routes; the first being the direct adsorption of OH- species on the surface sites and the second being the reaction of the acidic proton species H^+ with surface adsorbed O- species and subsequent adsorption [315, 316].

In conclusion, XRD and Raman characterisation techniques gave evidence of the formation of the $ZnCr_2O_4$ (zinc chromite) spinel phase, through the phase characterisation of the composites suggesting that the colour change that was observed in the sensor devices after gas exposure, was due to a solid-state reaction that occurred between both the Cr_2O_3 and ZnO phases within the bulk of the sensor matrix. XPS showed evidence of significant hydroxylation of the material surfaces after gas exposure, indicated by the presence of the shoulder in the O1s core level spectra of the individual sensor devices.

Calculation of the relative binding energies of the Cr and Zn species from XPS data, prior to gas sensing analysis, did not show any correlative pattern as a function of changing phase fraction of CTO and ZnO within the composite materials, as was observed between the W and Zn species in the WO_3–ZnO hetero-junction system reported in Chapter 3. Thus, no visible evidence of an electronic interaction between the Cr and Zn species could be reported.

5.2.3.6 Gas Sensing Properties of $ZnCr_2O_4$ (Zinc Chromite)

Studies on the gas sensing properties of the tertiary compound $ZnCr_2O_4$ are not prominent in the literature, however some reports have been observed for both chemical vapour and humidity sensing applications [317-319].

Niu *et al*. [317] reported on the gas sensing properties of various perovskite compounds based on ZnM_2O_4, where M = Fe, Co, Cr against Cl_2 and NO_2 (both oxidising gases) and C_2H_5OH, H_2S and acetone (reducing gases). The perovskite compounds were reported to be made by a novel micro-emulsion method which resulted in the production of ultrafine powders with spherical particles attributed to a uniform grain size distribution; with the $ZnCr_2O_4$ particles observed to have a mean size of 55 nm. The optimal operating temperature of the spinel oxide was found to be 305 ^oC; which was determined against its responsivity towards Cl_2. The perovskite was found to exhibit p-type conductivity with its resistance decreasing in the presence of the oxidising gases and increasing in the presence of the reducing gases. The group presented the responsivity results (where responsivity was calculated as a ratio of the resistances, subject to the nature of the gas i.e. oxidising or reducing) of the material against the variety of gases. They referenced a responsivity magnitude of 1 to be equivalent to nearly no gas sensing response. The group had reported that the responsivity of spinel towards 50 ppm of all gases was observed to be around 1 at 305 ^oC, except towards ethanol where its response was seen to be 2. Thus the study showed that the performance of $ZnCr_2O_4$ was poor.

In another study by Honeybourne *et al*. [318], the NO_2 and volatile sulphide sensing properties of copper, zinc and nickel chromite were reported, which were prepared via a metal nitrate decomposition process. When exposed to 20 ppm NO_2, the $ZnCr_2O_4$ showed a responsivity (which was a ratio of the change in the current of the material, as a function of the applied potential difference, as function of gas concentration) of 291.36 to the gas at 220 °C.

Both studies here present response results of the $ZnCr_2O_4$ phase towards very high concentrations of analytes, particularly with NO_2, the toxic limit value (TLV) of which is only 3 ppm [38, 172]. However, for the purposes of comparison, the former study by Nui *et al*. is more appropriate due to the nature of the response calculation, which is very similar to that implemented in this thesis. In their study, the group observed very low responses of the spinel compound towards 50 ppm of NO_2, ethanol and acetone. Comparatively in this study, the NO_2 concentrations being analysed are at ppb levels and that of acetone is a maximum of 10 ppm, indicating that is very unlikely that the spinel could be attributed to any form of response. The ethanol concentration reported by the group is relatively similar to that used in this study (10 ppm – 100 ppm), but again the literature study shows very little response behaviour towards the analyte, which may suggest poor response characteristics of the spinel present in the CTO-ZnO composite materials.

As the inference of when the spinel formed during the gas sensing experiments remains unknown, it is extremely difficult to determine the actual influence of the phase on the response properties of the composite materials. As mentioned earlier, the colour change of the sensor devices was only observed after removing the sensors from the gas sensing rig, once all gas sensing characterisation studies had been conducted.

.

5.2.4 Gas Sensing

5.2.4.1 Ethanol Sensing

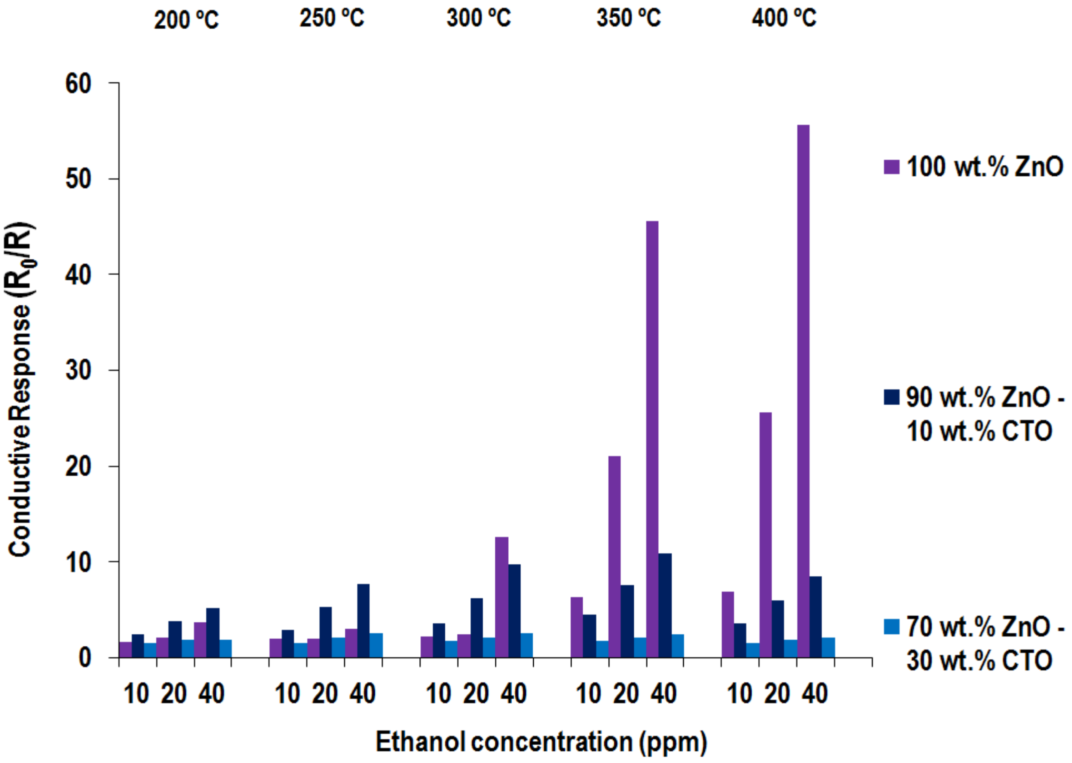

Figure 5–15. Conductive response of 100 wt.% ZnO, 90 wt.% ZnO – 10 wt.% CTO and 70 wt.% ZnO – 30 wt.% CTO sensor devices against 10, 20 and 40 ppm ethanol at 200, 250, 300, 350 and 400 °C.

Figure 5–15 shows that the conductive responses of the three sensor devices constituting the greatest concentration of ZnO: 100 wt.% ZnO, 90 wt.% ZnO – 10 wt.% CTO and 70 wt.% ZnO – 30 wt.% CTO, increased as a function of operating temperature; with the 100 wt.% ZnO sensor device exhibiting the highest response of 55.6 towards 40 ppm ethanol at 400 ºC. The responses of the two composite materials: 90 wt.% ZnO – 10 wt.% CTO and 70 wt.% ZnO – 30 wt.% CTO, under the same operating conditions, were not as profound as the pure ZnO counterpart. The chemiresistive behaviour (in the form of an increase in conductive behaviour) of the two composite materials, concurred with a report by Kim *et al*. [46]. The group reported that the conduction along composites, specifically nanocomposites, between p- and n-type oxide semiconductors, depends on the concentration, size and dispersion of the two phases. A limited number of p-type oxide particles dispersed discretely throughout the matrix of the host n-type semiconductor particles, influences the chemiresistivity of the device to be dominated by the n-type semiconductor particles located at the n-n and p-n interfaces. This reasoning explains the observed chemiresistive behaviour of both the 90 wt.% ZnO – 10 wt.% CTO and 70 wt.% ZnO – 30 wt.% CTO composites, whose conductivity is dominated by the ZnO particles. Previous reports on a ZnO-CuO composite system [89, 161, 288, 289, 320, 321] have also reported an observed transition from an n-type conduction regime for ZnO-rich compositions, to a p-type conduction regime for CuO–rich compositions. Such transitions have been accounted for by a switch from n-type grain connectivity to p-type grain connectivity.

Further observation of Figure 5–15 shows that the responses of both the 70 wt.% ZnO – 30 wt.% CTO and the 90 wt.% ZnO – 10 wt.% CTO devices are outperformed by the pure ZnO device, at operating temperatures in the range of 350 ºC – 400 ºC. At these higher temperatures, the response order of the three devices is dependent on the composition of ZnO and CTO, where greater ZnO, leads to a better response magnitude.

At lower operating temperatures of 200 ºC – 300 ºC however, the 90 wt.% ZnO – 10 wt.% CTO composite device outperformed the 100 wt.% ZnO and 70 wt.% ZnO – 30 wt.% CTO devices, exhibiting the best response of 7.6 against 40 ppm ethanol at 250 ºC, which was a 2.6-fold enhanced response compared to the pure ZnO counterpart, under the same operating conditions. Interestingly, the 70 wt.% ZnO-30 wt.% CTO sensor device exhibited baseline response ($R_0/R = 1$) towards all concentrations of ethanol, at all operating temperatures.

The enhanced response of the 90 wt.% ZnO – 10 wt. CTO composite sensor within the lower operating temperature range and that of the 100 wt.% ZnO sensor device within the higher operating temperature range, indicated the synergistic effect of both metal oxides as a function of operating temperature. This was apparent as ZnO is associated to poor response performance towards ethanol at lower operating temperatures (and effective response performance at high operating temperatures), and conversely CTO to enhanced response performance towards ethanol at low operating temperatures (and poor response performance at high operating temperatures); both trends of which will be discussed further in this section.

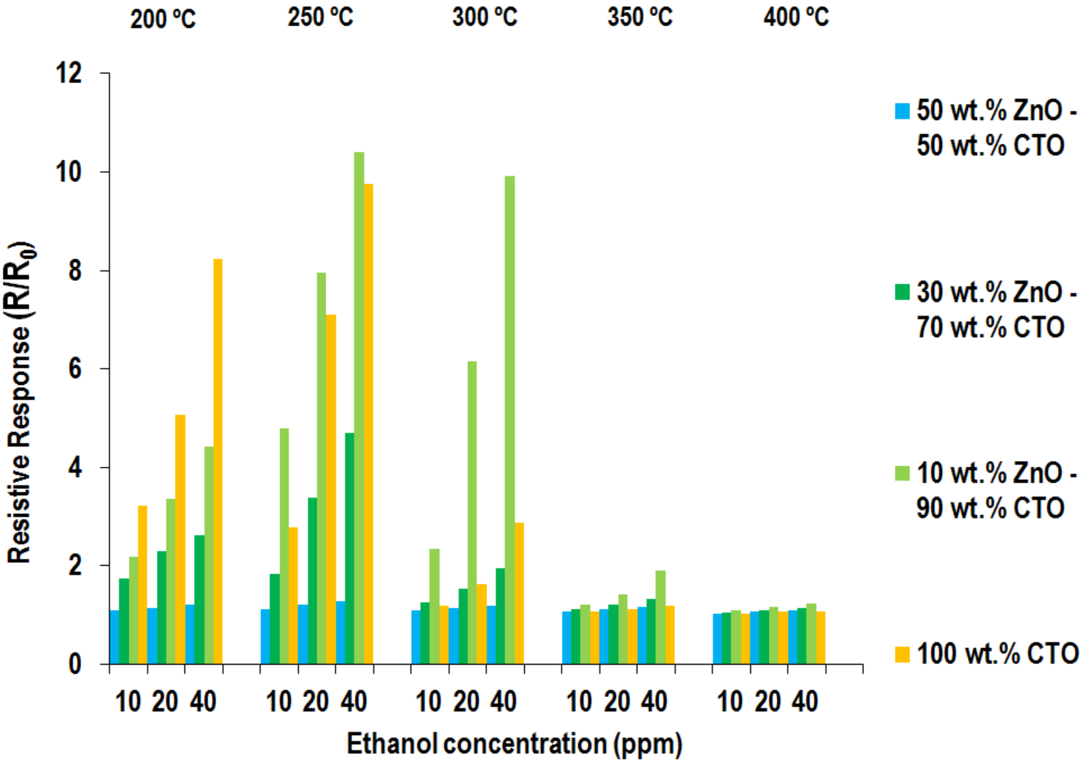

Figure 5–16. Resistive response of 50 wt.% ZnO – 50 wt.% CTO, 30 wt.% ZnO – 70 wt.% CTO, 10 wt.% ZnO – 90 wt.% CTO and 100 wt.% CTO sensor devices against 10, 20 and 40 ppm ethanol at 200, 250, 300, 350 and 400 °C.

Figure 5–16 shows an increase in resistive response of the 50 wt.% ZnO – 50 wt.% CTO, 30 wt.% ZnO – 70 wt.% CTO, 10 wt.% ZnO – 90 wt.% CTO and 100 wt.% CTO sensor devices when exposed to 10, 20 and 40 ppm of ethanol, at operating temperatures in the range of 200 °C – 500 °C.

This suggests that the conductivity of these devices was dominated by the p-type CTO particles. Again, this observation concurs with Kim *et al*. [46], who reported that as the concentration of p-type particles dispersed throughout n-type particles is increased, the percolative conduction path occurs along the p-type particles.

The same figure shows that all four sensors were associated to large magnitudes of resistive response towards ethanol, at the lower operating temperatures of 200 ºC – 300 ºC. However, at higher operating temperatures of 350 ºC – 400 ºC, all four devices performed poorly. This is a stark contrast to the response behaviour observed as function of temperature of the three n-type dominated sensors in Figure 5–15, which exhibited large conductive responses towards ethanol at 350 ºC – 400 ºC and significantly poorer responses in the temperature range of 200 ºC – 300 ºC. Figure 5–15 and Figure 5–

16 are therefore symmetrical to each other, presenting opposite response magnitude behaviours as a function of temperature modulation.

The observation of the enhanced response characteristics of ZnO towards ethanol, as a function of increasing operating temperature has been reported in the literature [69] and is accounted for by a greater conversion ratio of ethanol to acetaldehyde. The reaction of ethanol molecules on the surface of an n-type semiconductor such as ZnO [69], is characterised by the ethanol undergoing dehydrogenation, which yields acetal as the intermediate product, as opposed to a dehydration reaction in which ethene is the intermediate. The conversion of ethanol to acetal increases as a function of temperature, which ZnO is particularly responsive to.

The application of CTO as a sensor material for ethanol has been reported in many studies [126, 138], but reports of its performance against the analyte as a function of operating temperature, have not been found. However, the response behaviour of the metal oxide towards NH_3, as a function of temperature, was reported by Schmitt *et al.* [129]. They had reported the responses of an ink-jet printed CTO sensor towards increasing concentrations of NH_3 (10 ppm – 50 ppm) as a function of different operating temperatures in the range of 330 ºC – 570 ºC. In their study, it was found that the CTO sensor had the best response at the lower operating temperature of 330 ºC and the worst response at 570 ºC, which corroborates with the response behaviour observed in this study against ethanol. Both NH_3 and ethanol are combustible reducing gases and this indicates that their interaction chemistry is likely to be fundamentally similar with the CTO surface.

In a study by Suryawanshi *et al.* [292] the group had studied the gas response of Fe_2O_3-activated Cr_2O_3 thick-film sensors towards 10 ppm of NH_3 and ethanol (individually), as a function of increasing operating temperature in the range of 200 °C – 500 ºC. They had found that the response patterns of the modified Cr_2O_3 device towards both gases was very similar, with the optimal performance of the material observed to be at 250 ºC and 300 ºC, respectively. They had reported that the evenly distributed Fe_2O_3 defects upon the surface of the Cr_2O_3, would have made it possible to adsorb the oxygen ions at lower temperatures compared to pure Cr_2O_3. The adsorbed oxygen species are stable at these lower temperatures, possessing enough stability for the analyte molecules to interact with them before desorption, and in this way, the surface reactions progress. At higher temperatures however, the adsorption of the oxygen ions is likely to be very unstable with the thermodynamics promoting desorption of the species at a much faster rate, which lowers the chances of surface oxidation reactions of the target analytes, ultimately reducing the response performance of the sensor material. Analogously, the Ti ions with the matrix of the Cr_2O_3 in the CTO material, may have also promoted enhanced oxygen adsorption on the surface at lower operating temperatures, which may rationalise the better gas sensing behaviour of CTO towards ethanol at low temperatures. Another possible rationalisation, as observed with ZnO, could be that the CTO is more responsive to the intermediate products yielding from the surface oxidation reactions of ethanol, at lower operating temperatures.

Figure 5–16 shows that the 10 wt.% ZnO – 90 wt.% CTO composite sensor device was the best performing composite within the system, displaying a resistive response of 10.4 towards 40 ppm ethanol at 250 ºC, which is a 1.1-fold enhanced response with respect to the pure CTO counterpart under the same operating conditions. The same composite performed particularly well at 300 ºC, with a response of 9.9 toward 40 ppm ethanol at 300 ºC, which is a 3.4-fold enhanced response compared to the pure CTO counterpart.

The SEM micrograph of the 10 wt.% ZnO – 90 wt.% CTO composite sensor device observed in Figure 5–6 (k) and (l), showed evidence of the intimate mixing and dispersion of the ZnO particles within the CTO matrix, with the CTO particles coating the larger micron-sized ZnO particles. The visualisation of the packing structure associated to this composite, suggests the presence of mainly p-p homo- and some p-n hetero-junctions, but a rare number of n-n homo-junctions as observed in Figure 5–17.

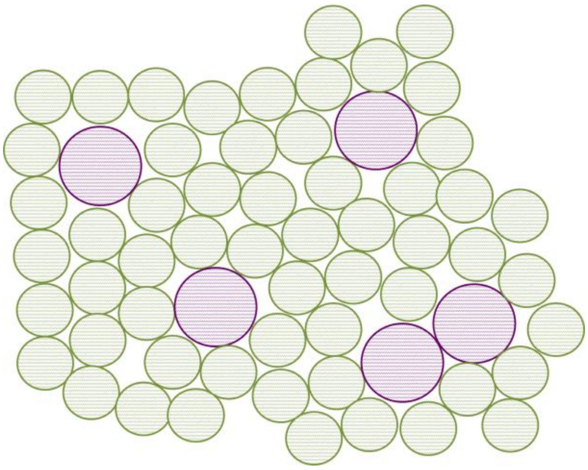

Figure 5–17. Schematic of packing structure of metal oxide grains in 10 wt.% ZnO - 90 wt.% CTO sensor device. In the diagram the green circles represent the smaller CTO particles and the larger purple circles, the larger ZnO particles. Although the diagram presents the grains to be perfectly spherical for simplicity, this perfect spherical nature is not assumed.

In accordance with Yamazoe *et al*. [170, 171] such a packing structure is a derivative of the stone-in-sand packing structure. Such packing between the grains is described to be no better, in terms of contact potential formation and its subsequent enhancement to the transduction function, than a random packing structure or packing structure dominated by homo-contacts. The ratio of the composition of ZnO : CTO in the composite, suggests that this composite is dominated by p-p homo-contacts that exist between the CTO grains, and therefore the enhanced response of this particular sensor device is surprising. However, the significant response may suggest that the localized p-n hetero-contacts between the CTO and ZnO grains within the composite matrix, are attributed to the formation of contact potentials between the hetero-junctions [170, 171], which may have greater influence over the conductivity of sensor device than the weaker p-type conductivity via the p-p percolation paths, and as such may act to enhance the transduction function of the device. Further, SEM micrographs of the sensor device seen in Figure 5–6 (k) and (l), showed the presence of loosely held grains within the sensor matrix, suggesting that the body, as well as the surface of material are accessible to the gas molecules. These factors may act synergistically to enhance the response behaviour of the device [70, 238].

In comparison to the response results of the CTO-ZnO system obtained against ethanol, Woo *et al.* [290] reported on the responsivity of ZnO–Cr_2O_3 hetero-nanostructures against a range of reducing gases, of which one was ethanol. From the range of hetero-structure architectures they had fabricated, the group had found that those based on the decoration of discrete p-type Cr_2O_3 nanoparticles on an n-type ZnO nanowire network, exhibited the best conductive response of 7 towards 5 ppm of ethanol at an operating temperature of 400 ºC. This response was a 2.2-fold enhanced response in comparison to pure ZnO nanowires. The second type of hetero-structure architectures they fabricated were ZnO (core) - Cr_2O_3 (shell) nanocables, which exhibited a resistive response of just over 1 towards 5 ppm ethanol at 400 ºC. The CTO –ZnO composites (displaying p-type behaviour) fabricated in this thesis, are comparable to Woo *et al.*'s nanocable based hetero-structures. Comparatively, the 10 wt.% ZnO – 90 wt.% CTO device (the best performing composite) was attributed to a resistive response of 1.2 towards 10 ppm ethanol at 200 ºC and exhibited a response of just above 1 at 400 ºC. However the same device was attributed to a response as high as 4.8 towards 10 ppm ethanol at 250 ºC, suggesting that its response towards 5 ppm of the analyte at 250 ºC, is likely to be higher than that achieved by the nanocables towards the same concentration of ethanol at 400 ºC.

Comparison of Woo *et al.*'s Cr_2O_3 nanoparticle decorated ZnO nanowires (displaying n-type behaviour) to the CTO-ZnO composites which displayed n-type behaviour, show that the hetero-structures from the literature study are better performers. The 90 wt.% ZnO – 10 wt.% CTO device (the best n-type dominated composite), displayed a response of 3.5 at 400 ºC towards 10 ppm ethanol. In contrast, Woo *et al.* were able to achieve a response of 7 to ½ the concentration of the analyte (5 ppm) at the same operating temperature. The group [290] had related the enhanced responsivity of the Cr_2O_3 nanoparticle decorated ZnO nanowire architecture, to be associated to a multiple number of factors. The first was a low agglomerated porous network structure of the nanowire based architectures, which allowed diffusion of the analyte to the entire sensing surface. The second was effectively the packing structure in the form of a uniform loading of the p-type Cr_2O_3 catalysts on the surface of the n-type nanowires, which allowed for the enlargement of the conduction path, which acted to enhance the transduction function. Thus, they had reported that this uniform deposition of a discrete configuration of p-type semiconductor nanostructures on the surface of the n-type semiconductor nanowires, was a powerful tool to achieve enhanced sensor performance.

In comparison to the 10 wt.% ZnO – 90 wt.% CTO device, the SEM micrograph of the 30 wt.% ZnO – 70 wt.% CTO composite observed in Figure 5–6 (i) and (j), which also displayed a p-type response behaviour, was seen to consist of a greater concentration and agglomeration of ZnO particles, accounted for by the increased ratio of ZnO : CTO particles. The increased concentration of the ZnO particles in this material, also suggests that they are likely to have been more delocalised within the sensor matrix in comparison to the 10 wt.% ZnO – 90 wt.% CTO device, where the ZnO particles are likely to be more localised. A schematic of this device is shown in Figure 5–18.

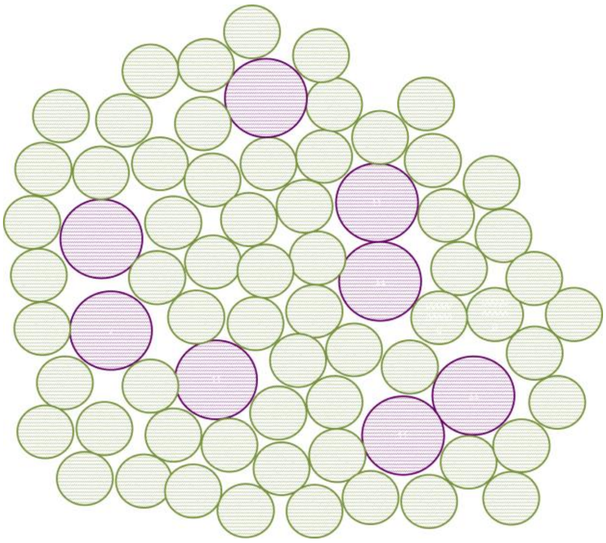

Figure 5–18. Schematic of packing structure of metal oxide grains in 30 wt.% ZnO - 70 wt.% CTO sensor device. In the diagram the green circles represent the smaller CTO particles and the larger purple circles, the larger ZnO particles. Although the diagram presents the grains to be perfectly spherical for simplicity, this perfect spherical nature is not assumed.

With a greater number of ZnO particles dispersed within a host matrix of CTO particles, the 30 wt.% ZnO – 70 wt.% CTO sensor is likely to be associated to a mixture of p-p and n-n homo- and p-n hetero-junctions. The increased n-n junction concentration induced by ZnO–ZnO grain contacts, may have acted to negate the enhancement effects of the p-n hetero-contacts and as such, reduce the transduction function of the sensor device, accounting for its poor performance in comparison to the 10 wt.% ZnO – 90 wt.% CTO composite. Yamazoe *et al*. [170, 171] suggested that only by competitively increasing the hetero-contact frequency with respect to the homo-contact frequency, would one really observe the hetero-junction enhancement effects, and such an increase can be achieved by optimising the packing structure. In the case of the 30 wt.% ZnO – 70 wt.% CTO sensor, the hetero-contacts potentially competed with the homo-contacts, which suggest difficulty in observing significant hetero-junction enhancement effects.

Of particular interest, were the response behaviours of both the 70 wt.% ZnO – 30 wt.% CTO device in Figure 5–15 and the 50 wt.% ZnO – 50 wt.% CTO device in Figure 5–16, which both exhibited response magnitudes of less than 2.5 towards all concentrations of ethanol, across all temperature ranges. Their almost negligible response magnitudes suggested that although their response behaviour was dominated by the n-type oxide in the case of the 70 wt.% ZnO – 30 wt.% CTO device, and by the p-type oxide in the case of the 50 wt.% ZnO – 50 wt.% CTO device, there was an overall cancellation effect [210]. This cancellation effect indicated significant contributions of both the p- and n- type oxides in each composite, negating the overall response signals.

Further the SEM micrographs of both the 70 wt.% ZnO – 30 wt.% CTO device and the 50 wt.% ZnO – 50 wt.% CTO device, observed in Figure 5–6 (e) & (f) and (g) & (h), respectively, show evidence of agglomeration of the ZnO and CTO particles into clusters rather than a more heterogeneous distribution of the particles amongst each other. Thus, the packing structure [170, 171] within both composites suggested minimal p-n junction formation and the greater statistical formation of n-n and p-p junctions, which are likely to promote cancellation effects due to a cancellation of n-type percolation paths and the p-type percolation paths. This behaviour was particularly evident in the 50 wt.% ZnO – 50 wt.% CTO sensor device, which showed all resistive responses to be close to baseline response ($R/R_0 = 1$).

Such cancellation behaviour has been reported by Savage *et al*. [161] on a semiconducting n-p titanium oxide system. In their investigation, certain mixtures of n-type anatase and p-type rutile resulted in minimal resistance change towards CO and CH_4. They had reported that based on a polychromatic percolation model, the two parallel conduction pathways based on n-n and p-p paths, with the particular ratios of mixtures they had investigated, cancelled each other out. In a similar study by Sun *et al*. [210], who reported on the gas sensing properties of WO_3 and Cr_2O_3 composites, they had found that a particular ratio of a WO_3 : Cr_2O_3 mixture (9:1 w/w) was attributed to a response transient with minimal resistance change towards 20 ppm CO. This feature they explained was due to a cancellation effect due to the interference of p- and n-type percolation paths. In their case, the cancellation trace (an effect that occurs due to cancellation of conduction that occur along the n-type percolation paths with that which occurs along the p-type percolation paths) was more explicit, in comparison to the result presented in this thesis, with half the resistance curve split into an observed increase in resistance and half into an observed decrease in resistance.

In another study by Bekermann *et al.*[169] the gas sensing properties of Co_3O_4 - ZnO nano-composites towards a range of analytes, which included ethanol, were reported. In their study they had varied the over-dispersion time via PECVD (Plasma-Enhanced Chemical Vapour Deposition) of Co_3O_4 on ZnO. They had found that greater thickness of Co_3O_4 on ZnO, resulted in the lowering of the response magnitude of the composite material towards the target analytes, in comparison to a composite consisting of a thinner layer of Co_3O_4 on ZnO. They had explained the poor performance of the composite containing the thicker layer of Co_3O_4 to be influenced by an electrical cancellation effect of the p- and n-type materials [169, 210].

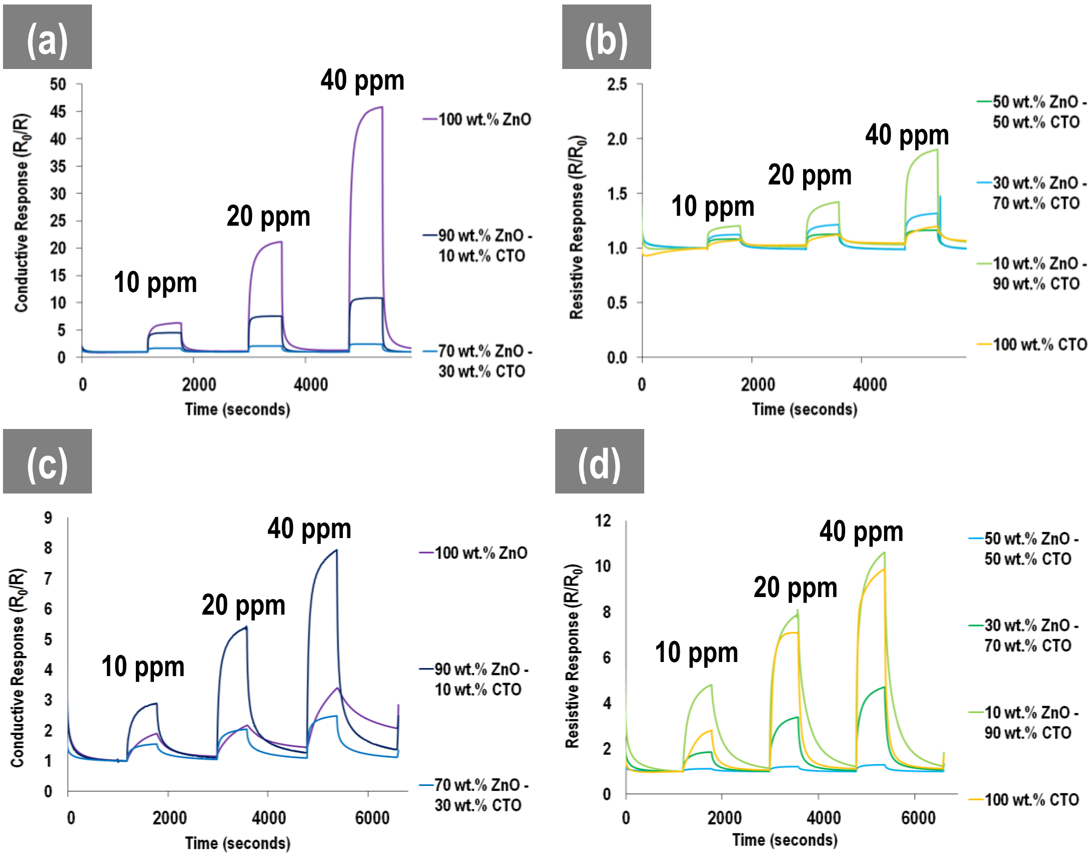

Figure 5–19. (a) Conductive response traces of 100 wt.% ZnO, 90 wt.% ZnO – 10 wt.% CTO and 70 wt.% ZnO – 30 wt.% CTO sensor devices at 350 ºC, (b) Resistive response traces of 50 wt.% ZnO – 50 wt.% CTO, 30 wt.% ZnO – 70 wt.% CTO, 10 wt.% ZnO – 90 wt.% CTO and 100 wt.% CTO sensor device at 350 ºC, (c) Conductive response traces of 100 wt.% ZnO, 90 wt.% ZnO – 10 wt.% CTO and 70 wt.% ZnO – 30 wt.% CTO sensor devices at 250 ºC and (d) Resistive response traces of 50 wt.% ZnO – 50 wt.% CTO, 30 wt.% ZnO – 70 wt.% CTO, 10 wt.% ZnO – 90 wt.% CTO and 100 wt.% CTO sensor at 250 ºC, all against increasing concentrations of ethanol.

The response traces for the CTO – ZnO sensor system against ethanol are presented in Figure 5–19 at operating temperatures of 350 ºC (Figures (a) and (b)) and 250 ºC (Figures (c) and (d)). Tabulation of the mean responses values of the sensor devices in the CTO-ZnO system from the repeat tests against exposure towards the various ethanol concentrations at 350 °C and 250 °C and the associated 95% confidence intervals have been presented in Table 5–3 and Table 5–4, respectively.

Table 5–3. Average responses of sensor devices in CTO-ZnO system from all repeat tests against various ethanol concentrations at 350 °C and associated errors in the form of 95% CIs.

	10 ppm		**20 ppm**		**40 ppm**	
Device	Average Response	95% CI	Average Response	95% CI	Average Response	95% CI
100 wt.% CTO	1.04	±0.03	1.08	±0.04	1.15	±0.05
90 wt.% CTO – 10 wt.% ZnO	1.14	±0.06	1.32	±0.10	1.69	±0.21
70 wt.% CTO – 30 wt.% ZnO	1.11	±0.01	1.20	±0.01	1.30	±0.02
50 wt.% CTO – 50 wt.% ZnO	1.08	±0.01	1.12	±0.01	1.16	±0.00
30 wt.% CTO – 70 wt.% ZnO	1.63	±0.05	2.00	±0.10	2.29	±0.14
10 wt.% CTO – 90 wt.% ZnO	4.31	±0.21	7.02	±0.71	9.95	±1.24
100 wt.% ZnO	6.69	±0.37	22.41	±2.41	Electronic capping out	

Table 5–4. Average responses of sensor devices in CTO-ZnO system from all repeat tests against various ethanol concentrations at 250 °C and associated errors in the form of 95% CIs.

	10 ppm		**20 ppm**		**40 ppm**	
Device	Average Response	95% CI	Average Response	95% CI	Average Response	95% CI
100 wt.% CTO	3.10	±0.54	7.24	±0.33	10.10	±0.40
90 wt.% CTO – 10 wt.% ZnO	4.69	±0.23	7.63	±0.93	10.10	±1.03
70 wt.% CTO – 30 wt.% ZnO	1.89	±0.07	3.34	±0.08	4.68	±0.06
50 wt.% CTO – 50 wt.% ZnO	1.12	±0	1.21	±0	1.29	±0
30 wt.% CTO – 70 wt.% ZnO	1.56	±0	2.02	±0.05	2.45	±0.07
10 wt.% CTO – 90 wt.% ZnO	2.84	±0.12	5.18	±0.49	7.61	±0.67
100 wt.% ZnO	2.01	±0.21	2.29	±0.24	3.69	±0.56

A change in the operational temperature of the system, showed a clear distinction in the response trace characteristics of the sensor devices. The faster responses at 350 ºC (Figures (a) and (b)) were observed by the steep increases in magnitude of the responses, upon switching on ethanol gas. In contrast, the response traces at 250 ºC (images (c) and (d)) were seen to increase in magnitude more gradually, upon introduction of ethanol.

The recoveries of the traces back to baseline response were also indicative of the temperature dependent kinetics; at 250 ºC for example, upon switching off the individual ethanol pulses, the return of the response signals were seen to be very gradual (shallow gradient), and in some cases, particularly with the ZnO dominant sensors, the signals did not have enough time to settle completely (baseline drift), before a new concentration pulse of ethanol was introduced. This shows that the lower temperature of operation did not provide sufficient thermal energy to promote rapid desorption of the ethanol molecules from the surface of the metal oxide materials. Further it suggests that at 250 ºC, the time given for the sensor to recover was not enough. The incomplete recovery of some of these sensing materials, particularly those dominated by ZnO, suggests that the sensor surfaces were pre-conditioned with ethanol molecules, prior to exposure to a new concentration pulse of the analyte. This pre-conditioning effectively artificially increased the response magnitudes of some of the devices with increasing concentrations of ethanol, suggesting an over-estimation of their response values.

At 350 ºC, the recovery of the response of the CTO dominant devices was steep, sharp and reversible [169], with the CTO dominant composites such as the 90 wt.% CTO – 10 wt.% ZnO sensor device associated to a t_{-90} (40 ppm) of 47 seconds and the 70 wt.% CTO – 30 wt.% ZnO associated to a t_{-90} (40 ppm) of 51 seconds and the CTO device itself associated to a t_{-90} (40 ppm) of 16 seconds. The signals of these CTO dominant devices were observed to reach baseline response in time before the next pulse of ethanol exposure. However at the same operating temperature, the 100 wt.% ZnO device was associated to a t_{-90} (40 ppm) of 640 seconds and the 90 wt.% ZnO – 10 wt.% CTO device to a t_{-90} (40 ppm) of 288 seconds (seen in Figure 5–19 (a)), indicating that the return of the signals to baseline of these ZnO dominated devices, was slower. At 250 ºC, the ZnO dominant composites in Figure 5–19 (c) were observed to be associated to greater baseline drift than the CTO dominant composites devices in Figure 5–19 (d). CTO possesses greater resistance to humidity effects and therefore is attributed to more stable response characteristics under slight variations of humidity [47, 120].

In general, comparison of the speed of the kinetics of response and recovery between the different operating temperatures was deduced through comparison of the t_{90} and t_{-90} values of the sensor devices. For example, the t_{90} (20 ppm) of the 100 wt.% ZnO sensor device at 350 °C was 177 seconds and at 250 °C was 363 seconds. Similarly the recovery time t_{-90} (20 ppm) of the same device at 350 °C was 504 seconds and at 250 °C was 543 seconds. The t_{90} (20 ppm) of the 90 wt.% ZnO – 10 wt.% CTO device was 35 seconds at 350 °C and 214 seconds at 250 °C. The same device showed a recovery t_{-90} (20 ppm) of 255 seconds at 350 °C and 745 seconds at 250 °C.

The 90 wt.% CTO – 10 wt.% ZnO sensor device was associated to a t_{90} (40 ppm) of 78 at 350 °C and 235 at 250 °C. The same device exhibited a t_{-90} (40 ppm) of 47 seconds at 350 °C and a t_{-90} (40 ppm) of 980 at 250 °C. The 100 wt.% CTO sensor device was associated to a t_{90} (40 ppm) of 24 at 350 °C and 180 at 250 °C, with t_{-90} (40 ppm) values of 16 and 561 at 350 °C and 250 °C, respectively. These comparisons give evidence of the reduced surface kinetics of the surface reactions, as a function of decreasing operating temperature.

Figure 5–19 illustrates the contrast in the shapes of the response traces of the ZnO heavy composites between Figure 5–19 (a) and (c), with respect to 350 and 250 ºC, respectively. At 250 ºC, the 100 wt.% ZnO sensor for example, is seen to be associated to an obvious shark fin [33] shape associated to an unsaturated surface and slow response behaviour. In contrast at 350 ºC, the shape of the ZnO response curve, as well the two other composite materials, is associated to a cross between shark-fin and box type [106] behaviour, and thus greater saturation of the sensor surfaces and faster response behaviour. The geometry of the response traces at the lower temperature, can be accounted for by reduced thermal energy which results in slower reaction kinetics of the ethanol molecules with the adsorbed oxygen ions on surface of the metal oxide, i.e. a smaller yield of surface reactions per unit time, hence a slower response is observed. At higher temperatures, more energy in the system implies faster kinetics, resulting in a greater yield of surface reactions per unit time. The near steady-state behaviour of the sensor devices at 350 ºC, evident from the flattening of the response traces, also indicated kinetically balanced surface adsorption and desorption reactions, suggesting the rate of the reaction of the ethanol molecules with the surface adsorbed oxygen species was as fast as the subsequent formation and instantaneous desorption of the reaction products – an influence of the thermodynamics of the operating temperature.

5.2.4.2 NO_2 Sensing

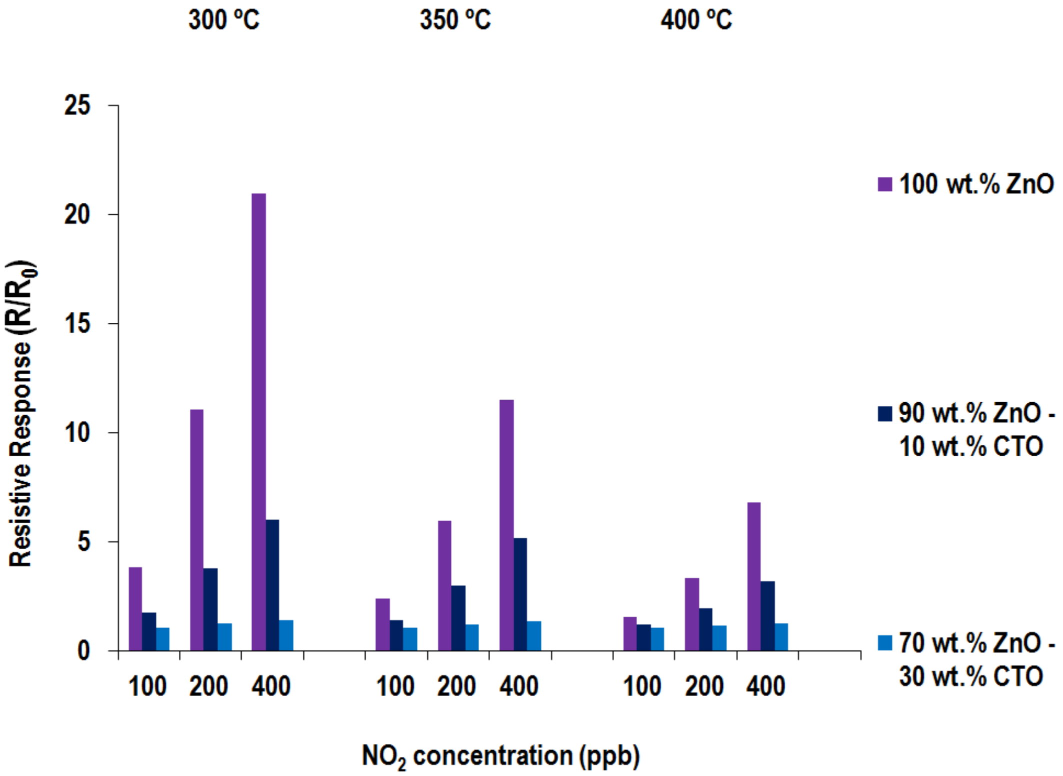

Figure 5–20. Resistive response of 100 wt.% ZnO, 90 wt.% ZnO – 10 wt.% CTO and 70 wt.% ZnO – 30 wt.% CTO sensor devices against 100, 200 and 400 ppb NO_2 at 300, 350 and 400 °C.

Figure 5–20 presents the resistive responses of the 100 wt.% ZnO, 90 wt.% ZnO – 10 wt.% CTO and 70 wt.% ZnO – 30 wt.% CTO sensor devices against varying concentrations of NO_2 as a function of increasing operating temperature. The increase in the resistive response of the two composite sensor devices: 90 wt.% ZnO – 10 wt.% CTO and 70 wt.% ZnO – 30 wt.% CTO, concurs with observations presented earlier towards ethanol, but in contrast here the conductivity of the both composites was dominated by the n-type ZnO particles.

The figure further shows that the 100 wt.% ZnO sensor device dominated the response, exhibiting a maximum resistive response of 21 towards 400 ppb NO_2 at 300 ºC, with its responsivity decreasing as a function of increasing operating temperature. The two composite materials in contrast, showed significantly lower responses across the range of operational temperatures, with respect to the 100 wt.% ZnO sensor device, with their responses decreasing as a function of decreasing concentration of ZnO and increasing operating temperature.

Interestingly the three sensor devices in Figure 5–20 exhibited opposite response characteristics towards NO_2, as a function of operating temperature, in comparison to that observed against ethanol in Figure 5–15. Against the reducing gas, the conductive response of the sensors increased as a function of increasing operating temperature, whereas against the oxidising gas, a decrease in resistive response was observed as a function of increasing operating temperature. Thus, the results show that the selectivity of these three devices of the system, towards the reducing or oxidising gas can be controlled as a function of temperature modulation, which from a point-of-view of practical applications, is very useful in a mixed-gas atmosphere. Bekermann *et al*. [169] had reported a similar observation in their study on the gas sensing properties of Co_3O_4 - ZnO nano-composites. They had reported greater selectivity of their composites towards 100 ppm ethanol and 500 ppm acetone at higher operating temperatures (400 °C) and better selectivity towards 5 ppm NO_2 at lower operating temperatures (200 °C). Such characteristics they reported, are of interest in view of technological exploitation of their sensors in mixed gas atmospheres, which are usually present in real world conditions.

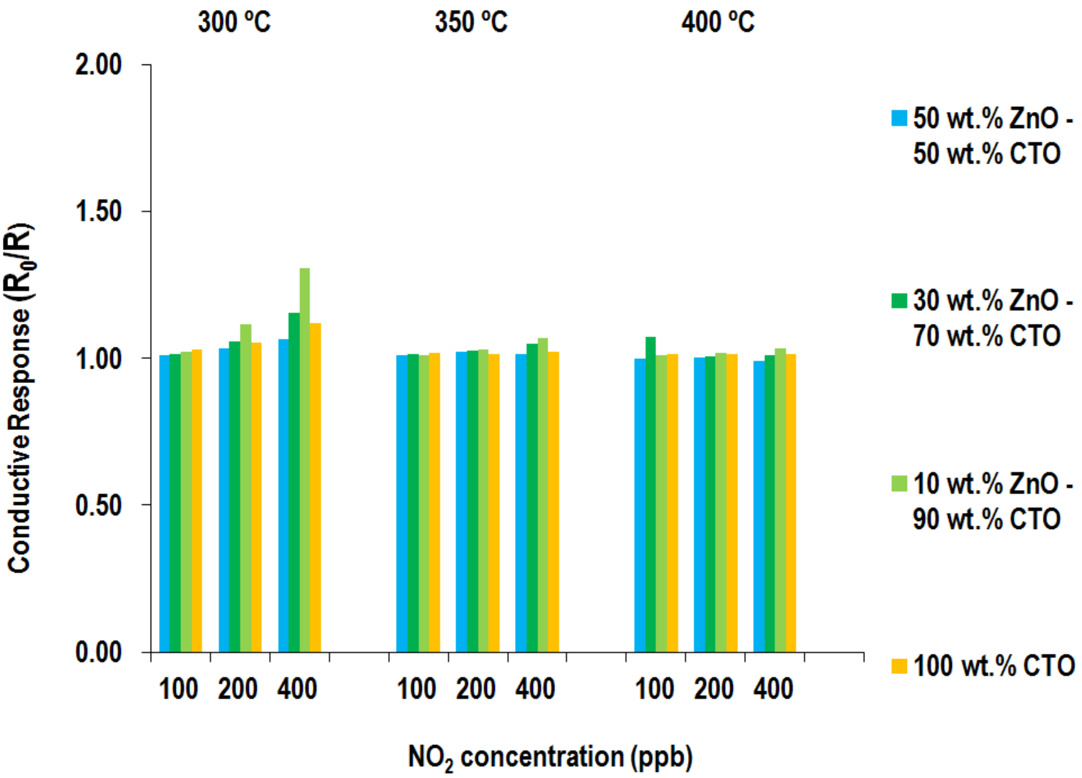

Figure 5–21. Conductive response of 50 wt.% ZnO – 50 wt.% CTO, 30 wt.% ZnO – 70 wt.% CTO, 10 wt.% ZnO – 90 wt.% CTO and 100 wt.% CTO sensor devices against 100, 200 and 400 ppb NO_2 at 300, 350 and 400 °C.

Figure 5–21 presents the conductive response characteristics of the 50 wt.% ZnO – 50 wt.% CTO, 30 wt.% ZnO – 70 wt.% CTO, 10 wt.% ZnO – 90 wt.% CTO and 100 wt.% CTO sensor devices as a function of increasing operating temperature. Of the four devices, the 10 wt.% ZnO – 90 wt.% CTO composite sensor exhibited minimal enhancement in response characteristics, with a response of 1.3 observed towards 400 ppb of NO_2 at 300 ºC. The responses observed by the four sensors here dominated by p-type behaviour were very poor and as such can practically be negated, particularly in comparison to the three devices dominated by n-type behaviour presented in Figure 5–20. However, the enhanced response of the 10 wt.% ZnO – 90 wt.% CTO composite demonstrated the enhancement effect of the hetero-junction nature of the materials.

Comparison of Figure 5–16 and Figure 5–21 showed that the four sensors dominated by p-type conduction displayed a decrease in response as a function of increasing operating temperature against both ethanol and NO_2. The four sensors were seen to exhibit selectivity towards ethanol at 300 °C and 350 °C, with significantly poorer responses observed towards NO_2 at the same operating temperatures. No selectivity however was observed at 400 °C. Therefore, in a mixed atmosphere of both analytes, these four sensors would selectively detect ppm levels of ethanol at the lower operating temperature range.

In general, the response properties of the CTO-ZnO system, showed that they are better suited for the detection of ethanol compared to NO_2. The 100-fold concentration difference between both analytes may have been a key factor which significantly contributed to the variation in response magnitudes observed. Response characteristics of the CTO-ZnO composite system against both ethanol and NO_2, showed that the sensors dominated by n-type percolation paths were associated to significantly better gas sensing responses in comparison to those sensors whose conductivity was dominated by the p-type percolation paths. Hubner *et al*. [46, 278] reported that the response of a p-type MOS gas sensor to a given gas is equivalent to the square root of that of an n-type MOS gas sensor, towards the same gas, if the morphological configuration of both sensor materials are identical. The reasoning behind this is due to difference in the layers i.e. EDL vs. HAL, which dominate the resistance/conduction of the individual metal oxides, details of which were alluded to earlier in the introduction of this Chapter. Although the morphological configurations of the CTO and ZnO metal oxides were not observed to be the same in this thesis, the poor performance of the p-type semiconducting oxide with respect to the n-type semiconducting oxide is consistent with the experimental results observed and is independent of the morphology.

In comparison to the 10 wt.% ZnO – 90 wt.% CTO composite, which showed a 1.2-fold enhanced conductive response compared to the pure CTO counterpart, against 400 ppb NO_2 at 300 °C as seen in Figure 5–21, Bekermann *et al*.[169] achieved a maximum resistive response of 1.1 from their Co_3O_4 – ZnO nano-composite system, when exposed to 5 ppm NO_2 at an operating temperature of 200 ºC. This highest response against NO_2 was achieved with minimum p-type Co_3O_4 loading in their nano-composite, and as the loading of the Co_3O_4 increased, they observed a decrease in resistive response magnitude. They had attributed this decrease to two factors; the first being the increased Co_3O_4 particle size and the second being the reduced system porosity as a function of increased Co_3O_4 loadings. In significant contrast, the CTO-ZnO composite study here showed that the general trend of the composites exhibiting p-type conductive behaviour, was an increase in conductive response towards NO_2 as a function of increasing CTO composition.

Similarly, in a study of a p-n junction system based on a Carbon Nanotube (CNT) - WO_3 nano-composite grown by thermal CVD, Hashishin *et al*. [322] had reported on the gas sensing properties of NO_2. They found that a 0.1 wt.% WO_3 – CNT composite exhibited a conductive behaviour towards the oxidising gas, suggesting that the conductivity of the material occurred through the apparent p-type CNT. The composite was associated with a response of 3.8 towards 5 ppm NO_2 at an operating temperature of 200 ºC [322], which was a 3.6-fold enhanced response in comparison to the pure CNT sensor. They had accounted for the enhanced response of the material through the formation of p-n junctions within that particular composite, which generated a large depletion layer within the CNT, resultantly inducing a large resistance of the material. The highly depleted surface state of the CNT increased the amount of NO_2 adsorption on the surface of the CNT, resulting in a higher response towards the oxidising analyte. With an increased loading of WO_3, for example higher than 1 wt.% WO_3, the conductivity was seen to be dominated by the connections between the WO_3 grains and resultantly, the number of the p-n hetero-junctions decreased and n-n homo-junctions increased. A 7 wt.% WO_3 – CNT composite displayed a conductive response of only 1, however given that WO_3 is an n-type semiconductor, presentation of this material's resistive response magnitude would have been a better representation of the gas sensing performance of the material. This reasoning suggests that despite the 10 wt.% ZnO – 90 wt.% CTO composite being dominated by the CTO homo-contacts i.e. p-p homo-junctions, the localised p-n hetero-junctions between the CTO and ZnO grains within the matrix of the sensor material, are likely to be associated to enhanced resistances due to the formation of contact potentials, enhancing the responsivity of the overall material to the surrounding NO_2 atmosphere. It is also suggests that from the group of p-typed dominated devices, this particular ratio of ZnO : CTO is the optimal combination of both metal oxides, to obtain enhanced responsivities.

Figure 5–22 presents the response traces of the composite system towards increasing NO_2 concentrations at an operating temperature of 300 ºC, which was the optimal performance temperature of all devices in the CTO-ZnO system, against the analyte. Tabulation of the mean responses values of the sensor devices in the CTO-ZnO system from the repeat tests against exposure towards the various NO_2 concentrations at 300 °C and the associated 95% confidence intervals have been presented in Table 5–5.

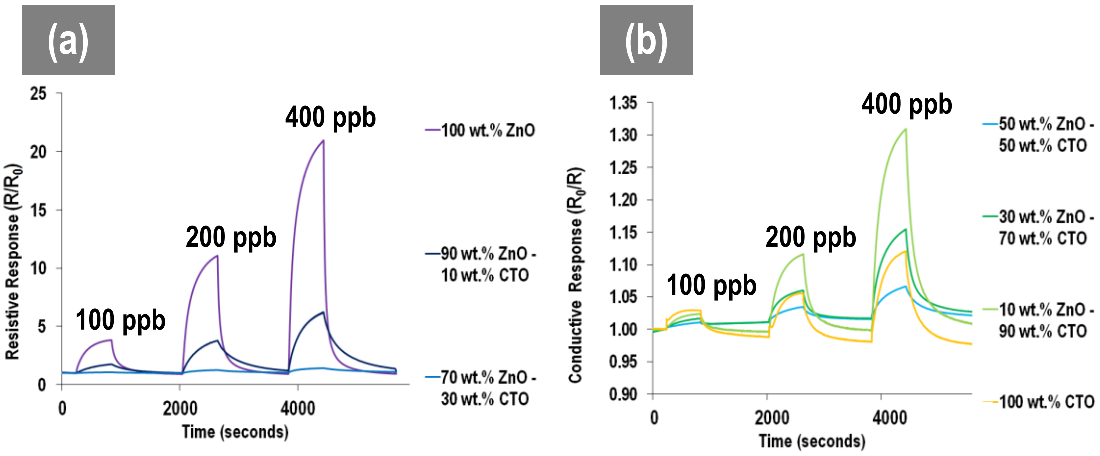

Figure 5–22. (a) Resistive response traces of 100 wt.% ZnO, 90 wt.% ZnO – 10 wt.% CTO and 70 wt.% ZnO – 30 wt.% CTO sensor devices and (b) Conductive response traces of 50 wt.% ZnO – 50 wt.% CTO, 30 wt.% ZnO – 70 wt.% CTO, 10 wt.% ZnO – 90 wt.% CTO and 100 wt.% CTO sensor devices towards 100, 200 and 400 ppb NO_2, at 300 ºC.

Table 5–5. Average responses of sensor devices in CTO-ZnO system from all repeat tests against various NO_2 concentrations at 300 °C and associated errors in the form of 95% CIs.

	100 ppb		**200 ppb**		**400 ppb**	
Device	Average Response	95% CI	Average Response	95% CI	Average Response	95% CI
100 wt.% CTO	1.03	±0	1.07	±0.01	1.13	±0.01
90 wt.% CTO – 10 wt.% ZnO	1.03	±0.01	1.13	±0.02	1.33	±0.03
70 wt.% CTO – 30 wt.% ZnO	1.02	±0	1.07	±0.01	1.16	±0.02
50 wt.% CTO – 50 wt.% ZnO	1.01	±0	1.04	±0.01	1.07	±0
30 wt.% CTO – 70 wt.% ZnO	1.08	±0.02	1.27	±0.01	1.19	±0.48
10 wt.% CTO – 90 wt.% ZnO	1.83	±0.16	3.78	±0.03	6.09	±0.27
100 wt.% ZnO	4.07	±0.47	10.65	±0.83	19.76	±2.40

The shark fin behaviour of all devices within the system, illustrates their slow response towards increasing concentrations of the analyte, which may be accounted for by the low operating temperature, relative to higher temperatures of 400 °C - 500 ºC. This lower operating temperature encourages slower kinetics of the surface reactions, which in turn slows down the resulting resistance change of the materials. Such slow kinetic behaviour is also illustrated through the gradual increasing gradient of the response curves, when NO_2 is switched on and their slow recovery to baseline response when the gas is switched off. The shark-fin behaviour also suggested the lack of saturation of the metal oxide surface sites, which may be accounted for by the lower concentration of NO_2 exposure for the available number of surface sites in the gas sensitive materials. In contrast, the response traces in Figure 5–19 exhibited significantly more saturated responses towards ethanol, particularly at 350 °C. This may be accounted for by the higher temperature of operation which would have likely promoted increased kinetics of surface adsorption and desorption reactions and subsequently increased the corresponding yield of resistance change per unit time. Further the higher concentration of exposure of ethanol would have also promoted greater saturation of surface sites.

In comparison to the response magnitudes of the 100 wt.% ZnO and 90 wt.% ZnO – 10 wt.% CTO devices, Figure 5–20 shows that the 70 wt.% ZnO – 30 wt.% CTO device exhibited minimal increase in response amplitude, towards all concentrations of NO_2 across the range of temperatures it was operated at, with the device seen to exhibit resistive responses between baseline response ($R/R_0 = 1$) and 2.5. Poor behaviour of this device was also observed towards ethanol as seen in Figure 5–15 and suggested effects of cancellation [210] between the n-type and p-type dominated percolation paths, which may have contributed to the low response magnitudes. Domination of cancellation behaviour in the 50 wt.% ZnO – 50 wt.% CTO sensor device was particularly apparent from Figure 5–21, as it exhibited resistive responses, equivalent to or just above baseline response ($R/R_0 = 1$), towards all concentrations of NO_2, at all operating temperatures.

In this study, cancellation effects were observed to be apparent against both ethanol and NO_2. However if the effect had been more dominant towards one analyte than the other, then selectivity due to cancellation could potentially be exploited in a mixed ethanol and NO_2 atmosphere. Such a selectivity by cancellation phenomenon was observed by Sun *et al*. [210] who had reported that within their system of WO_3 and Cr_2O_3 composites, the composite which had a 9 : 1 w/w WO_3 : Cr_2O_3 ratio, showed cancellation behaviour for 20 ppm CO, however towards 2, 5 and 10 ppm NO, the composite exhibited a marked change in resistance. This example demonstrates that in a mixed atmosphere of 20 ppm CO and 2, 5 or 10 ppm NO, their 9:1 w/w WO_3:Cr_2O_3 composite could potentially be exploited to selectively detect NO.

5.2.5 Further Gas Sensing Studies

Further gas sensing studies of the CTO – ZnO composite system were conducted towards a range of reducing gases including: acetone, CO, NH_3 and toluene (and ethanol which was evaluated earlier in the Chapter), at operating temperatures of 300 °C and/or 350 °C. Both these temperatures were associated to the system of sensors exhibiting stable baseline response behaviour against ethanol and were temperatures at which contributory behaviour of both metal oxides was observed. In terms of optimal response temperatures for devices exhibiting p-type behaviour, this was 250 °C, however at this temperature the devices dominated by n-type behaviour, showed poor responsivities toward ethanol, and further, their baseline stability was very poor. The optimal response temperature for the devices exhibiting n-type behaviour was 400 °C, however at this temperature the devices attributed to p-type behaviour, showed poor responsivities toward ethanol. Thus temperatures of 300 °C and 350 °C were temperatures at which both types of devices showed contributory behaviour of both metal oxides and so were chosen to conduct further gas sensing studies against the range of reducing gases.

Focus was on testing the system against various concentrations of acetone and toluene, as the system proved to be poor at responding towards significant concentrations of CO and NH_3, with response magnitudes seen to be ranging between baseline response (1) and 2, as observed in Figure 5–23 and Figure 5–24, respectively. Tabulation of the mean responses values of the sensor devices in the CTO-ZnO system from the repeat tests against exposure towards the various CO concentrations at 350 °C and the associated 95% confidence intervals have been presented in

Table 5–6.

5.2.5.1 CO Sensing

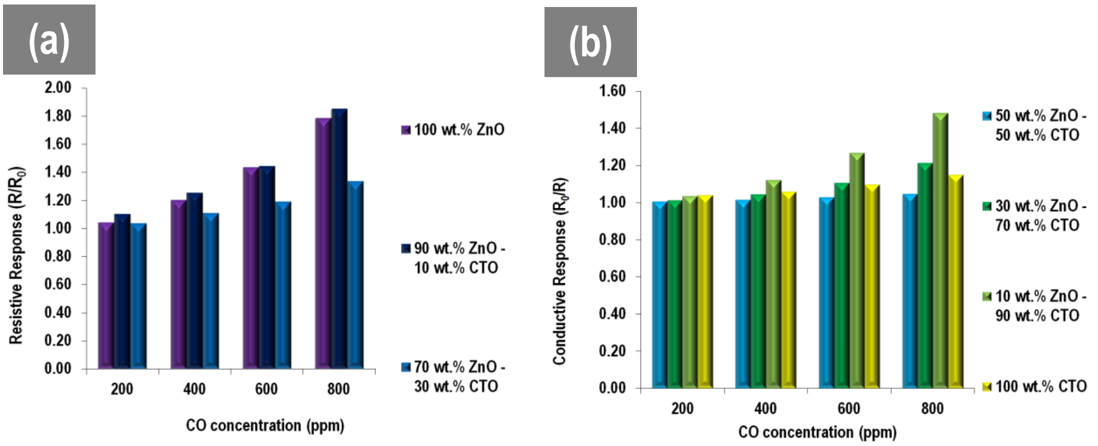

Figure 5–23. (a) Resistive response of 100 wt.% ZnO, 90 wt.% ZnO – 10 wt.% CTO, 70 wt.% ZnO – 30 wt.% CTO and (b) Conductive response of 50 wt.% ZnO – 50 wt.% CTO, 30 wt.% ZnO – 70 wt.% CTO, 10 wt.% ZnO – 90 wt.% CTO and 100 wt.% CTO sensor devices against 200, 400, 600 and 800 ppm CO at an operating temperature of 350 °C.

Table 5–6. Average responses of sensor devices in CTO-ZnO system from all repeat tests against various CO concentrations at 350 °C and associated errors in the form of 95% CIs.

	200 ppm		**400 ppm**		**600 ppm**		**800 ppm**	
Device	Average Response	95% CI	Average Response	95% CI	Average Response	95% CI	Average Response	95% CI
100 wt.% CTO	1.02	±0.02	1.05	±0.01	1.09	±0.01	1.14	±0.02
90 wt.% CTO – 10 wt.% ZnO	1.03	±0	1.12	±0.01	1.26	±0.02	1.47	±0.04
70 wt.% CTO – 30 wt.% ZnO	1.01	±0	1.04	±0	1.09	±0.01	1.19	±0.03
50 wt.% CTO – 50 wt.% ZnO	1.00	±0	1.01	±0.01	1.02	±0.01	1.04	±0.01
30 wt.% CTO – 70 wt.% ZnO	1.02	±0.01	1.08	±0.03	1.16	±0.04	1.26	±0.08
10 wt.% CTO – 90 wt.% ZnO	1.07	±0.03	1.21	±0.05	1.38	±0.09	1.68	±0.20
100 wt.% ZnO	1.02	±0.02	1.17	±0.03	1.39	±0.07	1.69	±0.14

Figure 5–23 presents the response results of the system of sensors against increasing concentrations of CO. The devices dominated by n-type behaviour displayed typical n-type response as seen in Figure 5–23 (a), and those dominated by p-type behaviour displayed typical p-type response as seen in Figure 5–23 (b). The responses were seen to be poor with the best performing n-type device being the 90 wt.% ZnO – 10 wt.% CTO device, which showed a resistive response of 1.9 towards 800 ppm of CO. The best performing sensor device which exhibited p-type behaviour was the 10 wt.% ZnO – 90 wt.% CTO which showed a conductive response of 1.5 towards 800 ppm CO.

5.2.5.2 NH_3 Sensing

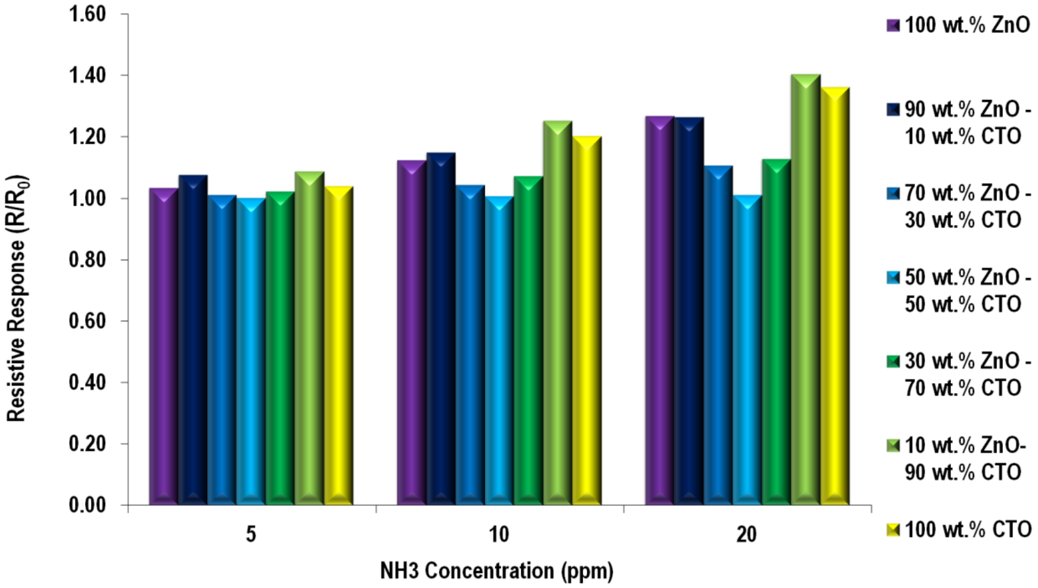

Figure 5–24. Resistive response of 100 wt.% ZnO, 90 wt.% ZnO – 10 wt.% CTO, 70 wt.% ZnO – 30 wt.% CTO, 50 wt.% ZnO – 50 wt.% CTO, 30 wt.% ZnO – 70 wt.% CTO, 10 wt.% ZnO – 90 wt.% CTO and 100 wt.% CTO sensor devices against 5, 10 and 20 ppm NH_3 at an operating temperature of 350 °C.

Figure 5–24 presents the resistive responses of all devices within the CTO-ZnO system against increasing concentrations of NH_3. Tabulation of the mean responses values of the sensor devices in the CTO-ZnO system from the repeat tests against exposure towards the various NH_3 concentrations at 350 °C and the associated 95% confidence intervals have been presented in Table 5–7.

Most device were seen to exhibit responses close to the baseline response ($R/R_0 = 1$). The best performing sensor device was the 10 wt.% ZnO – 90 wt.% CTO sensor device which exhibited a resistive response of 1.4 towards 20 ppm NH_3. Interestingly all sensor devices exhibited an increase in resistive response against the analyte; suggesting that the devices dominated by n-type conductivity exhibited an inverted p-type behaviour towards the reducing analyte. Such resistive response behaviour of n-type materials against NH_3, was observed in Chapter 3 and Chapter 4 which focused on WO_3 - ZnO and SnO_2 – ZnO composite systems, respectively. Such behaviour can be accounted for by the oxidation reaction of NH_3 on the surface of n-type metal oxides [114, 115], the reaction of which has been alluded to in Chapter 1, section 1.10.3.

Table 5–7. Average resistive responses of sensor devices in CTO-ZnO system from all repeat tests against various NH_3 concentrations at 350 °C and associated errors in the form of 95% CIs.

	5 ppm		**10 ppm**		**20 ppm**	
Device	Average Response	95% CI	Average Response	95% CI	Average Response	95% CI
100 wt.% CTO	1.05	±0.01	1.20	±0.03	1.35	±0.03
90 wt.% CTO – 10 wt.% ZnO	1.09	±0.01	1.26	±0.03	1.43	±0.06
70 wt.% CTO – 30 wt.% ZnO	1.02	±0.01	1.07	±0	1.13	±0.01
50 wt.% CTO – 50 wt.% ZnO	1.00	±0	1.01	±0.00	1.01	±0
30 wt.% CTO – 70 wt.% ZnO	1.02	±0.01	1.04	±0.02	1.10	±0.04
10 wt.% CTO – 90 wt.% ZnO	1.03	±0.04	1.12	±0.03	1.24	±0.03
100 wt.% ZnO	1.03	±0.01	1.11	±0.02	1.26	±0.03

5.2.5.3 Acetone Sensing

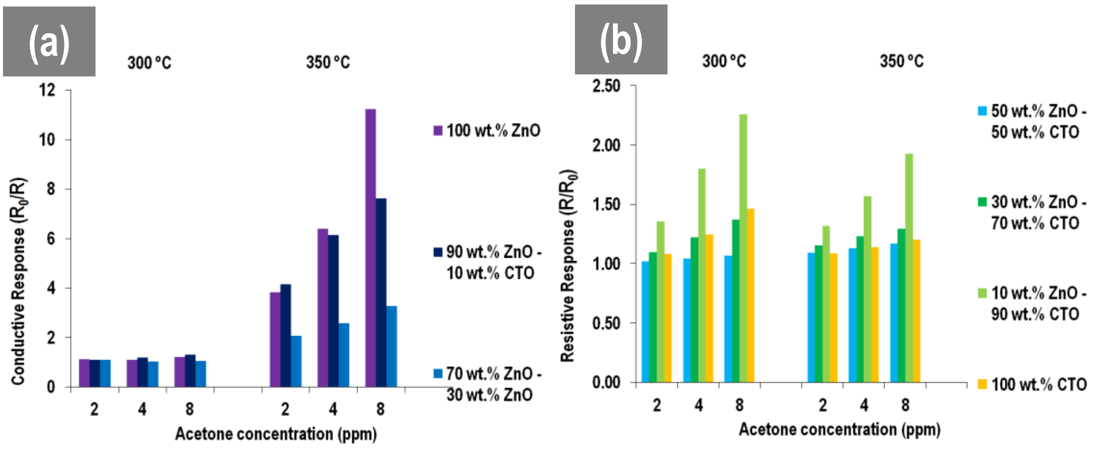

Figure 5–25. (a) Conductive response of 100 wt.% ZnO, 90 wt.% ZnO – 10 wt.% CTO and 70 wt.% ZnO – 30 wt.% CTO sensor devices and (b) Resistive response of 50 wt.% ZnO – 50 wt.% CTO, 30 wt.% ZnO – 70 wt.% CTO, 10 wt.% ZnO – 90 wt.% CTO and 100 wt.% CTO sensor devices against 2, 4, and 8 ppm of acetone at 300 and 350 °C.

Figure 5–25, presents the response magnitudes of the CTO - ZnO system against increasing concentrations of acetone at 300 °C and 350 °C. Tabulation of the mean responses values of the sensor devices in the CTO-ZnO system from the repeat tests against exposure towards the various acetone concentrations at 300 °C and 350 °C and the associated 95% confidence intervals have been presented in Table 5–8 and Table 5–9, respectively.

Table 5–8. Average responses of sensor devices in CTO-ZnO system from all repeat tests against various acetone concentrations at 300 °C and associated errors in the form of 95% CIs.

	2 ppm		**4 ppm**		**8 ppm**	
Device	Average Response	95% CI	Average Response	95% CI	Average Response	95% CI
100 wt.% CTO	1.15	±0.11	1.34	±0.16	1.49	±0.03
90 wt.% CTO – 10 wt.% ZnO	1.68	±0.62	2.44	±1.22	2.31	±0.09
70 wt.% CTO – 30 wt.% ZnO	1.14	±0.10	1.28	±0.13	1.37	±0.01
50 wt.% CTO – 50 wt.% ZnO	1.05	±0.05	1.08	±0.06	1.08	±0.01
30 wt.% CTO – 70 wt.% ZnO	1.25	±0.29	1.41	±0.51	1.24	±0.05
10 wt.% CTO – 90 wt.% ZnO	1.49	±0.75	1.80	±1.18	1.33	±0.05
100 wt.% ZnO	1.52	±0.76	2.08	±1.64	1.45	±0.05

Table 5–9. Average responses of sensor devices in CTO-ZnO system from all repeat tests against various acetone concentrations at 350 °C and associated errors in the form of 95% CIs.

	2 ppm		**4 ppm**		**8 ppm**	
Device	Average Response	95% CI	Average Response	95% CI	Average Response	95% CI
100 wt.% CTO	1.11	±0.01	1.16	±0.02	1.23	±0.01
90 wt.% CTO – 10 wt.% ZnO	1.33	±0.02	1.59	±0.02	1.95	±0.02
70 wt.% CTO – 30 wt.% ZnO	1.16	±0.01	1.23	±0.01	1.29	±0.02
50 wt.% CTO – 50 wt.% ZnO	1.09	±0.01	1.13	±0.01	1.17	±0.01
30 wt.% CTO – 70 wt.% ZnO	2.09	±0.09	2.77	±0.21	3.60	±0.34
10 wt.% CTO – 90 wt.% ZnO	4.24	±0.12	6.36	±0.28	9.28	±0.56
100 wt.% ZnO	3.85	±0.04	6.60	±0.10	9.93	±2.98

Part (a) presents the results of the devices dominated by n-type percolation paths and shows that these devices exhibited substantial activity at 350 °C, with the highest response observed to be 11.2 against 8 ppm of acetone by the 100 wt.% ZnO device. The two composites exhibited measureable responses, with the 90 wt.% ZnO – 10 wt.% CTO sensor device being the better mixed oxide device of the two, displaying a maximum response of 7.6 towards 8 ppm of the analyte at 350 °C. Both composites however, did not perform as well as the pure ZnO counterpart, with the response performance decreasing as a function of decreasing ZnO concentration and increasing CTO concentration. This trend suggested that the response order of the three devices, as observed with ethanol and NO_2, was dependent on the synergism of both metal oxides and in particular, ratio of the ZnO : CTO components, with the presence of ZnO enhancing the response characteristics or alternatively its absence and/or the addition of CTO diminishing the response. Thus, a complimentary effect of the presence of n-type and p-type based metal oxides, than a hetero-junction effect, was evident from the behaviour of these three sensor devices. In contrast at 300 °C, the responses of the three sensors were negligible.

Figure 5–25 part (b) illustrates that the sensors dominated by p-type conductivity exhibited significantly lower responses than those in (a) with the highest response of 2.3 exhibited by the 10 wt.% ZnO – 90 wt.% CTO composite toward 8 ppm acetone at 300 °C. The response magnitudes of the p-type dominated materials were seen to decrease as a function of increasing operating temperature however the results generally showed that the presence of ZnO in conjunction with CTO had a positive sensitisation effect on the response characteristics in comparison to the unmodified CTO counterpart. The behaviour, particularly of the 10 wt.% ZnO – 90 wt.% CTO composite exemplified an hetero-junction effect or the effective sensitisation behaviour of the n-type metal oxide towards the p-type metal oxide.

In general, the overall behaviour of the CTO - ZnO system towards acetone between 300 °C – 350 °C, was very similar to that exhibited against ethanol and NO_2 as seen in Figure 5–15 - Figure 5–16 and Figure 5–20 - Figure 5–21 respectively, in terms of performance correlation with firstly the operating temperature and secondly, the compositional variations. Most devices within the system were generally seen to exhibit selectivity towards ethanol, when comparing the responses between both ethanol and acetone between 300 °C - 350 °C. However, the 70 wt.% CTO – 30 wt.% ZnO sensor device was an exception which was seen to exhibit selectivity towards acetone at 350 ° C.

A number of papers have reported the acetone gas sensing properties of ZnO, in which the metal oxide is seen to possess a variety of different morphologies. A very small fraction of these studies have been cited here [323-325]. In one study, Zeng *et al*. [323] reported on the growth and selective acetone detection of ZnO nanorod systems, which exhibited an increase in response as a function of operating temperature between 200 °C – 300 °C towards 100 ppm acetone; with an optimal response of 30.4 observed at 300 °C, after which the response of the sensor decreased.

In another study, Pugh *et al*. [325] had reported on the gas sensing properties of zeolite modified ZnO. The metal oxide used in their study was identical to the ZnO used in this study, and it was found that the responsivity of the pure ZnO sensor increased as a function of operating temperature between 350 °C – 500 °C, with the highest response in the range of 17.5 – 18 towards 8 ppm of the analyte, at 500 °C. The differences in the optimal operating temperatures of the ZnO material between the literature report and the study in this thesis, can be accounted for by differing device architectures, operating rigs, etc., however both studies show that the acetone sensing performance of ZnO, increases as a function of operating temperature.

The acetone gas sensing properties of CTO are limited in the literature however in one study by Pokhrel *et al*. [127], it was reported that various $Cr_{2-x}Ti_xO_3$ powders (where x was varied between 0.1 - 0.5 in increments of 0.1), were prepared by a combustion technique followed by heat-treatment at 1000 °C for 12 hours. When the materials were tested against 1 ppm – 5 ppm acetone at an operating temperature of 400 °C, the relative response of the materials against the analyte was seen to increase as the value of x decreased, i.e. when x = 0.1 the best responsivity of 14 was achieved towards 5 ppm of the analyte. Instead, when x was increased to 0.5, the relative response towards 5 ppm was seen to be 7.3.

In another study, this time based on pure Cr_2O_3, Liu *et al*. [280] had reported on the acetone gas sensing properties of highly ordered mesoporous Cr_2O_3 samples, fabricated using a vacuum assisted impregnation route. Two samples of Cr_2O_3 were fabricated; the first using 2D hexagonal templates, which promoted the formation of Cr_2O_3 with a highly ordered hexagonal mesoporous structure, and the second sample was prepared using a 3D cubic template, which promoted the formation of Cr_2O_3, with a highly ordered 3D cubic mesoporous structure. Both samples were attributed to high specific surface areas and narrow pore size distributions, which enhanced the sensing properties of the materials. Both samples (hexagonal and 3D cubic) demonstrated responses of 11 and 14, respectively, towards 1000 ppm acetone. These responses were significantly enhanced compared to a bulk Cr_2O_3 counterpart, attributed to a response of 4 towards 1000 ppm acetone. Unfortunately the group did not report the operating temperature over which the gas sensing studies were conducted, however the stable baselines observed in the response traces of the sensors, suggested a high temperature of operation. In this CTO - ZnO study, the CTO consists of a matrix of Cr_2O_3 doped with Ti ions and therefore a majority of the material can be associated to the responsivity of Cr_2O_3. Therefore the poor responses achieved in this thesis by the CTO dominated materials, towards acetone, can be justified with respect to the poor response results of the bulk Cr_2O_3 towards 1000 ppm acetone reported by Liu *et al*. The group's study showed that in order for the Cr_2O_3 to exhibit superior acetone sensing properties, it would need to be fabricated around e.g. mesoporous or nanostructured frameworks.

Studies on the acetone sensing properties of a p-n hetero-junction system based on a combination of CTO and ZnO are rare in the literature. However, studies based on other p-n combinations have been reported; one example which loosely relates to the study reported in this thesis, was reported by Gao *et al*. [187] who had investigated the selective acetone sensing properties of WO_3-Cr_2O_3 thin films, prepared by a sol-gel method. Specifically, the group had prepared a range of Cr_2O_3 doped WO_3 sols, where the concentration of the Cr_2O_3 ranged from 0.5 mol%, 1.0 mol%, 5.0 mol% and 10 mol%. The sols were coated around Al_2O_3 ceramic tubes via a dip-coating process, sintered at 500 °C, quenched to maintain the WO_3 specific phases and subsequently examined for their acetone sensing properties. Their results showed that the 5 mol% Cr_2O_3 doped WO_3 film, was attributed to the highest responsivity of 8.91 towards 20 ppm acetone at 320 °C and also was selective towards acetone gas, amongst a range of other gases which included ethanol, ammonia, methanol, n-butanol and CO_2, at the same temperature. The best performance of this particular device was attributed to its optimal characteristics influenced by composition, microstructure, sintering temperature and quenching. Experimental results from this thesis, are comparable to the results achieved by Gao *et al*., for example the 90 wt.% ZnO – 10 wt.% CTO sensor device exhibited a response of 7.6 toward 8 ppm acetone at 350 °C, however at 20 ppm, it would be expected that the composite would exhibit a higher response (at 350 °C) than the literature study. Interestingly, both hetero-junction materials from the literature study by Gao *et al*. and the experimental study in this thesis, are attributed to packing-structures consisting of a host matrix of one metal oxide with a small addition/dispersion of a second metal oxide, analogous to Yamazoe *et al*'s stone-in-sand packing structure [170, 171], mentioned earlier. Such packing structures are seen to be effective for acetone detection, as well as for ethanol detection, as observed from result presented earlier in this Chapter.

5.2.5.4 Toluene Sensing

Figure 5–26 presents the resistive response magnitudes of the four devices within the system that were dominated by p-type conductivity, towards increasing concentrations of toluene at 300 °C and 350 °C. Tabulation of the mean responses values of the sensor devices in the CTO-ZnO system from the repeat tests against exposure towards the various ethanol concentrations at 350 °C and 250 °C and the associated 95% confidence intervals have been presented in Table 5–10 and

Table 5–11, respectively.

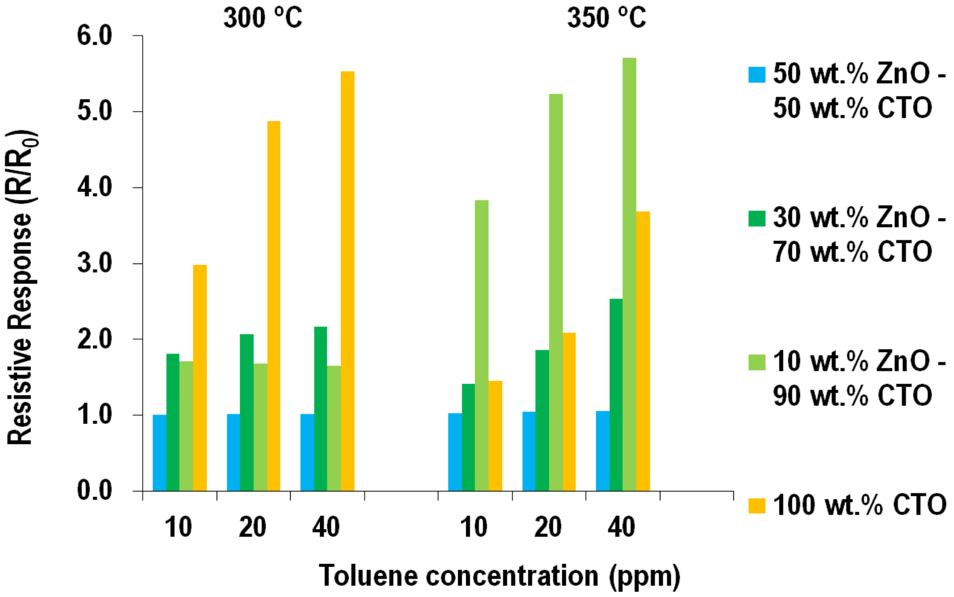

Figure 5–26. Resistive response of 50 wt.% ZnO – 50 wt.% CTO, 30 wt.% ZnO – 70 wt.% CTO, 10 wt.% -90 wt.% CTO and 100 wt.% CTO sensor devices against 10, 20 and 40 ppm toluene at 300 and 350 °C.

Table 5–10. Average resistive responses of sensor devices in CTO-ZnO system from all repeat tests against various toluene concentrations at 300 °C and associated errors in the form of 95% CIs.

	10 ppm		**20 ppm**		**40 ppm**	
Device	Average Response	95% CI	Average Response	95% CI	Average Response	95% CI
100 wt.% CTO	2.67	±0.69	4.75	±0.62	5.76	±0.36
90 wt.% CTO – 10 wt.% ZnO	1.64	±0.12	1.80	±0.12	1.89	±0.09
70 wt.% CTO – 30 wt.% ZnO	1.74	±0.15	2.02	±0.10	2.16	±0.06
50 wt.% CTO – 50 wt.% ZnO	1.01	±0	1.01	±0	1.02	±0

Table 5–11. Average resistive responses of sensor devices in CTO-ZnO system from all repeat tests against various toluene concentrations at 350 °C and associated errors in the form of 95% CIs.

	10 ppm		**20 ppm**		**40 ppm**	
Device	Average Response	95% CI	Average Response	95% CI	Average Response	95% CI
100 wt.% CTO	1.44	±0.05	2.04	±0.10	3.57	±0.21
90 wt.% CTO – 10 wt.% ZnO	3.63	±0.41	4.99	±0.48	5.60	±0.44
70 wt.% CTO – 30 wt.% ZnO	1.41	±0	1.85	±0	2.54	±0
50 wt.% CTO – 50 wt.% ZnO	1.03	±0	1.04	±0	1.06	±0

These devices were seen to dominate the responses, in comparison to the other three devices which were dominated by n-type conductivity. The three sensors dominated by n-type behaviour exhibited responses very close to baseline response, and therefore have not been presented. This suggested the very poor conductive response behaviour of the n-type dominated materials towards toluene.

Figure 5–26 shows that the 100 wt.% CTO sensor dominated the toluene response at 300 °C, with a maximum response of 5.5 towards 40 ppm. In contrast, the 10 wt.% ZnO – 90 wt.% CTO sensor exhibited the lowest response 1.6 (towards the same analyte concentration) at the same operating temperature. At 350 °C, a switch was observed with the 10 wt.% ZnO - 90 wt.% CTO composite sensor showing optimal response of 5.7 towards 40 ppm of the analyte. At this higher temperature however, the response of the pure CTO counterpart worsened, exhibiting a response of 3.7 under the same conditions, illustrating that the 10 wt.% ZnO - 90 wt.% CTO composite showed a 1.5-fold enhanced response compared to the pure CTO counterpart. The optimal performance of the 10 wt.% ZnO - 90 wt.% CTO sensor device at 350 °C, compared to 300 °C, exemplified how the operating temperature exerted an influential effect on tuning the responsivity of the composite. In general, no particular response order was observed as a function of changing ZnO or CTO concentration or as a function of changing operating temperature with toluene. In contrast, greater correlative trends with these variables, were observed with ethanol and acetone.

The detection of toluene via a hetero-junction system based on the combination of metal oxides studied in this thesis, has not been observed in the literature. Woo *et al*. [290] however, whose study was mentioned earlier, had reported on the detection of toluene by the use of Cr_2O_3-ZnO hetero-nanostructures. The largest response (conductive) they had observed was of 3 towards 5 ppm toluene, at an operating temperature of 400 °C, by a hetero-junction system containing semi-elliptical Cr_2O_3 nanoparticles dispersed on the surface of ZnO nanowires. This response was a two-fold enhanced response compared to pure un-treated ZnO nanowires. The response achieved of this literature material is comparable to the response achieved by the 10 wt.% ZnO - 90 wt.% CTO composite sensor in this thesis, however that in the literature was dominated by the n-type ZnO and that in this thesis, by the p-type CTO. The group has also reported on the response of continuous Cr_2O_3 shell layers that were uniformly coated around ZnO nanowires, which exhibited a resistive response of just above 1 towards 5 ppm toluene at 400 °C.

Table 5–12. Response magnitudes of CTO-ZnO composite system against various concentrations of ethanol, NO_2, acetone, and toluene gas at operating temperatures of 300 and 350 °C. The devices highlighted in orange are those which exhibited n-type conductive behaviour and those in green are those which exhibited p-type conductive behaviour. Where devices responses were observed to be below 1.5, associated cells have been block filled.

	100 Z	90 Z – 10 C	70 Z– 30 C	50 Z – 50 C	30 Z – 70 C	10 Z– 90 C	100 C		100 Z	90 Z – 10 C	70 Z– 30 C	50 Z – 50 C	30 Z – 70 C	10 Z– 90 C	100 C
Ethanol (300 °C)								**Ethanol (350 °C)**							
10 ppm	2.2	3.6	1.7	■	■	2.3	■	**10 ppm**	6.3	4.5	1.7	■	■	■	■
20 ppm	2.4	6.2	2.1	■	1.5	6.2	1.6	**20 ppm**	21.0	7.5	2.1	■	■	■	■
40 ppm	12.6	9.8	2.5	■	2.0	10.0	2.9	**40 ppm**	45.5	10.9	2.4	■	■	1.9	■
NO_2 (300 °C)								**NO_2 (350 °C)**							
100 ppb	3.8	1.8	■	■	■	■	■	**100 ppb**	2.4	■	■	■	■	■	■
200 ppb	11.1	3.8	■	■	■	■	■	**200 ppb**	6.0	3.0	■	■	■	■	■
400 ppb	21.0	6.0	■	■	■	■	■	**400 ppb**	11.5	5.2	■	■	■	■	■
Acetone (300 °C)								**Acetone (350 °C)**							
2 ppm	■	■	■	■	■	■	■	**2 ppm**	3.8	4.2	2.1	■	■	■	■
4 ppm	■	■	■	■	■	1.8	■	**4 ppm**	6.4	6.1	2.6	■	■	1.6	■
8 ppm	■	■	■	■	■	2.3	1.5	**8 ppm**	11.2	7.6	3.3	■	■	1.9	■
Toluene (300 °C)								**Toluene (350 °C)**							
10 ppm	■	■	■	■	1.8	1.7	3.0	**10 ppm**	■	■	■	■	■	3.8	1.5
20 ppm	■	■	■	■	2.1	1.7	4.9	**20 ppm**	■	■	■	■	1.9	5.2	2.1
40 ppm	■	■	■	■	2.2	1.7	5.5	**40 ppm**	■	■	■	■	2.5	5.7	3.7

Key:

100Z – 100 wt.% ZnO

90Z – 10C – 90 wt.% ZnO – 10 wt.% CTO

70Z – 30C – 70 wt.% ZnO – 30 wt.% CTO

50Z – 50C – 50 wt.% ZnO – 50 wt.% CTO

30Z – 70C –30 wt.% ZnO – 70 wt.% CTO

10Z - 90C – 10 wt.% ZnO – 90 wt.% CTO

100C – 100 wt.% CTO

5.3 Summary and Conclusions

Table 5–12 presents the response magnitudes of the group of CTO-ZnO composite devices against all the tested gases at both operating temperatures of 300 °C and 350 °C. Where device responses were observed to be below 1.5, associated cells have been block filled. The devices highlighted in orange are associated to those devices exhibiting n-type conductive behaviour and those in green are associated to those exhibiting p-type conductive behaviour.

The results of this study showed that 10 wt.% ZnO – 90 wt.% CTO sensor device exemplified the best response behaviour when combining the two metal oxides, which suggested that it contained the optimal composition (as well as optimal packing structure) of both semiconducting metal oxide grains. This was concluded through its enhanced response behaviour with respect to the pure CTO counterpart and other sensor devices dominated by p-type semiconducting behaviour, for example against ethanol at 250 °C - 300 °C or towards NO_2 at 300°C, amongst acetone and toluene as well.

Such a device consisted of n-type ZnO particles discretely dispersed into a host matrix of p-type CTO particles, and as such was primarily dominated by p-type conductivity. The significant enhancement associated to such a device, may suggest that the conductivity and enhancement effects of the localized p-n hetero-contacts may have greater influence of the conductivity than the weaker p-type conductivity via the p-p homo-contact dominated percolation paths, and as such may act to enhance the transduction function of the device. These results corroborate with the Hubner *et al*. and Pokhrel *et al*. [278, 282], who reported that the conduction through the HAL in the p-type metal oxide significantly weakens its response characteristics.

In some instances, the 90 wt.% ZnO – 10 wt.% CTO composite sensor device was also seen to show enhanced responsivities with respect to the pure ZnO counterpart against ethanol between 200 °C – 300 °C, however this enhancement effect was inconsistent between analytes and was not as profound as the enhancement that the 10 wt.% ZnO – 90 wt.% CTO sensor device showed with respect to the pure CTO counterpart. Such a device consisted of a dispersion of p-type CTO particles in a matrix of ZnO particles, and thus was dominated by n-type conductivity. The weaker response of such devices with respect to the pure ZnO counterpart, suggested that the stronger n-type dominated conductivity via the n-n homo-contact percolation paths swamped the localised p-n hetero-junction conductivity and potential enhancement effects towards the responsivity, and as such hardly displayed any enhancement upon combination of both metal oxides.

Interestingly, the 50 wt.% ZnO – 50 wt.% CTO sensor device exhibited responses close to 1 (base line response) towards all four gases at all operating temperatures, which suggested cancellation behaviour with this specific combination of ZnO and CTO materials. This may have been attributed to percolation paths between the ZnO–ZnO n-n homo-contacts and CTO-CTO p-p homo-contacts cancelling each other out, and as such, the net effect was null net conductivity. The response behaviour of the 30 wt.% ZnO – 70 wt.% CTO sensor device was also interesting as it exhibited cancellation behaviour against ethanol, acetone and NO_2 but exhibited quantifiable responses against toluene at 350 °C, indicating that in a mixed atmosphere of all four gases, the cancellation behaviour of this device may be exploited to selectively detect toluene.

XPS characterisation did not show any visible evidence of the electronic interaction between both metal oxides, however the packing structure and the ratio of homo : hetero contacts within the composite matrices, as well as the responsivities of the individual metal oxides were all thought to have contributed to the overall responsivity behaviour of the p-n hetero-junction composite system.

Overall the study showed that the system is complex, with two key types of devices within the system; one dominated by n-type conductivity and the second by p-type conductivity. The devices that were dominated by n-type conductivity were seen to show particularly large conductive responsivities towards ethanol at higher operating temperatures of 350 °C – 400 °C, resistive responsivities towards NO_2 at lower operating temperatures of 300 °C – 350 °C and conductive responsivities towards acetone at 350 °C. In contrast, selective devices dominated by p-type conductivity were associated to better ethanol responsivities (in comparison to the n-type devices) at lower operating temperatures of 200 °C – 250 °C, better acetone responsivities at 300 °C and superior toluene sensing characteristics, the latter of which the n-type dominated sensor devices did not exhibit. The temperature of operation was also seen to be a contributory factor to the overall behaviour of the p- and n-type composite materials towards ethanol, as each metal oxide was seen to have opposite response performances as a function of operating temperature.

Error analysis of the mean response values throughout the study showed that in general the responses between the repeat tests were repeatable and errors were minimal in value. This was a significantly different trend to that observed for both the previous n-n hetero-junction composite systems, which were associated to significantly larger magnitudes of error, particularly towards the gases towards which they showed largest responsivity magnitudes. The lower error magnitudes with this system, suggested poorer response behaviour in general, which was evident from the results presented, but also greater stability of the materials system. A further discussion of error sources and possible future outcome from the sources has been discussed in the final conclusions of the thesis in Chapter 7.

Chapter 6 : Emerging ZnO Materials for MOS Sensing

In the last three Chapters, materials and gas sensing characterisation analyses of various hetero-junction systems were presented, with a focus on mixed metal oxide material systems based on ZnO, as a route to achieving enhanced responsivities towards various analytes for Metal Oxide Semiconductor (MOS) based gas sensing applications. This Chapter focuses on the application of emerging ZnO materials, predominantly nanomaterials, for MOS sensing. Amongst the variety of materials investigated in this Chapter, detailed focus is on ZnO nanomaterials fabricated via continuous hydrothermal flow synthesis (CHFS), which is demonstrated as an emerging technique for the production of nanomaterials for MOS sensing technology. A study on the application of various ZnO ceramics made by Molten-Salt synthesis, Solid-State metathesis and Hydrothermal synthesis is also presented. Such materials demonstrate the potential for further research and development for new materials, including composite system, for MOS based gas sensing.

6.1 Introduction

The enhanced gas sensing characteristics of nanosized materials was demonstrated by Yamazoe in 1991 [19, 326]. Materials with high surface:bulk ratios can yield a large number of surface reactions and therefore can dramatically improve the response characteristics of sensor devices [19, 327]. Materials design for sensing applications is a subject of academic and commercial interest [328], particularly with nanomaterials, where there lies the possibility of developing new sensors with interesting one-dimensional particle morphologies, e.g. nanoribbons, wires and belts [329] and sensor functionalities such as enhanced responsivity and selectivity. Key interests in the area of materials design are the fabrication technology used to fabricate the materials, the fabricated materials and their associated morphologies and their functional performance.

ZnO in particular, is a very popular metal oxide when studying nanomaterials, as discussed in Chapter 1, demonstrating the ability to adopt an system of morphological architectures [76, 79, 83, 84], which have ranged from nanorods, nanowires, nanotubes, nanocages, nanoflowers, nanotetrapods [76, 79, 330], amongst a host of other structures, some of which have been reported to have whimsical names such as nanopropellers [76]. As such, ZnO has been reported to be the richest family of nanostructures among all materials [330], with a richer number of configurations than any known nanomaterial, including carbon nanotubes [330]. The synthesis technique, process conditions, precursors, pH of a system or concentration of the reactants are all thought to play influential role in controlling the morphology of ZnO nanoparticles [76].

Previous reports in the literature [142, 143] have established Continuous Hydrothermal Flow Synthesis (CHFS) as a promising technique for the production of nanostructured metal oxides for high performance MOS based gas sensing. The CHFS production method enables the production of large quantities of materials in hours with the ability to adjust the physical parameters of the synthesis conditions, such as temperature and pressure, and control particle characteristics [143, 331]. The method is also clean for the environment and energy efficient [143]. The route of fabrication generally involves a flow of supercritical water (T_c 374 °C and P_c 22.1 MPa), which reacts with aqueous room-temperature flows of metal salts in a confined jet mixer (CJM), precipitating and crystallising nanomaterials in the flow, in continuous mode [143]. The medium provided by the supercritical water allows the precipitation of the metal ions to occur rapidly, through a combination of hydrolysis and dehydration reactions, which precipitate and oxidize the metal ions rapidly to form oxide based nanomaterials [143].

Recently, Shi *et al.*[143] reported on the fabrication of high performance ZnO nanomaterials via this technique in a pilot plant scale reactor. In their study, they reported the preparation of ZnO nanomaterials by using fixed concentrations of $Zn(NO_3)_2.6H_2O$ (0.2 M) and KOH (0.5 M) precursors and an auxiliary reagent hydrogen peroxide, H_2O_2 (30 wt.% in H_2O). The oxidising agent was pumped in with $Zn\ (NO_3)_2.6H_2O$ in various volume ratios of 0, 0.05, 0.1, 0.15 and 0.25, and mixed with an aqueous flow feed of KOH. The mixed feed was then reacted with a flow of supercritical water. Five different samples of ZnO were reported and it was found that as the concentration of the H_2O_2 initially increased, the crystallite size of the particles decreased, and promoted high-surface area ZnO samples, with mainly nanorod like attributes. Volume ratios of H_2O_2 above 0.15 interestingly promoted an increase in crystallite size and thus decrease in surface area, with significant pointed rod type and prismatic growth of these samples reported to be observed by TEM. The ZnO samples were prepared as MOS sensor devices by drop coating slurries of the metal oxides, followed by heat-treatment for 600 °C for 2 hours. One of the ZnO materials (constituting a ratio of 0.15 H_2O_2 : $Zn(NO_3)_2.6H_2O$) exhibited a resistive response of 128 towards 10 ppm NO_2 at 350 °C and a response of over 80 when exposed to 4 ppm NO_2. They had reported these responses had compared favorably over other studies in the literature which had reported the gas sensing properties of nanoscaled ZnO materials, and showed CHFS as an effective technique for the fabrication of nanomaterials for MOS gas sensing applications.

In another study by Elouali *et al.* [142], the group had reported on the fabrication of nanostructured In_2O_3 in a laboratory scale CHFS reactor. The synthesis involved a dilute feed of $In\ (NO_3)_3.H_2O$ precursor which was reacted with a flow of supercritical water preheated to 400 °C, which resulted in the rapid crystallisation and precipitation of nanosized In_2O_3 particles. No auxiliary reagent was required in this reaction. TEM analysis showed a majority of particles to be well-defined round cubes of size 5 - 20 nm. Sensor devices of the material were fabricated by drop-coating a slurry of the In_2O_3 nanoparticles onto MOS sensor substrates followed by heat-treatment at 600 °C for 2 hours. Drop coating was varied, with one sensor substrate coated with two layers and another coated with three layers of the In_2O_3 slurry. Exposure of the sensor devices to increasing concentrations of ethanol at the optimal operating temperature of 300 °C, showed a largest response of 14.7 towards 20 ppm of the analyte by the three coat sensor. When the same device was exposed to increasing concentration of the NH_3, the highest response obtained was 1.8 against 10 ppm of the analyte at 450 °C, which was the optimal operating temperature of NH_3 in the study. Cross-sensitivity studies of the sensor devices against a range of gases, which apart from NH_3 (10 ppm, 450 °C) and ethanol (20 ppm, 300 °C), included NO_2 (16 ppb, 450 °C), butane (10 ppm, 450 °C) and CO (200 ppm, 450 °C), showed selectivity of the device towards ethanol, with a response 4 times larger towards ethanol than all other analytes.

Both these example studies, demonstrate the success of CHFS nanostructured metal oxides for MOS gas sensing applications. In this Chapter, new ZnO nanomaterials are prepared via the pilot plant scale CHFS reactor used by Shi *et al*. [143] and a detailed and comprehensive gas sensing analysis of the resulting materials have been presented. Further the potential of ZnO ceramic materials made by other relatively high temperature routes, specifically molten-salt, solid-state metathesis and hydrothermal synthesis has also been demonstrated, for MOS gas sensing.

6.2 Results and Analysis: Nanomaterials based on Continuous Hydrothermal Flow Synthesis (CHFS)

6.2.1 Transmission Electron Microscopy (TEM)

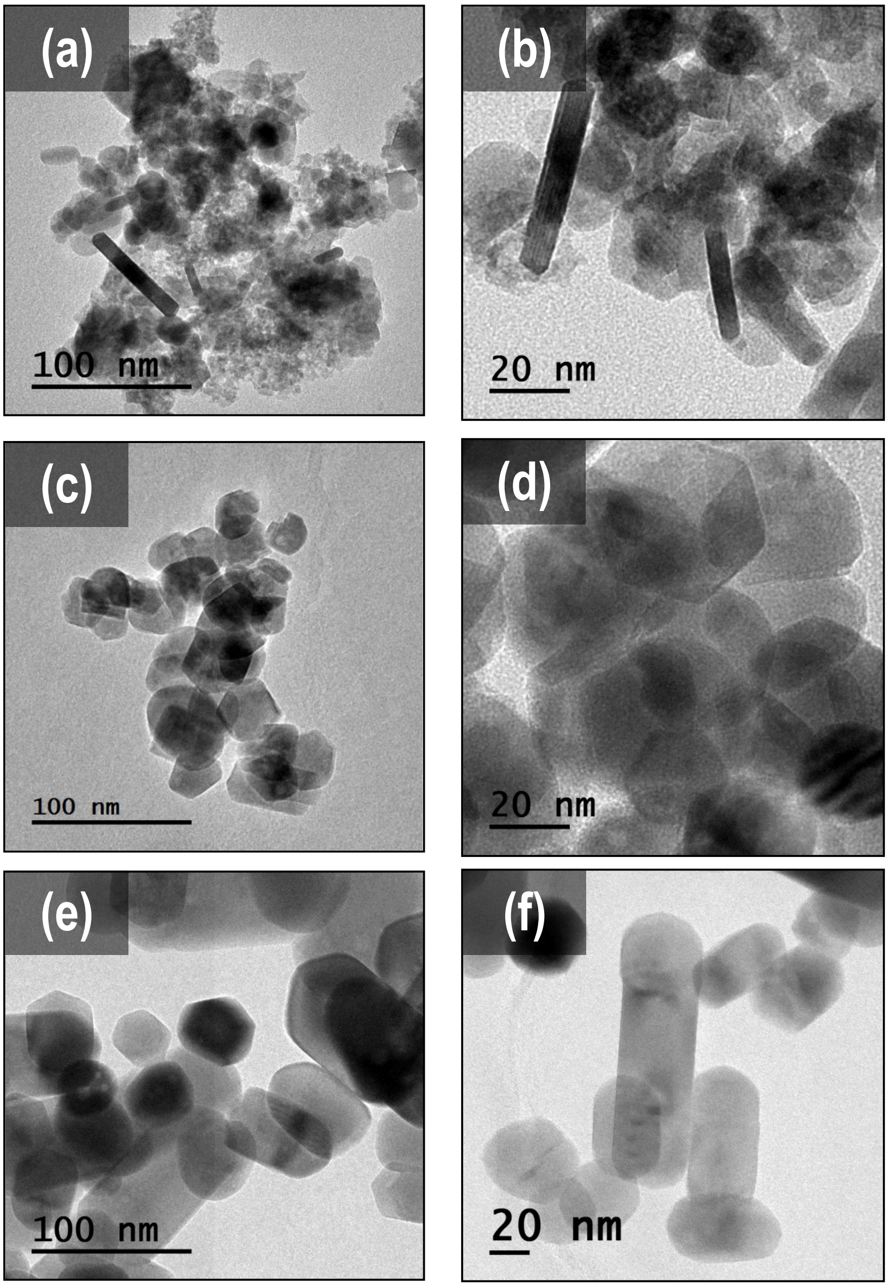

Figure 6–1. TEM images of as-prepared CHFS ZnO nanomaterials where (a) is of ZnO sample A with scale bar of 100 nm, (b) is of ZnO sample A with scale bar of 20 nm, (c) is of ZnO sample B with scale bar of 100 nm, (d) is of ZnO sample B with scale bar of 20 nm, (e) is of ZnO sample C with scale bar of 100 nm and (f) ZnO sample C with scale bar of 20 nm. Samples A, B and C were prepared by CHFS which involved a reaction of ambient flows of 0.1, 0.2, 0.45 M of $Zn (NO_3)_2.6H_2O$ aqueous solution and KOH aqueous solution respectively (each flowing at 200 mL min^{-1}), with a supercritical water flow at 450 °C and 240 bar (flowing at 400 mL min^{-1}) in a confined jet mixer.

TEM images of the ZnO samples A, B and C are reported Figure 6–1 and showed a variation in their morphology and particle sizes as a function of the changing precursor concentration. The wide and narrow rod-like, spherical and hexagonal particles in sample A, observed in Figure 6–1 (a) and (b) were observed to be in the size range of 5 nm - 75 nm, justified by analysis of the particle size distribution of the sample presented in Figure 6–2. Of these, the rods predominantly spanned a range of 25 nm – 70 nm and the spherical and hexagonal particles predominantly exhibited a size range of 10 nm – 25 nm.

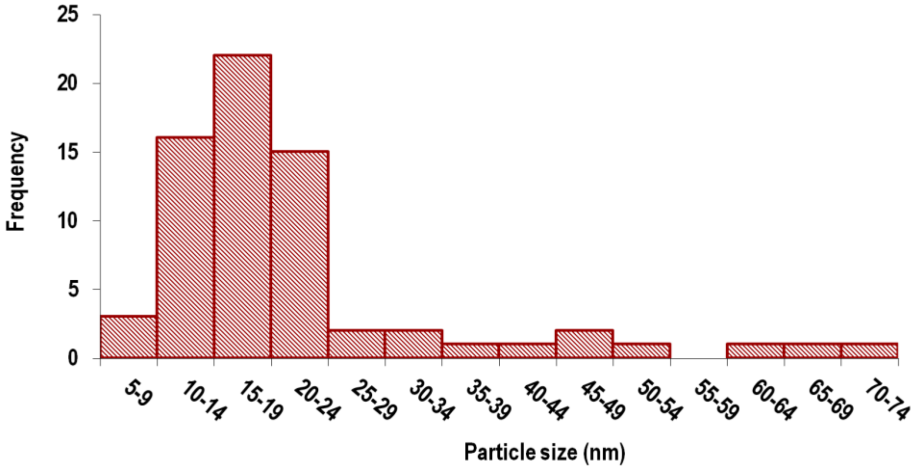

Figure 6–2. Particle size distribution calculated from TEM imaging of ZnO sample A prepared by CHFS which involved reaction of ambient flows of 0.1 M of Zn $(NO_3)_2.6H_2O$ aqueous solution and KOH aqueous solution (each flowing at 200 mL min^{-1}) with supercritical water flow at 450 °C and 240 bar (flowing at 400 mL min^{-1}) in a confined jet mixer.

The hexagonal and spherical particles in sample B observed in Figure 6–1 (c) and (d) were observed to span a range of particle sizes between 20 nm – 95 nm as observed in the corresponding particle size distribution plot in Figure 6–3, with most particles in the range of 30 nm - 45 nm.

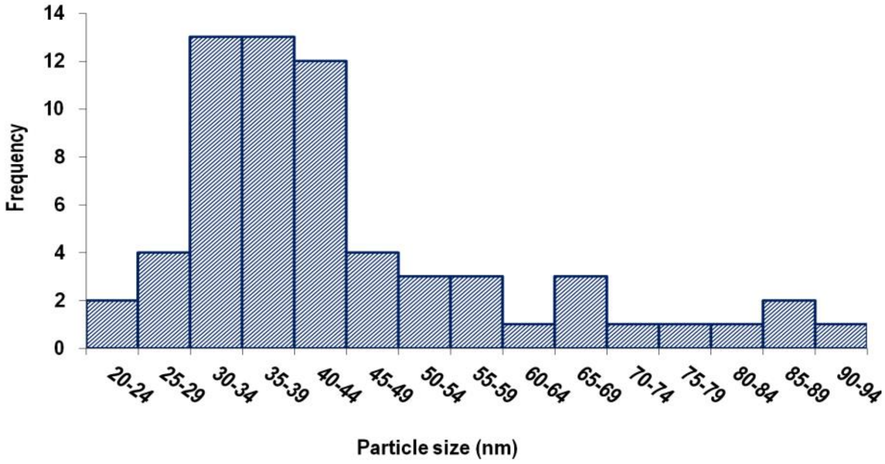

Figure 6–3. Particle size distribution calculated from TEM imaging of ZnO sample B prepared by CHFS which involved reaction of ambient flows of 0.2 M of Zn $(NO_3)_2.6H_2O$ aqueous solution and KOH aqueous solution (each flowing at 200 mL min^{-1}) with supercritical water flow at 450 °C and 240 bar (flowing at 400 mL min^{-1}) in a confined jet mixer.

Sample C as observed in Figure 6–1 (e) and (f) consisted of particles with mainly wide rod-like and spherical habits and few hexagonal habits. Particles were observed to exist in the range of 25 nm - 150 nm as observed in the associated particle size distribution plot in Figure 6–4, with a majority of the particles observed to be in the range of 40 nm – 70 nm.

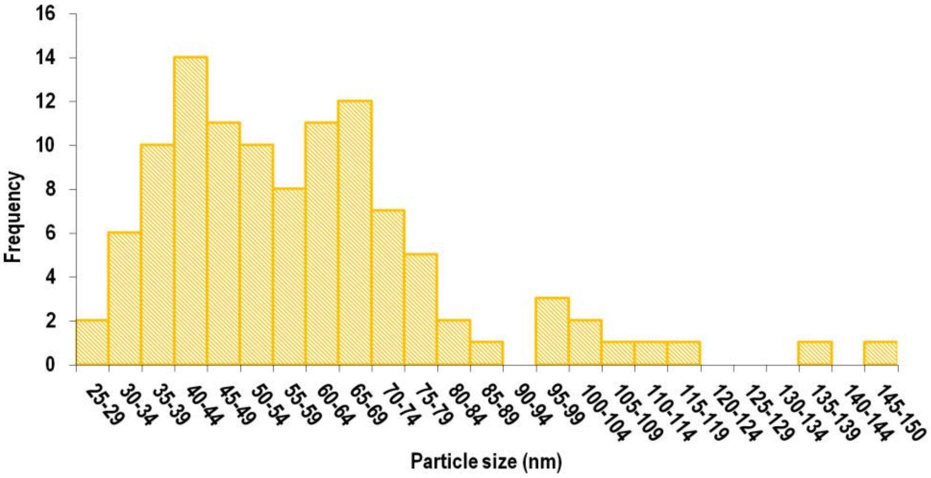

Figure 6–4. Particle size distribution calculated from TEM imaging of ZnO sample C prepared by CHFS which involved reaction of ambient flows of 0.45 M of Zn $(NO_3)_2.6H_2O$ aqueous solution and KOH aqueous solution (each flowing at 200 mL min^{-1}) with supercritical water flow at 450 °C and 240 bar (flowing at 400 mL min^{-1}) in a confined jet mixer.

The observed dimensions of the ZnO particles suggested that the average particle size increased with precursor concentration, perhaps due to influence on the surface energy for growth, suggesting an effective decrease in surface area. The increased particle count from sample A (Figure 6–2) to sample C (Figure 6–4) to analyse the particle size distribution, was also indicative of the increase in size of the particles from sample A to sample C, with the larger particle sizes in sample C being easy to identify. The extent of heterogeneity of the shapes of the ZnO particles was also observed to reduce as a function of increasing precursor concentration, with the shapes of the particles becoming more uniform with respect to each other. Both the observed trends in the size and morphological distribution as a function of precursor concentration were suggestive of the influence of precursor concentrations on the surface energy of growth of the ZnO particles. The observed hexagonal habits of the ZnO particles, corroborated with theory from the study by Shi *et al*. [143], in which it was reported that under normal hydrothermal conditions, in the absence of an oxidising agent such as H_2O_2, which promotes the solubility of the Zn species, the thermodynamically favoured morphology of ZnO is hexagonal [143].

Interestingly, during the experimental synthesis, it was observed that the ZnO nanoparticle product yield increased with precursor concentration. Based on previous work [143], it has been reported that in the hydrothermal reactor, when the zinc precursor, KOH and supercritical water meet, the following reactions occur [143]:

Equation 6–1
$$Zn^{2+} + 4OH^{-} \rightarrow Zn(OH)_4^{2-} \rightarrow ZnO_2^{2-} + 2H_2O$$

Equation 6–2
$$ZnO_2^{2-} + H_2O \leftrightarrow ZnO + 2OH^{-}$$

Equation 6–1 shows that increasing the zinc and KOH precursor concentration, promotes a greater number of Zn^{2+} ions to be formed which convert into soluble $Zn\,(OH)_4^{2-}$ species, which are the growth unit of ZnO. Thus, the ZnO nanomaterials are precipitated from the alkaline hydrothermal environment by the above reactions, with the dehydration reaction promoted by the reaction point temperature of 335 °C. Thus the higher yield of ZnO observed as a function of increasing precursor concentration is justified.

As suggested earlier in the introduction of this Chapter, previously Shi *et al*. [143] had reported on the NO_2 gas sensing properties of the highly sensitive ZnO nanorod and nanoprism based nanomaterials, which were made in the same reactor as the experimental study being reported in this thesis. The key difference between both studies however, was in the precursors used to fabricate the ZnO nanomaterials. In the literature study, Shi *et al*. had kept the concentration of the $Zn(NO_3)_2.6H_2O$ and

KOH precursors constant and hydrogen peroxide H_2O_2, (as an auxiliary reagent), was pumped in with the $Zn(NO_3)_2.6H_2O$ in various volume ratios of 0, 0.05, 0.1, 0.15 and 0.25, producing 5 differing ZnO samples. It was found that as the concentration of the H_2O_2 initially increased, the crystallite size of the particles decreased, promoting high-surface area ZnO samples, with mainly nanorod shapes. Volume ratios above 0.15 of the precursors however, promoted an increase in crystallite size and thus decrease in surface area, and significant pointed and prismatic growth of the nanorods was observed by TEM.

On a significantly smaller scale to the experimental study reported in this thesis, Ohara *et al.*[332] reported on the synthesis of fine ZnO nanorods by hydrothermal synthesis in supercritical water in a reactor that was reported to be only 5 cm^3 in volume. In their reaction, they used an aqueous $Zn(NO_3)_2.6H_2O$ solution which had a flow rate of 2 cm^3 min^{-1}, and reacted it with supercritical water, which was at a temperature of 450 °C and a flow rate of 10 cm^3 min^{-1}. Inside the reactor, the temperature and pressure of the supercritical water were maintained at 400 °C and 30 MPa, respectively. The reduced size of the physical parameters in this literature study, to that reported in this thesis, establishes a stark contrast in the scale of reactor and resultantly the yield of product possible. Interestingly, TEM analysis of the resulting ZnO nanoparticles by Ohara *et al*. showed that they were associated to a mean diameter of 150 nm and a width of 600 nm, suggesting the formation of much larger nanoparticles than those that have been reported in this thesis. Further, their TEM analysis showed pure nanorod formation, unlike the variation of morphology observed experimentally.

6.2.2 Scanning Electron Microscopy (SEM)

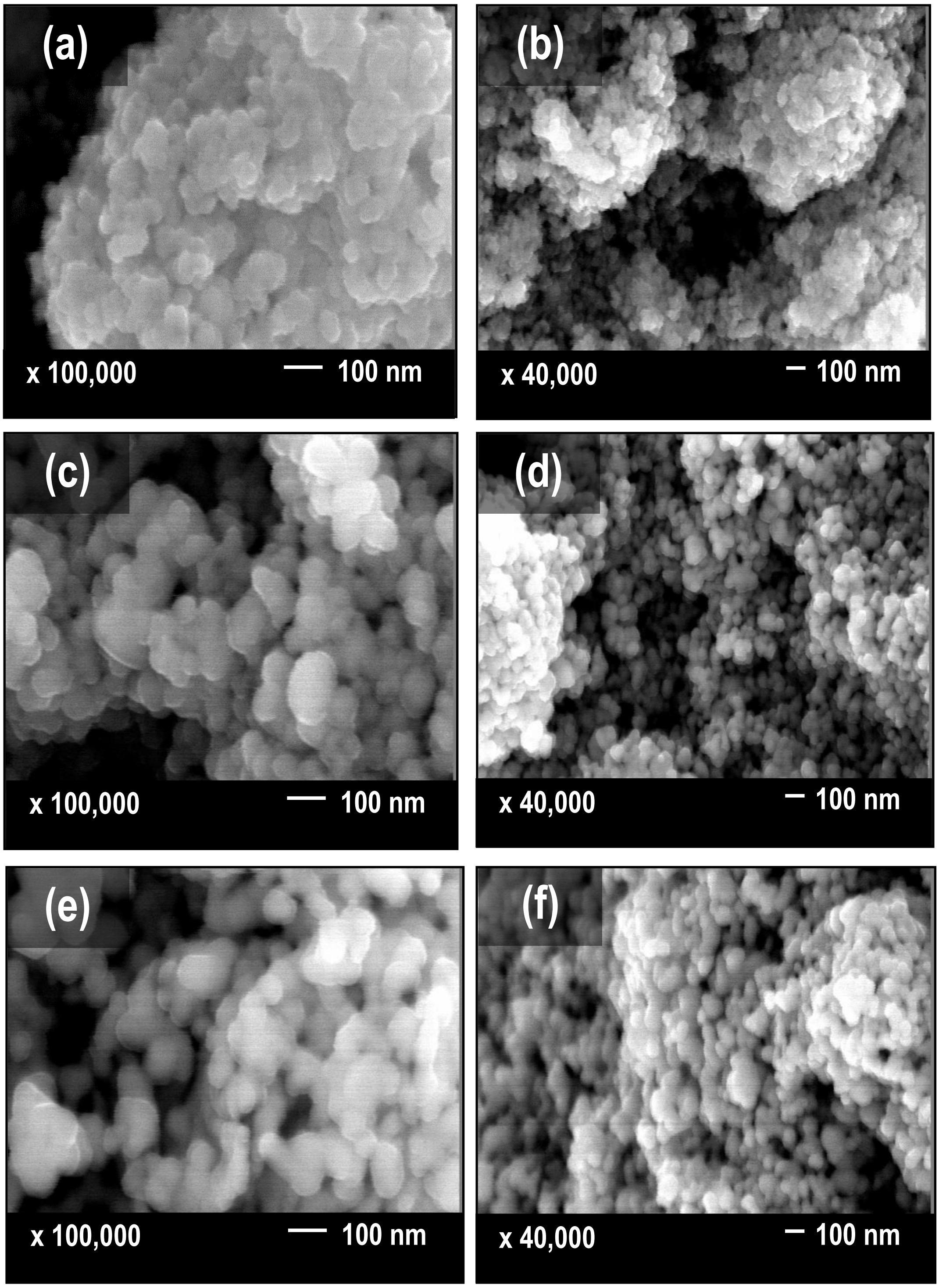

Figure 6–5. SEM images of (a) and (b) ZnO A at x 100,000 and x 40,000 magnification respectively, (c) and (d) ZnO B at x 100,000 and x 40,000 magnification respectively and (e) and (f) ZnO C at x 100,000 and x 40,000 magnification, respectively, after screen-printing onto gas sensor substrates and heat-treating at 600 °C. Samples A, B and C were prepared by CHFS which involved a reaction of ambient flows of 0.1, 0.2, 0.45 M of Zn $(NO_3)_2.6H_2O$ aqueous solution and KOH aqueous solution respectively (each flowing at 200 mL min^{-1}) with supercritical water flow at 450 °C and 240 bar (flowing at 400 mL min^{-1}) in a confined jet mixer.

SEM imaging of the CHFS fabricated ZnO samples in Figure 6–5, taken after the materials were individually screen-printed onto MOS sensor substrates and heat-treated at 600 °C, showed a variation in the morphology of the three individual ZnO sensor devices. Figure 6–5 (a) and (b) showed evidence of smaller ZnO particles attributed to significant agglomeration in sample A, as opposed to the larger grains in samples B and C, which were both observed to be associated to reduced inter-grain agglomeration, as seen in Figure 6–5 (c) & (d) and (e) & (f), respectively; particularly sample B.

Sample A from TEM imaging was observed to be composed of the smallest particle sizes of all three ZnO samples. Smaller nanoparticles (which are associated to larger surface areas due to a large surface:bulk ratio and therefore stronger intermolecular forces, compared to larger nanoparticles) are likely to be associated to agglomeration and dense packing upon heat-treatment (of 600°C), within the sensor matrix. The agglomeration can also be accounted for by the change in the particle size observed in sample A pre- and post- heat treatment. The as-prepared sample A was seen to be composed of nanoparticles predominantly in the range of 10 nm - 25 nm analysed via TEM imaging, with some nanorods exhibiting larger particle sizes than 25 nm. SEM imaging however, showed the particle sizes to be (measured from those particles that were visible upon the surface of the agglomerates) in the range 50 nm – 75 nm with some as large as 100 nm. This gave evidence that heat-treatment had promoted growth of the nanoparticles. The nanoparticles however, were so closely packed together in the sensor matrix as observed in Figure 6–5 (a), that only the particles on the surface of the agglomerates could be observed and measured, and those in the bulk could not be resolved.

In contrast, larger nanoparticles associated to lower surface:bulk ratios, implies greater thermal stability, and therefore less agglomeration upon heat-treatment. As such, larger nanoparticles provide effectively better surface site accessibility for the gaseous analyte molecules [70], through provision of diffusion pathways between the grain interfaces, to permeate through the body of the sensor matrix. SEM imaging shows reduced inter-grain agglomeration of samples B and C, however suggests growth of particles in both samples upon heat-treatment, with the former observed to be attributed to particle sizes of 50 nm - 150 nm as observed in Figure 6–5 (c) and the latter observed to be attributed to sizes of 110 nm - 200 nm as observed in Figure 6–5 (e).

Despite the inter-grain agglomeration observed in sample A, the provision of diffusion pathways were evident through the voids present between the agglomerates (i.e. inter-agglomerate diffusion) as observed in Figure 6–5 (b). Sample B and C in contrast, showed evidence of providing inter-grain and inter-agglomerate diffusion pathways for the gaseous analyte molecules.

6.2.3 Powder X-Ray Diffraction (PXRD)

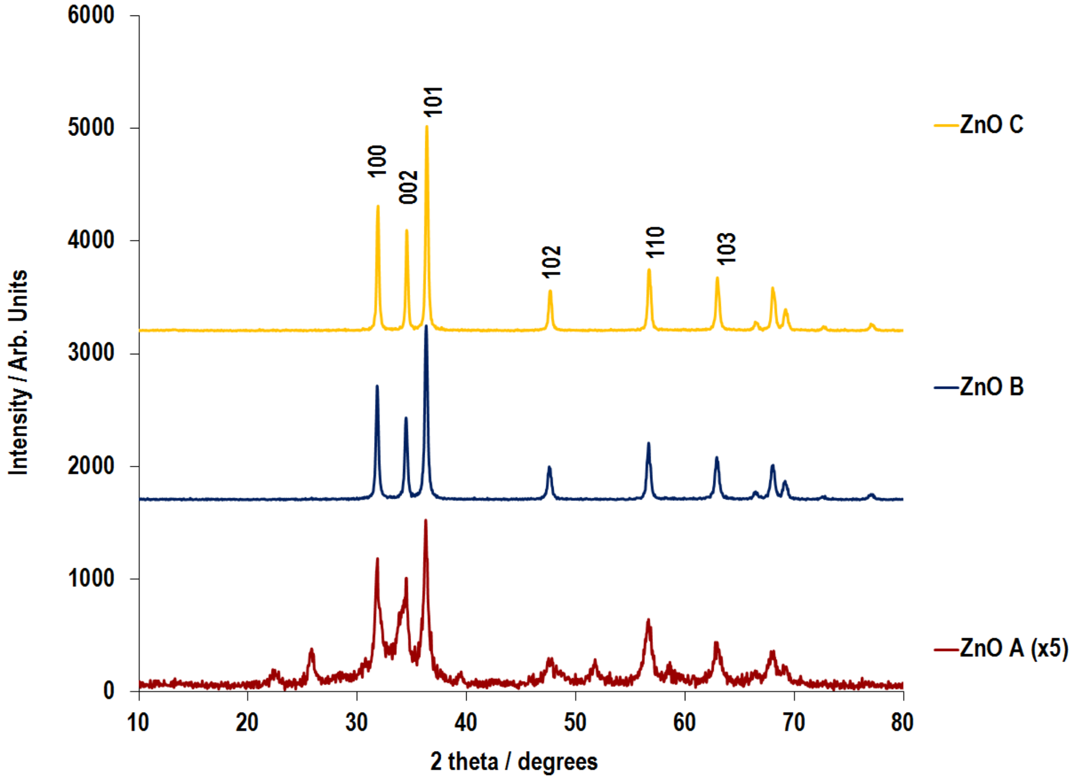

Figure 6–6. PXRD patterns of as-prepared CHFS ZnO samples ZnO A, ZnO B and ZnO C. Samples A, B and C were prepared by CHFS which involved a reaction of ambient flows of 0.1, 0.2, 0.45 M of Zn $(NO_3)_2.6H_2O$ aqueous solution and KOH aqueous solution respectively (each flowing at 200 mL min^{-1}), with a supercritical water flow at 450 °C and 240 bar (flowing at 400 mL min^{-1}) in a confined jet mixer.

PXRD data of the ZnO samples were in agreement with literature reports, which showed that the samples adopted a hexagonal wurtzite crystal structure [333], (JCPDS No. 36-1451) [143, 334]. The most intense reflections of the metal oxide have been labelled in Figure 6–6. The increasing peak intensity of the reflections in the range of 30-40 ° 2θ from sample A to sample C gave evidence of the increase in the apparent crystallinity of the ZnO materials. The greatest preferential intensity of the (101) reflection, suggested growth of the ZnO crystal structure in that plane.

6.2.4 Raman Spectroscopy

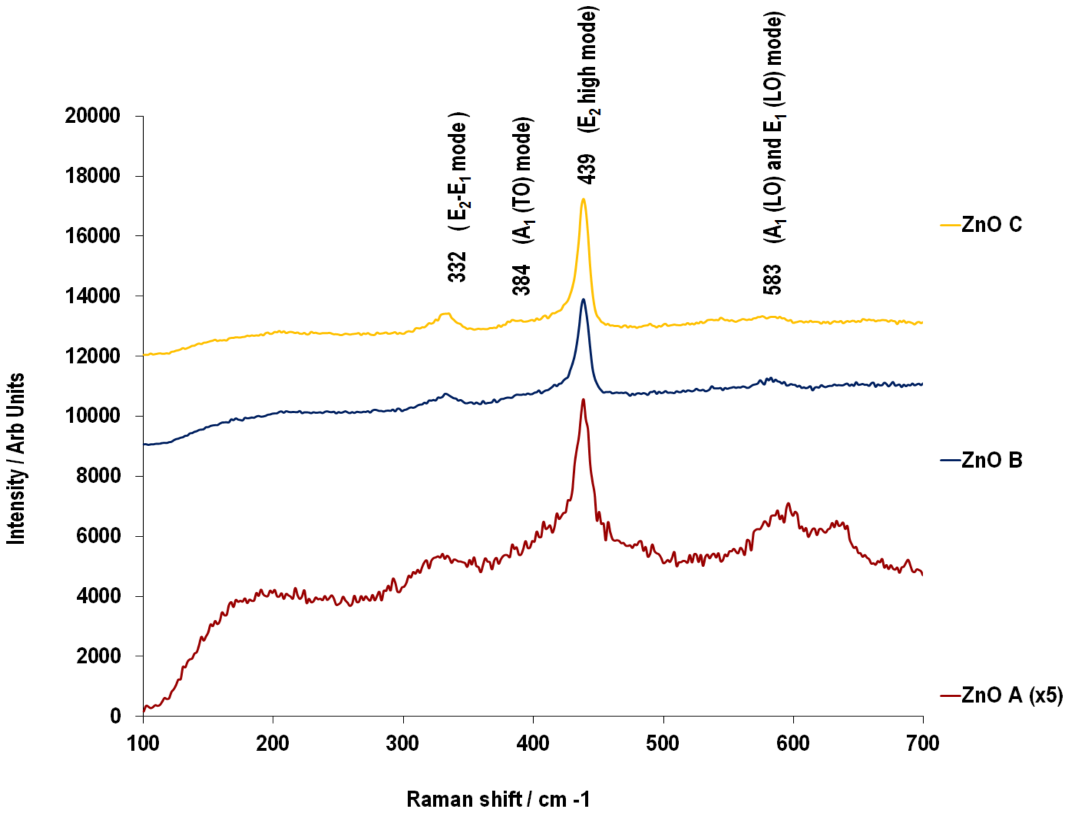

Figure 6–7. Raman spectra of as-prepared CHFS ZnO samples ZnO A, ZnO B and ZnO C. Samples A, B and C were prepared by CHFS which involved a reaction of ambient flows of 0.1, 0.2, 0.45 M of Zn $(NO_3)_2.6H_2O$ aqueous solution and KOH aqueous solution respectively (each flowing at 200 mL min^{-1}), with a supercritical water flow at 450 °C and 240 bar (flowing at 400 mL min^{-1}) in a confined jet mixer.

Raman spectroscopy of all three ZnO samples in Figure 6–7 suggested vibrations corresponding to wurtzite crystal structure [335, 336]. The vibration at around 439 cm^{-1} has been reported as a particularly characteristic feature of the wurtzite lattice and corresponds to the non-polar phonon E_2 high mode, associated to the O atom vibrations in the structure [335, 336]. The vibration observed at 332 cm^{-1} is a second order forbidden mode corresponding to a E_2-E_1 phonon mode [336]. The broad peak at 583 cm^{-1} is a combination of two modes, which explains its broadness, and corresponds to the A_1 (LO) and E_1 (LO) vibrational modes. The presence of the E_1 (LO) mode is disallowed, however, one reason for its presence has been associated to oxygen deficiencies in the ZnO materials [335, 336]. Finally, the peak at 384 cm^{-1}, corresponds to the A_1 (TO) mode, which is present in this case most likely due to induced disorder through structural influences [336]. The same Raman pattern was observed in a similar study by Shi *et al*. [143].

6.2.5 Brunauer-Emmet-Teller (BET) Surface Area measurements and Crystallite size

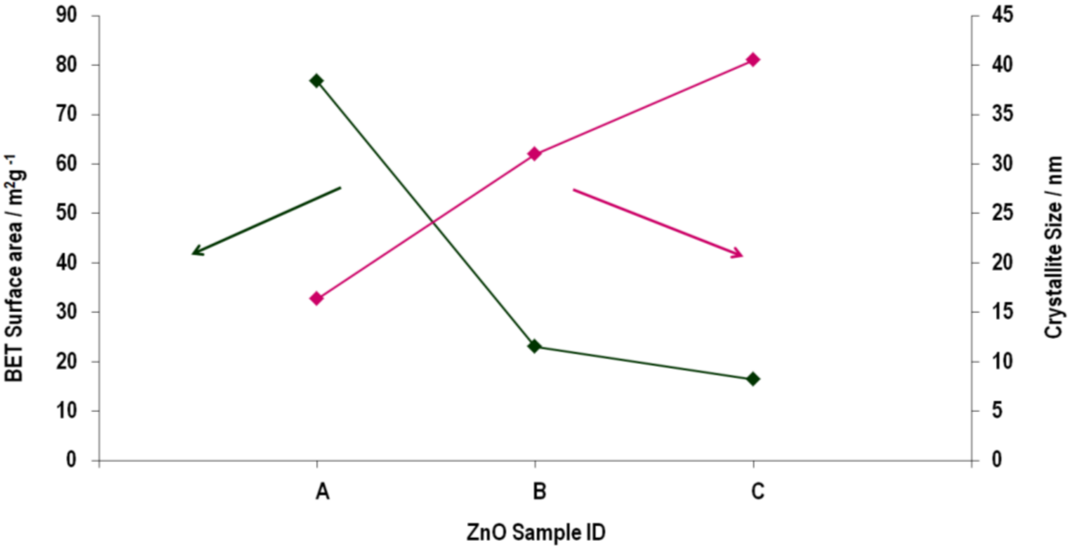

Figure 6–8. BET surface area vs. approximated Crystallite Size (Scherrer equation) of as-prepared CHFS samples ZnO A, ZnO B and ZnO C. Samples A, B and C were prepared by CHFS which involved a reaction of ambient flows of 0.1, 0.2, 0.45 M of Zn $(NO_3)_2.6H_2O$ aqueous solution and KOH aqueous solution respectively (each flowing at 200 mL min^{-1}), with a supercritical water flow at 450 °C and 240 bar (flowing at 400 mL min^{-1}) in a confined jet mixer.

BET results presented in Figure 6–8, revealed that the specific surface area of the ZnO samples decreased from sample A to C, i.e. as a function of precursor concentration. This trend corroborated with the TEM analysis in Figure 6–1, which established that the higher concentrations of both Zn $(NO_3)_2.6H_2O$ and KOH precursors, resulted in increasing particle size, suggesting a decrease in the specific surface area of the particles. This observed trend of the surface area reiterated the influence of precursor concentration on the surface energy of the particle growth and suggested that increasing concentration of precursor promoted greater surface energy to the particles, resulting in larger particle sizes.

The Scherrer equation (Equation 6–3) was used in conjunction with the PXRD data presented in Figure 6–6, to understand the general trend in crystallite size variation, by calculating the approximate crystallite sizes of the three different ZnO samples. These have been plotted against the associated BET surface areas in Figure 6–8.

Equation 6–3 $$D = \frac{k\lambda}{\beta \cos\theta}$$

In the calculation, *K,* the shape factor was assumed to be 0.90 [337], λ, the X-ray wavelength was 1.5418 Å, β was the full width half-maximum of the diffraction line and θ was the Bragg angle.

Figure 6–8 showed an inverse relationship between the crystallite size and the surface area, with the crystallite size seen to increase from sample A to sample C, as the surface area concurrently decreased. The crystallite size trend was in good agreement with the observed trend of particle sizes observed via TEM, as a function of precursor concentration.

6.2.6 Gas Sensing

6.2.6.1 Ethanol Sensing

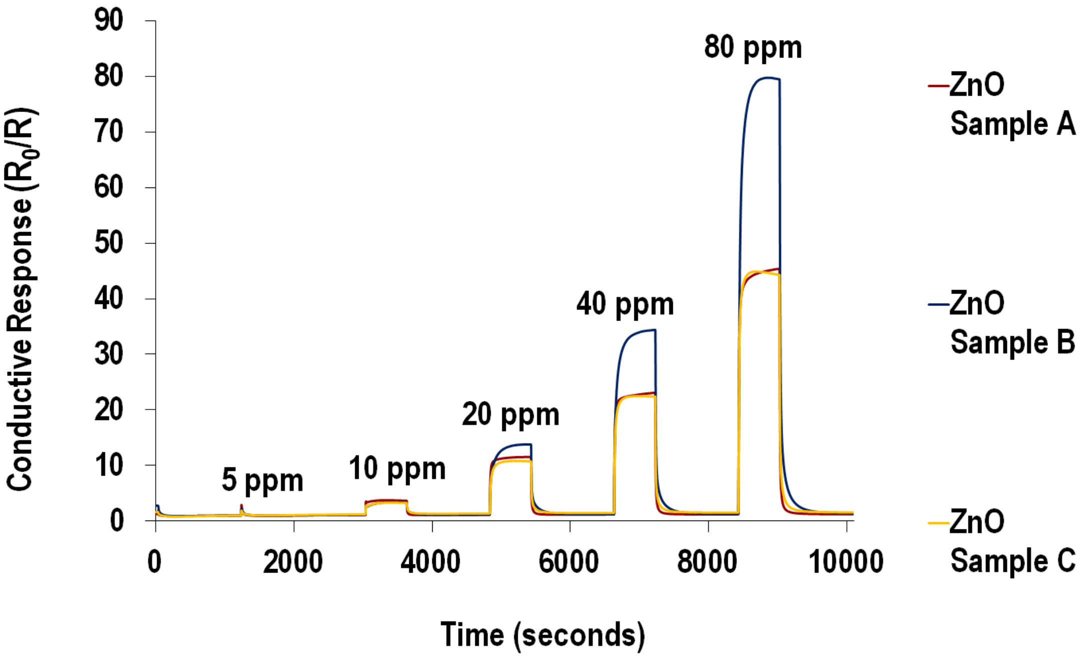

Figure 6–9. Conductive response traces of CHFS ZnO samples: ZnO A, ZnO B and ZnO C at 350 °C against 5, 10, 20, 40 and 80 ppm of ethanol. Samples A, B and C were prepared by CHFS which involved a reaction of ambient flows of 0.1, 0.2, 0.45 M of Zn $(NO_3)_2.6H_2O$ aqueous solution and KOH aqueous solution respectively (each flowing at 200 mL min^{-1}), with a supercritical water flow at 450 °C and 240 bar (flowing at 400 mL min^{-1}) in a confined jet mixer.

Figure 6–9 presents the conductive response traces of all three ZnO sensors at an operating temperature of 350 °C, against increasing concentrations of ethanol. Tabulation of the mean responses values of the sensor devices in the CHFS ZnO system from the repeat tests against exposure towards the various ethanol concentrations at 350 °C and the associated 95% confidence intervals have been presented in Table 6–1.

Table 6–1. Average conductive responses of sensor devices in CHFS ZnO system from all repeat tests against various ethanol concentrations at 350 °C and associated errors in the form of 95% CIs.

	10 ppm		20 ppm		40 ppm		80 ppm	
Device	Average Response	95% CI	Average Response	95% CI	Average Response	95% CI	Average Response	95% CI
ZnO sample A	3.93	±0.34	11.78	±0.51	23.36	±0.51	45.7	±0.69
ZnO sample B	3.53	±0.25	13.91	±0.24	34.25	±0.30	Electronic capping out	
ZnO sample C	3.63	±0.62	11.48	±1.30	23.27	±1.69	45.2	±0.20

350°C was the operating temperature at which all three sensor devices exhibited substantial conductive response towards ethanol (as observed further in Figure 6–13). In particular both sample A and sample C were observed to exhibit better responses at this operating temperature towards ethanol, in comparison to all remaining temperatures in the range of 300 °C – 500 °C.

Comparison of the response magnitudes of all three sensor devices at this temperature, showed that ZnO sample B outperformed ZnO samples A and C, with a response of 79.7 towards 80 ppm of ethanol, which was a 1.8-fold enhanced response with respect to samples A and C, which both interestingly exhibited the same response of 45 towards 80 ppm of the analyte.

In comparison to these response results, Wang *et al.* [235] reported on the ethanol gas sensing properties of ZnO nanorods, fabricated by a low temperature hydrothermal synthesis route, which performed optimally at 320 °C, with a response value of 22 towards 50 ppm and 26 towards 100 ppm. Rai *et al.* [338] also reported on the ethanol gas sensing properties of ZnO nanorods prepared via a microwave assisted hydrothermal method which had exhibited a response of 6.83 at an operating temperature of 400 °C towards 250 ppm. Wan *et al.* [339] reported on the gas sensing properties of ZnO nanowires, which were fabricated via a thermal evaporation method and deposited onto MEMS substrates. The group reported their ZnO materials to have a response of 32 against 100 ppm ethanol at 300 °C.

Figure 6–9 showed that sample B was associated to a significant increase in conductive response amplitude between an exposure of 40 ppm and 80 ppm of ethanol. In contrast, both ZnO samples A and C, showed a lower increase in response amplitude between both concentrations i.e. both samples saturated quicker than sample B. This behaviour has been more clearly presented in Figure 6–10.

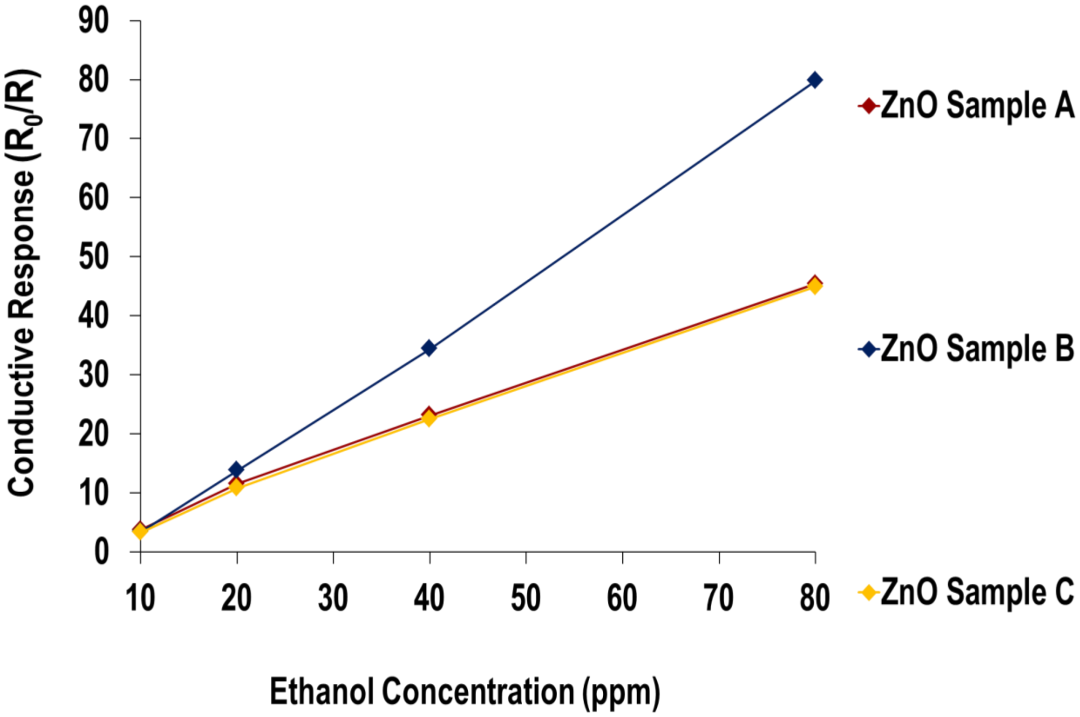

Figure 6–10. Conductive response of CHFS ZnO samples: ZnO A, ZnO B and ZnO C at 350 °C against 10, 20, 40 and 80 ppm of ethanol. Samples A, B and C were prepared by CHFS which involved a reaction of ambient flows of 0.1, 0.2, 0.45 M of Zn $(NO_3)_2.6H_2O$ aqueous solution and KOH aqueous solution respectively (each flowing at 200 mL min^{-1}), with a supercritical water flow at 450 °C and 240 bar (flowing at 400 mL min^{-1}) in a confined jet mixer.

Figure 6–10 illustrates the reduced gradient of conductive response profiles of both ZnO A and ZnO C, in comparison to ZnO B, as a function of increasing ethanol concentration. The reduced gradients indicate that both samples A and C do and will saturate a lot earlier than sample B as a function of the increasing concentrations of ethanol. This behaviour was suggestive of the limited number of surface sites in samples A and C, which implied a restricted number of adsorbed oxygen anions on the metal oxide surfaces, limiting the overall yield of ethanol reactions that could occur. As such, an increase in the concentration of ethanol from 40 ppm to 80 ppm, resulted in only small increases in the conductive response amplitudes for both the samples, as only a limited number of ethanol molecules could be accommodated on the metal oxide surfaces at 80 ppm, with respect to 40 ppm.

In contrast, the significant increase in conductive response of sample B between 40 ppm and 80 ppm was indicative of an increase in the yield of ethanol surface reactions occurring at 80 ppm relative to 40 ppm. This behaviour suggested a larger number of surface sites in sample B, resulting in an increased concentration of adsorbed anionic oxygen species. This would lead to a higher yield of ethanol species (associated to 80 ppm ethanol) being accommodated on the surface of the sample B, resulting in a significant increase in conductive response amplitude with respect to 40 ppm.

This difference in response behaviour between the three ZnO samples may be accounted for by the lower agglomerated network between the individual ZnO grains associated to sample B, as observed in Figure 6–5 (d). Such a microstructure can provide inter-grain (and inter-agglomerate) diffusion pathways [70] for the gaseous analyte molecules to permeate through, increasing the overall surface site interaction. In contrast, sample A was seen to be associated to significant agglomeration between the ZnO grains as observed in Figure 6–5 (a), accounted for by the impact of heat-treatment on the smaller nanoparticle sizes. This agglomeration is suggestive of reduced surface site accessibility for the ethanol analyte molecules and as such could have influenced its poorer response with respect to ZnO sample B. Korotchenkov [70] reported that agglomeration can result in “capsulated zones” forming within the matrix of the sensor, which are areas through which gas molecules cannot travel. As such, agglomeration proves detrimental for gas responsivity, which is what was observed with sample A. The larger particle sizes of ZnO sample C, as observed via TEM imaging Figure 6–1 (e) and (f), may justify its poor response performance with respect to sample B, with larger particle size associated to lower surface : bulk ratios, which indicates a reduced number of surface sites for the ethanol molecules to interact with.

Careful observation of Figure 6–9 shows that in terms of kinetics of response, ZnO sample C was attributed to significant saturation of its surface sites accounted by the flattened box shape of its response curves against all concentrations of ethanol, indicating that this sensor device was associated to a fast response with a t_{90} (80 ppm) calculated to be 46 seconds. The response curves of ZnO sample A were seen replicate those of ZnO sample C; with all exhibiting saturation of the surface sites and indicating a similar response speed to that of sample C, with the t_{90} (80 ppm) calculated to be 47 seconds. In contrast to both samples A and C, the response curves of ZnO sample B were attributed to greater curvature, indicating that the surface sites of the sample were not fully saturated. This suggested the availability of further surface sites that could be occupied and the sample was calculated to have a t_{90} (80 ppm) of 98 seconds, indicating a slower response speed of the sample, with respect to samples A and C. The study showed that the kinetics was compromised for the enhanced responsivity associated to ZnO sample B.

Figure 6–9 further indicated that the kinetics of recovery to baseline was the fastest for ZnO sample A with a t_{-90} (80 ppm) calculated to be 282 seconds. The fast recovery of this sample was observed by its very steep return to baseline after exposure to 80 ppm (and lower concentrations) of ethanol. ZnO sample C was the second fastest sample to recover with a t_{-90} (80 ppm) calculated to be 464 seconds.

The slower recovery of this sample was identified through its more gradual return to baseline after exposure of the different concentrations of ethanol relative to sample A. Of all three samples, it was evident from Figure 6–9, that sample B was associated to the slowest recovery with the approach of the response to baseline value observed to be very gradual. The calculated t_{-90} (80 ppm) value of 692 seconds of sample B suggested slow recovery, in comparison to both other ZnO samples.

The slow recovery of sample B, in comparison to samples A and C, may have been associated to the stronger adsorption or bonding of the products from the decomposition of ethanol, such as acetal to the surface of the metal oxide particles of the sample, in comparison to the propensity of the adsorption and bonding that the other two samples had for the decomposition products [340, 341]. The lower inter-grain agglomeration may also account for the slower recovery; with a greater number of surface sites to be recovered per unit time, accounting for slower kinetics of recovery. For example, when Kanan *et al*. [341] reported measuring the resistance measurements on a sample of porous WO_3 and non-porous WO_3 against exposure to various alcohols and dimethyl methylphophonate (DMMP), the group had reported observing a steep change in the increase in the resistance of the non-porous oxide relative to the porous oxide, which potentially suggested slower diffusion in the porous oxide, accounted for by the larger number of surface sites it provided for gas interaction.

The conductive response convergence of samples A and C is an interesting feature of both Figure 6–9 and Figure 6–10 and suggests that both ZnO samples may have been associated to an equivalent occupation of electrons in the conduction bands of the semiconducting oxides, resulting in a similar yield of ethanol surface reactions at 350 °C. Furthermore, the similar response behaviour between both samples suggests that the smaller particle sizes of sample A which were observed to promote significant inter-grain agglomeration, may have balanced out the larger particle sizes of sample C. Both factors contributing to lower surface:bulk ratios. As such, both factors contributed similarly to limiting the surface site accessibility of the ethanol molecules with the metal oxide matrices.

6.2.6.2 NO_2 Sensing

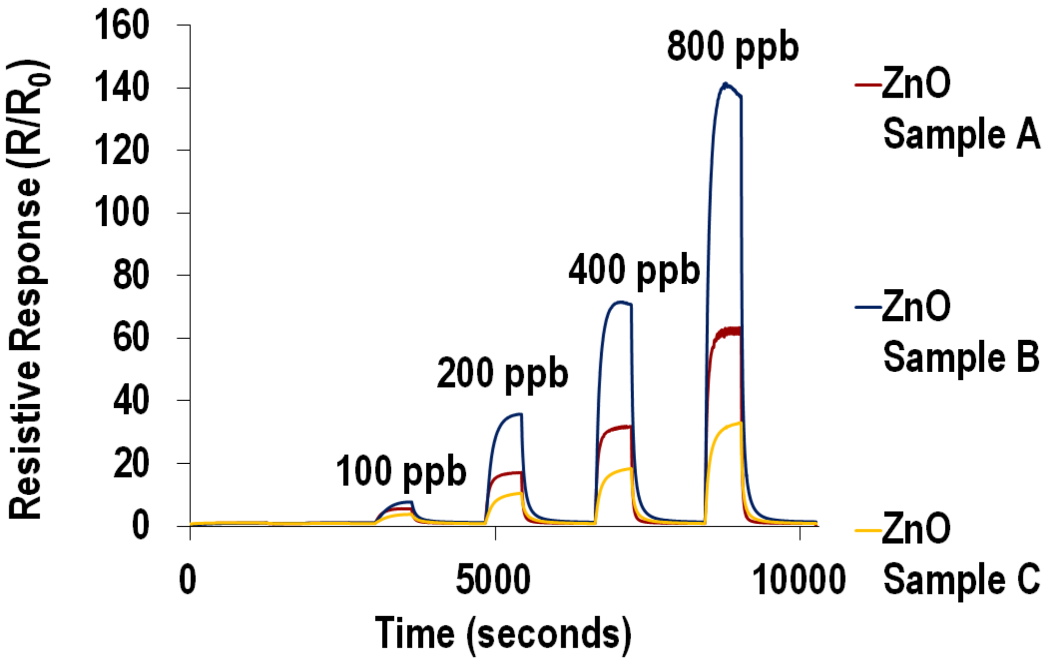

Figure 6–11. Resistive response traces of CHFS ZnO samples: ZnO A, ZnO B and ZnO C at 250 °C against 100, 200, 400 and 800 ppb of NO_2. Samples A, B and C were prepared by CHFS which involved a reaction of ambient flows of 0.1, 0.2, 0.45 M of Zn $(NO_3)_2.6H_2O$ aqueous solution and KOH aqueous solution respectively (each flowing at 200 mL min^{-1}), with a supercritical water flow at 450 °C and 240 bar (flowing at 400 mL min^{-1}) in a confined jet mixer.

Figure 6–11 presents the response curves of the CHFS based ZnO nanomaterials against increasing concentrations of NO_2 at 250 °C. Tabulation of the mean responses values of the sensor devices in the CHFS ZnO system from the repeat tests against exposure towards the various NO_2 concentrations at 250 °C and the associated 95% confidence intervals have been presented in Table 6–2.

Table 6–2. Average resistive responses of sensor devices in CHFS system from all repeat tests against various NO_2 concentrations at 250 °C and associated errors in the form of 95% CIs.

	100 ppb		200 ppb		400 ppb		800 ppb	
Device	Average Response	95% CI	Average Response	95% CI	Average Response	95% CI	Average Response	95% CI
ZnO sample A	4.86	±0.72	18.29	±2.93	31.66	±0.39	64.04	±1.36
ZnO sample B	6.38	±1.44	38.92	±4.34	80.71	±9.98	159.33	±21.53
ZnO sample C	3.54	±0.52	12.66	±3.58	19.45	±2.06	36.00	±5.90

250 °C was the was the operating temperature at which all three sensor devices exhibited substantial resistive response towards NO_2 (presented further in Figure 6–14); in particular both sample A and sample C were observed to exhibit better responses at this operating temperature to NO_2, in comparison to all remaining temperatures in the range of 300 °C – 500 °C.

Figure 6–11 shows that ZnO sample B gave a larger response towards all concentrations of NO_2 exposure (in comparison to both samples A and C), with the maximum response of this sensor device attributed to 141 against 800 ppb of the analyte. This was a 2.1 fold enhanced response in comparison to sample A (which exhibited a response of 65.7) and 4.3 fold enhanced response with respect to sample C (which exhibited a response of 33), under the same operating conditions.

In the study by Shi *et al*. [143], the optimal temperature of operation of ZnO nanomaterials fabricated in the CHFS pilot plant was 350 °C against NO_2, with the highest response of 128 achieved against 10 ppm of the analyte. Liu *et al*. [51] reported observing ZnO nanorods, with a diameter of ~33 nm, prepared by a hydrothermal method, exhibiting a response of 199 towards 5 ppm NO_2 in N_2 carrier gas at 250 °C. Ozturk *et al*. [342] reported on ZnO nanorods of size 60 nm, also fabricated by a hydrothermal method, exhibiting a response of 2.1 toward 1000 ppb NO_2 at 200 °C. These literature studies suggest that the ZnO nanomaterials reported in this thesis are successful for the detection of NO_2.

Analogous to the observation with ethanol, ZnO sample B was seen to exhibit a substantial increase in resistive response amplitude as a function of increasing concentration of NO_2, particularly between 400 ppb and 800 ppb. In contrast, ZnO samples A and C were seen to be attributed to shallower increases in resistive response as a function of increasing NO_2 concentration. This behaviour is presented more clearly in Figure 6–12.

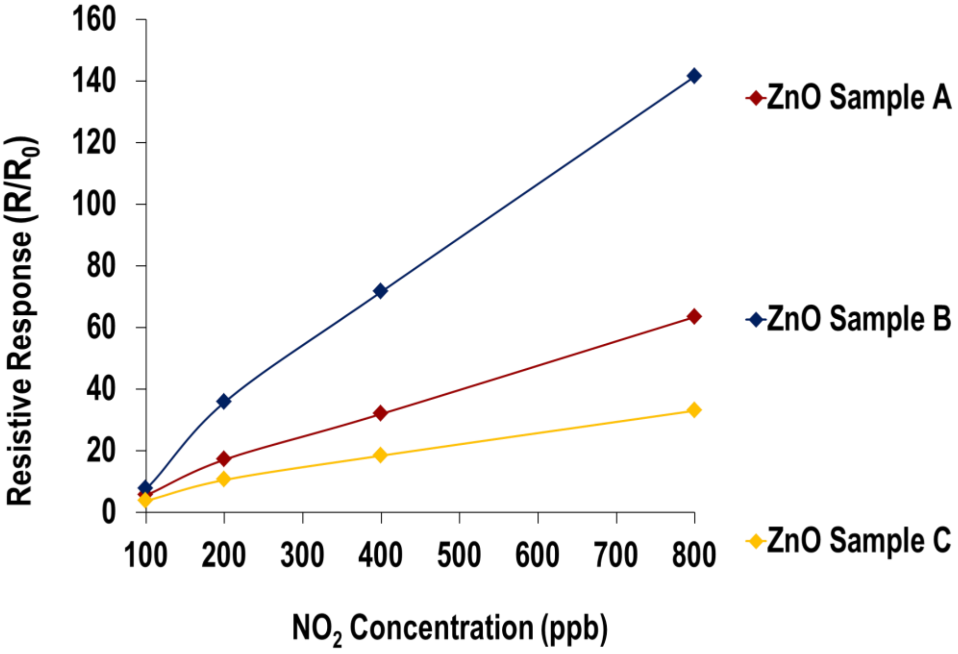

Figure 6–12. Resistive response of CHFS ZnO samples: ZnO A, ZnO B and ZnO C against increasing concentrations of NO_2 at 250 °C. Samples A, B and C were prepared by CHFS which involved a reaction of ambient flows of 0.1, 0.2, 0.45 M of Zn $(NO_3)_2.6H_2O$ aqueous solution and KOH aqueous solution respectively (each flowing at 200 mL min^{-1}), with a supercritical water flow at 450 °C and 240 bar (flowing at 400 mL min^{-1}) in a confined jet mixer.

The rapid increase in the resistive response of ZnO sample B was indicative of a substantial increase in yield of NO_2 surface reactions as a function of increasing NO_2 exposure concentration, which promoted a substantial abstraction of charge carriers (as a result of the NO_2 interaction with the surface of n-type semiconducting oxides) from the electron depletion layer, resulting in such a significant change in the conductivity of the material. A further indication of this response behaviour was the inherent change in the size of the electron depletion layer (Debye Length). If the sample did contain ZnO grains which were comparable to twice the size of the Debye Length, then the space charge region will have developed within the crystallites of the grains, inducing grain controlled conductivity, which is more responsive than grain boundary controlled conductivity [63, 68, 269], as discussed in Chapter 1. This may explain the larger and faster increase in conductivity of sample B compared to samples A and C. Furthermore, the possibility of a larger yield of NO_2 surface reactions on the surface of sample B is indicative of a highly populated conduction band or the availability of a larger number of surface sites in this material to promote an enhanced number of NO_2 surface reactions. The larger number of surface sites can be accounted for by the nano-sized particles as well as the lower inter-grain agglomeration observed between the grains via SEM imaging in Figure 6–5 (c) and (d) of the ZnO sample B sensor device.

In terms of the kinetics of response and recovery against NO_2, Figure 6–11 illustrated that ZnO sample C responded the slowest in comparison to both ZnO samples A and B, observed by its shark-fin response curve, which responded gradually upon exposure to the analyte. Calculation of t_{90} (800 ppb) value of the device was 293 seconds which was slower than sample A, which had a calculated t_{90} (800 ppb) value of 133 seconds and sample B which had a t_{90} (800 ppb) of 155 seconds. The kinetics of the recoveries of the samples were also seen to be attributed to a similar trend with sample C associated to the slowest recovery with a t_{-90} (800 ppb) value calculated to be 894 seconds, whilst for the sample A the t_{-90} (800 ppb) value was 645 seconds and that for sample B was 877 seconds. The long response and recovery times here are likely to have been influenced by the low temperatures of operation of 250 °C, in comparison to those observe for ethanol at 350 °C. An increase in the thermal energy in the system, through an increase in operating temperature is statistically likely to promote a larger concentration of electrons to the conduction band of ZnO, promoting faster response and recovery of the ZnO sensor materials towards NO_2.

Zhang *et al*. [343] had reported on the characterization and gas sensing properties of ZnO hollow spheres of sizes 200 nm – 360 nm, with shells of thickness 25 nm, which were prepared using carbon microsphere templates. The group had reported that their materials had shown an optimal response at 240 °C towards 10 ppm, 50 ppm and 100 ppm NO_2, with associated response of 140.6, 172.8 and 286.8, respectively. The respective response times towards each concentration were reported to be 31, 19 and 9 seconds respectively. In comparison to the literature study, the responsivities of the CHFS based ZnO materials presented in this thesis are better, given the ppb concentration range of NO_2 tested here, with ZnO sample B seen to exhibit a response of 141 toward 800 ppb NO_2 at 250 °C. The response times however, obtained by Zhang *et al*., were significantly better than those reported in this thesis, however, this could be accounted for the higher concentrations (in the ppm range) of NO_2 that Zhang *et al*. used which are likely to saturate the surface sites faster than ppb concentrations in the same time.

One of the key trends observed in terms of response and recovery times in this Chapter and also in the previous experimental Chapters for all sensor devices fabricated, is the slower recovery times relative to the response times. Choi *et al*. [344] have reported in their study, based on other works in the literature, that the response times of sensor devices based on the n-type semiconducting oxides are usually associated to shorter response times in comparison to recovery times, when the devices are exposed to reducing gases, independent of the n-type material used. They report that this trend indicates that the diffusion of the analyte gas to the surface and the body of the sensor matrix and its subsequent oxidation with the surface adsorbed anionic oxygen species such as O^- or O^{2-}, is generally shorter than a series of recovery reactions that take place. The recovery times of MOS sensors [344, 345] are said to be made up of a series of sequential steps which include the counter-diffusion of the oxidized product gases, the diffusion of oxygen species towards the metal oxide surface, and the adsorption, dissociation and ionization processes of the oxygen species; all of which are thought to slow down the overall recovery of the metal oxide. In the studies reported in this thesis, the slower recovery times relative to fast response times, are not limited to reducing gases, but are also seen for the oxidising gas, NO_2.

6.2.7 Key influential factors effecting responsivity order of ZnO samples A, B and C.

A key observation from Figure 6–9 - Figure 6–12 is the uncorrelated behaviours between the response magnitudes/orders of ZnO samples A and B, and their associated particle sizes. Smaller grain sizes were reported by Yamazoe to induce an increase in gas sensing responsivity [19, 326]. Given that sample A was associated to the smallest particle sizes of all three ZnO samples (and therefore a larger surface to bulk contribution) it was expected that it would exhibit the largest response [70]; instead, sample B has been observed to exhibit the best response magnitudes. Particle sizes however, are not the only physical contributions to the overall microstructure of the material, and therefore are not deterministic of the final response behaviours. There are various key physical factors that potentially played an influential role over the microstructure of both samples [70], contributing to the responsivity behaviours observed. These factors are briefly discussed in the following sections.

6.2.7.1 Effect of particle size and morphology

Sample A is composed of the smallest nanoparticles of all three ZnO samples and smaller nanoparticles (which are attributed to larger surface to bulk contributions and therefore stronger intermolecular forces, compared to larger nanoparticles), have greater propensity to be tightly agglomerated and densely packed within the sensor matrix. SEM imaging showed evidence of visible agglomeration of the grains in sample A in Figure 6–5 (a) and (b). In comparison, reduced inter-grain agglomeration was visible in samples B and C containing larger nanoparticles as observed in Figure 6–5 (c) & (d) and (e) & (f) respectively, particularly in sample B. Reduced agglomeration, implies greater surface site accessibility, promoting better access for the analyte molecules to the active surface sites [70], allowing the target gas to permeate and diffuse through the volume of the sensor matrix. Thus the dimensions of the particles play a key role in determining the packing structure [170] of the particles as well as the surface site accessibility within the gas sensing material.

It has also been reported that the external planes of nanocrystals participate in the interaction between the solid and gas, and therefore, play an important role in the determination of the gas sensing properties [70]. Additionally, the shape of the nanocrystal has been reported to determine the crystallographic planes, the inter-grain contacts and permeability of gas, among other physical factors [70]. This suggests that the morphology of the crystallites influences the observed gas sensing behaviour and that the greater concentration of hexagonal particles with multiple facets in sample B potentially provided a larger number of surfaces for surface reactions, in comparison to crystal morphologies which possess limited facets, such as spheres and rods, which dominated samples A and C. In this way, both particle size and morphologies may have been key influencing factors for the enhanced response behaviour of sample B in comparison to both A and C.

6.2.7.2 Effect of heat-treatment

Heat-treatment is another factor which can influence the surface area of the materials through promoting agglomeration, sintering and neck formation effects between the individual particles [63]. Further, it is well-established that heat-treatment can effect an increase in the size of particles [65, 346]. Comparison of the TEM images in Figure 6–1 and the post-heat treated particles via SEM in Figure 6–5 did show evidence of the growth of the nanoparticles after heat-treatment.

The formation of necks at the grain boundary, due to sintering [63], has been reported to take place at extremely high temperatures of annealing which lie in the range of 700 – 800 °C and greater [65, 70]. However 600 °C, (which was the heat-treatment temperature used in this study), is considered a substantially high temperature for nanomaterials and has been reported to promote agglomeration and potential sintering of ZnO nanoparticles [346]. SEM images of ZnO samples A, B and C seen in Figure 6–5 (a), (c) and (e), respectively, did show evidence of particle agglomeration between the particles post heat-treatment at 600 °C. Further, operation of the sensor devices at 400 °C - 500 °C during gas sensing experiments, may have also promoted microstructural changes to the nanomaterials. Singh *et al.* [233] reported on thermal sintering effects on ZnO nanomaterials, with temperatures as low at 600 °C, having an effect on the growth of the particles. For example, 6 nm particles at 400 °C, were reported to grow as large as 30 nm at 600 °C to as large as 65 nm at 800 °C, with agglomeration also observed as a function of temperature. Agglomeration can pose various problems for gas sensing applications, the first of which is lowering responsivity due to loss of grain boundary and neck contributions to the surface contribution [65], which results in lowering the surface site accessibility and the provision of diffusion pathways for the gaseous molecules to travel through. The second disadvantage of agglomeration is potentially slowing the speed of response as the diffusion through agglomerated particles can be more difficult and can take longer [346].

Here, agglomeration was seen to be more prominent with the smaller nanomaterial particles in sample A, in comparison to the larger nanomaterial particles in samples B and C. Such closures between the grains or these “capsulated zones” [70] can contribute to lowering the inter-grain diffusion of the gas molecules throughout the volume of the sensing matrix [70], thus, decreasing the overall response of the material. Heat treatment conditions are likely to affect the microstructure of smaller nanoparticles more dramatically due to weaker intermolecular forces existing between the grains in contrast to larger nanoparticles.

6.2.7.3 Effect of neck formation

The profound effects of heat-treatment on the grain boundaries of nanoparticles, which can promote neck formation effects between the grain interfaces, can result in the grain boundary contributions dominating the overall gas sensing performance of a material. If the extent of sintering between the particles is too profound, it can result in the inner region of the neck behaving like the bulk of the material, making only the surface of the particles sensitive, thus contributing to a lower responsivity [65]. In such a case, the sintering is so profound that it results in the loss of the grain boundary and neck contributions and this is possible with grains, particularly in the nm range, exposed to high temperatures. If however the particles can overcome the thermal energy barrier, then less sintering between the grain boundaries is likely which implies the grain boundaries and the neck region can contribute to the overall surface, making the material significantly more responsive [65]. In the case of this study the dimensions and the intermolecular forces of the nanoparticles, contribute to their instability under the applied heat-treatment conditions, which indicates significant domination of grain boundary contributions to the overall responsivity.

In a study by Jun *et al*. [346], commercial ZnO nanoparticles with an average crystallite size of ca. 120 nm, with an system of different shapes exhibited a response value of 150 toward 400 ppb NO_2 at 200 °C. In their study, heat-treatment was conducted at 400 °C for 12 hours, which was reported as the optimal heat-treatment temperature (as it maintained the porous network of grains and prevented substantial agglomeration of the nanoparticles). Neck formation effects as well as an increase in particle size (originally 70 nm) were also observed in the report however, their sensors displayed excellent responses. In comparison, Figure 6–11 and Figure 6–12 showed that ZnO sample B (which was heat-treated at 600 °C for 1 hour) was attributed to a response of 71 towards 400 ppb NO_2 at 250 °C. Comparison to Jun *et al*'s report suggests that the thermal treatment regime is something to be further experimented with, to evaluate the ideal heat-treatment regime to obtain the optimal microstructural development of the CHFS based ZnO nanomaterials.

Overall, various physical factors potentially play complex roles towards manipulating the microstructure of the nanomaterials and can help to explain the behaviour of the ZnO samples; in particular for ZnO samples A and B. In the case of ZnO sample C, physical attributes such as largest particle size, greater agglomeration (in comparison to ZnO sample B) and lack of multi-facetted crystallites, may have contributed to its weaker responsivity.

Figure 6–13 and Figure 6–14 present the temperature profile of the CHFS sensor devices between 250 °C and 500 °C, when exposed to 80 ppm of ethanol and 800 ppb of NO_2, respectively. The graphs show that the specific optimal operating temperatures for each device were different. For ethanol, sample A exhibited optimal performance at 300 °C with a response of 47, sample B at 400 °C with a response of 84 and sample C at 350 °C (also observed in Figure 6–9) was attributed to response of 45. All sensor devices were seen to exhibit substantial performance at an operating temperature of 350 °C, as mentioned earlier in the Chapter. With NO_2, samples A and C were not seen to be attributed to any specific optimal performance temperature, however were seen to exhibit the best performance at 250 °C, with sample A exhibiting a response of 63 and sample C a response of 33. Sample B in contrast was associated to a specific optimal operating temperature of 300 °C, with an associated response of 166, at this temperature.

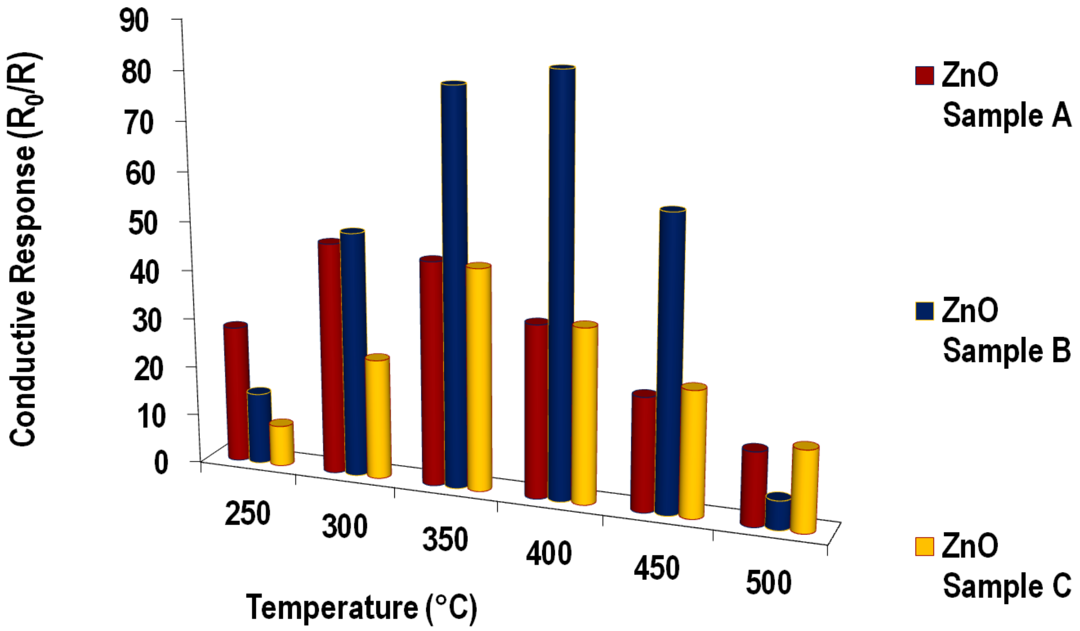

Figure 6–13. Conductive response of CHFS ZnO samples: ZnO A, ZnO B and ZnO C as a function of increasing operating temperature against 80 ppm of ethanol. Samples A, B and C were prepared by CHFS which involved a reaction of ambient flows of 0.1, 0.2, 0.45 M of Zn $(NO_3)_2.6H_2O$ aqueous solution and KOH aqueous solution respectively (each flowing at 200 mL min^{-1}), with a supercritical water flow at 450 °C and 240 bar (flowing at 400 mL min^{-1}) in a confined jet mixer.

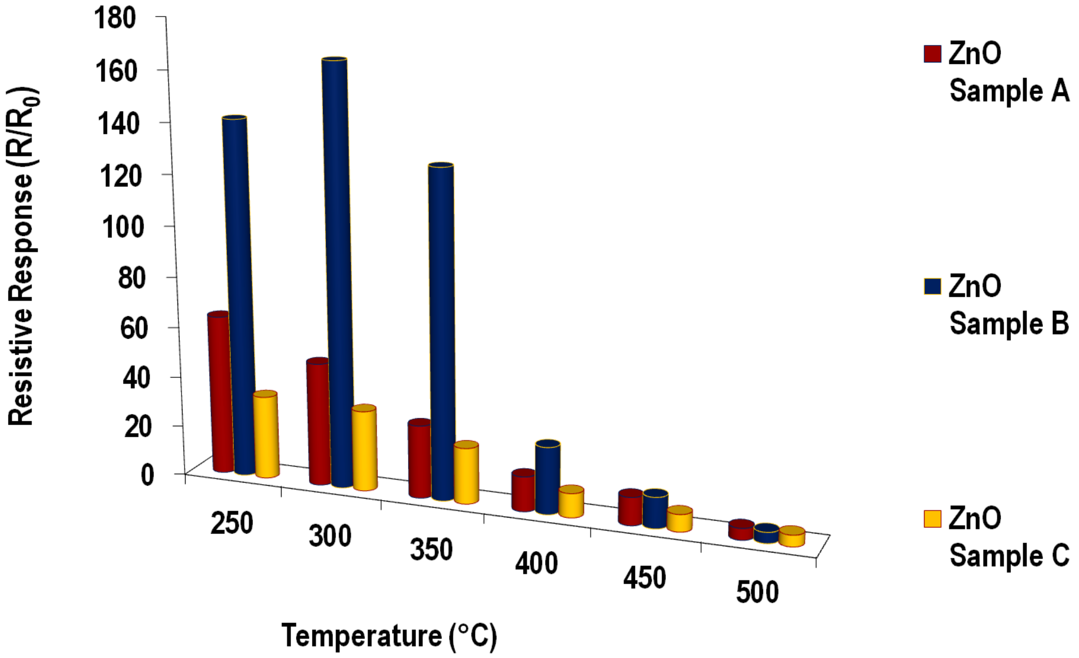

Figure 6–14. Resistive response of CHFS ZnO samples: ZnO A, ZnO B and ZnO C as a function of increasing operating temperature against 800 ppb of NO_2. Samples A, B and C were prepared by CHFS which involved a reaction of ambient flows of 0.1, 0.2, 0.45 M of Zn $(NO_3)_2.6H_2O$ aqueous solution and KOH aqueous solution respectively (each flowing at 200 mL min^{-1}), with a supercritical water flow at 450 °C and 240 bar (flowing at 400 mL min^{-1}) in a confined jet mixer.

The variation in the optimal performance as a function of temperature modulation for the three ZnO samples against both ethanol and NO_2 was indicative of the influence of temperature effects to obtain the optimal responsivity. In particular, the optimal response of ZnO sample B towards ethanol at 400 °C and NO_2 at 300°C, was a particular feature when comparing both Figure 6–13 and Figure 6–14and such behaviour has been reported previously in the literature. For example, Zhang e*t al.* [343], had reported that their ZnO hollow spheres, were attributed to optimal responsivity against oxidising NO_2 at 240 °C, but an optimal performance against reducing NH_3 at 220 °C. Such behaviour can be accounted for by the characteristic temperature-conductance profiles [20, 137, 208] not only for the target gas, but also for the gas sensitive metal oxides. Such profiles have been explained to be associated to a volcano - plot type or bell shape behaviour [347], where the response is greatest at the central temperature of the temperature range, but lowest at both its highest and lowest extremes, which is what was observed experimentally in Figure 6–14 and Figure 6–14. As discussed in Chapter 3, the shape of these profiles is reported to be influenced by a number of complex factors, which include the differing stabilities of the surface oxygen species adsorbed on the surface of the different materials and also the different optimum oxidising temperatures of the target analytes [343]. Further chemical and physical factors, such as the rates of adsorption and desorption of oxygen and the target analytes, or of oxidation products, the rate of surface decomposition of target analytes, the charge-carrier concentration (in the conduction band as well as the electron depletion layer) and the Debye length in the semiconductor also contribute to the response of the sensor and thus its conductance-temperature profile [137, 239]. In this case with nanomaterials, where grain-boundary conditions play a very prominent role, it is also possible that thermal influences on the microstructural behaviour of the materials are likely to have also influenced the shape of the conductance-temperature profiles against both ethanol and NO_2.

6.2.8 Further Gas Sensing Studies

Further gas sensing studies of the CHFS ZnO sensor devices was conducted against a range of reducing gases to include acetone, NH_3 and CO (and ethanol which has already been discussed), to evaluate their selectivity if put in a mixed atmosphere of reducing gases. Studies were conducted at the specific optimal operating temperatures (i.e. operating temperature specific to each sensor device) determined from their responsivities towards ethanol in Figure 6–13. These temperatures were: ZnO A – 300 °C, ZnO B – 400 °C and ZnO C – 350 °C.

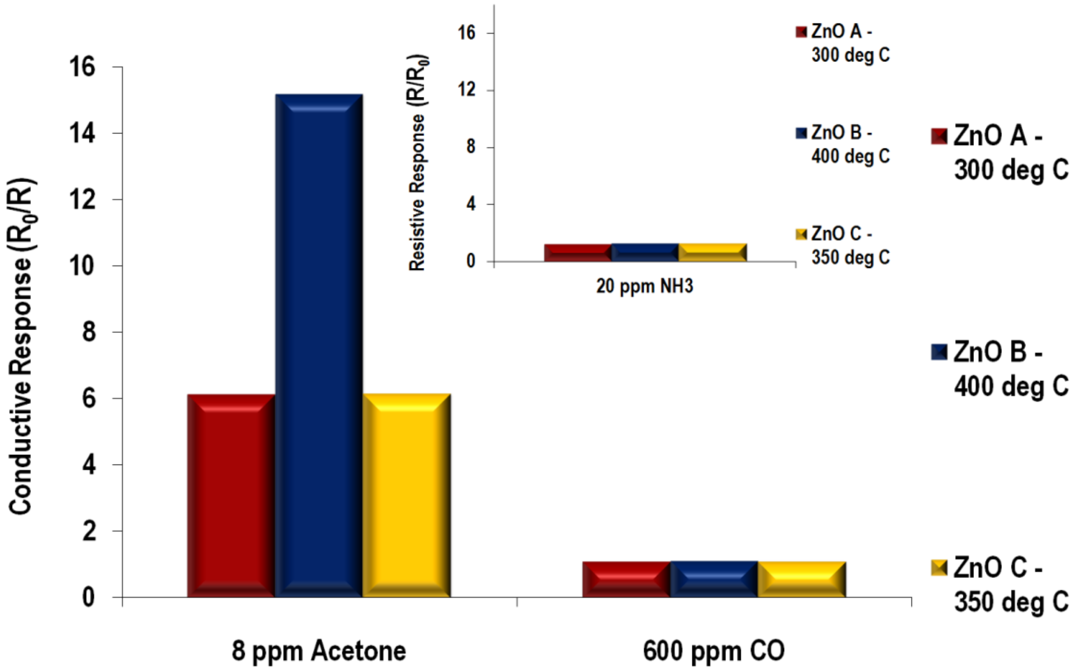

Figure 6–15. Conductive responses of CHFS ZnO samples: ZnO A sensor at 300 °C, ZnO B at 400 °C and ZnO C 350 °C against 8 ppm acetone and 600 ppm CO. The inset presents the resistive response of the sensor devices at the same operating temperatures against 20 ppm NH_3. Samples A, B and C were prepared by CHFS which involved a reaction of ambient flows of 0.1, 0.2, 0.45 M of Zn $(NO_3)_2.6H_2O$ aqueous solution and KOH aqueous solution respectively (each flowing at 200 mL min^{-1}), with a supercritical water flow at 450 °C and 240 bar (flowing at 400 mL min^{-1}) in a confined jet mixer.

Figure 6–15 presents the responses of the three devices against the highest concentration of each reducing gas tested at the specific optimal operating temperatures. The figure establishes that the system of three sensor devices showed minimal response towards CO and NH_3 with all devices exhibiting baseline response (R/R_0 or $R_0/R = 1$) towards both gases, despite the concentrations of both analytes being higher in comparison to acetone. Against 8 ppm acetone, the devices exhibited quantifiable responses, with ZnO sample B exhibiting the highest response of 15.1 at 400 °C. Both ZnO samples A and C were seen to exhibit the same response of 6.1 towards 8 ppm acetone at 300

°C and 350 °C, respectively. It was interesting to observe the same responsivities of both ZnO sample A and C at the differing operating temperatures towards acetone, as well as the same responsivities towards ethanol at 350 °C observed earlier in Figure 6–9 and Figure 6–10.

Table 6–3 tabulates the responsivities of the individual ZnO materials towards 10 ppm ethanol and 8 ppm acetone at the associated specific optimal operating temperatures.

Table 6–3. Comparison of conductive responses of ZnO A, ZnO B and ZnO C sensor devices at 300 °C, 400 °C and 350 °C respectively, against 8 ppm acetone and 10 ppm ethanol. Samples A, B and C were prepared by CHFS which involved a reaction of ambient flows of 0.1, 0.2, 0.45 M of Zn $(NO_3)_2.6H_2O$ aqueous solution and KOH aqueous solution respectively (each flowing at 200 mL min^{-1}), with a supercritical water flow at 450 °C and 240 bar (flowing at 400 mL min^{-1}) in a confined jet mixer.

Sensor device @ specific optimal operating temperature	**Conductive Response (R_0/R) against 8 ppm acetone**	**Conductive Response (R_0/R) against 10 ppm ethanol**
ZnO A @ 300 °C	**6.1**	**3.6**
ZnO B @ 400 °C	**15.2**	**5.0**
ZnO C @ 350 °C	**6.1**	**3.3**

Comparison of the conductive responses of the three sensors against 8 ppm acetone and 10 ppm ethanol, showed that all three sensors were attributed to higher responsivities against 8 ppm acetone, suggesting that in a mixed atmosphere of 10 ppm ethanol and 10 ppm acetone, the sensor devices are likely to be selective towards 10 ppm acetone.

A more detailed presentation of the response results against increasing concentrations of acetone has been presented in Figure 6–16 showing a detection limit of 1 ppm acetone for ZnO B and 2 ppm for both ZnO A and C. Tabulation of the mean responses values of the sensor devices in the CHFS ZnO system from the repeat tests against exposure towards the various acetone concentrations and the associated 95% confidence intervals have been presented in Table 6–4.

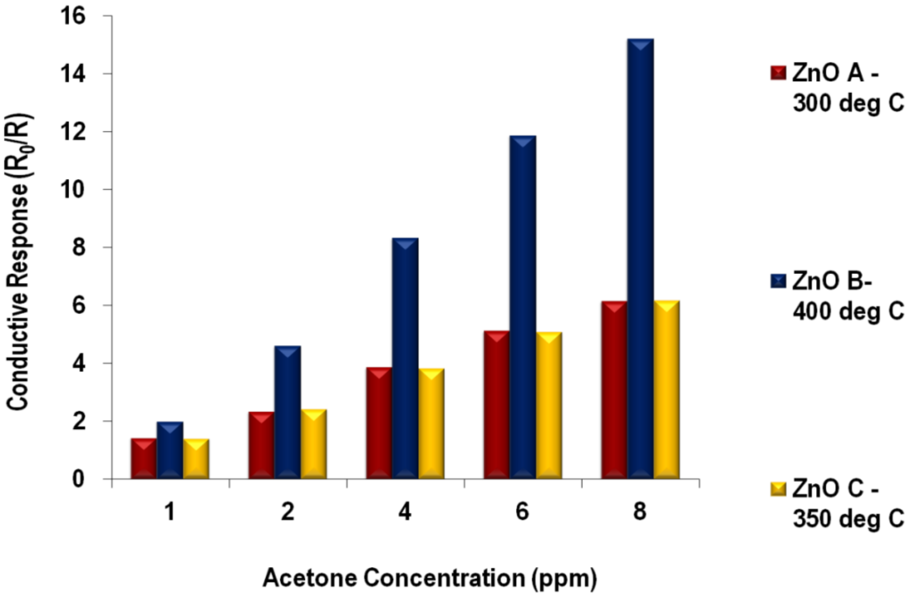

Figure 6–16. Conductive response of CHFS ZnO sensor devices: ZnO A at 300 °C, ZnO B at 400 °C and ZnO C at 350 °C as a function of increasing concentrations of acetone. Samples A, B and C were prepared by CHFS which involved a reaction of ambient flows of 0.1, 0.2, 0.45 M of Zn $(NO_3)_2.6H_2O$ aqueous solution and KOH aqueous solution respectively (each flowing at 200 mL min^{-1}), with a supercritical water flow at 450 °C and 240 bar (flowing at 400 mL min^{-1}) in a confined jet mixer.

Table 6–4. Average conductive responses of sensor devices in CHFS system from all repeat tests against various acetone concentrations at corresponding operating temperatures, and associated errors in the form of 95% CIs.

	1 ppm		**2 ppm**		**4 ppm**		**6 ppm**		**8 ppm**	
Device	Average Response	95% CI	Average Response	95% CI	Average Response	95% CI	Average Response	95% CI	Average Response	95% CI
ZnO sample A @ 300 °C	1.36	±0.07	2.31	±0.14	3.73	±0.31	4.97	±0.41	6.10	±0.47
ZnO sample B @ 400 °C	1.92	±0.10	4.46	±0.26	7.99	±0.70	11.38	±1.19	14.58	±1.74
ZnO sample C @ 350 °C	1.33	±0.07	2.28	±0.22	3.58	±0.44	4.75	±0.65	5.81	±0.84

The selective acetone detection by ZnO nanorod systems was recently reported by Zeng *et al.* [323]. In the study, the group reported the growth of ZnO nanorods system thin films via aqueous solution methods. Upon exposure to 100 ppm acetone at an operating temperature of 300 °C, the thin film sensor was found to exhibit a response of 30.4, which was significantly higher than a range of other test gases which included 100 ppm ethanol, to which the sensor only exhibited a response of 12, suggesting the sensor exhibited a 2.5-fold selective response towards acetone. When their sensor was exposed to 10 ppm of acetone, they had observed a response of 4, showing that comparatively the CHFS samples, particularly sample B, performed better however at 300 °C or higher operating temperatures. Direct comparison however between the two studies is difficult as the group reported the sensing properties of a thin film, which is attributed to significantly different microstructural properties than a screen-printed film. The group had further reported, based on various other studies in the literature that cross-sensitivity between acetone and ethanol was difficult to avoid but that they had observed selectivity towards acetone with their nanorod system sensor. In a similar way, the CHFS ZnO materials investigated in this Chapter, do potentially show selectivity towards acetone (with respect to ethanol) at low ppm concentrations.

6.3 Results and Analysis: ZnO ceramics synthesised via Molten-Salt synthesis, Solid-State metathesis and Hydrothermal synthesis

6.3.1 Scanning Electron Microscopy (SEM)

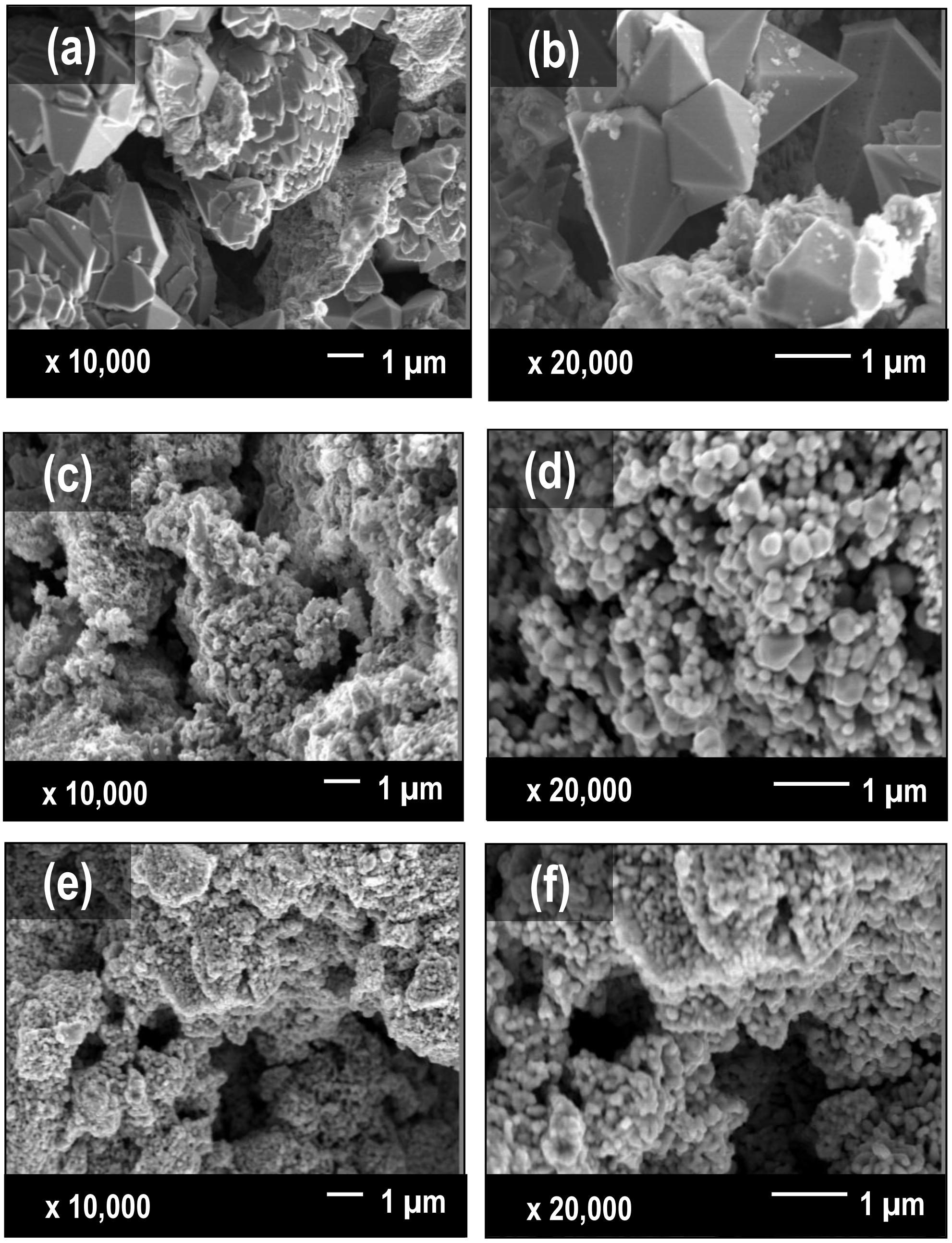

Figure 6–17. SEM images of (a) & (b) MS ZnO at x 10,000 & x 20,000 magnification respectively, (c) & (d) SS ZnO at x 10,000 & x 20,000 magnification respectively and (e) & (f) Zn ZnO at x 10,000 & x 20,000 magnification, respectively, after screen-printing onto gas sensor substrates and heat-treating at 600 °C. The ZnO ceramics were prepared by three different synthesis methods: Molten-Salt synthesis (MS-ZnO), Solid-State metathesis (SS-ZnO) and Hydrothermal synthesis (Zn-ZnO).

SEM imaging of the ceramic samples, showed that the first sample MS ZnO observed in Figure 6–17 (a) and (b), was attributed to micron sized hexagonal pyramidal habits with the height of the pyramids observed to be in the range of 1 – 1.5 µm. In contrast the other two ZnO samples SS ZnO and Zn ZnO were attributed to significantly smaller particles sizes, in the nano range. The former (SS ZnO), observed in Figure 6–17 (c) and (d) was seen to be attributed to particle sizes of 100 nm to as large as 750 nm with the particles exhibiting spherical habits. The latter sample (Zn ZnO) observed in Figure 6–17 (e) and (f) was associated to spherical habits but with particles sizes being significantly smaller of sizes in the range of 100 nm - 250 nm.

The imaging technique gave evidence that the Zn ZnO particles were seen to be more agglomerated, in comparison to the SS ZnO particles which exhibited greater spacing between the grains. This phenomenon as suggested earlier in the Chapter is likely attributed to the smaller sized Zn ZnO nanoparticles which are attributed to a lower thermal stability due to an increase in surface to bulk ratio as a function of decreasing particle size. As such, heat-treatment can lead to greater agglomeration and an overall decrease in the provision of diffusion channels in the material, for the gas molecules to permeate through. In contrast, the larger sized SS ZnO nanoparticles are likely to have stronger resilience to heat due to a greater bulk contribution, suggestive of why the SS ZnO nanoparticles are not seen to readily agglomerate together. Lower agglomeration of large sized nanoparticles suggests the presence of a larger number of inter-grain diffusion pathways, which can allow the gas molecules to travel into the body of the sensor matrix and interact with a larger number of surface sites, thus the material provides greater surface site accessibility. Larger agglomeration and potential sintering of the particles can promote the inner region of the neck to behave like the bulk of the material, and as such, only the outer regions of the neck will be gas sensitive [65]. For particles which are less agglomerated, a greater proportion of the neck can be considered gas sensitive and as such are better for gas sensing applications. Agglomeration is a key issue with nanomaterials particularly with smaller nanoparticles that are attributed to larger surface to bulk contributions, which are more likely to be compromised under high temperature heat-treatment regimes, which are a key requirement to stabilise the sensor baseline prior to gas sensing experiments [65]. The grain boundary contributions therefore are seen to play an influential role in the microstructures of both the SS and Zn ZnO nanomaterials, as was observed for the CHFS nanomaterials earlier in the Chapter.

6.3.2 PXRD (Powder X-Ray Diffraction)

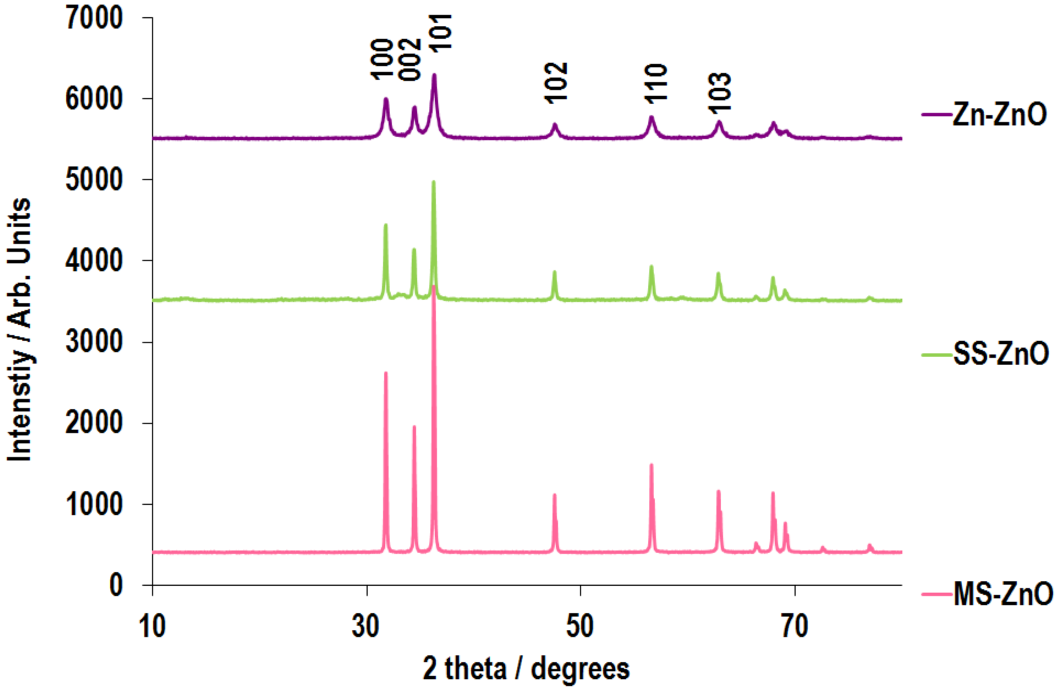

Figure 6–18. PXRD patterns of Zn ZnO, SS ZnO and MS ZnO samples. The ZnO ceramics were prepared by three different synthesis methods: Molten-Salt synthesis (MS-ZnO), Solid-State metathesis (SS-ZnO) and Hydrothermal synthesis (Zn-ZnO).

XRD data of the ZnO samples were in agreement with literature reports, which showed that the samples adopted a hexagonal wurtzite crystal structure [333], (JCPDS No. 36-1451) [143, 334]. The most intense reflections have been labelled in Figure 6–18. The increasing peak intensity of the reflections in the range of 30-40 ° 2θ from the Zn-ZnO to the MS-ZnO sample gave evidence for the increase in the apparent crystallinity of ZnO. The greatest preferential intensity of the (101) reflection, suggests the growth of the ZnO crystal structure in that plane. The peak broadening of the Zn-ZnO sample suggested that this sample was attributed to the smallest crystallite size of all three samples.

6.3.3 Gas Sensing

6.3.3.1 Ethanol Sensing

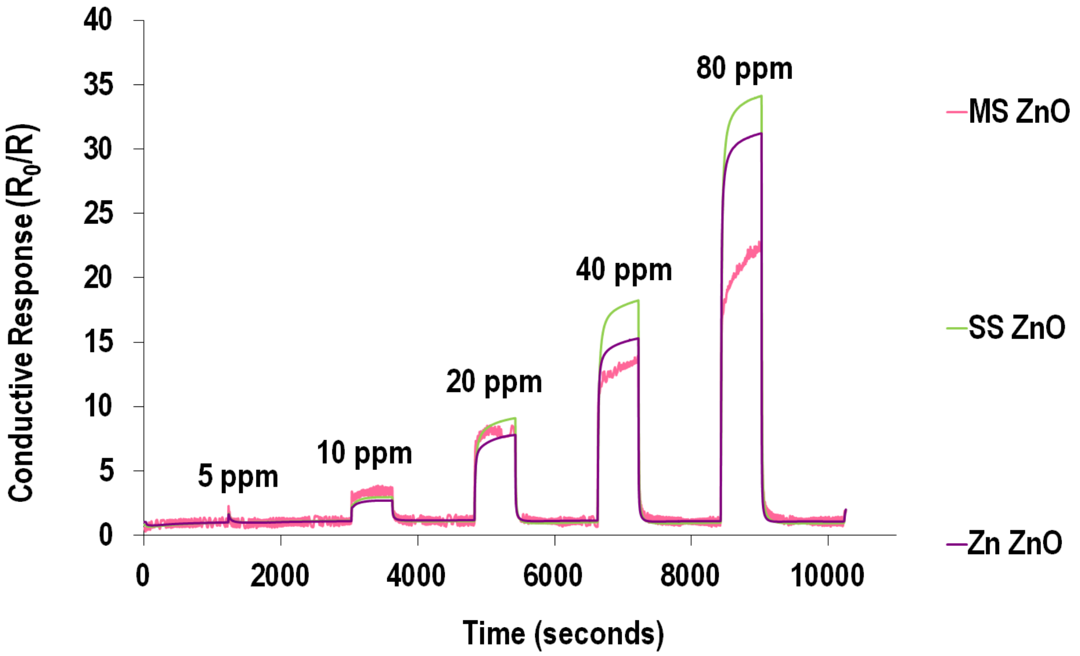

Figure 6–19. Conductive response traces of MS ZnO, SS ZnO and Zn ZnO sensor devices against increasing concentrations of ethanol at an operating temperature of 400 °C. The ZnO ceramics were prepared by three different synthesis methods: Molten-Salt synthesis (MS-ZnO), Solid-State metathesis (SS-ZnO) and Hydrothermal synthesis (Zn-ZnO).

Figure 6–19 presents the conductive response traces of all three sensor devices against increasing concentrations of ethanol at 400 °C, which was the operating temperature at which all three sensor devices exhibited substantial conductive response towards ethanol. The traces have been presented at this temperature as it gave the best signal to noise ratio for the MS ZnO sensor device, and was still a temperature at which both the SS and Zn ZnO sensor devices performed well at (observed further in Figure 6–25). Tabulation of the mean responses values of the MS, SS and Zn ZnO sensor devices from the repeat tests against exposure towards the various ethanol concentrations at 400 °C and the associated 95% confidence intervals have been presented in Table 6–5.

Table 6–5. Average conductive responses of sensor devices in Molten-Salt synthesis ZnO (MS-ZnO), Solid-State metathesis ZnO (SS-ZnO) and Hydrothermal synthesis ZnO (Zn-ZnO) system from all repeat tests against various ethanol concentrations at 400 °C and associated errors in the form of 95% CIs.

	10 ppm		20 ppm		40 ppm		80 ppm	
Device	Average Response	95% CI	Average Response	95% CI	Average Response	95% CI	Average Response	95% CI
MS ZnO	3.60	±0.32	8.05	±0.61	12.90	±1.25	20.61	±2.34
SS ZnO	3.25	±0.29	9.56	±0.53	18.45	±0.85	Electronic capping out	
Zn ZnO	2.83	±0.18	7.56	±0.45	14.37	±1.28	28.70	±3.32

The responses showed that the SS ZnO sensor device exhibited the best response characteristics of all three devices, with a maximum response of 34.2 towards 80 ppm of the analyte. The Zn ZnO sample was observed to exhibit a response of 31.2 towards 80 ppm of the analyte and the MS ZnO sensor device was seen to exhibit the weakest performance with a maximum response of 22.8 towards 80 ppm. Thus the SS ZnO device exhibited a response which was 1.1-fold enhanced with respect to the Zn ZnO device and 1.4-fold greater than the MS ZnO device. Comparison of the traces showed that the MS ZnO device was attributed to faster saturation than the SS and Zn ZnO devices accounted by its slower increase in response amplitude as a function of increasing concentration of ethanol. This trend is clearly presented in Figure 6–20, which shows the larger gradient of response increase of both the SS and Zn ZnO devices, and in contrast the smaller gradient of response increase of the MS ZnO device. This behaviour can be accounted for by the substantial difference in particle sizes between the MS-ZnO sample, which SEM showed was associated to be in the μm range, and both the SS and Zn samples, which were associated particle sizes in the nm range. The size contribution of the particle has a direct influence on the surface to bulk contribution, with smaller nm particles attributed to a larger contribution of surface:bulk ratios, which act to increase the yield of surface reactions between the analyte and the metal oxide surface, due larger surface site accessibility. Comparison of both the nanomaterial samples SS and Zn ZnO from Figure 6–19 and Figure 6–20, showed that the former was attributed to better responsivity, which can be accounted for the prominent inter-grain spacing [70] observed in the sample in Figure 6–17 (d), which provides greater pathways for interaction for the gaseous molecules. In comparison, the Zn ZnO sample was observed to have particles agglomerated together, potentially reducing the overall surface site accessibility of the gaseous molecules, resulting in a weaker response than the SS ZnO device. However the inter-agglomerate diffusion pathways [70] of the Zn ZnO sample contribute to provision of diffusion pathways for the gaseous molecules to permeate through, contributing to its observed responsivity.

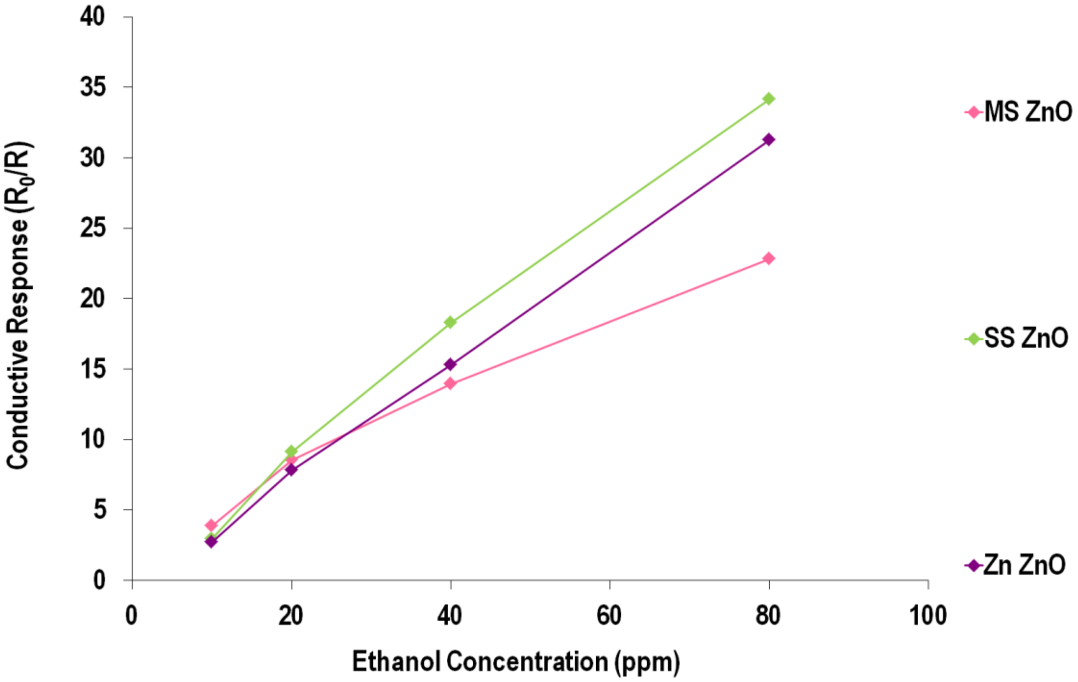

Figure 6–20. Conductive response of MS ZnO, SS ZnO and Zn ZnO sensor devices as a function of increasing ethanol concentration at an operating temperature of 400 °C. The ZnO ceramics were prepared by three different synthesis methods: Molten-Salt synthesis (MS-ZnO), Solid-State metathesis (SS-ZnO) and Hydrothermal synthesis (Zn-ZnO).

Comparison of the kinetics of response from the observed response traces of each ZnO sample in Figure 6–19, showed that the shape of the response trace of the MS ZnO sample was observed to vary as a function of increasing concentration of ethanol. At lower concentrations e.g. 20 ppm, the sample surface was seen to saturate, observed through its box shaped behaviour in comparison to both SS and Zn ZnO samples, which were attributed to unsaturated shark-fin behaviour at the same concentration. Thus the speed of response at 20 ppm of MS was faster with a t_{90} (20 ppm) calculated to be 47 seconds. In comparison the SS ZnO sample was observed to be the slowest device with the most gradual slope upon exposure to 20 ppm ethanol, and was calculated to have a t_{90} (20 ppm) of 153 seconds. The Zn ZnO sample was observed to have a relatively slow response at 20 ppm too, but not as slow as the SS sample, with a t_{90} (20 ppm) of 140 seconds.

At the higher concentration of 80 ppm of ethanol exposure, the kinetics of the MS ZnO device were seen to significantly change, as can be observed by the increasing slope of the associated response trace in Figure 6–19. The increasing slope suggested that the surface of the MS ZnO material was not saturated at 80 ppm subsequently suggesting that the response speed of the device significantly reduced with respect to its calculated speed at 20 ppm. Indeed the t_{90} (80 ppm) of the device was calculated to be 237 seconds, which was 5-fold slower response speed than that calculated at 20 ppm. Given the larger concentration of ethanol molecules in an 80 ppm exposure, a reduction in response kinetics at this higher concentration of ethanol exposure, relative to a lower concentration of ethanol exposure, is physically impossible as the yield in surface reactions per unit time is proportional to gas concentration, which results in an increase in the response speed of the device. This behaviour of the MS ZnO device was unusual, as the response trace of the MS device clearly showed surface saturation at lower concentrations of 10 ppm and 20 ppm exposure. The unusual behaviour may be explained by the influence of the electronic digitisation on the MS ZnO response signal, evident from Figure 6–19 and the associated response traces of this device observed in further figures i.e. Figure 6–21, Figure 6–22 and Figure 6–23. Noise was clearly evident in the signal of the MS ZnO device which looks likely to have interfered with the true nature of the response trace. This electronic digitisation may have been caused by the sporadic grain boundaries that existed between the hexagonal pyramidal grains of the material, which interrupted the smooth percolation pathways of the charge carriers. In contrast, the particles of both the SS and Zn devices were seen to be attributed to continuous grain boundaries between the spherical grains in the materials, providing smooth percolation pathways for the charge carriers to travel through the semiconducting metal oxides. Both the SS and Zn ZnO sensor devices were calculated to have significantly faster responses as a function of increasing concentration with t_{90} (80 ppm) values calculated to be 80 and 62 seconds respectively. The recoveries of both these devices at 80 ppm, t_{-90} (80 ppm), were calculated to be 186 and 94 seconds respectively and 20 ppm, the t_{-90} (20 ppm) values were 92 and 69, respectively. The erratic response of the MS device, invalidated and added unquantifiable error to the associated response and recovery values. The slower unsaturated response times of the SS ZnO device relative to the Zn ZnO device was suggestive of the larger number of surface sites that the SS ZnO device is associated to. This was accounted for earlier by the contribution of the inter-grain spacing observed via SEM imaging but also the small ZnO grain sizes of this material.

Figure 6–21 presents the conductive response traces of the three sensor devices against increasing concentrations of ethanol at a lower operating temperature of 300 °C. The response traces of the devices were seen to be significantly different to those observed at the higher temperature of 400 °C, accounting for the differences in thermal energy supplied to the sensor devices in the form of temperature.

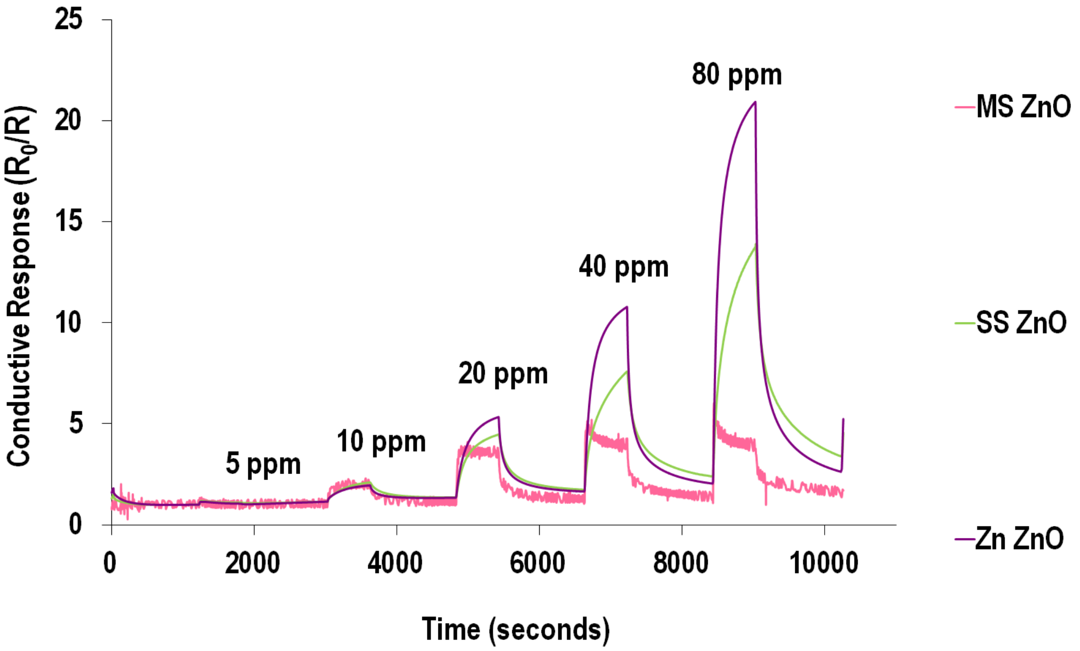

Figure 6–21. Conductive response traces of MS ZnO, SS ZnO and Zn ZnO sensor devices against increasing concentrations of ethanol at an operating temperature of 300 °C. The ZnO ceramics were prepared by three different synthesis methods: Molten-Salt synthesis (MS-ZnO), Solid-State metathesis (SS-ZnO) and Hydrothermal synthesis (Zn-ZnO).

It was interesting to observe a switch in the response orders of both the SS and Zn ZnO devices, with the latter performing better at the lower operating temperature of 300 °C as observed in Figure 6–21 and the former at 400 °C as observed in Figure 6–19 and Figure 6–20.

This switch suggests that chemical and physical factors, such as the rates of adsorption and desorption of oxygen species and the target analytes, or of oxidation products, the rate of surface decomposition of target analytes, the charge-carrier concentration (in the conduction band as well as the electron depletion layer) and the Debye length in the semiconductor contribute to the individual response of the sensor material and its characteristic conductance-temperature profile [137, 239].

Figure 6–21 shows that the response trace of the MS device as observed earlier in Figure 6–19, was associated to erratic behaviour and electrical noise. The discontinuity in the increase of the response amplitude of the sensor device between 20 ppm - 80 ppm showed that the sensor did not respond to increasing concentrations of ethanol exposure. In contrast, both the SS and Zn ZnO sensor devices were seen to exhibit an increase in conductive response as a function of increasing concentration; however, both devices were associated to significant baseline drift, suggesting the thermal energy in the system at 300 °C was not sufficient for the complete desorption of the analyte molecules, to fully recover the metal oxide surface and that water from the surface oxidation reactions of ethanol, may have also contributed to the drift. The unsaturated response traces of both devices indicated the slow response of the devices towards ethanol at 300 °C, in comparison to the faster responses observed at 400 °C in Figure 6–19. This was justified by the slower t_{90} (20 ppm) values of 323 seconds (SS ZnO) and 320 seconds (Zn ZnO) and t_{-90} (20 ppm) values of 624 seconds (SS ZnO) and 563 seconds (Zn ZnO), in comparison to those observed at 400 °C. Comparison of the response and recovery speeds at the higher concentration regions was difficult, as the baseline drift artificially shortened the t_{90} and t_{-90} values at 300 °C due to incomplete recovery of the surface of the material.

6.3.3.2 NO_2 Sensing

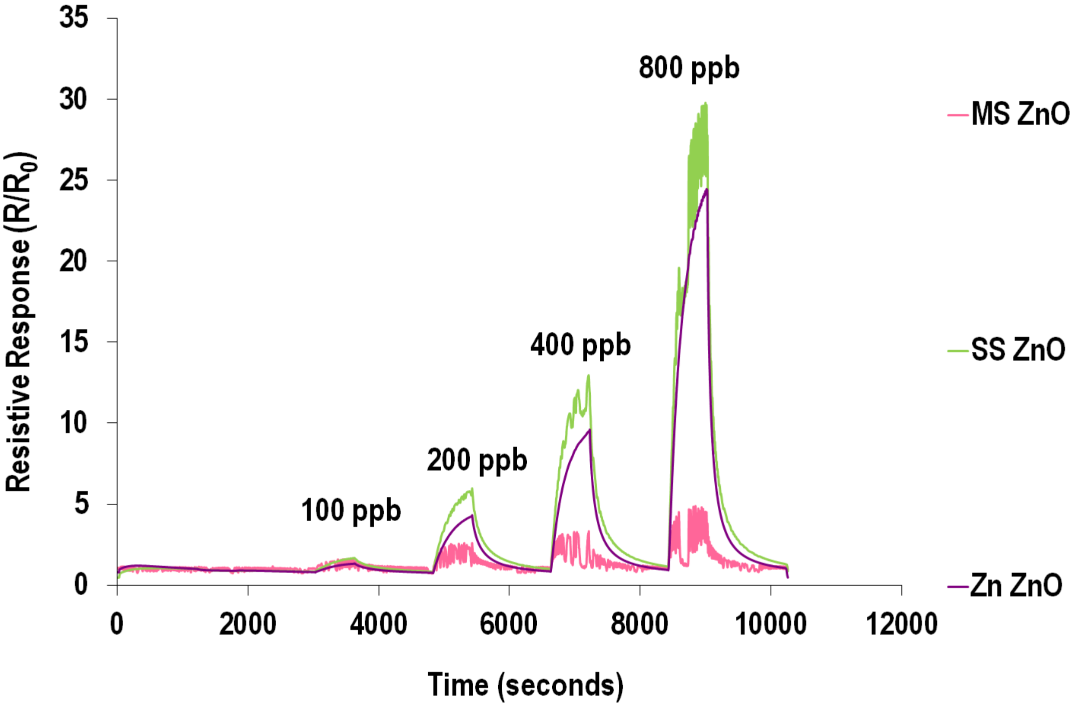

Figure 6–22. Resistive response traces of MS, SS ZnO and Zn ZnO sensor devices against increasing concentrations of NO_2 at an operating temperature of 300 °C. The ZnO ceramics were prepared by three different synthesis methods: Molten-Salt synthesis (MS-ZnO), Solid-State metathesis (SS-ZnO) and Hydrothermal synthesis (Zn-ZnO).

Figure 6–22 presents the resistive response traces of the MS, SS and Zn ZnO sensor devices at an operating temperature of 300 °C against increasing concentrations of NO_2. Although the optimal operating temperature of the SS and Zn ZnO devices was observed to be 250 °C presented further in Figure 6–24, the MS device had a very low signal:noise ratio at this lower temperature. Therefore the responses have been presented at 300 °C, at which the MS ZnO device was attributed to a high signal:noise ratio and was still a temperature at which both the SS and ZnO devices performed well at.

The figure shows that the MS sensor device was associated to negligible response towards NO_2 at 300 °C with a very poor signal:noise ratio, however a change in the responsivity of the material as a function of increasing NO_2 concentration could be observed. The SS ZnO was also seen to be affected by noise during NO_2 exposure at this temperature, however the maximum response of the device was calculated to be 25.5 towards 800 ppb of NO_2. The Zn ZnO sensor device in contrast showed a clear resistive response towards the analyte with a maximum response of 24.5 attributed to 800 ppb of NO_2. The traces illustrated that the response of both the SS and Zn devices were slow, accounted for by their gradual increase in resistive response upon exposure to NO_2 and the shark-fin nature of the response curves. This indicated that both materials had many available surface sites for the given concentration of the NO_2 they were exposed to and that neither of the surfaces were saturated. Further, the slow behaviour indicated that the operating temperature did not provide enough thermal energy to the system for yielding faster combustion reactions to promote surface site saturation.

The slow behaviour of both materials was accounted for by kinetic analysis which showed the t_{90} (200 ppb) values to be 429 seconds (SS ZnO) and 435 seconds (Zn ZnO) and the t_{-90} (200 ppb) values to be 957 seconds (SS ZnO) and 980 seconds (Zn ZnO). The kinetic analysis had to be conducted at the lower concentration of NO_2 exposure, as the SS device was attributed to significant noise at both 400 and 800 ppb.

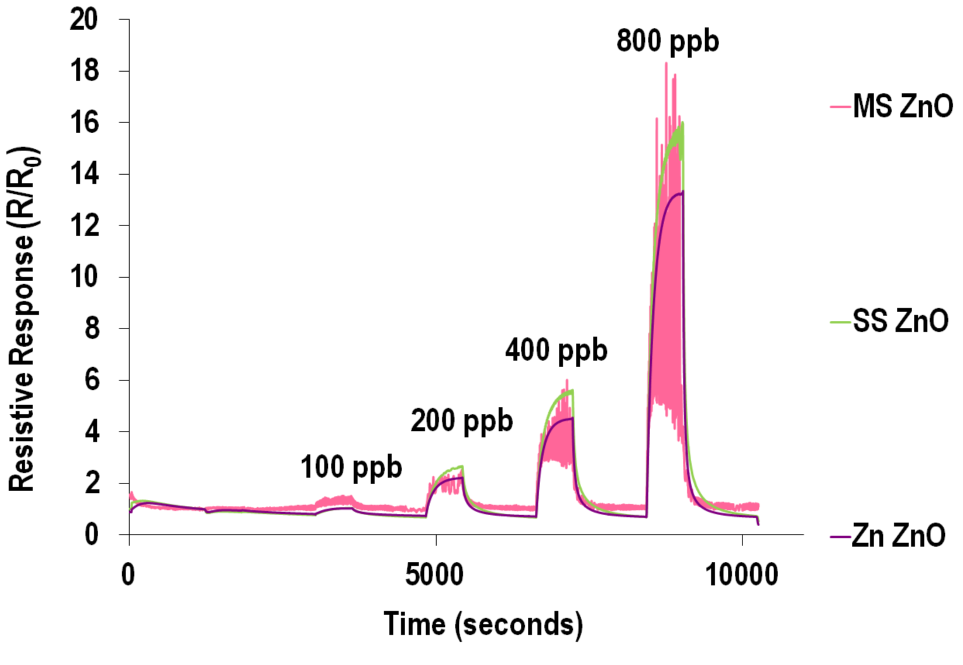

Figure 6–23. Resistive response traces of MS, SS and Zn ZnO sensor devices against increasing concentrations of NO_2 at an operating temperature of 350 °C. The ZnO ceramics were prepared by three different synthesis methods: Molten-Salt synthesis (MS-ZnO), Solid-State metathesis (SS-ZnO) and Hydrothermal synthesis (Zn-ZnO).

Figure 6–23 presents the resistive response traces of the MS, SS and Zn ZnO sensor devices at an operating temperature of 350 °C. Tabulation of the mean responses values of the MS, SS and Zn ZnO sensor devices from the repeat tests against exposure towards the various NO_2 concentrations at 350 °C and the associated 95% confidence intervals have been presented in Table 6–6.

Table 6–6. Average resistive responses of sensor devices in Molten-Salt synthesis ZnO (MS-ZnO), Solid-State metathesis ZnO (SS-ZnO) and Hydrothermal synthesis ZnO (Zn-ZnO) system from all repeat tests against various NO_2 concentrations at 350 °C and associated errors in the form of 95% CIs.

	100 ppb		**200 ppb**		**400 ppb**		**800 ppb**	
Device	Average Response	95% CI	Average Response	95% CI	Average Response	95% CI	Average Response	95% CI
SS ZnO	1.15	±0.10	2.92	±0.25	6.14	±0.59	17.77	±2.32
Zn ZnO	1.09	±0.05	2.32	±0.09	4.76	±0.21	14.28	±0.99

Comparison of Figure 6–22 and Figure 6–23 shows that an increase in the operating temperature by 50 °C speeded up the response and recovery kinetics, however compromised the responsivity. As observed in previous data, the MS device was attributed to significant digitisation, however both the SS and Zn ZnO sensor devices were seen to be attributed to clean response signal with each device associated to the highest observed response of 16 and 13 respectively, towards 800 ppb of NO_2. The faster kinetics was evident from the lower t_{90} (200 ppb) values which were observed to be 298 seconds (SS ZnO) and 251 seconds (Zn ZnO) and the lower t_{-90} (200 ppb) values which were 775 seconds (SS ZnO) and 602 seconds (Zn ZnO), relative to the same observed calculations at 300 °C. Figure 6–23 showed evidence of greater saturation of the surface sites of both the SS and Zn ZnO sensor devices at 350 °C, relative to 300 °C, observed through the greater curvature of the response traces at the higher operating temperature. In particular, the saturation was evident in the Zn ZnO device and was clearly thermally induced, with the higher thermal energy in the system promoting a greater number of surface reactions between the NO_2 molecules and the electrons in the conduction band of the metal oxide. As such, a larger number of electrons were abstracted from the conduction band, which limited the number of charge carriers which promoted the combustion reactions.

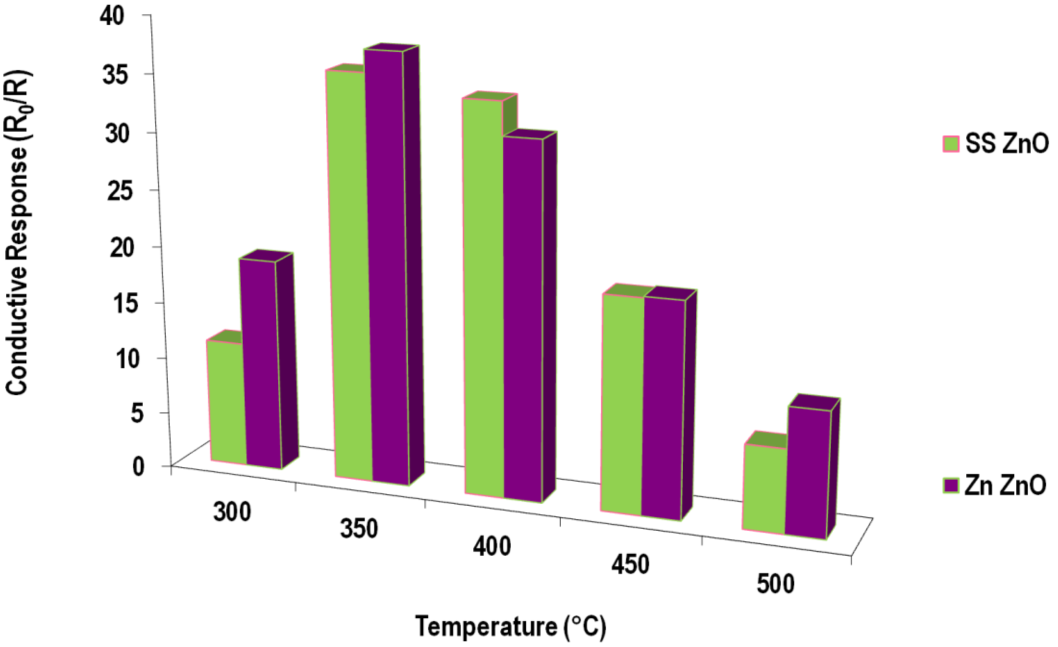

Figure 6–25. Conductive responses of SS ZnO and Zn ZnO sensor devices as a function of increasing operating temperature against 80 ppm of ethanol. The ZnO ceramics were prepared by two different synthesis methods: Solid-State metathesis (SS-ZnO) and Hydrothermal synthesis (Zn-ZnO).

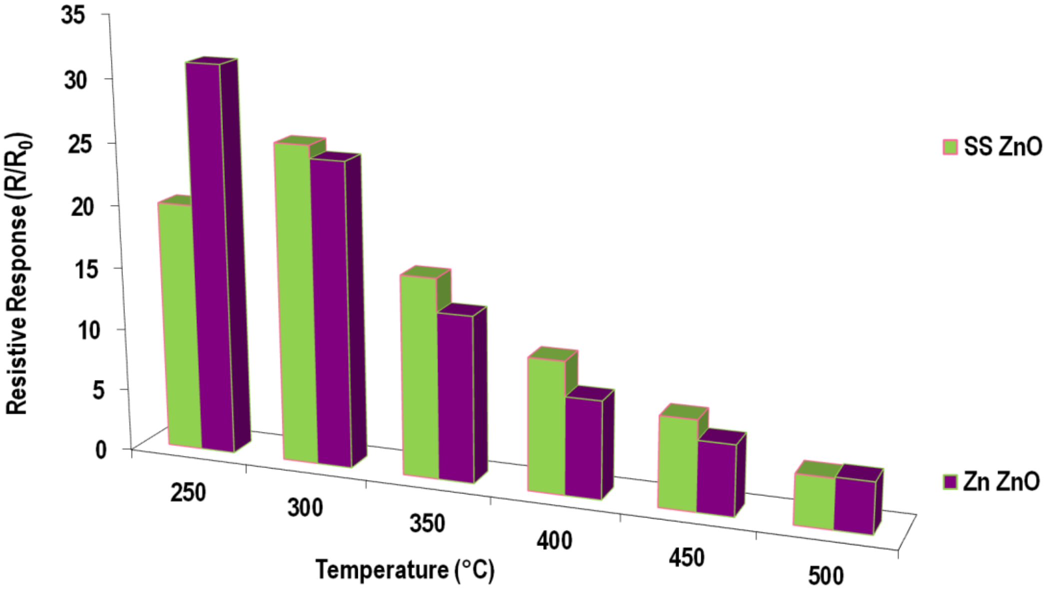

Figure 6–24. Resistive responses of SS ZnO and Zn ZnO sensor devices as a function of increasing operating temperature against 800 ppb of NO_2. The ZnO ceramics were prepared by two different synthesis methods: Solid-State metathesis (SS-ZnO) and Hydrothermal synthesis (Zn-ZnO).

Figure 6–24 and Figure 6–24 present the temperature profiles of the SS and Zn ZnO devices against both ethanol and NO_2, respectively. Both figures do not present the data for the MS ZnO sensor device due to the electronic digitised noise that distorted the response signals (discussed and observed earlier in Figure 6–19, Figure 6–21, Figure 6–22 and Figure 6–23), which add unquantifiable error to the final responsivities.

Figure 6–25 shows that the SS and Zn devices were associated to a specific optimal operating temperature of 350 °C, with conductive responses of 35.8 and 37.7 against 80 ppm of ethanol, respectively. Figure 6–24 shows that the specific optimal operating temperature of the SS ZnO device was 300 °C with a resistive response of 25.5 against 800 ppb NO_2, and that of the Zn ZnO device was 250 °C with a resistive response of 31.3.

As with the CHFS ZnO sensor devices discussed earlier in the Chapter, a variation in the optimal performance as a function of temperature modulation for the three ZnO samples against both ethanol and NO_2 was indicative of the influence of temperature effects to obtain the optimal responsivity. In particular, the optimal response of Zn ZnO sample towards ethanol at 350 °C and oxidising NO_2 at 250°C was a particular feature when comparing both graphs. Such temperature-conductance profiles [20, 137, 208] which are associated to a volcano - plot type or bell shape behaviour [347] as observed in Figure 6–24 and Figure 6–24 have been reported to be influenced by a number of complex factors, some of which have been alluded to earlier in the Chapter with respect to Figure 6–13 and Figure 6–14.

6.3.4 Further Gas Sensing Studies

Further gas sensing studies were conducted on the system of ZnO ceramic sensor devices against a range of reducing gases, which included acetone, NH_3 and CO (apart from ethanol evaluated above) at the specific optimal operating temperatures (i.e. operating temperature specific to each device) determined from their responsivities towards ethanol in Figure 6–25. This temperature was 350 °C for both SS and Zn ZnO sensor devices. This study was conducted in order to understand the selectivity of the devices if put in a mixed atmosphere of reducing gases.

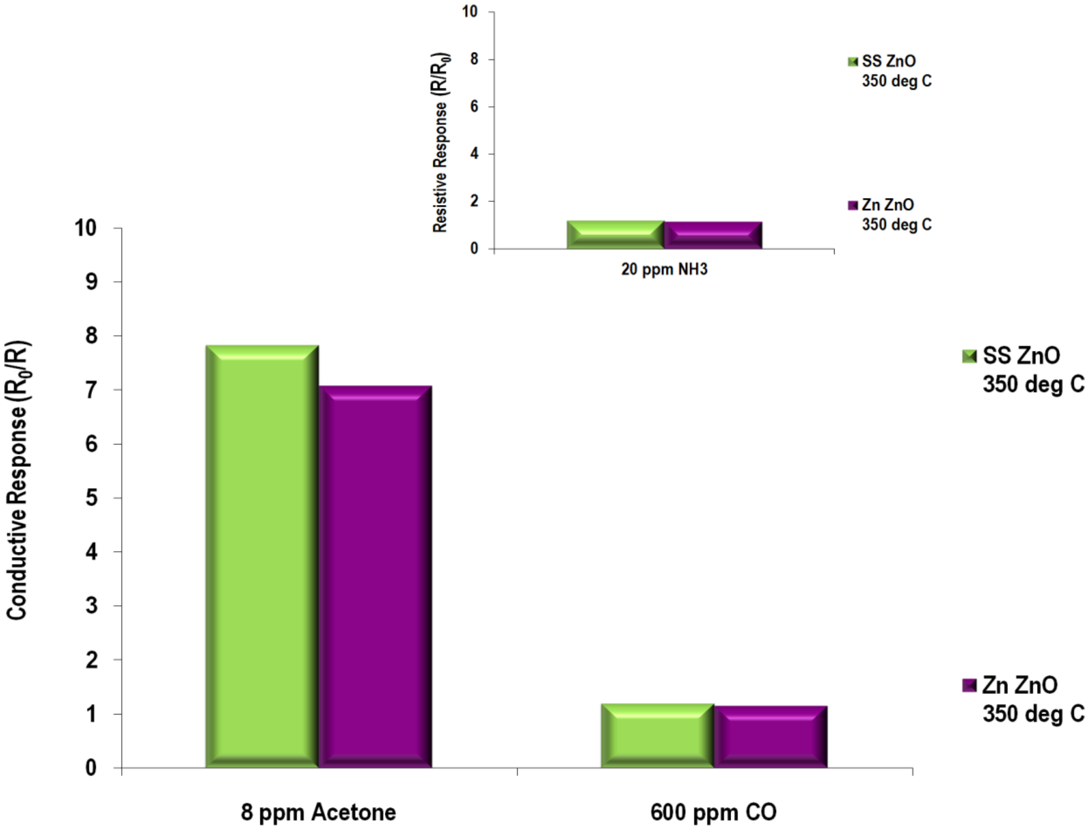

Figure 6–26. Conductive responses of SS and Zn ZnO sensor devices at 350 °C against 8 ppm Acetone and 600 ppm CO. The inset presents the resistive responses of both sensor devices at 350 °C against 20 ppm NH_3. The ZnO ceramics were prepared by two different synthesis methods: Solid-State metathesis (SS-ZnO) and Hydrothermal synthesis (Zn-ZnO).

Figure 6–26 presents the responses of the SS and Zn ZnO sensor devices against the highest concentration of each reducing gas tested, at the specific optimal operating temperature of each device, which was 350 °C for both.

The figure establishes that both the SS and Zn ZnO devices exhibited minimal response towards both 600 ppm CO and 20 ppm NH_3 with baseline response (R/R_0 or $R_0/R = 1$), as observed with the CHFS

ZnO samples earlier. Instead against 8 ppm acetone, both devices exhibited quantifiable responses, with SS ZnO sample exhibiting the highest response of 7.8 at 350 °C and the Zn ZnO sample attributed to a response of 7.1 at the same operating temperature.

Table 6–7 presents the responsivities of the individual ZnO materials towards 8 ppm acetone and 10 ppm ethanol at the associated optimal operating temperatures.

Table 6–7. Comparison of conductive responses of SS ZnO and Zn ZnO sensor devices at 350 °C against 8 ppm acetone and 10 ppm ethanol. The ZnO ceramics were prepared by two different synthesis methods: Solid-State metathesis (SS-ZnO) and Hydrothermal synthesis (Zn-ZnO).

Sensor device @ specific optimal operating temperature	Conductive Response (R_0/R) against 8 ppm acetone	Conductive Response (R_0/R) against 10 ppm ethanol
SS ZnO @ 350 °C	**7.8**	**3.4**
Zn ZnO @ 350 °C	**7.1**	**2.9**

Comparison of the conductive responses of both sensors against 8 ppm acetone and 10 ppm ethanol, showed that both devices were attributed to higher responsivities against 8 ppm acetone. The responsivities also indicate that in a mixed atmosphere of 10 ppm ethanol and 10 ppm acetone, the sensor devices are likely to be selective towards 10 ppm acetone.

A more detailed presentation of the response results against increasing concentrations of acetone has been presented in Figure 6–27, showing a detection limit of 2 ppm acetone for both devices. Like the CHFS ZnO materials, both the SS and Zn ZnO materials are seen to be attributed to selectivity towards acetone (with respect to ethanol) at low ppm concentrations. Tabulation of the mean responses values of the MS, SS and Zn ZnO sensor devices from repeat tests against exposure towards the various acetone concentrations at 350 °C and the associated 95% confidence intervals have been presented in Table 6–8 .

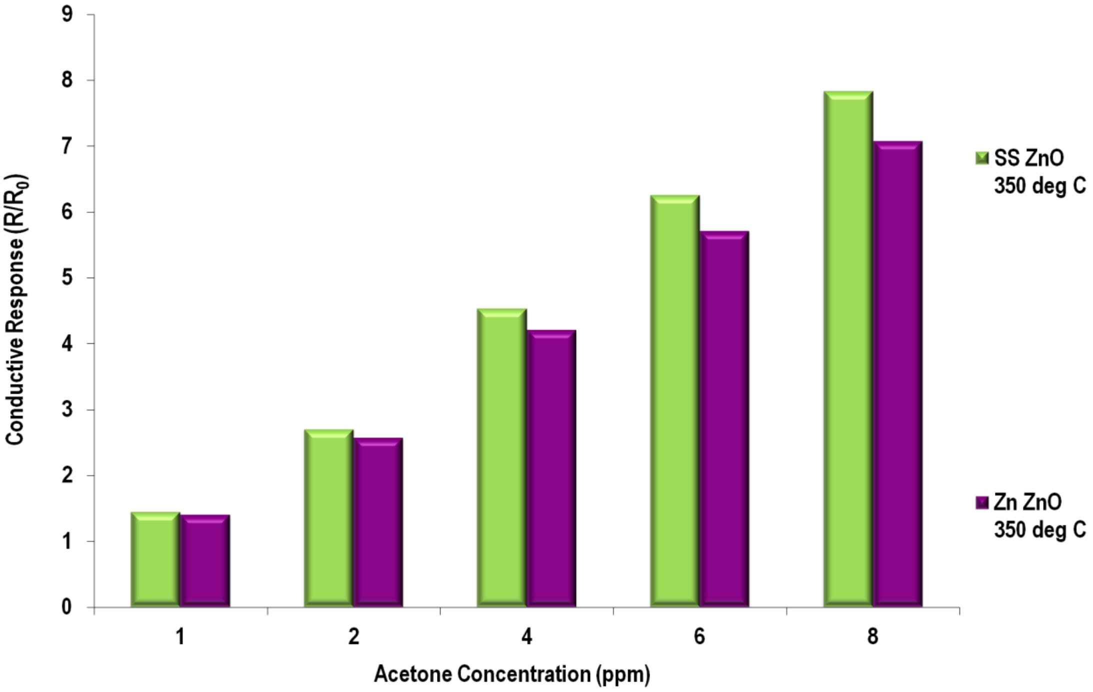

Figure 6–27. Conductive responses of ZnO sensor devices: SS ZnO and Zn ZnO as a function of increasing concentrations of acetone at the specific optimal operating temperatures, which was 350 °C for both devices. The ZnO ceramics were prepared by two different synthesis methods: Solid-State metathesis (SS-ZnO) and Hydrothermal synthesis (Zn-ZnO).

Table 6–8. Average conductive responses of sensor devices in Molten-Salt synthesis ZnO (MS-ZnO), Solid-State metathesis ZnO (SS-ZnO) and Hydrothermal synthesis ZnO (Zn-ZnO) system from all repeat tests against various acetone concentrations at 350 °C and associated errors in the form of 95% CIs.

	1 ppm		**2 ppm**		**4 ppm**		**6 ppm**		**8 ppm**	
Device	Average Response	95% CI	Average Response	95% CI	Average Response	95% CI	Average Response	95% CI	Average Response	95% CI
SS ZnO	1.39	±0.07	2.59	±0.28	4.33	±0.67	6.00	±1.07	7.77	±1.55
Zn ZnO	1.32	±0.11	2.38	±0.40	3.87	±0.82	5.26	±1.22	6.62	±1.59

Summary and Conclusions

Two systems of ZnO nanomaterial sensor devices, the first fabricated from CHFS (continuous hydrothermal flow synthesis) derived powder, which demonstrated a variety of sizes and shapes of ZnO nanoparticles using a pre-commercial CHFS pilot plant, and the second fabricated from ZnO powders derived from various relatively higher temperature synthesis routes, specifically molten-salt, solid-state and hydrothermal methods, were investigated.

Within the system of CHFS ZnO devices, the best performing sample (CHFS ZnO sample B) was attributed to observed responses of 84 towards 80 ppm ethanol at 400 °C, 15.2 towards 8 ppm acetone at 400 °C and 166 towards 800 ppb NO_2 at 300 °C.

Within the system of ZnO devices made by a range of high temperature routes, the best performing sample towards ethanol and NO_2 was the Zn ZnO sensor device which was attributed to a response of 37.7 against 80 ppm ethanol at 350 °C and 31.3 towards 800 ppb NO_2 at 250 °C. Towards the lower concentrations of acetone however, the SS ZnO device dominated the response, with the best observed response of 7.8 towards 8 ppm of the analyte.

Analysis of all gas sensing results indicated that in a mixed atmosphere of 10 ppm of acetone and ethanol, both sensors (and in fact all other remaining ZnO sensors in both systems) are potentially attributed to selectivity towards acetone.

Within both systems, it was found that the particle size, morphology and grain boundary conditions at the grain interfaces had significant effect on the overall responsivity and kinetic properties of the materials. In particular, factors like inter-grain agglomeration through heat-treatment and resulting surface-site accessibility, sintering effects, electron path percolation and crystal faceting were observed to be some of the key variables in assimilating sensor behaviour.

Chapter 7 : Final Conclusions and Future Work

This thesis has presented investigations of various hetero-junction systems and ZnO based nanomaterial systems for metal oxide semiconductor (MOS) based gas sensing applications.

The underlying aims of the investigations of the hetero-junction systems were:

- To understand if composite materials and random packing structures were attributed to enhanced gas responsivities with respect to pure metal oxide counter parts
- To interpret possible causes for any enhancement effects observed or not observed
- To interpret the existence of electronic interactions or synergistic effects within the composite metal oxide systems
- To understand if selectivity could be achieved with hetero-junction devices
- To understand effects of microstructure, metal oxide composition, junction effects, packing structure, temperature and analyte concentration on the response properties

The underlying aims of the nanomaterial systems were:

- To identify influential microstructural factors on the response behaviours of nanomaterials
- To assess the potential of emerging fabrication technologies as a route to synthesis of ZnO nanomaterials for MOS gas sensing

7.1 Final Conclusions

In order to address the aims of the hetero-junction study, various systems of sensor devices based on various n-n (WO_3-ZnO and SnO_2-ZnO) and p-n (CTO-ZnO) composite metal oxide combinations were fabricated. Within each composite system, a simple route to the fabrication of a group of hetero-junction sensor devices was demonstrated by forming various inks though a simple mechanical mixing technique. Each ink contained a specific ratio of both component metal oxides, and was screen-printed onto individual MOS sensor substrate strips, which after further processing, ultimately led to the formation of a system of the five composite sensors and two pure unmodified reference counterparts.

In order to address the aims of the ZnO based nanomaterials study, three ZnO nanomaterial samples were fabricated by CHFS, and three other ZnO samples fabricated by molten salt, solid-state metathesis and hydrothermal synthesis. Like the hetero-junction systems, sensors of the ZnO materials were fabricated by primarily forming various inks of each material. Each ink was screen-printed onto individual MOS sensor substrate strips, which after further processing, ultimately led to the formation of a system of the 6 ZnO sensor devices (two systems with three devices each).

XRD and Raman characterisation techniques were implemented to ensure the composite nature of the hetero-junction systems. The techniques also gave evidence of the presence of tertiary phases in the WO_3-ZnO n-n hetero-junction system in the form of zinc tungstate ($ZnWO_4$) and in the CTO-ZnO p-n hetero-junction system in the form of zinc chromite ($ZnCr_2O_4$). The formation of $ZnWO_4$ inevitably formed due to the nature of heat-treatment of the WO_3-ZnO sensor devices. This tertiary phase however, was present as a minority phase and was evaluated to have no response properties towards the key target analytes: NO_2 and ethanol at the associated optimal operating temperatures of 300 °C and 350 °C, and therefore any enhanced response behaviour of the composites was evaluated to occur as a result of the combination of the individual metal oxides.

The formation of $ZnCr_2O_4$, was found to be present in the CTO-ZnO composite materials after the sensor devices were removed from the gas sensing test rig, at the end of gas sensing characterisation tests, however it was unclear at what particular stage of the gas sensing characterisation tests, the tertiary phase had actually formed. Experimental results showed that it was inconclusive as to whether the formation of this tertiary phase had any positive or negative impact on the overall responsivity of the composite material.

7.1.1 Cross Comparisons

Gas sensing experiments of each sensor system, demonstrated the enhanced response behaviour of the composite materials with respect to the pure counterparts. For example in the case of NO_2 sensing, the WO_3-ZnO sensor system proved the most effective hetero-junction system, with devices like the 30 wt.% WO_3 – 70 wt.% ZnO and the 10 wt.% WO_3 – 90 wt.% ZnO composites exhibiting enhanced response magnitudes of 140 and 147, respectively, towards 800 ppb NO_2 at 300 °C in comparison to both the WO_3 and ZnO counterparts, which both displayed responses of 42.7 and 23.4, respectively, under the same operating conditions.

Cross comparison of the response behaviour of the WO_3-ZnO hetero-junction system, with the other two hetero-junction systems studied, established it to be most effective for NO_2 sensing. In the case of the SnO_2-ZnO and CTO-ZnO systems, the composites demonstrated poor responsivity towards NO_2 with respect to the pure ZnO sensor devices. In the case of the former system, the response increased as a function of increasing ZnO concentration in the sensors and decreasing SnO_2 concentration. In the case of the CTO-ZnO system, the n-type ZnO dominated devices showed increased responsivity as a function of increasing ZnO concentration and decreasing CTO concentration, and the p-type CTO dominated devices all showed responses close to baseline response. Thus, in both systems both the pure ZnO sensor devices displayed the largest responses towards NO_2.

In the case of the ZnO based nanomaterials, CHFS ZnO sample B, was seen to be attributed to comparable NO_2 response to the 10 wt.% WO_3 – 90 wt.% ZnO composite, with a response of 141.5 towards an exposure of 800 ppb but at a lower operating temperature of 250 °C. Thus the CHFS material was seen to exhibit a comparably response to NO_2 at the lowest operating temperature; demonstrating a combination of significant responsivity and lowered power consumption. The SS- and Zn- ZnO devices were seen to perform poorly against NO_2 with respect to the CHFS based sensor devices (response range from 18 – 71 towards 400 ppb NO_2) at 250 °C with responses of 13.0 and 9.6, respectively, towards 400 ppb of NO_2 at an operating temperature of 300 °C, but were associated to responses comparable to devices within the WO_3-ZnO composite system such as the pure WO_3 and ZnO devices towards 400 ppb NO_2 at 300 °C, as observed Chapter 3.

In the case of ethanol sensing, both the WO_3-ZnO and SnO_2-ZnO n-n hetero-junction systems contained composite materials which exhibited enhanced responsivities towards the analyte, in comparison to the respective pure counterpart materials. In the former system, the 30 wt.% WO_3 – 70 wt.% ZnO and the 50 wt.% WO_3 – 50 wt.% ZnO sensor devices both exhibited a 1.6-fold and 6.6-fold enhanced response with respect to the pure WO_3 and ZnO sensor devices, respectively, towards 100 ppm ethanol at operating temperatures of 350 °C. In the second system, the 50 wt.% ZnO - 50 wt.% SnO_2 composite was seen to be attributed to a 4.5-fold and 12.3-fold enhanced response with respect to the pure SnO_2 and pure ZnO counterparts, respectively, towards 100 ppm of ethanol at 300 °C. Further, the 30 wt.% ZnO – 70 wt.% SnO_2 sensor device was also seen to exhibit a 4.2-fold and 11.6-fold enhanced response with respect to the pure SnO_2 and pure ZnO counterparts, respectively, again towards 100 ppm of ethanol at 300 °C.

In comparison, CHFS ZnO sample B, was associated to a response of 79.9 towards 80 ppm ethanol at an operating temperature of 350 °C. This response was comparable to the response magnitudes of the 50 wt.% ZnO – 50 wt.% SnO_2 and 30 wt.% ZnO – 70 wt.% SnO_2 composite sensors towards the same concentration of ethanol, but at a lower operating temperature of 300 °C; an example being the 50 wt.% ZnO - 50 wt.% SnO_2 sensor device, which exhibited the highest response of 76 at 300 °C towards 80 ppm ethanol. In a similar way, the responsivity of the Zn ZnO material fabricated by hydrothermal synthesis, was observed to exhibit comparable responsivity magnitudes (10.3) towards 40 ppm of ethanol at 300 °C to the n-type dominated 10 wt.% CTO – 90 wt.% ZnO composite, which exhibited a response of 9.8 towards 40 ppm of ethanol at 300 °C. Thus, the study showed that under certain experimental conditions the nanomaterials were able to perform as well as the composite materials. In the case of the CTO-ZnO composite system, the 10 wt.% ZnO – 90 wt.% CTO material was the best performing composite, dominated by p-type conductivity, showing a response of 10.0 towards 40 ppm ethanol at an operating temperature of 300 °C, with respect to the pure CTO counterpart which showed a response of 2.9 under the same conditions.

Composite materials such as the 30 wt.% WO_3 – 70 wt.% ZnO composite which demonstrated enhanced responses towards both NO_2 and ethanol with respect to its pure WO_3 and ZNO counterparts or the 50 wt.% ZnO – 50 wt.% SnO_2 and 30 wt.% ZnO – 70 wt.% SnO_2 composites, which demonstrated enhanced responses towards ethanol with respect to their pure ZnO and SnO_2 counter parts, were thought to be associated to delocalised contact potentials (i.e. contact potentials which are dispersed among the sensor matrix), which acted to enhance their response magnitudes, with respect to the pure materials. In this way, the investigation showed that composite materials and random packing structures of the grains, within the matrix of the sensor device, was an effective way of increasing the responsivity behaviour.

Composite materials such as the 10 wt.% ZnO – 90 wt.% CTO composite which displayed an enhanced response towards ethanol at 250 °C - 300 °C or towards NO_2 at 300°C, amongst acetone and toluene as well, with respect to the pure CTO material and other sensor devices dominated by p-type semiconducting behaviour, contained n-type ZnO particles dispersed discretely throughout the matrix of the host p-type CTO semiconductor particles. Such packing structures which contained a discrete dispersion of one metal oxide in the host matrix of the second host metal oxide, were thought to be associated to enhanced resistances at the n-n or p-n interfacial hetero-junction which dominated the conductivity of the material, as opposed to the n-n or p-p homo-junction which existed between the homo-contacts. In short, the ratio of homo : hetero contacts played an influential role in the responsivity towards different analytes. The 10 wt.% ZnO – 90 wt.% CTO device was the best performing composite sensor in the whole of the system, and it was thought that the p-n hetero-junctions that existed between the CTO and ZnO grains dominated the device resistance over the weaker p-p homo-contact dominated percolation paths; accounted by the weaker response of p-type semiconducting oxides, and as such displayed significant enhancement with respect to the pure CTO counterpart. Thus the enhanced response of the composites with the p-n hetero-junction system were thought to be dominated by the synergy of both metal oxides when combined together, with electronic effects at the p-n hetero-junction thought to contribute further.

Such packing structures which contained localised contact potentials within the sensor matrix, were also seen to be effective sensing candidates in the n-n mixed metal oxides systems; an example being the 10 wt.% WO_3 – 90 wt.% ZnO sensor device mentioned earlier, which contained particles of WO_3 dispersed discretely throughout the matrix of ZnO grains, exhibiting a 7-fold and 3.5-fold enhanced response with respect to the pure ZnO and WO_3 counterparts, respectively, towards 800 ppb NO_2 at an operating temperature of 300 °C.

The investigations showed that highly random packing structures as well as those which contained a discrete dispersion of grains of one metal oxide in the host matrix of grains of the second metal oxide grains, were both effective candidates for sensing.

The hetero-junction studies reported in this thesis have contributed uniquely to the gas sensing field, by reporting on gas sensing properties of various combinations of metal oxides in which very limited studies have to date been reported in the literature. This is particularly apparent with both the WO_3-ZnO and CTO-ZnO metal oxide combinations, the second of which has never been studied.

In the case of the WO_3-ZnO system, comparison of the results with those reported by An *et al*. and Siriwong *et al*., mentioned earlier in the introduction of Chapter 3, showed the ability of the composites to detect significantly lower concentrations of NO_2 as well as demonstrating their potential towards acetone and ethanol detection, which both literature studies have not demonstrated. In the case of the SnO_2-ZnO, much research around this combination of metal oxides has already been well-established in the literature, however the study reported in this thesis is unique in its route to the preparation of the composite materials and also in the actual ratios of each metal oxide studied which is also true for both the WO_3-ZnO and CTO-ZnO composite systems. The simple change in the ratio of metal oxides in the composite systems, has also allowed the study of the effect of a variety of packing structures on responsivity and selectivity properties. The simple mechanical mixing route to the fabrication of the composite materials, has been demonstrated as an easy and a potentially commercial route for the fabrication of hetero-junction sensors.

Studies of CHFS based materials for gas sensing have been reported a couple of times in literature for example by Elouali *et al*. and Shi *et al*. however the study conducted in this thesis has demonstrated for the first time, the ability to fabricate and successfully test screen-printed CHFS based sensors, which have conventionally always been deposited by drop coating. Further, the study here reports a more in-depth gas sensing analysis, over a wider range of gases and concentrations, which previous studies have not reported. The study has further enhanced the commercial viability of the CHFS process for gas sensing applications, by demonstrating the ability to screen-print nanomaterials, which already have the commercial edge as the synthesis process allow the manufacture of such materials in large amounts, useful for mass production of sensor devices.

Cross comparison of the nanomaterial based ZnO sensors made by CHFS and those made by other high temperature routes, showed the former group of ZnO materials exhibited larger responsivities to the target analytes, for example the best CHFS response (associated to ZnO sample B) recorded against 80 ppm of ethanol was 79.7 at 350 °C and against 800 ppb NO_2 was 141 at 250 °C. In contrast, the best response of the ZnO ceramics made via the high temperature routes (specifically solid state metathesis) was 34.2 against 80 ppm ethanol at 400 °C and 25.5 towards 800 ppb of NO_2 at 300 °C. Response results against acetone showed that the best performing ZnO nanomaterial made via CHFS (ZnO sample B) was associated to a response of 15.2 towards 8 ppm of acetone at 400 °C, whereas the sensor made via solid state metathesis, displayed a response of 7.8 towards 8 ppm at a lower operating temperature of 350 °C. Thus in general the CHFS sensors were associated to larger responsivities at lower operating temperatures, making them the more attractive from a commercial perspective.

Microstructural influences of the materials, on the responsivity performance was deduced through imaging of the sensor devices through SEM. The technique showed evidence of loosely packed nature of the grains in most composite devices, attributed to thick-film deposition technology, which gave evidence of diffusion and percolation pathways, for the gaseous molecules to travel into and out of the body of the sensor matrices. Such microstructures were thought to contribute to the enhanced responsivity of the composite materials as they enabled an increased surface site accessibility of the analyte molecules, increasing the overall yield of surface reactions.

Further, particle size difference observed through this imaging technique showed the stark difference between some combination of metal oxides, such as for example in the SnO_2-ZnO system in which a mixture of SnO_2 agglomerated grains and the individual ZnO grains were observed or in the CTO-ZnO system in which nanosized CTO particles and micron sized ZnO particles were observed. Such stark differences in particle sizes were also though to contribute to the hetero-junction effects attributed to these systems, apart from the hetero-junction effects induced by the chemical in-homogeneity of the materials.

The assessment of microstructural factors influential on the response performance of ZnO nanomaterials showed that the smallest particle size of a material was not the determining factor of the highest responsivity. Factors such as heat-treatment regime which subsequently affected the inter-grain agglomeration and sintering effects, as well as the electron path percolation and morphological crystal faceting were all identified as influential to the overall responsivity and kinetic properties of the materials, as these factors contributed to surface site accessibility of the gaseous analytes as well as the charge carrier conductivity. The study showed that balance between these properties was required, where a small particle size, with limited agglomeration and sintering as a result of heat-treatment and larger morphological faceting of the metal oxide grains, made up for a microstructure that promoted the best responsivity. Thus, grain-boundary contributions at the grain interfaces were significant for nanomaterials, accounted for by their large surface : bulk ratios and as such, microstructure played an influential role on their overall response properties.

The nanomaterials study demonstrated both CHFS and the other synthesis methods to be successful as a route to ceramics for metal oxide semiconductor gas sensing applications, with a variety of morphologies (nano-rods, nano-hexagons, nano-spheres and larger hexagonal pyramids) and particle sizes fabricated. From a commercial and synthetic perspective, cross comparison of the routes of fabrication of the nanomaterials from CHFS vs. those made from high temperature routes, suggested that the former route was more attractive fabrication route offering the capability to produce large quantities of ZnO nanomaterials in minutes and the versatility to alter the morphological characteristics of the ZnO particles by a simple change in the precursor concentrations, within the same system. Previous literature studies have also established this synthesis route to producing effective nanomaterials for gas sensing applications. In contrast, the molten salt synthesis route, solid-state metathesis route and the hydrothermal synthesis route were seen to offer limited variation in the morphological characteristics of the ZnO particles within the associated samples and were also associated to limited yield of the formed product, assimilated from the samples received from Dr. Poduska.

XPS analysis was conducted on the individual sensor devices within each hetero-junction system, to verify any electronic interactions between the individual metal oxide components. The analysis technique showed a very strong correlation between the relative binding energies as a function of increasing WO_3 phase fraction, and as such indicated an electronic interaction between both the WO_3 and ZnO components, which was thought to contribute to the enhanced gas sensing properties associated to the WO_3-ZnO composite system. In contrast a weaker correlation was seen between the relative binding energies as a function of increasing SnO_2 phase fraction suggesting a very weak electronic interaction, between the individual metal oxide components with the SnO_2-ZnO hetero-junction system. No correlation was seen in the CTO-ZnO system and as such, no evidence of an electronic interaction could be deduced between the p-and n- type materials.

The XPS analysis of the composite materials was a further advancement and novelty of the studies reported in this thesis, with no such analysis observed in literature before. The observation of electronic interactions between the individual metal oxide components, particularly in the WO_3-ZnO composite system, was evidenced and suggested the existence of hetero-junction electronic effects between both metal oxides which were thought to act to enhance responsivity properties. The simple preparation route of a variety of composite sensors within a particular hetero-junction system, contributed to the ease and structure with which this XPS analysis could be conducted and interpreted.

Temperature was variable that was seen to counteract the hetero-junction effects in the composite systems. In particular with both n-n hetero-junction systems, the degradation of the electronic enhancement was evident at higher operating temperatures and was thought to be due to energetically easier charge transfer within the semiconductors, which effectively decreased the effective energy barrier, and thus resistance, at the junction; weakening the overall junction effect. Thus higher temperatures could not promote junction effects to play effective roles in enhancing gas sensing response.

Apart from the electronic interactions, the synergy of the individual metal oxides upon their combination was deduced as a major contributory factor to the enhanced response properties of all three composite systems. In the case of the WO_3-ZnO composite system, the superior sensing properties of WO_3 towards NO_2 and ZnO towards ethanol, contributed to the group of devices performing well against both NO_2 and ethanol, which was not observed with the other hetero-junction systems investigated.

In the case of the SnO_2-ZnO composite system, the synergy of both metal oxides as oxidation catalysts for VOCs was potentially evident from the enhanced responsivities that the combination of both metal oxides exhibited towards ethanol and acetone. In contrast, towards increasing concentrations of NO_2 and CO, all devices were seen to increase as a function of increasing concentration of ZnO and increasing concentrations of SnO_2, respectively. As such the synergy of both materials was evident from the response properties.

In the case of the CTO-ZnO system, conductivity was 2-fold; a weaker response of the p-type semiconducting oxide due to conductivity via the hole accumulation layer (HAL) and the stronger response of the n-type semiconducting oxide due to conductivity via the electron depletion layer (EDL) balanced each other out and as such, played a synergistic role in the observed response behaviour. The 10 wt.% ZnO – 90 wt.% CTO composite sensor device was a good example of such a device, which contained n-type ZnO particles dispersed discretely throughout the matrix of the host p-type CTO semiconductor particles. In such a device, the p-n hetero-junctions were thought to dominate the resistance of the device in comparison to the weaker p-p homo-contact percolation paths that dominate the sensor matrix, and as such the device was thought to exhibit enhanced response behaviour. In contrast, 90 wt.% ZnO – 10 wt.% CTO composite sensor device which contained p-type CTO particles dispersed discretely throughout the matrix of the host n-type ZnO semiconductor particles, showed minimal enhancement and this was thought to be due to the n-n percolation paths which dominated the sensor matrix, which had significant influence over the resistance of the device over the potentially weaker p-n hetero-contacts.

A further synergistic effect seen in this CTO-ZnO system, was the evidence of the resistance of those materials integrated with the p-type CTO material, towards effects of humidity generated by surface induced chemical reactions, due to the nature of the conductivity of the p-type semiconducting oxide dominated by the HAL. Its incorporation into the composite sensors, saw baseline stability being promoted for the composites towards potential humidity effects, due to by-products such as water formed on the surface of the metal oxides, from combustion reactions of ethanol. In particular this was evident at the lower end of the operating temperature at 250 °C, where those devices dominated by p-type conductivity were seen to be attributed to a stable baseline compared to those devices dominated by n-type conductivity.

Thus, synergy was recurring theme within the investigations of the hetero-junction systems interpreted through the gas sensing behaviour of the materials; this was accompanied by potential electronic enhancement effects, which to some extent could be verified by XPS. Both factors were considered to be influential causes for the enhanced response behaviours observed .All hetero-junction studies also showed how the responsivity and selectivity of a composite sensor device could be tuned by a simple change in the concentration of either of the metal oxides (and therefore the packing structure of the grains), within the composite matrix.

Gas testing and analysis of the hetero-junction systems, to a range of other gases; specifically acetone, NH_3, CO and toluene (in addition to the two main target gases ethanol and NO_2), showed that the hetero-junction devices did exhibit potential selectivity.

In the WO_3-ZnO system for example, the 10 wt.% WO_3 – 90 wt.% ZnO sensor device, which contained particles of WO_3 dispersed discretely throughout the matrix of ZnO grains, was particularly interesting as it showed the largest response of 148 towards 800 ppb NO_2 at an operating temperature of 300 °C and a response of only 4 towards 100 ppm ethanol at the same operating temperature. This suggested that in a mixed atmosphere containing the associated concentration ranges of ethanol (ppm levels) and NO_2 (ppb levels), the composite sensor can potentially exhibit successful selectivity towards NO_2. In another example, comparison of the responsivities of the 30 wt.% WO_3 – 70 wt.% ZnO and 50 wt.% WO_3 – 50 wt.% ZnO sensor devices towards 10 ppm of ethanol and acetone, showed that both devices, particularly the 30 wt.% WO_3 – 70 wt.% ZnO composite device could selectively detect acetone, if put in a mixed gas atmosphere of equal concentrations of ethanol and acetone.

In the case of the SnO_2-ZnO composite system, the 50 wt.% ZnO - 50 wt.% SnO_2 and the 30 wt.% ZnO – 70 wt.% SnO_2 sensor devices were seen to be attributed to conductive responses of 1.5 and 2.0 towards 10 ppm ethanol at 300 °C but larger response of 8.3 and 11.8 respectively, towards 10 ppm of acetone at the same operating temperature. In contrast, the 70 wt.% ZnO - 30 wt.% SnO_2 sensor device was seen to be attributed to the largest conductive response of 33 towards 10 ppm of acetone but only a conductive response of 2.1 to the 10 ppm of ethanol at 300 °C. This therefore demonstrated that within the SnO_2-ZnO sensor system, composites could selectively detect acetone and ethanol, depending on the composition of each metal oxide.

In the case of the CTO-ZnO system, selectivity through cancellation (due to the cancelling out of n- and p- type percolation paths) was evident with the 30 wt.% ZnO – 70 wt.% CTO sensor device which exhibited cancellation behaviour against ethanol, acetone and NO_2 but exhibited quantifiable responses against toluene at 350 °C, indicating that in a mixed atmosphere of all four gases, the cancellation behaviour of this device may be exploited to selectively detect toluene. Thus a key recurring theme from the investigations was how a simple change in the composition (and therefore packing structure) of the metal oxides, within the composites, could tune the responsivity and selectivity of the sensor device towards either a reducing or oxidising analyte. The study also showed how a simple addition of ZnO to CTO, was able to change the selectivity of the material. For example at an operating temperature of 300 °C, the pure CTO sensor device was seen to display selectivity towards toluene, however at the same operating temperature, the 10 wt.% ZnO – 90 wt.% CTO sensor device showed selectivity towards ethanol. Thus some examples existed in the study which showed how a simple change in the concentration of either metal oxide could tune the responsivity and selectivity of a sensor device towards a particular analyte.

Both the composite and the nanomaterial systems demonstrated, that if put in a mixed atmosphere of ethanol and acetone, both groups of sensor devices are potentially likely to selectively detect acetone. Due to their compositional nature, the opportunity to tune the selectivity was clearly more flexible in the composite devices than in the nanomaterial devices, through the variation of the concentration contribution of the individual metal oxide components.

7.1.2 Sources of Error

In terms of error analysis that has been briefly alluded to, throughout each Chapter, the concentration of the analyte and the composition of the sensor devices, were 2 of the physical factors observed to contribute significantly to the errors on the response magnitudes. In terms of concentration, the error magnitude increased with an increasing gas concentration. In particular, if a sensor was very responsive to a particular analyte e.g. the WO_3-ZnO based devices particularly responsive to NO_2 / ethanol or the SnO_2-ZnO devices particularly responsive to ethanol / acetone, then such a device was associated to significant error. One reason for this may have been the formation of more by-products at the higher concentrations of gas exposure. This may have caused cross-sensitivity issues contributing to the significant magnitudes of errors on the devices at the higher analyte concentrations. Further, exposure to the higher concentrations may have also lead to progressive contamination issues on the metal oxide surface, which was not as probable with exposures to the low gas concentrations. Such larger errors were not limited to the composite devices, but were also apparent with the ZnO nanomaterials, such as that observed with the CHFS sample B upon exposure to 800 ppb NO_2. More specifically for the composite materials, larger errors were also prevalent with those composites which had a significant contribution of both metal oxides, in comparison to those composites which had a biased contribution of one metal oxide or the single metal oxide devices. This was particularly apparent with the WO_3-ZnO composites and the SnO_2-ZnO composites. This trend suggested that the composite sensors in general were associated to instability, which may be a result of the fabrication process or the presence of two very responsive and active metal oxides in each of the hetero-junction devices. The combination of two metal oxides with very potent response properties are likely to contribute to greater error, as a multiple number of reactions and catalytic effects are likely to occur on the metal oxide surface. Due to the significant errors on the composites, comparative responsivity and selectivity performance between the composites was difficult to conclude, as the mean response values and associated errors overlapped with each other between devices. This was particularly apparent with the SnO_2-ZnO composite materials, where significant overlap in response magnitude and associated errors towards ethanol and acetone.

In terms of the ZnO based nanomaterials, all devices were associated to significantly low magnitudes of error except for CHFS sample B. This sample was the most responsive and as such the magnitude of error increased with the large response of the device. Possible factors may have been the active nature of the material and the instability of microstructure during gas runs, as a function of temperature.

In general, the error analysis shows that changes in the error values were not seen to be random, when evaluated as a function of analyte concentration or composition of the device. However randomness was observed between the repeat tests, with response magnitude following no specific order with repeat tests.

Other sources of errors on the response magnitudes, may have been potential temperature fluctuations of the sensor devices, whilst in operation. Given that the nature of heating is dependent on the resistance of the platinum heater track, fluctuations in temperature are very likely to have occurred with the deviation in the platinum resistance being promoted by atmospheric temperature changes, minor fluctuations in gas flow on the sensor devices and instability of the electronics that controlled the temperature. More technically, an inherent error associated to the MFC, which would have subsequently affected flow rate, would also contribute to fluctuations in the response with all MFCs being associated to a minimum error of 2 %. The electronic measurement circuits and digital multi-meter for direct resistance measurements in the gas sensing rig, are also contributory source of errors.

7.1.3 Application Possibilities

From the investigations conducted, the gas sensing studies of the various hetero-junction systems demonstrated the materials (depending on the combination of metal oxides used) to be applicable for a variety of applications.

The first of the applications was for NO_2 sensing, which is an important analyte to detect from exhausts released from cars, power plants or combustion engines. In 2000, the world health organisation (WHO) [348] had reported, through information from various sources, that the maximum 24-hour average outdoor NO_2 concentration was measured to be 0.21 ppm (210 ppb) and the maximum 30 minute or 1 hour average was measured to be 0.5 ppm (500 ppb). Further, they had reported that the annual mean concentration of NO_2 in urban areas throughout the world was in the range of 0.01 ppm –

0.05 ppm (10 ppb - 50 ppb). The hourly average NO_2 concentrations near very busy roads exceeded 0.5 ppm (500 ppb). In the UK itself, the maximum hourly concentrations of NO_2, during peak times on roads, were reported to in the range of 0.25 ppm – 0.40 ppm (250 ppb - 400 ppb).

Another source, which gave an overview on an urban area survey in the UK, reported that the annual mean concentrations of NO_2 were detected to be in the range of 10 - 45 ppb in the UK, with fossil fuel combustion from power stations and combustion due to transportation contributing to a total of 65% of the anthropogenic source of NO_2 production [349]. NO_2 levels due to transportation varied significantly throughout the day, but during time of rush hour traffic the values peaked, with maximum daily means being as high as 200 ppb and had reported that the maximum one hourly mean to be as high as 600 ppb [349]. Both sources suggest that during peak times on roads, globally and nationally the NO_2 concentrations significantly increase with respect to the background, and illustrate the contribution of the analyte emissions from the car exhausts. The concentration ranges reported thus illustrate the potential to use the composite sensors devices, studied in this thesis, which are able to detect ppb ranges of NO_2, for practical NO_2 detection applications.

A second potential application of the sensor devices would be for ethanol detection for use in food and drink quality control processes such as food packing safety or in breathalysers for the detection of alcohol content in the breath of drunk drivers. In the case of the second application, the concentration ranges of ethanol in the blood ae determined from its concentration in the breath, which can be related to the extent of intoxication [175]; for example symptoms of haziness suggest concentrations in the range of 130 – 260 ppm in the breath, slight drunkenness suggests concentrations in the range of 260 – 390 ppm in the breath and drunkenness is associated to concentrations of 390-650 ppm in the breath [175]. These ppm levels demonstrate the potential to use of the composite sensors, which have ppm ethanol detection capability, for practical breathalyser applications.

A third application of the sensor devices is for the detection of acetone as a key biomarker for diabetic patients, with individuals suffering from this disease found with levels of over 1.8 ppm of acetone [23] in their breath. As such the composite sensor devices demonstrated potential in medical sensing applications.

A final potential application of the composite sensor devices is for toluene detection in the environment. As a guideline, from a range of organic gases, toluene was measured to have the mean highest concentration of 17 ppb in Turin in Italy, with a similar magnitude of concentration measured at sites in the USA, UK and Australia, as per a report cited by the WHO [350]. Correa *et al*. [351] had reported that whilst filling up gasoline in 11 different gasoline stations in Rio de Janeiro, Brazil, resulted in the emission of 10 ppb of toluene in the ambient air between 2008 and 2009. The environmental protection agency (EPA) [352] has referred to a report by the US Dept. of Health and Human Services from 2000, in which it had reported that the highest toluene concentrations are measured indoors through the use of common household products such as paints, varnishes, synthetic fragrances and via cigarette smoke, with a measured average concentration of 8 ppm. The same department had also reported urban and rural concentrations of toluene to be 3 ppm and 320 ppb, respectively with emission sources ranging from cars and during production, use and disposal of industrial and consumer products that contain toluene. The thesis has presented response results of some of the CTO based composites exhibiting responses towards 100 ppm toluene; which suggests the potential for the sensors to detect low concentrations of the analyte, particularly in indoor and urban environments in the US.

7.1.4 Drawbacks

Despite the advantages towards the responsivity, potential selectivity and wide applicability of the composite materials for gas sensing applications, a number of drawbacks of the systems were apparent. Some of these have already been integrated into the source of errors above in section 7.1.2. Further to these form a commercial perspective, one of the key disadvantages was the slow response and recovery kinetics.

Poor kinetics was particularly apparent with the composite materials in the n-n hetero-junction systems and was seen to be promoted by the increased number of surface sites in hetero-junction materials. The increased number of surface sites available for the given concentration of gas exposure lead to the slow and gradual saturation of the surface. This parameter also lead to the slower gradual recovery of the surface sites upon switching off the gas exposure, with time needed for the surface sites to fully recover from the large number of adsorbed gas molecules. The t_{90} and t_{-90} values obtained in the 100s of seconds showed that the kinetics of response and recovery were compromised for the response performance, which to some extent made the sensors impractical in environments where fast responses and recoveries are required. In this way, the investigation illustrated a potential disadvantage for the application of a hetero-junction MOS gas sensing system. A suggested earlier in the introduction, typical response times for sensor devices in commercial application are required to be in the 10s of seconds for critical warnings. Solutions to lower the response times from 100s of seconds achieved in this investigation, to 10s of seconds, may include the inclusion of catalytic dopants or zeolite layers in/on the existing sensor materials , as a kinetic solution, a proposal of which has been mentioned in the future work.

The summary of final conclusions shows how the aims of the project were fulfilled through various examples seen in the experimental investigations. Potential suggestions that can further develop the research work presented in this thesis have been suggested in the following section.

7.2 Future Work

Development of the research work in this thesis can be extended in many directions, given the diverse nature of the investigation. An assessment of the conducted research work presented in this thesis, has highlighted some key future investigations that have been proposed below.

A first future proposal is the design of the hetero-junction systems around alternate structural architectures / packing structures of both the metal oxides in question, which can promote potentially better electronic hetero-junction enhancement effects and greater stability of the devices. Examples include core-shell architectures as well as layered architectures. In the core-shell, it would be interesting to explore the individual gas sensing performances of packing structures where each metal oxide is either a core or a shell (e.g. WO_3-ZnO core-shell and ZnO-WO_3 core-shell or CTO-ZnO core-shell and ZnO-CTO core-shell), and compare and contrast them. In the layered, packing structures in which the stacking order of the metal oxides is varied (e.g. ZnO on SnO_2 or SnO_2 on ZnO), are important to consider. With layered architectures, the direction of gas flow is an important variable towards responsivity behaviour. The flow can be directed towards the hetero-interface side-on with the gas permeating through both metal oxides at once. Alternatively gas flow can be directed face-on allowing the gas to permeate from metal oxide layer on top down to the metal oxide layer below it. This opens up a study on the deposition techniques that can be used to deposit layers of metal oxides in stack form, on the gas sensor substrates, and how each technique can change the orientation of the metal oxide layered architectures on the gas sensor substrates. Given that both the layered and core-shell architectures can be built with an system of deposition techniques such as chemical vapour deposition (CVD) or atomic layer deposition (ALD) (both thin-film techniques), or an amalgamation of both thick-film and thin-film techniques, then microstructural variations are also likely to play an influential role on the overall response properties. Thus, investigation based on changing the architecture of the hetero-junction system, open up a whole new avenue of studies that can be explored.

Another interesting study in the future, would be visualise the homo– and hetero- contacts in the hetero-junction composite devices by using computer tomography or back-scattered scanning electron microscopy (SEM) imaging techniques, the latter of which should be able to visualise the different metal oxides within the matrix of the metal oxide composite by elemental mass difference. Such techniques will aid the qualitative and quantitative interpretation of the homo- and hetero- contacts and shed light for deeper interpretation of their influencing roles towards the gas sensing properties.

Further developments to the composite hetero-junction study, from a more theoretical perspective, can be investigation of the formation of the tertiary phases as a function of processing temperature. In particular, low temperatures are of key interest as the formation of a tertiary phase could be avoided but at the same time the organic vehicle burned off to form a composite sensor with robust adherence of the substrate, if left long enough. These sensor devices can then be investigated to understand their response properties and compared to the current devices, which contain the presence of the tertiary phases. This evaluation will better contribute to the understanding of the role of the tertiary phase on the response properties. Further investigations on the hetero-junction composite systems can be conducted on the catalytic modification through doping of noble metal such as gold or integration of zeolites layers, to improve the associated response and recovery kinetics for practical applications.

A further interesting study would be to see how the responsivity of the hetero-junction composite devices varies as a function of changing the p-type metal oxide, while keeping ZnO as the n-type metal oxide and then varying the n-type metal oxide, while keeping the p-type metal oxide constant to for example CTO. Particular to the utilisation of CTO, changing the stoichiometry of the Cr:Ti ratio within the CTO, and understanding the effect of this change to the responsivity to the CTO-ZnO p-n hetero-junction composite system, is also another study of interest.

In terms of gas sensing studies, one of the key potential investigations that has recurred throughout the investigation of the hetero-junction systems is the evaluation of the system of these devices in mixed gas atmospheres of for example ethanol and NO_2, or ethanol and acetone, as well as other gas combinations. In particular it would be interesting to investigate the selectivity of each hetero-junction system towards a particular alcohol. Given the nature of the similar chemistry of alcohols on metal oxide surfaces, potential selectivity towards a specific alcohol would be of particular interest, and opens up a study of shape selectivity of hetero-junction systems. Shape-selectivity can also be achieved by the integration of zeolite layers on the metal oxide materials, and hence the integration of zeolites to the composite materials and subsequent investigation of alcohol selectivity is another avenue that can be explored.

Further studies can incorporate the testing of multiple sensors of the same composition, in order to assimilate the batch-to–batch repeatability of the response characteristics. Further, routes to the assimilation of the selectivity properties of the composite devices with respect to each other can be investigated, which due to the overlapping of error values could not be deduced in this thesis. Longevity testing of the individual sensor devices (or alternatively called sensor ageing) is another suggestion, in order understand the performance of the sensors over a long period time – i.e. do they have the same response performance after for example 6 months or 1 year or does the performance deteriorate with time. Another investigation associated to the longevity testing is the baseline resistance drift over the time. Longevity tests like this will allow to gauge in to the commercial potential of the devices when put into practical real life situations. Gas testing in this thesis was limited to certain concentration ranges and operating temperatures, however future work can consider testing the sensor devices over larger analyte concentration ranges and operating temperatures. This testing will widen the application possibilities of the sensors devices to those already highlighted. The gas testing carried out in this thesis was purely under dry conditions, however in reality, moisture is always present in the ambient air and as such; future work can also encompass testing the sensor devices under humid conditions.

Of particular interest in correspondence to both the underlying themes of this thesis, i.e. the hetero-junction systems and the nanomaterial systems, would be to combine the ZnO nanomaterials with other metal oxide nanomaterials to develop nanomaterial based hetero-junction systems. Such systems encapsulate the combined advantages of size, morphology and chemical & electronic sensitisation effects and contribute to the research and development of a host of new hetero-junction based on metal oxide sensor systems for MOS gas sensing applications. A further interest would be to bring together the best performing composite and nanomaterial based sensors, and combine them together in an electronic nose type system, and investigate the responsivity and selectivity performance of the group of devices.

Ultimately this investigation is for research and development of sensor devices for practical monitoring applications and as such the sensors are envisaged to be integrated into portable devices. Thus, testing the viability of the devices for practical applications requires evaluation of their response behaviour towards target analytes out in the field, in addition to the ideal laboratory environment.

Publications

Journals

1. A.J.T. Naik, R. Gruar, C.J. Tighe, I.P. Parkin, J.A. Darr and R. Binions**, *Environmental Sensing Semiconducting Nanomaterials made using a Continuous Hydrothermal Synthesis Pilot Plant,*** submitted to Sensors and Actuators B: Chemical**,** Accepted**.**
2. A.J.T. Naik, I.P. Parkin, and R. Binions, ***Gas Sensing Studies of a n-n Hetero-Junction System Based on WO_3 and ZnO Composites***. Sensors Journal, IEEE. 2014; 14 (9): 3137-3147.
3. P.T. Hernandez, A.J.T. Naik, E.J. Newton, S.M.V. Hailes, and I.P. Parkin, ***Assessing the potential of metal oxide semiconducting gas sensors for illicit drug detection markers***. Journal of Materials Chemistry A. 2014; 2 (23): 8952-8960.
4. D.C. Pugh, E.J. Newton, A.J.T. Naik, S.M.V. Hailes, and I.P. Parkin, ***The gas sensing properties of zeolite modified zinc oxide***. Journal of Materials Chemistry A. 2014; 2 (13): 4758-4764.
5. L. Shi, A.J.T. Naik, J.B.M. Goodall, C. Tighe, R. Gruar, R. Binions, I.P. Parkin, and J. Darr, ***Highly Sensitive ZnO Nanorod- and Nanoprism-Based NO_2 Gas Sensors: Size and Shape Control Using a Continuous Hydrothermal Pilot Plant***. Langmuir. 2013; 29 (33): 10603-10609.
6. A.J.T. Naik, C. Bowman, N. Panjwani, M.E.A. Warwick, and R. Binions, ***Electric field assisted aerosol assisted chemical vapour deposition of nanostructured metal oxide thin films***. Thin Solid Films. 2013; 544 (0): 452-456.
7. A.J.T. Naik, M.E.A. Warwick, S.J.A. Moniz, C.S. Blackman, I.P. Parkin, and R. Binions, ***Nanostructured tungsten oxide gas sensors prepared by electric field assisted aerosol assisted chemical vapour deposition***. Journal of Materials Chemistry A. 2013; 1 (5): 1827-1833.
8. N. Panjwani, A. Naik, M.E.A. Warwick, G. Hyett, and R. Binions, ***The Preparation of Titanium Dioxide Gas Sensors by the Electric Field Assisted Aerosol CVD Reaction of Titanium Isopropoxide in Toluene***. Chemical Vapor Deposition. 2012; 18 (4-6): 102-106.
9. A.J.T. Naik, S. Ismail, C. Kay, M. Wilson, and I.P. Parkin, ***Antimicrobial activity of polyurethane embedded with methylene blue, toluidene blue and gold nanoparticles against Staphylococcus aureus; illuminated with white light***. Materials Chemistry and Physics. 2011; 129 (1–2): 446-450.

Publsihed Conference Proceedings

1. A.J.T. Naik, I.P. Parkin, and R. Binions. ***Gas sensing studies of an n-n hetero-junction metal oxide semiconductor sensor system based on WO_3 and ZnO composites***. in *SENSORS, 2013 IEEE*. 2013.
2. A.J.T. Naik, R. Gruar, C.J. Tighe, I.P. Parkin, J.A. Darr and R. Binions**, *Environmental Sensing Semiconducting Nanomaterials made using a Continuous Hydrothermal Synthesis Pilot Plant,*** 15th International Meeting on Chemical Sensors 2014 (IMCS 2014). Proceedings found at: http://www.imcs2014.org/proceedings

Book Chapters

1. R. Binions and A.J.T. Naik, ***Chapter 13: Metal oxide semiconductor gas sensors in environmental monitoring*** in ***Semiconductor Gas Sensors***. 2013, Woodhead Publishing, Edited by R. Jaaniso and O.K. Tan. p.433-46

References

1. M.E. Franke, T.J. Koplin, and U. Simon, ***Metal and metal oxide nanoparticles in chemiresistors: Does the nanoscale matter?*** Small. 2006; 2 (1). 36-50.

2. Y. Wang and J.T.W. Yeow, ***A Review of Carbon Nanotubes-Based Gas Sensors***. Journal of Sensors. 2009; 2009. 1-24.

3. G.I.A. Inc. ***Global Chemical Sensors Market to Reach $17.28 Billion by 2015, According to New Report by Global Industry Analysts, Inc.*** 2010, PRWeb [date accessed: 6th July 2011]; Available from: http://www.prweb.com/releases/chemical/sensors/prweb3609734.htm.

4. X. Liu, S. Cheng, H. Liu, S. Hu, D. Zhang, and H. Ning, ***A Survey on Gas Sensing Technology***. Sensors. 2012; 12 (7). 9635-9665.

5. P. Grundler, ***Chapter 1: Introduction***, in ***Chemical Sensors***, 2007, Springer-Verlag: Berlin Heidelberg, Germany. pp. 1-13.

6. J. Janata, ***Chapter 5: Electrochemical Sensors***, in ***Priciples of Chemical Sensors***, 2009, Springer US: New York, USA. pp. 99-118.

7. Wikipedia. ***Electrochemical Gas Sensor***. 25th June 2014 [date accessed: 23rd January 2015]; Available from: http://en.wikipedia.org/wiki/Electrochemical_gas_sensor#cite_note-1.

8. P. Grundler, ***Chapter 7: Electrohemical Sensors***, in ***Chemical Sensors***, 2007, Springer-Verlag: Berlin Heidelberg, Germany. pp. 137-197.

9. P. Grundler, ***Chapter 8: Optical Sensors***, in ***Chemical Sensors***, 2007, Springer-Verlag: Berlin Heidelberg, Germany. pp. 199-225.

10. P. Grundler, ***Chapter 6: Thermometric and Calorimetric Sensors***, in ***Chemical Sensors***, 2007, Springer-Verlag: Berlin Heidelberg, Germany. pp. 133-136.

11. P. Grundler, ***Chapter 5: Conductivity Sensors and Capacitive Sensors***, in ***Chemical Sensors***, 2007, Springer-Verlag: Berlin Heidelberg, Germany. pp. 123-132.

12. G.F. Fine, L.M. Cavanagh, A. Afonja, and R. Binions, ***Metal Oxide Semi-Conductor Gas Sensors in Environmental Monitoring***. Sensors. 2010; 10 (6). 5469-5502.

13. N. Taguchi, ***Gas-Detecting Device U.S. Patent : 3,631,436***, 1971.

14. T. Seiyama, A. Kato, K. Fujiishi, and M. Nagatani, ***A New Detector for Gaseous Components Using Semiconductive Thin Films***. Analytical Chemistry. 1962; 34 (11). 1502-1503.

15. A. D'Amico and C. Di Natale, ***A contribution on some basic definitions of sensors properties***. IEEE Sensors Journal. 2001; 1 (3). 183-190.

16. P.T. Moseley, ***Solid state gas sensors***. Measurement Science & Technology. 1997; 8 (3). 223-237.

17. G. Korotcenkov, ***Metal oxides for solid-state gas sensors: What determines our choice?*** Materials Science and Engineering B-Solid State Materials for Advanced Technology. 2007; 139 (1). 1-23.

18. G. Eranna, B.C. Joshi, D.P. Runthala, and R.P. Gupta, ***Oxide materials for development of integrated gas sensors - A comprehensive review***. Critical Reviews in Solid State and Materials Sciences. 2004; 29 (3-4). 111-188.

19. E. Comini and G. Sberveglieri, ***Metal oxide nanowires as chemical sensors***. Materials Today. 2010; 13 (7–8). 36-44.

20. N. Barsan, D. Koziej, and U. Weimar, ***Metal oxide-based gas sensor research: How to ?*** Sensors and Actuators B: Chemical. 2007; 121 (1). 18-35.

21. A. Ponzoni, E. Comini, G. Sberveglieri, J. Zhou, S.Z. Deng, N.S. Xu, Y. Ding, and Z.L. Wang, ***Ultrasensitive and highly selective gas sensors using three-dimensional tungsten oxide nanowire networks***. Applied Physics Letters. 2006; 88 (20). 203101~1 - 203101~3.

22. B. Hoffheins, ***Chapter 14: Solid state, resistive gas sensors***, in ***Handbook of Chemical and Biological Sensors***, R.F. Taylor and J.S. Schultz, Editors, 1996, Institute of Physics Publishing Ltd.: Bristol, United Kingdom pp. 371-398.

23. P. Varsani, A. Afonja, D.E. Williams, I.P. Parkin, and R. Binions, ***Zeolite-modified WO_3 gas sensors – Enhanced detection of NO_2***. Sensors and Actuators B: Chemical. 2011; 160 (1). 475-482.

24. H. Tang, M. Yan, H. Zhang, S. Li, X. Ma, M. Wang, and D. Yang, ***A selective NH_3 gas sensor based on Fe_2O_3–ZnO nanocomposites at room temperature***. Sensors and Actuators B: Chemical. 2006; 114 (2). 910-915.

25. T. Tsyrkina, L. Obvintseva, V. Kuchaev, A. Avetisov, S. Penkin, I. Sukhareva, and M. Dmitrieva, ***Research of the interaction mechanism between HCl and semiconductor metal oxides***. Procedia Chemistry. 2009; 1 (1). 184-187.

26. S. Kanan, O. El-Kadri, I. Abu-Yousef, and M. Kanan, ***Semiconducting Metal Oxide Based Sensors for Selective Gas Pollutant Detection***. Sensors. 2009; 9 (10). 8158-8196.

27. S. Di Carlo and M. Falasconi ***Chapter 14: Drift Correction Methods for Gas Chemical Sensors in Artificial Olfaction Systems: Techniques and Challenges*** in ***Advances in Chemical Sensors***, W. Wang, Editor, 2012, InTech, Available from http://cdn.intechopen.com/pdfs-wm/26356.pdf [date accessed: 2nd February 2015]. pp. 305 - 327.

28. M. Schüler, T. Sauerwald, and A. Schütze, ***Metal oxide semiconductor gas sensor self-test using Fourier-based impedance spectroscopy***. Journal of Sensors and Sensor Systems. 2014; 3. 213 - 221.

29. B. Ruhland, T. Becker, and G. Müller, ***Gas-kinetic interactions of nitrous oxides with SnO_2 surfaces***. Sensors and Actuators B: Chemical. 1998; 50 (1). 85-94.

30. A.D. Wilson and M. Baietto, ***Applications and Advances in Electronic-Nose Technologies***. Sensors. 2009; 9 (7). 5099-5148.

31. E. Comini, G. Faglia, and G. Sberveglieri, ***Chapter 2: Electrical-Based Gas Sensing***, in ***Solid State Gas Sensing***, E. Comini, G. Faglia, and G. Sberveglieri, Editors, 2009, Springer US: New York, USA. pp. 47-107.

32. C.S. Blackman, X. Correig, V. Katko, A. Mozalev, I.P. Parkin, R. Alcubilla, and T. Trifonov, ***Templated growth of tungsten oxide micro/nanostructures using aerosol assisted chemical vapour deposition***. Materials Letters. 2008; 62 (30). 4582-4584.

33. S. Ashraf, R. Binions, C.S. Blackman, and I.P. Parkin, ***The APCVD of tungsten oxide thin films from reaction of WCl_6 with ethanol and results on their gas-sensing properties***. Polyhedron. 2007; 26 (7). 1493-1498.

34. G. Shaw, I.P. Parkin, K.F.E. Pratt, and D.E. Williams, ***Control of semiconducting oxide gas-sensor microstructure by application of an electric field during aerosol-assisted chemical vapour deposition***. Journal of Materials Chemistry. 2005; 15 (1). 149-154.

35. D.G. Rickerby and A.M. Serventi, ***Chapter 6: Nanostructured Metal Oxide Gas Sensors for Air-Quality Monitoring***, in ***Enviro-nanotechnology***, 2010, Elsevier: Oxford, United Kingdom. pp. 99-136.

36. S. Capone, A. Forleo, L. Francioso, R. Rella, P. Siciliano, J. Spadavecchia, D.S. Presicce, and A.M. Taurino, ***Solid state gas sensors: State of the art and future activities***. Journal of Optoelectronics and Advanced Materials. 2003; 5 (5). 1335-1348.

37. O.A. Afonja, ***Ph.D Thesis: Use of Zeolites to Effect Discrimination in Metal Oxide Semiconductor Gas Sensors***. *Chapter 1 : Introduction : p. 31*, Dept. of Chemistry, University College London (UCL), London, United Kingdom. 2012.

38. K. Wetchakun, T. Samerjai, N. Tamaekong, C. Liewhiran, C. Siriwong, V. Kruefu, A. Wisitsoraat, A. Tuantranont, and S. Phanichphant, ***Semiconducting metal oxides as sensors for environmentally hazardous gases***. Sensors and Actuators B: Chemical. 2011; 160 (1). 580-591.

39. S.G. Sensors. ***Solidsense SEC H_2S Sensor Temperature Dependence***. SolidsenS Gas Sensors [date accessed [cited 8th September 2014]; Available from: http://www.solidsense.de/Application%20Notes/Application%20Note%20SS-002%20Rev.01%20-%20Temperature%20Dependence%20of%20SEC%20H2S%20Sensor.pdf.

40. ***Emerson Process Management : Detecting Hydrogen Sulfide Gas and Understanding its Danger in the Field***. 10th September 2014, Emerson Process Management [date accessed: 30th January 2015]; Available from: http://www2.emersonprocess.com/siteadmincenter/PM%20Rosemount%20Analytical%20Documents/FGD_TWP_H2S_Hydrogen_Sulfide_Gas_Understand_Danger.pdf.

41. V.E. Henrich and P.A. Cox, ***Chapter 5: Electronic structure of transition-metal oxides*** in ***The Surface Science of Metal Oxides***, 1994, Cambridge Universtiy Press: Cambridge, UK. pp. 158-245.

42. R. Turton, ***Chapter 5: Semiconductors*** in ***The Physics of Solids*** 2000, Oxford University Press Inc.: New York, USA. pp. 117-148.

43. P. Hofman, ***Chapter 7: Semiconductors*** in ***Solid State Physics***, 2008, Wiley - VCH: Berlin, Germany. pp. 113-133.

44. P. Atkins and J. de Paula, ***Chapter 15: Metallic, Ionic and Covalent Solids*** in ***Elements of Physical Chemistry***, 2005, Oxford University Press Inc.: New York, USA. pp. 375-402.

45. C. Wang, L. Yin, L. Zhang, D. Xiang, and R. Gao, ***Metal Oxide Gas Sensors: Sensitivity and Influencing Factors***. Sensors. 2010; 10 (3). 2088-2106.

46. H.-J. Kim and J.-H. Lee, ***Highly sensitive and selective gas sensors using p-type oxide semiconductors: Overview***. Sensors and Actuators B: Chemical. 2014; 192. 607-627.

47. D. Niemeyer, D.E. Williams, P. Smith, K.F.E. Pratt, B. Slater, C.R.A. Catlow, and A. Marshall Stoneham, ***Experimental and computational study of the gas-sensor behaviour and surface chemistry of the solid-solution*** $Cr_{2-x}Ti_xO_3$ ***(X≤0.5)***. Journal of Materials Chemistry. 2002; 12 (3). 667-675.

48. V. Jayaraman, K.I. Gnanasekar, E. Prabhu, T. Gnanasekaran, and G. Periaswami, ***Preparation and characterisation of*** $Cr_{2-x}Ti_xO_{3+\delta}$ ***and its sensor properties***. Sensors and Actuators B: Chemical. 1999; 55 (2–3). 175-179.

49. T. Akamatsu, T. Itoh, N. Izu, and W. Shin, ***NO and*** NO_2 ***Sensing Properties of*** WO_3 ***and*** Co_3O_4 ***Based Gas Sensors***. Sensors. 2013; 13 (9). 12467-12481.

50. ***Royal Society of Chemistry : Drop Coating***. [date accessed: 26th January 2015]; Available from: http://www.rsc.org/publishing/journals/prospect/ontology.asp?id=CMO:0002163&MSID=b9nr00004f.

51. F.-T. Liu, S.-F. Gao, S.-K. Pei, S.-C. Tseng, and C.-H.J. Liu, ***ZnO nanorod gas sensor for*** NO_2 ***detection***. Journal of the Taiwan Institute of Chemical Engineers. 2009; 40 (5). 528-532.

52. D. Briand and J. Courbat, ***Chapter 6: Micromachined semiconductor gas sensors*** in ***Semiconductor gas sensors***, R. Jaaniso and O.K. Tan, Editors, 2013, Woodhead Publishing: Cambridge, UK. pp. 220-260.

53. M. Blaschke, T. Tille, P. Robertson, S. Mair, U. Weimar, and H. Ulmer, ***MEMS Gas-Sensor Array for Monitoring the Perceived Car-Cabin Air Quality***. IEEE Sensors Journal. 2006; 6 (5). 1298-1308.

54. S. Vallejos, T. Stoycheva, P. Umek, C. Navio, R. Snyders, C. Bittencourt, E. Llobet, C. Blackman, S. Moniz, and X. Correig, ***Au nanoparticle-functionalised*** WO_3 ***nanoneedles and their application in high sensitivity gas sensor devices***. Chemical Communications. 2011; 47 (1). 565-567.

55. A.J.T. Naik, M.E.A. Warwick, S.J.A. Moniz, C.S. Blackman, I.P. Parkin, and R. Binions, ***Nanostructured tungsten oxide gas sensors prepared by electric field assisted aerosol assisted chemical vapour deposition***. Journal of Materials Chemistry A. 2013; 1 (5). 1827-1833.

56. R. Binions, C.J. Carmalt, and I.P. Parkin, ***A comparison of the gas sensing properties of solid state metal oxide semiconductor gas sensors produced by atmospheric pressure chemical vapour deposition and screen printing***. Measurement Science and Technology. 2007; 18 (1). 190-200.

57. D. James, S.M. Scott, Z. Ali, and W.T. O'Hare, ***Chemical sensors for electronic nose systems***. Microchimica Acta. 2005; 149 (1-2). 1-17.

58. Wikipedia. ***Physical vapor deposition***. [date accessed: 27th January 2015]; Available from: http://en.wikipedia.org/wiki/Physical_vapor_deposition.

59. Wikipedia. ***Chemical vapor deposition***. [date accessed: 27th January 2015]; Available from: http://en.wikipedia.org/wiki/Chemical_vapor_deposition.

60. R. Binions and A.J.T. Naik, ***Chapter 13: Metal oxide semicoductor gas sensors in environmental monitoring*** in ***Semiconductor gas sensors***, R. Jaaniso and O.K. Tan, Editors, 2013, Woodhead Publishing: Cambridge, UK. pp. 433-466.

61. F. Maury, ***Trends in precursor selection for MOCVD***. Chemical Vapor Deposition. 1996; 2 (3). 113-116.

62. N. Barsan and U. Weimar, ***Conduction model of metal oxide gas sensors***. Journal of Electroceramics. 2001; 7 (3). 143-167.

63. S. Sharma and M. Madou, ***A new approach to gas sensing with nanotechnology***. Philosophical Transactions of the Royal Society A: Mathematical, Physical and Engineering Sciences. 2012; 370 (1967). 2448-2473.

64. S.W. Lee, P.P. Tsai, and H. Chen, ***Comparison study of SnO_2 thin- and thick-film gas sensors***. Sensors and Actuators B: Chemical. 2000; 67 (1–2). 122-127.

65. S.C. Naisbitt, K.F.E. Pratt, D.E. Williams, and I.P. Parkin, ***A microstructural model of semiconducting gas sensor response: The effects of sintering temperature on the response of chromium titanate (CTO) to carbon monoxide***. Sensors and Actuators B: Chemical. 2006; 114 (2). 969-977.

66. G. Chabanis, I.P. Parkin, and D.E. Williams, ***A simple equivalent circuit model to represent microstructure effects on the response of semiconducting oxide-based gas sensors***. Measurement Science & Technology. 2003; 14 (1). 76-86.

67. R.W.J. Scott, S.M. Yang, G. Chabanis, N. Coombs, D.E. Williams, and G.A. Ozin, ***Tin Dioxide Opals and Inverted Opals: Near-Ideal Microstructures for Gas Sensors***. Advanced Materials. 2001; 13 (19). 1468-1472.

68. C. Xu, J. Tamaki, N. Miura, and N. Yamazoe, ***Grain size effects on gas sensitivity of porous SnO_2-based elements***. Sensors and Actuators B: Chemical. 1991; 3 (2). 147-155.

69. J. Xu, J. Han, Y. Zhang, Y. Sun, and B. Xie, ***Studies on alcohol sensing mechanism of ZnO based gas sensors***. Sensors and Actuators B: Chemical. 2008; 132 (1). 334-339.

70. G. Korotcenkov, ***The role of morphology and crystallographic structure of metal oxides in response of conductometric-type gas sensors***. Materials Science and Engineering: R: Reports. 2008; 61 (1–6). 1-39.

71. S. Mridha and D. Basak, ***Investigation of a p-CuO/n-ZnO thin film heterojunction for H_2 gas-sensor applications***. Semiconductor Science and Technology. 2006; 21 (7). 928-932.

72. D. Barreca, G. Carraro, E. Comini, A. Gasparotto, C. Maccato, C. Sada, G. Sberveglieri, and E. Tondello, ***Novel Synthesis and Gas Sensing Performances of CuO–TiO_2 Nanocomposites***

Functionalized with Au Nanoparticles. The Journal of Physical Chemistry C. 2011; 115 (21). 10510-10517.

73. X. Gou, G. Wang, J. Yang, J. Park, and D. Wexler, ***Chemical synthesis, characterisation and gas sensing performance of copper oxide nanoribbons***. Journal of Materials Chemistry. 2008; 18 (9). 965-969.

74. N. Yamazoe and K. Shimanoe, ***Chapter 1: Fundamentals of semiconductor gas sensors*** in ***Semiconductor gas sensors***, R. Jaaniso and O.K. Tan, Editors, 2013, Woodhead Publishing: Cambridge, UK. pp. 3-34.

75. N. Yamazoe, J. Tamaki, and N. Miura, ***Role of hetero-junctions in oxide semiconductor gas sensors***. Materials Science and Engineering: B. 1996; 41 (1). 178-181.

76. A. Moezzi, A.M. McDonagh, and M.B. Cortie, ***Zinc oxide particles: Synthesis, properties and applications***. Chemical Engineering Journal. 2012; 185–186. 1-22.

77. A. Janotti and C. G. Van de Walle, ***Fundamentals of zinc oxide as a semiconductor***. Reports on Progress in Physics. 2009; 72 (12). 126501~1 - 126501~ 29.

78. Ü. Özgür, Y.I. Alivov, C. Liu, A. Teke, M.A. Reshchikov, S. Doğan, V. Avrutin, S.-J. Cho, and H. Morkoç, ***A comprehensive review of ZnO materials and devices***. Journal of Applied Physics. 2005; 98 (4). 041301~1 - 041301~102.

79. M.J.S. Spencer, ***Gas sensing applications of 1D-nanostructured zinc oxide: Insights from density functional theory calculations***. Progress in Materials Science. 2012; 57 (3). 437-486.

80. Wikipedia. ***Zinc Oxide***. 13th February 2015, Wikipedia [date accessed: 16th February 2015]; Available from: http://en.wikipedia.org/wiki/Zinc_oxide.

81. P. Šulcova and M. Trojan, ***New green pigments; ZnO–CoO***. Dyes and Pigments. 1999; 40 (1). 83-86.

82. N. Padmavathy and R. Vijayaraghavan, ***Enhanced bioactivity of ZnO nanoparticles—an antimicrobial study***. Science and Technology of Advanced Materials. 2008; 9 (3). 035004~1 - 035004~7.

83. S. Xu and Z.L. Wang, ***One-dimensional ZnO nanostructures: Solution growth and functional properties***. Nano Research. 2011; 4 (11). 1013-1098.

84. N. Yu, X. Li, X. Ma, Z. Mao, and B. Dong, ***Sunflower arrays: ZnO nanostructures on patterned sapphire***. Materials Today. 2013; 16 (1–2). 44-45.

85. E. Oh, H.-Y. Choi, S.-H. Jung, S. Cho, J.C. Kim, K.-H. Lee, S.-W. Kang, J. Kim, J.-Y. Yun, and S.-H. Jeong, ***High-performance NO_2 gas sensor based on ZnO nanorod grown by ultrasonic irradiation***. Sensors and Actuators B: Chemical. 2009; 141 (1). 239-243.

86. X.B. Li, S.Y. Ma, F.M. Li, Y. Chen, Q.Q. Zhang, X.H. Yang, C.Y. Wang, and J. Zhu, ***Porous spheres-like ZnO nanostructure as sensitive gas sensors for acetone detection***. Materials Letters. 2013; 100. 119-123.

87. H. Nanto, H. Sokooshi, and T. Usuda, ***Smell sensor using aluminium-doped zinc oxide thin film prepared by sputtering technique***. Sensors and Actuators B: Chemical. 1993; 10 (2). 79-83.

88. H. Nanto, T. Minami, and S. Takata, ***Zinc oxide thin film ammonia gas sensors with high sensitivity and excellent selectivity***. Journal of Applied Physics. 1986; 60 (2). 482-484.

89. D.H. Yoon, J.H. Yu, and G.M. Choi, ***CO gas sensing properties of ZnO–CuO composite***. Sensors and Actuators B: Chemical. 1998; 46 (1). 15-23.

90. G. Uozumi, M. Miyayama, and H. Yanagida, ***Fabrication of a CuO-infiltrated ZnO composite and its gas sensing properties***. Journal of Materials Science. 1997; 32 (11). 2991-2996.

91. B.P.J. de Lacy Costello, R.J. Ewen, P.R.H. Jones, N.M. Ratcliffe, and R.K.M. Wat, ***A study of the catalytic and vapour-sensing properties of zinc oxide and tin dioxide in relation to 1-butanol and dimethyldisulphide***. Sensors and Actuators B: Chemical. 1999; 61 (1–3). 199-207.

92. J.H. Yu and G.M. Choi, ***Electrical and CO gas sensing properties of ZnO–SnO$_2$ composites***. Sensors and Actuators B: Chemical. 1998; 52 (3). 251-256.

93. X. Song and L. Liu, ***Characterization of electrospun ZnO–SnO$_2$ nanofibers for ethanol sensor***. Sensors and Actuators A: Physical. 2009; 154 (1). 175-179.

94. M. Batzill and U. Diebold, ***The surface and materials science of tin oxide***. Progress in Surface Science. 2005; 79 (2–4). 47-154.

95. ***Chemistry : WebElements Peridic Table (professional edition) : Tin (IV)Oxide***. 18th April 2004, The University of Sheffield and WebElements Ltd, UK. [date accessed: 16th February 2015]; Available from: http://jpkc.whut.edu.cn/web18/main/wangluo/webelements/webelements/compounds/text/sn/o2sn1-18282105.html.

96. S.H. Mohamed, ***SnO$_2$ dendrites–nanowires for optoelectronic and gas sensing applications***. Journal of Alloys and Compounds. 2012; 510 (1). 119-124.

97. H.M. Yates, P. Evans, D.W. Sheel, S. Nicolay, L. Ding, and C. Ballif, ***The development of high performance SnO$_2$:F as TCOs for thin film silicon solar cells***. Surface and Coatings Technology. 2012; 213. 167-174.

98. F.A. Akgul, C. Gumus, A.O. Er, A.H. Farha, G. Akgul, Y. Ufuktepe, and Z. Liu, ***Structural and electronic properties of SnO$_2$***. Journal of Alloys and Compounds. 2013; 579. 50-56.

99. G.G. Mandayo, E. Castaño, F.J. Gracia, A. Cirera, A. Cornet, and J.R. Morante, ***Strategies to enhance the carbon monoxide sensitivity of tin oxide thin films***. Sensors and Actuators B: Chemical. 2003; 95 (1–3). 90-96.

100. A. Reungchaiwat, T. Wongchanapiboon, S. Liawruangrath, and S. Phanichphant, ***Home-made Detection Device for a Mixture of Ethanol and Acetone***. Sensors. 2007; 7 (2). 202-213.

101. R.S. Niranjan and I.S. Mulla, ***Spin coated tin oxide: a highly sensitive hydrocarbon sensor***. Materials Science and Engineering: B. 2003; 103 (2). 103-107.

102. H. Zheng, J.Z. Ou, M.S. Strano, R.B. Kaner, A. Mitchell, and K. Kalantar-zadeh, ***Nanostructured Tungsten Oxide – Properties, Synthesis, and Applications***. Advanced Functional Materials. 2011; 21 (12). 2175-2196.

103. W.B. Cross, I.P. Parkin, S.A. O'Neill, P.A. Williams, M.F. Mahon, and K.C. Molloy, ***Tungsten oxide coatings from the aerosol-assisted chemical vapor deposition of $W(OAr)_6$ ($Ar=C_6H_5$, C_6H_4F-4, $C_6H_3F_2$-3,4); photocatalytically active gamma-WO_3 films***. Chemistry of Materials. 2003; 15 (14). 2786-2796.

104. A.A. Ashkarran, A. Iraji zad, M.M. Ahadian, and S.A.M. Ardakani, ***Synthesis and photocatalytic activity of WO_3 nanoparticles prepared by the arc discharge method in deionized water***. Nanotechnology. 2008; 19 (19). 195709~1 - 195709~7.

105. C.S. Blackman and I.P. Parkin, ***Atmospheric Pressure Chemical Vapor Deposition of Crystalline Monoclinic WO_3 and WO_{3-x} Thin Films from Reaction of WCl_6 with O-Containing Solvents and Their Photochromic and Electrochromic Properties***. Chemistry of Materials. 2005; 17 (6). 1583-1590.

106. S. Ashraf, C.S. Blackman, R.G. Palgrave, and I.P. Parkin, ***Aerosol-assisted chemical vapour deposition of WO_3 thin films using polyoxometallate precursors and their gas sensing properties***. Journal of Materials Chemistry. 2007; 17 (11). 1063-1070.

107. R.S. Khadayate, J.V. Sali, and P.P. Patil, ***Acetone vapor sensing properties of screen printed WO_3 thick films***. Talanta. 2007; 72 (3). 1077-1081.

108. E. Rossinyol, A. Prim, E. Pellicer, J. Arbiol, F. Peiró, A. Cornet, J.R. Morante, L.A. Solovyov, B. Tian, T. Bo, and D. Zhao, ***Mesostructured WO_3 as a sensing material for NO_2 detection***. MRS Online Proceedings Library - Symposium R - Nanostructured Materials and Hybrid Composites for Gas Sensors and Biomedical Applications. 2006; 915. R06-09.

109. Y. Qin, M. Hu, and J. Zhang, ***Microstructure characterization and NO_2-sensing properties of tungsten oxide nanostructures***. Sensors and Actuators B: Chemical. 2010; 150 (1). 339-345.

110. A. Ponzoni, E. Comini, M. Ferroni, and G. Sberveglieri, ***Nanostructured WO_3 deposited by modified thermal evaporation for gas-sensing applications***. Thin Solid Films. 2005; 490 (1). 81-85.

111. C. Ge, C. Xie, D. Zeng, and S. Cai, ***Formaldehyde-, Benzene-, and Xylene-Sensing Characterizations of Zn–W–O Nanocomposite Ceramics***. Journal of the American Ceramic Society. 2007; 90 (10). 3263-3267.

112. I.T. Horvath ***Catalysis by Solid Acids,*** in ***Encyclopedia of Catalysis Volume 2***, 2003, Wiley-Interscience, Available from https://chms.ucdavis.edu/research/web/catalysis/PDF%20Pubs/Gates%20Pub%20-%20355.pdf [date accessed: 5th February 2015]. pp. 103-142.

113. V. Oison, L. Saadi, C. Lambert-Mauriat, and R. Hayn, ***Mechanism of CO and O_3 sensing on WO_3 surfaces: First principle study***. Sensors and Actuators B: Chemical. 2011; 160 (1). 505-510.

114. I. Jiménez, A.M. Vila, A.C. Calveras, and J.R. Morante, ***Gas-sensing properties of catalytically modified WO_3 with copper and vanadium for NH_3 detection***. IEEE Sensors Journal. 2005; 5 (3). 385-391.

115. I. Jiménez, M.A. Centeno, R. Scotti, F. Morazzoni, A. Cornet, and J.R. Morante, ***NH_3 Interaction with Catalytically Modified Nano-WO_3 Powders for Gas Sensing Applications***. Journal of The Electrochemical Society. 2003; 150 (4). H72-H80.

116. G. Chabanis, I.P. Parkin, and D.E. Williams, ***Microspheres of the gas sensor material $Cr_{2-x}Ti_xO_3$ prepared by the sol-emulsion-gel route***. Journal of Materials Chemistry. 2001; 11 (6). 1651-1655.

117. A.M. Nartowski and A. Atkinson, ***Sol-Gel Synthesis of Sub-Micron Titanium-Doped Chromia Powders for Gas Sensing***. Journal of Sol-Gel Science and Technology. 2003; 26 (1-3). 793-797.

118. S.P. McBride and R. Brydson, ***Analytical transmission electron microscopy and surface spectroscopy of ceramics: The microstructural evolution in titanium-doped chromia polycrystals as a function of sintering conditions***. Journal of Materials Science. 2004; 39 (22). 6723-6734.

119. T.P. Trainor, P.J. Eng, G.E. Brown Jr, I.K. Robinson, and M.D. Santis, ***Crystal truncation rod diffraction study of the α-Al_2O_3 (1 -1 0 2) surface***. Surface Science. 2002; 496 (3). 238-250.

120. C. Peter, J. Kneer, K. Schmitt, A. Eberhardt, and J. Wöllenstein, ***Preparation, material analysis, and morphology of $Cr_{2-x}Ti_xO_{3+z}$ for gas sensors***. physica status solidi (a). 2013; 210 (2). 403-407.

121. ***Crystallography 365***. [date accessed: 16th February 2015]; Available from: https://crystallography365.wordpress.com/.

122. G.S. Henshaw, D.H. Dawson, and D.E. Williams, ***Selectivity and composition dependence of response of gas-sensitive resistors. Part 2.-Hydrogen sulfide response of $Cr_{2-x}Ti_xO_{3+y}$***. Journal of Materials Chemistry. 1995; 5 (11). 1791-1800.

123. J. Du, Y. Wu, and K.-L. Choy, ***Controlled synthesis of gas sensing $Cr_{2-x}Ti_xO_3$ films by electrostatic spray assisted vapour deposition and their structural characterisation***. Thin Solid Films. 2006; 497 (1–2). 42-47.

124. G.A. Shaw, I.P. Parkin, and D.E. Williams, ***Atmospheric pressure chemical vapour deposition of $Cr_{2-x}Ti_xO_3$ (CTO) thin films (≤ 3 µm) on to gas sensing substrates***. Journal of Materials Chemistry. 2003; 13 (12). 2957-2962.

125. D. Niemeyer, ***Ph.D Thesis: The gas sensitive material $Cr_{(2-x)}Ti_xO_3$***. *Chapter 5 : Gas sensing behaviour of the solid solution $Cr_{2-x}Ti_xO_3$: pp. 65 - 67*, Dept. of Chemistry, University College London (UCL), London, United Kingdom. 2001.

126. O.A. Afonja, ***Ph.D Thesis: Use of Zeolites to Effect Discrimination in Metal Oxide Semiconductor Gas Sensors***. *Chapter 1 : Introduction : p. 35*, Dept. of Chemistry, University College London (UCL), London, United Kingdom. 2012.

127. S. Pokhrel, Y. Ming, L. Huo, H. Zhao, and S. Gao, ***$Cr_{2-x}Ti_xO_3$ ($x \leq 0.5$) as CH_3COCH_3 sensitive resistors***. Sensors and Actuators B: Chemical. 2007; 125 (2). 550-555.

128. D.H. Dawson, G.S. Henshaw, and D.E. Williams, ***Description and characterization of a hydrogen sulfide gas sensor based on $Cr_{2-y}Ti_yO_{3+x}$***. Sensors and Actuators B: Chemical. 1995; 26 (1–3). 76-80.

129. K. Schmitt, C. Peter, and J. Wöllenstein, ***Chapter 8: Chromium Titanium Oxide-Based Ammonia Sensors***, in ***Solid State Gas Sensors - Industrial Application***, M. Fleischer and M. Lehmann, Editors, 2012, Springer - Verlag: Berlin Heidelberg, Germany. pp. 113-135.

130. D.E. Williams, ***Semiconducting oxides as gas-sensitive resistors***. Sensors and Actuators B: Chemical. 1999; 57 (1–3). 1-16.

131. T. Sathitwitayakul, M.V. Kuznetsov, I.P. Parkin, and R. Binions, ***The gas sensing properties of some complex metal oxides prepared by self-propagating high-temperature synthesis***. Materials Letters. 2012; 75. 36-38.

132. A.B. Gadkari, T.J. Shinde, and P.N. Vasambekar, ***Ferrite Gas Sensors***. IEEE Sensors Journal. 2011; 11 (4). 849-861.

133. X.F. Chu, S.M. Zhou, W.B. Zhang, and H.F. Shui, ***Trimethylamine sensing properties of nano-$LaFeO_3$ prepared using solid-state reaction in the presence of PEG400***. Materials Science and Engineering B-Advanced Functional Solid-State Materials. 2009; 164 (1). 65-69.

134. J.H. Yu and G.M. Choi, ***Selective CO gas detection of Zn_2SnO_4 gas sensor***. Journal of Electroceramics. 2002; 8 (3). 249-255.

135. L.F. Yang, Y.G. Xie, H.Y. Zhao, X.H. Wu, and Y.D. Wang, ***Preparation and gas-sensing properties of $NiFe_2O_4$ semiconductor materials***. Solid-State Electronics. 2005; 49 (6). 1029-1033.

136. C.L. Zhu, Y.J. Chen, R.X. Wang, L.J. Wang, M.S. Cao, and X.L. Shi, ***Synthesis and enhanced ethanol sensing properties of α-Fe_2O_3/ZnO heteronanostructures***. Sensors and Actuators B: Chemical. 2009; 140 (1). 185-189.

137. A.P. Lee and B.J. Reedy, ***Temperature modulation in semiconductor gas sensing***. Sensors and Actuators B: Chemical. 1999; 60 (1). 35-42.

138. R. Binions, A. Afonja, S. Dungey, D.W. Lewis, I.P. Parkin, and D.E. Williams, ***Discrimination Effects in Zeolite Modified Metal Oxide Semiconductor Gas Sensors***. IEEE Sensors Journal. 2011; 11 (5). 1145-1151.

139. O.A. Afonja, ***Ph.D Thesis: Use of Zeolites to Effect Discrimination in Metal Oxide Semiconductor Gas Sensors***. *Chapter 2 : Experimental Design and Procedure : pp. 53 - 55*, Dept. of Chemistry, University College London (UCL), London, United Kingdom. 2012.

140. Y. Hiranaka, T. Abe, and H. Murata, ***Gas-dependent response in the temperature transient of SnO2 gas sensors***. Sensors and Actuators B: Chemical. 1992; 9 (3). 177-182.

141. G. Jimenez-Cadena, J. Riu, and F.X. Rius, ***Gas sensors based on nanostructured materials***. Analyst. 2007; 132 (11). 1083-1099.

142. S. Elouali, L.G. Bloor, R. Binions, I.P. Parkin, C.J. Carmalt, and J.A. Darr, ***Gas Sensing with Nano-Indium Oxides (In_2O_3) Prepared via Continuous Hydrothermal Flow Synthesis***. Langmuir. 2011; 28 (3). 1879-1885.

143. L. Shi, A.J.T. Naik, J.B.M. Goodall, C. Tighe, R. Gruar, R. Binions, I. Parkin, and J. Darr, ***Highly Sensitive ZnO Nanorod- and Nanoprism-Based NO_2 Gas Sensors: Size and Shape Control Using a Continuous Hydrothermal Pilot Plant***. Langmuir. 2013; 29 (33). 10603-10609.

144. L.I. Trakhtenberg, G.N. Gerasimov, V.F. Gromov, T.V. Brelysheva, and O.J. Ilegbusi, ***Gas Semiconducting Sensors Based on Metal Oxide Nanocomposites***. Journal of Materials Science Research. 2012; 1 (2). 56-68.

145. B.P.J. de Lacy Costello, R.J. Ewen, N. Guernion, and N.M. Ratcliffe, ***Highly sensitive mixed oxide sensors for the detection of ethanol***. Sensors and Actuators B: Chemical. 2002; 87 (1). 207-210.

146. S. Bai, D. Li, D. Han, R. Luo, A. Chen, and C.L. Chung, ***Preparation, characterization of WO_3–SnO_2 nanocomposites and their sensing properties for NO_2***. Sensors and Actuators B: Chemical. 2010; 150 (2). 749-755.

147. M. Ivanovskaya, D. Kotsikau, G. Faglia, and P. Nelli, ***Influence of chemical composition and structural factors of Fe_2O_3/In_2O_3 sensors on their selectivity and sensitivity to ethanol***. Sensors and Actuators B: Chemical. 2003; 96 (3). 498-503.

148. S. Kaciulis, L. Pandolfi, S. Viticoli, G. Sberveglieri, E. Zampiceni, W. Wlodarski, K. Galatsis, and Y.X. Li, ***Investigation of thin films of mixed oxides for gas-sensing applications***. Surface and Interface Analysis. 2002; 34 (1). 672-676.

149. K. Zakrzewska, ***Mixed oxides as gas sensors***. Thin Solid Films. 2001; 391 (2). 229-238.

150. S. Yu-Sheng and Z. Tian-Shu, ***Preparation, structure and gas-sensing properties of ultramicro $ZnSnO_3$ powder***. Sensors and Actuators B: Chemical. 1993; 12 (1). 5-9.

151. P. Wadkar, D. Bauskar, and P. Patil, ***High performance H_2 sensor based on $ZnSnO_3$ cubic crystallites synthesized by a hydrothermal method***. Talanta. 2013; 105. 327-332.

152. M. Radecka, K. Zakrzewska, and M. Rękas, ***SnO_2–TiO_2 solid solutions for gas sensors***. Sensors and Actuators B: Chemical. 1998; 47 (1–3). 194-204.

153. Y. Zhu, X. Su, C. Yang, X. Gao, F. Xiao, and J. Wang, ***Synthesis of TiO_2-WO_3 nanocomposites as highly sensitive benzene sensors and high efficiency adsorbents***. Journal of Materials Chemistry. 2012; 22 (28). 13914-13917.

154. C.R. Young, N. Menegazzo, A.E. Riley, C.H. Brons, F.P. DiSanzo, J.L. Givens, J.L. Martin, M.M. Disko, and B. Mizaikoff, ***Infrared Hollow Waveguide Sensors for Simultaneous Gas Phase Detection of Benzene, Toluene, and Xylenes in Field Environments***. Analytical Chemistry. 2011; 83 (16). 6141-6147.

155. B.M. Reddy and A. Khan, ***Recent Advances on TiO_2-ZrO_2 Mixed Oxides as Catalysts and Catalyst Supports***. Catalysis Reviews. 2005; 47 (2). 257-296.

156. B.P.J. de Lacy Costello, R.J. Ewen, N.M. Ratcliffe, and P. Sivanand, ***Thick film organic vapour sensors based on binary mixtures of metal oxides***. Sensors and Actuators B-Chemical. 2003; 92 (1-2). 159-166.

157. Y.-J. Chen, G. Xiao, T.-S. Wang, F. Zhang, Y. Ma, P. Gao, C.-L. Zhu, E. Zhang, Z. Xu, and Q.-h. Li, ***Synthesis and enhanced gas sensing properties of crystalline CeO_2/TiO_2 core/shell nanorods***. Sensors and Actuators B: Chemical. 2011; 156 (2). 867-874.

158. L.J. Van Ruyven, ***Phenomena at Heterojunctions***. Annual Review of Materials Science. 1972; 2 (1). 501-528.

159. E.-O. Encyclopedia. ***Abrupt Junction***. [date accessed: 12th June 2012]; Available from: http://www.encyclo.co.uk/define/abrupt%20junction.

160. E.F. Schubert. ***17: Band Diagrams of Heterostructures: pages 186-202***. [date accessed: 12th June 2012]; Available from: http://www.ecse.rpi.edu/~schubert/Course-ECSE-6968%20Quantum%20mechanics/Ch17%20Heterostructures.pdf.

161. N. Savage, B. Chwieroth, A. Ginwalla, B.R. Patton, S.A. Akbar, and P.K. Dutta, ***Composite n–p semiconducting titanium oxides as gas sensors***. Sensors and Actuators B: Chemical. 2001; 79 (1). 17-27.

162. Wikipedia. ***Homojunction***. 16th December 2011 [date accessed: 25th May 2012]; Available from: http://en.wikipedia.org/wiki/Homojunction.

163. J.F. Wager, ***Transparent electronics: Schottky barrier and heterojunction considerations***. Thin Solid Films. 2008; 516 (8). 1755-1764.

164. M. Jayalakshmi and K. Balasubramanian, ***Hydrothermal Synthesis of CuO-SnO_2 and CuO-SnO_2-Fe_2O_3 Mixed Oxides and Electrochemical Characterization in Neutral Electrolyte***. International Journal of Electrochemical Science. 2009; 4 (4). 571-581.

165. R. van der Krol and H.L. Tuller, ***Electroceramics - the role of interfaces***. Solid State Ionics 2002; 150 (1-2). 167-179.

166. D.K. Roy, ***Chapter 2: Physics of pn junctions***, in ***Physics of Semiconductor Devices***, 2004, Universities Press (India) Private Ltd. : Hyderabad, India. pp. 97-203.

167. Wikipedia. ***Band bending***. 13th May 2012 [date accessed: 10th June 2012]; Available from: http://en.wikipedia.org/wiki/Band_bending.

168. W. Zeng, T. Liu, and Z. Wang, ***Enhanced gas sensing properties by SnO_2 nanosphere functionalized TiO_2 nanobelts***. Journal of Materials Chemistry. 2012; 22 (8). 3544-3548.

169. D. Bekermann, A. Gasparotto, D. Barreca, C. Maccato, E. Comini, C. Sada, G. Sberveglieri, A. Devi, and R.A. Fischer, ***Co_3O_4/ZnO Nanocomposites: From Plasma Synthesis to Gas Sensing Applications***. ACS Applied Materials & Interfaces. 2012; 4 (2). 928-934.

170. N. Yamazoe and K. Shimanoe, ***Basic approach to the transducer function of oxide semiconductor gas sensors***. Sensors and Actuators B: Chemical. 2011; 160 (1). 1352-1362.

171. N. Yamazoe and K. Shimanoe, ***Proposal of contact potential promoted oxide semiconductor gas sensor***. Sensors and Actuators B: Chemical. 2013; 187. 162-167.

172. I.-C. Chen, S.-S. Lin, T.-J. Lin, C.-L. Hsu, T.J. Hsueh, and T.-Y. Shieh, ***The Assessment for Sensitivity of a NO_2 Gas Sensor with $ZnGa_2O_4$/ZnO Core-Shell Nanowires—a Novel Approach***. Sensors. 2010; 10 (4). 3057-3072.

173. U.S. E.P.A. ***Nitrogen Dioxode - Health***. 15th August 2014 [date accessed: 13th October 2014]; Available from: http://www.epa.gov/oaqps001/nitrogenoxides/health.html.

174. S. Zhan, D. Li, S. Liang, X. Chen, and X. Li, ***A Novel Flexible Room Temperature Ethanol Gas Sensor Based on SnO_2 Doped Poly-Diallyldimethylammonium Chloride***. Sensors. 2013; 13 (4). 4378-4389.

175. K. Mitsubayashi, K. Yokoyama, T. Takeuchi, and I. Karube, ***Gas-Phase Biosensor for Ethanol***. Analytical Chemistry. 1994; 66 (20). 3297-3302.

176. Matheson. ***Threshold Limit Values (TLV) and Immediately Dangerous to Life and Health (IDLH) values***. TLVs from Threshold Limit Vlaues and Biological Exposure Indices, copyright 2005 by American Conference of Governmental Industrial Hygienists (ACGIH) and IDLH values from the NIOSH Pocket Guide to Chemical Hazards 2004, published by National Institute for Occupational Safety and Health (NIOSH) [date accessed: 11th October 2014] Available from: https://www.mathesongas.com/pdfs/products/threshold-limit-values-(tlv).pdf.

177. K. Mirabbaszadeh and M. Mehrabian, ***Synthesis and properties of ZnO nanorods as ethanol gas sensors***. Physica Scripta. 2012; 85 (3). 035701~1 - 035701~8.

178. Wikipedia. ***Blood alcohol content***. 10th September 2014, Wikipedia [date accessed: 10th September 2014]; Available from: http://en.wikipedia.org/wiki/Blood_alcohol_content.

179. H. Ogawa, M. Nishikawa, and A. Abe, ***Hall measurement studies and an electrical-conduction model of tin oxide ultrafine particle films***. Journal of Applied Physics. 1982; 53 (6). 4448-4455.

180. A. Tricoli, M. Righettoni, and A. Teleki, ***Semiconductor Gas Sensors: Dry Synthesis and Application***. Angewandte Chemie International Edition. 2010; 49 (42). 7632-7659.

181. R.S. Khadayate, R.B. Waghulde, M.G. Wankhede, J.V. Sali, and P.P. Patil, ***Ethanol vapour sensing properties of screen printed WO_3 thick films***. Bulletin of Materials Science. 2007; 30 (2). 129-133.

182. B. Timmer, W. Olthuis, and A. van den Berg, ***Ammonia sensors and their applications—a review***. Sensors and Actuators B: Chemical. 2005; 107 (2). 666-677.

183. Y. Qiao, Z. Gao, Y. Liu, Y. Cheng, M. Yu, L. Zhao, Y. Duan, and Y. Liu, ***Breath Ketone Testing: A New Biomarker for Diagnosis and Therapeutic Monitoring of Diabetic Ketosis***. BioMed Research International. 2014; 2014. 1-5.

184. Wikipedia. ***Ketosis***. 2nd October 2014 [date accessed: 11th October 2014]; Available from: http://en.wikipedia.org/wiki/Ketosis.

185. Wikipedia. ***Ketogenic diet***. 3rd October 2014 [date accessed: 11th October 2014]; Available from: http://en.wikipedia.org/wiki/Ketogenic_diet.

186. CDC. ***Centre for Diseases Control and Prevention : Occupational Safety and Health Guideline for Acetone***. 1988 [date accessed: 11th October 2014]; Available from: http://www.cdc.gov/niosh/docs/81-123/pdfs/0004.pdf.

187. P. Gao, H. Ji, Y. Zhou, and X. Li, ***Selective acetone gas sensors using porous WO_3–Cr_2O_3 thin films prepared by sol–gel method***. Thin Solid Films. 2012; 520 (7). 3100-3106.

188. M. Parmar, C. Balamurugan, and D.-W. Lee, ***PANI and Graphene/PANI Nanocomposite Films — Comparative Toluene Gas Sensing Behavior***. Sensors. 2013; 13 (12). 16611-16624.

189. H. Ma, Y. Xu, Z. Rong, X. Cheng, S. Gao, X. Zhang, H. Zhao, and L. Huo, ***Highly toluene sensing performance based on monodispersed Cr_2O_3 porous microspheres***. Sensors and Actuators B: Chemical. 2012; 174. 325-331.

190. Wikipedia. ***Sick Building Syndrome***. 10th September 2014, Wikipedia [date accessed: 10th September 2014]; Available from: http://en.wikipedia.org/wiki/Sick_building_syndrome.

191. CDC. ***Centre for Diseases Control and Prevention : Occupational Safety and Health Guideline for Toluene***. September 1978 [date accessed: 11th October 2014]; Available from: http://www.cdc.gov/niosh/docs/81-123/pdfs/0619.pdf.

192. S. Santra, P.K. Guha, S.K. Ray, F. Udrea, and J.W. Gardner. ***SOI CMOS integrated zinc oxide nanowire for toluene detection***. in *The 5th IEEE International Nanoelectronics Conference (INEC)*. 2013. Singapore: IEEE. 119-121.

193. A.N. Trushkin, M.E. Grushin, I.V. Kochetov, N.I. Trushkin, and Y.S. Akishev, ***Decomposition of toluene in a steady-state atmospheric-pressure glow discharge***. Plasma Physics Reports. 2013; 39 (2). 167-182.

194. O.A. Afonja, ***Ph.D Thesis: Use of Zeolites to Effect Discrimination in Metal Oxide Semiconductor Gas Sensors***. *Chapter 3 : Test Rig Development, Construction and Operation: pp. 66 - 87*, Dept. of Chemistry, University College London (UCL), London, United Kingdom. 2012.

195. A.R. Phani, M. Passacantando, L. Lozzi, and S. Santucci, ***Structural characterization of bulk $ZnWO_4$ prepared by solid state method***. Journal of Materials Science. 2000; 35 (19). 4879-4883.

196. R.I. Gruar, C.J. Tighe, and J.A. Darr, ***Scaling-up a Confined Jet Reactor for the Continuous Hydrothermal Manufacture of Nanomaterials***. Industrial & Engineering Chemistry Research. 2013; 52 (15). 5270-5281.

197. C.Y. Ma, C.J. Tighe, R.I. Gruar, T. Mahmud, J.A. Darr, and X.Z. Wang, ***Numerical modelling of hydrothermal fluid flow and heat transfer in a tubular heat exchanger under near critical conditions***. The Journal of Supercritical Fluids. 2011; 57 (3). 236-246.

198. C.J. Tighe, R.Q. Cabrera, R.I. Gruar, and J.A. Darr, ***Scale Up Production of Nanoparticles: Continuous Supercritical Water Synthesis of Ce–Zn Oxides***. Industrial & Engineering Chemistry Research. 2013; 52 (16). 5522-5528.

199. C.J. Tighe, R.I. Gruar, C.Y. Ma, T. Mahmud, X.Z. Wang, and J.A. Darr, ***Investigation of counter-current mixing in a continuous hydrothermal flow reactor***. The Journal of Supercritical Fluids. 2012; 62. 165-172.

200. M. Wojdyr, ***Fityk: a general-purpose peak fitting program***. Journal of Applied Crystallography. 2010; 43 (Part 5 No.1). 1126-1128.

201. LaSurface.com. ***Database***. [date accessed: 15th January 2013]; Available from: http://www.lasurface.com/database/elementxps.php.

202. A.P. Dementjev, A. de Graaf, M.C.M. van de Sanden, K.I. Maslakov, A.V. Naumkin, and A.A. Serov, ***X-Ray photoelectron spectroscopy reference data for identification of the C_3N_4 phase in carbon–nitrogen films***. Diamond and Related Materials. 2000; 9 (11). 1904-1907.

203. K.J. Boyd, D. Marton, S.S. Todorov, A.H. Al-Bayati, J. Kulik, R.A. Zuhr, and J.W. Rabalais, ***Formation of C–N thin films by ion beam deposition***. Journal of Vacuum Science & Technology A. 1995; 13 (4). 2110-2122.

204. O.A. Afonja, ***Ph.D Thesis: Use of Zeolites to Effect Discrimination in Metal Oxide Semiconductor Gas Sensors***. *Chapter 3 : Test Rig Development, Construction and Operation: pp. 67 - 68*, Dept. of Chemistry, University College London (UCL), London, United Kingdom. 2012.

205. O.A. Afonja, ***Ph.D Thesis: Use of Zeolites to Effect Discrimination in Metal Oxide Semiconductor Gas Sensors***. *Appendix A - Test Rig Design : p. 203*, Dept. of Chemistry, University College London (UCL), London, United Kingdom. 2012.

206. O.A. Afonja, ***Ph.D Thesis: Use of Zeolites to Effect Discrimination in Metal Oxide Semiconductor Gas Sensors***. *Chapter 3 : Test Rig Development, Construction and Operation: p. 60*, Dept. of Chemistry, University College London (UCL), London, United Kingdom. 2012.

207. C. Siriwong, K. Wetchakun, A. Wisitsoraat, and S. Phanichphant. ***Gas sensing properties of WO_3-doped ZnO nanoparticles synthesized by flame spray pyrolysis***. in *IEEE Sensors Conference Proceedings*. 2009. Christchurch, New Zealand: IEEE. 118-123.

208. R. Chutia and M. Bhuyan. ***Study of temperature modulated tin oxide gas sensor and identification of chemicals***. in *2nd National Conference on Computational Intelligence and Signal Processing (CISP)*. 2012. Don Bosco College of Enginnering and Technology (DBCET) Guwahati, India: IEEE. 181-184.

209. S. An, S. Park, H. Ko, and C. Lee, ***Enhanced NO_2 gas sensing properties of WO_3 nanorods encapsulated with ZnO***. Applied Physics A. 2012; 108 (1). 53-58.

210. C. Sun, G. Maduraiveeran, and P. Dutta, ***Nitric oxide sensors using combination of p- and n-type semiconducting oxides and its application for detecting NO in human breath***. Sensors and Actuators B: Chemical. 2013; 186. 117-125.

211. O.A. Afonja, ***Ph.D Thesis: Use of Zeolites to Effect Discrimination in Metal Oxide Semiconductor Gas Sensors***. *Chapter 1 : Introduction : p. 29*, Dept. of Chemistry, University College London (UCL), London, United Kingdom. 2012.

212. D. Polsongkram, P. Chamninok, S. Pukird, L. Chow, O. Lupan, G. Chai, H. Khallaf, S. Park, and A. Schulte, ***Effect of synthesis conditions on the growth of ZnO nanorods via hydrothermal method***. Physica B: Condensed Matter. 2008; 403 (19–20). 3713-3717.

213. N.D.M. Sin, M.F. Kamel, R.I. Alip, Z. Mohamad, and M. Rusop, ***The Electrical Characteristics of Aluminium Doped Zinc Oxide Thin Film for Humidity Sensor Applications***. Advances in Materials Science and Engineering. 2011; 2011. 974906~1- 974906~5.

214. Y. Zhang, F. Zhu, J. Zhang, and L. Xia, ***Converting Layered Zinc Acetate Nanobelts to One-dimensional Structured ZnO Nanoparticle Aggregates and their Photocatalytic Activity***. Nanoscale Research Letters. 2008; 3 (6). 201-204.

215. J. Yan, Y. Shen, F. Li, and T. Li, ***Synthesis and Photocatalytic Properties of $ZnWO_4$ Nanocrystals via a Fast Microwave-Assisted Method***. The Scientific World Journal. 2013; 2013. 458106~1 - 458106~8.

216. S. Ghosh, S.S. Acharyya, S. Adak, L.N.S. Konathala, T. Sasaki, and R. Bal, ***Selective oxidation of cyclohexene to adipic acid over silver supported tungsten oxide nanostructured catalysts***. Green Chemistry. 2014; 16 (5). 2826-2834.

217. E. Cazzanelli, C. Vinegoni, G. Mariotto, A. Kuzmin, and J. Purans, ***Low-Temperature Polymorphism in Tungsten Trioxide Powders and Its Dependence on Mechanical Treatments***. Journal of Solid State Chemistry. 1999; 143 (1). 24-32.

218. Y. Huang, M. Liu, Z. Li, Y. Zeng, and S. Liu, ***Raman spectroscopy study of ZnO-based ceramic films fabricated by novel sol–gel process***. Materials Science and Engineering: B. 2003; 97 (2). 111-116.

219. R. Loudon, ***The Raman effect in crystals***. Advances in Physics. 2001; 50 (7). 813-864.

220. S. Choopun, N. Hongsith, P. Mangkorntong, and N. Mangkorntong, ***Zinc oxide nanobelts by RF sputtering for ethanol sensor***. Physica E: Low-dimensional Systems and Nanostructures. 2007; 39 (1). 53-56.

221. Y. Liu, H. Wang, G. Chen, Y.D. Zhou, B.Y. Gu, and B.Q. Hu, ***Analysis of Raman spectra of $ZnWO_4$ single crystals***. Journal of Applied Physics. 1988; 64 (9). 4651-4653.

222. A. Kalinko and A. Kuzmin, ***Raman and photoluminescence spectroscopy of zinc tungstate powders***. Journal of Luminescence. 2009; 129 (10). 1144-1147.

223. E.I. Ross-Medgaarden and I.E. Wachs, ***Structural Determination of Bulk and Surface Tungsten Oxides with UV−vis Diffuse Reflectance Spectroscopy and Raman Spectroscopy***. The Journal of Physical Chemistry C. 2007; 111 (41). 15089-15099.

224. M.C. Biesinger, L.W.M. Lau, A.R. Gerson, and R.S.C. Smart, ***Resolving surface chemical states in XPS analysis of first row transition metals, oxides and hydroxides: Sc, Ti, V, Cu and Zn***. Applied Surface Science. 2010; 257 (3). 887-898.

225. S. Rajagopal, D. Nataraj, D. Mangalaraj, Y. Djaoued, J. Robichaud, and O.Y. Khyzhun, ***Controlled Growth of WO_3 Nanostructures with Three Different Morphologies and Their Structural, Optical, and Photodecomposition Studies***. Nanoscale Research Letters. 2009; 4 (11). 1335-1342.

226. O.Y. Khyzhun, ***XPS, XES and XAS studies of the electronic structure of tungsten oxides***. Journal of Alloys and Compounds. 2000; 305 (1–2). 1-6.

227. X. Cao, W. Wu, N. Chen, Y. Peng, and Y. Liu, ***An ether sensor utilizing cataluminescence on nanosized $ZnWO_4$***. Sensors and Actuators B: Chemical. 2009; 137 (1). 83-87.

228. J. Tamaki, T. Fujii, K. Fujimori, N. Miura, and N. Yamazoe, ***Application of metal tungstate-carbonate composite to nitrogen oxides sensor operative at elevated temperature***. Sensors and Actuators B: Chemical. 1995; 25 (1–3). 396-399.

229. L. You, Y. Cao, Y.F. Sun, P. Sun, T. Zhang, Y. Du, and G.Y. Lu, ***Humidity sensing properties of nanocrystalline $ZnWO_4$ with porous structures***. Sensors and Actuators B: Chemical. 2012; 161 (1). 799-804.

230. K.D. Schierbaum, U. Weimar, W. Göpel, and R. Kowalkowski, ***Conductance, work function and catalytic activity of SnO_2-based gas sensors***. Sensors and Actuators B: Chemical. 1991; 3 (3). 205-214.

231. D.E. Williams and K.F.E. Pratt, ***Microstructure effects on the response of gas-sensitive resistors based on semiconducting oxides***. Sensors and Actuators B: Chemical. 2000; 70 (1–3). 214-221.

232. Y.D. Wang, Z.X. Chen, Y.F. Li, Z.L. Zhou, and X.H. Wu, ***Electrical and gas-sensing properties of WO_3 semiconductor material***. Solid-State Electronics. 2001; 45 (5). 639-644.

233. R.C. Singh, O. Singh, M.P. Singh, and P.S. Chandi, ***Synthesis of zinc oxide nanorods and nanoparticles by chemical route and their comparative study as ethanol sensors***. Sensors and Actuators B: Chemical. 2008; 135 (1). 352-357.

234. M.R. Waugh, ***Eng.D Thesis: The Synthesis, Characterisation and Application of Transparent Conducting Thin Films***. *Chapter 7 : Gas Sensing: pp. 236-237*, Dept. of Chemistry, University College London (UCL), London, United Kingdom. 2011.

235. L. Wang, Y. Kang, X. Liu, S. Zhang, W. Huang, and S. Wang, ***ZnO nanorod gas sensor for ethanol detection***. Sensors and Actuators B: Chemical. 2012; 162 (1). 237-243.

236. A.M. El-Sayed, F.M. Ismail, M.H. Khder, M.E.M. Hassouna, and S.M. Yakout, ***Effect Of CeO_2 Doping On The Structure, Electrical Conductivity And Ethanol Gas Sensing Properties Of Nanocrystalline ZnO Sensors***. International Journal on Smart Sensing and Intelligent Systems. 2012; 5 (3). 606-623.

237. S.D. Shinde, G.E. Patil, D.D. Kajale, D.V. Ahire, V.B. Gaikwad, and G.H. Jain, ***Synthesis of ZnO nanorods by hydrothermal method for gas sensing applications***. International Journal on Smart Sensing and Intelligent Systems. 2012; 5 (1). 57-70.

238. N. Barsan, M. Schweizer-Berberich, and W. Göpel†, ***Fundamental and practical aspects in the design of nanoscaled SnO_2 gas sensors: a status report***. Fresenius' Journal of Analytical Chemistry. 1999; 365 (4). 287-304.

239. J. Mizsei, ***How can sensitive and selective semiconductor gas sensors be made?*** Sensors and Actuators B: Chemical. 1995; 23 (2–3). 173-176.

240. M.R. Waugh, ***Eng.D Thesis: The Synthesis, Characterisation and Application of Transparent Conducting Thin Films***. *Chapter 7 : Gas Sensing: p. 247*, Dept. of Chemistry, University College London (UCL), London, United Kingdom. 2011.

241. W. Gao, Y. Ling, X. Liu, and J. Sun, ***Simple point contact WO_3 sensor for NO_2 sensing and relevant impedance analysis***. International Journal of Minerals, Metallurgy, and Materials. 2012; 19 (12). 1142-1148.

242. Y.-Q. Wu, M. Hu, and X.-Y. Wei, ***A study of transition from n- to p-type based on hexagonal WO_3 nanorods sensor***. Chinese Physics B. 2014; 23 (4). 040704-1 - 040704-7.

243. C. Zhang, M. Debliquy, A. Boudiba, H. Liao, and C. Coddet, ***Sensing properties of atmospheric plasma-sprayed WO_3 coating for sub-ppm NO_2 detection***. Sensors and Actuators B: Chemical. 2010; 144 (1). 280-288.

244. X. Li, R. Ramasamy, and P.K. Dutta, ***Study of the resistance behavior of anatase and rutile thick films towards carbon monoxide and oxygen at high temperatures and possibilities for sensing applications***. Sensors and Actuators B: Chemical. 2009; 143 (1). 308-315.

245. A. Gurlo, N. Barsan, A. Oprea, M. Sahm, T. Sahm, and U. Weimar, ***An n- to p-type conductivity transition induced by oxygen adsorption on $\alpha - Fe_2O_3$***. Applied Physics Letters. 2004; 85 (12). 2280-2282.

246. J.L. Solis, V. Golovanov, V. Lantto, and S. Leppävuori, ***A study of dual conductance response to carbon monoxide of CdS and α-$SnWO_4$ thin films***. Physica Scripta. 1994; T54. 248-251.

247. Y. Anno, T. Maekawa, J. Tamaki, Y. Asano, K. Hayashi, N. Miura, and N. Yamazoe, ***Zinc-oxide-based semiconductor sensors for detecting acetone and capronaldehyde in the vapour of consomme´soup***. Sensors and Actuators B: Chemical. 1995; 25 (1–3). 623-627.

248. K.-W. Kim, P.-S. Cho, S.-J. Kim, J.-H. Lee, C.-Y. Kang, J.-S. Kim, and S.-J. Yoon, ***The selective detection of C_2H_5OH using SnO_2–ZnO thin film gas sensors prepared by combinatorial solution deposition***. Sensors and Actuators B: Chemical. 2007; 123 (1). 318-324.

249. I.-S. Hwang, S.-J. Kim, J.-K. Choi, J. Choi, H. Ji, G.-T. Kim, G. Cao, and J.-H. Lee, ***Synthesis and gas sensing characteristics of highly crystalline ZnO–SnO_2 core–shell nanowires***. Sensors and Actuators B: Chemical. 2010; 148 (2). 595-600.

250. J.Y. Park, S.-W. Choi, and S.S. Kim, ***A model for the enhancement of gas sensing properties in SnO_2–ZnO core–shell nanofibres***. Journal of Physics D: Applied Physics. 2011; 44 (20). 205403~1 - 205403~4.

251. J.-A. Park, J. Moon, S.-J. Lee, S.H. Kim, H.Y. Chu, and T. Zyung, ***SnO_2–ZnO hybrid nanofibers-based highly sensitive nitrogen dioxides sensor***. Sensors and Actuators B: Chemical. 2010; 145 (1). 592-595.

252. S.-W. Choi, J.Y. Park, and S.S. Kim, ***Synthesis of SnO_2–ZnO core–shell nanofibers via a novel two-step process and their gas sensing properties***. Nanotechnology. 2009; 20 (46). 465603~1 - 465603~6.

253. X. Song, Z. Wang, Y. Liu, C. Wang, and L. Li, ***A highly sensitive ethanol sensor based on mesoporous ZnO–SnO_2 nanofibers***. Nanotechnology. 2009; 20 (7). 075501~1 - 075501~5.

254. L.C. Tien, D.P. Norton, B.P. Gila, S.J. Pearton, H.-T. Wang, B.S. Kang, and F. Ren, ***Detection of hydrogen with SnO_2-coated ZnO nanorods***. Applied Surface Science. 2007; 253 (10). 4748-4752.

255. G. Lu, J. Xu, J. Sun, Y. Yu, Y. Zhang, and F. Liu, ***UV-enhanced room temperature NO_2 sensor using ZnO nanorods modified with SnO_2 nanoparticles***. Sensors and Actuators B: Chemical. 2012; 162 (1). 82-88.

256. S. Wei, Y. Zhang, and M. Zhou, ***Toluene sensing properties of SnO_2–ZnO hollow nanofibers fabricated from single capillary electrospinning***. Solid State Communications. 2011; 151 (12). 895-899.

257. W. Tang, J. Wang, P. Yao, and X. Li, ***Hollow hierarchical SnO_2-ZnO composite nanofibers with heterostructure based on electrospinning method for detecting methanol***. Sensors and Actuators B: Chemical. 2014; 192. 543-549.

258. D.T. Thanh Le, D.D. Trung, N.D. Chinh, B.T. Thanh Binh, H.S. Hong, N. Van Duy, N.D. Hoa, and N. Van Hieu, ***Facile synthesis of SnO_2–ZnO core–shell nanowires for enhanced ethanol-sensing performance***. Current Applied Physics. 2013; 13 (8). 1637-1642.

259. L. Xu, R. Xing, J. Song, W. Xu, and H. Song, ***ZnO-SnO_2 nanotubes surface engineered by Ag nanoparticles: synthesis, characterization, and highly enhanced HCHO gas sensing properties***. Journal of Materials Chemistry C. 2013; 1 (11). 2174-2182.

260. J.A. Toledo-Antonio, R. Gutiérrez-Baez, P.J. Sebastian, and A. Vázquez, ***Thermal stability and structural deformation of rutile SnO_2 nanoparticles***. Journal of Solid State Chemistry. 2003; 174 (2). 241-248.

261. X. Liu, J. Zhang, X. Guo, S. Wu, and S. Wang, ***Enhanced sensor response of Ni-doped SnO_2 hollow spheres***. Sensors and Actuators B: Chemical. 2011; 152 (2). 162-167.

262. O. Lupan, L. Chow, G. Chai, A. Schulte, S. Park, and H. Heinrich, ***A rapid hydrothermal synthesis of rutile SnO_2 nanowires***. Materials Science and Engineering: B. 2009; 157 (1–3). 101-104.

263. S.H. Sun, G.W. Meng, G.X. Zhang, T. Gao, B.Y. Geng, L.D. Zhang, and J. Zuo, ***Raman scattering study of rutile SnO_2 nanobelts synthesized by thermal evaporation of Sn powders***. Chemical Physics Letters. 2003; 376 (1–2). 103-107.

264. ***Fiz Karlsruhe ICSD via the National Chemical Database Service***. 2014, Royal Society of Chemistry [date accessed: 17th June 2014]; Available from: http://cds.rsc.org.

265. A.A. Bolzan, C. Fong, B.J. Kennedy, and C.J. Howard, ***Structural Studies of Rutile-Type Metal Dioxides***. Acta Crystallographica Section B. 1997; 53 (3). 373-380.

266. S. Baruah and J. Dutta, ***Zinc stannate nanostructures: hydrothermal synthesis***. Science and Technology of Advanced Materials. 2011; 12 (1). 013004~1 - 013004~18.

267. S.A. Halawy and M.A. Mohamed, ***The effect of different ZnO precursors on the catalytic decomposition of ethanol***. Journal of Molecular Catalysis A: Chemical. 1995; 98 (2). L63-L68.

268. H. Cheong and M. Lee, ***Sensing characteristics and surface reaction mechanism of alcohol sensors based on doped SnO_2***. Journal of Ceramic Processing Research. 2006; 7 (3). 183 - 191.

269. M.R. Waugh, ***Eng.D Thesis: The Synthesis, Characterisation and Application of Transparent Conducting Thin Films***. *Chapter 7 : Gas Sensing: pp. 233 - 235*, Dept. of Chemistry, University College London (UCL), London, United Kingdom. 2011.

270. Y. Shimizu and M. Egashira, ***Basic Aspects and Challenges of Semiconductor Gas Sensors***. MRS Bulletin. 1999; 24 (06). 18-24.

271. S. Rani, S.C. Roy, M.C. Bhatnagar, and D. Kanjilal. ***p-type gas sensing behaviour in high energy ion beam irradiated un-doped SnO_2 thin films***. in *IEEE Sensors Conference Proceedings*. 2008. Lecce, Italy: IEEE. 886-889.

272. T. Kida, A. Nishiyama, Z. Hua, K. Suematsu, M. Yuasa, and K. Shimanoe, ***WO_3 Nanolamella Gas Sensor: Porosity Control Using SnO_2 Nanoparticles for Enhanced NO_2 Sensing***. Langmuir. 2014; 30 (9). 2571-2579.

273. H. Xu, X. Chen, J. Zhang, J. Wang, B. Cao, and D. Cui, ***NO_2 gas sensing with SnO_2–ZnO/PANI composite thick film fabricated from porous nanosolid***. Sensors and Actuators B: Chemical. 2013; 176. 166-173.

274. S.V. Ryabtsev, A.V. Shaposhnick, A.N. Lukin, and E.P. Domashevskaya, ***Application of semiconductor gas sensors for medical diagnostics***. Sensors and Actuators B: Chemical. 1999; 59 (1). 26-29.

275. J.-B. Yu, H.-G. Byun, M.-S. So, and J.-S. Huh, ***Analysis of diabetic patient's breath with conducting polymer sensor array***. Sensors and Actuators B: Chemical. 2005; 108 (1–2). 305-308.

276. Y. Xue-Jun, H. Tian-Sheng, X. Wei, C. Kun, and X. Xing, ***High Performance Micro CO Sensors Based on ZnO-SnO_2 Composite Nanofibers with Anti-Humidity Characteristics***. Chinese Physics Letters. 2012; 29 (12). 120702~1 - 120702~4.

277. A.M. Soleimanpour, A.H. Jayatissa, and G. Sumanasekera, ***Surface and gas sensing properties of nanocrystalline nickel oxide thin films***. Applied Surface Science. 2013; 276. 291-297.

278. M. Hübner, C.E. Simion, A. Tomescu-Stănoiu, S. Pokhrel, N. Bârsan, and U. Weimar, ***Influence of humidity on CO sensing with p-type CuO thick film gas sensors***. Sensors and Actuators B: Chemical. 2011; 153 (2). 347-353.

279. Y. Li, J. Liang, Z. Tao, and J. Chen, ***CuO particles and plates: Synthesis and gas-sensor application***. Materials Research Bulletin. 43 (8–9). 2380-2385.

280. H. Liu, X. Du, X. Xing, G. Wang, and S.Z. Qiao, ***Highly ordered mesoporous Cr_2O_3 materials with enhanced performance for gas sensors and lithium ion batteries***. Chemical Communications. 2012; 48 (6). 865-867.

281. Z. Wen, L. Zhu, W. Mei, L. Hu, Y. Li, L. Sun, H. Cai, and Z. Ye, ***Rhombus-shaped Co_3O_4 nanorod arrays for high-performance gas sensor***. Sensors and Actuators B: Chemical. 2013; 186. 172-179.

282. S. Pokhrel, C.E. Simion, V. Quemener, N. Bârsan, and U. Weimar, ***Investigations of conduction mechanism in Cr_2O_3 gas sensing thick films by ac impedance spectroscopy and work function changes measurements***. Sensors and Actuators B: Chemical. 2008; 133 (1). 78-83.

283. N. Barsan, C. Simion, T. Heine, S. Pokhrel, and U. Weimar, ***Modeling of sensing and transduction for p-type semiconducting metal oxide based gas sensors***. Journal of Electroceramics. 2010; 25 (1). 11-19.

284. A. Biaggi-Labiosa, F. Solá, M. Lebrón-Colón, L.J. Evans, J.C. Xu, G.W. Hunter, G.M. Berger, and J.M. González, ***A novel methane sensor based on porous SnO_2 nanorods: room temperature to high temperature detection***. Nanotechnology. 2012; 23 (45). 455501~1 - 455501~8.

285. K. Arshaka, K. Twomey, and D. Egan, ***A Ceramic Thick Film Humidity Sensor Based on MnZn Ferrite***. Sensors. 2002; 2 (2). 50-61.

286. K.-M. Kim, H.-M. Jeong, H.-R. Kim, K.-I. Choi, H.-J. Kim, and J.-H. Lee, ***Selective Detection of NO_2 Using Cr-Doped CuO Nanorods***. Sensors. 2012; 12 (6). 8013-8025.

287. N.G. Cho, H.-S. Woo, J.-H. Lee, and I.-D. Kim, ***Thin-walled NiO tubes functionalized with catalytic Pt for highly selective C_2H_5OH sensors using electrospun fibers as a sacrificial template***. Chemical Communications. 2011; 47 (40). 11300-11302.

288. H. Youl Bae and G. Man Choi, ***Electrical and reducing gas sensing properties of ZnO and ZnO–CuO thin films fabricated by spin coating method***. Sensors and Actuators B: Chemical. 1999; 55 (1). 47-54.

289. J.D. Choi and G.M. Choi, ***Electrical and CO gas sensing properties of layered ZnO–CuO sensor***. Sensors and Actuators B: Chemical. 2000; 69 (1–2). 120-126.

290. H.-S. Woo, C.W. Na, I.-D. Kim, and J.-H. Lee, ***Highly sensitive and selective trimethylamine sensor using one-dimensional ZnO–Cr_2O_3 hetero-nanostructures***. Nanotechnology. 2012; 23 (24). 245501~1 - 245501~10.

291. D.R. Patil, L.A. Patil, and P.P. Patil, ***Cr_2O_3-activated ZnO thick film resistors for ammonia gas sensing operable at room temperature***. Sensors and Actuators B: Chemical. 2007; 126 (2). 368-374.

292. D.N. Suryawanshi, D.R. Patil, and L.A. Patil, ***Fe_2O_3-activated Cr_2O_3 thick films as temperature dependent gas sensors***. Sensors and Actuators B: Chemical. 2008; 134 (2). 579-584.

293. L.Y. Jiang, S. Xin, X.L. Wu, H. Li, Y.G. Guo, and L.J. Wan, ***Non-sacrificial template synthesis of Cr_2O_3-C hierarchical core/shell nanospheres and their application as anode materials in lithium-ion batteries***. Journal of Materials Chemistry. 2010; 20 (35). 7565-7569.

294. A.H. Hill, A. Harrison, C. Dickinson, W. Zhou, and W. Kockelmann, ***Crystallographic and magnetic studies of mesoporous eskolaite***. Microporous and Mesoporous Materials. 2010; 130 (1–3). 280-286.

295. Z. Ma, Z. Xiao, J.A. van Bokhoven, and C. Liang, ***A non-alkoxide sol-gel route to highly active and selective Cu-Cr catalysts for glycerol conversion***. Journal of Materials Chemistry. 2010; 20 (4). 755-760.

296. S. Sōmiya, S. Hirano, and S. Kamiya, ***Phase relations of the Cr_2O_3-TiO_2 system***. Journal of Solid State Chemistry. 1978; 25 (3). 273-284.

297. W.H. Baur and A.A. Khan, ***Rutile-type compounds. IV. SiO_2, GeO_2 and a comparison with other rutile-type structures***. Acta Crystallographica Section B. 1971; 27 (11). 2133-2139.

298. J. Yan, G. Wu, N. Guan, L. Li, Z. Li, and X. Cao, ***Understanding the effect of surface/bulk defects on the photocatalytic activity of TiO_2: anatase versus rutile***. Physical Chemistry Chemical Physics. 2013; 15 (26). 10978-10988.

299. O.A. Afonja, ***Ph.D Thesis: Use of Zeolites to Effect Discrimination in Metal Oxide Semiconductor Gas Sensors***. *Chapter 4 : Characterization & Selection of Sensing Element : pp. 89 - 91*, Dept. of Chemistry, University College London (UCL), London, United Kingdom. 2012.

300. D. Segal, ***Chemical synthesis of ceramic materials***. Journal of Materials Chemistry. 1997; 7 (8). 1297-1305.

301. V. Swamy, A. Kuznetsov, L.S. Dubrovinsky, R.A. Caruso, D.G. Shchukin, and B.C. Muddle, ***Finite-size and pressure effects on the Raman spectrum of nanocrystalline anatase TiO_2*** Physical Review B. 2005; 71 (18). 184302.

302. J. Mougin, N. Rosman, G. Lucazeau, and A. Galerie, ***In situ Raman monitoring of chromium oxide scale growth for stress determination***. Journal of Raman Spectroscopy. 2001; 32 (9). 739-744.

303. R.J. Meier, ***Vibrational spectroscopy: a 'vanishing' discipline?*** Chemical Society Reviews. 2005; 34 (9). 743-752.

304. C. Aprile, L. Maretti, M. Alvaro, J.C. Scaiano, and H. Garcia, ***Long-lived (minutes) photoinduced charge separation in a structured periodic mesoporous titania containing 2,4,6-triphenylpyrylium as guest***. Dalton Transactions. 2008; (40). 5465-5470.

305. J. Zuo, C. Xu, B. Hou, C. Wang, Y. Xie, and Y. Qian, ***Raman Spectra of Nanophase Cr_2O_3***. Journal of Raman Spectroscopy. 1996; 27 (12). 921-923.

306. P.M. Sousa, A.J. Silvestre, and O. Conde, ***Cr_2O_3 thin films grown at room temperature by low pressure laser chemical vapour deposition***. Thin Solid Films. 2011; 519 (11). 3653-3657.

307. D. Gingasu, I. Mindru, D.C. Culita, L. Patron, J.M. Calderon-Moreno, S. Preda, O. Oprea, P. Osiceanu, and E. Morena Pineda, ***Investigation of nanocrystalline zinc chromite obtained by two soft chemical routes***. Materials Research Bulletin. 2014; 49. 151-159.

308. H. Sawada, ***Electron Density Study of Spinels: Zinc Chromium Oxide*** Materials Research Bulletin. 1997; 32 (7). 873-878.

309. Z. Wang, P. Lazor, S.K. Saxena, and G. Artioli, ***High-Pressure Raman Spectroscopic Study of Spinel ($ZnCr_2O_4$)***. Journal of Solid State Chemistry. 2002; 165 (1). 165-170.

310. C. Vargas-Hernández, O. Almanza, and J.F. Jurado, ***EPR, μ -Raman and Crystallographic properties of spinel type $ZnCr_2O_4$***. Journal of Physics: Conference Series. 2009; 167 (1). 012037~1 - 012037~4.

311. Z.V. Marinković Stanojević, N. Romčević, and B. Stojanović, ***Spectroscopic study of spinel $ZnCr_2O_4$ obtained from mechanically activated $ZnO–Cr_2O_3$ mixtures***. Journal of the European Ceramic Society. 2007; 27 (2–3). 903-907.

312. K.L. Purvis, G. Lu, J. Schwartz, and S.L. Bernasek, ***Surface Characterization and Modification of Indium Tin Oxide in Ultrahigh Vacuum***. Journal of the American Chemical Society. 2000; 122 (8). 1808-1809.

313. J.B. Miller, S.L. Bernasek, and J. Schwartz, ***Surface Hydroxylation of Single Crystal Aluminum(110) in Ultrahigh Vacuum***. Langmuir. 1994; 10 (8). 2629-2635.

314. J.F. McAleer, P.T. Moseley, J.O.W. Norris, D.E. Williams, and B.C. Tofield, ***Tin dioxide gas sensors. Part 2.-The role of surface additives***. Journal of the Chemical Society, Faraday Transactions 1: Physical Chemistry in Condensed Phases. 1988; 84 (2). 441-457.

315. E. Traversa, ***Ceramic sensors for humidity detection: the state-of-the-art and future developments***. Sensors and Actuators B: Chemical. 1995; 23 (2–3). 135-156.

316. E. McCafferty and A.C. Zettlemoyer, ***Adsorption of water vapour on α-Fe_2O_3***. Discussions of the Faraday Society. 1971; 52. 239-254.

317. X. Niu, W. Du, and W. Du, ***Preparation and gas sensing properties of ZnM_2O_4 (M = Fe, Co, Cr)***. Sensors and Actuators B: Chemical. 2004; 99 (2–3). 405-409.

318. C.L. Honeybourne and R.K. Rasheed, ***Nitrogen dioxide and volatile sulfide sensing properties of copper, zinc and nickel chromite***. Journal of Materials Chemistry. 1996; 6 (3). 277-283.

319. M. Bayhan, T. Hashemi, and A.W. Brinkman, ***Sintering and humidity-sensitive behaviour of the $ZnCr_2O_4$–$K_{22}CrO_4$ ceramic system***. Journal of Materials Science. 1997; 32 (24). 6619-6623.

320. G.M. Choi and S.T. Jun, ***Modelling of Electrical Conductivity of n-p Ceramic Composite Using Equivalent Circuits***. MRS Online Proceedings Library - 1995 MRS Fall Meeting - Symposium T - Electrically based Microstructural Characterization 1995; Volume 411. 301-306.

321. S.-T. Jun and G.M. Choi, ***Composition Dependence of the Electrical Conductivity of ZnO(n)–CuO(p) Ceramic Composite***. Journal of the American Ceramic Society. 1998; 81 (3). 695-699.

322. T. Hashishin and J. Tamaki, ***Conductivity-Type Sensor Based on CNT-WO_3 Composite for NO_2 Detection***. Journal of Nanomaterials. 2008; 2008. 352854~1 - 352854~4.

323. Y. Zeng, T. Zhang, M. Yuan, M. Kang, G. Lu, R. Wang, H. Fan, Y. He, and H. Yang, ***Growth and selective acetone detection based on ZnO nanorod arrays***. Sensors and Actuators B: Chemical. 2009; 143 (1). 93-98.

324. X. Wang, W. Wang, and Y.-L. Liu, ***Enhanced acetone sensing performance of Au nanoparticles functionalized flower-like ZnO***. Sensors and Actuators B: Chemical. 2012; 168. 39-45.

325. D.C. Pugh, E.J. Newton, A.J.T. Naik, S.M.V. Hailes, and I.P. Parkin, ***The gas sensing properties of zeolite modified zinc oxide***. Journal of Materials Chemistry A. 2014; 2 (13). 4758-4764.

326. N. Yamazoe, ***New approaches for improving semiconductor gas sensors***. Sensors and Actuators B: Chemical. 1991; 5 (1–4). 7-19.

327. A. Kolmakov and M. Moskovits, ***Chemical Sensing and Catalysis by One-Dimensional Metal-Oxide Nanostructures***. Annual Review of Materials Research. 2004; 34 (1). 151-180.

328. N. Yamazoe, ***Toward innovations of gas sensor technology***. Sensors and Actuators B: Chemical. 2005; 108 (1–2). 2-14.

329. K.J. Choi and H.W. Jang, ***One-Dimensional Oxide Nanostructures as Gas-Sensing Materials: Review and Issues***. Sensors. 2010; 10 (4). 4083-4099.

330. Z.L. Wang, ***Nanostructures of zinc oxide***. Materials Today. 2004; 7 (6). 26-33.

331. M. Chen, C.Y. Ma, T. Mahmud, J.A. Darr, and X.Z. Wang, ***Modelling and simulation of continuous hydrothermal flow synthesis process for nano-materials manufacture***. The Journal of Supercritical Fluids. 2011; 59. 131-139.

332. S. Ohara, T. Mousavand, T. Sasaki, M. Umetsu, T. Naka, and T. Adschiri, ***Continuous production of fine zinc oxide nanorods by hydrothermal synthesis in supercritical water***. Journal of Materials Science. 2008; 43 (7). 2393-2396.

333. S. Turner, S.M.F. Tavernier, G. Huyberechts, E. Biermans, S. Bals, K.J. Batenburg, and G. Tendeloo, ***Assisted spray pyrolysis production and characterisation of ZnO nanoparticles with narrow size distribution***. Journal of Nanoparticle Research. 2010; 12 (2). 615-622.

334. N. Boukos, C. Chandrinou, K. Giannakopoulos, G. Pistolis, and A. Travlos, ***Growth of ZnO nanorods by a simple chemical method***. Applied Physics A. 2007; 88 (1). 35-39.

335. G. Mohan Kumar, P. Ilanchezhiyan, J. Kawakita, M. Subramanian, and R. Jayavel, ***Magnetic and optical property studies on controlled low-temperature fabricated one-dimensional Cr doped ZnO nanorods***. CrystEngComm. 2010; 12 (6). 1887-1892.

336. T. Ngo-Duc, K. Singh, M. Meyyappan, and M. M. Oye, ***Vertical ZnO nanowire growth on metal substrates***. Nanotechnology. 2012; 23 (19). 194015~1 - 194015~5.

337. S.J.S. Qazi, A.R. Rennie, J.K. Cockcroft, and M. Vickers, ***Use of wide-angle X-ray diffraction to measure shape and size of dispersed colloidal particles***. Journal of Colloid and Interface Science. 2009; 338 (1). 105-110.

338. P. Rai, H.-M. Song, Y.-S. Kim, M.-K. Song, P.-R. Oh, J.-M. Yoon, and Y.-T. Yu, ***Microwave assisted hydrothermal synthesis of single crystalline ZnO nanorods for gas sensor application***. Materials Letters. 2012; 68. 90-93.

339. Q. Wan, Q.H. Li, Y.J. Chen, T.H. Wang, X.L. He, J.P. Li, and C.L. Lin, ***Fabrication and ethanol sensing characteristics of ZnO nanowire gas sensors***. Applied Physics Letters. 2004; 84 (18). 3654-3656.

340. J. Zhang, X. Li, J. White, and P.K. Dutta, ***Effects of Surface and Morphological Properties of Zeolite on Impedance Spectroscopy-Based Sensing Performance***. Sensors. 2012; 12 (10). 13284-13294.

341. S.M. Kanan, A. Waghe, B.L. Jensen, and C.P. Tripp, ***Dual WO_3 based sensors to selectively detect DMMP in the presence of alcohols***. Talanta. 2007; 72 (2). 401-407.

342. S. Öztürk, N. Kılınç, and Z.Z. Öztürk, ***Fabrication of ZnO nanorods for NO_2 sensor applications: Effect of dimensions and electrode position***. Journal of Alloys and Compounds. 2013; 581. 196-201.

343. J. Zhang, S. Wang, Y. Wang, M. Xu, H. Xia, S. Zhang, W. Huang, X. Guo, and S. Wu, ***ZnO hollow spheres: Preparation, characterization, and gas sensing properties***. Sensors and Actuators B: Chemical. 2009; 139 (2). 411-417.

344. K.-I. Choi, H.-R. Kim, K.-M. Kim, D. Liu, G. Cao, and J.-H. Lee, ***C_2H_5OH sensing characteristics of various Co_3O_4 nanostructures prepared by solvothermal reaction***. Sensors and Actuators B: Chemical. 2010; 146 (1). 183-189.

345. J.-H. Lee, ***Gas sensors using hierarchical and hollow oxide nanostructures: Overview***. Sensors and Actuators B: Chemical. 2009; 140 (1). 319-336.

346. J.H. Jun, J. Yun, K. Cho, I.-S. Hwang, J.-H. Lee, and S. Kim, ***Necked ZnO nanoparticle-based NO_2 sensors with high and fast response***. Sensors and Actuators B: Chemical. 2009; 140 (2). 412-417.

347. S. Ahlers, G. Müller, and T. Doll, ***A rate equation approach to the gas sensitivity of thin film metal oxide materials***. Sensors and Actuators B: Chemical. 2005; 107 (2). 587-599.

348. ***Air Quality Guidelines for Europe - Second Edition, Chapter 7.1 - Nitrogen dioxide***. 2000, World Health Organisation Regional Office for Europe, Copenhagen, Denmark [date accessed: 1st February 2015]; Available from: http://www.euro.who.int/__data/assets/pdf_file/0017/123083/AQG2ndEd_7_1nitrogendioxide.pdf.

349. ***Air Pollution***. [date accessed: 1st February 2015]; Available from: http://www.air-quality.org.uk/introduction.php.

350. ***Air Quality Guidelines for Europe - Second Edition, Chapter 5.14 - Toluene***. 2000, World Health Organisation Regional Office for Europe, Copenhagen, Denmark [date accessed: 1st February 2015]; Available from: http://www.euro.who.int/__data/assets/pdf_file/0020/123068/AQG2ndEd_5_14Toluene.PDF.

351. S.M. Correa, G. Arbilla, M.R.C. Marques, K.M.P.G. Oliveira, and W. Kockelmann, ***The impact of BTEX emssions from gas stations into the atmosphere***. Atmospheric Pollution Research. 2012; 3 (2). 163-169.

352. U.S. E.P.A. ***Technlogy Transfer Network - Air Toxics Web Site - Toluene***. 18th October 2013, Environmental Protection Agency [date accessed: 1st February 2015]; Available from: http://www.epa.gov/airtoxics/hlthef/toluene.html#ref1.

Appendix

Preceding repeat gas response data

Presented here are examples of preceding repeat gas sensing tests (to the final gas sensing tests, data of which has been presented in the main body of the thesis and reproduced here in the appendix again) of the various sensor devices studied in this thesis.

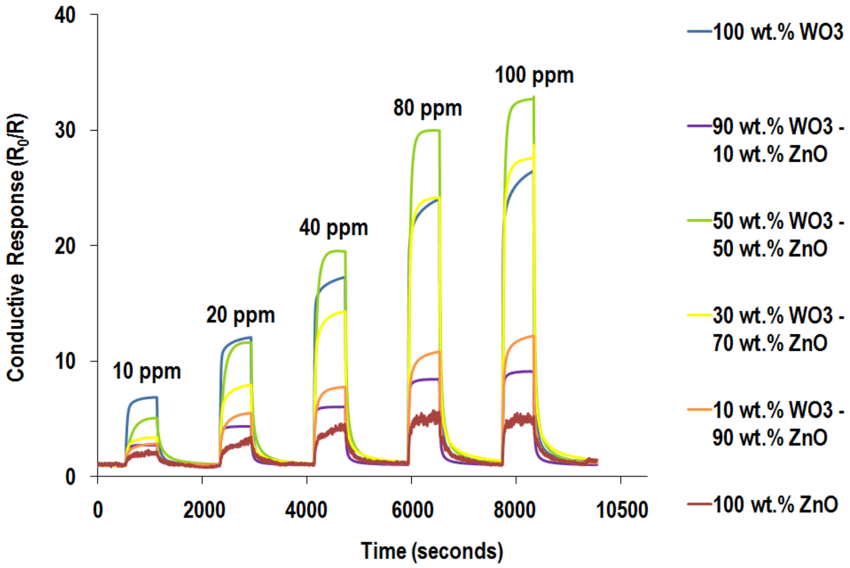

Figure A - 1. Repeat test of WO_3-ZnO composite system when exposed to increasing concentrations of ethanol at an operating temperature of 350 ºC as presented in the main body of thesis in Figure 3–10.

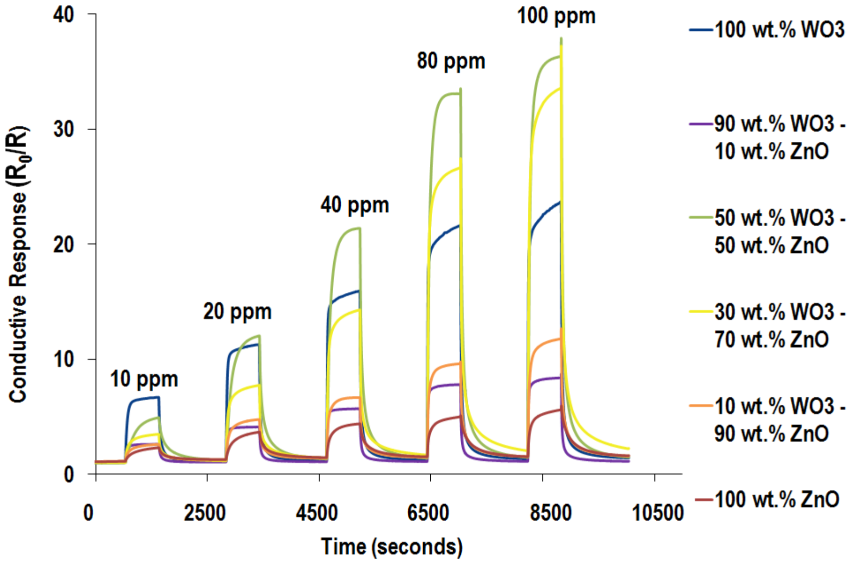

Figure A - 2. Figure 3–10 reproduced from main body of thesis.

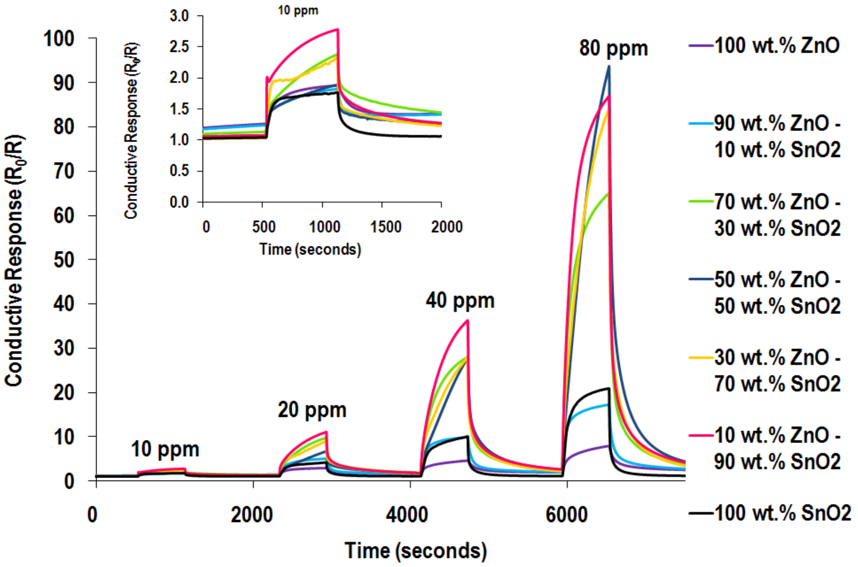

Figure A - 3. Repeat test of SnO$_2$-ZnO composite system when exposed to increasing concentrations of ethanol at an operating temperature of 300 ºC as presented in the main body of thesis in Figure 4–7.

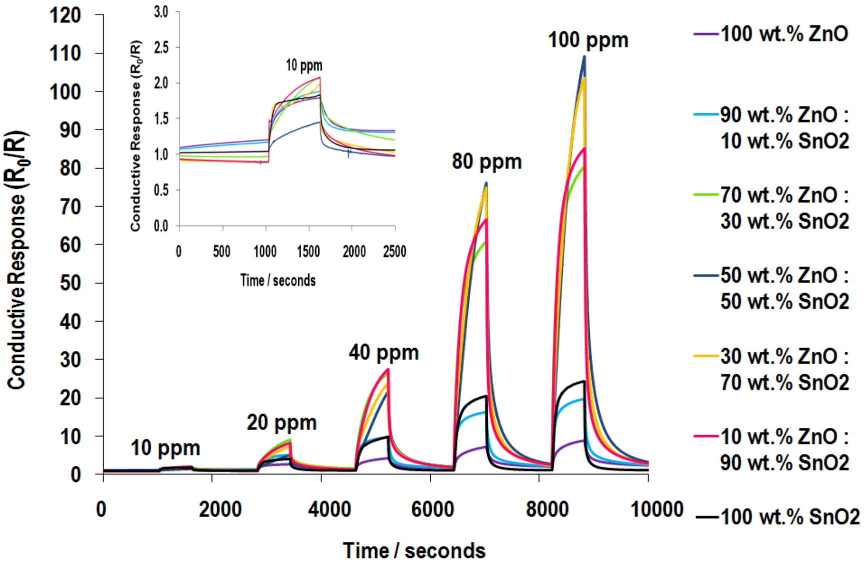

Figure A - 4. Figure 4–7 reproduced from main body of thesis

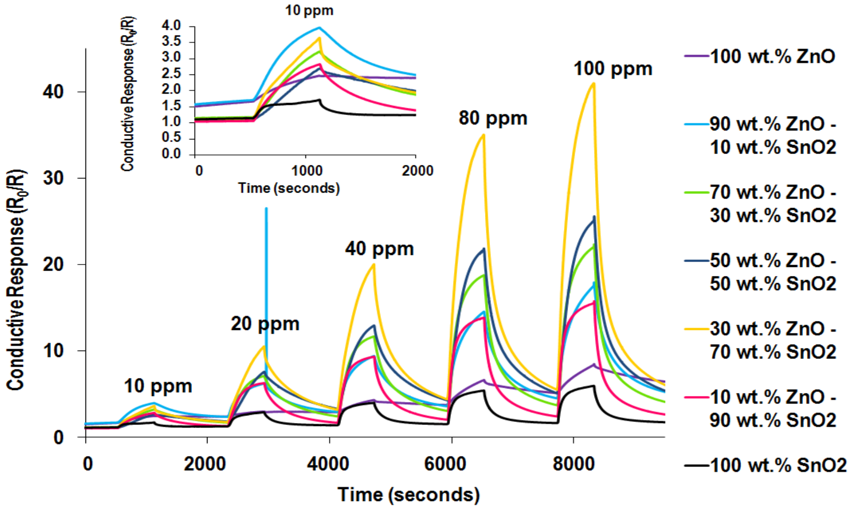

Figure A - 5. Repeat test of SnO_2-ZnO composite system when exposed to increasing concentrations of ethanol at an operating temperature of 200 ºC as presented in the main body of thesis in Figure 4–10.

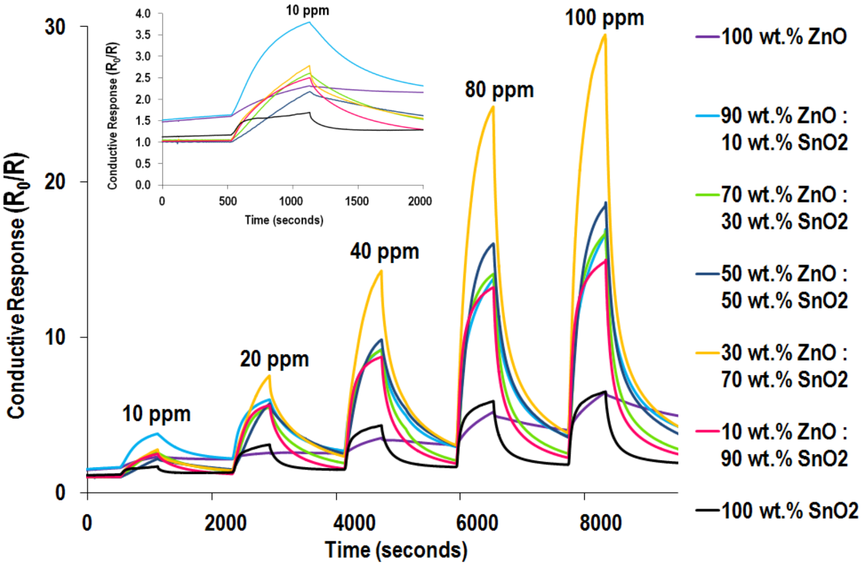

Figure A - 6. Figure 4–10 reproduced from main body of thesis.

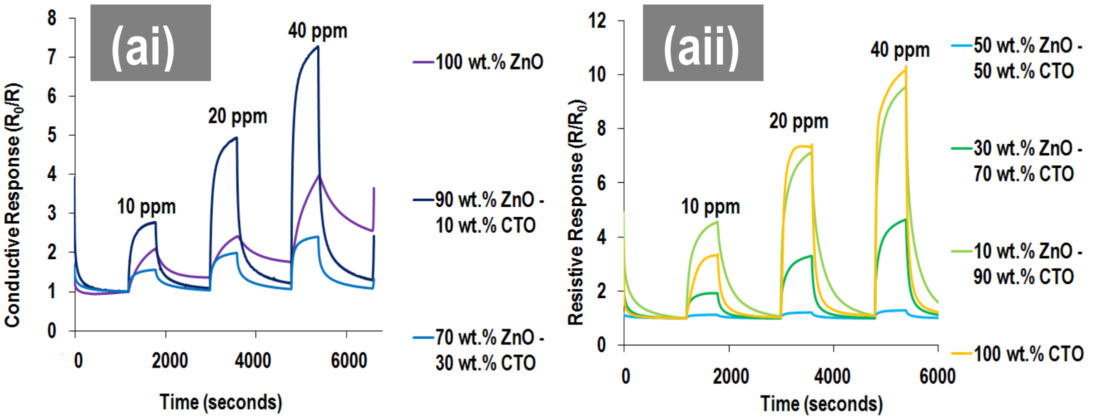

Figure A - 7. Repeat test of CTO-ZnO composite system when exposed to increasing concentrations of ethanol at 250 °C in (ai) and (aii) as presented in the main body of thesis in Figure 5–19 (c) and (d).

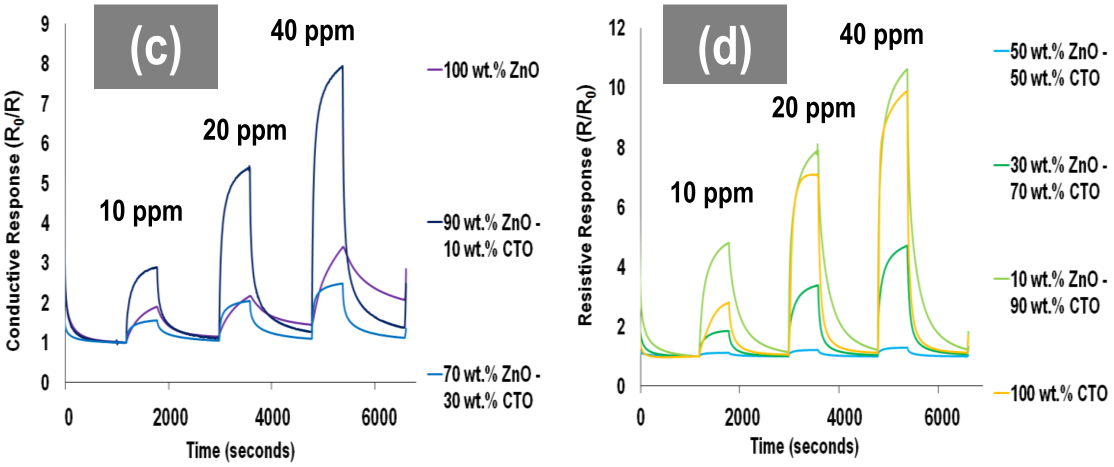

Figure A - 8. Figure 5–19 (c) and (d) reproduced from main body of thesis.

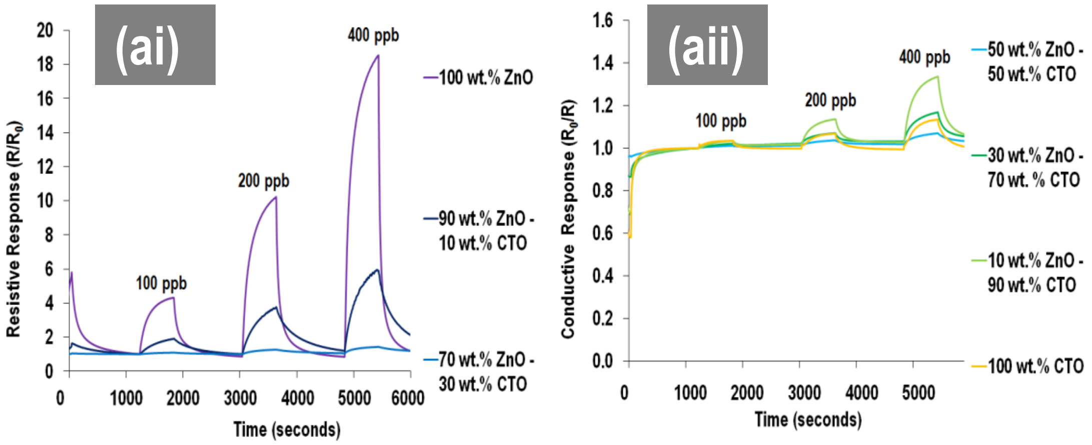

Figure A - 9. Repeat test of CTO-ZnO composite system when exposed to increasing concentrations of NO_2 at 300 ºC in (bi) and (bii) as presented in the main body of thesis in Figure 5–22 (a) and (b).

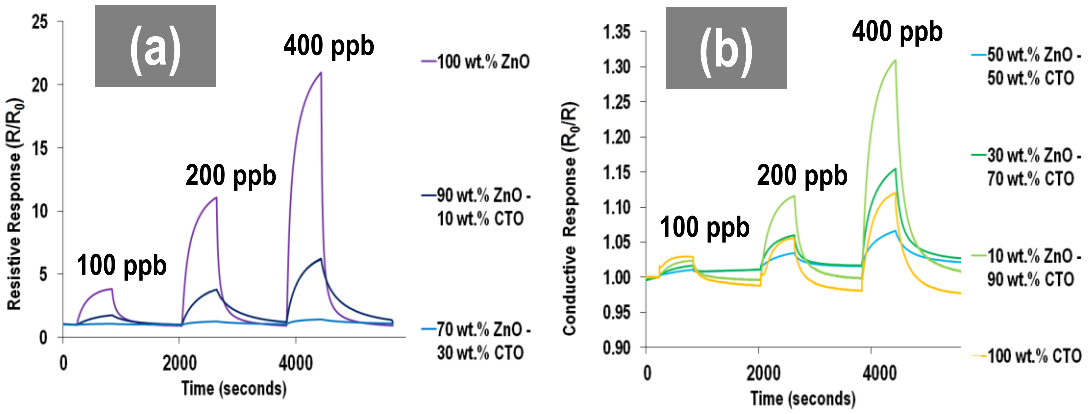

Figure A - 10. Figure 5–22 (a) and (b) reproduced from main body of thesis.

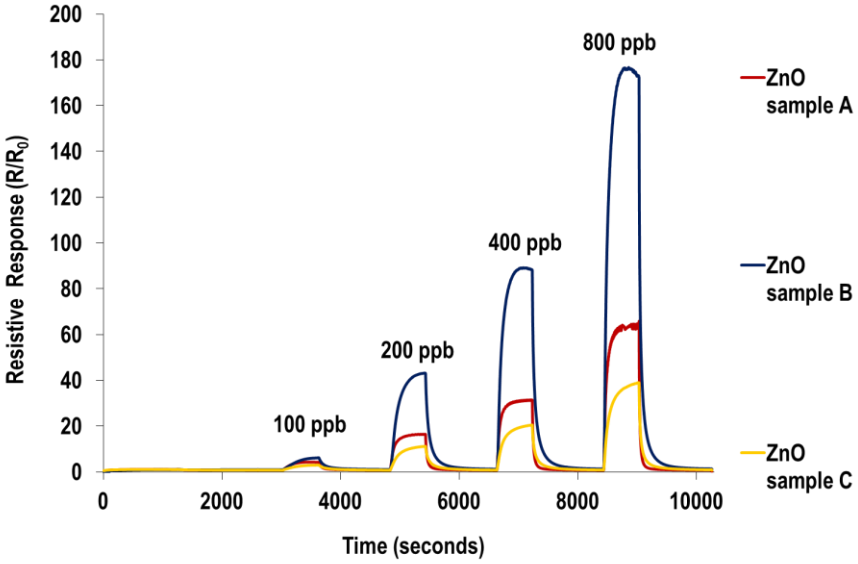

Figure A - 11. Repeat test of CHFS ZnO system against increasing concentrations of NO_2 at 300 °C as presented in the main body of thesis in Figure 6–11.

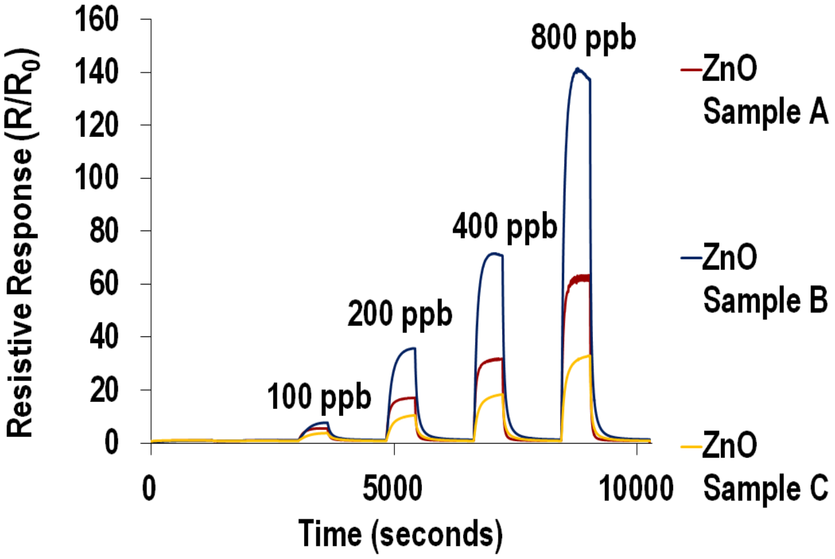

Figure A - 12. Figure 6–11 reproduced from main body of thesis

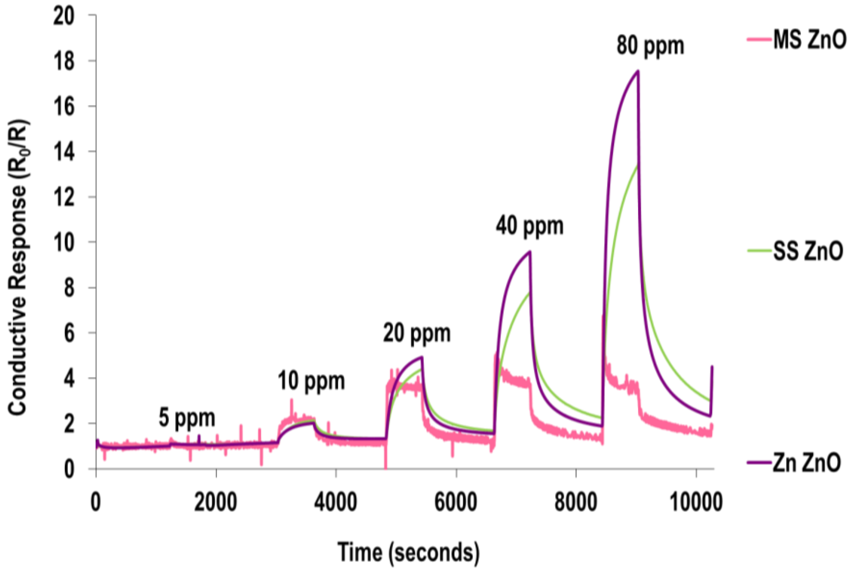

Figure A - 13. Repeat test of MS ZnO, SS ZnO and Zn ZnO sensor devices against increasing concentrations of ethanol at an operating temperature of 300 °C. The ZnO ceramics were prepared by three different synthesis methods: Molten-Salt synthesis (MS-ZnO), Solid-State metathesis (SS-ZnO) and Hydrothermal synthesis (Zn-ZnO) as presented in the main body of thesis in Figure 6–21.

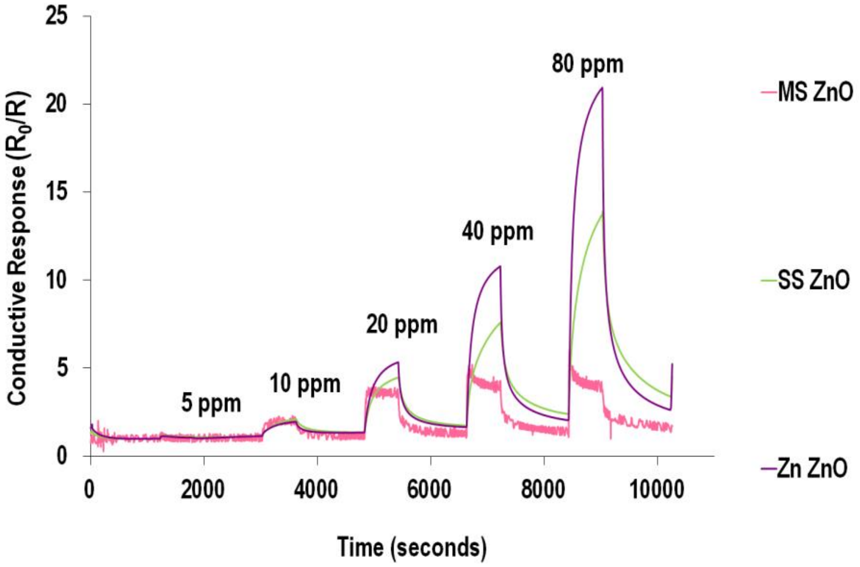

Figure A - 14. Figure 6–21 reproduced from main body of thesis.

Baseline resistances

The following tables present the ranges within which the baseline resistances for each sensor device investigated in this thesis, at the corresponding operating temperature, lie.

System 1: WO_3 – ZnO composites

Table A - 1. Baseline resistance ranges in ohms for all sensor devices studied within WO_3-ZnO composite system at operating temperatures of 500, 450, 400, 350 and 300 ºC.

Device	500 ºC (ohms)	450 ºC (ohms)	400 ºC (ohms)	350 ºC (ohms)	300 ºC (ohms)
100 wt.% WO_3	1.4 – 1.7 x 10^{4}	1.9 – 2.1 x 10^{4}	2.8 – 3.4 x 10^{4}	0.7 – 1.4 x 10^{5}	0.6 – 2.4 x 10^{5}
90 wt.% WO_3 – 10 wt.% ZnO	1.5 – 5.5 x 10^{6}	1.7 – 5.8 x 10^{6}	2.5 – 7.2 x 10^{6}	0.5 – 4.6 x 10^{7}	0.1 – 3.7 x 10^{7}
50 wt.% WO_3 – 50 wt.% ZnO	2.9 – 5.2 x 10^{5}	5.8 – 10.5 x 10^{5}	1.6 – 1.9 x 10^{6}	0.4 – 1.8 x 10^{7}	0.5 – 12.0 x 10^{6}
30 wt.% WO_3 – 70 wt.% ZnO	0.4 – 1.8 x 10^{5}	0.6 – 2.7 x 10^{5}	1.0 – 4.6 x 10^{5}	1.1 – 1.7 x 10^{6}	0.4 – 4.8 x 10^{6}
10 wt.% WO_3 – 90 wt.% ZnO	1.1 – 7.5 x 10^{4}	1.9 – 11.6 x 10^{4}	0.3 – 2.2 x 10^{5}	2.2 – 8.5 x 10^{5}	0.2 – 3.5 x 10^{6}
100 wt.% ZnO	2.6 – 2.9 x 10^{4}	5.4 – 8.1 x 10^{4}	8.6 – 24.8 x 10^{4}	7.0 – 10.1 x 10^{5}	0.5 – 3.8 x 10^{6}

System 2: SnO_2 – ZnO composites

Table A - 2. Baseline resistance ranges in ohms for all sensor devices studied within SnO_2-ZnO composite system at operating temperatures of 500, 450, 400, 350 and 300 °C.

Device	500 °C (ohms)	450 °C (ohms)	400 °C (ohms)	350 °C (ohms)	300 °C (ohms)
100 wt.% SnO_2	1.7 - 2.7 x 10^5	5.0 – 7.0 x 10^5	1.3 – 1.6 x 10^6	2.2 – 2.5 x 10^6	3.5 – 3.8 x 10^6
90 wt.% SnO_2 – 10 wt.% ZnO	1.0 – 1.8 x 10^6	2.2 – 3.5 x 10^6	5.2 – 7.3 x 10^6	0.9 – 1.4 x 10^7	1.2 – 1.7 x 10^7
70 wt.% SnO_2 – 30 wt.% ZnO	1.3 – 2.7 x 10^6	2.9 – 4.9 x 10^6	6.6 – 9.9 x 10^6	1.2 – 1.6 x 10^7	1.5 – 2.0 x 10^7
50 wt.% SnO_2 – 50 wt.% ZnO	2.5 – 4.5 x 10^6	6.4 – 9.5 x 10^6	1.3 – 1.8 x 10^7	2.3 – 2.5 x 10^7	1.1 – 2.8 x 10^7
30 wt.% SnO_2 – 70 wt.% ZnO	3.9 – 9.6 x 10^5	0.8 – 1.7 x 10^6	1.3 – 2.5 x 10^6	2.5 – 5.5 x 10^6	2.1 – 3.0 x 10^6
10 wt.% SnO_2 – 90 wt.% ZnO	0.8 – 2.7 x 10^5	1.0 – 2.5 x 10^5	0.8 – 1.8 x 10^5	1.5 – 1.8 x 10^5	1.1 – 4.4 x 10^5
100 wt.% ZnO	0.3 – 1.2 x 10^5	0.1 - 27 x 10^6	0.04 - 26 x 10^6	0.06 – 70 x 10^6	0.03 - 27 x 10^7

System 3: CTO-ZnO composites

Table A - 3. Baseline resistance ranges in ohms for all sensor devices studied within CTO-ZnO composite system at operating temperatures of 500, 450, 400 and 350 °C.

Device	500 °C (ohms)	400 °C (ohms)	350 °C (ohms)	300 °C (ohms)
100 wt.% CTO	3.6 – 3.7 x 10^4	8.5 – 10.1 x 10^4	1.8 – 2.2 x 10^5	4.7 – 5.3 x 10^5
90 wt.% CTO – 10 wt.% ZnO	2.7 – 2.9 x 10^4	8.4 – 11.3 x 10^4	1.9 – 2.6 x 10^5	6.1 – 9.0 x 10^5
70 wt.% CTO – 30 wt.% ZnO	8.0 – 8.3 x 10^3	2.1 – 3.2 x 10^4	4.2 – 6.6 x 10^4	1.1 – 1.9 x 10^5
50 wt.% CTO – 50 wt.% ZnO	4.4 – 5.2 x 10^3	0.9 – 1.0 x 10^4	1.7 – 1.9 x 10^4	4.2 - 4.4 x 10^4
30 wt.% CTO – 70 wt.% ZnO	1.2 – 1.4 x 10^5	3.3 – 4.2 x 10^5	6.9 – 8.4 x 10^5	1.3 – 2.0 x 10^6
10 wt.% CTO – 90 wt.% ZnO	1.7 – 1.8 x 10^6	4.2 – 6.7 x 10^6	8.7 – 14.1 x 10^6	1.4 – 3.2 x 10^7
100 wt.% ZnO	9.4 – 16.0 x 10^5	2.2 – 10.6 x 10^5	0.4 – 2.7 x 10^6	0.6 – 5.5 x 10^6

System 4: Emerging ZnO materials

Table A - 4. Baseline resistance ranges in ohms for all sensor devices studied within nanostructured ZnO material systems at operating temperatures of 500, 450, 400, 350 and 300 ºC.

Device	500 ºC (ohms)	450 ºC (ohms)	400 ºC (ohms)	350 ºC (ohms)	300 ºC (ohms)
CHFS ZnO A	0.4 – 1.3 x 10^6	0.4 – 1.5 x 10^6	0.7 – 1.5 x 10^6	1.5 – 1.8 x 10^6	2.0 – 2.6 x 10^6
CHFS ZnO B	1.6 – 1.9 x 10^5	0.1 – 2.1 x 10^6	1.3 – 4.5 x 10^5	2.3 – 4.6 x 10^5	4.5 – 7.1 x 10^5
CHFS ZnO C	0.6 – 3.1 x 10^5	0.7 – 2.1 x 10^5	1.7 – 1.8 x 10^5	3.8 – 4.9 x 10^5	7.2 – 11.0 x 10^5
SS ZnO	0.7 – 3.4 x 10^6	0.7- 2.3 x 10^6	1.3 – 2.1 x 10^6	4.0 – 6.5 x 10^6	1.4 – 2.3 x 10^7
Zn ZnO	0.5 – 4.1 x 10^5	0.6 – 1.5 x 10^5	1.3 – 2.0 x 10^5	2.9 – 5.8 x 10^5	0.8 – 1.2 x 10^6